Neutron scattering studies of two-dimensional antiferromagnetic spin fluctuations in insulating and superconducting S = ½ systems

Christensen, Niels Bech

Publication date:
2005

Document Version
Publisher's PDF, also known as Version of record

RISØ

Risø-PhD-7(EN)

Neutron scattering studies of two-dimensional antiferromagnetic spin fluctuations in insulating and superconducting S = 1/2 systems

Niels Bech Christensen

Risø National Laboratory
Roskilde
Denmark
January 2005

Neutron scattering studies of two-dimensional antiferromagnetic spin fluctuations in insulating and superconducting $S = 1/2$ systems

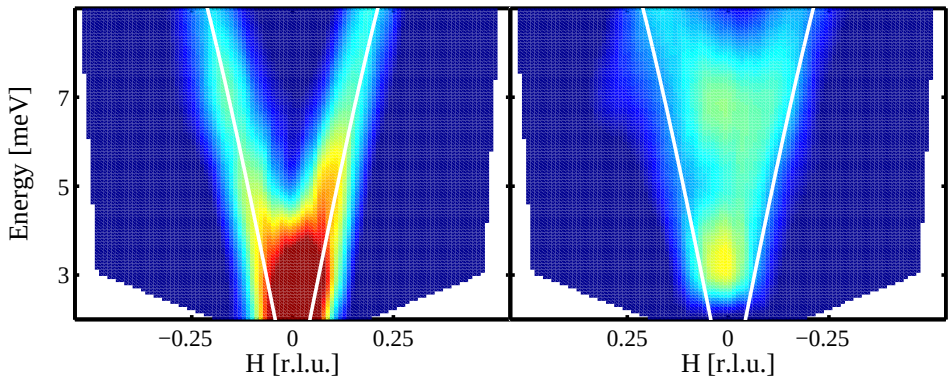

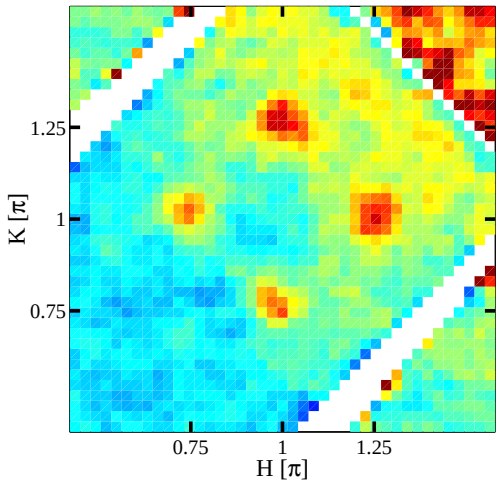

Niels Bech Christensen

Materials Research Department
Risø National Laboratory
4000 Roskilde, Denmark

Abstract:

In this thesis, neutron scattering techniques are used to study the magnetic excitations in two materials which derive from two-dimensional square lattices of $S = 1/2$ spins. Within these planes, nearest neighbor spins are known to interact predominantly via antiferromagnetic Heisenberg exchange interactions. By contrast, interactions between spins in neighboring planes are negligible small for most purposes. In particular, the magnetic fluctuation spectra of these systems are two-dimensional, and this makes them well suited for time-of-flight neutron scattering experiments designed to shed light on important outstanding questions concerning − at the most fundamental level − the nature of the respective ground states.

- $Cu(DCOO)_2 \cdot 4D_2O$ is a two-dimensional $S = 1/2$ Heisenberg antiferromagnet on a square lattice. Theoretically, the ground state has long range order at $T = 0$ K, but quantum fluctuations are strong and lead to a large reduction in the ordered sublattice moment relative to classical expectations. This thesis reports on experiments designed to clarify the fate of the disordered part of the moment.

  Combining time-of-flight and polarized triple axis neutron scattering it is shown that despite the strongly quantum fluctuating nature of the system, the low-energy excitations are excellently described by linear spin wave theory. In particular, a continuum of longitudinally polarized multimagnon excitations existing above a dispersion cone of transversely polarized single-magnon excitations is identified. Such a multimagnon continuum has never before been observed in the square lattice $S = 1/2$ Heisenberg model. Its experimental verification proves that a substantial fraction of the disordered moment is associated with excitations involving more than one magnon. At higher energies, the intensities of the single-magnon excitations have been discovered to be characterized by a non-uniform renormalization away from the simplest model predictions. The momentum dependence of this intensity renormalization tracks that of a non-uniform renormalization of the single-magnon energies. Using polarization analysis, it is shown that the high-energy spin fluctuation spectrum consists of renormalized, transversely polarized single-magnon excitations and weak but finite continua of longitudinally and transversely polarized multimagnon excitations. The intensities and characteristic energy scales of all components of the high-energy excitation spectrum agree with state-of-the-art Quantum Monte Carlo computations to very high degree of accuracy.

- The $La_{2-x}Sr_xCuO_4$ crystals studied in the second part of this thesis are members of the class of materials known as high-temperature superconductors. In these systems, superconductivity is achieved by doping holes into the two-dimensional, square lattice $S = 1/2$ Heisenberg antiferromagnet La_2CuO_4. In the process, static antiferromagnetism is destroyed but strong, two-dimensional antiferromagnetic fluctuations persist into the superconducting phase. The cause of superconductivity is unknown, but it is a commonly held belief that the antiferromagnetic fluctuations play an important role.

  The central contribution made by this thesis is the identification of a dispersion in the excitation spectrum of the dominant incommensurate magnetic fluctuations. This discovery points to the existence of a common spin fluctuation spectrum in all superconducting cuprates. It is further shown that the existence of dispersing excitations does not require phase coherent superconductivity and that the dispersion persist to 100 K in underdoped $La_{2-x}Sr_xCuO_4$. Studies of the temperature dependence of the intensities associated with the dispersive magnetic fluctuations in optimally doped $La_{2-x}Sr_xCuO_4$ have in addition revealed a spectral weight shift which displays qualitative and quantitative similarities to the widely studied resonance mode in other families of high-temperature superconductors, with the important difference that it occurs at incommensurate rather than commensurate wavevectors. These discoveries put strong constraints on theories for the magnetic excitations in high-temperature superconductors.

Preface

This thesis is submitted in partial fulfillment of the requirements for obtaining the Ph.D. degree in physics from the Niels Bohr Institute at the University of Copenhagen, Denmark.

The work reported was carried out under the supervision of Jens Jensen from the University of Copenhagen and Desmond F. McMorrow from Risø National Laboratory and University College London.

Niels Bech Christensen

Copenhagen, November 2004

Contents

1 Introduction

On the following pages I present the results of neutron scattering experiments designed to study the magnetic excitations of two materials: the band insulator $Cu(DCOO)_2{\cdot}4D_2O$ (CFTD), and the high-temperature superconductor $La_{2-x}Sr_xCuO_4$ (LSCO). While these systems are very different in their electrical properties, their magnetic properties display strong similarities. In both systems, neighboring $S = 1/2$ spins in a square lattice geometry are coupled by antiferromagnetic Heisenberg exchange interactions, yielding a preference for antiparallel alignment. At the same time, spins in different planes are almost completely oblivious of each others existence, implying that the magnetic properties have a strongly two-dimensional character. This low dimensionality combines with antiferromagnetism and the extreme quantum nature of $S = 1/2$ spins to make such systems strongly non-classical and highly fluctuating.

In the case of CFTD, the problem one is confronted with is the following. For two-dimensional, $S = 1/2$ Heisenberg antiferromagnets on a square lattice, it is known theoretically that long-range magnetic order can be established only at $T = 0$ K, but even here − in the absence of thermal fluctuations − quantum fluctuations are very strong and prevent a significant fraction of the spin quantum number S from participating in static antiferromagnetic order. Furthermore, the nature of the quantum mechanical ground state is unknown. In the first part of this thesis, state-of-the-art neutron scattering techniques are employed to investigate the fate of the part of moment which remains disordered at $T = 0$ K. This is done in the interest of providing fresh insight about the ground state.

In LSCO, superconductivity is obtained by chemically doping holes into La_2CuO_4 which − like CFTD − is an example of a two-dimensional $S = 1/2$ Heisenberg antiferromagnet on a square lattice. The introduction of holes rapidly destroys the antiferromagnetic order of La_2CuO_4 and causes LSCO to be even more quantum fluctuating than LSCO. Miraculously, the hole-doping process also transforms the insulator La_2CuO_4 into a high-temperature superconductor, the ground state of which is a matter of fierce debate. One commonly held view is that the antiferromagnetic spin fluctuations left behind after the destruction of static antiferromagnetism play a key role in establishing superconducting correlations, but exactly how this happens has been a mystery for many years. In the second part of this thesis, neutron scattering is used in the study of the spin excitation spectrum of LSCO, in order to shed new light on this important problem in contemporary solid state physics.

It has been my intention to make this thesis readable to advanced undergraduate and graduate students as well as to researchers in the fields investigated. Thus, in the course of writing I have not hesitated to insert extra clarifying remarks and references to other interesting and related pieces of work. In the end, this has made for a very long thesis. I can only hope that the results presented will make the reading of these pages worthwhile in spite of my propensity for wordiness.

Before concluding this introduction, I would like to express my gratitude to a number of people with whom I have had the good fortune to work and discuss physics. They include Collin Broholm, Almut Schröder, Yiming Qiu, Bella Lake, Gabriel Aeppli, Stephen M. Hayden, Toby G. Perring, Joel Mesot, Raffaele Gilardi, Andrew Harrison, Radu Coldea, Andrew T. Boothroyd, Mechthild Enderle, Andrew Wildes, Anne Stunault, Jiri Kulda, Peter Vordervisch, Peter Smeibidl, Martin von Zimmermann, N. Mangkorntong, T. Sasagawa, M. Nohara, Hidenori Takagi, Thom E. Mason, Louis-Pierre Regnault, Per Hedegård, Brian Møller Andersen, Linda Udby, Thomas Bagger Stibius Jensen, Niels Hessel Andersen, Per-Anker Lindgård, Luise Theil Kuhn, Peter Kjær Willendrup, Christian Bahl, Asger Bech Abrahamsen, Bente Lebech, Kurt Clausen, Stine Nyborg Klausen and Anne Egebjerg. I would like to thank Kim Lefmann for many helpful comments concerning the physics of high-temperature superconductors. Further, I am greatly indebted to Henrik Moodysson Rønnow and Desmond Francis McMorrow for combining collaboration and supervision with friendship, and to Jens Jensen for many years of patience. Outside the physics community, I feel obliged to thank family and friends for their kindness and support in hard times. Last but not least, I wish to thank Thomine Hansen for being part of my life.

2 Neutron scattering

In this chapter I will present the essentials required to understand the neutron scattering experiments reported in this thesis. Since a number of standard textbooks and papers are available on the subject [1, 2, 3, 4, 5], I will not enter into details of the derivations, concentrating instead on the implications of the resulting mathematical expressions. Details pertaining to the specific studies of LSCO and CFTD are postponed to chapters 4, 5 and 6.

The outline of the chapter is as follows. Selected aspects of the theory of neutron scattering are presented in section 2.1. Section 2.2 then discusses triple axis spectrometers while section 2.3 is concerned with direct-geometry time-of-flight spectrometers. Finally, in section 2.4 the concept of a resolution function is introduced and discussed with special emphasis on identifying its contributions for the two types of instruments.

2.1 Basic theory

In order to understand why neutrons have become one of the prime tools of choice for solid state experimentalist wishing to understand structural and magnetic properties of materials, a good place to start is by a comparison of length scales. The relation between neutron energy E, mass m_n and wavelength λ is $E = h^2/2m_n\lambda^2$. From this one sees, that a thermal neutron, i.e. one with $E = k_BT$ for $T \simeq 300$ K has an energy of $\simeq 26$ meV and wavelength of $\simeq 2$ Å, a length scale of the same order of magnitude as typical interatomic distances. Because neutrons are electrically neutral, they are able to penetrate deeply into solid state materials without being deflected by Coulomb forces. In particular neutrons may experience close encounters with atomic nuclei, with which they interact through the strong nuclear force. The existence of an interaction together with the identity of length scales imply that the crystal structure of the material studied will reveal itself through interference effects.

Despite overall electrical neutrality neutrons do have an internal electric structure as they are made up of charged quarks. This leads to the existence of a finite magnetic moment which in turn interacts with the orbital and spin angular momenta of unpaired electrons through the dipole-dipole interaction. By the same arguments as presented above for interactions with nuclei, neutrons are therefore also sensitive to magnetic structure.

The magnitude of the magnetic cross-section is generally of the same order of magnitude as the nuclear cross-section. Both are however rather small, reflecting that neutrons interact only weakly with matter, a property which simplifies theoretical treatment since one can effectively disregard all processes in which the neutron is scattered twice. In an actual experiment however, multiple scattering events can be very important and neglecting their influence may easily lead to wrong conclusions. The flip side of the weak-interaction coin is that neutron scattering is an intensity limited technique. Studies of solid state excitations in particular typically require large single-crystalline samples.

Typical excitation energies in solid state materials are of the same order of magnitude as the energy of a thermal neutron, i.e. in the meV range. By recording the energy changes of scattering events in which neutrons impart energy to (or conversely, gain energy from) the system studied, one may extract information about the dynamics of the lattice and magnetic degrees of freedom. This is however only practical if the energy resolution $\Delta E/E$ is sufficiently good to discriminate against scattering of different origin.

A quantitative description of the neutron scattering experiments we are going to present in this thesis starts with basic definitions of neutron energy and momentum transfers. We have in mind the situation sketched in Fig. 1: An incident neutron of well-defined wavevector $\mathbf{k}_i$, momentum $\hbar\mathbf{k}_i$ and energy $E_i = \hbar^2k_i^2/2m_n$ scatters from a generic sample, changing its momentum and energy to $\hbar\mathbf{k}_f$ and $E_f = \hbar^2k_f^2/2m_n$ in the process. We then define the neutron momentum and energy transfers $\hbar\mathbf{Q}$ and $\hbar\omega$ by

$$\hbar\mathbf{Q} = \hbar\mathbf{k}_i - \hbar\mathbf{k}_f \quad (1)$$

$$\hbar\omega = E_i - E_f = \frac{\hbar^2}{2m_n}(k_i^2 - k_f^2) \quad (2)$$

In addition, the spin state of the neutron may change, and recording such changes yields additional

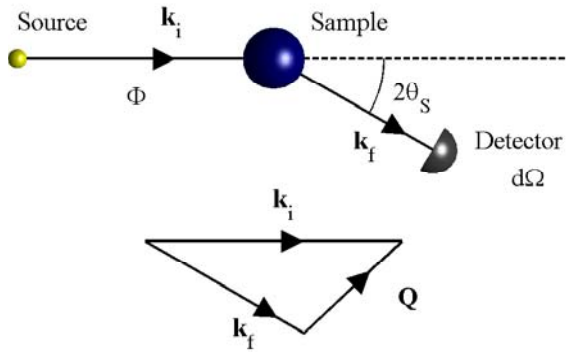

Figure 1: Schematic of a neutron scattering experiment. Monochromatic neutrons of flux Φ, wavevector $\mathbf{k}_i$ and energy $E_i = \hbar^2 k_i^2/2m$ emanating from a source (e.g. a monochromator or a system of choppers) transfer momentum $\hbar\mathbf{Q} = \hbar(\mathbf{k}_i - \mathbf{k}_f)$ and energy $\hbar\omega = \hbar^2(k_i^2 - k_f^2)/2m_n$ to the sample and are scattered through an angle $2\theta_S$ towards a detector subtending the solid angle element $d\Omega$. In a triple-axis spectrometer (Section 2.2) an analyzer crystal is inserted in the exit beam to affect the energy analysis. In a direct geometry time-of-flight spectrometer (Section 2.3), k_f is obtained from measured times of flight and known angles and lengths of the instrument. The scattering triangle in the bottom part of the figure shows an inelastic scattering event with $k_f \leq k_i$.

insights as we shall learn in section 2.1.3. It is important to make clear that when studying crystalline materials, the momentum transferred to the sample should be viewed as crystal momentum and is only defined modulo $\hbar$ times a reciprocrocal lattice vector. This is a direct consequence of the replacement of the full translational invariance of the vaccum by the discrete translational invariance of the crystal lattice. Because of the well matched energy and length scales discussed above, neutron scattering has a large dynamic range in both $\mathbf{Q}$ and $\hbar\omega$.

To set the experimental stage, we must define the cross-sections for neutron scattering processes. To do this we refer again to Fig. 1. A beam of neutrons of flux Φ and wavevector $\mathbf{k}_i$ impinge on a target (the scattering system). We arrange a detector subtending the solid angle $d\Omega$ at a large distance from the sample position and record the number $I_{d\Omega\ dE_f}$ of neutrons with energies between E_f and $E_f + dE_f$ reaching the detector per second. This number must be proportional to the incident flux Φ, the solid angle element $d\Omega$ and the energy window dE_f. Per definition, the constant of proportionality is the partial differential scattering cross-section $(d^2\sigma/d\Omega\ dE_f)$:

$$I_{d\Omega\ dE_f} = \left(\frac{d^2\sigma}{d\Omega\ dE_f}\right) \Phi\ d\Omega\ dE_f \tag{3}$$

If one does not specify a particular energy range for the neutrons detected but integrates over all neutron events which lead to scattering into $d\Omega$ one obtains the differential cross-section $I_{d\Omega}$:

$$I_{d\Omega} = \left(\frac{d\sigma}{d\Omega}\right) \Phi\ d\Omega \tag{4}$$

Finally, and for completeness, the ratio of the total number of scattered neutrons I to the incident flux is per definition the total cross-section σ:

$$I = \sigma\ \Phi \tag{5}$$

It is evident that the three cross-sections introduced above should be thought of as probabilities though they are measured in units of area, and that they satisfy the relations $(d\sigma/d\Omega) = \int dE_f\ (d^2\sigma/d\Omega\ dE_f)$ and $\sigma = \int d\Omega\ (d\sigma/d\Omega)$. Note however, that the definitions do not take into account the spin states of the incident and scattered neutrons, or the logical possibility that spin may be imparted to the system in the scattering process. When working with polarized neutrons on a triple axis spectrometer the neutron spin states prior to and after scattering are known quantities. The component of the neutron spin along a given axis, which we take as the z-axis and which is normally defined by a guide field, can be either $s^z = +1/2$ (spin up "u") or $s^z = -1/2$ (spin down "d"). By recording the spin states of the neutron, each of the cross-sections (3)-(5) may be decomposed into four components in a natural way. For example $(d^2\sigma/d\Omega\ dE_f)_{u\to d}$ is the partial differential cross-section for processes in which the incident neutron has spin up, and the interaction causes this spin to flip. If an unpolarized incident beam is viewed as consisting of

equal numbers of $s^z = +1/2$ and $s^z = -1/2$ neutrons, the total partial differential cross-section appearing in Eq. (3) is related to the four spin-dependent cross-sections in a natural manner:

$$\left(\frac{d^2\sigma}{d\Omega\ dE_f}\right) = \frac{1}{2}\left(\left(\frac{d^2\sigma}{d\Omega\ dE_f}\right)_{u\to u} + \left(\frac{d^2\sigma}{d\Omega\ dE_f}\right)_{d\to d} + \left(\frac{d^2\sigma}{d\Omega\ dE_f}\right)_{u\to d} + \left(\frac{d^2\sigma}{d\Omega\ dE_f}\right)_{d\to u}\right) \quad (6)$$

For the moment we defer explicit treatment of changes in the neutron spin state to section 2.1.3.

In order to make contact with experiment, one must develop theoretical expressions for the cross-sections Equations (3)-(5) in terms of $\mathbf{Q}$ and $\hbar\omega$ for a general interaction V between a neutron and a scattering system. Denoting by λ_i and λ_f particular quantum mechanical states of the system with energies E_{λ_i} and E_{λ_f}, one can derive the differential cross-section $(d\sigma/d\Omega)_{\lambda_i\to\lambda_f}$ for processes in which the interaction V causes the system to make the transition $\lambda_i \to \lambda_f$ while the neutron changes its wavevector from a given value $\mathbf{k}_i$ to $\mathbf{k}_f$ with $\mathbf{k}_f$ restricted to the direction defined by the detector angle $d\Omega$, but with no restriction on $k_f = |\mathbf{k}_f|$, i.e. corresponding to Eq. (4). The required expression is

$$\left(\frac{d\sigma}{d\Omega}\right)_{\lambda_i\to\lambda_f} = \frac{k_f}{k_i}\left(\frac{m_n}{2\pi\hbar^2}\right)^2 |\langle \mathbf{k}_f\lambda_f\ |V|\ \mathbf{k}_i\lambda_i\rangle|^2 \quad (7)$$

To arrive at Eq. (7), one employs Fermi's golden rule to relate the number of transitions per second from the neutron plus system state $|\mathbf{k}_i, \lambda_i\rangle$ to $|\mathbf{k}_f, \lambda_f\rangle$ with $\mathbf{k}_f$ in $d\Omega$ to the squared matrix element $|\langle \mathbf{k}_f\lambda_f| V |\mathbf{k}_i\lambda_i\rangle|^2$. The remaining factors originate from the density of final neutron states of momenta $\mathbf{k}_f$ in the direction of $d\Omega$ divided by the flux $\Phi \propto k_i$. Since λ_i, λ_f and k_i are all given quantities, energy conservation $E_{\lambda_i} + E_i = E_{\lambda_f} + E_f$ can be incorporated straightforwardly by using the properties of δ-functions. This step leads to the expression

$$\left(\frac{d^2\sigma}{d\Omega\ dE_f}\right)_{\lambda_i\to\lambda_f} = \frac{k_f}{k_i}\left(\frac{m_n}{2\pi\hbar^2}\right)^2 |\langle \mathbf{k}_f\lambda_f\ |V|\ \mathbf{k}_i\lambda_i\rangle|^2\ \delta(E_{\lambda_i} - E_{\lambda_f} + \hbar\omega) \quad (8)$$

for the partial differential cross-section in the presence of a general interaction V.

2.1.1 Nuclear cross-section

To proceed further an explicit expression for the interaction V must be introduced. As discussed in great detail by Squires [1], the relevant formula for the case of nuclear scattering is

$$V_{\rm nuc}(\mathbf{r}) = \frac{2\pi\hbar^2}{m_n}\ b\ \delta(\mathbf{r}) \quad (9)$$

The presence of a δ-function expresses the physical fact that the range of the strong forces responsible for nuclear scattering is of the order of the nuclear radius $\sim 10^{-15}$ m − orders of magnitude smaller than the neutron wavelength. The quantity b is known as the scattering length, and depends on the total spin angular momentum of the nucleus plus neutron system (Either $I + 1/2$ or $I - 1/2$ where I is the nuclear spin quantum number). In this manner, the dependence of the matrix element $|\langle \mathbf{k}_f\lambda_f\ |V|\ \mathbf{k}_i\lambda_i\rangle|^2$ on the spin state of the neutron is hidden inside b. In addition, the scattering length depends on the particular isotope studied, and varies erratically between different isotopes of the same element as well as between the elements themselves. No existing theory is capable of predicting the numbers b from first principles.

Equations (7) and (8) involve a specific transition $\lambda_i \to \lambda_f$ of the scattering system, over which the experimenter has no control. To obtain the cross-section defined by Eq. (3) one has to sum over all final states λ_f and subsequently average over initial states λ_i employing Boltzmann statistics, i.e. associating the a factor $P_{\lambda_i} = \exp(-E_{\lambda_i}\beta)/Z$ with each initial state λ_i. Here $\beta = 1/k_BT$ and the partition function $Z = \sum_{\lambda_i}\exp(-E_{\lambda_i}\beta)$ ensures the condition $\sum_{\lambda_i} P_{\lambda_i} = 1$. The thermal expectation value of an operator A is then given by $\langle A\rangle = \sum_{\lambda_i} P_{\lambda_i}\langle\lambda_i\,|A|\,\lambda_i\rangle$. By introducing time-dependent Heisenberg operators $A(t) = \exp(iHt/\hbar)A\exp(-iHt/\hbar)$, with H denoting the Hamiltonian of the system studied, the partial differential cross-section for nuclear scattering can be split into two components:

$$\left(\frac{d^2\sigma}{d\Omega\ dE_f}\right)_{\rm coh} = \frac{\sigma_{\rm coh}}{4\pi}\frac{k_f}{k_i}\frac{1}{2\pi\hbar}\sum_{\boldsymbol{jj'}}\int_{-\infty}^{\infty} dt\exp(-i\omega t)\langle\exp(-i\mathbf{Q}\cdot\mathbf{R}_{\boldsymbol{j'}}(0))\exp(i\mathbf{Q}\cdot\mathbf{R}_{\boldsymbol{j}}(t))\rangle \quad (10)$$

$$\left(\frac{d^2\sigma}{d\Omega\ dE_f}\right)_{\rm inc} = \frac{\sigma_{\rm inc}}{4\pi}\frac{k_f}{k_i}\frac{1}{2\pi\hbar}\sum_{\boldsymbol{j}}\int_{-\infty}^{\infty} dt\exp(-i\omega t)\langle\exp(-i\mathbf{Q}\cdot\mathbf{R}_{\boldsymbol{j}}(0))\exp(i\mathbf{Q}\cdot\mathbf{R}_{\boldsymbol{j}}(t))\rangle \quad (11)$$

Here $R_{\boldsymbol{j}}(t)$ is the Heisenberg operator for the position coordinate of a nuclei indexed j in the scattering system. The quantities $\sigma_{\rm coh} = 4\pi(\bar{b})^2$ and $\sigma_{\rm inc} = 4\pi(\bar{b^2} - (\bar{b})^2)$ depend on the relative abundances f_i of nuclei with scattering lengths b_i (depending in turn, as already noted, on both the total spin state of neutron plus nucleus system and on the total number of nucleons inside the atomic nucleus) through the weighted averages $\bar{b^n} = \sum_i f_i b_i^n$.

The results (10) and (11) are known as the coherent and incoherent partial differential cross-sections respectively. The former measures the scattering that would be observed if all nuclei had the average scattering length $\bar{b}$. Because of the double sum $\sum_{jj'}$ it contains interference terms and as such gives rise to peaks in the detector. By contrast, the incoherent scattering $(d^2\sigma/d\Omega\ dE_f)_{\rm inc}$ describes the scattering from the random deviations of the actual distribution of b_i from the average $\bar{b}$. Owing to this randomness, incoherent scattering is featureless in $\mathbf{Q}$, but can still be of great practical importance. The classic example, and one that is relevant for the studies of CFTD reported in chapter 3 is the difference in the spin-incoherent scattering from hydrogen and deuterium. The coherent and incoherent scattering from these two isotopes are determined by $\sigma_{\rm coh,H} = 1.8$, $\sigma_{\rm inc,H} = 20.2$ for hydrogen and $\sigma_{\rm coh,D} = 5.6$, $\sigma_{\rm inc,D} = 2.0$ for deuterium (in units of barns: 1b = 10^{-28} m^2). Since $\sigma_{\rm coh,H} \ll \sigma_{\rm inc,H}$ Eq. (11) tells us that there is always a large featureless incoherent background in hydrogen-rich samples which is potentially detrimental to the study of weak signals. One should therefore strive whenever possible work to with deuterated samples.

2.1.2 Magnetic cross-section

The interaction between the magnetic moment $\boldsymbol{\mu}_n$ of a neutron and the electrons inside the scattering system originates from its Zeeman interaction $V = -\boldsymbol{\mu}_n \cdot \mathbf{B}$ with the magnetic field distribution inside the sample. The latter has contributions from both the spin and orbital angular momenta of unpaired electrons. In terms of the nuclear and Bohr magnetons $\mu_N = e\hbar/2m_p = 5.051\ 10^{-27}$ J T^{-1} and $\mu_B = e\hbar/2m_e = 9.274\ 10^{-24}$ J T^{-1} with m_p and m_e being the proton and electron masses, the magnetic moments of a neutron and an electron are given by $\boldsymbol{\mu}_n = -\gamma\mu_N\boldsymbol{\sigma}_n$ and $\boldsymbol{\mu}_e = -2\mu_B\mathbf{s}$ respectively. Here $\gamma = 1.913$ is the gyromagnetic ratio of the neutron, $\boldsymbol{\sigma}_n = 2\mathbf{s}_n$ is its Pauli spin operator and $\mathbf{s}$ is the operator for the electron spin.

If we denote by $\mathbf{p}$ the electron momentum operator, by $\mathbf{R}$ a distance vector measured from this electron and introduce the unit vector $\hat{\mathbf{R}} = \mathbf{R}/\,|\,\mathbf{R}\,|$, the total Zeeman interaction with the field produced by this electron can be derived from electromagnetic theory:

$$V_{\rm mag}(\mathbf{r}) = -\frac{\mu_0}{4\pi}\,2\gamma\mu_N\mu_B\,\boldsymbol{\sigma}_n \cdot \left(\nabla \times \left(\frac{\mathbf{s}\times\hat{\mathbf{R}}}{|\,\mathbf{R}\,|^2}\right) + \frac{1}{\hbar}\frac{\mathbf{p}\times\hat{\mathbf{R}}}{|\,\mathbf{R}\,|^2}\right) \tag{12}$$

The first contribution originates from the field created by the magnetic moment associated with the electronic spin angular momentum. The motion of the electronic charge − related to its orbital angular momentum − may be viewed as giving rise to current elements, and hence to field distributions which are computable from the law of Biot and Savart and which account the second term in Eq. (12).

As in the case of nuclear scattering, after inserting (12) in (8) one now switches to Heisenberg operators, sums over the initial and final system states λ_i and λ_f using Boltzmann statistics for the former. Since we are not considering polarized neutron scattering in this section, we must also sum over the final neutron spin states σ_f and average over σ_i assuming an unpolarized incoming beam. We shall further assume LS-coupling, i.e. that the spin and orbital angular momentum of the electrons combine to yield effective resultant ionic spin and orbital angular momenta. For electrons localized close to atomic positions $\mathbf{R}_{\boldsymbol{ld}}$ in a non-Bravais crystal with unit cells defined by vectors $\boldsymbol{l}$ and with each atom inside the cell defined by a vector $\boldsymbol{d}$ measured relative to $\boldsymbol{l}$, the resulting partial differential cross-section for magnetic scattering is

$$\left(\frac{d^2\sigma}{d\Omega\ dE_f}\right)_{\rm mag} = \frac{(\gamma r_0)^2}{2\pi\hbar}\frac{k_f}{k_i}\sum_{\alpha\beta}(\delta_{\alpha\beta} - \hat{\mathbf{Q}}_\alpha\hat{\mathbf{Q}}_\beta)\sum_{\boldsymbol{l'd'ld}}\frac{1}{4}g_{\boldsymbol{d'}}g_{\boldsymbol{d}}F^*_{\boldsymbol{d'}}(\mathbf{Q})F_{\boldsymbol{d}}(\mathbf{Q})$$
$$\times\int_{-\infty}^{\infty}dt\exp(-i\omega t)\langle\exp\{-i\mathbf{Q}\cdot\mathbf{R}_{\boldsymbol{l'd'}}(0)\}\exp\{i\mathbf{Q}\cdot\mathbf{R}_{\boldsymbol{ld}}(t)\}\rangle\langle S^\alpha_{\boldsymbol{l'd'}}(0)S^\beta_{\boldsymbol{ld}}(t)\rangle \tag{13}$$

Here $r_0 = 2.818\ 10^{-15}$ m is the classical radius of an electron, and the symbols $S_{\boldsymbol{ld}}$ represent the total angular momenta of the ions mentioned above. The numbers $g_{\boldsymbol{d}}$ are then the Landé splitting

factors of these ions defined as $g = g_S + g_L$ with $g_S = 1 + (S(S+1) - L(L+1)) / (J(J+1))$ and $g_L = 1/2 + (L(L+1) - S(S+1)) / (2J(J+1))$. For spin-only scattering, $g = g_S = 2$. In writing down Eq.(13) it has been assumed that correlations between space and spin coordinates can be neglected. The functions $F_{\boldsymbol{d}}(\mathbf{Q})$ are magnetic form factors and enter because the objects giving rise to magnetic scattering are clouds of unpaired electrons, which have a finite physical extent and cannot be represented mathematically by δ-functions as in the case of the nuclear scattering Eq. (9). In calculations of scattering amplitudes the finite extent of the electron clouds gives rise to phase-shifts which express themselves in the form factor. $F_{\boldsymbol{d}}(\mathbf{Q})$ is explicitly given by the Fourier transform over all spatial coordinates of the normalized density of unpaired electrons $s_{\boldsymbol{d}}(\mathbf{r})$ of the ion located at $\boldsymbol{d}$

$$F_{\mathbf{d}}(\mathbf{Q}) = \int d\mathbf{r} \exp(i\mathbf{Q}\cdot\mathbf{r}) s_{\boldsymbol{d}}(\mathbf{r}) \tag{14}$$

Finally the factor $\sum_{\alpha\beta}(\delta_{\alpha\beta} - \hat{\mathbf{Q}}_\alpha \hat{\mathbf{Q}}_\beta)$ in (13) encapsulates the fact that in magnetic scattering processes from electrons only the component of the moment perpendicular to the scattering vector $\mathbf{Q}$ is visible. In an unfortunate collapse of terminology, this factor is commonly referred to as the polarization factor, even though it is always present, for unpolarized and polarized neutrons alike.

Comparing the coherent and incoherent nuclear cross-sections (10) and (11) with Eq.(13) for magnetic scattering it is apparent that the physics of interest is in all cases contained in thermal averages of quantum mechanical expectation values of two point correlation functions between electron angular momentum and nuclear position operators $\mathbf{S}$ and $\mathbf{R}$, which are Fourier transformed in both space and time to yield the partial differential cross-sections. As pointed out by van Hove [3, 4] it is useful to separate these four-dimensional Fourier transforms which depend only on the momentum and energy transfers $\hbar\mathbf{Q}$ and $\hbar\omega$, from quantities depending on properties of the scattered particles such as $\mathbf{k}_i$ and $\mathbf{k}_f$. Generalizing the notation of [2] to non-Bravais crystals with one species of magnetic ion, the case relevant to both LSCO and CFTD, we can write

$$\left(\frac{d^2\sigma}{d\Omega\, dE_f}\right)_{\text{mag}} = \frac{1}{\hbar}\frac{k_f}{k_i} p^2 \exp(-2W) \sum_{\alpha\beta} (\delta_{\alpha\beta} - \hat{\mathbf{Q}}_\alpha \hat{\mathbf{Q}}_\beta) S^{\alpha\beta}(\mathbf{Q},\omega) \tag{15}$$

for scattering processes that are elastic in the lattice variables $\mathbf{R}_{\boldsymbol{ld}}$. The factor $p = (\gamma r_0/2) g F(\mathbf{Q})$ contains some of the trivial factors in Eq. (13). We have further made the simplifying assumption that zero-point vibrations of the atoms in the unit cell about their equilibrium positions, represented by a set of Debye-Waller factors $\exp(-2W_{\boldsymbol{d}})$ may effectively be replaced by one overall exponential factor $\exp(-2W)$ which can be moved outside the Fourier transforms in the scattering function $S^{\alpha\beta}(\mathbf{Q},\omega)$ given by

$$S^{\alpha\beta}(\mathbf{Q},\omega) = \frac{1}{2\pi} \sum_{\boldsymbol{l'd'ld}} \exp(-i\mathbf{Q}\cdot\{\boldsymbol{l'} + \boldsymbol{d'} - \boldsymbol{l} - \boldsymbol{d}\}) \int_{-\infty}^{\infty} dt \exp(-i\omega t) \langle S^{\alpha}_{\boldsymbol{l'd'}}(0) S^{\beta}_{\boldsymbol{ld}}(t)\rangle \tag{16}$$

A useful property of $S(\mathbf{Q},\omega)$ is that it is connected to the imaginary part of the generalized magnetic susceptibility $\chi(\mathbf{Q},\omega) = \chi'(\mathbf{Q},\omega) + i\chi''(\mathbf{Q},\omega)$ through the fluctuation-dissipation theorem [6]

$$S(\mathbf{Q},\omega) = [\, n(\omega) + 1\,]\, \chi''(\mathbf{Q},\omega) = \frac{\chi''(\mathbf{Q},\omega)}{1 - \exp(-\hbar\omega/k_B T)} \tag{17}$$

where $n(\omega) = 1/(\exp(\hbar\omega/k_B T) - 1)$ is the Bose occupation factor. The significance of this result of linear-response theory lends itself to the fact that $\chi(\mathbf{Q},\omega)$ is often computable from first principles theories.

2.1.3 Polarization analysis

To discuss polarized neutron scattering we must generalize our notation somewhat. It turns out, that for each scattering process, one can define an effective scattering length operator $\hat{b}$, which can be written in the form $\hat{b} = A + B\,\boldsymbol{\sigma}_n \cdot \mathbf{I}$, in terms of two constants A and B and an operator $\mathbf{I}$, all determined by the type of scattering process considered [1]. Following [2], we take as our starting point for this short discussion of polarized neutron scattering the expression

$$\left(\frac{d^2\sigma}{d\Omega\, dE_f}\right)_{s_i \to s_f} = \frac{k_f}{k_i} \sum_{if} P_{\lambda_i} \mid \langle \lambda_f \mid \sum_{\boldsymbol{l}} \exp(i\mathbf{Q}\cdot\mathbf{r}_{\boldsymbol{l}}) U_{\boldsymbol{l}}^{s_i s_f} \mid \lambda_i \rangle \mid^2 \delta(E_{\lambda_i} - E_{\lambda_f} + \hbar\omega) \tag{18}$$

with the enclosed operator $U_{\boldsymbol{l}}^{s_i s_f}$ given by a matrix element with respect to the neutron spin states before and after the scattering event

$$U_{\boldsymbol{l}}^{s_i s_f} = \langle s_f \mid b_{\boldsymbol{l}} - p_{\boldsymbol{l}}\, \boldsymbol{\sigma}_n \cdot \mathbf{S}_{\boldsymbol{l}\perp} + B_{\boldsymbol{l}}\, \boldsymbol{\sigma}_n \cdot \mathbf{I}_{\boldsymbol{l}} \mid s_i \rangle \tag{19}$$

In this notation introduced by Moon, Riste and Koehler in their seminal paper on polarization analysis [5], $\mathbf{S}_{\boldsymbol{l}\perp}$ is the component of the spin at position $\boldsymbol{l}$ perpendicular to the scattering wavevector $\mathbf{Q}$, i.e. $\mathbf{S}_{\boldsymbol{l}\perp} = \hat{\mathbf{Q}} \times \mathbf{S}_{\boldsymbol{l}} \times \hat{\mathbf{Q}}$ (this gives rise to the polarization factor discussed in relation to Eq. (13)). As in the previous subsection we use the notation $p_{\boldsymbol{l}} = (\gamma r_0/2) g_{\boldsymbol{l}} F(\mathbf{Q})$ and $I_{\boldsymbol{l}}$ is the nuclear moment of the ion at site $\boldsymbol{l}$. In contrast to the treatment of nuclear scattering in section 2.1.1, Eq. (19) explicitly separates the spin-dependent part of the total nuclear scattering amplitude $B_{\boldsymbol{l}}\, \boldsymbol{\sigma}_n \cdot \mathbf{I}_{\boldsymbol{l}}$ from the spin-independent part $b_{\boldsymbol{l}}$ that depends only on the type of isotope studied.

If the initial and final neutron polarizations are specified in terms of their spin-component along a particular polarization direction ζ at the sample position, then in terms of a spatial coordinate system (ξ, η, ζ) (defined such that the ζ-direction is along the polarization, and the ξ and η-directions are perpendicular both to the polarization and to each other), one can show [5] that the four possible matrix elements are given by

$$\begin{aligned} U^{++} &= b - pS_{\perp\zeta} + BI_\zeta \\ U^{--} &= b + pS_{\perp\zeta} - BI_\zeta \\ U^{+-} &= -p(S_{\perp\xi} + iS_{\perp\eta}) + B(I_\xi + iI_\eta) \\ U^{-+} &= -p(S_{\perp\xi} - iS_{\perp\eta}) + B(I_\xi - iI_\eta) \end{aligned} \tag{20}$$

Case-by-case examination of these four expressions suffices to pave the way for the exposition of polarized measurements on CFTD in chapter 5. For a start, let us disregard the electronic magnetic contribution, i.e. we assume that all three components $S_{\perp\xi}$, $S_{\perp\eta}$ and $S_{\perp\zeta}$ of $\mathbf{S}_{\boldsymbol{l}\perp}$ vanish. It is then clear that coherent nuclear scattering governed by b − for example nuclear Bragg reflections and scattering from phonons − contributes solely to processes ($++$ and $--$) in which the polarization state of the neutron is unchanged. These are commonly referred to as non-spin-flip (NSF) channels as opposed to the spin-flip (SF) channels $+-$ and $-+$ where the neutron spin state is altered. As we discussed in section 2.1.1 there are two contributing factors to nuclear incoherent scattering: Isotope incoherence resulting from randomness in the distribution of $b_{\boldsymbol{l}}$-values between the sites $\boldsymbol{l}$ for fixed $\boldsymbol{\sigma}_n + \mathbf{I}$ and nuclear spin incoherence arising from randomness in the possible values of the sum $\boldsymbol{\sigma}_n + \mathbf{I}$ for fixed isotope number. Since isotope incoherence is contained in the factor b it contributes to the NSF channels only. Nuclear spin incoherent scattering on the other hand, gives rise to both SF and NSF scattering as do scattering from electronic spins $S_\perp$, the difference being that the component of the electronic spin parallel to $\mathbf{Q}$ does not give rise to scattering. In the case most commonly encountered, the nuclear spins remain disordered $\langle I_\xi^2 \rangle = \langle I_\eta^2 \rangle = \langle I_\zeta^2 \rangle = 1/3 \langle I^2 \rangle = I(I+1)/3$ and mutually uncorrelated. Under these circumstances it follows from Eq. (21) that two-thirds of the nuclear spin incoherent scattering is spin-flip and one-third non-spin-flip. Turning to the electronic magnetic contribution it follows from (21) that the component of $\mathbf{S}_{\boldsymbol{l}\perp}$ along the polarization direction at the sample contributes to the NSF scattering while components of $\mathbf{S}_{\boldsymbol{l}\perp}$ perpendicular to the polarization gives rise to SF scattering. An important special case of this general result occurs when the polarization is parallel to the scattering vector $\mathbf{Q}$. In this case, $S_{\perp\zeta} = 0$ and all magnetic scattering occurs in the SF channel.

2.2 Triple axis spectrometers

Conceptually, a triple axis spectrometer is an extremely simple machine. It is based only on the Bragg's law and simple geometry in reciprocal space. In a triple axis experiment a beam of neutrons traverses a path through the instrument determined by the settings of three angles θ_{S}, θ_{M} and θ_{A}. The first of these is defined in Fig. 1, while θ_{M} and θ_{A} will be discussed now. Figure 2 shows a triple axis spectrometer with a monochromator crystal located in the beam path leading to the sample position, and an analyzer crystal located in the path from sample to detector. Monochromators and analyzers are either perfect crystals or crystals that have been deformed in a controlled manner to obtain certain characteristic properties. Typical monochromator and analyzer materials are pyrolytic graphite (PG), silicon and germanium. For polarized experiments Heusler (Cu_2MnAl) crystals are used. The latter have a lower reflectivity than the other choices, and scatter only neutrons with a particular spin state, immediately implying longer counting times.

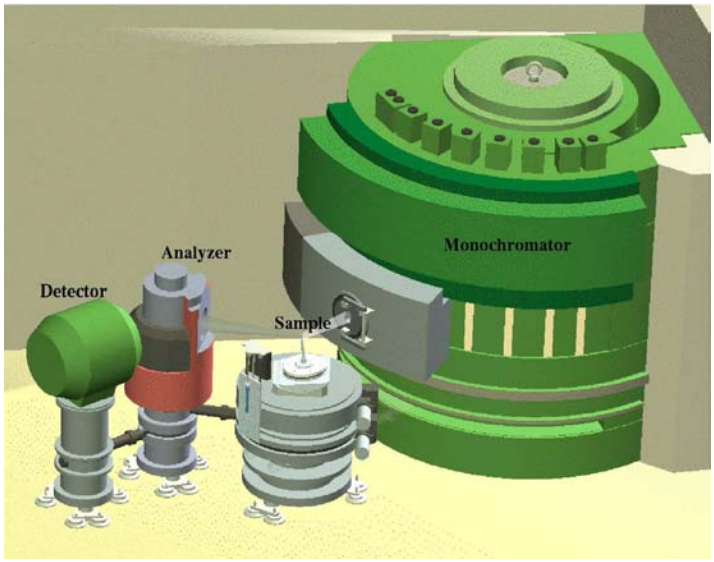

Figure 2: The layout of a triple axis spectrometer, here exemplified by the IN8 spectrometer at ILL, Grenoble. A monochromatic neutron beam at the sample position is produced by a monochromator crystal. Neutrons scattered from the sample are subsequently Bragg reflected from the analyzer into the detector tank. In a typical experiment either k_i or k_f remains fixed. This is achieved by fixing either $\theta_{\rm M}$ or $\theta_{\rm A}$ appearing in Eqs. (21)-(22). Scans in $(\mathbf{Q}, \omega)$-space are executed by controlled motions of the sample orientation, the sample scattering angle $\theta_{\rm S}$ and either $\theta_{\rm M}$ or $\theta_{\rm A}$ depending on which of these is fixed.

This may seem like a high price to pay, but is counterbalanced by the ability through polarized triple axis spectroscopy to separate the individual components of the cross-section. The theoretical basics of this separation was presented in the previous section, and we will see it experimentally demonstrated in chapter 5.

At the monochromator and analyzer positions neutrons are reflected according to Bragg's law

$$n\lambda = 2d\sin\theta_i \tag{21}$$

$$n\tau = 2k\sin\theta_i \tag{22}$$

Here n is and integer and $i = \mathrm{M}, \mathrm{A}$ for monochromator and analyzer respectively. The setting of the angle θ_i causes a family of crystal planes characterized by their distance d (or equivalently, by their reciprocal lattice vector $\boldsymbol{\tau}$) to diffract exactly those neutrons with wavelengths $\lambda = 2\pi/k$ determined by equation (21). Hence, a monochromator transforms a polychromatic beam of neutrons to a beam of neutrons with wavenumbers k, $2k$ etc. corresponding to neutron energies $E = \hbar^2k^2/2m$, $4E$ and so on. Under normal circumstances we are primarily interested in the neutrons which correspond to $n = 1$ in the above expressions, and regard the remaining, higher order neutrons ($n \geq 2$) as a nuisance, which is normally dealt with efficiently by the use of neutron filters of e.g. pyrolythic graphite, beryllium or beryllium oxide. Disregarding higher order neutrons for now we can consider the neutron beam after the monochromator as consisting only of neutrons with a particular wavevector $\mathbf{k}_i$ determined from (22). When this beam hits the sample, the scattered neutrons leave the sample along a distribution of directions and with a distribution of energies and spin directions determined by the spin-dependent partial differential scattering cross-sections $(d^2\sigma/d\Omega\, dE_f)_{\mathrm{s_i}\to\mathrm{s_f}}$ in Eq. (6). By varying the scattering angle $\theta_{\rm S}$ between $\mathbf{k}_i$ and $\mathbf{k}_f$, the angular distribution can be probed. At the same time, one can analyze the energy distribution in each given direction by varying the analyzer angle $\theta_{\rm A}$ defining the direction towards the detector. Additional information may be gleaned by considering not only the change in momentum and energy of the neutron in the scattering process, but also possible changes in its spin state. The angular, energy and spin distributions contain full information about the scattering events which took place inside the sample, and may in principle be inverted to unveil the physics of the sample expresses in its Hamiltonian H.

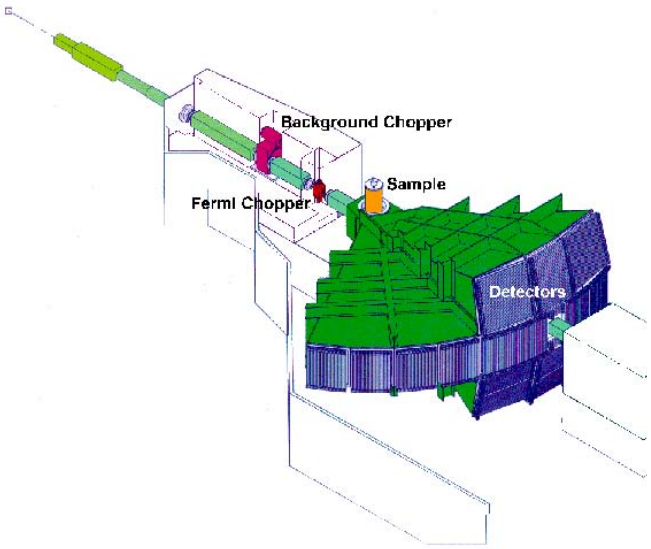

Figure 3: The layout of the MAPS spectrometer at ISIS. A monochromatic beam is produced by chopping the beam emanating from a water moderator. After scattering from the sample, the neutrons are detected in a 16 m^2 bank of position sensitive detectors, consisting of 147456 individually accessible pixel elements. The central, rectangular part of the detector bank extends to 20 degrees along the vertical and horizontal directions. The high angle bank extends from 20 to 60 degrees along the horizontal direction.

2.3 Direct geometry time-of-flight spectrometers

Time-of-flight spectrometers are used at reactor sources by deliberately pulsing the continuous incident beam or at spallation sources. At the latter, neutron pulses are typically created by letting high energy proton pulses hit a heavy ion target. At the ISIS facility, Rutherford Appleton Laboratory, where the experiments reported in chapters 4 and 7 were performed, a tantalum target is used and the pulse frequency is 50 Hz. A broad distinction may be drawn between direct-geometry and indirect-geometry time-of-flight instruments. In the latter, one uses a white incident beam, and perform energy analysis of the scattered neutrons by means of crystal analyzers. By contrast, direct-geometry instruments use a monochromatic incident beam and will be discussed below.

Figure 3 shows the MAPS (MultiArray Position Sensitive) spectrometer at the ISIS pulsed neutron source. This particular instrument was used for both studies of CFTD and LSCO. The neutrons produced in the spallation process are first moderated by inelastic scattering in water at room temperature to thermalize the neutrons emanating from the target. A monochromatic pulse is then produced by the use of chopper technology: First, a background chopper positioned 8.5 m after the moderator is installed. It rotates at the frequency of the proton pulse and is phased to close the beam path when the proton beam hits the target. This prevent unwanted byproducts (epithermal neutrons, pions etc.) of the spallation process from entering the detector tank, where they would otherwise thermalize and give rise to a large background. A further purpose of the background chopper is to remove the pulse components which would have given rise to frame overlap at the detector position i.e. the situation in which the slowest neutrons in a given pulse are overtaken by the fastest ones from the next pulse, see Fig. 5. Second, a Fermi chopper located 10 m after the moderator can be phased relative to the neutron pulses from the target. This allows one to select any given E_i. The Fermi choppers at MAPS are capable of spinning at frequencies between 50 and 600 Hz. The choice of chopper frequency has a determining influence on the flux at the sample position and on the energy resolution. At the sample position 12 m from the moderator, the neutrons are scattered as dictated by the scattering function $S(\mathbf{Q}, \omega)$ of the sample.

Because $\mathbf{k}_i$ and the chopper-sample distance are known quantities, one can calculate the time it takes the neutron beam to reach the sample. The latest generation of direct-geometry time of flight spectrometers are equipped with large arrays of position sensitive detectors. For example, MAPS has 147456 physical pixel elements spread out on a 16 m^2 ^{3}He detector array positioned 6 m from the sample position. For each pixel the time-of-flight from the pulse creation to the detector is recorded. An inelastically scattered neutron reaches the detector before or after an elastically

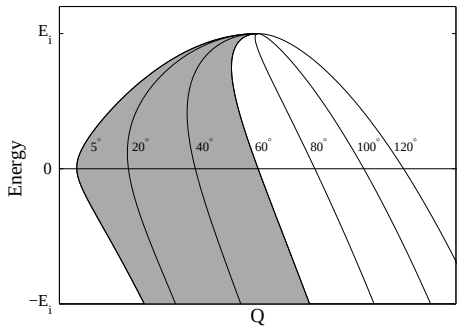

Figure 4: Available phase space for direct geometry time-of-flight spectrometry derived from the expression $\hbar^2Q^2/2m = 2E_i - \hbar\omega - 2\cos 2\theta_S(E_i(E_i-\hbar\omega))^{1/2}$ which in turn follows from the cosine rule applied to the scattering triangle in Fig. 1 and Eq. (2). The lines indicate the trajectories as a function of $Q = |\mathbf{Q}|$ and $\hbar\omega$ for detectors at fixed angles, and the grey area represents the region which may be investigated with the MAPS spectrometer which has detectors extending to $2\theta_S = 60$ degrees.

scattered one depending on whether it gained or lost energy in the scattering process it underwent. From the measured times, the sample-detector distances and the polar and azimuthal angles of a given detector measured with respect to $\mathbf{k}_i$, it is straightforward to compute the momentum and energy changes $\mathbf{Q}$ and $\hbar\omega$ of all detected neutrons. Each pixel represents a trajectory in 4 dimensional $(\mathbf{Q}, \hbar\omega)$ space with the spacing of the individual energy bins limited by the number of time-channels selected for each detector. Energy and momentum conservation requires the trajectories to be parabolas

$$\left(\frac{\hbar^2 k_i^2}{2m} - \hbar\omega\right) = \left(\frac{\hbar^2}{2m}\right)\left[\ |\mathbf{Q}_\perp|^2 + (k_i - |\mathbf{Q}_\parallel|)^2\right] \tag{23}$$

We have used the symbols $\mathbf{Q}_\parallel$ and $\mathbf{Q}_\perp$ for the components of $\mathbf{Q}$ along and perpendicular to $\mathbf{k}_i$, i.e. $\mathbf{Q}_\parallel = (\mathbf{Q}\cdot\hat{\mathbf{k}}_i)\mathbf{k}_i$ and $\mathbf{Q}_\perp = \mathbf{Q} - \mathbf{Q}_\parallel$. There are two reasons for explicitly separating these perpendicular vectors. First, it makes direct contact with our experiments, and second, that it is convenient for the discussion of $\mathbf{Q}$-resolution in section 2.4.2.

It is the intersection of these time-of-flight parabolas with the sample scattering function $S(\mathbf{Q},\omega)$ that determines what is measured in a given experiment. The use of large arrays of position-sensitive detectors makes it possible to map out large portions of $S(\mathbf{Q},\omega)$ while retaining favorable resolution conditions. The region of (Q,ω)-space accessible to direct geometry time-of-flight spectrometers is displayed in Fig. 4.

The power of the time-of-flight approach is particularly striking when $S(\mathbf{Q},\omega)$ is independent of one or more components of $\mathbf{Q}$, as occurs e.g. in low dimensional magnets such as $Cu(DCOO)_2{\cdot}4D_2O$ and $La_{2-x}Sr_xCuO_4$. Generally, the detectors will then pick up more intensity for a given sample orientation, and one can envisage special orientations providing very efficient data collection. For the 2D systems studied in this thesis, we employed configurations with the 2D planes oriented perpendicular to $\mathbf{k}_i$. In this case the role of $\mathbf{Q}_\perp$ is played by the in-plane component $\mathbf{Q}_{2D}$ of the wavevector transfer As $\hbar\omega$ varies at fixed $\mathbf{Q}_{2D}$, $\mathbf{Q}_\parallel$ changes according to Eq. (23), but this variation is irrelevant for the 2D magnetic signal, since $S(\mathbf{Q},\omega)$ is independent of the out-of-plane component of $\mathbf{Q}$. The situation is different when we consider phonon scattering, which contributes to the background in our experiments. Because single-phonon branches typically disperse along all three components of $\mathbf{Q}$, it is clear that such branches will intersect the parabola (23) in a restricted part of $(\mathbf{Q},\omega)$ space. It can happen that the phonon branch intersects the parabola (23) in the same region as the magnetic scattering, and this situation is potentially detrimental to the data analysis. Being delocalized in $\mathbf{Q}$ and ω, multiphonon scattering cuts the parabola everywhere and is primarily a cause for concern owing to its rapid increase with $|\mathbf{Q}|$.

Figure 5 shows a typical direct geometry time-of-flight experiment in a space vs. time graph. The initial pulse of neutrons leaves the moderator with a distribution of velocities and gives rise to a distribution of arrival times at the background chopper position. Appropriate phasing of the two choppers relative to the pulses allows the selection of any E_i present in the original distribution. At each detector, the neutrons arrive with a velocity distribution reflecting $S(\mathbf{Q},\omega)$. By connecting each detector to a multichannel analyzer, every single pulse yields a spectrum in ω and after many pulses, the average distribution gives a good representation of $S(\mathbf{Q},\omega)$.

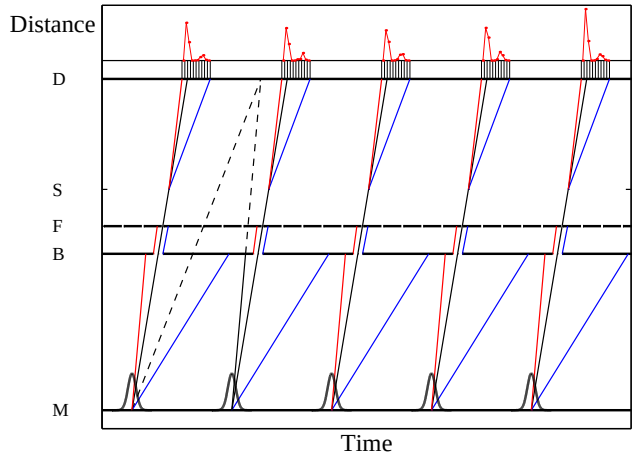

Figure 5: Time-of-flight diagram showing the propagation of a pulse from the moderator to the detector. Moderator, background chopper, Fermi chopper, sample and detector positions are indicated by capital letters M, B, F, S and D respectively. At each stage, the slowest neutrons are indicated in blue and the fastest in red. The ones having energy E_i are indicated by solid black lines. Frame overlap is shown by the dashed black lines. In the particular example shown, the Fermi chopper spins at five times the frequency of the neutron source. At the sample position the incoming beam undergoes scattering processes described by the sample scattering function $S(\mathbf{Q},\omega)$ giving rise to a distribution of velocities between the sample and a detector capable of multichannel analysis. Each pulse then samples $S(\mathbf{Q},\omega)$. At the end of the run, all pulses are summed.

2.4 The experimental resolution function

So far we have considered ideal scattering experiments with the incident and final neutron wavevectors $\mathbf{k}_i$ and $\mathbf{k}_f$ and scattering angle $2\theta_S$ being sharply defined quantities. In doing so we have neglected that experimentally, the neutron path through any instrument − from source to detector − has a finite extent in the directions perpendicular to the ideal path. We have also neglected the finite wavelength spreads of the neutrons reflected from monochromators and analyzers on a triple axis spectrometer or emanating from the moderator and choppers of a direct geometry time-of-flight instrument. What this means is that while neutrons arriving at the detector are on average characterized by $\mathbf{k}_i$, $\mathbf{k}_f$ and $2\theta_S$, accounting for the distributions $\{\mathbf{k}_i\}$, $\{\mathbf{k}_f\}$ and $\{2\theta_S\}$, around the average values is essential for a full analysis. The concept of a resolution function encapsulates these statements.

An essential realization is that the resolution function depends only on the configuration of the instrument and is independent of what we are really interested in − the scattering function $S(\mathbf{Q},\omega)$ describing the physics of the sample. In this section, we consider the resolution function and its contributions for triple axis and time-of-flight spectrometers.

2.4.1 The resolution function for triple axis spectrometers

The brief discussion below is based on the book by Shirane, Shapiro and Tranquada [2], and on original publications by Cooper and Nathans [7], Chesser and Axe [8] and by Popovici [9]. These references deal with triple axis spectrometers, but the core terminology is more general and equations (24)-(27) should extend to time-of-flight spectrometers.

The previous sections have shown that whether we are considering magnetic scattering or nuclear scattering it is always possible to write the neutron-scattering cross-section in the form

$$\left(\frac{d^2\sigma}{d\Omega\, dE_f}\right) = \frac{k_f}{k_i}\tilde{S}(\mathbf{Q},\omega) \tag{24}$$

using a suitably defined $\tilde{S}(\mathbf{Q},\omega)$. We are going to consider the intensity $I(\mathbf{Q}_0,\omega_0)$ measured at the nominal setting $(\mathbf{Q}_0,\omega_0)$ of the instrument. To this end we choose a Cartesian coordinate system $(\mathbf{Q}_\parallel,\mathbf{Q}_\perp,\mathbf{Q}_z)$ defined relative to the wavevector transfer $\mathbf{Q}_0$ in the following manner: The wavevector $\mathbf{Q}_\parallel$ is along $\mathbf{Q}_0$, $\mathbf{Q}_\perp$ is perpendicular to $\mathbf{Q}_0$ in the horizontal scattering plane and $\mathbf{Q}_z$ is along the vertical direction. It can then be shown that

$$I(\mathbf{Q}_0,\omega_0) = \int d\omega\, d\mathbf{Q}\, R(\mathbf{Q}-\mathbf{Q}_0,\omega-\omega_0)\tilde{S}(\mathbf{Q},\omega) \tag{25}$$

This important relation says that the intensity measured in the setting $(\mathbf{Q}_0, \omega_0)$ of the instrument should really be viewed as a four-dimensional convolution of the scattering function $\tilde{S}(\mathbf{Q}, \omega)$ with the resolution function $R(\mathbf{Q} - \mathbf{Q}_0, \omega - \omega_0)$. The latter may be written in the form

$$R(\mathbf{Q} - \mathbf{Q}_0, \omega - \omega_0) = R_0 \exp\left(-\frac{1}{2}\Delta\vartheta \underline{M} \Delta\vartheta\right) \tag{26}$$

where the quantity $\Delta\vartheta$ is a four-vector depending on the difference from the nominal setting

$$\Delta\vartheta = \left(\mathbf{Q}_\parallel - \mathbf{Q}_0, \mathbf{Q}_\perp, \mathbf{Q}_z, \frac{m}{\hbar Q_0}(\omega - \omega_0)\right) \tag{27}$$

and $\underline{M}$ is a 4×4 matrix with entries depending on $\mathbf{k}_i$, $\mathbf{k}_f$ and $2\theta_\mathrm{S}$ as well as on all parameters necessary to describe the beam path and energy distribution. The quantity R_0 is a normalization factor for the resolution function and as such depends on the same quantities as $\underline{M}$. Contours of constant value of R are determined by equations of the type $\Delta\vartheta \underline{M} \Delta\vartheta = c$-number, the solutions to which are nested four-dimensional ellipsoids. The volume of these resolution ellipsoids can be changed by altering the instrument configuration, but that may also affect the count rate. The experimental aim is to find the configuration which maximizes the signal-to-noise ratio while retaining non-preventive counting times.

For triple axis instruments the calculation of the resolution function was considered by Cooper and Nathans [7] who analyzed the resolution function $R(\mathbf{Q}, \omega)$ analytically based on Gaussian approximations for the monochromator and analyzer mosaic spreads and for the linear Soller collimators typically inserted to reduce the angular divergence of the beam. They found that $\underline{M}$ and R_0 depend on $\hbar\omega$, k_i,$\mathbf{Q}$, on the lattice parameters of the monochromator and analyzer crystals d_M and d_A, as well as on their mosaicities and on the horizontal and vertical angular divergences of the collimators. Because the focus in [7] was on the orientation of the resolution ellipsoid and not on intensity issues, the normalization factor R_0 was not derived analytically. This was subsequently done by Chesser and Axe [8]. A substantial generalization of the formalism of [7, 8] was supplied by Popovici [9], allowing spatial effects on the resolution function to be treated efficiently. These include the effects of the lengths of the individual sections of the instrument, the areas of the source and detector as well as the size and shape of the sample, monochromator and analyzer crystals. In particular, the effects of curving the latter two for intensity gain purposes is explicitly present in the formulation of [9].

A few comments of practical importance based on [2]: First, the matrix $\underline{M}$ in (26) is generally not diagonal and so the principal axes of the resolution ellipsoids are generally not aligned with the vectors $(\mathbf{Q}_\parallel, \mathbf{Q}_\perp, \mathbf{Q}_z)$. However, under not so restrictive assumptions, the vertical component of the resolution function effectively decouples from the remaining three. In this case the vertical resolution function is simply a Gaussian function of $\mathbf{Q}_z$ the extent of which is typically much larger than the projections in the plane spanned by $\mathbf{Q}_\parallel$ and $\mathbf{Q}_\perp$. When studying low dimensional systems this can be turned into a virtue by orienting a high-symmetry axis along $\mathbf{Q}_z$. The integration along $\mathbf{Q}_z$ in (25) then involves a function $\tilde{S}(\mathbf{Q}, \omega)$ which does not depend of $\mathbf{Q}_z$ and this increases the intensity measured at a given point $(\mathbf{Q}, \omega)$ compared with that found using alternative sample orientations. Second, a common occurrence particularly when mapping out dispersion surfaces is the appearance of focusing effects reflecting the orientation of the resolution ellipsoid relative to the dispersion surface. It is possible through clever choices of the instrument setup, to optimize the orientation of the resolution ellipsoid for a given experiment, e.g. for studying the energy-broadening of a dispersion surface or its detailed lineshape. Finally, it should be mentioned that it follows from Eq. (25) that the resolution function R can be measured experimentally by scanning across a Bragg reflection at $\mathbf{Q} = \boldsymbol{\tau}$, where $\tilde{S}(\mathbf{Q}, \omega) \propto \delta(\omega)\delta(\mathbf{Q} - \boldsymbol{\tau})$.

Having determined the resolution function, the typical way to account for resolution corrections when analyzing triple axis data is to choose a model for the expected scattering and then carry out the convolution (25) numerically before fitting to the experimental data. In performing the integration one would then use the analytic formulas for $\underline{M}$ and R_0 derived in [7, 8] or their generalizations in [9].

2.4.2 Resolution for time-of-flight spectrometers

For a time-of-flight spectrometer such as MAPS it is natural to consider the energy and momentum resolution separately. The short treatment given here is based on [10].

Let us start by studying the contributions to the energy resolution for a given detector. It is most convenient to work in the time-domain rather than explicitly in terms of energies. In the experimental situation neutrons emanate from the moderator with a distribution of energies and times determined ultimately by the moderation histories inside the moderator. This is a complicated matter and way outside the scope of this section. The net effect however, is to create a pulse of neutrons characterized by a distribution of energies. Furthermore, the neutrons having a particular energy E_c are distributed in time with a width $\Delta t_m(E_c)$. The Fermi chopper is open for passage only in a certain time-window Δt_c (determined by its design and frequency) centered around the arrival time t_c, inside which it picks out neutrons having the selected energy E_c, but owing to the existence of the time distribution $\Delta t_m(E)$ also some neutrons with higher and lower energy. Formally, the neutrons leaving the Fermi chopper are distributed in time according to the convolution of Δt_c and Δt_m. Approximating both by Gaussians, the total time-spread becomes

$$\Delta t = \sqrt{\Delta t_m^2(E_i) + \Delta t_c^2} \tag{28}$$

Together with t_c and the distance L_0 from the moderator to the chopper, this quantity determines the incident energy resolution. The time resolution on the exit side is determined by the chopper pulse width Δt_c, the chopper-sample distance L_1 and the sample-detector distance L_2. Combining the two contributions, the fractional energy resolution at the detector is given by [10, 11]

$$\frac{\Delta\hbar\omega}{E_i} = \left(\left(2\frac{\Delta t_c}{t_c} \left(1 + \frac{L_1 + L_2}{L_3} \left(1 - \frac{\hbar\omega}{E_i} \right)^{3/2} \right) \right)^2 + \left(2\frac{\Delta t_m}{t_c} \left(1 + \frac{L_2}{L_3} \left(1 - \frac{\hbar\omega}{E_i} \right)^{3/2} \right) \right)^2 \right)^{1/2} \tag{29}$$

from which it follows that for a given E_i the energy resolution improves with increasing energy transfer.

Turning to the resolution in momentum transfer, the general prescription for its calculation would be to first derive an analytic expression for $\mathbf{Q}$ in terms of the spectrometer variables, and then to analyze how $\mathbf{Q}$ is affected by small changes in these. Windsor [10] gives a detailed discussion on how this can be done in the case of diffraction. Rather than extending his discussion to the case of inelastic scattering based on Eq. (23), we restrict ourselves to a rather simplified treatment with particular emphasis on the particular instrument used to perform the experiments reported in chapters 4 and 7. Each pixel is defined by fixed polar and azimuthal angles with respect to $\mathbf{k}_i$. They form a regular array of obviously finite extent regions identified by average values $(\mathbf{Q}_0, \omega_0)$. In the experimental situation, the values of $S(\mathbf{Q}, \omega)$ are being summed in a finite interval around this average and identified with $S(\mathbf{Q}_0, \omega_0)$. The physical size of each pixel thus contributes to the $\mathbf{Q}$-resolution, and it seems fair that with the highly pixelated detectors on MAPS this is the dominant effect. A second contribution comes from the finite energy spread in the incident beam. Since neutrons with slightly different energies scatter to different angles by the same physical processes, the $\mathbf{Q}$-resolution is degraded by the energy resolution. The angular divergence of the incident beam similarly leads to angular spreads at the detector position. In addition, the finite size of the sample also leads to a worsening of the $\mathbf{Q}$ resolution on account of the possibility that neutrons scattered by the same processes may hit adjacent detectors instead of the same one. The effects of the sample size and finite energy resolution can effectively be viewed as a Gaussian smearing, which is convolved with the basically square resolution function contribution from the pixel size. Any other contributions to the $\mathbf{Q}$-resolution neglected here would yield extra blurring, and would tend to make the resolution ellipsoid more and more Gaussian. It stands to reason that the net result is to yield a resolution function which samples $S(\mathbf{Q}, \omega)$ as suggested by equation 25.

One point of relevance to our studies of LSCO is that the projection of the $\mathbf{Q}$-resolution onto the plane of the detectors is essentially isotropic. This situation should be compared with that of a triple axis spectrometer, where the resolution function is typically extended along one of the in-plane components of $\mathbf{Q}$. This immediately makes for slightly less ambiguous data analysis in the time-of-flight case, particularly so at higher energy transfers where the $\mathbf{Q}$-resolution on a triple axis spectrometer becomes worse, but where the $\mathbf{Q}$-resolution on a direct geometry time-of-flight spectrometer at least contains one contribution − the dominant one − which improves, because (as can be seen from Fig. 4) the same number of detectors collect data in a smaller section of $Q = |\mathbf{Q}|$ as $\hbar\omega$ increases.

3 CFTD − a model quantum magnet

The purpose of the present chapter is to provide an understanding of why it is that the experiments reported in chapters 4 and 5 transcend the level of pure characterization of the specific material $Cu(DCOO)_2{\cdot}4D_2O$ and should rather be viewed as investigations of the theoretical model known as the 2D quantum Heisenberg antiferromagnet on a square lattice, abbreviated to 2DQHAFSL. Strictly speaking, the term "quantum" refers to any quantized spin value S, but here we investigate the extreme quantum limit $S = 1/2$ where fluctuation effects are expected to be largest.

The outline of the chapter is as follows: Section 3.1 gives a brief introduction to the Heisenberg model in general and to some of the outstanding problems connected with it. Amongst other lessons, we shall see that quantum fluctuations in the spin degrees of freedom lead to renormalizations of classical results, obtained by treating the spins as ordinary vectors rather than quantum mechanical operators consisting of Cartesian components which do not commute, thus making the "real" spin-direction an ill-defined concept. In section 3.2 we turn to a more detailed account of the physical properties of $S = 1/2$ Heisenberg spins on a square lattice. Mainly to demonstrate the degree of consensus between various theoretical and numerical approaches we shall talk a bit about the quantum renormalizations in this particular case, but the main focal point will be attempts to calculate the spin excitation spectrum of the 2DQHAFSL.

Next, in section 3.3 we turn to the experimental situation, and start by a brief exposition of selected experimental results from optical spectroscopy which probe the spin excitations. Such studies have historically provided substantial impetus to the theoretical investigations of the 2DQHAFSL and still lack a full understanding. This unsatisfactory situation persists partly because there exists insufficient experimental information about the full spin excitation spectrum of the 2DQHAFSL, a situation which the work presented in chapters 4 and 5 aims to remedy. The inclusion of optical studies also serves to emphasize the potential importance of higher order spin couplings. In addition, section 3.3 contains a discussion of how a few specific materials including CFTD have been identified as being good representations of the 2DQHAFSL model. Pivotal in this respect have been neutron scattering studies of the temperature dependence of the correlation length ξ in the paramagnetic phase. We shall touch briefly on these experiments and the theory behind them, but will mainly concentrate on a more in-depth presentation of existing neutron scattering studies of the spin wave (single-magnon) spectra of three systems which have been believed to be good realizations of the 2DQHAFSL model. This discussion brings higher-order exchange terms in the spin Hamiltonian to the forefront again, but should demonstrate that CFTD is an excellent embodiment of the pure 2DQHAFSL model, without any need for consideration of such processes. Having established this point, section 3.4 concludes the chapter with a review of the known structural and magnetic properties of CFTD as they have been reported in the literature.

3.1 The Heisenberg model

The problem in which we are interested is that of the Heisenberg model of localized spins on a lattice

$$H = J \sum_{\langle \boldsymbol{j},\boldsymbol{k} \rangle} \mathbf{S}_{\boldsymbol{j}} \cdot \mathbf{S}_{\boldsymbol{k}} \tag{30}$$

Here $\mathbf{S}_{\boldsymbol{j}} = (\mathbf{S}^x_{\boldsymbol{j}}, \mathbf{S}^y_{\boldsymbol{j}}, \mathbf{S}^z_{\boldsymbol{j}})$ are quantum mechanical operators and J is a number characterizing the strength of the exchange interaction between any pair of spins. We imagine that only nearest neighbor spins interact and choose the notation $\sum_{\langle j,k \rangle}$ to represent a summation over all nearest neighbor sites − each interaction being counted once.

If rather than quantum mechanical operators the spins are thought of as a classical vectors, then $J < 0$ and $J > 0$ favor parallel and antiparallel orientations of neighboring vectors $\mathbf{S}_{\boldsymbol{j}}$ and $\mathbf{S}_{\boldsymbol{k}}$ respectively, i.e. the two cases correspond to ferromagnetism and antiferromagnetism. Energy minimization is achieved for $J < 0$ by allowing all spin-vectors to point along a certain direction, which we can take as the z-direction. For $J > 0$, the energy is minimized when all nearest neighbor spin-vectors are antiparallel to each other. This state is known as the Néel state. For simple lattices, it is possible to minimize all individual interaction energies of the vector spins simultaneously. It is clear that in such cases, the fully polarized and Néel state are the classical ground states for ferromagnets and antiferromagnets respectively.

If we instead treat the angular momenta $\mathbf{S}_j$ as quantum mechanical operators, we are forced to modify these conclusions. To see this most clearly, we shall use the raising and lowering operators $\mathbf{S}_j^{\pm} = \mathbf{S}_j^x \pm i\mathbf{S}_j^y$ known from standard textbooks on quantum mechanics [12] to rewrite Eq. (30) in the form

$$H = J \sum_{\langle j,k \rangle} \left(\mathbf{S}_j^z \mathbf{S}_k^z + \frac{1}{2} \left(\mathbf{S}_j^+ \mathbf{S}_k^- + \mathbf{S}_j^- \mathbf{S}_k^+ \right) \right) \tag{31}$$

The quantum analogue of the classical ferromagnetic ground state is constructed by allowing all spins to have their maximum expectation value of $\mathbf{S}^z$ for the given spin quantum number S. In one dimension, and for $S = 1/2$ we may write this state $|F\rangle = |\ldots \uparrow\uparrow\uparrow\uparrow \ldots\rangle$. Similarly, the quantum analogue of the classical Néel state is written $|N\rangle = |\ldots \uparrow\downarrow\uparrow\downarrow \ldots\rangle$. Operating with H in (31) on $|F\rangle$ shows that $|F\rangle$ is an eigenstate of H. In fact it is also the ground state. On the other hand, the term $\frac{1}{2}(\mathbf{S}_j^+ \mathbf{S}_k^- + \mathbf{S}_j^- \mathbf{S}_k^+)$ gives rise to finite matrix element between the quantum Néel state $|N\rangle$ and states such as $|\ldots \downarrow\uparrow\uparrow\downarrow \ldots\rangle$. This shows that the Néel state cannot be the quantum mechanical ground state of the Heisenberg antiferromagnet in any dimension. But what is then the true ground state? For dimensions greater than one, the answer is not known, and the question stands as one of the fundamental unsolved problems in solid state physics. Having said that, let us focus on what is known about the Heisenberg antiferromagnet.

Rigorous bounds for the ground state energy E_0 of a system of N Heisenberg spins each having z nearest neighbors were derived by Anderson [13]

$$-\frac{1}{2} NzJS^2 \left(1 + \frac{1}{zS} \right) < E_0 < -\frac{1}{2} NzJS^2 \tag{32}$$

The upper bound $-\frac{1}{2}NzJS^2$ is the classical ground state energy. Equation (32) tells us that the largest scope for variations away from the classical result exists when the number of nearest neighbors and the spin quantum number S are smallest. Considering the nature of one of the traditional ways of attacking spin Hamiltonians, this should come as no great surprise: In mean-field theory one starts by introducing the mean value $\langle \mathbf{S}_i \rangle$ of the spin operator $\mathbf{S}_i$ at site i. The true exchange interaction $\mathbf{S}_j \cdot \mathbf{S}_k$ is then rewritten in the form $[\langle \mathbf{S}_j \rangle + (\mathbf{S}_j - \langle \mathbf{S}_j \rangle)] \cdot [\langle \mathbf{S}_k \rangle + (\mathbf{S}_k - \langle \mathbf{S}_k \rangle)]$. Next, the term $(\mathbf{S}_j - \langle \mathbf{S}_j \rangle) \cdot (\mathbf{S}_k - \langle \mathbf{S}_k \rangle)$ describing correlation between fluctuations is neglected, leaving a constant term and a term resembling the Zeeman interaction of an isolated magnetic moment in an external magnetic field determined by the values of $\langle \mathbf{S}_i \rangle$. On general grounds, replacing the real interactions in (30) by effective fields can be expected to become a better approximation as the number of interactions z is increased, i.e. for higher dimensions. Similarly, the neglect of correlations between spin fluctuations is expected to become a better approximation as their relative importance decreases. Considering that one signature of quantum mechanics is that the expectation value of the operator $\mathbf{S}^2$ is $S(S+1)$ rather than the classical result S^2, a semi-quantitative estimate of the effect of the spin quantum number is obtained by taking the ratio $S(S+1)/S^2 = (1 + 1/S)$. If this ratio is interpreted as a measure of the effects of quantum mechanics, then deviations away from classical physics are expected to go as $1/S$, i.e. to be most dramatic for low spin and in particular for $S = 1/2$.

Another central issue is whether the ground state has magnetic order or not. In three dimensions, this appears to be the case for systems with interactions described by the Heisenberg, XY ($H_{\mathrm{XY}} = J \sum_{\langle j,k \rangle} \left(\mathbf{S}_j^x \mathbf{S}_k^x + \mathbf{S}_j^y \mathbf{S}_k^y \right)$) and Ising ($H_{\mathrm{Ising}} = J \sum_{\langle j,k \rangle} \mathbf{S}_j^z \mathbf{S}_k^z$) Hamiltonians. By contrast, the corresponding models in one spatial dimension are all disordered, even at absolute zero. In this sense, one may argue that two dimensions is the critical dimension for magnetic order to establish itself. However, there are rigorous restrictions: A general theorem due to Mermin and Wagner states that magnetic order at finite temperature is prohibited in 2D or less for systems with continuous degrees of freedom such as the Heisenberg and XY models. On the other hand, the Ising model has a discrete order parameter and Onsager proved that magnetic order does exist at finite temperature i 2 dimensions. The 2D XY model is a rather special case because a topological phase transition − unaccompanied by symmetry-breaking − takes place between two disordered phases. Finally, this leads us to the case of interest here − the 2D Heisenberg model. As discussed by Manousakis [14], long range antiferromagnetic order has been proven to exist at $T = 0$ K for the 2D square lattice for any $S \geq 1$. On the other hand, no rigorous proof for the existence or non-existence of order in the same model with $S = 1/2$ has surfaced. There exists a proof stating

that the ground state is a singlet $S^z_{\rm tot} = \sum_{\boldsymbol{r}} \langle \mathbf{S}^z_{\boldsymbol{r}} \rangle = 0$ (see [14] for a discussion), but this result does not by itself imply magnetic order, and leaves room for more exotic states such as the resonating valence band (RVB) state [15]. Originally introduced for the triangular lattice, the physics of this disordered, spin-liquid state has hovered over much of condensed matter magnetism ever since it resurfaced in efforts to shed light on high-T_c superconductivity [16]. One very attractive aspect of RVB states is that in certain guises their energy can be very close to the best estimates of the ground state energy of the 2DQHAFSL [14]. A second favorable property of RVB states, mostly relevant to superconductivity, is that spin pairing is a built-in property. Returning to the question of magnetic order, it is by now well established through a combination of theory and simulations that at $T = 0$ K, the spin rotation symmetry of the 2DQHAFSL is indeed broken and magnetic order is established. However, quantum fluctuations in the spin degrees of freedom significantly renormalize various physical observables away from the values they would take in the corresponding classical ($S \to \infty$) models [14].

The previous statement begs the question: What is meant by quantum fluctuations? We have already seen that the Néel state cannot be the quantum mechanical ground state since parts of the Hamiltonian have finite overlap with states in which pairs of nearest neighbor spins are flipped relative to the Néel state. A system initially prepared in the Néel state must make virtual transitions to such nearby states. The proneness of the Néel state to such fluctuations changes the values of physical observables away from their values in the classical Néel state. In the fully polarized ferromagnetic state no such virtual transitions occur and so all physical observables remain fixed at their classical values. A beautiful experimental demonstration of these ideas was provided by Coldea *et al.* [17] who used neutron scattering to determine the parameters of the spin Hamiltonian of the frustrated antiferromagnet Cs_2CuCl_4. They did so by applying a magnetic field sufficiently high to overcome the exchange couplings and transform the system into an effective ferromagnet. The trick is that while the exchange constants of the antiferromagnet are renormalized (see Eq. (38) below) and their values cannot be determined without additional information, this is not so for the ferromagnet. Thus, measurements of the spin wave spectrum gives the exchange constants directly.

3.1.1 Quantum renormalizations

For the purposes of the discussion in the present chapter, the most important quantum corrections are those of the sublattice magnetization m, the spin wave velocity c_s, the spin stiffness constant ρ_s and of the perpendicular susceptibility $\chi_\perp$.

The sublattice magnetization (per spin) is defined by $m = N^{-1} \left| \sum_{\boldsymbol{r}=(\boldsymbol{x},\boldsymbol{y})} (-1)^{\boldsymbol{x}+\boldsymbol{y}} \langle \mathbf{S}^z_{\boldsymbol{r}} \rangle \right|$ in units where $g\mu_B$ has been set to unity. It is reduced by quantum fluctuations from its saturation value $m = S$ by ΔS^z

$$m = S - \Delta S^z \tag{33}$$

The quantum renormalizations of c_s, ρ_s and $\chi_\perp$ are expressed in a common mathematical format, through constants Z_c, Z_ρ and Z_χ multiplied onto the classical values of each quantity. For example, the spin wave velocity is the slope of the single-magnon dispersion $\omega_{\boldsymbol{q}}$ (see below) in the limit $\boldsymbol{q} \to (\pi, \pi)$ and its renormalization constant Z_c is defined by

$$c_s = Z_c \, c_s^{\rm cl} = Z_c \sqrt{2z} JS \tag{34}$$

The spin stiffness constant is a measure of the change in energy of the system imposed by a slow and non-uniform twist of the spins away from the quantization axis. It quantifies the rigidity of the spin system to non-uniform rotations and is analogous to the superfluid density in a superfluid [6, 18, 19]. The definition of Z_ρ is

$$\rho_s = Z_\rho \, \rho_s^{\rm cl} = Z_\rho \, JS^2 \tag{35}$$

Finally, the perpendicular susceptibility measures the response of a system to an external magnetic field applied in a direction perpendicular to the staggered magnetization. The defining equation reads $\chi_\perp = N^{-1} \delta \langle \sum_{\boldsymbol{r}} \mathbf{S}^x_{\boldsymbol{r}} \rangle / \delta H_\perp$ [20]. Since transverse fields couple to the operators $\mathbf{S}^+$ and $\mathbf{S}^-$ which create and destroy magnons, it naturally emerges that $\chi_\perp$ is related to the intensity of single-magnon scattering. The associated quantum renormalization constant Z_χ is

$$\chi_\perp = Z_\chi \, \chi_\perp^{\rm cl} = Z_\chi \, \frac{1}{2zJ} \tag{36}$$

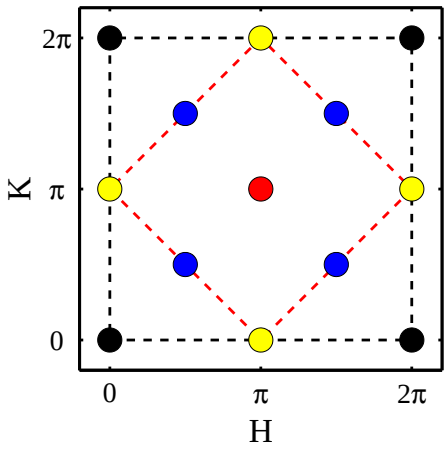

Figure 6: The full 2D Brillouin zone of a square lattice with nearest neighbor distance $a = 1$ is the region bounded by the dashed black line. If 2D Néel antiferromagnetic order exist, a magnetic Bragg peak occurs at $\mathbf{Q}_{2D} = (\pi, \pi)$ (red circle), reflecting a doubling of the unit cell. The dashed red line then marks the antiferromagnetic Brillouin zone boundary (ZB) which surrounds $\mathbf{Q}_{2D} = (\pi, \pi)$, connects four equivalent $\mathbf{Q}_{2D} = (\pi, 0)$ positions (yellow circles) and passes through four equivalent $\mathbf{Q}_{2D} = (\pi/2, \pi/2)$ positions (blue circles). The locations of the nuclear Bragg peaks of the square lattice are indicated by black circles.

The three defining equation (34)-(36) use the notation employed in [18] in which the nearest neighbor distance has been set to unity. Note that the classical quantities satisfy the hydrodynamic relation ${c_s^{\rm cl}}^2 = \rho_s^{\rm cl}/\chi_\perp^{\rm cl}$, and that our notation suppresses the fact that the renormalization factors Z_c, Z_ρ and Z_χ depend on S and tend to unity as $S \to \infty$, reflecting the approach to the classical limit of vector spins.

3.2 The 2D quantum Heisenberg antiferromagnet on a square lattice

Having discussed Heisenberg antiferromagnets at a general level, we proceed to take a closer look at its behavior for $S = 1/2$ spins residing on a square lattice.

3.2.1 Spin wave theories

One very successful approach to spin Hamiltonians is spin wave theory. Anderson [21] was the first to provide a careful treatment of antiferromagnetic spin waves, taking into account their zero-point energy. This allowed a calculation of the ground state energies for simple lattices in one, two and three dimensions. The resulting energies ranged between the rigorous bounds in Eq.(32) and for the 1D case further agreed well with Bethes exact solution (see e.g. [22]), even though the latter does not have long range order as explicitly assumed in spin wave theory. For the 2D case of our interest, an evaluation of the reduction in the ordered moment at $T = 0$ K yielded $m = 0.303$, i.e. a reduction of $\Delta S^z = 0.197$. The spin wave dispersion relation in D dimensions is

$$\omega_{\boldsymbol{q}}^{\rm A} = 2DJS\sqrt{1 - \gamma_{\boldsymbol{q}}^2} \tag{37}$$

with $\gamma_{\boldsymbol{q}} = (1/z)\sum_{\boldsymbol{\delta}} \exp(i\boldsymbol{q}\cdot\boldsymbol{\delta})$ where $\boldsymbol{\delta}$ are the nearest neighbor vectors. In the remainder of this thesis, the use of the subscripted notation $\omega_{\boldsymbol{q}}$ refers to the 2D reciprocal space shown in figure 6, i.e. the subscript $\boldsymbol{q}$ is really $\mathbf{Q}_{2D} = (H, K)$ (the nearest neighbor distance a is set to unity) and $\omega_{\boldsymbol{q}} = \omega(\mathbf{Q}_{2D})$. By Taylor expansion around (π, π) in the $D = 2$ case, it is easy to verify the value $\sqrt{2z}SJ$ given in Eq. (34) for the classical spin wave velocity. The dispersion (37) is gapless, implying zero energy cost for uniform rotations of all the ordered moments, and takes a constant value $2J$ in $D = 2$ along the antiferromagnetic zone boundary (ZB) which connects the four equivalent $(\pi, 0)$ points in the 2D Brillouin zone. Experimentally, $\omega_{\boldsymbol{q}}$ can be measured using inelastic neutron scattering. Fits to the expression (37) then yield the exchange constant J. While Andersons treatment was semiclassical, later work by Kubo [23] demonstrated the equivalence of this approach to the Holstein Primakoff (HP) method [24] which has since become the favored one. In appendix A we use the HP approach in its simplest guise − the so-called linear spin wave

theory − to derive the dispersion (37) and the intensities expected when scattering neutrons from a $S = 1/2$, square lattice Heisenberg antiferromagnet. It will be seen there, that the HP approach involves formally expanding a square root in powers of $\boldsymbol{n_i}/(2S)$, where $\boldsymbol{n_i}$ is a number operator, counting the number of spin flips on site $\boldsymbol{i}$. Physically, the HP expansion corresponds to taking interactions between spin waves into account to successively higher precision. Replacing the square root by unity yields linear spin wave theory, which Kubo showed to be equivalent to Andersons semiclassical theory. More generally, spin wave theory should be regarded as an expansion in the parameter $1/(zS)$ [20]. Within the HP version of spin wave theory we may accept that this is so, since one can argue that the thermal average of $\boldsymbol{n_i}$ is ultimately related to the reduction in the ordered moment, which in turn goes roughly as $1/z$.

Later, Oguchi calculated the quantum correction to order $1/(2S)$ of the spin wave dispersion $\omega_{\boldsymbol{q}}$ and found it to be proportional to $\omega_{\boldsymbol{q}}$ itself, i.e.

$$\omega_{\boldsymbol{q}}^{\mathrm{O}} = Z_c^{\mathrm{O}} \omega_{\boldsymbol{q}}^{\mathrm{A}} \tag{38}$$

with $Z_c^{\mathrm{O}} = 1.1579$ [25]. The use of the notation Z_c − a quantity defined in the limit $\mathbf{Q}_{2\mathrm{D}} \rightarrow (\pi, \pi)$ − for the renormalization of the dispersion over all of $\mathbf{Q}_{2\mathrm{D}}$-space is validated by the proportionality of the first order correction to $\omega_{\boldsymbol{q}}$ itself. Whether or not higher order corrections to (37) yield $\mathbf{Q}_{2\mathrm{D}}$-dependent renormalizations of the dispersion and neutron intensities is a central issue here and in chapters 4 and 5.

The existence of a quantum renormalization factor Z_c has an important experimental implication for neutron scattering studies. Once the dispersion $\omega_{\boldsymbol{q}}$ has been measured, a fit to the linear spin wave form (37) of the dispersion will now output a renormalized effective exchange $J_{\mathrm{eff}} = Z_c J$ rather than simply J. In the absence of additional information, it is a priori impossible to deduce the raw exchange J from the dispersion alone.

Proceeding to higher order in the HP expansion leads to much complication but was accomplished by Igarashi [26] who found corrections to second order in $1/(2S)$ for Z_ρ, Z_χ and m. He further evaluated the second order change in the spin wave dispersion $\omega_{\boldsymbol{q}}$ and from its limiting behavior for $\mathbf{Q}_{2\mathrm{D}} \rightarrow (\pi, \pi)$ derived the quantum renormalization Z_c of the spin wave velocity. Finally, an evaluation of Z_c through the use of the hydrodynamic relation $c^2 = \rho_s/\chi_\perp$ allowed a consistency check of the theory: $Z_c = (Z_\rho/Z_\chi)^{1/2}$ agreed within errors with Z_c evaluated directly from the dispersion $\omega_{\boldsymbol{q}}$ and corrected to the same order in $1/(2S)$.

An alternative way of tackling spin wave theory is through the use of the Dyson-Maleev (DM) formalism. This has been extensively employed by Canali and coworkers [20, 27, 28], who have used it to compute the Raman line shape [27] in order to address anomalous experimental results in La_2CuO_4 (see section 3.3.1). Using the same theoretical machinery, the second order correction to $\omega_{\boldsymbol{q}}$ was studied over the whole antiferromagnetic Brillouin zone [28]. At all wavevectors studied the second order correction to the magnon energy is positive, but importantly a small variation in $\omega_{\boldsymbol{q}}$ was found along the antiferromagnetic zone boundary: $\omega(\pi, 0)$ and $\omega(\pi/2, \pi/2)$ are larger than Oguchi's result (38) by roughly 4 and 2 percent respectively, i.e. there is a dispersion along the zone boundary. By contrast, if the relevant expressions for $\omega_{\boldsymbol{q}}$ in the HP spin wave theory [26] are analyzed numerically it turns out that $\omega(\pi, 0)$ and $\omega(\pi/2, \pi/2)$ are identical [29]. Evaluating the second order correction for $\mathbf{Q}_{2\mathrm{D}} \rightarrow (\pi, \pi)$, Canali and collaborators further found the second order correction to Z_c. In a subsequent publication [20], the second order corrections to both transverse susceptibility and sublattice magnetization were given. In table 1 we compare the results of Canali and coworkers for the renormalized quantities with those of Igarashi, with series expansions from the Ising limit to be discussed in the next section and with a selected numerical result. To complete the picture, we have computed Z_ρ for the DM spin wave theory assuming the validity of the hydrodynamic relation $Z_\rho = Z_c^2 Z_\chi$.

3.2.2 Excitation spectra in spin wave theories

We now turn to comment on calculations of the transverse and longitudinal scattering functions $S^{+-}(\mathbf{Q}_{2\mathrm{D}}, \omega)$ and $S^{zz}(\mathbf{Q}_{2\mathrm{D}}, \omega)$ relevant for neutron scattering experiments. Within spin wave theories, $S^{+-}(\mathbf{Q}_{2\mathrm{D}}, \omega)$ and $S^{zz}(\mathbf{Q}_{2\mathrm{D}}, \omega)$ hold information on odd-order and even-order magnon processes respectively. They have been computed to order $1/S^2$ both in the HP formalism by Igarashi and by Canali and Wallin using DM. To this order in the spin wave expansion, the transverse scattering function is the sum of a sharp single-magnon contribution and a continuum

Quantum corrections				
Theory	Z_c	Z_χ	Z_ρ	m
Linear SWT	1	1	1	0.303
$1/(2S)$ HP SWT	1.158	0.449	0.765	0.303
$1/(2S)^2$ HP SWT	1.1794 ± 0.0002	0.514 ± 0.001	0.724 ± 0.003	0.3069
$1/S^2$ DM SWT	1.1765 ± 0.0002	0.4844 ± 0.00010	(0.6705 ± 0.00027)	0.3069 ± 0.00020
Series expansion	1.18 ± 0.02	0.52 ± 0.03	0.72 ± 0.04	0.3025 ± 0.0075
QMC				0.30 ± 0.02

Table 1: Numerical values of various quantum corrections. By the definitions (34)-(36) linear spin wave theory yields renormalization factors Z_c, Z_χ and Z_ρ equal to unity. The value for m was given by Anderson [21]. The order $(1/2S)$ Holstein Primakoff results for Z_c and m summarize references [23, 25], while all second order Holstein Primakoff results and the first order results for Z_χ and Z_ρ are taken from [26]. Second order corrected values of Z_c, Z_χ and m, derived using the Dyson-Maleev formalism are from [20, 27, 28]. For completeness, we have supplemented these values with Z_ρ derived by assuming that the hydrodynamic relation $c^2 = \rho_s/\chi_\perp$ remains valid, i.e. by taking $Z_\rho = Z_c^2 Z_\chi$. The series expansion results are found in [30] and QMC results are from [31]. More elaborate comparisons between various theoretical and computational approaches to the 2DQHAFSL are given in the review paper [14].

contribution from three-magnon processes, whereas the longitudinal scattering function consist of antiferromagnetic Bragg peaks and two-magnon continuum contribution

$$S^{+-}(\mathbf{Q}_{2D},\omega) = S_1(\mathbf{Q}_{2D})\,\delta(\omega-\omega_{\boldsymbol{q}}) + S_3(\mathbf{Q}_{2D},\omega) \quad (39)$$

$$S^{zz}(\mathbf{Q}_{2D},\omega) = S_0\,\delta(\omega)\,\delta(\mathbf{Q}_{2D}-(\pi,\pi)) + S_2\,(\mathbf{Q}_{2D},\omega) \quad (40)$$

Here $\omega_{\boldsymbol{q}}$ is the dispersion calculated to the same order in $1/S$ [26, 28].

Igarashi studied $S^{+-}(\mathbf{Q}_{2D},\omega)$ and $S^{zz}(\mathbf{Q}_{2D},\omega)$ in HP spin wave theory for wavevectors inside the antiferromagnetic zone boundary [32]. As it does in linear spin wave theory (see Appendix A), the single-magnon intensity $S_1(\mathbf{Q}_{2D})$ diverges near $\mathbf{Q}_{2D} = (\pi,\pi)$. Going to second order in $1/S$ does not remove this leading divergence, but introduces minor corrections into its detailed $\mathbf{Q}_{2D}$-dependence. More interesting is the three-magnon continuum $S_3(\mathbf{Q}_{2D},\omega)$. As one would naively expect for three-magnon processes it is nonzero only for energies above the sharp one-magnon branch $\omega_{\boldsymbol{q}}$ and has an upper energy limit of three times the zone boundary energy $2Z_cJ$. Whereas $S_3(\mathbf{Q}_{2D},\omega)$ is broad in energy, it is featureless as a function of $\mathbf{Q}_{2D}$ and remains finite in the limit $\mathbf{Q}_{2D} \to (\pi,\pi)$. For the particular wavevector $\mathbf{Q}_{2D} = (\pi, 31/160\pi)$ close to the zone boundary point $(\pi,0)$ the single-magnon energy is close to its limiting value $2Z_cJ$ and $S_3((\pi,31/160\pi),\omega)$ peaks around $1.6 \times 2Z_cJ$. The ratio of the energy-integrated three-magnon intensity to the single-magnon intensity is $S_3((\pi,31/160\pi))/S_1((\pi,31/160\pi)) = 0.376$. By contrast, for a wavevector close to (π,π), Igarashi finds a lower ratio $S_3((\pi,143/160\pi))/S_1((\pi,143/160\pi)) = 0.132$, showing that three-magnon processes are more important near the ZB. Generally speaking, the integrated three-magnon intensities $S_3(\mathbf{Q}_{2D})$ were found to be an order of magnitude smaller than the single-magnon intensities $S_1(\mathbf{Q}_{2D})$.

The inelastic part $S_2(\mathbf{Q}_{2D},\omega)$ of the longitudinal scattering function was found to be nonzero only at energies above $\omega_{\boldsymbol{q}}$ and to extend to twice the zone-boundary energy, as expected for two-magnon processes. For all wavevectors, $S_2(\mathbf{Q}_{2D},\omega)$ peaks just above the single-magnon branch. As a function of $\mathbf{Q}_{2D}$ at constant ω, $S_2(\mathbf{Q}_{2D},\omega)$ therefore has peaks immediately inside the dispersion cone. The intensity along this maximum increases as $(\mathbf{Q}_{2D}-(\pi,\pi))^{-1}$ in the limit $\mathbf{Q}_{2D} \to (\pi,\pi)$. At high energies and near the zone boundary, the numerically evaluated $S_2(\mathbf{Q}_{2D},\omega)$ becomes negative. Igarashi attributes this failure to a breakdown in the convergence of the $1/S$ expansion at high $\mathbf{Q}_{2D}$ and ω.

Canali and Wallin used the DM spin wave theory to study $S^{+-}(\mathbf{Q}_{2D},\omega)$ and $S^{zz}(\mathbf{Q}_{2D},\omega)$ at all wavevectors in the Brillouin zone [20]. The main features of their results are similar to those of Igarashi [32], but there are also differences, in particular for the longitudinal two-magnon response. The transverse scattering $S^{+-}(\mathbf{Q}_{2D},\omega)$ consist of a delta-function at $\omega_{\boldsymbol{q}}$ and for $\omega \geq \omega_{\boldsymbol{q}}$ a broad sideband of three-magnon excitations extending to a maximum of three times the zone boundary energy. As in [26], the leading term in the $\mathbf{Q}_{2D}$-dependence of the one-magnon spectral weight is identical to that derived from linear spin wave theory. The inclusion of higher order terms in the

spin wave expansion renormalizes the perpendicular susceptibility by $Z_\chi < 1$, and as a direct consequence the one-magnon intensity drops. The energy integrated intensity of the three-magnon continuum is negligible near the nuclear and magnetic Bragg positions $(2\pi, 0)$ and (π, π) but rises as the zone boundary is approached. The ratio $S_3(\mathbf{Q}_{2D})/S_1(\mathbf{Q}_{2D})$ was evaluated at several wavevectors including $(\pi, \pi/5) \simeq (\pi, 0)$ and $(\pi/2, \pi/2)$. For both of these wavevectors $S_3(\mathbf{Q}_{2D})/S_1(\mathbf{Q}_{2D})) \simeq 0.23$. We can compare this result directly with $S_3((\pi, 31/160\pi))/S_1((\pi, 31/160\pi)) = 0.376$ from [32] to learn that the three-magnon cross-section near the ZB is about 50% larger in the HP spin wave theory. The same effect is seen near (π, π) although the data in [20] and [32] are not as directly comparable in this case. Despite this quantitative disagreement, it is noteworthy that just as in the HP case, the DM result for $S_3((\pi, \pi/5))$ is peaked around 1.5 times the zone boundary energy, and that the same holds true for the three-magnon response at $(\pi/2, \pi/2)$.

The longitudinal scattering function $S^{zz}(\mathbf{Q}_{2D}, \omega)$ calculated to first order in the DM spin wave theory has a double-peak structure, with one sharp peak located at the position $\omega_{\boldsymbol{q}}$ of the single-magnon mode and another − attributed to a resonant two-magnon process − between $\omega_{\boldsymbol{q}}$ and twice the zone boundary energy. Without magnon-magnon interactions, the high-energy peak is the most intense, but inclusion of interactions reduces its spectral weight to the point that for some wavevectors it becomes hardly visible in the longitudinal spectrum. However, this washing-out effect induced by interaction is less effective near the zone boundary and the high-energy peak survives here. In particular, $S^{zz}(\mathbf{Q}_{2D}, \omega)$ is predicted to display secondary peaks around 1.7 and 1.4 times the zone boundary energy at the wavevectors $(\pi, 0)$ and $(\pi/2, \pi/2)$ respectively. Finally, we mention that near $\mathbf{Q}_{2D} = (\pi, \pi)$ the high-energy peak merges with the low-energy peak at $\omega_{\boldsymbol{q}}$ to give the expected elastic Bragg peak.

3.2.3 Series expansions from the Ising limit

In a number of papers [19, 30, 33, 34], R. R. P. Singh and coworkers have used series expansion around the Ising limit to estimate thermodynamic properties of the 2DQHAFSL, i.e. they expand around the Ising limit $\alpha = 0$ of the Hamiltonian

$$H = J \sum_{\langle \boldsymbol{i}, \boldsymbol{j} \rangle} S_i^z S_{\boldsymbol{j}}^z + \alpha (S_i^x S_{\boldsymbol{j}}^x + S_i^y S_{\boldsymbol{j}}^y). \tag{41}$$

In [19, 30], this method was employed to calculate m as well as Z_χ and Z_ρ. Then, using the series in α for $\chi_\perp$ and ρ_s and assuming the validity of the hydrodynamic relation $c^2 = \rho_s/\chi_\perp$ an estimate of the renormalization factor Z_c was obtained. These results are listed in table 1 and compare very well with the results obtained from the Holstein Primakoff [26] spin wave theory. For Z_c and m the agreement is also good with the results from the Dyson-Maleev [20, 27, 28] versions of spin wave theory. However, in this case, the agreement with Z_χ (and consequently with the derived quantity Z_ρ) is less impressive. In order to obtain a consistent picture, this discrepancy deserves further theoretical attention.

From the point of view of our experiments the most relevant papers are [33] and [34], in which direct information about the spin excitation spectra is extracted. In [33] the transverse equal-time structure factor $S^\perp(\mathbf{Q}_{2D}) = \sum_{\boldsymbol{r}} \exp(i\mathbf{Q}_{2D} \cdot \mathbf{r}) \langle S_{\mathbf{0}}^x S_{\boldsymbol{r}}^x + S_{\mathbf{0}}^y S_{\boldsymbol{r}}^y \rangle$ was computed using the so-called single-mode approximation, which assumes that the spectral weight present in the frequency-dependent spectrum $S^\perp(\mathbf{Q}_{2D}, \omega)$ − which is not computed − is due to single-magnon processes only. Because of the nature of the single-mode approximation, these calculations yield only an upper bound on the spin wave energies, and therefore also on the renormalization factor Z_c. Indeed the values resulting from extrapolations of Z_c near $\mathbf{Q}_{2D} = (0, 0)$ ($Z_c = 1.44 \pm 0.1$) and $\mathbf{Q}_{2D} = (\pi, \pi)$ ($Z_c = 1.36 \pm 0.13$) are substantially larger than the more direct estimates from series expansion ($Z_c = 1.18 \pm 0.02$ [19, 30]) and spin wave theory [26, 28] given in table 1. Considering the excellent correspondence between Z_c evaluated by various techniques, the large Z_c-values found using the single-mode approximation, implies that this method fails rather badly for the 2DQHAFSL, and that consequently a non-negligible fraction of the total transverse spectral weight $S^\perp(\mathbf{Q}_{2D}, \omega)$ must be assigned to multimagnon processes.

In a subsequent paper by Singh and Gelfand [34] the full single-magnon dispersion $\omega_{\boldsymbol{q}}$ was computed to tenth order in the expansion parameter α. They found that the dispersion along the line $H = K$ is nearly uniformly renormalized with respect to the linear spin wave result Eq. (37). By extrapolation to $\mathbf{Q}_{2D} = (0, 0)$, they obtained the renormalization factor $Z_c \simeq 1.18$ in agreement with the more direct series evaluations in [30]. By contrast, along the antiferromagnetic

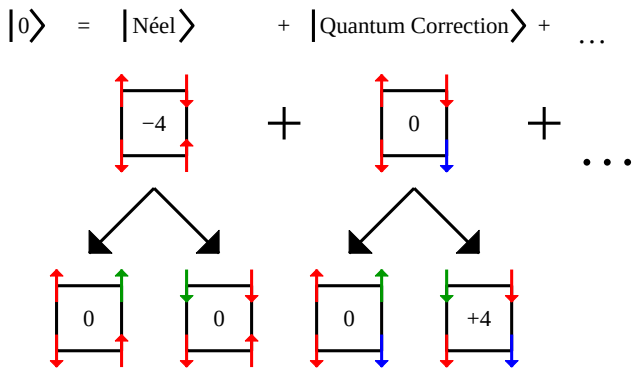

Figure 7: Origin of the zone boundary dispersion (adapted from [35]) in the 2DQHAFSL. Since the Néel state is not the ground state of the 2D Heisenberg model, but on the other hand not such a bad approximation, it is sensible to take a perturbative approach and add correction terms denoted |Quantum Correction⟩ to the Néel state |Néel⟩. The leading corrections are terms in which one spin on the plaquette has been flipped relative to the Néel state (blue arrows). Inside each plaquette is written the sum of bond energies with parallel and antiparallel nearest neighbors contributing $+1$ and -1 respectively. Now, consider spin flips away from the states |Néel⟩ and |Quantum Correction⟩. The former are energetically degenerate for spin flips (green arrows) along [10] (black arrows pointing towards the left) and [11] (black arrows pointing towards the right) relative to the site in the lower right corner. By contrast, spin flips along the [10] direction relative to the flipped spin in |Quantum Correction⟩ are less energetic than those along [11] because in the former case, the energy gain of the spin flip is compensated by a loss of bond energy along [10]. The end result is spin waves of larger energy at $(\pi/2, \pi/2)$ than at $(\pi, 0)$.

zone boundary $H + K = \pi$, there is a shallow minimum at $\mathbf{Q}_{2D} = (\pi, 0)$ where the single-magnon energy is about 7% lower than at the center of the zone boundary $\mathbf{Q}_{2D} = (\pi/2, \pi/2)$, implying the existence of a dispersion in the single-magnon energies along the antiferromagnetic zone boundary. As we saw previously, such a dispersion was also obtained in the DM spin wave theory of Canali, Girvin and Wallin when taken to second order in $1/S$ [28]. It is however important to realize that there exist a subtle difference between the two cases: In [34] the single-magnon energy at $(\pi, 0)$ lies below the linear spin wave dispersion when the latter is uniformly renormalized by $Z_c = 1.18$. By contrast, in [28] it is the spin wave energy at $(\pi/2, \pi/2)$ which lies above the uniformly renormalized curve. Moreover, the magnitude of the ZB dispersion found in [28] is smaller, the energy difference between $(\pi, 0)$ and $(\pi/2, \pi/2)$ being approximately 3%.

The origin of the ZB dispersion can be understood qualitatively by considering the cartoon picture provided in Fig. 7. As we have already seen, the Néel state cannot be the true quantum many-body ground state. Thus, a full understanding of the excitations require at the very least that correction terms be added to the Néel state. Adding correction terms removes the degeneracy between spin waves propagating along the [10] and [11] directions of reciprocal space, with the end result that spin waves become more energetic when propagating along the [11] direction.

In addition to the dispersion $\omega_{\boldsymbol{q}}$, Singh and Gelfand obtained the ratio of the spectral weight of multimagnon excitations to the total transverse spectral weight $S^{\perp}(\mathbf{Q}_{2D})$ previously studied in [33]. This ratio was obtained over the full Brillouin zone, and specifically it was found that at $\mathbf{Q}_{2D} = (\pi, 0)$ the multimagnon weight constitutes roughly $24 \pm 5\%$ of the total spectral weight, whereas the corresponding number at $\mathbf{Q}_{2D} = (\pi/2, \pi/2)$ is $9 \pm 3\%$. Working backwards from the results in [34] we can then deduce that the single-magnon weight at $(\pi, 0)$ is about 80% of the single-magnon weight at $(\pi/2, \pi/2)$, although the combined error bars are not inconsistent with equal single-magnon weights at the two wavevectors. It is noted here because Quantum Monte Carlo (QMC) also provides evidence that the single-magnon weights are different at the two wavevectors, as we shall see below.

3.2.4 Numerical techniques

A very strong piece of evidence that the ground state of the Heisenberg Hamiltonian (30) supports magnetic order comes from numerical work of Reger and Young [31]. These authors used QMC on lattices up to $N \times N = 12 \times 12$ in size and arrived at a value for the ground state staggered magnetization of $m = 0.30 \pm 0.02$, which agrees with both spin wave theory and series expansion results.

Turning to numerical investigations of the excitation spectrum, Syljuåsen and Rønnow [36]

used QMC to calculate the relative energies at $(\pi, 0)$ and $(\pi/2, \pi/2)$ for lattice up to 32×32. Finite-size scaling was then employed to extrapolate to the thermodynamic limit $N \to \infty$. Results were obtained at several temperatures and the results extrapolated to $T = 0$ K, where $\omega(\pi, 0)$ was found to be 6% smaller than $\omega(\pi/2, \pi/2)$. The procedure used to extract the relative energies averages over the longitudinal and transverse fluctuations and this adds to the uncertainty in the ZB dispersion, as does the extrapolations to infinite size and to $T = 0$ K. Even bearing these remarks in mind, the agreement with [34] is quite good. It is important to note that no ZB dispersion was found for lattices smaller than 8×8, as one must then consider it a many-particle effect.

Finally, Sandvik and Singh [37] used state-of-the-art QMC algorithms to study the single-magnon dispersion and amplitude as well as the multimagnon spectrum of the 2DQHAFSL. These results will be discussed further in direct relation to the experimental results presented in chapters 4 and 5. At this stage we shall merely mention that their results indicate a ZB dispersion of $1 - \omega(\pi, 0)/\omega(\pi/2, \pi/2) = 0.1$, accompanied by a decreased spectral weight for single-magnon excitations at $(\pi, 0)$ relative to $(\pi/2, \pi/2)$, and sizeable multimagnon contributions extending to energies much higher than typical zone boundary energies.

3.3 Experimental studies of 2DQHAFSL systems

Convincing evidence that La_2CuO_4, CFTD and other systems are well described by the 2DQHAFSL comes from determination of the components of the spin Hamiltonian by investigation of the spin excitations by neutron scattering and also from experiments probing the temperature dependence of spin-spin correlation length ξ using two-axis neutron scattering. The purpose of this section is to describe these experiments in order to provide the underlying framework in which the experiments reported in chapters 4 and 5 can be understood. However, we start by presenting some puzzling results from Raman scattering [38, 39] and optical absorption [40]. These experiments are drastically add at odds with linear spin wave theory, and introduce what will be a general theme in this section, namely that of further neighbor exchange terms versus multimagnon excitations. Moreover, they add flavor to the issues addressed here by adding the high-T_c parent compound La_2CuO_4 to the equation.

3.3.1 Raman scattering and optical absorption

Raman scattering is a second-order process involving the absorption and subsequent emission (quantum mechanics also allows the time-reversed process where emission precedes absorption) of a photon in an inelastic process where the state of the atomic or electronic system studied is changed. The quantum mechanical operator responsible for the transitions is the electric dipole moment operator. Single dipole transitions are associated with a selection rule $\Delta J = \pm 1$ on the total angular momentum J, so for Raman scattering the selection rule becomes $\Delta J = 0, \pm 2$ [41]. In particular the technique is sensitive to two-magnon scattering but not to single-magnon scattering events which have $\Delta J = 1$. Further, in linear spin wave theory, two-magnon Raman scattering is dominated by zone boundary magnons since the single-magnon density of states has a singularity at the zone boundary energy.

Lyons *et al.* [38] studied the Raman scattering from La_2CuO_4 in the two channels named B_{1g} and A_{1g}. These symbols refer to particular transitions in the photon polarization in the scattering process (see e.g. [42]). The B_{1g} spectrum contained peaks with an unusually broad line shape, inconsistent with linear spin wave theory. When identified as resulting from two-magnon processes these peaks led to a quantitative estimate for the nearest neighbor superexchange J in reasonable agreement with more direct neutron scattering determinations. Lyons *et al.* suggested that the anomalously broad two-magnon peak was explained by strong quantum fluctuations enforced by the combination of low spin and dimensionality in La_2CuO_4. Similar results for the B_{1g} Raman spectra were obtained by Sugai *et al.* [39] who studied five different insulating cuprates (La_2CuO_4, $YBa_2Cu_3O_{6.2}$, $Bi_2Sr_2Ca_{0.5}Y_{0.5}Cu2O_{8+y}$, Nd_2CuO_4 and Pr_2CuO_4) and contrasted their findings in these systems with those obtained on the insulating and isostructural material La_2NiO_4 which has $S = 1$ Ni spins replacing the $S = 1/2$ Cu spins of the cuprates. The B_{1g} cuprate spectra taken at $T = 30$ K were very broad with tails extending to $\sim 8J$, and in addition to the two-magnon peaks discussed in [38] contained secondary peaks at $\sim 4J$. The energy $4J$ is near twice the zone boundary magnon energy which would classically be the cut-off for two-magnon processes in light

scattering experiments. However, when magnon-magnon interactions are taken into account the picture becomes more complex [43]. Sugai and collaborators identified their $4J$ peaks (which were absent in the nickelate) as evidence of four-magnon cyclic exchange (or ring-exchange) processes in which the incident photon causes the spins of four Cu^{2+} ions residing at the corners of an elementary Cu_4O_4 plaquette to exchange their values. In this picture, the high energy tails of the B_{1g} spectra are due to interacting magnons created on four sites which are not all on the same plaquette. A back-of-the-envelope estimate of the ratio of the strength of cyclic exchange $J_\square$ to the nearest neighbor J yields $J_\square/J \sim 0.5$-0.6. Later in this section we shall see that neutron scattering experiments of Coldea *et al.* [44] have since provided direct evidence for the existence of sizeable cyclic exchange terms in the Hamiltonian of La_2CuO_4. The neutron estimate of $J_\square/J = 0.41 \pm 0.07$ at $T = 10$ K ($J_\square/J = 0.27 \pm 0.06$ at $T = 295$ K) is not far off the Raman value. One important aspect of the spin physics of the 2DQHAFSL disregarded in the theoretical foundation behind the analysis of the Raman data is the existence of higher order magnon continua above the single-magnon branches. A full account of the Raman spectra should take such processes into account. At the very least, their neglect would imply that estimates of $J_\square$ remain semiquantitative upper limits. Given such uncertainties, the agreement between the two estimates is astounding.

It is well known and will be discussed further below that one can get the Heisenberg model from the large-U limit of the Hubbard model at half-filling. Roger and Delrieu [45] showed that starting from an extended (three-band) Hubbard model which takes into account the oxygen sites between Cu sites in the cuprates, as well as nearest neighbor Coulomb interactions, one gets a spin Hamiltonian dominated by four-spin ring-exchange terms when taking the $U \to \infty$ limit. With this quartic ring-exchange Hamiltonian, the ground state is magnetically ordered with a sublattice magnetization $m = 0.225 \pm 0.025$ and more importantly, has a Raman spectrum which is in much better accord with experiment, than if one had started from the quadratic Heisenberg model.

Moving on to optical absorption, Perkins *et al.* [40] found several intense bands in transmission spectra from four undoped cuprates (La_2CuO_4, Nd_2CuO_4, Pr_2CuO_4 and $Sr_2CuO_2Cl_2$) which they interpreted as processes where the absorbed photon causes an electron to change its orbital state which in turn causes magnons to be excited via the exchange interactions. In La_2CuO_4 the absorption bands are consistent with one through four-magnon processes, though this identification is not based on rock-solid theory for such processes, but on simplistic arguments. Moreover, when classical theory is applied − as in the case of Raman scattering − it underestimates the peak widths. Subsequent explicit calculations in a model involving lattice vibrations as well as magnon processes reached the conclusion that the high-energy absorption bands are due to multimagnons [46].

3.3.2 Correlation length studies

The theoretical framework underlying studies of the temperature dependence of the correlation length was provided by Chakravary, Halperin and Nelson [47, 48] (CHN) who in this ground-breaking work showed that the 2DQHAFSL can be mapped onto another model − the quantum non-linear sigma model (QNLσM) − in which $\xi(T)$ can be calculated explicitly using renormalization group theory. The theory introduces a coupling constant g, which plays the role of $1/zS$ in spin wave theory and represents the effect of quantum fluctuations in the Néel state. As a function of g and temperature CHN derived the phase diagram shown in figure 8. There are three identifiable regimes separated by a quantum critical point at $g = g_c$ and each characterized by a unique temperature dependence of ξ for which CHN gave explicit mathematical expressions. The three regimes are known as the renormalized classical region, the quantum critical region and the quantum disordered region. The renormalized classical regime stands out by having Néel order at $T = 0$ K (Solid blue line) and CHN found that an isolated Heisenberg layer belongs in this region. The CHN expression for $\xi(T)$ in the renormalized classical regime was later refined by higher precision calculations by Hasenfratz and Niedermayer (CHN-HN), who found that to leading order ξ diverges exponentially in $1/T$ in a manner determined by the spin wave velocity c_s and the spin-stiffness constant ρ_s. Within spin wave theory, c_s and ρ_s are related to J by equations (34) and (35). Since Z_c and Z_ρ in these expressions have been calculated accurately (table 1), it follows that $\xi(T)$ is completely specified if J is a known quantity. In the quantum critical regime $\xi \propto (T - T_{\rho_s})^{-1}$ is expected, with $T_{\rho_s} \to 0$ as $g \to g_c$ and otherwise positive [49]. To complete the picture, a weakly temperature dependent ξ which stays finite as $T \to 0$ is expected in the quantum disordered region. In addition to calculations of $\xi(T)$, CHN also discussed the

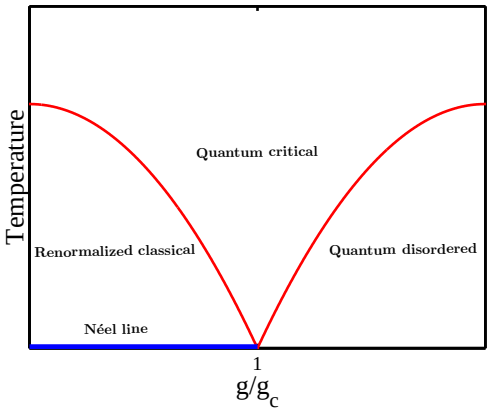

Figure 8: 2DQHAFSL phase diagram by Chakravarty, Halperin and Nelson [47, 48]. The parameter g in a broad sense represents the effect of quantum fluctuations. Below a critical threshold g_c, the system is characterized by Néel order at $T = 0$ K (solid blue line). At temperatures lower than a crossover line above the Néel line, physical observables evolve classically, but their numerical values are renormalized by quantum fluctuations. At $g = g_c$ and $T = 0$ K, there is a transition to a quantum disordered regime existing below another crossover line. Above the two crossover lines, the state of the system is quantum critical. In each of the three separate regions there exists a definite prediction for the temperature dependence of the thermodynamic coherence length ξ as measured in a two-axis neutron scattering experiment.

temperature dependence of the $\mathbf{Q}_{2D} = \mathbf{0}$ limit of the instantaneous spin-spin correlation function $S(\mathbf{Q}_{2D})$ and found $S(\mathbf{Q}_{2D} = \mathbf{0}) \sim \xi(T)^2 T^2$ (CHN express wavevectors relative to the antiferromagnetic zone center, so $\mathbf{0}$ really means $\mathbf{Q}_{2D} = (\pi, \pi)$). Finally, note that the phase diagram offers the possibility of crossovers as a function of temperature from the renormalized classical or quantum disordered regions to the quantum critical regime. Through detailed measurements of the temperature dependences of ξ and $S(\mathbf{0})$ it should be possible to confirm such crossovers.

Experimental data to test the theory are available from two-axis neutron scattering studies of $\xi(T)$ and $S(\mathbf{0})$ in $Sr_2CuO_2Cl_2$ [50, 49], La_2CuO_4 [51, 52] and CFTD [53]. In all these studies a configuration with $\mathbf{k}_f$ perpendicular to the 2D planes was employed. This configuration takes advantage of the fact that for 2D magnets each point in $\mathbf{Q}_{2D}$ space is a rod in $\mathbf{Q}_{3D}$ space. The measured intensity becomes proportional to $\int_{-\infty}^{E_i} S(\mathbf{Q}_{2D}, \omega)\, d\omega$.

This is a natural time and place to mention that while the CHN-HN theory considers $\xi(T)$ to diverge as $T = 0$ K is approached, all real materials considered good approximations to the 2DQHAFSL have small perturbation terms in their Hamiltonians which are responsible for transitions to three dimensional long range order at a finite Néel temperature T_N. The correlation length then diverges at T_N rather than at $T = 0$ K. Moreover, in a critical regime $(T - T_N)/T_N \ll 1$ all terms in the Hamiltonian affect the temperature dependence of ξ, and so the CHN-HN theory loses its predictive power. Thus experiments to compare the CHN-HN theory with real antiferromagnets are performed at temperatures above T_N and outside the critical regime.

For completeness, we should also mention how the 2D antiferromagnets discussed in this chapter go about developing three-dimensional antiferromagnetic order despite the fact that their interplane exchange couplings are perhaps four or five orders of magnitude weaker than the dominant nearest neighbor exchange J. A rough mathematical criterion for the temperature at which the transition occurs may be formulated: If α_{eff} is a suitably defined combined measure of the magnitudes of small perturbing terms in the Hamiltonian, measured in units of J, and the correlation length $\xi(T)$ is expressed in units of the lattice constant, then we expect T_N to be given approximately by $\alpha_{\text{eff}}\xi(T_N)^2 \sim 1$ [51]. This so-called "pancake" argument expresses the physical reality that no matter how small the interplane coupling becomes, the exponential divergence of $\xi(T)$ always wins. If $\alpha_{\text{eff}}\xi(T)^2$ is viewed as an effective coupling summed over the correlated area, the pancake argument says 3D order occurs when this number becomes of order one.

Greven *et al.* [50, 49] found excellent quantitative agreement between $\xi(T)$ for $Sr_2CuO_2Cl_2$ and Monte Carlo simulations. Taking $J = 125$ meV from two-magnon Raman scattering, both agree with the CHN-HN expression for ξ in the renormalized classical regime without any adjustable parameters. No crossover to quantum critical behavior could be discerned. By contrast their finding $S(\mathbf{0}) \sim \xi^2$ does not agree with the CHN prediction $S(\mathbf{0}) \sim \xi^2 T^2$, but is in agreement with data on both the $S = 1$ system K_2NiF_4 [49] and with early experiments by Keimer *et al.* on

La_2CuO_4 [51]. Birgeneau and coworkers [52] improved on the latter La_2CuO_4 studies by taking data at a series of incident energies E_i to ensure that integration over all relevant fluctuations $S(\mathbf{Q}_{2D}, \omega)$ is properly performed in the two-axis geometry. Their findings closely parallel those of [49] and agree within errors with the $\xi(T)$ data reported in [51]. With $J = 135$ meV taken from studies of the spin wave spectrum of La_2CuO_4 [54], the correlation length in La_2CuO_4 is fully accounted for with no adjustable parameters by the CHN-HN expression for $\xi(T)$ in the renormalized classical regime. In particular there was no hint of a crossover to quantum critical behavior. Further, the behavior $S(\mathbf{0}) \sim \xi^2$ agrees with [49], although the door is kept open for a possible crossover from $S(\mathbf{0}) \sim \xi^2 T^2$ to $S(\mathbf{0}) \sim \xi^2$ as a function of increasing temperature. Rønnow *et al.* investigated $\xi(T)$ and $S(\mathbf{0})$ in CFTD [53]. CFTD has the significant advantage over $Sr_2CuO_2Cl_2$ and La_2CuO_4 that the exchange energy $J = 6.3$ meV known from spin wave studies is much lower than the typical $J \sim 1500$ K common to the cuprates. This enabled Rønnow *et al.* to study $\xi(T)$ and $S(\mathbf{0})$ over a much broader range in T/J than had previously been possible, and in particular extending to $T \geq J$. While the temperature dependence of ξ was once again found to be consistent with QMC and the CHN-HN expression but with no suggestion of crossover to quantum criticality, that of $S(\mathbf{0})$ differed from $S(\mathbf{0}) \sim \xi^2$ as found in [49] and [52]. Instead the CHN prediction $S(\mathbf{0}) \sim \xi^2 T^2$ was consistent with the data.

Summing up, there is a very impressive agreement between the experimental $\xi(T)$ data from three materials $Sr_2CuO_2Cl_2$, La_2CuO_4 and CFTD and the CHN-HN expression, valid in the renormalized classical region of the phase diagram. There are no adjustable parameters involved in either case, and the agreement is excellent over a large combined span in T/J. However, in neither case is the expected crossover behavior seen. One possible explanation is that the crossover is really a property of the QNLσ (continuum) model. It may or may not occur for spins confined to 2D lattice sites [52]. If the mapping of the 2DQHAFSL onto the QNLσM breaks down before the crossover occurs in the latter, then its experimental absence is naturally explained. The overall picture concerning $S(\mathbf{0})$ is more ambiguous, and further experiments on other materials are probably needed to clarify why $S(\mathbf{0}) \sim \xi^2$ in $Sr_2CuO_2Cl_2$ while in CFTD the CHN expectation $S(\mathbf{0}) \sim \xi^2 T^2$ appears to be realized.

3.3.3 Single-magnon excitation spectrum

Three papers have been published in which the single-magnon part of the excitation spectrum of supposed $S = 1/2$, square lattice Heisenberg antiferromagnets have been measured. We shall take a little space to discuss these results as they have generated substantial interest and taken together emphasize a question of great importance to theories regarding high-T_c, namely which theoretical model is the correct starting point for a description of these systems. We start by discussing $Sr_2Cu_3O_4Cl_2$ [55], then CFTD [56] and finally move on to La_2CuO_4 [44].

$Sr_2Cu_3O_4Cl_2$ [55] is a complex material consisting of two interpenetrating square sublattices (Cu_I and Cu_{II}) of $Cu^{2+}, S = 1/2$ ions. Each sublattice, when considered in isolation is described by Eq. (30). It so happens that the molecular fields created by one sublattice vanishes on any site belonging to the other sublattice. This implies that classically one sublattice does not know about the existence of the other, and therefore they are free to order independently of each other, giving rise to a degenerate ground state and two sets of Goldstone modes, reflecting that the energy cost of rotating all spins on a given sublattice is zero. A more elaborate treatment reveals that the degeneracy can be lifted by quantum fluctuations [57] or by disorder or thermal fluctuations [58], creating a gap in the excitation spectrum. This order-from-disorder physics makes $Sr_2Cu_3O_4Cl_2$ very interesting from the viewpoint of fundamental quantum magnetism and is the main focal point of [55]. The Cu_I sublattice orders three dimensionally at $T_{N,I} = 385 \pm 2$ K, while the Cu_{II} sublattice remains disordered down to a lower temperature $T_{N,II} = 40.0 \pm 0.2$ K. In the phase where only the Cu_I spins are ordered, the predominantly transverse fluctuations in their moment direction lead to an effective Ising anisotropy in the inter-sublattice exchange couplings, which in turn favors colinear ordering of the Cu_{II} spins with the Cu_I spins below $T_{N,II}$.

The spin excitation spectrum was studied in a $T = 0$ K spin wave theory in which intersublattice interactions are expanded to fourth order to incorporate spin wave interactions. Using this model, Kim *et al.* were able to obtain a consistent description of the experimental spin wave spectra both for $T < T_{N,II}$ and for $T_{N,I} > T > T_{N,II}$. The fluctuation driven gap predicted by theory [57] is seen directly at the 2D magnetic zone center. In addition, the single-magnon dispersion of the low temperature phase was measured along the symmetry directions in the 2D reciprocal

space of the Cu_{II} sublattice. From the zone boundary energy, the value $J_{II} = 10.5$ meV was deduced for the exchange coupling within sublattice II. The most interesting feature in the single-magnon spectrum of $Sr_2Cu_3O_4Cl_2$ is a zone boundary dispersion between $(\pi, 0)$ and $(\pi/2, \pi/2)$. Its magnitude $1 - \omega(\pi, 0)/\omega(\pi/2, \pi/2) = 0.07$ is in perfect agreement with the series expansion results discussed in section 3.2.3, and indeed the whole single-magnon spectrum could be well modeled with $J_{II} = 10.5$ meV using the dispersion given in [34].

This was the first observation of a ZB dispersion in a material thought to well described by the 2DQHAFSL. However, the observed zone boundary dispersion can also be explained within the bounds of linear spin wave theory in case a nonzero antiferromagnetic next-nearest neighbor (NNN) interaction $J_{II,NNN}$ exists. The experiment [55] did not offer any possibility for making a distinction between the two cases, but Kim *et al.* rejected this explanation on the grounds that the sheer magnitude of the measured energy difference between $(\pi, 0)$ and $(\pi/2, \pi/2)$ − which within linear spin wave theory is related to $J_{II,NNN}$ − is inconsistent with a $J_{II} = 10.5$ meV which is already low and a $J_{II,NNN}$ which must be substantially lower than J_{II} because of the larger NNN distance between Cu_{II} sites.

The first experiments designed to determine the full spin wave dispersion and exchange constants of CFTD were carried out by Clarke *et al.* [59]. With the sample oriented with the 2D-planes in the horizontal scattering plane, they determined the single-magnon dispersion along $\mathbf{b}^*$, which in CFTD is equivalent to the [11] direction of 2D reciprocal space. From a least-squares fit to the measured dispersion, the in-plane exchange integral was determined to be $J = 6.3 \pm 0.2$ meV after correcting for higher order terms in the $1/(2S)$ expansion by assuming $Z_c = 1.18$. This result agrees well with $J = 6.1 \pm 0.1$ meV deduced from dc-susceptibility measurements [60] to be discussed further in section 3.4. An experimentally observed gap of magnitude $\Delta = 0.38 \pm 0.02$ meV at the zone center $\mathbf{Q}_{2D} = (\pi, \pi)$ was included in the fit. While Clarke *et al.* were unable to determine its origin because polarization analysis was not available to them, they argued that a Dzyaloshinsky-Moriya antisymmetric exchange interaction $\mathbf{D} \cdot \mathbf{S}_i \times \mathbf{S}_j$ is the most likely cause. Such a term had previously been proposed to explain susceptibility data in CFTD [61].

Extending on the experiments in [59], Rønnow an coworkers [56] used time-of-flight neutron scattering to study the excitation spectrum in a larger portion of 2D reciprocal space. The instrument used was HET at ISIS. This matters because at the time of the experiment, the **Q**-resolution of HET was much worse than that presently attainable at MAPS. In particular, measurements of the spin wave spectrum along the zone boundary from $\mathbf{Q}_{2D} = (\pi, 0)$ to $\mathbf{Q}_{2D} = (\pi/2, \pi/2)$ were not possible. This turned out to be an important restriction since − just as in $Sr_2Cu_3O_4Cl_2$ − a pronounced dip of relative magnitude $1 - \omega(\pi, 0)/\omega(\pi/2, \pi/2) = 0.06 \pm 0.01$ was discovered in the single-magnon energy at $\mathbf{Q}_{2D} = (\pi, 0)$. Along the [11] direction in 2D reciprocal space, the measured dispersion agreed well with linear spin wave theory. Once again assuming $Z_c = 1.18$, the data taken along this direction lead to $J = 6.31 \pm 0.02$ meV in agreement with [59]. Further, if one uses classical theory to fit high-temperature susceptibility data it is possible to obtain an estimate of J directly, and then to deduce the quantum renormalization factor from the ratio $Z_c = J_{\text{eff}}/J$. Using this approach Rønnow *et al.* found $Z_c = 1.21 \pm 0.05$, in agreement with the theoretical values given in table 1.

As in the case of $Sr_2Cu_3O_4Cl_2$, the authors of [53] note that their observed ZB dispersion could also be attributed to finite antiferromagnetic NNN interactions (of magnitude $J' \simeq 0.06J$). However, both the QMC data [36] discussed in section 3.2.4 and exact diagonalizations of $\sqrt{32} \times \sqrt{32}$ spin clusters yield finite energy differences between $\mathbf{Q}_{2D} = (\pi, 0)$ and $\mathbf{Q}_{2D} = (\pi/2, \pi/2)$. The QMC calculations extrapolate to a 6% ZB dispersion while the exact diagonalization yields 4.8%. Further, the observed ZB dispersion could be fitted very well using the series expansions of Singh and Gelfand [34] of the pure, nearest neighbor problem. All these results suggest that one should interpret the ZB dispersion as a true quantum effect of the 2DQHAFSL rather than resulting from additional terms in the Hamiltonian. There may still be finite NNN interactions, but by Occams razor we should not take them into account when explaining the ZB dispersions observed in $Sr_2Cu_3O_4Cl_2$ and CFTD. Finally, it is worth noting that neither QMC nor exact diagonalization give a ZB dispersion if applied to small lattice sizes. Consequently, understanding the microscopics of the effect requires consideration of many spins.

In the high-T_c parent compound La_2CuO_4, an early set of experiments by Hayden, Aeppli and coworkers had combined triple axis [54, 62] and time-of-flight [63] neutron scattering to establish the existence of well defined spin waves throughout the Brillouin zone. However, the **Q**-resolution in these experiments was coarse, and so it was impossible to resolve any dispersion along the zone-

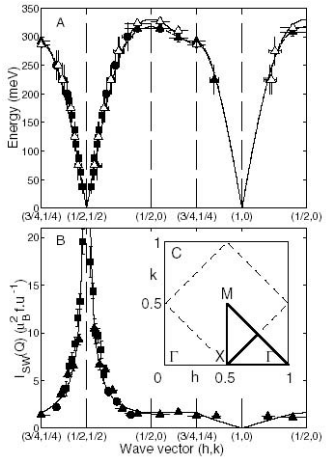

Figure 9: Single-magnon dispersion (A) and intensity (B) in La_2CuO_4 from [44] for $T = 10$ K (open symbols) and $T = 295$ K (closed symbols) along the path of square lattice reciprocal space illustrated in the inset (C). The different types of symbols correspond to the three different incident energies employed.

boundary. Since further neighbor exchange terms have their largest effect for wavevectors along the zone boundary, only an upper bound could be placed on their magnitude.

With the appearance of time-of-flight spectrometers equipped with position sensitive detectors, the **Q**-resolution attainable has improved dramatically, and so Coldea *et al.* [44] revisited the single-magnon spectrum in La_2CuO_4 to search for such further neighbor exchange terms. The result of the experiment was a determination of the spin wave dispersion and intensities over the entire Brillouin zone, see figure 9. Here too, a ZB dispersion was identified, but contrary to the observations in $Sr_2Cu_3O_4Cl_2$ and CFTD the magnon energy at $\mathbf{Q}_{2D} = (\pi, 0)$ was now higher than that at $\mathbf{Q}_{2D} = (\pi/2, \pi/2)$. In other words, the zone boundary dispersion in La_2CuO_4 has the opposite sign. Its magnitude at $T = 10$ K was $1 - \omega(\pi/2, \pi/2)/\omega(\pi, 0) = 0.13$, dropping to 0.08 at $T = 295$ K.

As explained by Coldea *et al.* the measured dispersion is perfectly consistent with the Heisenberg model supplemented by ferromagnetic NNN interactions. However, a more satisfactory explanation can be obtained if one starts from the one-band Hubbard model

$$H_{\text{Hubbard}} = -t \sum_{\langle i,j\rangle,\sigma} (c^\dagger_{i\sigma} c_{j\sigma} + \text{H.c.}) + U \sum_i n_{i\uparrow} n_{i\downarrow} \tag{42}$$

Here $c^\dagger_{i\sigma}$ ($c_{i\sigma}$) creates (annihilates) an electron with spin $\sigma \in \{\uparrow, \downarrow\}$ at site number i and the first summation is over nearest neighbor sites of the square lattice. The operator $n_{i\sigma} = c^\dagger_{i\sigma} c_{i\sigma}$ counts the number of electrons in the spin state σ at site i. The first term in (42) describes hopping of electrons between neighboring sites, while the second represents the energy penalty for having two electrons with opposite spins on the same site. When U is very large, electron hopping is entirely suppressed in the half-filled case (where the number of electrons is equal to the number of sites), and the only remaining degrees of freedom are the spins of the localized electrons. It is well known that in the large-U limit a second order perturbation expansion of Eq. (42) leads to antiferromagnetic Heisenberg interactions (see e.g. [22]) with $J = 4t^2/U$. For finite t/U, further neighbor quadratic interactions and more complex terms obtain when the perturbation expansion is continued to progressively higher order in t/U. The terms of the expansion involve electrons virtually hopping around the lattice, reaching sites further and further from their starting point before returning home. Coldea *et al.* considered an expansion of H_{Hubbard} to fourth order in t/U. In this manner they obtained nearest neighbor, next-nearest neighbor, third-nearest neighbor and ring-exchange interactions J, J', J'' and $J_\square$. The ring-exchange interaction derives from an electron taking a trip around an elementary Cu_4O_4 plaquette and is expressed as a biquadratic term

$$H_\square = J_\square \sum_{\langle i,j,k,l\rangle} \left[(\mathbf{S}_i \cdot \mathbf{S}_j)(\mathbf{S}_k \cdot \mathbf{S}_l) + (\mathbf{S}_i \cdot \mathbf{S}_l)(\mathbf{S}_k \cdot \mathbf{S}_j) - (\mathbf{S}_i \cdot \mathbf{S}_k)(\mathbf{S}_j \cdot \mathbf{S}_l) \right] \tag{43}$$

in the spin Hamiltonian. Here, sites i through l are labeled clockwise around a plaquette. The spin

interaction parameters J, J', J'' and $J_\square$ are in turn expressed in terms of the electronic parameters t and U.

Including the quantum renormalization Z_c and performing a fit with J and $J_\square$ as free parameters ($J' = J'' = J_\square/20$ according to the perturbation expansion relations between U and t and the spin exchange parameters) lead to excellent agreement with the data for both the dispersion and the single-magnon intensities over the entire Brillouin zone at both $T = 10$ K and $T = 295$ K, as can be seen in Fig. 9. From the fitted exchange constants, U and t could be derived. At $T = 10$ K, the results $J = 146.3 \pm 4$ meV and $J_\square = 61 \pm 8$ meV ($J' = J'' = 3.1 \pm 0.4$ meV) correspond to $t = 0.30 \pm 0.02$ eV and $U = 2.2 \pm 0.4$ eV ($U/t = 7.3 \pm 1.4$). The data obtained at $T = 295$ K lead to $J = 138.3 \pm 4$ meV and $J_\square = 38 \pm 8$ meV ($J' = J'' = 2 \pm 0.5$ meV) and this corresponds to $t = 0.33 \pm 0.02$ eV and $U = 2.9 \pm 0.4$ eV ($U/t = 8.8 \pm 1.3$). These values of t and U are in excellent agreement with values derived from ARPES and optical spectroscopy − techniques which are directly sensitive to these electronic parameters. Incidentally, the nearest neighbor exchange at $T = 295$ K, $J = 138.3 \pm 4$ meV agrees well with the room temperature value $J = 132 \pm 4$ meV derived from the pure Heisenberg model renormalized by $Z_c = 1.18$ in [63], showing that the inclusion of a significant ring-exchange interaction does not lead to large changes in value of the nearest neighbor exchange.

The situation is this: A good description of the data can be obtained both within a J-J' spin-based model, and via a perturbation expansion of the electron-based Hubbard model, leading to an effective spin Hamiltonian with ring-exchange interactions. Coldea *et al.* list several reasons why the latter explanation is preferable: First, a ferromagnetic J' is at odds with theoretical suggestions that J' should be antiferromagnetic. Second, the Raman scattering and infrared absorption data discussed in section 3.3.1 displayed widths in frequency which could not be accounted for by the pure Heisenberg model. In this connection finite ring-exchange were suggested as a possible cause although multimagnons were also a recurrent theme. Third, numerical work had suggested $J_\square/J = 0.3$, similar to the experimental value 0.27 ± 0.06 ($T = 295$ K). Fourth, the exchange energies in the spin ladder compound $Sr_{14}Cu_{24}O_{41}$, which may be viewed as stacked Cu_4O_4 plaquettes, are most easily rationalized if a finite ring-exchange is included. Finally, the impressive agreement of neutron scattering − a charge-neutral spectroscopic tool − with the results of direct charge probes for t and U is an additional argument for preferring the Hubbard model as a starting point.

Following the experiment by Coldea *et al.* , Goff and coworkers have attempted to find evidence for the existence of ring-exchange in La_2CuO_4 by studying the diffuse magnetic scattering in $S(\mathbf{Q}_{2D})$ above T_N, using polarization analysis to separate the magnetic signal from incoherent and nuclear scattering in a manner less crude than is possible without polarization analysis. So far, the results of these experiments are suggestive but not conclusive concerning the existence of a ring-exchange in La_2CuO_4 [64].

Figure 10 shows in a qualitative manner how one may think of the ZB dispersion in La_2CuO_4 . This is the analogy of Fig. 7, but starts from the Hubbard model Eq. (42) since t and U are the dominant energy scales. In this case, we take doubly occupied sites as the correction terms to the Néel state. Taking the kinetic energy associated with electrons jumping to the unoccupied site into account, one finds that spin waves propagating along [10] are the most energetic.

3.3.4 Reactions and consequences

Next, we shall mention some responses to work on $Sr_2Cu_3O_4Cl_2$ [55], CFTD [56] and − mostly − La_2CuO_4 [44]. The most immediate consequence of the results reported in [44] and perhaps the most important is theoretical and has to do with identifying the minimal model for understanding high-T_c superconductivity in the cuprates. The two favored models (see e.g. [65]) are the Hubbard model Eq. (42) and the so-called t-J model (see e.g. [65, 66]). The latter is obtained from the Hubbard Hamiltonian by projecting out doubly-occupied sites to find a Hamiltonian of the form

$$H_{t-J} = \sum_{ij\sigma} t_{ij}\, c^\dagger_{i\sigma} c_{j\sigma} + \sum_{\langle ij \rangle} J_{ij}\, \mathbf{S}_i \cdot \mathbf{S}_j \tag{44}$$

where for generality allowance has been made for hopping terms beyond the nearest neighbor hopping t appearing in (42). Since the experiments of Coldea *et al.* show that t/U is non-zero, the disregard of double-occupancy underlying (44) is problematic at best, and the Hubbard model should be a more natural point of departure.

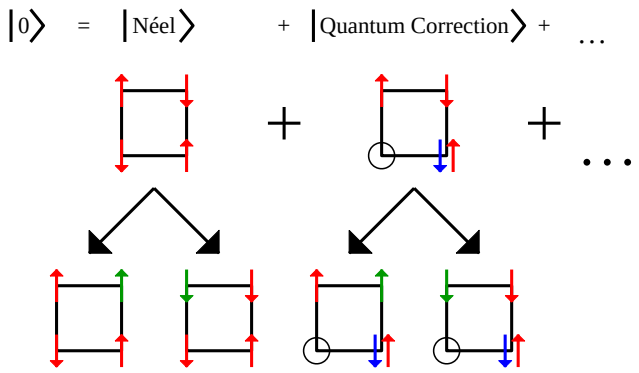

Figure 10: Origin of the zone boundary dispersion in La_2CuO_4 (adapted from [35]). In this case, if the U in Hubbard model is finite, there will be corrections to the Néel state involving pairs of doubly occupied and unoccupied sites, the latter represented here by circles. As in Fig. 7, the spin waves from the Néel state have the same energy whether they propagate along [10] (black arrows pointing towards the left) or along [11] (black arrows pointing towards the right) relative to the site in the lower right corner. The difference to the case of CFTD lies in the possibility that the (green) electron whose spin is flipped can jump back to the unoccupied site when it is displaced along [11] relative to the doubly occupied site. This possibility does not exist if the flipped spin is displaced along [10] from the doubly occupied site. This leads to a reduction in kinetic energy for spin waves propagating along [11] relative to those along [10]. In this case the magnon energy at $(\pi/2, \pi/2)$ is smaller than at $(\pi, 0)$.

Another of the fundamental questions of the high-T_c problem is why hole-doping and electron-doping are different: Starting from the antiferromagnetic parent compounds, one can dope either holes (as in e.g. $La_{2-x}Sr_xCuO_4$) or electrons (as in e.g. $Nd_{2-x}Ce_xCuO_4$) into the CuO_2 planes. The evidence is that the antiferromagnetic state is much more robust to electron doping than it is to hole-doping. For example, a hole concentration of $\sim 2\%$ is sufficient to suppress the commensurate antiferromagnetism of La_2CuO_4 whereas electron doping levels as high as $\sim 15\%$ are needed in $Nd_{2-x}Ce_xCuO_4$. How can this behavior arise from the particle-hole symmetric Hamiltonian (42)? It has been shown that supplementing Eq. (42) by a next-nearest neighbor electron hopping term, one can obtain − using realistic parameters − a phase diagram with the correct doping asymmetry. However, if a finite t' hopping term is present, the parameters derived from a Hubbard model treatment of the spin wave spectrum will be different from those obtained without t'-processes. Following this line of reasoning, A. Singh and Goswami [67] used an RPA approach to fit the experimental spin wave spectrum of La_2CuO_4 given in [44]. They find that for wavevectors along the zone-boundary, there are two competing effects, each of which by itself leads to a ZB dispersion between $(\pi, 0)$ and $(\pi/2, \pi/2)$. First, double occupancy effects of order $(t/U)^2$ lead to $\hbar\omega(\pi, 0) > \hbar\omega(\pi/2, \pi/2)$. Second, competing interaction effects ("competing" since t' leads to an antiferromagnetic NNN exchange interaction J' which in turn enhances quantum fluctuations in the Néel state and thus competes with the effect of J) of order $(t'/t)^2$ lead to the opposite behavior, $\hbar\omega(\pi, 0) < \hbar\omega(\pi/2, \pi/2)$. For the relevant regime of t/U and t'/t, Singh and Goswami find that these two effects are of comparable order of magnitude. From the experimental observation $\hbar\omega(\pi, 0) > \hbar\omega(\pi/2, \pi/2)$ in La_2CuO_4, it follows that double-occupancy effects are dominant in this material. Having established this, the energy difference between $(\pi, 0)$ and $(\pi/2, \pi/2)$ can be used to obtain an upper bound $t'/t \sim 0.3$. Thus, in order to neutralize the effect of competing interactions, t/U must be even larger than estimated in [44]. Explicit analysis assuming $|t'/t| = 0.25$ yields $U/t = 6.7$, $t = 0.34$ eV and $U = 2.3$ eV. Compared with [44] where $t' = 0$, the double occupancy factor $(t/U)^2$ is enhanced by nearly 20% [67].

Peres and Araújo [68] treat the data of [44] starting from the Hubbard model, but without carrying out the perturbation expansion. Instead, treating the Hubbard model at half-filling in a spin-density wave ground state with nesting vector (π, π), they compute the transverse susceptibility by summing all ladder diagrams. The resulting dispersion is then evaluated numerically in various limits. Using values of t and U consistent with the values quoted by Coldea and coworkers, Peres and Araújo obtain excellent agreement with the experimental data, proving that an effective spin model such as the one used by Coldea *et al.* is not necessary to explain the data, and that charge fluctuations are important in the cuprates. The good agreement between the two approaches should not come as a surprise: If written down in real-space coordinates, it would be clear that the ladder summation contains the same physics as the perturbation expansion, namely

that of electrons hopping coherently around the lattice in larger and larger orbits [68].

The work in [68] is essentially a mean-field treatment of the Hubbard model and is therefore only approximate. To bolster its conclusion that charge fluctuations are important in the cuprates Sengupta, Scalettar and R. R. P. Singh [69] used QMC techniques to study the magnon dispersion along the magnetic zone boundary as a function of U/t in the 2D Hubbard model and compared their results with QMC studies of the pure Heisenberg model. They make the single-mode approximation, which we encountered in section 3.2.3 and which amounts to the assumption that the spectral weight at each wavevector is entirely accounted for by single-magnon processes. In neglecting multimagnon continuum excitations this approach provides only an upper limit on the single-magnon energies, but is expected to give reliable estimates for the dispersion along the zone boundary. Indeed, using $U/t = 6$, their calculated dispersion along the symmetry directions probed in [44] is in excellent agreement with experiment away from the gapless points $\mathbf{Q}_{2\mathrm{D}} = (0,0)$ and $\mathbf{Q}_{2\mathrm{D}} = (\pi,\pi)$ (QMC generally has problems in predicting long wavelength properties because it involves computations on small lattice sizes). Focusing on the ZB dispersion as a function of U/t, Sengupta *et al.* found that the Hubbard model magnon energy at $\mathbf{Q}_{2\mathrm{D}} = (\pi,0)$ is larger than at $\mathbf{Q}_{2\mathrm{D}} = (\pi/2,\pi/2)$ for $U/t < 8$. The relative magnitude of the ZB dispersion grows with decreasing U/t, i.e. upon approaching the limit of strongly delocalized electrons where a description in terms of spin operators breaks down. The dispersion curve along the zone boundary is flat within statistical errors for $U/t = 8$ and this point marks the onset of a qualitative transition in the spectrum. At higher U/t, the ZB dispersion changes sign and $\omega(\pi/2,\pi/2) \geq \omega(\pi,0)$ as observed in CFTD and $Sr_2Cu_3O_4Cl_2$. This is also the behavior found for the pure Heisenberg model obtained in the high $U/t \gg 1$ limit, where the most reliable QMC estimate is $1 - \omega(\pi,0)/\omega(\pi/2,\pi/2) \simeq 0.1$ [37]. An open theoretical question raised by [69] is whether the Hubbard model in the intermediate U/t regime near the crossover point $U/t \sim 8$ is equivalent to Heisenberg model supplemented by a ring-exchange term.

We may add that the analysis presented in [69] points to a possible explanation of why the dispersion in $Sr_2Cu_3O_4Cl_2$ is unlike that in La_2CuO_4 when both materials are Cu-based with exchange interactions mediated through intervening oxygens. A larger U/t for $Sr_2Cu_3O_4Cl_2$ may be casually rationalized by considering that U is an atomic property and that the distance between the nearest neighbor Cu_{II} ions in $Sr_2Cu_3O_4Cl_2$ is a factor of $\sqrt{2}$ larger than the nearest neighbor Cu_I distance, which in turn should correspond closely to La_2CuO_4 . Correspondingly we would expect $t_{II}^{NN}/t_I^{NN} \ll 1$ (the relevant exchange constants derived in [55] are $J_I = 4t_I^2/U = 130$ meV and $J_{II} = 10$ meV) and so a larger U/t for the Cu_{II} sublattice. According to [69] this should give a ZB dispersion with $\omega(\pi/2,\pi/2) \geq \omega(\pi,0)$ as observed. Clearly these remarks are oversimplified as they neglect the microscopic differences between La_2CuO_4 and $Sr_2Cu_3O_4Cl_2$, but still, to test the QMC work in [69] it would be very interesting to see whether a zone boundary dispersion similar to that in La_2CuO_4 is present for the Cu_I sublattice of $Sr_2Cu_3O_4Cl_2$.

Katanin and Kampf [70] argue that the use of a single quantum renormalization factor Z_c to extract the exchange integrals is not correct if further neighbor interactions or ring-exchange terms are present. To prove their case, they study a Heisenberg model modified by next-nearest neighbor, third-nearest neighbor, interplane and ring-exchange terms using a self-consistent spin wave theory taken to order $1/S$ in the Dyson-Maleev formalism. They find that each interaction term leads to one or more renormalization factors, which differ from the single value $Z_c = 1.18$ employed in [44] to obtain all exchange constants J, J', J'' and $J_\Box$. Using these individual renormalization factors, the La_2CuO_4 dispersion at $T = 10$ K was refitted and it was found that the parameters $J = 151.9$ meV and $J' = J'' = 0.025J$ differ only slightly from those deduced in [44], but that the ring-exchange term $J_\Box = 0.24J$ is 50% lower. Further, it is shown how inclusion of exchange interactions beyond nearest neighbors lead to values of the renormalization constants Z_c, Z_ρ and Z_χ which differ substantially from those of the nearest neighbor Heisenberg model given in table 1. By way of independent experimental evidence, it counts in favor of the arguments of [70] that the exchange constants derived from fitting the La_2CuO_4 data lead to estimates of the spin stiffness constant ρ_s and the Néel temperature T_N which are in agreement with measurements. We may also note that although Katanin and Kampf consider only La_2CuO_4 explicitly, the points they raise should apply to $Sr_2Cu_3O_4Cl_2$ and CFTD as well.

Finally, we comment on a more recent publication by Katanin and Kampf [71] where the Raman spectra discussed in section 3.3.1 are analyzed on the basis of the modified coupling parameters derived in [70]. The aim was to check whether a consistent description of the Raman data could be obtained with a Heisenberg model with ring exchange. While this analysis achieves excellent

agreement with experimental Raman spectra [38, 39] in terms of the two-magnon Raman peak position, the asymmetry of the experimental peak shape and its width is not accounted for simply by a finite ring-exchange. Ring-exchange does give rise to high energy spectral weight but not enough to explain the data. The authors of [71] consider other sources of broadening such as damping resulting from spin-phonon coupling but still fail to reproduce the asymmetry of the experimental data. They conclude that spin-charge coupling may also have to be considered. We may add, that multimagnon excitations is a plausible source of broadening towards high energies not considered in [71].

In conclusion, we have seen that the three materials $Sr_2Cu_3O_4Cl_2$, CFTD and La_2CuO_4 all display a zone boundary dispersion. In $Sr_2Cu_3O_4Cl_2$ and CFTD, the observed dispersions have shallow minima at $\mathbf{Q}_{2D} = (\pi, 0)$ and display a dispersion along the zone boundary with $1 - \omega(\pi, 0)/\omega(\pi/2, \pi/2) \sim 0.07$. These observations are excellently described by a series expansion treatment of the pure Heisenberg model with no need for including additional terms in the Hamiltonian. These conclusions are further supported by numerical evidence from QMC and exact diagonalization. By contrast, the single-magnon dispersion curve of La_2CuO_4 displays a zone boundary dispersion with the opposite sign, $1 - \omega(\pi/2, \pi/2)/\omega(\pi, 0) \sim 0.13$ the explanation of which requires the existence of a finite ring-exchange term in the Hamiltonian. It has been proposed that the difference between zone boundary dispersions in the two cases can be understood within the Hubbard model solely from the ratio U/t. In this picture, La_2CuO_4 corresponds to small U/t and the insulator CFTD to the large-U/t limit where the Hubbard model maps onto the Heisenberg model. The copper-oxide material $Sr_2Cu_3O_4Cl_2$ should then be viewed as an intermediate case, in which case the agreement with the series expansion treatment of the Heisenberg model would become largely coincidental.

In view of the discovery of large ring-exchange terms in the Hamiltonian of La_2CuO_4 it would be very interesting to investigate theoretically whether adding a ring-exchange term to the Heisenberg model Eq. (30) modifies the temperature dependences of ξ and $S(\mathbf{0})$. If so, it would be natural to ask whether such modifications are sufficient to fully explain the discrepancies between the existing experimental data on these quantities in La_2CuO_4 and CFTD and in particular whether a Heisenberg model plus ring-exchange leads to $S(\mathbf{0}) \sim \xi^2$ (as observed in La_2CuO_4) rather than $S(\mathbf{0}) \sim \xi^2 T^2$ (as predicted by CHN and observed in CFTD), while at the same time not modifying the T-dependence of ξ noticeably relative to the CHN-HN prediction with which both the La_2CuO_4 and CFTD data agree astonishingly well.

Focusing on CFTD, its excitation spectrum appears to be very well described by state-of-the-art theoretical and numerical work on the Heisenberg model. Further, the experiments to probe the temperature dependence of ξ and $S(\mathbf{0})$ in CFTD have reached good agreement with the broadly accepted CHN-HN model. Thus, we are well justified in viewing studies of CFTD as studies of the 2DQHAFSL.

3.4 Properties of CFTD

This section briefly recounts some properties of CFTD as they are described in the literature. There exists studies of both the hydrate $Cu(HCO_2)_2{\cdot}4H_2O$ (CFTH), the partially deuterated version $Cu(HCO_2)_2{\cdot}4D_2O$ (CFTHD) and fully deuterated $Cu(HCO_2)_2{\cdot}4D_2O$. Full deuteration is essential for neutron scattering experiments because the high incoherent scattering from hydrogen would otherwise give rise to a $\mathbf{Q}$-independent signal, complicating analysis of low energy data in general and diffraction data in particular. For other techniques such as NMR, deuteration of the crystal bound water make it possible to probe the hydrogens in the formate groups only.

When comparing the magnetic properties of the three different variants, it is of course essential that no significant changes to the spin Hamiltonian result from partial or full deuteration, and this indeed appears to be the case.

3.4.1 Structural properties

Kiriyama, Ibamoto and Matsuo used X-rays to determine the structure of CFTH [72]. They found that at room temperature the structure is monoclinic with space group $P2_1/a$, lattice parameters $a = 8.18 \pm 0.02$ Å, $b = 8.15 \pm 0.02$ Å, $c = 6.35 \pm 0.02$ Å , monoclinic angle $\beta = 101.1 \pm 0.3°$ and two formula units per unit cell. In this structure each Cu^{2+} ion is surrounded by four oxygen atoms belonging to four different formate molecules in an approximately square configuration parallel to

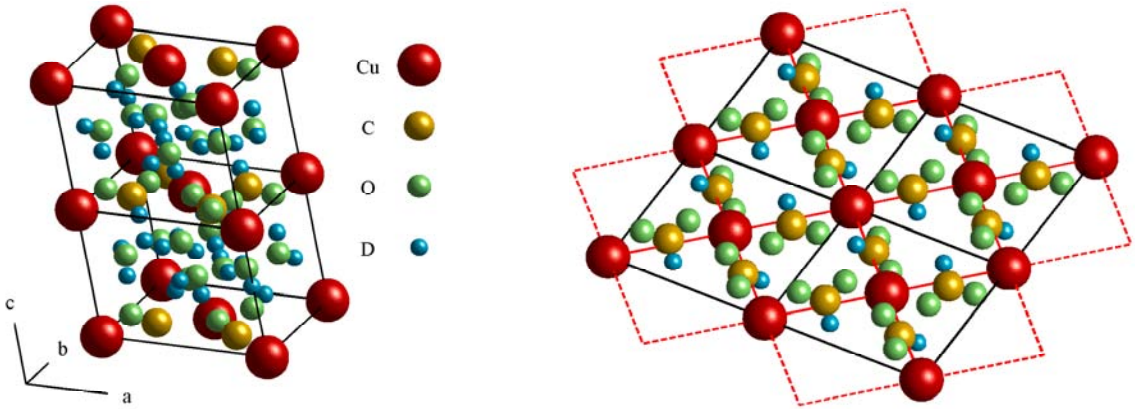

Figure 11: Left: Crystal structure of $Cu(DCOO)_2{\cdot}4D_2O$ at low temperatures. The lattice parameters at 120K are $a = 8.113$ Å, $b = 8.119$ Å, $c = 12.45$ Å and the monoclinic angle $\beta = 100.79°$. Right: A single copper formate layer viewed from above. The red lines indicate the nearly square lattice of Cu^{2+} ions, rotated 45 degrees with respect to the 2D structural and magnetic unit cells (black lines) which coincide in the antiferromagnetically ordered state.

(001). The copper formate layers in themselves are body-centered (see Fig. 11) with a nearest neighbor Cu-Cu distance $\sqrt{a^2+b^2}/2 = 5.77$ Å. Each unit cell contains two crystallographically distinct types of water molecules: The octahedral coordination of the Cu^{2+} ions is completed by water molecules above and below the copper-formate planes at distances larger than the in-plane Cu-O bonds, i.e. the octahedra are elongated along **c**. Moreover, the Cu-H_2O bonds are oriented differently for the two Cu^{2+} ions in the unit cell. The second crystallographic type of water molecule is not coordinated to copper and resides between the copper formate layers.

A first order [73] paraelectric to antiferroelectric phase transition takes place at 236.1 K in CFTH. This transition is related to hydrogen ordering [73] and is accompanied by a doubling of the crystallographic unit cell along the **c**-direction. The low temperature space group is $P2_1/n$. The fully deuterated analog $Cu(DCO_2)_2{\cdot}4D_2O$ has the same space groups as $Cu(HCO_2)_2{\cdot}4H_2O$, and the lattice parameters change only slightly: $a = 8.184$ Å, $b = 8.137$ Å, $c = 6.323$ Å and $\beta = 100.79°$ at 296 K and $a = 8.113$ Å, $b = 8.119$ Å, $c = 12.45$ Å and $\beta = 100.79°$ at 120 K. The antiferroelectric transition temperature depends only weakly on the hydration state: 236.1 K, 245.6 K and 246.1 K are found for $Cu(HCO_2)_2{\cdot}4H_2O$, $Cu(HCO_2)_2{\cdot}4D_2O$ and $Cu(DCO_2)_2{\cdot}4D_2O$ respectively. We conclude, that from a structural viewpoint the three different species are very similar. Figure 11 displays the structural unit cell in the low temperature phase.

3.4.2 Magnetic properties

Turning to magnetic properties, interest in CFTD/CFTH took off following high-temperature susceptibility measurements on CFTH powder, performed by Martin and Waterman [74]. The susceptibility showed a Curie-Weiss behavior with a Curie-Weiss constant $\Theta = -175$ K. Given the clear two-dimensionality of the crystal structure derived in [72], the large negative Curie-Weiss constant was attributed two-dimensional antiferromagnetism with exchange interactions mediated by formate groups and a Néel temperature below the boiling point of nitrogen, which had set the lower temperature limit of the susceptibility measurements.

Subsequently, Flippen and Friedberg [61] measured the magnetic susceptibility of single crystalline and powdered hydrates CFTH at lower temperatures. Using an ac-technique they discovered a peak in the powder susceptibility which was naturally explained by antiferromagnetic order below $T_N = 16.8$ K. Single crystal ac-susceptibility with the field applied along the crystallographic axes contained similar peaks, but in addition revealed anisotropies in the response along different directions. These anisotropies were interpreted as arising from weak ferromagnetism made possible by a Dzyaloshinsky-Moriya interaction leading to canting in the otherwise antiferromagnetic spin structure, but this suggestion could not be confirmed directly. Similar peaks and anisotropies were obtained from dc and ac-susceptibility work on single crystals by Kobayashi and Haseda [75], who also attributed the anisotropies to weak ferromagnetism, in this case with an antiferromagnetic easy axis close to the crystallographic **a** axis. In analyzing the susceptibility data, Kobayashi and Haseda took into account that the difference in out-of-plane Cu-H_2O directions between inequivalent Cu sites leads to a staggered g-tensor, with components $g = 2.1$ in the planes perpendicular

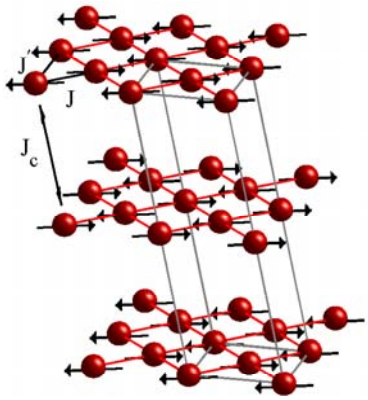

Figure 12: The ordered magnetic structure below T_N determined in [80]. The magnetic moments orient themselves in the **ac** plane, 8 ± 1 degrees away from **a**, i.e. approximately 3 degrees from $\mathbf{a}^*$. Also indicated are the nearest-neighbor exchange interaction J, the next-nearest neighbor interaction J' and the inter-plane exchange J_c. The grey lines show the magnetic unit cell.

to the Cu-H_2O directions, $g = 2.4$ along these directions, and an average of $g_{\text{av}} = 2.19$ [75, 76]. They observed no changes in the dielectric properties of CFTH near $T_N = 17.0 \pm 0.2$ K [75], thus making it unlikely that the origin of the susceptibility anomalies observed at this temperature lies in additional ferroelectric transitions. Further indication that the low temperature peaks in the susceptibility are due to long range antiferromagnetic order came from proton NMR experiments performed by van der Leeden, van Dalen and de Jongh [77] who studied the magnetism of CFTH and partially deuterated CFTHD at liquid helium temperatures. Substituting the waters of hydration between the planes by D_2O allowed a separation of the signal from the hydrogens in the formate molecules surrounding the Cu^{2+} ions from the signal produced by the hydrogens in the water molecules of CFTH. Spectra obtained with the external field rotated around the **a** axis contained four lines with a 360° periodicity, consistent with antiferromagnetic order.

In addition to the low temperature anomalies discussed above, a broad maximum in the ac-susceptibility around 60 K was identified with the external field applied along a direction close to the crystallographic **a** axis [75]. Independent confirmation of this maximum in the susceptibility came from electron spin resonance data of Seehra [78]. In attempts to arrive at a unified description of the susceptibility data below 80 K, both Flippen and Friedberg [61] and Kobayashi and Haseda [75] propose a model of two-dimensional magnetism in CFTD with strong antiferromagnetic correlations following from the large Curie-Weiss constant. Considering the possible exchange paths, the latter group went on to agree with Martin and Waterman [74] that the dominant super-exchange path between Cu^{2+} ions occurs through the intervening formate molecules, while inter-plane exchange paths are much weaker. The smallness of the interlayer exchange J_c was directly confirmed in a mean-field analysis of the field-dependence of the magnetization in CFTH by Yamagata and coworkers [76, 79], who estimated an interlayer exchange constant of order $10^{-5}J$. Kobayashi and Haseda further suggested that the broad maximum in the ac-susceptibility near 60 K occurs due to 2D short range antiferromagnetic order which is followed by 3D antiferromagnetic order setting in around 17 K. Elaborating on this picture, the authors of [61] discuss how the absence of specific heat anomalies around 60 K is consistent with gradual ordering of the Cu^{2+} spins. Entropy changes associated with antiferromagnetism will then occur gradually, consistent with the observation of only a weak reduction of the spin entropy at T_N. This view was subsequently confirmed by Seehra [60] who analyzed susceptibility data using a high-temperature series expansion for a 2D, $S = 1/2$ Heisenberg antiferromagnet and showed that the broad maximum near 60 K can be quantitatively accounted for using a nearest neighbor exchange constant $J = 71.5 \pm 3.0$ K. This firmly established CFTD/CFTH as a good example of a 2D, S=1/2 Heisenberg antiferromagnet.

Zero-field NMR by Dupas and Renard on $Cu(HCO_2)_2{\cdot}4D_2O$ [81] revealed two resonance lines, the temperature dependences of which were studied near $T = 0$ K and $T = T_N$. These measurements made it possible to study the sublattice magnetization of the antiferromagnet. By calculating the expected frequencies of the resonance lines in a dipole model, it was concluded that the ordered sublattice moment at $T = 0$ K deviates strongly from the full value 1/2. More precisely, it was estimated that $m = 0.265$.

Combining polarized with unpolarized neutron diffraction Burger, Fuess and Burlet [80] were able to directly determine the ordered spin structure and sublattice magnetization in a model independent manner. The zero-field spin structure consists of four sublattices as depicted in Fig. 12. Further, an upper limit of $\Delta\mu = 0.005(6)\mu_B$ was put on any ordered ferromagnetic component, showing that there is essentially no weak ferromagnetism to be taken into account in the absence of an external field. In the antiferromagnetically ordered phase the moments orient themselves 8 ± 1 degrees away from the **a**-axis − in the direction towards $\mathbf{a}^*$ − and have a magnitude of $0.48 \pm 0.02\,\mu_B$ at zero temperature, in good agreement with the NMR result. The temperature dependence of the (101) reflection − the magnetic Bragg reflection closest to the origin − was recorded and found to be well described by the mean-field, Brillouin function for $S = 1/2$. Finally, it was found that in an external field, a ferromagnetic moment along the **b**-axis is generated, explaining why indications of weak ferromagnetism had been spotted in susceptibility data.

With this, we conclude this section, and thereby also this introductory chapter. The main message has been that while a substantial amount of theoretical and experimental work has been done on the 2DQHAFSL, there are still important unresolved issues involved in connecting theory with experiment. The most important of these revolve around the issue of higher-energy excitations in the pure Heisenberg model versus the need to include interactions coupling spins beyond their nearest neighbors. We have seen that the physical properties of CFTD can be understood by considering it a manifestation of the 2DQHAFSL. In particular, neutron scattering studies of the temperature dependences of ξ and $S(\mathbf{0})$ are in excellent agreement with theory, while the single-magnon energies contain a zone boundary dispersion predicted by a variety of different theoretical and numerical approaches to the 2DQHAFSL. Many of these theories and computational techniques have suggested the existence of a non-negligible spectral weight associated with multimagnon excitations, in particular for wavevectors near $\mathbf{Q}_{2\mathrm{D}} = (\pi, 0)$ where the single-magnon energy is reduced from the value it takes in the simplest of approaches − linear spin wave theory. However, such multimagnon excitations have never been directly identified in the 2DQHAFSL. In chapters 4 and 5 we use neutron scattering techniques to investigate the full excitation spectrum of CFTD in order to elucidate these issues from an experimental viewpoint.

4 Single-magnon spectrum in CFTD

In this chapter we present the results of a time-of-flight experiment performed with the objective of studying the $T = 0$ K single-magnon dispersion $\omega_{\boldsymbol{q}}$ and intensities $I_{\boldsymbol{q}}$ of the 2DQHAFSL model system CFTD. Our main discovery is that the zone boundary dispersion found by Rønnow *et al.* is accompanied by a large anomaly in the single-magnon intensity along the zone boundary. No existing theory appears capable of quantitatively capturing the anomalies in both $\omega_{\boldsymbol{q}}$ and $I_{\boldsymbol{q}}$.

As discussed in the previous chapter $\hbar\omega_{\boldsymbol{q}}$ has already been studied in CFTD by Clarke *et al.* [59] and later by Rønnow *et al.* who found a zone boundary dispersion between $(\pi/2, \pi/2)$ and $(\pi, 0)$ [29, 56]. The experiment reported here was performed using the MAPS spectrometer (see Fig. 3) at the ISIS facility, Rutherford Appleton Laboratory, and is in at least two ways an improvement over the experiment of Rønnow and coworkers. First, each detector bank of the HET (High Energy Transfer) spectrometer used by Rønnow and coworkers were at the time only pixelated along one direction and integrated over momentum transfers perpendicular to this directions. With the chosen sample orientation they had good momentum-resolution conditions only along the [11] and [10] directions of square lattice reciprocal space. By contrast, MAPS is equipped with large detector banks which are highly pixelated along both perpendicular directions, immediately implying improved momentum resolution conditions over HET. Second, gaps between the HET detectors made it impossible for Rønnow *et al.* to study the dispersion relation over the full Brillouin zone. In particular they did not probe the dispersion along the magnetic zone boundary, i.e. between the two high symmetry positions $(\pi/2, \pi/2)$ and $(\pi, 0)$. Using the MAPS spectrometer it is possible to investigate $\omega_{\boldsymbol{q}}$ and $I_{\boldsymbol{q}}$ over the full Brillouin zone.

Figure 13(a) shows the single-magnon dispersion surface $\hbar\omega_{\boldsymbol{q}} = 2Z_c J(1-\gamma_{\boldsymbol{q}})^{1/2}$ expected from linear spin wave theory (LSW; see appendix A) with the quantum renormalization factor Z_c of the energy scale explicitly included. The color variation on the dispersion surface indicates the expected intensity variation $I_{\boldsymbol{q},\mathrm{LSW}} \propto [(1-\gamma_{\boldsymbol{q}})/(1+\gamma_{\boldsymbol{q}})]^{1/2}$. The dashed red lines run along the magnetic Brillouin zone boundary along which $\hbar\omega_{\boldsymbol{q}}$ takes its maximum value $2J_{\mathrm{eff}} = 2Z_c J$. Fig. 13(b) displays raw MAPS data at three different energy transfers $\hbar\omega$ for in-plane momentum transfers $\mathbf{Q}_{2\mathrm{D}}$ inside the magnetic Brillouin zone surrounding (π, π). These color maps are averages over data from the four equivalent Brillouin zones closest to the origin (centered on the crystallographic in-plane momenta $(H, K) = \pm(1, 0)$ and $\pm(0, 1)$ − all four of which correspond to $\mathbf{Q}_{2\mathrm{D}} = (\pi, \pi)$) and over energy transfers in the ranges $\hbar\omega + \delta\hbar\omega = 5.5 \pm 0.5$ meV, 9 ± 1 and 14 ± 1 meV. It is clear that the single-magnon mode dominates at all energy transfers but that its intensity drops as $\hbar\omega$ increases.

For further illustration of the capabilities of the MAPS spectrometer we present in Figure 14 a color map of the intensities along the crystallographic $\mathbf{b}^*$-direction corresponding to a [11] direction in the first Brillouin zone of the square lattice, i.e. along a diagonal in Fig. 13(a). Dispersing

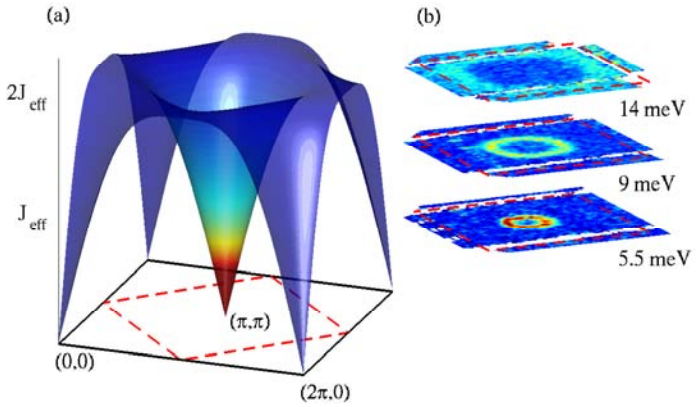

Figure 13: (a): Linear spin wave dispersion surface in the square lattice Brillouin zone. The dashed red line runs along the magnetic zone boundary separating the magnetic Brillouin zone centered on $\mathbf{Q}_{2\mathrm{D}} = (\pi, \pi)$ from the nuclear zone centered on $(2\pi, 2\pi)$ and equivalent points. The color scale of the dispersion surface indicates the expected intensity of single-magnon scattering in linear spin wave theory. According to Eq. (129) this diverges at (π, π). The single-magnon energy is $2J_{\mathrm{eff}}$ over the entire magnetic Brillouin zone boundary. (b): Raw MAPS data in the magnetic Brillouin zone obtained by averaging over the four zones closest to the origin. The constant energy slices are averages over the energy intervals 5.5 ± 0.5 meV, 9 ± 1 and 14 ± 1 meV.

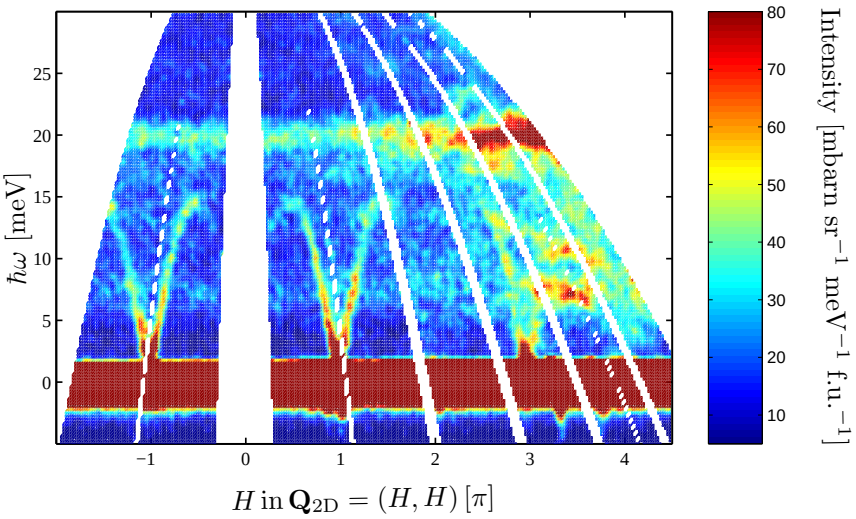

Figure 14: Color map of the measured intensities along a path $(0KL)$ in the reciprocal space of CFTD. To obtain this map intensities were averaged over all H-values between -0.05 and 0.05 and for presentational purposes were smoothed using a Gaussian filter. If desired, the L-value for each point can be deduced from Eq. (23) using the known incident energy and the orientation of the sample. The units on the horizontal axis were converted from crystallographic notation to 2D, square lattice reciprocal space notation. The intensities have been converted from counts per time-bin to absolute units mbarn sr^{-1} meV^{-1} f.u.$^{-1}$ as explained in the text.

away from $-(\pi,\pi)$, (π,π) and $3(\pi,\pi)$ are sharp single-magnon branches. Upon approaching the zone boundary points of the type $(2l+1)(\pi/2,\pi/2)$ with l an integer, the single-magnon modes gradually loose intensity but are also visible inside the nuclear zones surrounding $(0,0)$ and $(2\pi,2\pi)$. In addition to single-magnon scattering, there is an intense band due to incoherent scattering surrounding $\hbar\omega = 0$ meV and two roughly non-dispersive phonon bands around $\hbar\omega =$ 7-8 meV and $\hbar\omega = 20$ meV. The 20 meV phonon is believed to be related to the motion of the water molecules involved in the antiferroelectric transition at 246.1 K $\sim$ 21 meV whereas the lower-energy mode is an acoustic phonon emanating from the crystallographic (101) and (111) reflections [29]. As is expected for displacement modes, the intensities of the phonon bands increase with increasing $|\mathbf{Q}|$ and this precludes reliable analysis of data from the magnetic zone around $3(\pi,\pi)$ (equivalent to $(H,K) = (0,3)$) where in addition, the magnetic modes would be reduced by the form factor variation. Consequently, the results presented in this chapter are all obtained by analyzing data from the four Brillouin zones closest to the origin.

The outline of this chapter is as follows. Section 4.1 contains a description of the experimental setup and related details. In section 4.2 we discuss the methods employed in the data analysis before turning to a presentation of the results in section 4.3.

4.1 Experimental details

The sample studied consisted of two single crystals grown from solution in the group of Andrew Harrison at the University of Edinburgh. The total mass of the two crystals was 10.61 g. Prealignment had taken place at ILL, Grenoble, but since the samples dry out quickly (and visibly) within minutes when exposed to air and furthermore react strongly with the aluminium sample holder it was necessary to transport them to ISIS by hand, separated from the holder. Here, the sample mount was reassembled immediately prior to its attachment to the cold finger of a continuous cycle refrigerator with a nominal base temperature of 7 K. Rapid cooling through the antiferroelectric transition temperature 246.1 K halts the above-mentioned chemical reactions which could otherwise have rendered the experiment significantly more complicated.

The two crystals were comounted with their $\mathbf{c}^*$-axes parallel to the incident neutron wavevector $\mathbf{k}_i$ and with the $\mathbf{a}$-axis vertical. The 2D planes are then perpendicular to $\mathbf{k}_i$ and $\mathbf{a}^*$ oriented 10.79 degrees away from the vertical. This setup had previously been employed with success in the experiments of Rønnow *et al.* , and is the maximally symmetric configuration mentioned in section 2.3 for studying two-dimensional magnetism. The incident energy was chosen to be $E_i = 36.25$

meV. With this E_i, five Brillouin zones are intersected by the time-of-flight parabola. With a Fermi chopper frequency of 200 Hz the energy resolution was ~ 1.15 meV FWHM at $\hbar\omega = 0$ meV improving to ~ 0.8 meV at $\hbar\omega = 15$ meV. Data were taken at base temperature, $T = 7$ K, and the total counting time for this run was roughly 11 hours.

At the end of the experiment, a number of manipulations were carried out to transform the data to a format suitable for continued analysis. In this step, faulty detectors are masked off using appropriate software, and the kinematic factor (k_f/k_i) appearing in the partial differential cross-section for magnetic scattering (13) is removed from the raw count rates in the remaining good detectors. The corrected count rates $(k_i/k_f)(d^2\sigma/(d\Omega\ dE_f))$ are then converted to absolute units (millibarns per steradian per meV per formula unit, abbreviated mbarn sr^{-1} meV^{-1} $\mathrm{f.u.}^{-1}$) by callibration of the instrument using the incoherent scattering from a vanadium standard specimen. This step also corrects the data for differences in the efficiencies of individual detectors.

For the experiments decribed in this chapter the total available 147456 pixel elements on MAPS were binned together in groups of four, so that after the removal of bad detectors the resulting data file contained 33977 individually adressable pixels. The number of energy bins (or more precisely: Time bins) per pixel is also chosen in software. We used 180 energy bins per pixel element, spanning energy transfers $\hbar\omega$ from -9.875 to 34.875 meV in steps of 0.25 meV. The data set from one run thus contains information from a total of $33977 \times 180 \simeq 6.1 \times 10^6$ detectors, each probing a different point on the time-of-flight parabola.

4.2 Data analysis

The analysis of the data can be divided into three steps: The first step consist in producing the data to be fitted. In the second step, the data are fitted to determine the position and intensities of the single-magnon excitations at a given energy or momentum transfer. In the final step, the resulting dispersion and intensity variations $\hbar\omega_{\boldsymbol{q}}$ and $I_{\boldsymbol{q}}$ are analyzed using the theoretical predictions of linear spin wave theory which are derived in appendix A. In this section, we describe the first two steps in some detail, postponing the last step to section 4.3.

4.2.1 MSlice details

Each data file from MAPS comes in the form of a large file containing essentially the intensities in absolute units as a function of energy-transfer and the polar and azimuthal angles with respect to $\mathbf{k}_i$. The Matlab package Mslice developed by R. Coldea reads this file and once the user has supplied the crystal structure and sample orientation allows one to convert the data to intensities as a function of either three of the four variables $\hbar\omega$, H, K and L. The three momenta could also be along off-axis directions in reciprocal space, but for CFTD we chose $\hbar\omega$ and the two in-plane components H and K. The value of fourth variable is implied by the energy and momentum conservation laws. We have already seen two examples of raw data presented in this manner. In Fig. 13, data were displayed as a function of in-plane momentum transfer (H, K) (converted to square lattice reciprocal space notation) by averaging over a few energy bins. In Fig. 14 the average was performed over a small interval of H values and the resulting color map as a function of K-values and $\hbar\omega$ was presented with the K-values converted to momentum transfers along the [11] direction of the square lattice reciprocal space.

With the data on the form of intensities versus any three out of the quartet $(H, K, L, \hbar\omega)$, Mslice allows one to create cuts through the data as a function of either H, K, L or $\hbar\omega$. These cuts mimic the constant energy or momentum scans obtained on triple-axis spectrometers but are easier to decode visually since the almost square detector elements on the MAPS spectrometer give a small squarish resolution ellipsoid rather than the elongated, sometimes cigar-shaped resolution ellipsoid more typical of triple-axis machines. The cut is defined by a direction, a bin size along this direction and two ranges of averaging over two other variables. Taking CFTD as an example, the cut could run along H, in which case the averages would be over K and $\hbar\omega$ with L fixed by the conservation laws. The intensity and associated errorbar of each point in a cut are then computed by MSlice as averages over the intensities and errorbars of all the individual detectors on the time-of-flight parabola being averaged over for that particular point.

Resolution corrected fits are prepared by outputting the cuts in a manner where the detector information (including the intensities, the associated errorbars and detector numbers in a particular index file) is retained for all detectors contributing to an individual point. A cut-file structured

in this manner is then passed to the least-squares fitting program Tobyfit [82] developed by T. G. Perring for further analysis. Since it applies both to the analysis of CFTD and to that of LSCO data in chapter 7 we shall say a bit more about the way Tobyfit affects data fitting in section 4.2.2.

To analyze the CFTD data, it is natural to use constant-$\hbar\omega$ cuts at low energy transfer where the single-magnon dispersion is steep, but to use constant-$\mathbf{Q}_{2D}$ cuts for momentum transfers near the magnetic zone boundary where there is little change in magnon energy with $\mathbf{Q}_{2D}$. As explained above cut-files are produced by averaging over $\hbar\omega$ and/or momentum transfers. Because the single-magnon mode becomes gradually less intense as $\mathbf{Q}_{2D}$ approaches the magnetic zone boundary and further weakens on entering the nuclear zones surrounding $(2\pi, 2\pi)$ positions, it was necessary when producing the cut-files to allow the area $\delta\mathbf{Q}_{2D}$ of the in-plane momentum regions being averaged over to vary with $\mathbf{Q}_{2D}$ for the high-energy constant-$\mathbf{Q}_{2D}$ cuts. Similarly, for low-energy constant-$\hbar\omega$ cuts running along e.g. the H direction, the size of the momentum region being averaged over along K was allowed to increase with increasing $\hbar\omega$. As we shall see below, such increases do not lead to any problems when fitting the data in Tobyfit.

The data were analyzed along the path of in-plane wavevector transfers shown in Fig. 17(a). It should be noted, that inside each of the four Brillouin zones analyzed there are two equivalent $\langle 11 \rangle$ directions and two equivalent $\langle 10 \rangle$ directions, giving a total of eight equivalent cuts per direction. All of these cuts can be analyzed because of the wide reciprocal space coverage and good, isotropic momentum resolution of the MAPS spectrometer. For momenta closer to the magnetic zone boundary, the expected (and observed) intensity decrease along with the reduction in reciprocal space coverage with increasing $\hbar\omega$ sometimes make it necessary to create cuts which average over all available equivalent regions in order to obtain sensible counting statistics. In particular, this was necessary near $\mathbf{Q}_{2D} = (\pi, 0)$. However, more generally we attempted − whenever statistics allowed it − to work with several symmetry-equivalent cuts.

4.2.2 Tobyfit details

To analyze data in Tobyfit, the user must supply the cut-file(s) to be fitted as well as a duplicate of the detector index-file used by Mslice when generating the cut-files. This, the crystal structure, sample orientation and incident neutron energy must be input by the user to allow Tobyfit to identify the momentum and energy transfers of all detectors contributing to a given point in a cut-file. The user also supplies the name of the instrument (which the program translates into fixed instrument lengths etc.) and the Fermi chopper frequency. From all the informations at hand, Tobyfit is capable of calculating the resolution function for all $(H, K, L, \hbar\omega)$. The parameters determining the contribution to the resolution function from the moderator can be fixed by fitting the isotropic incoherent scattering from vanadium or the incoherent line of the sample.

To fit the data, a parametrized model must be defined. In Tobyfit a model consist of a background model plus a model for $S(\mathbf{Q}, \omega)$ − the scattering of primary interest. Both of these models are user-defined, though preexisting models may also be picked.

In choosing a model for $S(\mathbf{Q}, \omega)$, the user must first decide whether the model should include both a well-defined dispersion surface and a well-defined intensity variation over this surface, or whether it is more natural that the model only specifies the lineshape as a function of momentum transfer. The former option is the natural choice for studies of the spin waves in CFTD (see section 4.2.3) whereas the latter is more appropriate in a situation where the observed scattering contains broad features for which an educated guess for the exact mathematical form of the energy dependence of the intensity is not available, as is the case in our studies of the high T_c superconductors $La_{2-x}Sr_xCuO_4$ in chapter 7. Tobyfit provided templates for the user to write his own models of either kind mentioned above. In both cases, it is optional to include the Bose occupation factor $(n(\omega) + 1)$ and the square of the magnetic form factor $|F(\mathbf{Q})|$ for the magnetic ion being studied in the calculation of the intensity before convolution with the resolution function and subsequent fitting of the experimental data takes place.

Prior to any fitting, the user must decide between two different ways of implementing the integration (25) involved in the resolution convolution. The first is a Monte Carlo routine and the second a simplified method in which the convolution is approximated by a summation over a (user-defined) number of detectors surrounding each of the detectors contributing to a given point in a cut-file. The choice of integration method affects the degree of detail in which Tobyfit treats the resolution function, but leaves the user with a very large freedom of choice for exactly which resolution contributions should be included and which should not. All results presented in this

chapter were obtained by employing the second method, summing over a 12 point grid for each detector.

Tobyfit makes it possible to fit up to 10 cut-files from the same run simultaneously using the same model for $S(\mathbf{Q},\omega)$. Since a typical MAPS data set is quite large, this can substantially speed up the process of reducing the data set to physical quantities of interest such as peak intensities, positions, widths etc. A further advantage of the parallel fitting option is that since Tobyfit deduces the values of (H,K,L) and $\hbar\omega$ for all detectors contributing to a point in a cut-file (Since what is being computed is a convolution of $S(\mathbf{Q},\omega)$ with the instrument resolution function, some of the detectors contributing to the intensity calculated for a given point in a cut-file may lie outside the region being averaged over in Mslice for that particular point) it is possible to carry out effectively multi-dimensional fits over extended regions of $(H,K,L,\hbar\omega)$ by producing cut-files along momentum or energy tranfer in a side-by-side fashion. As we shall see in chapter 7, this was the procedure chosen for analyzing the LSCO time-of-flight data. For CFTD it was more natural to fit equivalent cuts from different Brillouin zones simultaneously.

The ability to compute all $(H,K,L,\hbar\omega)$ is also what ensures that moderate increases in the in-plane momentum regions $\delta\mathbf{Q}_{2\mathrm{D}}$ being averaged over for constant-momentum cuts do not affect the final results. This is so because Tobyfit calculates the single-magnon energies and intensities for all detectors contributing to a given point in a cut-file and then averages them to make contact with the averaging affected by Mslice in producing cut-files. The same applies to analysis of advanced cuts generated by averaging over several equivalent regions belonging to different Brillouin zones.

Before fitting the user must finally choose whether the program should regard a given background model as local to a particular cut-file or as global. In the latter case, when fitting a set of several cut-files simultaneously, the same background model is assumed for all cuts, whereas in the former case the parameters determining the background variation are allowed to vary independently for each cuts being fitted. We chose always to work with a local background definition. After fitting the data, the variations in the parameters determining the background can then be checked for mutual consistency.

4.2.3 Model and extraction of energies and intensities

To find the positions and intensities of the single-magnon peaks in constant-momentum or constant-energy cuts the data were fitted in Tobyfit using the expectations of linear spin wave theory. Thus we choose a model for $S(\mathbf{Q},\omega)$ in which the dispersion and the intensity variation over the dispersion surface are determined by two fitting parameters E_{fit} and A_{fit}:

$$S(\mathbf{Q},\omega) = I_{\boldsymbol{q}}\,\delta(\omega-\omega_{\boldsymbol{q}}) \tag{45}$$

$$I_{\boldsymbol{q}} = A_{\mathrm{fit}}\,[n(\omega_{\boldsymbol{q}})+1]\,|\,F(\mathbf{Q})\,|^2\,\sqrt{\frac{1-\gamma_{\boldsymbol{q}}}{1+\gamma_{\boldsymbol{q}}}} \tag{46}$$

$$\hbar\omega_{\boldsymbol{q}} = E_{\mathrm{fit}}\sqrt{1-\gamma_{\boldsymbol{q}}^2} \tag{47}$$

The notation chosen is the same as that employed in appendix A with subscripted $\boldsymbol{q}$'s equivalent to $\mathbf{Q}_{2\mathrm{D}}$. The quantity $\gamma_{\boldsymbol{q}}$ was introduced in chapter 3.

The equations emphasize that the model dispersion (47) depends only on the components of the crystal momentum transfer corresponding to the reciprocal space of the square lattice, whereas the intensities (46) are influenced by the variation of the square of the free Cu^{2+} form factor with 3D momentum transfer $\mathbf{Q}$ as well as by the Bose occupation factor. Section 2.1.2 showed that the observed intensities are further influenced by the Debye-Waller factor and by the polarization factor in the neutron scattering cross-section. We have neglected the former since it is expected to vary slowly with $\mathbf{Q}$ over the parts of the Brillouin zone where single-magnon modes are visible. The polarization factor has been excluded for reasons to be discussed further in section 4.3.2.

Each time a cut (or a series of equivalent cuts) is fitted, Tobyfit outputs one energy parameter E_{fit}, one amplitude parameter A_{fit}, the statistical errorbars ΔE_{fit} and ΔA_{fit} as well as a matrix containing the correlation coefficients between the parameters varied in the fit. The correlation between the values of E_{fit} and A_{fit} was always found to be negligible. Because the background is treated as local to each cut, the program also outputs one (for constant-$\hbar\omega$ cuts the background is expected to be flat) or more (for constant-$\mathbf{Q}_{2\mathrm{D}}$ cuts the background is treated as sloping or quadratic) background parameters per cut being fitted. For both constant-$\hbar\omega$ and constant-$\mathbf{Q}_{2\mathrm{D}}$

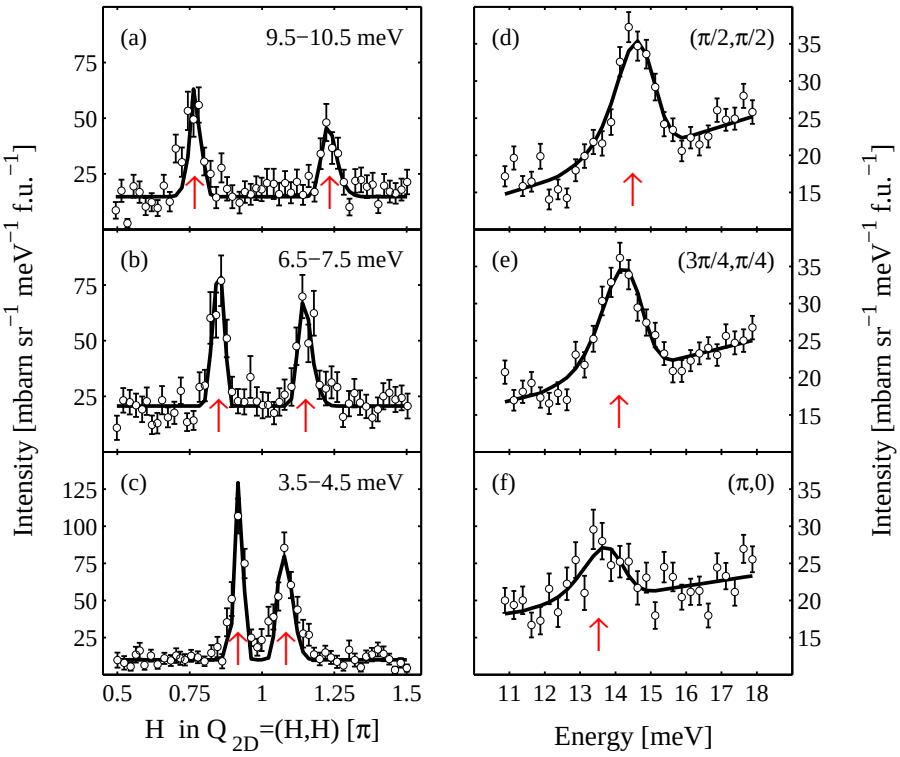

Figure 15: Examples of fits to the data. The fitted positions of the single-magnon modes are indicated by the red arrows in all plots. (a)-(c) Constant-$\hbar\omega$ cuts along the [11] direction. Note the changing intensity scales. (d)-(f) Constant-$\mathbf{Q}_{2D}$ cuts along the zone boundary. Both the zone boundary dispersion and the reduced intensity at $(\pi, 0)$ are clearly seen.

cuts we checked that $E_{\rm fit}$ and $A_{\rm fit}$ obtained by fitting N symmetry-equivalent cuts simultaneously are are identical within errors to the values one obtains by first fitting the N cuts one by one and subsequently averaging the individual results $\{E_{\rm fit,i}\}$ and $\{A_{\rm fit,i}\}$.

It is very important to realize that the parameters $E_{\rm fit}$ and $A_{\rm fit}$ are local to each cut (or series of simultaneously fitted equivalent cuts). Their significance is that they yield the best description of the data they were obtained from in the precise sense of the single-magnon intensity and position being given by (46) and (47) respectively. In particular, the values of $E_{\rm fit}$ and $A_{\rm fit}$ obtained from a fit of any one constant-$\hbar\omega$ (or constant-$\mathbf{Q}_{2D}$) cut are not expected to give a satisfactory description of the single-magnon dispersion and intensities over the entire Brillouin zone. Instead we treat $E_{\rm fit}$ and $A_{\rm fit}$ as effective parameters, the variations of which over the Brillouin zone contain in them any anomalies we might encounter in the dependence of the single-magnon positions and intensities. In principle, the intensity parameter $A_{\rm fit}$ further contains the polarization factor in the neutron scattering cross-section which was left out of Eq. (46).

Using the fitted values of $E_{\rm fit}$ and $\Delta E_{\rm fit}$ along with our knowledge of the average values of $\mathbf{Q}_{2D}$ (for constant-wavevector cuts) or $\hbar\omega$ (for constant-energy cuts) it is straightforward to employ Eq. (47) to compute the actual positions in $\hbar\omega$ or $\mathbf{Q}_{2D}$ (for constant-wavevector and constant-energy cuts respectively) of the single-magnon mode as well as the associated statistical errorbars. For constant-energy cuts, the errorbar on $\mathbf{Q}_{2D}$ can subsequently be converted to an errorbar on $\hbar\omega_{\boldsymbol{q}}$ using Eq. (47) in order to facilitate comparisons of the observed dispersion to various model predictions. In a similar manner, Eq. (46) allows us to calculate the spectral weight $I_{\boldsymbol{q}}$ of the single-magnon scattering at the intersections between the dispersion surface and the time-of-flight parabola. In determining the statistical errorbar $\delta I_{\boldsymbol{q}}$, it should be noted that for constant-energy cuts $\delta I_{\boldsymbol{q}}$ has contributions from $\delta E_{\rm fit}$ as well as from $\delta A_{\rm fit}$. The reason is that $I_{\boldsymbol{q}}$ depends on $\gamma_{\boldsymbol{q}}$ which in turn is deduced by inverting Eq. (47).

4.3 Results

Having described how single-magnon energies and intensities are extracted from $E_{\rm fit}$ and $A_{\rm fit}$, we continue with a presentation of our results.

Examples of fits performed in Tobyfit are shown in Fig. 15. Panels (a)-(c) display results of constant-$\hbar\omega$ cuts along a [11] direction in the reciprocal space of the square lattice. Eight equivalent [11] cuts were fitted, but the ones shown all correspond to the same cut in the 3D reciprocal space of CFTD. The solid black lines represent the best least-squares fit with the red arrows marking the location of the single-magnon peaks. The dispersion and loss of intensity with increasing $\hbar\omega$ are clearly seen. Panels (d)-(f) are fits of constant-$\mathbf{Q}_{\rm 2D}$ cuts for three equally spaced wavevector transfers on the magnetic Brillouin zone. We point to two central features in the data in (d)-(f). First, the locations of the single-magnon peaks at the three momenta are clearly not identical and certainly inconsistent with any conjecture that the zone boundary dispersion could be an unfortunate artifact of the resolution function convolution Eq. (25). The fitted magnon energies at $(\pi/2,\pi/2)$ and $(\pi,0)$ are 14.49 ± 0.06 meV and 13.52 ± 0.16 meV respectively, corresponding to a zone boundary dispersion of magnitude $7\pm1\%$, consistent with the value $6\pm1\%$ obtained in [56]. Second, not only is the single-magnon energy at $(\pi,0)$ reduced from its value at $(\pi/2,\pi/2)$, there is also a dramatic reduction in the spectral weight associated with the single-magnon peak at $(\pi,0)$ relative to $(\pi/2,\pi/2)$. The intensity of the magnon at $(\pi,0)$ is just $46\pm12\%$ of that of the $(\pi/2,\pi/2)$ magnon. Note in passing that the background levels are roughly identical in the three cuts shown in Fig. 15(d)-(f). Therefore, the decreased spectral weight at $(\pi,0)$ cannot simply be due to the effect of an unfortunate phonon branch intersecting the single-magnon branch.

The spectral weight drop at $(\pi,0)$ was not noted by Rønnow and co-workers, nor has anything similar been reported for the two other systems $Sr_2Cu_3O_4Cl_2$ [55] and La_2CuO_4 [44] which are known to display a zone boundary dispersion. It is thus a new phenomenon observed for the first time in the present experiment.

This section is subdivided into four subsection. First, section 4.3.1 is devoted to a presentation of the results for the single-magnon dispersion $\hbar\omega_{\boldsymbol{q}}$. Then we turn to analyze the intensity distribution $I_{\boldsymbol{q}}$ along the dispersion surface. Section 4.3.2 shows that in contrast with our expectations discussed in the previous section, we are unable to pick out the variation of the polarization factor in the neutron scattering cross-section from the fitted intensity parameters $A_{\rm fit}$. Following a discussion of the possible reasons for this failure, section 4.3.3 proceeds to analyze $I_{\boldsymbol{q}}$ itself. Finally, in section 4.3.4, we briefly discuss indications of multimagnon continuum scattering in the time-of-flight data.

4.3.1 Single-magnon dispersion $\hbar\omega_{\boldsymbol{q}}$

Taking the values of $E_{\rm fit}$ from all constant-$\hbar\omega$ and constant-$\mathbf{Q}_{\rm 2D}$ cuts and converting to single-magnon energies as explained in section 4.2.3, we are able to produce the data displayed in Fig. 16. The path of wavevectors along which $\hbar\omega_{\boldsymbol{q}}$ is plotted, is reproduced in Fig. 17(a). For easy comparison, it is precisely the same path along which Coldea and coworkers investigated the single-magnon spectrum of La_2CuO_4 [44]. Figure 16(a) represents an extension of Fig. 2 in [56] to a larger portion of 2D reciprocal space including, in particular, the zone boundary between $(\pi/2,\pi/2)$ and $(\pi,0)$. For the parts of reciprocal space covered in both experiments, the single-magnon energies found appear to be in good agreement. It is particularly noteworthy that the magnitude of the zone boundary dispersion is identical in the two experiments and − most importantly − $\hbar\omega_{\boldsymbol{q}}$ has a shallow local minimum at $(\pi,0)$.

To analyze the dispersion we note that the linear spin wave theory expression $\hbar\omega_{\boldsymbol{q}} = 2J_{\rm eff}(1-\gamma_{\boldsymbol{q}}^2)^{1/2}$ provides a good description of all the data along the [11] direction. For completeness, we include the gap $\Delta = 0.38$ meV measured by Clarke and coworkers [59] via the phenomenological form

$$\hbar\omega_{\boldsymbol{q},\rm LSW} = \sqrt{\Delta^2 + (2J_{\rm eff}(1-\gamma_{\boldsymbol{q}}^2)^{1/2})^2} \tag{48}$$

This yields an effective exchange $J_{\rm eff} = 7.30\pm0.02$ meV. The value of $J_{\rm eff}$ in insensitive to the inclusion of Δ which − owing to its small magnitude − only has appreciable effect at wavevectors very close to (π,π). As was repeatedly pointed out in chapter 3, studies of the single-magnon dispersion by themselves do not allow the physical exchange constant J to be deduced unambiguously since the energy scale is renormalized by quantum fluctuations. Following the standard

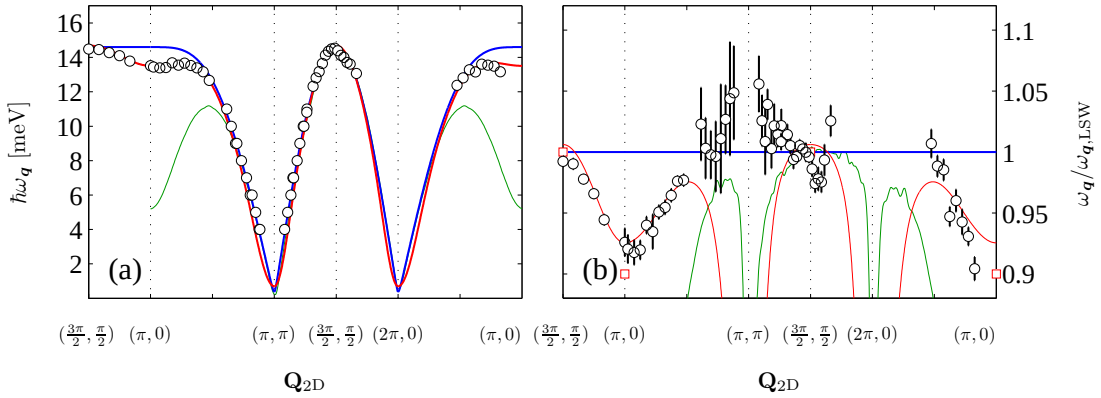

Figure 16: (a): Single-magnon dispersion relation in CFTD as a function of $\mathbf{Q}_{2D}$ along the path indicated in Fig. 17(a). Errorbars are contained within the symbols. Blue line: Nearest neighbor spin wave theory Eq. (48), including a gap of $\Delta = 0.38$ meV. Red line: Dispersion derived by the series expansion method [34]. The green line is the prediction of the π-flux phase approach to the Heisenberg model [83]. (b): Ratio of the measured dispersion to the nearest-neighbor linear spin wave result Eq. (48). The lines are the same as in panel (a) while the open red squares at $(\pi, 0)$ and $(3\pi/2, \pi/2)$ are from QMC studies of the 2DQHAFSL [37, 84]. The scatter in the green line is caused by numerical noise. Note that $(3\pi/2, \pi/2)$ is equivalent to $(\pi/2, \pi/2)$.

approach we assume $Z_c = 1.18$ and obtain thereby $J = 6.18 \pm 0.02$ meV. This is inconsistent with $J = 6.31 \pm 0.02$ meV quoted in [56], but in absolute numbers the difference is not too dramatic.

It should emphasized, that although we are using the same functional form to fit the experimental data as we used to obtain the single-magnon energies in Tobyfit, this is not a limitation in the approach. We could in principle have chosen another model for $S(\mathbf{Q}, \omega)$ in Tobyfit since the resulting fitted parameters are always used to invert the model equations to yield the real position and spectral weight of the excitations. These positions and intensities are therefore independent of the choice of model as long as it is reasonable, which the chosen model Eq. (45) certainly is in the sense of reproducing the observed lineshapes as well as exemplified in Fig. 15.

The solid blue line in Fig. 16(a) represents the dispersion (48). It is clear that it fails in an extended region surrounding $(\pi, 0)$. In order to bring this discrepancy with linear spin wave theory forward most clearly, we have divided the experimental data by the expected energy (48) with $J_{\mathrm{eff}} = 7.30$ meV. The result is shown in Fig. 16(b). In addition to the zone boundary anomaly around $(\pi, 0)$ we see a substantial degree of scatter in the normalized single-magnon energies near the zone center (π, π). Though largely consistent with Eq. (48) within the combined errors, we cannot exclude a small positive anomaly in the normalized single-magnon energies near (π, π). A possible explanation for such an effect could be that the lowest-energy part of the dispersion is not exactly as we have assumed. However, even if this is not the case, and an anomali were to be verified by more careful measurements, it is certainly much less dramatic than the zone boundary dispersion. We will not consider it further here.

Within linear spin wave theory, inclusion of further neighbor interactions also lead to the development of zone boundary dispersions. Fig. 70(a) in appendix A shows that a zone boundary dispersion with the correct sign $1 - \omega(\pi, 0)/\omega(\pi/2, \pi/2) > 0$ is obtained if finite antiferromagnetic next-nearest neighbor interactions are present. If in Eq. dispersion (48) we replace $2J_{\mathrm{eff}}(1-\gamma_{\boldsymbol{q}}^2)^{1/2}$ by the more general result (116), the best agreement with the data is found with unrenormalized exchange integrals $J = 8.27$ meV and $J' = 0.78$ meV. As discussed by Katanin and Kampf [70] in the presence of interactions beyond nearest neighbors, each interaction has its own renormalization factor which must be determined self-consistently.

On the other hand, as discussed in section 3.3.3 there exist convincing numerical evidence against including further-neighbor interactions in the spin Hamiltonian underlying the single-magnon dispersion $\hbar\omega_{\boldsymbol{q}}$ in order to explain the zone boundary dispersion. Both QMC and exact diagonalization studies of the nearest-neighbor only Heisenberg Hamiltonian have produced zone boundary dispersions with the correct symmetry and magnitude. Moreover, as we shall discuss below, the high-energy single-magnon dispersion computed using series expansion techniques is in very good agreement with the measured dispersions in both CFTD [56] and $Sr_2Cu_3O_4Cl_2$ [55]. Finally, Fig. 70(b) shows that neither ferromagnetic nor antiferromagnetic next-nearest neighbor interaction yield intensity variations along the zone boundary while Fig. 15(d)-(f) clearly indicates

a large intensity difference between $(\pi/2, \pi/2)$ and $(\pi, 0)$.

If we use the series expansion dispersion [34] we are able to obtain excellent agreement with the data at high energies, in particular along the zone boundary. The series expansion approach is expected to be valid only at short wavelengths and high energy scales, so we have not attempted a fit to the experimental data, but simply scale the theoretical dispersion to yield optimum agreement with the data above $\hbar\omega = 10$ meV. The red lines in Fig. 16 correspond to $J = 6.16$ meV, where once again we are assuming a single energy scale renormalization factor $Z_c = 1.18$.

The red squares at the two zone boundary points $(\pi, 0)$ and $(\pi/2, \pi/2)$ are taken from a Quantum Monte Carlo calculation of the full spin excitation spectrum of the 2DQHAFSL by Sandvik and Singh [37, 84], who found magnon energies of $2.16J$ and $2.40J$ respectively at the two points, corresponding to a zone boundary dispersion of 10% (Other QMC investigations of the 2DQHAFSL have yielded smaller zone boundary dispersions [36]). In Fig 16(b) we have normalized these numbers to unity at $(\pi/2, \pi/2)$.

The final comparison we want to make at this stage is with a completely different class of theory [85, 86, 83] in which the high energy degrees of freedom of the Heisenberg model are fermionic (charge 0, spin 1/2 spinons) while the low energy ones are bosonic Goldstone modes (spin waves). In technical terms, the starting point of these approaches is the Hubbard model Eq. (42) in the limit of half-filling and for $U/t \gg t$. As discussed in chapter 3 this leads to the Heisenberg model with $J = 4t^2/U$. Each spin operator in the Heisenberg Hamiltonian is then written as a pair of fermions and the quartic coupling term resulting from the substitution is decoupled in a mean-field treatment where moving a fermion around an elementary plaquette of the square lattice adds a phase of exactly π, corresponding to a magnetic flux of $\Phi_0/2 = hc/2e$ piercing each plaquette. These fermions are then forced to obey the constraint that only one fermion is present at each site. Analyzing such a model one can construct a state − the π-flux state − which has an energy close to the best numerical values for the Heisenberg model. However, energywise, an even better state is obtained by combining the π-flux state with a spin-density-wave state. This may be done variationally, resulting in a staggered magnetization agreeing well with the best values obtained for the Heisenberg model [85].

While such theories might seem wildly exotic, a comparison can be motivated from an experimental viewpoint since the spin excitation spectrum (obtained from underlying fermion bands found by diagonalizing an effective π-flux + spin-density-wave Hamiltonian) calculated by Hsu [85] agrees qualitatively with the observations in CFTD and $Sr_2Cu_3O_4Cl_2$: Along the line $(\pi, \pi) \rightarrow (\pi, 0)$ there is a maximum in the dispersion of the lowest-energy spin excitations well before $(\pi, 0)$. Further, there is a zone boundary dispersion with $\hbar\omega(\pi/2, \pi/2) > \hbar\omega(\pi, 0)$. Quantitatively, the theoretical energy variation along the zone boundary is however far greater than seen experimentally: $1 - \omega(\pi, 0)/\omega(\pi/2, \pi/2) = 0.64$. For illustration, the green lines in Fig. 16 are from work by Syljuåsen and Lee [83] (Kindly provided by O. F. Syljuåsen) who − using the π-flux ansatz − investigated the spin excitation spectrum of the Heisenberg model in an external magnetic field. The effect of a field is interesting from a theoretical viewpoint since it is expected − by analogy with 1D systems where spinons are theoretically and experimentally well established − to bring out any fermionic character of the spin excitations more clearly. The green lines in Fig 16 correspond to the $H = 0$ T limit, but evidently fail to provide an accurate description of the experimental data despite the qualitative similarities.

The full spectrum of transversely polarized excitations of the π-flux phase theory has been computed by Ho *et al.* [86] using the random phase approximation. They find that in addition to the lowest-lying, magnon-like excitations (which they refer to as RVB-excitons) studied by Hsu [85], there is nonvanishing weight associated with a higher-energy spectrum of particle-hole (spinon) excitations. In this picture, a spin-flip excitation should be associated with a pair of such spinons. This theory predicts an energy gap between the exciton and the spinon continuum which vanishes at $(\pi, 0)$. Moreover, the spectral weigh of the transverse continuum is predicted to be substantially larger near $(\pi, 0)$ than near $(\pi/2, \pi/2)$. In principle, these two effects could conspire to lead to an overestimation of the energy of the lowest lying mode at $(\pi, 0)$ in analysis of experimental data [83] thus improving the agreement with [85]. However, since the time-of-flight data are averages over transverse and longitudinal spin excitations, we cannot make any direct comparisons with [86] at this stage. To do so, we must first separate the transversely polarized spin excitations from the longitudinally polarized ones. This is done in the next chapter where we return to the predictions of the π-flux phase description of the Heisenberg model.

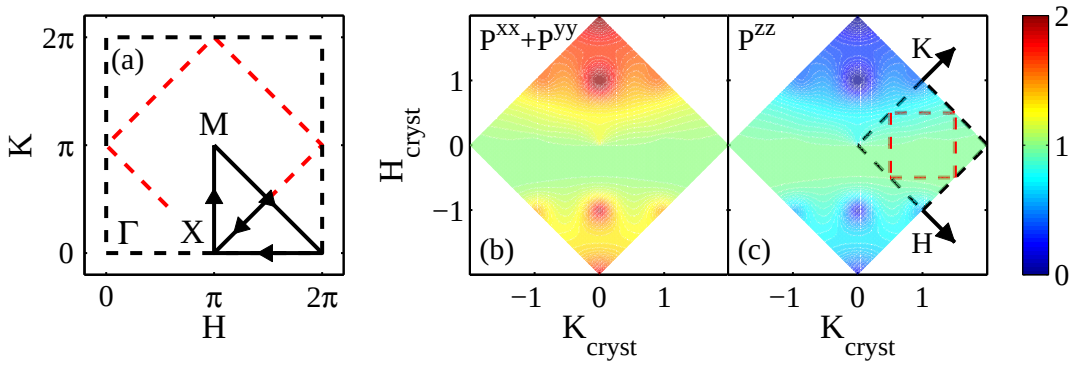

Figure 17: (a) Wavevector path in the reciprocal space of the square lattice probed in the experiment. In this figure only, we use the subscripted notation $(H_{\rm cryst}, K_{\rm cryst})$ for the crystallographic Miller indices and (H, K) for the Miller indices in the reciprocal space of the square lattice. (b) Expected polarization factor $P^{xx} + P^{yy}$ for fluctuations perpendicular to the ordered moment direction, calculated on a linear spin wave theory dispersion surface $\hbar\omega_{\boldsymbol{q}} = 2Z_c J\sqrt{1-\gamma_{\boldsymbol{q}}^2}$ with the nearest neighbor exchange $J = 6.31$ meV taken from [56] and $Z_c = 1.18$. (c) Expected polarization factor P^{zz} for the ordered moment and for fluctuations along the ordered moment direction.

4.3.2 Polarization factor variation

The neutron scattering cross-section contains the term

$$\sum_{\alpha,\beta}(\delta_{\alpha\beta} - \hat{\mathbf{Q}}_\alpha\hat{\mathbf{Q}}_\beta)S^{\alpha\beta}(\mathbf{Q},\omega) \tag{49}$$

which expresses the physical fact, that one observes only the components of the magnetic moment which are at right angles to the total wavevector transfer $\mathbf{Q}$. In this section, we analyze the variation of $A_{\rm fit}$ in constant-energy cuts taken at low energy transfers in the four Brillouin zones closest to the origin. The object is to test to which extent the expected variation of the polarization factor is reflected in the values of $A_{\rm fit}$ extracted from Tobyfit.

Employing the notation of appendix A where the ordered moment is taken to be along the z-direction, the polarization factors multiplying the scattering functions $S^{xx}(\mathbf{Q},\omega)$ and $S^{yy}(\mathbf{Q},\omega)$ describing single-magnon scattering are $P^{xx} = (1-\hat{\mathbf{Q}}_x^2)$ and $P^{yy} = (1-\hat{\mathbf{Q}}_y^2)$ respectively. Since by symmetry we expect $S^{xx}(\mathbf{Q},\omega) = S^{yy}(\mathbf{Q},\omega)$ below T_N, the effective polarization factor for single-magnon scattering becomes $P^{xx} + P^{yy} = (2 - \hat{\mathbf{Q}}_x^2 - \hat{\mathbf{Q}}_y^2)$. The polarization factor for scattering from the (static or longitudinally polarized fluctuating) components of the moment along z is $P^{zz} = (1 - \hat{\mathbf{Q}}_z^2)$.

With the sample oriented with its 2D planes perpendicular to $\mathbf{k}_i$ and with the ordered sublattice moment almost precisely along $\mathbf{a}^*$ [80] one would expect to find that the single-magnon modes observed at wavevector transfers close to $\mathbf{a}^*$ are generally more intense than those for wavevector transfers close to $\mathbf{b}^*$.

To estimate the magnitude of this expected intensity anisotropy more precisely we use the known incident neutron energy E_i and the value $J = 6.31 \pm 0.02$ meV deduced by Rønnow *et al.* [56] to compute the polarization factor variations everywhere in the four Brillouin zones closest to the origin. To this end, we assume that linear spin wave theory is valid so that we have the result $\hbar\omega_{\boldsymbol{q}} = 2Z_c J(1-\gamma_{\boldsymbol{q}}^2)^{1/2}$ for all wavevectors. The effect of the zone boundary dispersion observed by Rønnow *et al.* is not considered, since at this stage we are only interested in the variation of $A_{\rm fit}$ for wavevectors $\mathbf{Q}_{\rm 2D}$ away from the zone boundary. We start by calculating $\hbar\omega_{\boldsymbol{q}}$ everywhere inside the four Brillouin zones of the square lattice lying closest to the origin. Next, we use the known sample orientation and crystal structure to convert the square lattice reciprocal space to corresponding H and K values in the real 3D reciprocal of CFTD. The plane in 3D reciprocal space corresponding to the square lattice reciprocal space is tilted $\beta - 90 = 10.79$ degrees away from the vertical because CFTD is monoclinic. To obtain the out-of-plane component L we use the Eq. (23) describing the time-of-flight parabola. Having thus found $\mathbf{Q} = H\mathbf{a}^* + K\mathbf{b}^* + L\mathbf{c}^*$, it is straightforward to calculate $P^{xx} + P^{yy}$ and P^{zz} by simply expressing the unit vector $\hat{\mathbf{Q}} = (\hat{\mathbf{Q}}_x, \hat{\mathbf{Q}}_y, \hat{\mathbf{Q}}_z)$ in a Cartesian frame spanned by two orthogonal unit vectors $\mathbf{u}_x$ and $\mathbf{u}_y$ in the $\mathbf{bc}$-plane perpendicular to $\mathbf{a}^*$ and a third unit vector $\mathbf{u}_z$ along $\mathbf{a}^*$.

Figure 17(b) and (c) shows the results for $P^{xx} + P^{yy}$ and P^{zz} (Note the subscripted notation used in these plots only to avoid confusion between Miller indices in 2D and 3D reciprocal space). The asymmetry between the up and down directions is caused by the monoclinic crystal structure which leads to different values of L for points in 3D reciprocal space which correspond to equivalent points in the reciprocal space of the square lattice. Figure 17(b) predicts a low-energy ratio approaching 2 between the effective polarization factors $P^{xx} + P^{yy}$ near the crystallographic $(H, K) = (1, 0)$ and $(0, 1)$ positions. It was however recognized at an early stage of the analysis that the experimental data do not show such a large variation.

To illustrate this, we have grouped the amplitude parameters A_{fit} resulting from fits of eight equivalent low-energy, constant-$\hbar\omega$ cuts along the [11] direction into two sets: One set for the four cuts going horizontally and vertically through $(H, K) = (1, 0)$ and $(H, K) = (-1, 0)$ in Fig. 17(b) and another set for the four cuts going through $(H, K) = (0, 1)$ and $(H, K) = (0, -1)$. Comparing the four values of A_{fit} within each set, we find that they do not show the systematic variation implied for $P^{xx} + P^{yy}$ in Fig. 17(b). This is not so surprising given that the expected variation is rather small over the four equivalent cuts in each set and could well be hidden from view by the experimental errorbars on A_{fit}. Since the four values of A_{fit} in each set are mutually consistent at all energies in the range 3.5-11.5 meV investigated, we have calculated an average over the four A_{fit}-values for each each energy transfer and for each set. These are plotted versus 2D momentum transfer in Fig. 18(a). It is evident that the single-magnon intensities are systematically larger in the upper and lower detector banks (Red symbols. Momentum transfers around $\mathbf{a}^*$) than in the horizontal detector banks (Blue symbols. Momentum transfers around $\mathbf{b}^*$). Qualitatively, this is in agreement with the expected variation in $P^{xx} + P^{yy}$ seen in Fig. 17, as is the fact that $P^{xx} + P^{yy}$ for the horizontal banks appears independent of energy transfer. However, quantitatively there is a large discrepancy. To bring this forward, we have taken the ratio between the averaged values of A_{fit} in the vertical and horizontal detector banks and compare this ratio with the theoretical expectation in Fig. 18(b). The comparison shows that while there is systematically 10-20 percent more intensity for momentum transfers near $\mathbf{a}^*$ than for momentum transfers near $\mathbf{b}^*$, the magnitude of this anisotropy is far below the theoretical expectation indicated by the solid black line. Moreover, the anisotropy does not appear to depend on energy (or momentum) transfer in an obvious manner because of the much larger scatter in the values of $P^{xx} + P^{yy}$ for the vertical detector banks than for the horizontal ones.

How can we rationalize the unexpected reduction in the intensity anisotropy? First, twinning between the **a** and **b** crystal directions which have roughly equal length lattice constants could well produce the effect we are seeing since the moment are along $\mathbf{a}^*$. However, we can argue against this possibility on the grounds that during the alignment of the crystals, the critical step was the identification of allowed and disallowed Bragg reflections (H, K, L) and (K, H, L). Having found the allowed reflection, the crystal was reoriented to search extensively for the disallowed one. Since none were found, we can say with some confidence that neither of the two crystals were substantially twinned.

A second possibility is to speculate that maybe the ordered moment is not close to $\mathbf{a}^*$. The literature does contain suggestions of a moment direction away from $\mathbf{a}^*$, but these found a natural explanation in the neutron diffraction studies of Burger *et al.* [80] as arising from weak ferromagnetism in the presence of an external magnetic field. Since the evidence of a moment direction close to $\mathbf{a}^*$ in [80] appears solid it is an assumption we are reluctant to abandon. However in the face of the data in Fig. 18(b), we should at least consider the logical possibility of an different moment direction. For example, if the moments are parallel to $\mathbf{c}^* \parallel \mathbf{k}_i$ we would expect only a very small difference in the intensities of spin waves in the horizontal and vertical detector banks. The magnitude of this difference (a result of the monoclinic crystal structure) is expected to be of the order $\cos(\beta)^2$ which is a only few percent. Clearly this fails to explain the data in Fig. 18(b) but the argument shows that one might plausibly obtain better agreement with the experimental data if the moment direction is assumed to be closer to $\mathbf{c}^*$ than to **a**. However, as we shall see in chapter 5, the data from our polarized neutron scattering studies of the excitation spectrum of CFTD are inconsistent with a moment direction close to **c** whereas good agreement is obtained when they are analyzed under the explicit assumption of a moment direction parallel to $\mathbf{a}^*$.

A third idea is to ask whether in fact $S^{xx}(\mathbf{Q}_{2\text{D}}, \omega) \neq S^{yy}(\mathbf{Q}_{2\text{D}}, \omega)$ in the ordered phase of CFTD. Because crystal field effects are known to cause such asymmetries in the excitation spectra of rare earth systems, deviations from the circular symmetry implied by $S^{xx}(\mathbf{Q}_{2\text{D}}, \omega) = S^{yy}(\mathbf{Q}_{2\text{D}}, \omega)$ towards ellipticity cannot immediately be ruled out, but would obviously be an ugly dent in our

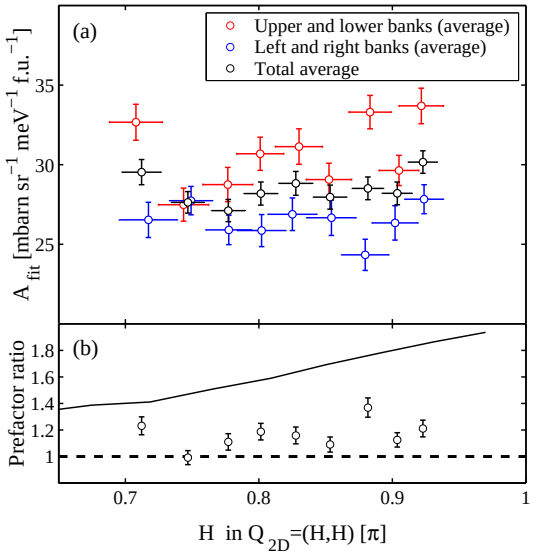

Figure 18: Checks of the polarization factor variation for low energy, constant-$\hbar\omega$ cuts along the [11] direction of the square lattice reciprocal space. (a) Averaged amplitude prefactors $\langle A_{\rm fit}\rangle$ obtained from the fitted parameters $J^{\rm fit}$ and $A^{\rm fit}$ as described in the text. The vertical and horizontal errorbars are related through Eq. (47). Each red (blue) symbol represents an average over the individual results of least-squares fits of four equivalent [11] directions going through the two (π,π) points in the vertical (horizontal) detector banks. The black symbols are the average of all eight equivalent cuts at each energy transfer. The horizontal axis shows 2D momentum transfer along the [11] direction. From left to right, the points correspond to constant energy cuts within the ranges 11.5 ± 0.5 meV to 3.5 ± 0.5 meV in steps of 1 meV. (b) Ratio $\langle A_{\rm fit,vert}\rangle/\langle A_{\rm fit,horz}\rangle$ of the amplitude prefactors in the vertical and horizontal detector banks. The solid line is the theoretically expected $T=0$ K behavior, calculated from the effective polarization factor $P^{xx}+P^{yy}$ for single-magnon scattering shown as a color map in Fig. 17(b).

picture of CFTD as an ideal 2DQHAFSL. Even if crystal field effects were absent, there is no argument to rule out a different origin. We can however ask for a quantitative estimate of the asymmetry required to reproduce Fig. 18(b). For this purpose, we neglect the monoclinic symmetry of the crystal and assume a moment direction parallel to $\mathbf{a}^*\parallel\mathbf{a}$. In this case, fluctuations in the moment direction parallel to $\mathbf{c}^*\parallel\mathbf{c}$ would by symmetry be multiplied by identical polarization factors in the vertical and horizontal banks. The only intensity difference would be due to fluctuations along $\mathbf{b}^*\parallel\mathbf{b}$ for which the relevant polarization factor $P^{\boldsymbol{bb}}$ is close to zero for parallel wavevector transfers (i.e. for wavevectors in the horizontal bank) and approaches unity for wavevector transfers near $\mathbf{a}^*$ (i.e. for wavevectors in the vertical bank). Thus, even without considering the orientation of the principal axes of elliptically polarized excitations, the observed 10-20 percent intensity difference between the orthogonal banks would imply a very large anisotropy $S^{\boldsymbol{cc}}(\mathbf{Q}_{\rm 2D},\omega)\geq 5S^{\boldsymbol{bb}}(\mathbf{Q}_{\rm 2D},\omega)$ in the single-magnon response. Perhaps the best evidence against a large anisotropy between fluctuations in the directions perpendicular to $\mathbf{a}^*$ is provided by the polarized triple axis neutron scattering measurements discussed in the next chapter. With polarized neutrons we are able to separate from each other three perpendicular components $S^{xx}(\mathbf{Q}_{\rm 2D},\omega)$, $S^{yy}(\mathbf{Q}_{\rm 2D},\omega)$ and $S^{zz}(\mathbf{Q}_{\rm 2D},\omega)$ of the scattering function of the sample. In doing so, we can directly check for any anisotropies between spin fluctuations along the relevant directions $\mathbf{b}^*$ and $\mathbf{c}$. No such anomalies were found, and we are therefore justified in rejecting the possibility of significant anisotropy in the single-magnon response.

A fourth possibility, which in a sense supersedes the previous two, is that perhaps the temperature at the sample position was in fact higher than was read off from the temperature controller during the experiment. For example, if the sample temperature was actually greater than T_N, we would expect no anisotropy between the intensities of paramagnetic magnon-like excitations probed in orthogonal detector banks because all spin-directions become equivalent above T_N. Thus, because we indisputably do see a clear anisotropy we know that spin rotational symmetry must have been broken and therefore $T<T_N$. In the opposite limit, at $T=0$ K, linear spin wave theory predicts that $S^{xx}(\mathbf{Q}_{\rm 2D},\omega)=S^{yy}(\mathbf{Q}_{\rm 2D},\omega)$ consists solely of single-magnon scattering whereas $S^{yy}(\mathbf{Q}_{\rm 2D},\omega)$ has an elastic contribution from the static ordered moment as well as an inelastic two-magnon contribution continuously distributed over momentum space, and over energies between the single-magnon energy and two times the zone boundary energy. It is in this limit the

solid black line in Fig. 18(b) is expected. For temperatures between 0 K and T_N, the evolution of the components of $S(\mathbf{Q}_{2D}, \omega)$ must happen continuously since the transition at T_N is a second order phase transition. Therefore, the ratio of single-magnon intensities near $\mathbf{a}^*$ and $\mathbf{b}^*$ must also evolve continuously, from the high-temperature value 1 to a low-temperature, low-energy limit approaching 2. The diffraction study by Burger, Fuess and Burlet [80] shows that at our experimental base temperature 7 K, the ordered moment is near its saturation value. If we assume that the same applies to the inelastic contributions, then we are justified in expecting a ratio near 2 at low energies. However, if the temperature at the sample position was actually closer to T_N, then the observed deviation from the low-temperature expectation is a natural consequence of the continuous redistribution of intensities in a second order phase transition.

One might also speculate whether the presence excitations other than the single-magnon modes studied in this chapter would be capable of producing the effect seen in Fig. 18(b). Glancing at linear spin wave theory as it is presented in appendix A, we would expect two-magnon excitations to be most relevant in this respect. Because these excitations are polarized along $\mathbf{a}^*$ the polarization factor associated with two-magnon excitations at $T = 0$ K is P^{zz} displayed in Fig. 17(c). However, since P^{zz} approaches unity for wavevectors along $\mathbf{b}^*$ and is close to zero for wavevectors along $\mathbf{a}^*$, two-magnon excitations would only be visible in the horizontal detector banks. If we tentatively assume that two-magnon excitations are present between the single-magnon branches (Chapter 5 will show that this is indeed the case), then they would tend to reduce the values of A_{fit} obtained from data in the horizontal banks from the correct ones, i.e. they would tend to yield a prefactor ratio larger than 2 rather than one close to unity.

In conclusion to this section, we have seen that the experimental data contain an anisotropy in the single-magnon amplitudes which is reduced from what one would have expected from the polarization factor variation at low temperatures. In order to explain this observation we have outlined a number of possible contributing factors. Considering the evidence from this experiment together with that of the experiment reported in chapter 5, we find the most likely cause of the observed reduction in intensity anisotropy to be that the sample temperature was higher than indicated by the temperature controller, but we cannot be completely certain that this is the only contributing factor. If the temperature were the sole factor behind the observed reduction in anisotropy, one could in principle regard the low-energy limit $\sim 1.2 - 1.4$ in Fig. 18(b) as a subtle measure of $S^{xx}(\mathbf{Q}_{2D}, \omega) - S^{zz}(\mathbf{Q}_{2D}, \omega)$, but without a detailed model for the temperature evolution of $S^{xx}(\mathbf{Q}_{2D}, \omega)$ and $S^{zz}(\mathbf{Q}_{2D}, \omega)$ it is not possible to continue this line of reasoning.

To proceed further, we note that since the polarization factor discrepancy is between experimental and theoretical intensity ratios rather their individual absolute values, there is no obvious reason to prefer analyzing data from one direction over the other. Indeed, restricting attention to one direction in $\mathbf{Q}$-space or to a particular set of detectors would make it impossible to study $\hbar\omega_{\boldsymbol{q}}$ and $I_{\boldsymbol{q}}$ over the entire Brillouin zone. The need to use all available data is particularly pressing for wavevectors $\mathbf{Q}_{2D}$ near the zone boundary where intensities become quite weak. Consequently, we have elected to leave the polarization factor out of the model Eq. (45) used by Tobyfit. Instead, when analyzing intensities we resign ourselves to making statements only about the averages of the intensities observed in the horizontal and vertical detector banks. These are shown as black symbols in Fig. 18(a) and are roughly independent of energy transfer. One might say that we approach the intensity analysis as if we were studying paramagnetic fluctuations and not fluctuations in an ordered antiferromagnet. By averaging over amplitudes A_{fit} which differ by 10-20 percent (some of which should depend on energy), we must concede a source of error of magnitude 5-10 percent in our further intensity analysis.

4.3.3 Single-magnon intensity $I_{\boldsymbol{q}}$

The significance of the intensity $I_{\boldsymbol{q}}$ is seen most clearly when it is realized that at zero temperature, the diagonal components of $S^{\alpha\beta}(\mathbf{Q}, \omega)$ defined in Eq. (16) are simply proportional to

$$S^{\alpha\alpha}(\mathbf{Q}, \omega) = \sum_m |\langle m | S^{\alpha}_{\mathbf{Q}} | 0 \rangle|^2 \ \delta(\hbar\omega - E_m) \tag{50}$$

where $|0\rangle$ is the ground state with energy $E_0 = 0$ and the sum runs over all excited states $|m\rangle$. The enclosed operator $S^{\alpha}_{\mathbf{Q}}$ is just the Fourier transform of $S^{\alpha}_{\boldsymbol{ld}}$. Thus, at low temperature what we are really measuring is a set of squared matrix elements of $S^{\alpha}_{\boldsymbol{Q}}$ connecting the ground state to the excited states. In the linear spin wave approach to the 2DQHAFSL we assume that the

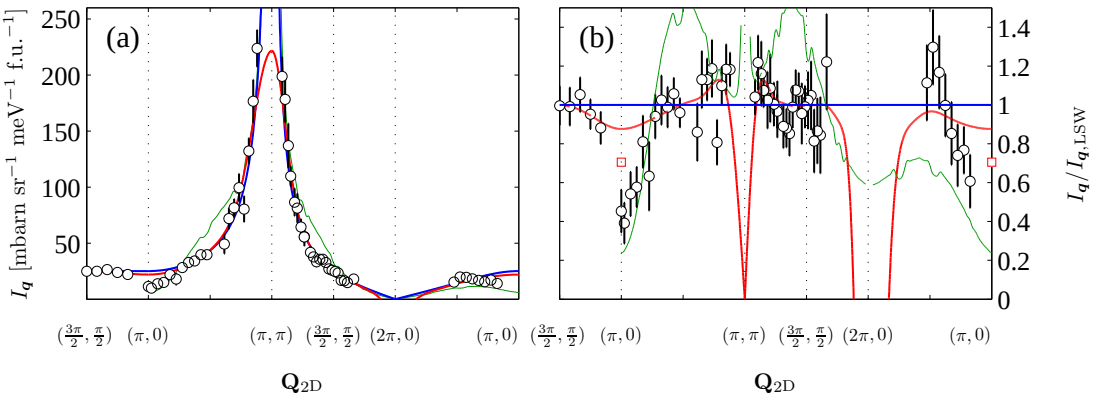

Figure 19: (a): Single-magnon intensities $I_{\boldsymbol{q}}$ in CFTD. The blue, red and green lines have the same significance as in Fig. 16. As discussed in section 4.3.2 the values of $I_{\boldsymbol{q}}$ presented here are averages over all detector banks. (b): Ratio of the observed intensities to the prediction of nearest neighbor linear spin wave theory as described in the text. The open red squares at $(\pi, 0)$ are from QMC studies of the 2DQHAFSL [37, 84]. Rapid variations in the green lines are caused by numerical noise in the data from [83].

ground state $|\,0\rangle$ is the long range ordered Néel state. The operators $S^{\alpha}_{\mathbf{Q}}$ with $\alpha = x,y$ then create a spin wave and $I_{\boldsymbol{q}}$ is a measure of the probability of creating a magnon with wavevector $\mathbf{Q}$ in the Néel state. By contrast, if $|\,0\rangle$ is not known, the interpretation of $I_{\boldsymbol{q}}$ is more involved. It holds information not only about the excited states $|\,m\rangle$ but also about the unknown ground state $|\,0\rangle$ itself.

In section 4.3.1 we discussed our results for the single-magnon dispersion displayed in figure 16(a). Figure 19(a) shows the corresponding values of the single-magnon intensity $I_{\boldsymbol{q}}$ defined by Eq. (46).

Since the single-magnon dispersion was found to be well described along the [11] direction by the expression (48), we fit the experimental intensities along the same direction by the linear spin wave theory expression $I_{\boldsymbol{q},\mathrm{LSW}} = I_{\pi/2}[(1-\gamma_{\boldsymbol{q}})/(1+\gamma_{\boldsymbol{q}})]^{1/2}$ where $I_{\pi/2}$ is the intensity at $(\pi/2, \pi/2)$. Having obtained $I_{\pi/2}$, we calculate the expected single-magnon intensity over the full momentum space path investigated (blue lines). Precisely as we observed for the single-magnon dispersion, the linear spin wave prediction for the intensities is in good agreement with the data except for the region around $(\pi, 0)$. Dividing the data by the linear spin wave prediction with the prefactor equal to $I_{\pi/2}$, we obtain Fig. 19(b) from which it is clear that near $(\pi, 0)$ spin wave theory overestimates the spectral weight by roughly a factor of two. Thus, in qualitative terms, the dependence of the single-magnon intensity with $\mathbf{Q}_{2\mathrm{D}}$ appears to mimic that of the single-magnon energy. Quantitatively, we find that the spectral weight of the magnon at $(\pi, 0)$ amounts to only $46 \pm 12\%$ of the spectral weight of the magnon at $(\pi/2, \pi/2)$. These numbers do not include the 5-10% error related to our failure to detect the full polarization factor variation in A_{fit}. However, even this source of error is insufficient to yield equal intensities at $(\pi, 0)$ and $(\pi/2, \pi/2)$.

In the light of the comments made in the first paragraph of this section, the intensity dip at $(\pi, 0)$ can be interpreted as implying either

- The need for to include terms in the spin Hamiltonian coupling spins beyond their nearest neighbors.
- That the Néel state is a good approximation of the ground state of the 2DQHAFSL in two dimensions, but linear spin wave theory is incapable of accurately predicting the properties of the excited states.
- That the Néel state is not a good approximation of the ground state of the 2DQHAFSL in two dimensions.

Inclusion of a finite next-nearest neighbor interaction J' in linear spin wave theory does not heal the discrepancy observed near $(\pi, 0)$ since the intensities of zone boundary magnons are unaffected by such a term in the spin Hamiltonian, see Fig. 70(b). As discussed already in section 4.3.1, we consider this a strong argument against assigning the zone boundary dispersion to further neighbor interactions.

Slightly better agreement is found using the series expansion approach [34] which does give a dip in the single-magnon intensity at $(\pi, 0)$ relative to $(\pi/2, \pi/2)$ (Red lines. Note that the series expansion result is only valid at high energies and therefore the discrepancies on approaching (π, π) and $(2\pi, 0)$ are not physically significant). The magnitude of the dip is however too small to account for the observed intensity variation even when allowance is made for a 5-10% error on all intensities. Thus, even though the agreement between the series expansion result for $\hbar\omega_{\boldsymbol{q}}$ and experimental data for CFTD and $Sr_2Cu_3O_4Cl_2$ (as well as with QMC and exact diagonalization) hints that the zone boundary dispersion is a property of the pure Heisenberg model, the theory appears incomplete in its overestimation of the corresponding intensities.

Quantum Monte Carlo calculations of the transverse and longitudinal spectra of the Heisenberg model lead to a zone boundary dispersion of 10% (See Fig. 16) and a spectral weight ratio of 0.71 for zone-boundary magnons at $(\pi, 0)$ and (π, π) [37, 84]. We include the latter prediction as open red squares at $(\pi, 0)$ in Fig. 19(b). Taking into account the 5-10% intensity error of uncertain origin, this numerical approach comes quite close to the experimentally observed intensity difference. In the next chapter we shall see that the same QMC computations yield excellent agreement with the full spectrum of excitations at both zone boundary position. Since QMC does not assume the Néel state as the ground state, and is essentially exact modulo numerical error its agreement with experiment can be viewed as a fingerprint of a non-negligible reduction from unity in the overlap between the true ground state and the Néel state.

Finally, the π-flux phase description of the Heisenberg model (green lines; from [83]) yields reasonable agreement with the observed intensity difference between $(\pi, 0)$ and $(\pi/2, \pi/2)$, but unfortunately does not predict the variation along the zone boundary. Furthermore, it overestimates the observed intensities along the paths leading from the zone center at (π, π) to both $(\pi, 0)$ and $(\pi/2, \pi/2)$.

4.3.4 Multimagnons

It is interesting to note, that despite significant quantitative differences seen in Figs. 16 and 19, the dispersion and the intensities of the lowest lying spin excitation predicted by the π-flux phase theory have qualitative characteristics similar to those seen in our experiment. However, as we have discussed above and will return to in the next chapter, QMC also yields a good description of our observations. To go one step further in comparing these approaches to the Heisenberg model to experiment, we must consider higher energy excitations forming continua above the main spin wave branches.

In spin models these would correspond to multimagnon excitations. For the particular case of linear spin wave theory, appendix A shows that they are longitudinally polarized two-magnon excitations. Transversely and longitudinally polarized excitations of still higher order result when spin wave theory is carried to higher order. In the flux-phase description of the Heisenberg model, the higher energy excitations are spin 1/2 spinons. Because a spin-flip neutron scattering process has $\Delta s^z = 1$, a single neutron must necessarily excite a pair of spinons.

We finish this chapter with a discussion of multimagnon excitations in the MAPS data. As mentioned above, linear spin wave theory predicts a continuum of longitudinally polarized two-magnon excitations at energies above the single-magnon branches. Fig. 72 shows that at $T = 0$ K, roughly a third of the total integrated spectral weight $S(S+1)$ is expected to be associated with the longitudinal continuum scattering. Although this continuum does have some internal structure (See Fig. 71 for a 1D example or Fig. 26 for 2D examples) its defining characteristic is that it is spread out over $\mathbf{Q}_{2D}$ and $\hbar\omega$. If at all visible, the signature of multimagnon scattering should therefore be weak extra scattering above the single-magnon branch which cannot be accounted for by our model (45) for $S(\mathbf{Q}, \omega)$.

Figure 20(a) displays a constant-$\hbar\omega$ cut along a [10] direction through $(H, K) = (0, 1)$ where Fig. 17(c) shows that $P^{zz} \simeq 1$ at $T = 0$ K, meaning that longitudinally polarized excitations, if they are sufficiently intense and the background scattering is low enough, ought to be visible. The solid black line represents a fit performed in Tobyfit using our model (45). While the agreement between fit and data is good in terms of the single-magnon position, intensity and background level outside the two counterpropagating spin wave branches, there is clearly more intensity than predicted by the model in the region between the two peaks as casually indicated by the grey box. This observation is qualitatively consistent with multimagnons, but does not constitute a proof of their existence since we are unable to unambiguously assign an origin to the excess scattering.

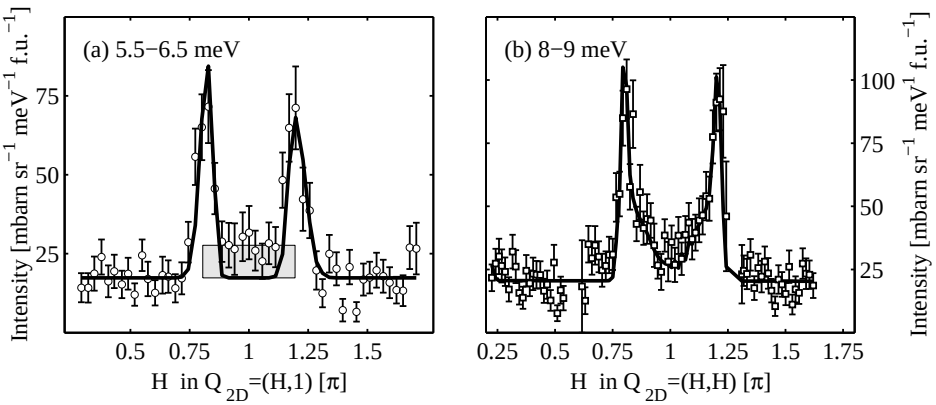

Figure 20: Possible multimagnon signatures. (a) An example of a fit of a constant-$\hbar\omega$ cut in which there is excess spectral weight between the two main peaks. The height above background of the grey box represents an average over the intensities of the nine centermost points. (b) A cut obtained in the rotated geometry described in the text. The solid line is a fit to the model (45) and is in excellent agreement with the data without any need for multimagnon excitations.

Remembering from Fig. 14 that there are phonon bands cutting through the region surrounding the zone center at (π, π), scattering from phonons is a particularly worrying alternative cause of the extra intensity we see.

The fit displayed in Fig. 20(a) is not the only example of a fit where extra intensity is seen which cannot be accounted for by the resolution convoluted model, but might plausibly be explained by multimagnon scattering. Not all these examples are as pleasing to the eye as that shown in Fig. 20(a). More typically they have features reminiscent of the fit displayed in Fig. 15(c), where the intensity distribution between the peaks appears slightly skewed towards one (or both) of the single-magnon peaks. Such behavior might seem odd for continuum scattering, but even the two-magnon spectrum computed in linear spin wave theory does have weak maxima immediately inside the single-magnon branches as can be seen in Fig. 26. Thus, lineshape anomalies of the type mentioned do not in themselves constitute a strong argument against the idea that multimagnon scattering is present in the data. A more serious concern is that the excess scattering between the single-magnon peaks does not seem to depend monotonically on $\hbar\omega$. Once again, phonon scattering could plausibly explain such a behavior.

As further discouraging sign of the difficulty of isolating clear evidence for multimagnon scattering in the time-of-flight data, we present a single cut obtained in a rotated scattering geometry as we shall now explain. By rotating the sample by 90 degrees around the vertical, the $\mathbf{b}^*$ direction of the reciprocal space of CFTD becomes parallel to $\mathbf{k}_i$. The $\mathbf{a}$ axis remains vertical while the undispersing $\mathbf{c}^*$-direction is along the horizontal axis perpendicular to $\mathbf{k}_i$. In this geometry, the time-of-flight parabola cuts through single-magnon modes dispersing along $\mathbf{a}^*$, but also through an extended interval of (H, L)-space corresponding to the region of $\mathbf{Q}_{2D}$-space between the single-magnon peaks. We can effectively increase our sensitivity to any scattering occurring between the peaks by creating cuts which average over a large interval of L values. By choosing $E_i = 25$ meV (the Fermi chopper frequency was 150 Hz), we arranged a situation where maximum sensitivity to such multimagnon scattering is obtained near $\hbar\omega = 8$ meV where the energy resolution is ~ 0.6 meV FWHM. The data presented in Fig. 20(b) is the result of such a cut, averaging over the energy range $8 - 9$ meV. As in Fig. 20(a) there appears at first sight to be additional scattering between the two counterpropagating magnon modes as expected for multimagnon scattering. Further, the lineshape looks asymmetric, and this could be a real feature of a multimagnon spectrum as already discussed. However, the solid black line in Fig. 20(b) is the result of a full resolution-corrected fit of our model (45) and yields quite good agreement with the experimental data. Between the single-magnon peaks, the predominant trend is for the data points to lie above the calculated curve, but the errorbars, even in this optimized scattering geometry, allow us to conclude neither the presence nor the absence of multimagnon scattering.

The data presented in this section have shown that it is unclear whether multimagnon excitations were seen at MAPS. In particular, scattering from phonons could easily disrupt attempts to unambiguously identify continuum contributions to the spin excitation spectrum. In the next chapter, we describe how to use polarized neutron scattering to do this much more efficiently.

5 Polarized neutron scattering studies of multimagnon states in CFTD

In the experiments discussed in this chapter, we have employed polarized triple axis spectrometry to separate the transverse and longitudinal spin excitation spectra $S^{xx}(\mathbf{Q}_{2D},\omega) = S^{yy}(\mathbf{Q}_{2D},\omega)$ and $S^{zz}(\mathbf{Q}_{2D},\omega)$ from each other and from coherent nuclear scattering. We have discovered for the first time, that for energies $\hbar\omega$ of order J and lower, the 2DQHAFSL supports a continuum of longitudinally polarized multimagnon states at energies above the single-magnon branch. This result is evident from the colormaps in figure 21. We shall see that the intensity of the low energy longitudinal continuum is in good agreement with the prediction of linear spin wave theory for two-magnon processes. Having demonstrated the existence of multimagnon scattering at energies $\hbar\omega \sim J$, we proceed to investigate higher order spin excitations at the two magnetic zone boundary points $(\pi, 0)$ and $(\pi/2, \pi/2)$. We find that while there are clear multimagnon contributions at both wavevectors, the intensities of which agree well with linear spin wave theory, Quantum Monte Carlo computations yield a slightly better agreement.

The previous chapter dealt with the single-magnon dispersion in CFTD at low temperatures. The analysis was performed assuming that the energy width of the dispersion is zero, corresponding to the theoretical cross-section (45) in the linear spin wave approximation. Higher order magnon contributions were entirely disregarded in the modeling of the observed intensities. In this chapter we attempt to do better.

Direct attempts to observe higher order magnon excitations in the MAPS data are problematic because of the presence scattering from phonons. While the latter may in principle be identified via their temperature dependence and then subtracted to obtain the remnant magnetic contributions, it should be kept in mind that higher order magnon processes are spread out in $\mathbf{Q}$ and $\hbar\omega$ and are therefore associated with significantly smaller intensities at any given point than the single-magnon intensities Eq. (129), even if the total integrated intensities associated with one- and multimagnon excitations are of similar magnitudes when quantum fluctuations are sufficiently strong (see Fig 72). In view of this, it is unlikely that a subtraction procedure could be made sufficiently controlled to obtain solid evidence for higher order magnons. A much more powerful technique in this respect is polarized neutron scattering, which allows the various contributions to the total observed scattering at any point in $(\mathbf{Q},\omega)$ space to be identified individually. In particular the transverse $S^{xx}(\mathbf{Q}_{2D},\omega) = S^{yy}(\mathbf{Q}_{2D},\omega)$ and longitudinal $S^{zz}(\mathbf{Q}_{2D},\omega)$ scattering functions (see Fig. 23) can be distinguished from each other and from coherent nuclear scattering from phonons. In order to do precisely this, two experiments using polarization analysis were performed at the IN20 and IN22 triple axis spectrometers at the Institute Laue Langevin (ILL) in Grenoble, France.

The outline of this chapter is as follows: In section 5.1 we present some details of relevance for the understanding the experiment. Section 5.2 contains a presentation of our method for

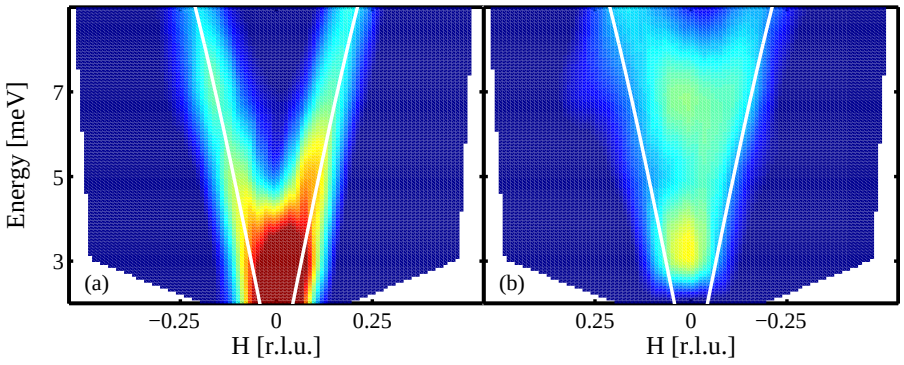

Figure 21: Low energy excitations in CFTD for wavevectors $\mathbf{Q} = (H10)$. (a) Color map of the transverse spin fluctuations $T(\mathbf{Q}_{2D},\omega) = S^{xx}(\mathbf{Q}_{2D},\omega) + S^{yy}(\mathbf{Q}_{2D},\omega)$ derived from the polarization analysis described in this chapter. (b) Color map of the longitudinal spin fluctuations $L(\mathbf{Q}_{2D},\omega) = S^{zz}(\mathbf{Q}_{2D},\omega)$. The solid white lines in (a) and (b) represent the linear spin wave dispersion which best describes the time-of-flight data for $\mathbf{Q}_{2D}$ along the direction from $\mathbf{Q}_{2D} = (0,0)$ to $\mathbf{Q}_{2D} = (\pi,\pi)$. For ease of comparison, the longitudinal intensities have been scaled as appropriate to be able to present the data on the same color scale. Counting times were between 2 and 4 minutes per point in six different polariziation channels.

reducing the raw, measured intensities to $S^{xx}(\mathbf{Q}_{2D},\omega) + S^{yy}(\mathbf{Q}_{2D},\omega)$ and $S^{zz}(\mathbf{Q}_{2D},\omega)$. Further, we discuss our model and the implementation of resolution corrections to its predictions. We then present our experimental results in section 5.3. Along the way, we discuss the significance of our findings, compare with theory and comment on outstanding issues. Finally, in section 5.4 we draw conclusions for the CFTD part of this thesis.

5.1 Experimental details

Figure 22 depicts the generic setup used in polarized triple axis spectrometry. Below, we shall discuss the individual elements of this setup with a view to the particular characteristics of the two spectrometers actually employed.

Heusler (Cu_2MnAl) monochromators and analyzers were used in both polarized experiments. The operating principle behind these neutron optical elements is to take advantage of the fact that Cu_2MnAl is magnetic, and to arrange a situation where the nuclear and magnetic contributions to the total cross-section of a particular Bragg reflection $\mathbf{Q} = \mathbf{G}$ balance and cancel each other for neutrons with a particular spin direction while the cross-section for neutron of opposite spin remains finite [2]. Under these circumstances, a polychromatic and unpolarized incident beam would be transformed into a monochromatic and polarized exit beam. When magnetized by strong permanent magnets the Heusler (111) reflection has the desired properties. At IN20 the Heusler (111) monochromator is doubly focusing and consists of 75 single crystal plates arranged in a 15×5 array 230 mm wide and 150 mm high. The 15 columns allow the horizontal focusing to be varied, while the vertical focusing is fixed. On the exit side, the analyzer consists of 11 single crystalline Heusler slabs, in total 170 mm wide and 150 mm high, with variable horizontal focusing. On IN22, the Heusler monochromator is vertically focusing with an area of 140×120 mm^2 while the Heusler analyzer is horizontally focusing and has an area of 150×100 mm^2.

To perform polarization analysis it is important to be able to control the spin state of the neutron beam from the monochromator to the sample position and − after the scattering event − from the sample to the analyzer. This is achieved by making use of the fact that in the presence of an external magnetic field, the spin of a neutron will perform Larmor precessions about the axis of said field. Moreover, the spin of the neutron will adiabatically follow a rotation in the external field direction provided the latter changes sufficiently slowly on a time-scale set by the neutron velocity. IN20 and IN22 are equipped with permanent magnet vertical guide fields (denoted 1, 2 and 3 in Fig. 22) inserted in the sections of the beam path leading to and from the sample position. These fields maintain the polarization state produced by the Heusler monochromator, and that of the neutrons which make their way towards the analyzer. Employing the same principle, a system of computer-controlled solenoid coils surrounding the sample position produces weak fields which cause an adiabatic rotation of the beam polarization to give any desired direction at the sample position and, following the scattering event, delivers the neutron beam with the wavevector and energies of interest (determined by the settings of the angles θ_M, θ_S and θ_A) back into the guide field section.

As we saw in section 2.1.3, the neutron scattering cross-sections may be divided into four individual components depending on the neutron spin state prior to and following the scattering event. In order to address the individual constituent components of the cross-sections, one must be able to flip the neutron spin at will. To do this, one can use a Mezei spin-flipper. This is a device consisting of a two flat solenoid coils. One coil acts to compensate the guide field, whereas the second produces a magnetic field transverse to the guide field axis. By adjusting the current in this second coil, the spin state of the neutron can be made to rotate by exactly 180 degrees around the transverse field, thus flipping the spin state with respect to the guide field. IN22 is equipped with a single flipper coil located after the sample table, whereas IN20 has two flippers installed before and after the sample position. The data presented in this chapter from the IN20 experiment were obtained using only the flipper on the exit side.

We can now see how the individual terms in Eq.(6) can be measured separately in an idealized experiment: If the Heusler monochromator and analyzers both reflect/transmit only spin $s^z = +1/2$ neutrons (spin up "u") and the spin-flipper is located in the exit beam path, the spin-flip (SF) and non-spin-flip (NSF) cross-sections $(d^2\sigma/d\Omega\, dE_f)_{u\to d}$ and $(d^2\sigma/d\Omega\, dE_f)_{u\to u}$ are measured with the flipper coil currents turned on and off respectively.

In both polarized experiments, the crystals to be studied were mounted with their copper-formate planes in the horizontal scattering plane. In this case, the neutron wavevector transfer $\mathbf{Q}$

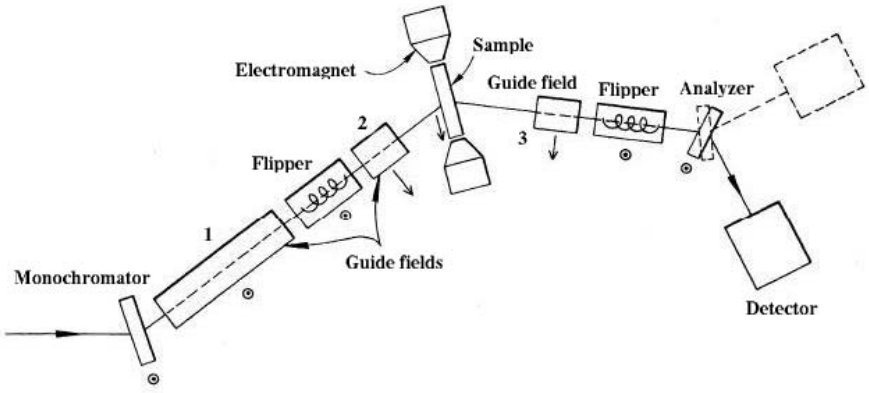

Figure 22: Schematic of the setup used in polarized triple axis neutron scattering (adapted from [5]). The individual elements in the setup are discussed in the text.

can be identified with $\mathbf{Q}_{2\mathrm{D}}$ modulo a reciprocal lattice vector. The samples masses were 7.6 grams (IN20) and 3.2 grams (IN22), and in both cases helium flow (orange) cryostats capable of cooling to temperatures around 1.5 degrees Kelvin were used.

All the data presented in this chapter were obtained with the spectrometers in the W-configuration at a fixed final neutron energy $E_f = 14.68$ meV ($k_f = 2.662$ Å^{-1}). Pyrolytic graphite filters were inserted in $\mathbf{k}_f$ to remove higher order contamination of the exit beam. In order to maximize the count rate for magnetic signal, the instruments were shortened as much as possible and we refrained from inserting collimators in $\mathbf{k}_i$ or $\mathbf{k}_f$. The beam sizes were thus defined solely by slits and diaphragms.

5.2 Analysis

In chapter 3 we saw that below the 3D ordering temperature $T_N = 16.2$ K, the ordered moments are contained in the **ac** plane, and oriented 8 degrees from the **a** axis, away from the **c**-axis. In the monoclinic crystal structure of CFTD, this means that the moments are 3.1 degrees from the $\mathbf{a}^*$ direction. Since there could be small uncertainties in the moment direction, the analysis presented here assumes $\langle \mathbf{S} \rangle \parallel \mathbf{a}^*$. In due course, we shall see that a small rotation of $\langle \mathbf{S} \rangle$ away from the $\mathbf{a}^*$-direction has virtually no effect on our results. With the sublattice moment along $\mathbf{a}^*$, the transverse components $S^{xx}(\mathbf{Q}_{2\mathrm{D}}, \omega)$ and $S^{yy}(\mathbf{Q}_{2\mathrm{D}}, \omega)$ of the scattering function are identical by symmetry and equal to the spatial and temporal Fourier transform of two-point correlation functions between components of the spins contained in the plane spanned by $\mathbf{b}^*$ and the crystallographic **c** axis. Similarly, the inelastic part of the longitudinal scattering function $S^{zz}(\mathbf{Q}_{2\mathrm{D}}, \omega)$ describes correlations between the fluctuating spin components along $\mathbf{a}^*$. Figure 23 illustrates this in a classical, precessing-vector image of the spin excitations.

A quantitative analysis starts by the introduction of the polarization P of the neutron beam. If N_u and N_d are the number of neutrons with $s^z = +1/2$ and $s^z = -1/2$ respectively inside a given volume enclosing a section of the beam path and with the z-direction defined by the guide field direction, P is determined by the ratio

$$P = \frac{N_u - N_d}{N_u + N_d} \tag{51}$$

A fully polarized beam, *i.e.* one with either N_u or N_d equal to zero gives $P = \pm 1$ whereas an unpolarized beam with $N_u = N_d$ gives $P = 0$. We may also speak of a vector polarization $\mathbf{P}$ of magnitude (51) and oriented along the local field direction which varies along the beam path. For the experiments reported here, $\mathbf{P}$ at the sample position was along one of three directions. For briefness, we shall refer to these as α-, β- and γ-polarization:

- α-polarization: $\mathbf{P}$ in the scattering plane, parallel to the scattering vector $\mathbf{Q}$.
- β-polarization: $\mathbf{P}$ in the scattering plane, perpendicular to $\mathbf{Q}$.

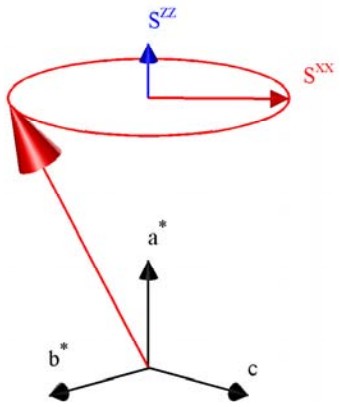

Figure 23: Schematic illustration of transverse and longitudinal fluctuations in the classical interpretation of a spin wave as a vector precessing around the direction of the ordered moment. When the latter is along the $\mathbf{a}^*$ as is approximately the case in CFTD, the transverse parts $S^{xx}(\mathbf{Q}_{2\mathrm{D}},\omega)$ and $S^{yy}(\mathbf{Q}_{2\mathrm{D}},\omega)$ of the scattering function describe the scattering from oscillations in the moment transverse to $\mathbf{a}^*$ (horizontal red arrow labeled S^{xx}) while the longitudinal scattering function $S^{zz}(\mathbf{Q}_{2\mathrm{D}},\omega)$ contains the contribution from fluctuations of the spin parallel to $\mathbf{a}^*$ (blue arrow labeled S^{zz}) as well as the magnetic Bragg peaks at $\mathbf{Q}_{2\mathrm{D}} = (\pi,\pi)$ positions.

- γ-polarization: $\mathbf{P}$ perpendicular to the scattering plane and to $\mathbf{Q}$.

For each of the above polarization directions it was possible to record both spin-flip and non-spin-flip scattering, making a total of six channels.

To further simplify the presentation we shall introduce shorthand notations T and L for the transverse and longitudinal components of the scattering function in the magnetically ordered phase for temperatures well below T_N

$$\begin{aligned} T/2 &= S^{xx}(\mathbf{Q}_{2\mathrm{D}},\omega) = S^{yy}(\mathbf{Q}_{2\mathrm{D}},\omega) \\ L &= S^{zz}(\mathbf{Q}_{2\mathrm{D}},\omega) \end{aligned} \tag{52}$$

where we have made explicit that the symmetry of the (pure) Heisenberg model requires that there is no difference between fluctuations along the two directions perpendicular to the ordered sublattice moment. We may then write

$$T = S^{xx}(\mathbf{Q}_{2\mathrm{D}},\omega) + S^{yy}(\mathbf{Q}_{2\mathrm{D}},\omega) = \frac{1}{2}\left(S^{+-}(\mathbf{Q}_{2\mathrm{D}},\omega) + S^{-+}(\mathbf{Q}_{2\mathrm{D}},\omega)\right) \tag{53}$$

With the neutron wavevector transfer $\mathbf{Q}$ in the (001) plane of CFTD, the longitudinal spin fluctuations L are most efficiently probed with $\mathbf{Q}$ mostly along the $\mathbf{b}^*$ axis. This is because the polarization factor $\sum_{\alpha\beta}(\delta_{\alpha\beta} - \hat{Q}_\alpha\hat{Q}_\beta)$ in the neutron scattering cross-section prevents us from seeing components of the spin in the direction of $\mathbf{Q}$. It follows that maximum sensitivity to L is obtained by arranging scans such that $\mathbf{Q}$ is perpendicular to the direction of the ordered moment, $\mathbf{Q}\cdot\langle\mathbf{S}\rangle \simeq 0$. We chose to perform scans in the vicinity of the (010) and (030) reciprocal lattice positions. It is important to realize that although in terms of 3D Bragg reflections, neither of these positions correspond to antiferromagnetic reciprocal lattice vectors, they are both equivalent to $\mathbf{Q}_{2D} = (\pi,\pi)$ in terms of 2D spin fluctuations owing to the two-dimensionality of the magnetic properties of CFTD.

In order to extract the transverse and longitudinal scattering functions T and L from the raw data, we must take into consideration

- Polarization corrections applied because $P \neq \pm 1$ in any real experiment.
- Angular corrections for the polarization factor $\sum_{\alpha\beta}(\delta_{\alpha\beta} - \hat{Q}_\alpha\hat{Q}_\beta)$ in the cross-section for magnetic scattering.
- Resolution corrections.

As an appetizer before these corrections are discussed in detail, we describe the ideal case where polarization conditions are perfect and $\mathbf{Q} \parallel \mathbf{b}^*$.

Based on the general rules outlined in section 2.1.3, we can immediately write down six equations for the intensities I^{η}_{NSF} and I^{η}_{SF} in the non-spin-flip and spin-flip channels when the polarization $\mathbf{P}$ at the sample position is in the η direction ($\eta \in \{\alpha, \beta, \gamma\}$). They are expressed in terms of $T/2$, L, the coherent nuclear scattering N and separate background levels B_{NSF} and B_{SF} for the non-spin-flip and spin-flip channels. For easy reference, we shall reiterate the general results from section 2.1.3:

- The components of $\mathbf{S}_{\perp}$ which are perpendicular to the polarization $\mathbf{P}$ produce spin-flip scattering, while the components along $\mathbf{P}$ produce non-spin-flip scattering. In particular, when $\mathbf{P} \parallel \mathbf{Q}$ (α-polarization) all magnetic scattering is spin-flip scattering.
- Coherent nuclear scattering is non-spin-flip scattering.
- Isotope incoherent nuclear scattering is non-spin-flip scattering.
- Nuclear spin incoherent scattering is one-third non-spin-flip and two-thirds spin-flip scattering.

Applied to the case in question we arrive at

$$\begin{aligned} I^{\alpha}_{\mathrm{NSF}} &= B_{\mathrm{NSF}} + N & I^{\alpha}_{\mathrm{SF}} &= B_{\mathrm{SF}} + T/2 + L \\ I^{\beta}_{\mathrm{NSF}} &= B_{\mathrm{NSF}} + N + L & I^{\beta}_{\mathrm{SF}} &= B_{\mathrm{SF}} + T/2 \\ I^{\gamma}_{\mathrm{NSF}} &= B_{\mathrm{NSF}} + N + T/2 & I^{\gamma}_{\mathrm{SF}} &= B_{\mathrm{SF}} + L \end{aligned} \tag{54}$$

Disregarding extrinsic background sources, B_{NSF} and B_{SF} are in turn comprised of contributions from isotope and spin incoherent nuclear scattering $N^{\mathrm{iso}}_{\mathrm{inc}}$ and $N^{\mathrm{spin}}_{\mathrm{inc}}$

$$B_{\mathrm{NSF}} = \frac{2}{3}N^{\mathrm{spin}}_{\mathrm{inc}} \qquad B_{\mathrm{SF}} = N^{\mathrm{iso}}_{\mathrm{inc}} + \frac{1}{3}N^{\mathrm{spin}}_{\mathrm{inc}} \tag{55}$$

The set of equations (54) demonstrate that by simple subtractions we can separate the quantities $B_{\mathrm{NSF}} + N$, L and $T/2$ from the three non-spin-flip channels and B_{SF}, L and $T/2$ from the three spin-flip channels

$$\begin{aligned} T/2 &= I^{\gamma}_{\mathrm{NSF}} - I^{\alpha}_{\mathrm{NSF}} & T/2 &= I^{\alpha}_{\mathrm{SF}} - I^{\gamma}_{\mathrm{SF}} \\ L &= I^{\beta}_{\mathrm{NSF}} - I^{\alpha}_{\mathrm{NSF}} & L &= I^{\alpha}_{\mathrm{SF}} - I^{\beta}_{\mathrm{SF}} \\ B_{\mathrm{NSF}} + N &= I^{\alpha}_{\mathrm{NSF}} & B_{\mathrm{SF}} &= I^{\beta}_{\mathrm{SF}} + I^{\gamma}_{\mathrm{SF}} - I^{\alpha}_{\mathrm{SF}} \end{aligned} \tag{56}$$

An important practical lesson drawn from Eqs. (54) is that counting all three spin-flip channels is more efficient in determining the magnetic contributions L and $T/2$ than counting all three non-spin-flip channels, since for equal counting times the total magnetic contribution to $I^{\alpha}_{\mathrm{SF}} + I^{\beta}_{\mathrm{SF}} + I^{\gamma}_{\mathrm{SF}}$ is $T + 2L$ whereas for the NSF channels one gets only $T/2 + L$. For this reasons our general approach was to count predominantly in the spin-flip channels, but to check the consistency of the subtraction procedure (56) by comparing L and $T/2$ derived from the non-spin-flip channels with L and $T/2$ calculated from the spin-flip channels.

5.2.1 Polarization corrections

During a polarized neutron scattering experiment, the polarization of the beam is not perfect, $P \neq \pm 1$. There are many factors contributing to this failure including finite monochromator and analyzer reflectivities for the minority spin species, inhomogeneities in the guide field directions, beam depolarization by the sample, reduced flipper efficiency and so on. Deviations from perfect polarization implies that with the guide field along the η direction, some of the events recorded in the detector in what would nominally be the spin-flip channel, should in reality be assigned to neutrons which have not had their spins flipped with respect to the η-direction, and vice versa. We will use the notation O^{η}_{ch} ($\mathrm{ch} \in \{\mathrm{NSF}, \mathrm{SF}\}$) for the observed intensities and retain the symbols I^{η}_{ch} introduced in Eq. (54) for the intensities corrected for polarization effects. Corrections for imperfect polarization should be performed before the quantities of interest (Here: L and T) are extracted.

The polarization $\mathbf{P}$ defined above is a quantity which varies along the beam path and the detailed spatial variation of which is of little practical interest. In terms of its effect it is useful to think of the depolarization process as occuring in three steps

1. Depolarization of an initially perfectly polarized beam along its path to the sample position. We represent this by a number p_i with the understanding that $p_i = 1$ and $p_i = 0$ correspond to no and full depolarization respectively.

2. Depolarization by the sample itself, represented by a depolarization factor $(1-d)$, with $d = 0$ and $d = 1$ meaning no and full depolarization respectively.

3. Depolarization of the beam leaving the sample along its path to the detector. We represent this by a number p_f defined in the same manner as p_i.

In appendix B we show how this subdivision procedure leads us to introduce an effective polarization $P_{\text{eff}} = p_i(1-d)p_f$, which is a single number quantifying the efficiency of a given polarization setup for distinguishing the various components of the total neutron scattering cross-section. An alternative measure of the same thing is the so-called flipping ratio R. The flipping ratio and the effective polarization are interrelated by

$$R = \frac{1+P_{\text{eff}}}{1-P_{\text{eff}}} \qquad\qquad P_{\text{eff}} = \frac{R-1}{R+1} \tag{57}$$

We may distinguish three special situations. $R = 1$ corresponds to an effectively unpolarized beam $P_{\text{eff}} = 0$ while $R = 0$ and $R = \infty$ correspond to $P_{\text{eff}} = -1$ and $P_{\text{eff}} = 1$ respectively. The divergence of R when $P_{\text{eff}} \to 1$ makes the flipping ratio a less meaningfully defined quantity in this limit. Given that the choice of sign in the numerator of our definition for the polarization Eq. (51) is arbitrary, the same comment applies to the physically symmetric case $P_{\text{eff}} \to -1$.

There are various strategies one can employ to measure R experimentally. One is by taking advantage of the all-important rule that with the guide field exactly along the scattering vector $\mathbf{Q}$, the magnetic response occurs in the spin-flip channel only. This was the approach taken at IN22 and IN20, where paramagnetic spin fluctuations were measured at a temperatures just above T_N. Such fluctuations resemble spin waves provided $\mathbf{Q}_{\text{2D}} - (\pi,\pi) \geq \xi(T)^{-1}$ [49, 62] (This condition is fulfilled at the energies and temperatures at which we study these paramagnetic excitations) with the important difference that in the absence of broken spin-rotation symmetry there is no longer any distinction between longitudinal and transverse fluctuations. Instead we define $M(\mathbf{Q}_{\text{2D}},\omega)/3 = S^{xx}(\mathbf{Q}_{\text{2D}},\omega) = S^{yy}(\mathbf{Q}_{\text{2D}},\omega) = S^{zz}(\mathbf{Q}_{\text{2D}},\omega)$ and expect to find

$$\begin{aligned}
I^{\alpha}_{\text{NSF}} &= B_{\text{NSF}} + N & I^{\alpha}_{\text{SF}} &= B_{\text{SF}} + \frac{2}{3}M \\
I^{\beta}_{\text{NSF}} &= B_{\text{NSF}} + N + \frac{1}{3}M & I^{\beta}_{\text{SF}} &= B_{\text{SF}} + \frac{1}{3}M \\
I^{\gamma}_{\text{NSF}} &= B_{\text{NSF}} + N + \frac{1}{3}M & I^{\gamma}_{\text{SF}} &= B_{\text{SF}} + \frac{1}{3}M
\end{aligned} \tag{58}$$

If no coherent nuclear scattering, e.g. from phonons occurs in the region of interest, $N = 0$, and we can safely attribute peaks in I^{α}_{NSF} to imperfect effective polarization $P_{\text{eff}} < 1$ and deduce the flipping ratio R from the ratio of the peak magnetic intensities in the spin-flip and non-spin-flip channels I^{α}_{SF} and I^{α}_{NSF} (see also appendix B). A converse approach consists in measuring the coherent phonon scattering with the guide field along $\mathbf{Q}$ in a region where $M = 0$. In this case, R is deduced from the ratio of the peaked signal in the non-spin-flip channel to the remnant peak in the spin-flip channel. It would also be possible to estimate R from Bragg intensities or from the nuclear spin incoherent scattering of vanadium. Having made these remarks, let us now proceed with our determination of R.

Figs. 24 (a) and (b) display the nominal SF and NSF scattering respectively, measured for an energy transfer of $\hbar\omega = 5$ meV at 18.4 K at IN20. It is immediately clear that under the assumption $N \simeq 0$ the intensity ratios are in qualitative agreement with Eqs. (58): The highest and lowest intensities are found for the SF and NSF α-polarization data, whereas the remaining channels are of comparable intensity. Upon closer examination of the NSF α-polarization channel, we see small hints of extra intensity near the positions (marked by red arrows) of the two peaks in the corresponding SF channel. An estimate of R can be obtained by taking the ratio of the peak-over-background intensities in the SF and NSF channels for α-polarization data. The peak intensities are averages taken at the locations of the red arrows whereas the background intensities are averages taken from the first and last points in the two scans, marked by black arrows. One

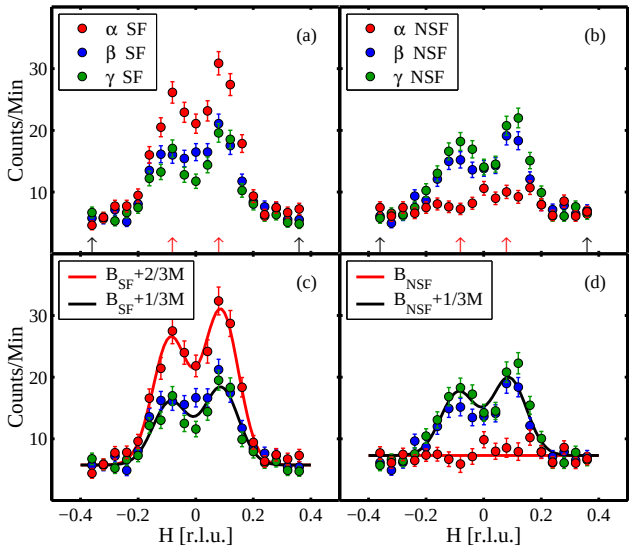

Figure 24: Paramagnetic scattering around (010) at $\hbar\omega = 5$ meV at IN20 and $T = 18.4$ K. The intensities are expressed in terms of the equivalent IN22 intensities, as discussed in the text. (a) Raw spin-flip data. (b) Raw non-spin-flip data. The red and black arrows in (a) and (b) indicate the positions where the peak and background intensities used to derive the flipping ratio R are obtained. The asymmetry between the peaks at positive values and negative values of H can be understood as arising because of the orientation of the resolution ellipsoid. Focusing and defocusing occurs for positive and negative H respectively. Having determined $R = 15$, panels (c) and (d) show the results of correcting the raw data for the beam depolarization using Eqs. (60) and subsequently fitting to two-Gaussians line shapes representing the expectations (58) for paramagnetic fluctuations. Counting times were 2 minutes per point in each polarization channel.

finds $R = 15$ corresponding to a polarization $P_{\rm eff} = 0.875$. Using a similar procedure, we found $R = 21$ and $P_{\rm eff} = 0.909$ at IN22.

Once the effective polarization $P_{\rm eff}$ or the flipping ratio R are known it is straightforward to make the appropriate polarization corrections. In any given direction η of the guide field, the set of equations relating the measured spin-flip and non-spin-flip intensities $O^\eta_{\rm SF}$ and $O^\eta_{\rm NSF}$ to I^η_{SF} and I^η_{NSF} read

$$\begin{bmatrix} O^\eta_{\rm SF} \\ O^\eta_{\rm NSF} \end{bmatrix} = \frac{1}{2} \begin{bmatrix} (1+P_{\rm eff}) & (1-P_{\rm eff}) \\ (1-P_{\rm eff}) & (1+P_{\rm eff}) \end{bmatrix} \begin{bmatrix} I^\eta_{\rm SF} \\ I^\eta_{\rm NSF} \end{bmatrix} \tag{59}$$

This matrix equation is easily inverted for $\eta = \alpha$, β, γ provided $P_{\rm eff} \neq 0$. In terms of R we have

$$\begin{bmatrix} I^\eta_{\rm SF} \\ I^\eta_{\rm NSF} \end{bmatrix} = \begin{bmatrix} R/(R-1) & -1/(R-1) \\ -1/(R-1) & R/(R-1) \end{bmatrix} \begin{bmatrix} O^\eta_{\rm SF} \\ O^\eta_{\rm NSF} \end{bmatrix} \tag{60}$$

Figure 24 (c) and (d) shows the result of such corrections of the raw data presented in panels (a) and (b) using $R = 15$. The background levels $B_{\rm NSF}$, $B_{\rm SF}$ were then determined directly from these polarization corrected data. This revealed that $B_{\rm NSF} > B_{\rm SF}$ as we would have expected from Eq. (55). These background estimates do not include extrinsic contributions, which would however contribute equally to $B_{\rm NSF}$ and $B_{\rm SF}$ and could have been measured experimentally by turning the analyzer crystal. Disregarding resolution corrections, we then fitted the polarization corrected, spin-flip α-polarization data to a two-Gaussians profile in order to fix $2M/3$. With the background levels and overall scale of the magnetic intensities fixed as described above, the solid red and black lines in Fig. 24 all follow from Eqs. (58) without additional fitting. Given the crudeness of the approach, the overall agreement is very good as shown by the reduced χ^2 values ($\chi^2_{\rm red} = 1.08$, 1.34, 1.20, 1.05, 2.12 and 1.58 for α, β and γ SF channels and α, β and γ NSF channels, in that order). This gives us confidence that even though we may not have used the optimal method of deducing R, the value found must essentially be correct. We estimate the error in the polarization to be $\Delta P = 0.075$, corresponding to the statistical uncertainty $\Delta R = 9.6$ in the determination of R at IN20. While this is very likely an overestimate of the real uncertainty in P, this value of ΔP is included in the calculations of errorbars in the remainder of this chapter.

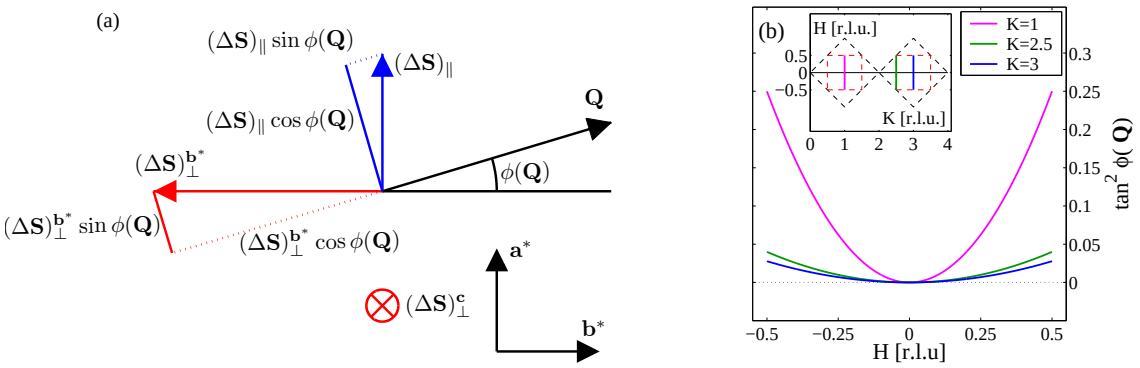

Figure 25: Angular corrections for polarized measurements. (a): When $\mathbf{Q}$ rotates away from the $\mathbf{b}^*$ direction, the components of the fluctuating part $\Delta\mathbf{S} = \mathbf{S} - \langle\mathbf{S}\rangle$ of the spin along $\mathbf{a}^*$, $\mathbf{b}^*$ and $\mathbf{c}$ (denoted $(\Delta S)_\parallel$, $(\Delta S)^{\mathbf{b}^*}_\perp$ and $(\Delta S)^{\mathbf{c}}_\perp$ respectively) can in turn be decomposed into their components along $\mathbf{Q}$ and perpendicular to $\mathbf{Q}$. The components along $\mathbf{Q}$ shown in dotted lines are never observed on account of the polarization factor in the neutron scattering cross-section. The components perpendicular to $\mathbf{Q}$ occur in the spin-flip or non-spin-flip channels depending on the direction of the polarization vector $\mathbf{P}$. Since the cross-section contributions T and L depend on two-point correlation functions between spins, they are modified by factors $\sin^2\phi(\mathbf{Q})$ or $\cos^2\phi(\mathbf{Q})$ when the polarization factor is taken into account. Equation (61) expresses these considerations in mathematical form. (b): The trigonometric function $\tan^2\phi(\mathbf{Q})$ appearing in Eq. (62) versus H for the three values of K indicated in the inset.

5.2.2 Angular corrections

When spin rotation symmetry is broken for $T \leq T_N$ there are additional corrections to be made when the wavevector transfer $\mathbf{Q}$ is not perpendicular to the direction of the ordered sublattice moment, i.e. when $\mathbf{Q}\cdot\mathbf{a}^* \neq 0$. There are two reasons for this which we attempt to illustrate in Fig. 25(a).

First, the polarization factor $\sum_{\alpha\beta}(\delta_{\alpha\beta} - \hat{Q}_\alpha\hat{Q}_\beta)$ in the cross-section plays a role since it always prevents us from seeing components of the electronic spins along $\mathbf{Q}$. When the scattering vector rotates, the inaccessible component of $\mathbf{Q}$ changes as well. To be quantitative, we must introduce the angle $\phi(\mathbf{Q})$ between the $\mathbf{b}^*$ direction and the scattering vector $\mathbf{Q}$ in the $\mathbf{a}^*\mathbf{b}^*$ plane. From the form of the polarization factor it then follows that the spin fluctuations along $\boldsymbol{a}^*$, i.e. L, get weighted by a factor $(1 - \sin^2\phi(\mathbf{Q})) = \cos^2\phi(\mathbf{Q})$, while spin fluctuations along $\boldsymbol{b}^*$ and $\boldsymbol{c}$, both given by $T/2$, are weighted by $\sin^2\phi(\mathbf{Q})$ and 1 respectively.

Second, what polarization analysis adds is the ability to direct these three components into the SF and NSF channels. The selection rules describing their distribution were stated on page 57. As $\mathbf{Q}$ rotates, the polarization vector $\mathbf{P}$, being tied to that of $\mathbf{Q}$, changes direction with respect to the direction of the ordered sublattice moment. This means that e.g. the spin-flip intensity, being determined by the components of the fluctuating spin perpendicular to $\mathbf{P}$, becomes a linear combination of L and $T/2$ with coefficients determined by $\phi(\mathbf{Q})$.

Combining these considerations we can write down two matrix equations relating the spin-flip and non-spin-flip intensities I^η_{SF} and I^η_{NSF} to the transverse and longitudinal magnetic intensities $T/2$ and L

$$\begin{bmatrix} I^\alpha_{\mathrm{NSF}}(\mathbf{Q},\omega) \\ I^\beta_{\mathrm{NSF}}(\mathbf{Q},\omega) \\ I^\gamma_{\mathrm{NSF}}(\mathbf{Q},\omega) \end{bmatrix} = \begin{bmatrix} 1 & 0 & 0 \\ 1 & \sin^2\phi(\mathbf{Q}) & \cos^2\phi(\mathbf{Q}) \\ 1 & 1 & 0 \end{bmatrix} \begin{bmatrix} B_{\mathrm{NSF}}(\mathbf{Q},\omega) + N(\mathbf{Q},\omega) \\ \frac{1}{2}T(\mathbf{Q},\omega) \\ L(\mathbf{Q},\omega) \end{bmatrix}$$
$$\begin{bmatrix} I^\alpha_{SF}(\mathbf{Q},\omega) \\ I^\beta_{SF}(\mathbf{Q},\omega) \\ I^\gamma_{SF}(\mathbf{Q},\omega) \end{bmatrix} = \begin{bmatrix} 1 & 1+\sin^2\phi(\mathbf{Q}) & \cos^2\phi(\mathbf{Q}) \\ 1 & 1 & 0 \\ 1 & \sin^2\phi(\mathbf{Q}) & \cos^2\phi(\mathbf{Q}) \end{bmatrix} \begin{bmatrix} B_{\mathrm{SF}}(\mathbf{Q},\omega) \\ \frac{1}{2}T(\mathbf{Q},\omega) \\ L(\mathbf{Q},\omega) \end{bmatrix} \quad (61)$$

The reader is warned that at this stage we have still not taken resolution effects into consideration, and hence the intensities I^η_{SF} and I^η_{NSF} should not be directly compared to theory. When $\phi(\mathbf{Q}) = 0$, Eqs. (61) reduce to Eqs. (54), as they should. The above matrix equations can be inverted when the determinants of the matrices do not equal zero. This constraint is not a cause for concern in the analysis, since it only happens when $\mathbf{Q} \parallel \mathbf{a}^*$, a situation which never occured in the experiments.

The inverse equations read

$$\begin{aligned}
\begin{bmatrix} B_{\rm NSF}+N \\ \frac{1}{2}T \\ L \end{bmatrix} &= \begin{bmatrix} -1 & 1 & 1 \\ 1 & 0 & -1 \\ 1 & -(1+\tan^2\phi(\mathbf{Q})) & \tan^2\phi(\mathbf{Q}) \end{bmatrix} \begin{bmatrix} I^{\alpha}_{\rm NSF} \\ I^{\beta}_{\rm NSF} \\ I^{\gamma}_{\rm NSF} \end{bmatrix} \\
\begin{bmatrix} B_{\rm SF} \\ \frac{1}{2}T \\ L \end{bmatrix} &= \begin{bmatrix} 1 & 0 & 0 \\ -1 & 0 & 1 \\ -1 & (1+\tan^2\phi(\mathbf{Q})) & -\tan^2\phi(\mathbf{Q}) \end{bmatrix} \begin{bmatrix} I^{\alpha}_{SF} \\ I^{\beta}_{SF} \\ I^{\gamma}_{SF} \end{bmatrix}
\end{aligned} \tag{62}$$

The forms of the inverse matrices show that it is only for the longitudinal scattering $L(\mathbf{Q},\omega)$ that corrections need be made. The entries determining $B_{\rm SF}(\mathbf{Q},\omega)$, $B_{\rm NSF}(\mathbf{Q},\omega)+N(\mathbf{Q},\omega)$ and the transverse response $T(\mathbf{Q},\omega)/2$ contain no trigonometric factors, and so are simply given by the corresponding expressions in (56).

The magnitude of the angular corrections to the longitudinal scattering can be estimated from corresponding entries in the inverse matrices. Taking the difference of the expressions for $L(\mathbf{Q},\omega)$ in Eq. (62) and those in (56) which correspond to $\phi(\mathbf{Q})=0$, it turns out that the correction terms are $\pm\tan^2\phi(\mathbf{Q})[I^{\beta}_{\rm ch}(\mathbf{Q},\omega)-I^{\gamma}_{\rm ch}(\mathbf{Q},\omega)]$ with the upper (lower) sign chosen for ch=SF (NSF). Clearly the largest effects are to be expected when $\phi(\mathbf{Q})$ is largest, but even then a partial compensation occurs because of the minus sign inside the bracket. Figure 25(b) plots $\tan^2\phi(\mathbf{Q})$ versus H for the three values of K at which we present data ($K=1$, $K=2.5$ and $K=3$ in reciprocal lattice units) and illustrates that only for data taken in the magnetic zone centered on $(0,1,0)$, and for $\mathbf{Q}$ approaching the magnetic zone boundary do angular corrections become non-negligible. For $\mathbf{Q}=(\pm0.5,1,0)$ the angular correction factor is 25 percent, but even in this extreme case the formulae (61) and (62) should handle the corrections without any difficulties. Note in passing that even if our assumption $\langle\mathbf{S}\rangle \parallel \mathbf{a}^*$ is not quite true and e.g. the moment is rotated 3.1 degrees off this direction [80], the corrections for this fact will be of order $\tan^2(3.1)\, I^{\eta}_{\rm ch}(\mathbf{Q},\omega)\simeq 0.003\, I^{\eta}_{\rm ch}(\mathbf{Q},\omega)$ or less, a number well within the errorbars of the present analysis.

In conclusion to this section and the preceding one, we have seen that for scans performed in the vicinity of the $\mathbf{b}^*$ direction, we can derive non-resolution corrected estimates of $T(\mathbf{Q},\omega)/2 = S^{xx}(\mathbf{Q},\omega)=S^{yy}(\mathbf{Q},\omega)$ and $L(\mathbf{Q},\omega)=S^{zz}(\mathbf{Q},\omega)$ directly from the raw intensities $O^{\gamma}_{SF/NSF}(\mathbf{Q},\omega)$ when all six polarization channels are measured. This is achieved by using first Eq. (59) and then (62). In processing the data in Fig. 24(c) and (d) it was not necessary to perform angular corrections because the broken spin-rotation invariance underlying equations (61)-(62) is not present above T_N, and instead we have Eqs. (58).

5.2.3 Model and resolution corrections

The polarization and angular corrections discussed above are performed on a point-by-point basis and can be done both before and after taking resolution effects into account. Our approach has been to reduce the raw data to T and L before considering resolution effects. Then, a concrete model is chosen and its predictions for T and L convolved with the experimental resolution function, before comparisons with the experimental curves. In this section, we discuss the implementation of resolution corrections to the one and two-magnon cross-sections derived from linear spin wave theory.

In appendix A a detailed treatment of our linear spin wave model is provided. Within this framework one finds that single-magnon scattering is transversely polarized, whereas two-magnon scattering is longitudinally polarized. Higher order processes are not considered. Thus, when in this chapter we compare our data to computations using results from linear spin wave theory, T is interpreted as single-magnon scattering and L as two-magnon scattering, even though higher order processes do in principle contribute to both T and L and do in principle redistribute the spectral weight between them.

If we restrict our attention to the pure 2DQHAFSL case and to zero temperature, the cross-sections T and L can be found from equations (128) and (135) derived in appendix A

$$\begin{aligned}
T(\mathbf{Q},\omega) &\propto \frac{S-\Delta S^z}{2}\sqrt{\frac{1-\gamma_{\mathbf{Q}}}{1+\gamma_{\mathbf{Q}}}}\,[n(\omega_{\mathbf{Q}})+1]\delta(\omega-\omega_{\mathbf{Q}}) \\
L(\mathbf{Q},\omega) &\propto \frac{2}{N}\sum_{\boldsymbol{q}}\frac{1}{2}(u_{\boldsymbol{q}}v_{\boldsymbol{q}+\mathbf{Q}}-u_{\boldsymbol{q}+\mathbf{Q}}v_{\boldsymbol{q}})^2[n(\omega_{\boldsymbol{q}})+1][n(\omega_{\boldsymbol{q}+\mathbf{Q}})+1]\,\delta(\hbar\omega-\hbar\omega_{\boldsymbol{q}}-\hbar\omega_{\boldsymbol{q}+\mathbf{Q}})
\end{aligned} \tag{63}$$

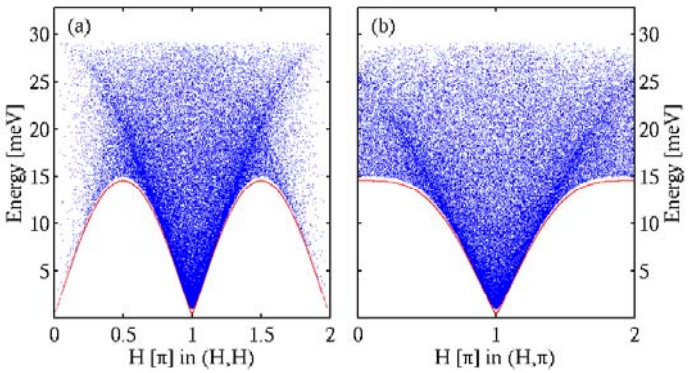

Figure 26: Sections through the clouds of 4×10^6 single-magnon (red points) and 4×10^6 two-magnon processes (blue points) described in the text. (a) $(0,0) \rightarrow (2\pi, 2\pi)$ direction (b) $(0,\pi) \rightarrow (2\pi,\pi)$ direction.

The geometrical factor $\gamma_{\boldsymbol{q}}$ and the dispersion $\omega_{\boldsymbol{q}}$ were introduced in chapter 3. The dispersion relation is derived in appendix A where the general expressions for $u_{\boldsymbol{q}}$ and $v_{\boldsymbol{q}}$ and the reduction ΔS^z in the ordered sublattice moment are also given.

In the same appendix, we give a description of how one can use a Monte Carlo routine to compute the cross-sections T and L numerically from Eqs. (63). We used this approach to generate 4×10^6 single-magnon events and 4×10^6 two-magnon events in the first Brillouin zone. In Fig. 26 we present two cuts through these neutron clouds along the [10] and [11] directions of 2D reciprocal space. To produce plots with a finite number of events, all one-magnon and two-magnon events inside a slender sliver in $\mathbf{Q}$-space were included. The red and blue points are single-magnon and two-magnon processes respectively. Several features should be noted. First, at fixed $\mathbf{Q}_{\rm 2D}$ the two-magnon intensity is non-zero only for energies between the one-magnon energy at the same $\mathbf{Q}_{\rm 2D}$ and twice the zone boundary energy $2J_{\rm eff}$, but is otherwise relatively weakly energy-dependent. Second, the two-magnon scattering is generally highest at low $\hbar\omega$ near $\mathbf{Q}_{\rm 2D} = (\pi,\pi)$ and lowest for wavevectors approaching the nuclear Bragg positions. Third, the longitudinal continuum contains weak maxima dispersing away from the single-magnon dispersion cone and extending all the way to the maximum two-magnon energy. At the zone boundary points $(\pi/2, \pi/2)$ and $(\pi, 0)$ the energies of these maxima are in good agreement with [20] where $L(\mathbf{Q}_{\rm 2D}, \omega)$ is predicted to have a two-peak structure with the most energetic mode being located at 1.4 and 1.7 times the zone boundary energy. Fourth, the one-magnon dispersion does not go to zero at $(0,0)$ and (π,π) because the Monte Carlo calculation uses very slightly modified expressions for the weight and dispersion for one-magnon processes. The weight-formulae are altered in order to obtain non-divergent maximum weights as discussed in appendix A. At the same time, by modifying the dispersion relation, we can effectively simulate the fact that experiments reveal a finite gap for one-magnon processes at $\mathbf{Q}_{\rm 2D} = (\pi,\pi)$ [59]. Because the modified single-magnon dispersion is employed in calculating the two-magnon energies, a related artifact is the appearance of a small gap between the single-magnon and two-magnon events, which becomes particularly prominent near the zone boundary points $(\pi, 0)$ and $(\pi/2, \pi/2)$. To check that the introduction of a finite gap in the one-magnon spectrum and cutoffs in the weight factors do not lead to non-physical spectra, one can perform various checks, e.g. to see that the gap between the one- and two-magnon Monte Carlo spectra vanishes as the gap in the theoretical one-magnon dispersion used as an input to the routine is reduced to zero. Indeed this is the case. Another important sanity check is that the shape of the density of states $S(\omega)$ for the two spectra must not be altered away from the forms one would expect in a simple picture. This is also easily verified numerically.

The parameters determining the resolution function were pinned down by a combination of fitting energy scans through the incoherent line centered on $\hbar\omega = 0$ meV and matching the focussing effects seen in constant energy scans like e.g. Fig. 27. This procedure effectively limits the scope for variations in the parameters determining the orientations and lengths of the principal axes of the resolution ellipsoid. It should be noted that throughout the analysis, we employed the formulae derived by Cooper and Nathans [7], in their corrected and normalized form [8]. By doing so, we neglect the influence of the additional contributing factors considered by Popovici [9] or − at least − treat them indirectly by incorporating their effect in effective values of the Copper-Nathans parameters. Following the discussion in chapter 2, the resolution parameters allow us to compute

a 4-by-4 matrix $\underline{M}$ and a normalization factor R_0 for each point in a given scan.

Having determined both the resolution function and the event clouds with which we must convolute it according to the general prescription (25) for treating resolution effects, we are ready to step to the implementation of the convolution itself. We can write $\tilde{S}(\mathbf{Q},\omega)$ in (25) as a sum over $N = 4\times10^6$ delta-functions in four-dimensional $(\mathbf{Q},\omega)$ space, $\tilde{S}(\mathbf{Q},\omega) = \sum_{i=1}^{N} \delta(\mathbf{Q}-\mathbf{Q}_i)\delta(\omega-\omega_i)$ and show that the integral reduces to a simple sum over exponential factors evaluated at the wavevectors and energies of the event clouds

$$\begin{aligned} I(\mathbf{Q}_0,\omega_0) &= \int d\omega\, d\mathbf{Q}\, R_0 \exp\left(-\frac{1}{2}\Delta\vartheta(\mathbf{Q}-\mathbf{Q}_0,\omega-\omega_0)\underline{M}\Delta\vartheta(\mathbf{Q}-\mathbf{Q}_0,\omega-\omega_0)\right)\tilde{S}(\mathbf{Q},\omega) \\ &= R_0\sum_{i=1}^{N}\exp\left(-\frac{1}{2}\Delta\vartheta(\mathbf{Q}_i-\mathbf{Q}_0,\omega_i-\omega_0)\underline{M}\Delta\vartheta(\mathbf{Q}_i-\mathbf{Q}_0,\omega-\omega_0)\right) \end{aligned} \tag{64}$$

Because the resolution function has a finite extent, it is not necessary to sum over all N events. Computation time is saved by selecting a finite region around each point $(\mathbf{Q}_0,\omega_0)$ inside which the exponential factors in (64) give non-zero contributions to the total sum.

In appendix A we discuss how the ratios between the total wavevector and energy-integrated Bragg, single-magnon and two-magnon intensities are fixed by a single number, the reduction ΔS^z in the staggered moment in the ground state. The total weights are given by $(S-\Delta S^z)$, $(S-\Delta S^z)(2\Delta S^z+1)$ and $\Delta S^z(\Delta S^z+1)$ respectively. It is straightforward to include these ratios in our model. We simply associate a weight factor $(S-\Delta S^z)(2\Delta S^z+1)$ with all single-magnon processes and a weight factor $\Delta S^z(\Delta S^z+1)$ with all two-magnon processes. Since the event clouds consist of equal numbers of points in $(\mathbf{Q},\omega)$-space, this procedure clearly yields the correct energy and wavevector integrated one-magnon and two-magnon spectral weights. In practice, we carry out the sum (64) for each event cloud and then multiply each sum by its associated weight. Having done this for each point in a given scan the resulting curves can be compared with the experimental data. Such comparisons involve only a single overall scale factor for the computed intensities since ΔS^z completely fixes the ratio between one-magnon and two-magnon processes.

The form factor squared $|F(\mathbf{Q})|^2$ also affects the magnetic intensities as a function of $|\mathbf{Q}|$. However, it varies by only a very small amount in each individual scan presented here (The worst cases are constant-$\hbar\omega$ scans through (010) where $|F(\mathbf{Q})|^2$ for free Cu^{2+} ions varies between 0.941 at (010) and 0.927 at (1/2 1 0), a 1.5% drop). We have therefore not corrected for its effect since it is always well within the experimental errorbars.

5.3 Results

We now move to a discussion of the experimental results. First we shall make a few comparisons between the two experiments, and between temperatures above and below T_N. This is useful for demonstrating that the experiments gave consistent results and for establishing in an indirect manner that spin-rotation symmetry is broken at the lowest temperatures. We then discuss our results for the low energy, low temperature behaviour of T and L, before finally presenting results for the transverse and longitudinal spectra at two high symmetry positions $\mathbf{Q}_{2D} = (\pi,0)$ and $\mathbf{Q}_{2D} = (\pi/2,\pi/2)$ on the magnetic Brillouin zone boundary.

5.3.1 Comparisons

Since the IN20 experiment focused predominantly on energy transfers $\hbar\omega \simeq J$ whereas the IN22 experiment dealt almost exclusively with energies $\hbar\omega \simeq 2J$ and above, it is important for us to establish their mutual consistency in order to link the two sets of measurements together. We will demonstate this correspondence in two ways: By comparing constant-$\hbar\omega$ scans taken at energy transfers $\hbar\omega \sim J$ at the two instruments, and by comparing constant-$\mathbf{Q}$ scans taken at the magnetic zone boundary.

Throughout this chapter, the IN20 intensities have been scaled down by an overall factor of 4.75 to account for the difference in sample mass (7.6 grams at IN20 versus 3.2 grams at IN22) and for an approximate factor of 2 between the incident fluxes at the energy transfers studied and with the instrument configurations chosen [87]. All intensities are therefore in units of expected IN22 counting times for a crystal weighing 3.2 grams.

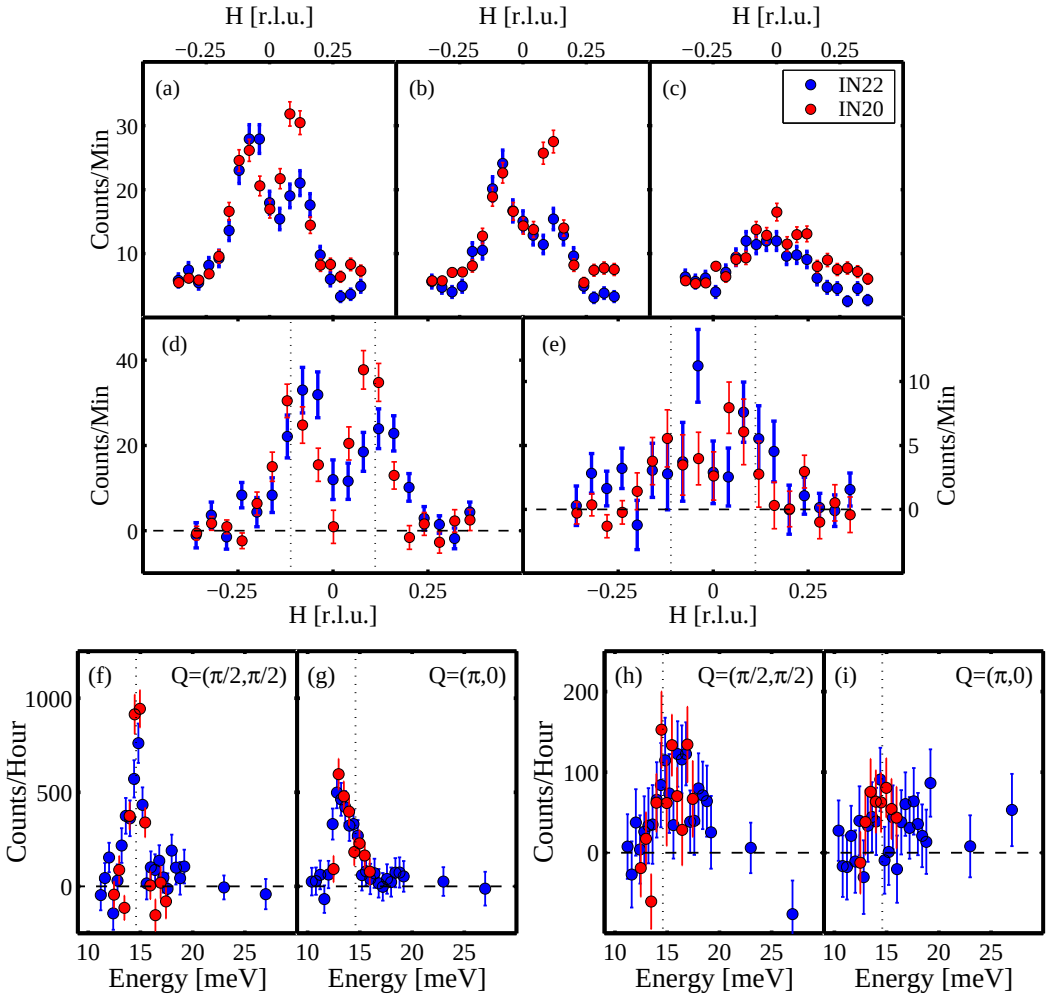

Figure 27: Raw and processed data for $T \ll T_N$ from the IN20 and IN22 experiments. The IN20 data has been scaled down by a factor 4.75, corresponding to an approximate flux ratio of 2 between the two instruments for $\mathbf{k}_f = 2.662$ Å^{-1} and $\hbar\omega = 5$ meV [87] multiplied by the ratio of sample masses (7.6 g/3.2 g)= 2.375. (a) Raw SF α-polarization channels. (b) Raw SF β-polarization channels. (c) Raw SF γ-polarization channels. By assuming perfect polarization, we can deduce the transverse and longitudinal scattering functions $T(\mathbf{Q}_{2D},\omega) = S^{xx}(\mathbf{Q}_{2D},\omega) + S^{yy}(\mathbf{Q}_{2D},\omega)$ and $L(\mathbf{Q}_{2D},\omega) = S^{zz}(\mathbf{Q}_{2D},\omega)$ from (a)-(c). These are shown in panels (d) and (e) respectively. The dotted lines indicate the expected positions of the one-magnon peaks with J obtained from the time-of-flight data presented in chapter 4. In panels (f)-(i) we compare IN20 and IN22 results (this time corrected for both polarization and angular factors) for the transverse and longitudinal cross-sections at two high-symmetry positions on the magnetic zone boundary. (f) Transverse spin fluctuations T for $\mathbf{Q}_{2D} = (\pi/2, \pi/2)$. (g) Transverse spin fluctuations for $\mathbf{Q}_{2D} = (\pi, 0)$. (h) Longitudinal spin fluctuations L for $\mathbf{Q}_{2D} = (\pi/2, \pi/2)$. (i) Longitudinal spin fluctuations for $\mathbf{Q}_{2D} = (\pi, 0)$. The dotted lines in (f)-(i) have the same significance as in (d) and (e). Counting times were roughly 3 (IN22) and 4 (IN20) minutes per point per channel for the data in (a)-(c). For the high-energy data in (f)-(i), counting times varied with energy transfer being typically $\sim$ 12-14 minutes per point per SF channel (IN20) and $\sim$ 32-35 minutes per point per SF channel ($\sim$ 7 minutes per point per NSF channel) below 20 meV. The two highest energy points in (f)-(i) were counted for $\sim$ 16 minutes in each NSF channel and $\sim$ 32 minutes in each SF channel.

Figure 27 displays data obtained at IN20 and IN22 at the lowest temperature attained ($T = 1.5$ K for IN20, $T = 1.9$ K at IN22). Panels (a)-(c) compares the raw spin-flip α, β and γ-polarization data respectively at $\hbar\omega = 5$ meV. It is immediately apparent that with the simple scaling by 4.75 we get almost the same count rate at the two instruments for all three polarization channels. The agreement is very satisfactory given the combined uncertainties in e.g. the estimated flux ratio, differences in slit settings (possibly leading to differences in the fractions of the samples being illuminated), beam polarization etc. Next, we notice that the orientation of the resolution ellipsoid differs in the two cases. Focusing occurs for positive and negative values of H in the IN20 and IN22 scans respectively. The IN22 data further display a slight offset and a sloping background level. Because the IN22 data taken at 5 meV included only the spin-flip channels we are unable

to perform corrections for beam polarization. If we nevertheless assume perfect polarization for both experiments and carry out corrections for the angular factors, we obtain the estimates of $T(\mathbf{Q}_{2D}, \omega)$ and $L(\mathbf{Q}_{2D}, \omega)$ shown in Figure 27 (d) and (e). As for the raw data in (a)-(c) the two independent estimates of T and L are very similar once scaled by 4.75. The ratios of the areas under the longitudinal and transverse spectra are also closely similar for the two experiments. Numerical estimates yield 0.19 ± 0.03 and 0.25 ± 0.03 for the IN20 and IN22 data respectively. The assumption of zero beam depolarization has only a minor effect on this correspondence since the flipping ratios in the two experiments were similar ($R = 15$ for IN20, $R = 21$ for IN22). Moreover, the peak separations in T are consistent with each other and with the expected single-magnon dispersion − indicated by the dotted vertical lines − derived from the analysis of the MAPS data presented in chapter 4. Of course simple one-dimensional integrations cannot replace a full resolution-corrected analysis, but for the simple purpose of establishing consistency between the two experiments it is sufficient and the result gratifying.

Fig. 27 (f)-(i) compares the IN20 and IN22 transverse and longitudinal spectra obtained at the two positions $\mathbf{Q}_{2D} = (\pi/2, \pi/2)$ and $\mathbf{Q}_{2D} = (\pi, 0)$ on the magnetic Brillouin zone boundary after corrections for depolarization and for angular factors. The IN20 data for $(\pi/2, \pi/2)$ were obtained at $\mathbf{Q} = (-0.5\,3\,0)$ and need to be corrected according to Eqs. (62) whereas the corresponding data from the IN22 experiment were taken at an on-axis position $\mathbf{Q} = (0\,2.5\,0)$ and hence no corrections are necessary. In both experiments, the $(\pi, 0)$ data were taken at $\mathbf{Q} = (0.5\,2.5\,0)$. As in Fig. 27(a)-(e) we find that when the IN20 intensities are scaled down by a factor of 4.75 excellent agreement is found for both T and L at both $(\pi/2, \pi/2)$ and $(\pi, 0)$. Again, the dotted vertical lines locate the positions of the single-magnon peaks expected if linear spin wave theory had adequately described the zone boundary response. The discrepancy between these expectations and the actual zone-boundary magnon energies reflects the ZB dispersion studied in chapter 4: The peak position is well accounted for at $(\pi/2, \pi/2)$ but not at $(\pi, 0)$.

The spectra obtained for T and L in themselves bear witness to the efficiency of polarization analysis in separating magnetic from non-magnetic scattering. We see this from the fact that in panels (f)-(i), the intensities drop to zero within errors for energies below the position of the single-magnon peak in T for each wavevector. This is the expected behavior since the single-magnon energy marks the lower limit for magnetic scattering at all wavevectors. Similarly, in panels (d) and (e) the intensity drops to zero within errors for values of H larger than that expected for single-magnon scattering in T. However, because no polarization corrections were applied in this case, statements regarding the virtues of polarization analysis are less persuasive.

It is interesting to note that the line shapes and relative intensities of the transverse response obtained in the two experiments are in close agreement at both reciprocal lattice positions: In both experiments the highest peak intensity and the narrowest energy width is found at $(\pi/2, \pi/2)$ whereas the response at $(\pi, 0)$ has a smaller peak intensity and appears to be broader in $\hbar\omega$. While this could well be a resolution effect, it could also imply a smaller lifetime for single-magnons at $(\pi, 0)$ relative to single-magnons at $(\pi/2, \pi/2)$. Whether or not there is an intrinsic component to the apparent broader linewidth at $(\pi, 0)$ is clearly a complicated issue since in addition to the orientation of the resolution ellipsoid with respect to the idealized linear spin wave dispersion used in our model (63), we should also recall that an energy broadening can result from the zone boundary dispersion itself if resolution conditions are right. We shall discuss this question later. At this stage, we restrict ourselves to noting that the agreement between the transverse lineshapes in the two experiments would be a little surprising had the zone boundary dispersion not existed because the data of panels (a)-(e) clearly show that the resolution ellipsoids in the two experiments had a different orientation with respect to the dispersion surface at low energies. Taken together, the close correspondence between both low and high-energy data from two separate experiments unambiguously establish the connection between the IN20 and IN22 experiments.

Before turning to a more careful analysis of the low-energy response studied at IN20, we shall briefly compare $\hbar\omega = 5$ meV data for temperatures just above T_N and at our base temperature. This is to demonstrate indirectly − by comparing polarized inelastic data − that spin-rotation symmetry is broken at low temperatures. In Fig. 28 (a)-(f) we plot the IN20 data in all six channels, scaled down by a factor 4.75, but with no corrections done for nonideal polarization or angular factors. The data below and above T_N should be compared to our expectations (54) and (58) for the magnetically order and disordered state respectively. Broken spin-rotation symmetry should manifest itself below T_N as a reduction in spin fluctuations along the preferred direction, i.e. along $\mathbf{a}^*$ and in concomitant increases in the fluctuations along $\mathbf{b}^*$ and the crystallographic $\mathbf{c}$

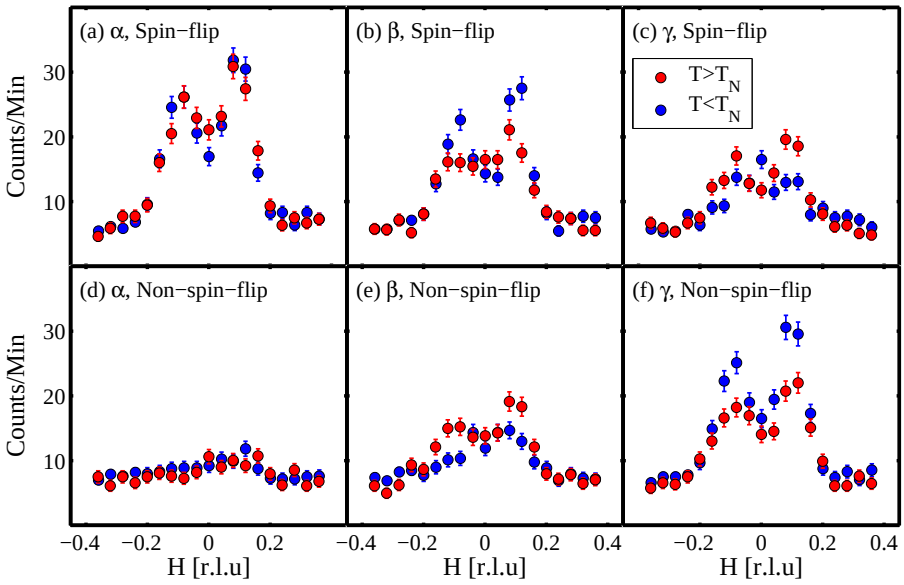

Figure 28: Raw IN20 data taken at 1.5 K $\ll T_N = 16.8$ K [61] and at 18.4 K $> T_N$. The intensities are scaled down by a factor of 4.75 to compare with IN22 intensities, as discussed in the text. (a) SF α-polarization. (b) SF β-polarization. (c) SF γ-polarization. (d) NSF α-polarization. (e) NSF β-polarization. (f) NSF γ-polarization. Comparing Eq. (54) with Eq. (58), we find signatures of the qualitative changes implied by broken spin-rotation symmetry ($L < M/3 < T/2$) in panels (b), (c), (e) and (f). Counting times were ~ 2 ($T > T_N$) and ~ 4 ($T < T_N$) minutes per point in each of the six polarization channels.

direction. In other words, we expect $L < M/3 < T/2$. The data in Fig. 28 compare favorably with these simple expectations. In the absence of explicit measurements of the temperature dependence of the order parameter through the tracking of the variation in the peak intensity of one of the magnetic Bragg peaks, T_N is not known accurately for any of the three crystals studied. Viewed in this light figure 28 tell us that $T_N = 16.8$ K [61] is consistent with the experimental data in the sense that clear qualitative changes in the spectra have occured between base temperature and just above the quoted Néel temperature.

We may also state with confidence that the ordered spin direction must be close to $\mathbf{a}^*$. If this were not the case, our program defined by Eqs. (59) and (61) from reducing the raw experimental data to T and L would have led to discrepancies, since it is based on the assumption $\langle \mathbf{S} \rangle \parallel \mathbf{a}^*$. No such discrepancies were found. In particular, we note that the moment cannot possibly have been along $\mathbf{c}$. This last comment relates back to our discussion in chapter 4 about the reduced polarization factor anisotropy in the MAPS data.

5.3.2 Low energy response

We turn now to a more in-depth discussion of the low energy response. Figure 29 shows our results for $L(\mathbf{Q}_{2D}, \omega)$ and $T(\mathbf{Q}_{2D}, \omega)$ obtained at $\hbar\omega = 5$ meV and $\hbar\omega = 9$ meV. Before discussing the modelling of the data, it is worth noting − as we did in connection with figure 27 − that in all four panels the response falls to zero within errors at the outside of the positions of the peaks in the transverse response. This yet again demonstrates how well the polarization analysis separates the magnetic components of the total cross-section from the nuclear and background contributions.

The solid lines represent the one-magnon and two-magnon cross-sections in the linear spin wave approximation described in section 5.2.3. As noted there, the ratio of the total (energy and wavevector) integrated one-magnon spectral weight to the total integrated two-magnon spectral weight is fixed by the reduction ΔS^z in the ordered moment from the full value $S = 1/2$. The red and blue lines are obtained using $m = S - \Delta S^z = 0.30$, close to the best theoretical estimates given in table 1. The overall scalefactor for the intensities is fixed by optimizing χ^2_{red} for the transverse data at 5, 7 (included in Fig. 30) and 9 meV. At optimal correspondance with the transverse data, the calculated values of χ^2_{red} at the three energies are 2.30, 2.23 and 2.37. We should emphasize that no real fits are involved in our analysis. Rather, with the ratio of one-magnon to two-magnon scattering fixed by ΔS^z, the overall scale is obtained by simply scaling the calculated predictions

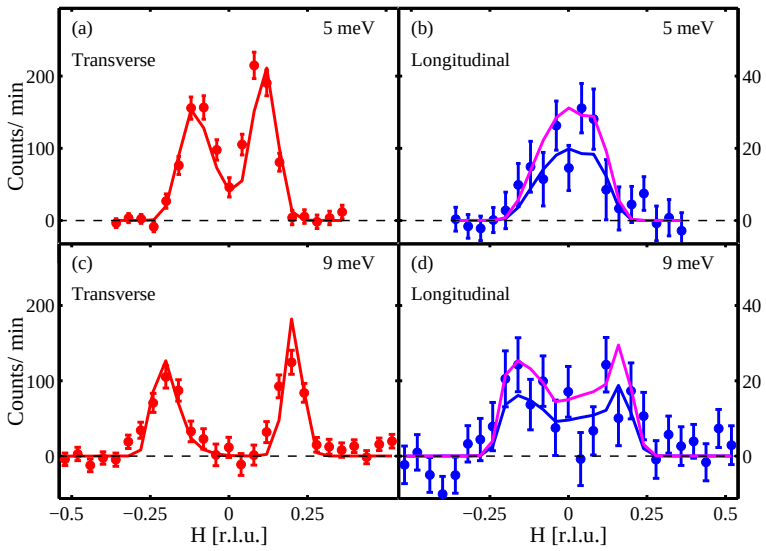

Figure 29: Low energy excitations in CFTD for wavevectors $\mathbf{Q} = (H10)$. (a) Transverse response $T(\mathbf{Q}_{2D}, \omega) = S^{xx}(\mathbf{Q}_{2D}, \omega) + S^{yy}(\mathbf{Q}_{2D}, \omega)$ at 5 meV. (b) Longitudinal response $L(\mathbf{Q}_{2D}, \omega) = S^{zz}(\mathbf{Q}_{2D}, \omega)$ at 5 meV. (c) Transverse response at 9 meV. (d) Longitudinal response at 9 meV. The solid red and blue lines are obtained by convoluting the instrumental resolution with the linear spin wave cross-section (using $\Delta S^z = 0.2$) as described in the text. The magenta lines in (b) and (d) are the corresponding results with $\Delta S^z = 0.26$. The two-peak structure of the model calculations in (d) is a real feature of the model as can be seen by comparing with figure 26. Counting times for $\hbar\omega = 5$ and 9 meV were ~ 4 and ~ 2 minutes per point per polarization channel, i.e. roughly 24 and 12 minutes per point in total or 12 and 6 minutes per point in the plots of $T(\mathbf{Q}_{2D}, \omega)$ and $L(\mathbf{Q}_{2D}, \omega)$ individually.

to the experimental spectra in the transverse channel.

Since the neutron diffraction measurements by Burger *et al.* indicate a slightly smaller ordered sublattice moment $m = S - \Delta S^z = 0.24 \pm 0.01$ (assuming $g = 2$), we have also computed the two-magnon spectrum corresponding to this value. To do this we simply rescale the two-magnon intensities according to Eqs. (138) keeping the one-magnon lineshape fixed and thus obtain the magenta lines in Figure 29 (b) and (d). Based on inspection of the longitudinal spectra the agreement with the data appears to change very little on going from $\Delta S^z = 0.20$ to $\Delta S^z = 0.26$. Based on the goodness-of-fit measure χ^2_{red} we reach the same conclusion: χ^2_{red} equals 0.76, 1.96 and 1.08 for 5, 7 and 9 meV with $\Delta S^z = 0.2$. The corresponding values calculated with $\Delta S^z = 0.26$ are 0.90, 1.34 and 1.31. Consequently, given the combined uncertainties we must refrain from passing judgement on the value of ΔS^z obtained Burger *et al.* and resign ourselves to qualitative statements regarding the correspondence between experiment and model.

It is clear that the experimental data for both L and T are well described by the linear spin wave calculation at the energies shown in Fig. 29. Even the intensity dip near $H = 0$ in (d) is theoretically accounted for as the Monte Carlo event cloud displayed in Fig 26 and used in calculating the two-magnon response contains the same feature in the shape of weak intensity maxima just above the single-magnon branch.

Figure 21 displays color maps of $T(\mathbf{Q}_{2D}, \omega) = S^{xx}(\mathbf{Q}_{2D}, \omega) + S^{yy}(\mathbf{Q}_{2D}, \omega)$ and $L(\mathbf{Q}_{2D}, \omega) = S^{zz}(\mathbf{Q}_{2D}, \omega)$ at energies extending to $\hbar\omega \sim J_{\text{eff}} = Z_c J$. In order to present the data on the same color scale, the longitudinal response has been multiplied by 5. The maps were produced directly from the raw data taken at $\hbar\omega = 2$, 3, 5, 7 and 9 meV by the subtraction procedure (56), i.e. without performing corrections for polarization or angular factors. The reason is simply that doing so would require that all six polarization channels were measured, and this was only the case for 5, 7 and 9 meV. By comparing the correct T and L, obtained using (60) and (62) at these three energies, with the approximations of T and L one gets from Eq. (56), we have verified that the error is small. At its largest, it is only marginally outside the experimental errorbars, and this happens only for the transverse response at wavevectors between the two counterpropagating magnon branches. In other word, the color maps of Fig. 21 are an excellent representation of the true longitudinal and transverse spectra. The solid white lines represent the dispersion relation Eq. (48) used in chapter 4 to fit the single-magnon dispersion along the [11] direction. We have set $J = J_{\text{eff}}/Z_c \simeq 7.30/1.18 = 6.18$ meV − the value obtained from this fit. Evidently the single-

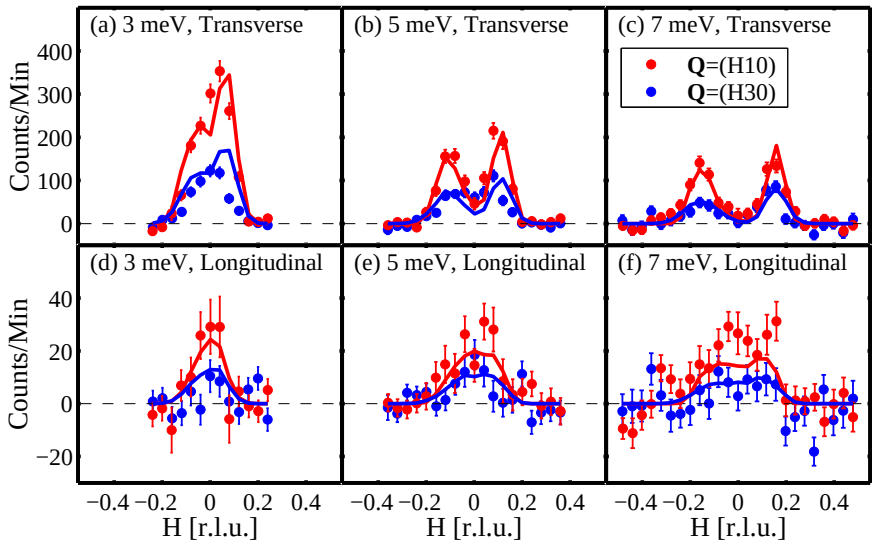

Figure 30: Comparisons of $L(\mathbf{Q}_{2D},\omega)$ and $T(\mathbf{Q}_{2D},\omega)$ at low energies obtained by transverse scans around $\mathbf{Q}=(010)$ (red points) and $\mathbf{Q}=(030)$ (blue points). The solid lines are the linear spin wave cross-sections convolved with the experimental resolution function. As explained in the text, the total ($\mathbf{Q}$ and ω-integrated) two-magnon scattering is equal to the total one-magnon scattering multiplied by a numerical constant which depends only on ΔS^z – the reduction of the sublattice moment caused by quantum fluctuations. The red and blue lines in (a)-(d) correspond to $\Delta S^z = 0.2$ (the theoretical expectation, see table 1) for scans around (010) and (030) respectively. The magenta (For (010) data) and black (for (030) data) lines in (c) and (d) were computed by keeping the transverse cross-sections fixed and then scaling the longitudinal cross-sections to obtain their expected values for $\Delta S^z = 0.25$ (the experimental value from [80]). One overall intensity scale factor was used for all the simulated cross-sections of this plot and for those of Fig. 29. The resolution corrected cross-sections calculated for wavevectors in the vicinity of (030) were further corrected for the drop of the free Cu^{2+} formfactor squared between (010) and (030). Counting times per point per polarization channel were ~ 2, ~ 4 and ~ 2 minutes at $\hbar\omega = 3$, 5 and 7 meV respectively for wavevectors around (010). For wavevectors near (030) they were ~ 2 minutes at all energies.

magnon dispersion in the transverse color map is well described by the theoretical form Eq. (48), and there is no need for additional parameters. We may also note that the transverse color map clearly reveals the focusing effects at positive H caused by the orientation of the resolution ellipsoid.

The longitudinal response displayed in Fig. 21(b) is clearly much more spread out in wavevector-space than the transverse response, and crucially is almost completely contained inside the one-magnon dispersion cone as expected for two-magnon scattering. When this appears not to be the case (as it does for negative H near $\hbar\omega = 7$ meV), it can be attributed to the combined influence of $\mathbf{Q}$-resolution, counting statistics and the way the graphics is being handled.

Having said this, the apparent modulations in longitudinal intensity with energy are however only partially a result of the graphical handling. For example, the longitudinal response at $\hbar\omega = 2$ meV is almost completely at background level, and this accounts for the hole at the lowest energies in Fig. 21(b). We shall return to this later as it may possibly have a deep significance, but for the time being our main purpose in presenting the data in the form of color maps is to provide a easy-to-grasp visual demonstration that we can clearly distinguish a low energy continuum of longitudinally polarized multimagnon scattering which within linear spin wave theory is interpreted as two-magnon scattering. The agreement between the data and the predictions of linear spin wave theory is generally very good for both T and L.

The low energy response discussed this far was obtained by transverse, constant-$\hbar\omega$ scans around the crystallographic (010) position. During the IN20 experiment, we also did a few transverse, constant energy scans around the equivalent wavevector (030). Figure 30 compares the transverse and longitudinal spectra obtained around (010) and (030) for the three energy transfers where data are available in both zones. The $\hbar\omega = 5$ meV data for wavevectors around (010) in panels (b) and (e) were already presented in Fig. 29. In all cases, the intensities are larger for scans through (010). This is expected given the reduction in the value of the squared form factor $|F(\mathbf{Q})|^2$. However, a casual analysis based on the integrated intensities under the curves shows that the magnetic intensities T and L both fall off more rapidly than dictated by the variation in the squared free Cu^{2+} form factor – $|F((010))|^2$ / $|F((030))|^2$= 1.58. On the other hand, the ratio

of the longitudinal to transverse integrals in the two zones remain identical within errorbars which are admittedly rather large owing to the poorer quality of the data taken around $\mathbf{Q} = (030)$. To investigate the rapid fall-off further, it is neccesary to go beyond simple one-dimensional integrals and to consider more carefully the evolution of the resolution ellipsoid with $\mathbf{Q}$ to see if changes in its volume can account for the observations.

The solid lines figure 30 are the results of resolution corrected calculations of our model cross-sections (63) with the variation in the square of the formfactor removed. The single overall scale factor for the intensities was fixed at the same value as was used in the model calculations in Fig. 29. In all panels, red and blue lines are computed with $\Delta S^z = 0.2$ and correspond to wavevector transfers around (010) and (030) respectively. Both inspection and computations of $\chi^2_{\rm red}$ reveal that the agreement between theory and experiment is reasonably good, with the transverse data at low energies being the main exception. We take this as evidence that the resolution function variation between the zones around (010) and (030) captures most of the experimentally observed intensity change, and note that the response at the lowest energies once again stands out as possible region to look for quantitative deviations away from the predictions of linear spin wave theory.

5.3.3 High energy response

Having studied the low energy response, we shall now investigate the high-energy behaviour of $T(\mathbf{Q}_{\rm 2D}, \omega)$ and $L(\mathbf{Q}_{\rm 2D}, \omega)$. The presence of a zone boundary dispersion in the single-magnon spectrum − a feature not predicted by spin wave theory − makes it relevant to ask whether or not there are also anomalies in the multimagnon components of T and L. Since we base our analysis on a linear spin wave approximation in which T has no multimagnon component and L consists solely of two-magnon excitations, we are restricted to inquiring how well this particular approximation accounts for the observed spectra. Further, polarized neutron scattering experiments being time-consuming, we focussed our attention on the high-symmetry points $(\pi/2, \pi/2)$ and $(\pi, 0)$ on the magnetic zone boundary where the single-magnon energy is highest and lowest respectively.

The data presented in this section were obtained at the IN22 triple axis spectrometer for wavevectors on the zone boundary enclosing $\mathbf{Q} = (030)$. To be precise, all $\mathbf{Q}_{\rm 2D} = (\pi/2, \pi/2)$ data were taken at $\mathbf{Q} = (0\,2.5\,0)$ and all $\mathbf{Q}_{\rm 2D} = (\pi, 0)$ data at $(0.5\,2.5\,0)$. Figure 31 displays our results for $T(\mathbf{Q}_{\rm 2D}, \omega)$ and $L(\mathbf{Q}_{\rm 2D}, \omega)$. These data are corrected for imperfect polarization and the off-axis $(\pi, 0)$ data also for a small angular factor associated with the rotation of $\mathbf{Q}$ away from the $\boldsymbol{b}^*$ axis (see Fig 25).

Let us start by considering the transverse responses shown in panels (a) and (b). First we notice that the main peaks in the transverse responses at the two wavevectors clearly do not occur at the same energy, immediately confirming a dispersion along the zone boundary. The dotted vertical lines mark the location of the single-magnon peak at $(\pi/2, \pi/2)$ in the MAPS experiment, where the data along the $(\pi, \pi) \rightarrow (0, 0)$ direction were fitted to the linear spin wave dispersion (48) with $\Delta = 0.38$ meV fixed. As mentioned already, the fit yielded $J_{\rm eff} = Z_c J = 7.30$ meV or $J = 6.18$ meV when we set $Z_c = 1.18$. This leads to a zone boundary energy of 14.59 meV which is in excellent agreement with the polarized data at $(\pi/2, \pi/2)$, but is significantly higher than the peak energy at $(\pi, 0)$.

Second, there is an apparent suppression of peak intensity at $(\pi, 0)$ compared with $(\pi/2, \pi/2)$, but this drop appears to be compensated by an increased peak width. When comparing IN20 and IN22 data in Fig. 27 we already mentioned that this possible lineshape effect was also present in the scarcer zone boundary data from IN20. Since resolution conditions were not identical in the two experiments we tentatively concluded that the broadening could possibly be associated with the resolution ellipsoid orientation with respect to a single-magnon dispersion which has a local miminum at $(\pi, 0)$. To make this conclusion firmer the calculated width of the single-magnon peak was investigated as a function of wavevector transfer along the zone boundary. Because our theoretical transverse cross-section has neither zone boundary dispersion nor continuum scattering above the single-magnon peak, the results give a lower limit on the effects of resolution alone. We find that around the full zone boundary, the FWHM of the calculated curves vary by as much as 30%. However, the widths of the particular curves computed for $(0\,2.5\,0)$ and $(0.5\,2.5\,0)$ are almost identical, and therefore the variation in the FWHM of the experimental curves in panels (a)-(b) (and in panels (f)-(g) of Fig. 27) by roughly 30% is very likely to have a contribution from other sources, notably the ZB dispersion and possibly also transverse continuum scattering at higher energies. The magnitude of the former effect could be investigated more accurately by adding

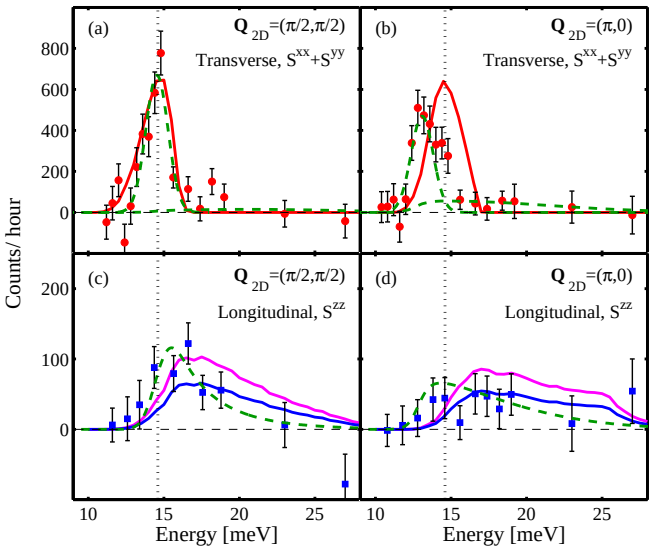

Figure 31: High-energy excitations in CFTD for wavevectors on the magnetic zone boundary surrounding the crystallographic (030) position. (a) and (b) display the transverse excitations $T(\mathbf{Q}_{2D},\omega) = S^{xx}(\mathbf{Q}_{2D},\omega) + S^{yy}(\mathbf{Q}_{2D},\omega)$ at $\mathbf{Q}_{2D} = (\pi/2,\pi/2)$ and $\mathbf{Q}_{2D} = (\pi,0)$ respectively. (c) and (d) display the longitudinal excitations $L(\mathbf{Q}_{2D},\omega) = S^{zz}(\mathbf{Q}_{2D},\omega)$ at $(\pi/2,\pi/2)$ and $(\pi,0)$ respectively. Dotted vertical lines represent the expected zone boundary single-magnon energies with $J = 6.18$ meV and the same dispersion used to fit the time-of-flight data of the previous chapter. In all four panels, solid lines are the results of the linear spin wave model calculation described in the text. The longitudinal intensities are fixed by the quantum reduction ΔS^z in the ordered moment. Blue and magenta lines in (c) and (d) correspond to $\Delta S^z = 0.2$ and $\Delta S^z = 0.26$ respectively. Dashed green lines are the Quantum Monte Carlo model calculations of Sandvik and Singh with the energy scale set by J and one $\mathbf{Q}_{2D}$-independent overall scale factor for the intensities fixed by comparing the theoretical and experimental one-magnon parts of the spectra. Counting times varied with energy transfer, typical values below 20 meV being $\sim$ 32-35 minutes per point per SF channel and $\sim$ 7 minutes per point per NSF channel. The two highest energy points were counted for $\sim$ 16 minutes in each NSF channel and $\sim$ 32 minutes in each SF channel.

a next-nearest neighbor interaction to yield the correct zone boundary dispersion in the Monte Carlo event cloud, but this has not been done. In connection with the latter possibility (that the lineshape broadening at $(\pi,0)$ has a contribution from transverse continuum scattering) we notice that the transverse spectra at both $(\pi/2,\pi/2)$ and $(\pi,0)$ appear to have additional small but finite spectral weight at energies above the main single-magnon peak. The errorbars are however quite significant. To have some kind of ad hoc quantitative measure we average over all points above $\hbar\omega = 16$ meV using the squared inverse errorbars as weight factors. The resulting numbers are 59 ± 26 and 37 ± 25 counts per hour for $(\pi/2,\pi/2)$ and $(\pi,0)$ respectively $-$ in both cases above zero, but only just so.

Turning to the longitudinal data plotted in panels (c)-(d) it is clear that for both wavevectors non-negligible intensity exists above the position of the single-magnon peaks in the corresponding transverse channels (dotted vertical lines), whereas the intensity levels drops to background level below the actual zone boundary energies. These features are fully consistent with interpreting the data in terms of a continuum of longitudinally polarized multimagnon states above the single-magnon dispersion relation. At $(\pi/2,\pi/2)$, L appears to have internal structure with a peak around $\hbar\omega \simeq 16$ meV while any such structure is less evident at $(\pi,0)$. For numerical comparison we have once again evaluated the average count rate for energies above 16 meV, and find 47 ± 13 and 41 ± 13 counts per hour for $(\pi/2,\pi/2)$ and $(\pi,0)$ respectively. These numbers are of the same order of magnitude as the transverse averages computed above but with significantly smaller errorbars.

The solid red lines in (a) and (b) represent resolution corrected calculations of $T(\mathbf{Q}_{2D},\omega)$ using the expression given in Eq. (63) with the exchange constant $J = 6.18$ meV entering $\omega_{\mathbf{Q}}$ taken from the time-of-flight experiment of chapter 4 and as usual renormalized by Z_c. An overall intensity scalefactor was found by matching the calculated curve with the measured $T(\mathbf{Q}_{2D},\omega)$ at $(\pi/2,\pi/2)$. There is a certain freedom of choice at this point owing not only to uncertainties in the determinations of the resolution function parameters and flipping ratio, but also more fundamentally to the fact that we do not know the relative single-magnon and multimagnon contributions to T immediately above the single-magnon peak position. The chosen scalefactor is a compromise between such considerations. With the overall intensity scale fixed, the ratio of one-magnon to

two-magnon scattering is again fixed by the quantum reduction ΔS^z of the ordered moment. The solid blue lines in (c) and (d) are thus resolution corrected calculations of the theoretical two-magnon spectrum $L(\mathbf{Q}_{2D}, \omega)$ given in Eq. (63) with $\Delta S^z = 0.2$ − the theoretical expectation for a 2DQHAFSL.

A comparison of the calculated longitudinal spectra with the experimental data reveals overall good agreement. Qualitatively, we first note that the intensity scale of the two-magnon scattering is of the right order of magnitude. Second, the calculated continuum is slightly flatter at $(\pi, 0)$ than at $(\pi/2, \pi/2)$, as appears to be the case for the data as well. Quantitatively, an evaluation of $\chi^2_{\rm red}$ yields 1.70 at $(\pi/2, \pi/2)$ and 0.54 at $(\pi, 0)$. The agreement is slightly worse if the calculated spectra are rescaled to the values they would take if $\Delta S^z = 0.26$. In this case we find $\chi^2_{\rm red} = 1.80$ at $(\pi/2, \pi/2)$ and $\chi^2_{\rm red} = 1.42$ at $(\pi, 0)$.

For the transverse response, the agreement between experiment and calculation is clearly best − although not perfect − for the one-magnon peak at $(\pi/2, \pi/2)$. This is no surprise since we fixed the overall intensity scale factor here, and further, since in the time-of-flight experiments the $(0, 0) \rightarrow (2\pi, 2\pi)$ direction was the one fitted to deduce the effective exchange constant $J_{\rm eff} = Z_c J$ used as input in the model calculations. An evaluation of $\chi^2_{\rm red}$ yields 2.79 at $(\pi/2, \pi/2)$. With respect to the peak position, the agreement is evidently hopeless for the transverse response at $(\pi, 0)$, as already discussed. The intensity mismatch is smaller, with theory overshooting the observed peak intensity. The trend is opposite at $(\pi/2, \pi/2)$, where the scaled computations are lower than the maximum intensity point. The model thus predicts a peak intensity ratio of 1.01, whereas the experimental value is 1.5 ± 0.3. If we look at integrated intensities instead of peak intensities, we find an experimental ratio 1.09 ± 0.11, i.e. the integrated intensities are identical within the errors. These numbers should be compared to the large intensity dip seen in the time-of-flight data presented in Fig. 19 in chapter 4. There, we found that the single-magnon intensity at $(\pi, 0)$ was only $46 \pm 12\%$ of the single-magnon intensity at $(\pi/2, \pi/2)$. The actual fits leading to this conclusion were displayed in Fig 15. In considering the momentum variation of the intensity derived from our time-of-flight experiments it should be kept in mind that we were unable to verify the expected low-temperature variation of the polarization factor in the cross-section for magnetic scattering. In turn, this forced us to admit a 5-10% error on all intensities. This source of error is not included in the results presented in Fig. 19. To make contact with the triple-axis data, we must consider whether there is consistency between the single-magnon intensity ratios between $(\pi, 0)$ and $(\pi/2, \pi/2)$ in the two experiments. However, because we have not yet collected all potential pieces in the puzzle, it is more natural to postpone the discussion of this issue.

5.3.4 Quantum Monte Carlo and discussion

In this section we continue with our discussion revolving around Fig. 31, focussing on numerical work on the 2DQHAFSL. We also discuss the interrelation between the results of the time-of-flight and triple axis experiments and investigate outstanding questions raised by the data presented in the chapter.

The dashed green lines in Fig. 31 are the results of QMC work by Sandvik and Singh [37] who computed $S^{xx}(\mathbf{Q}_{2D}, \omega)$ and $S^{zz}(\mathbf{Q}_{2D}, \omega)$ explicitly at the wavevectors studied in our experiment. Their model for $T(\mathbf{Q}_{2D}, \omega)/2 = S^{xx}(\mathbf{Q}_{2D}, \omega)$ includes a sharp delta-function peak associated with one-magnon excitations and a continuum of multimagnon states at energies higher than the one-magnon states, whereas the model for $L(\mathbf{Q}_{2D}, \omega) = S^{zz}(\mathbf{Q}_{2D}, \omega)$ consists of a continuum of longitudinally polarized multimagnon states:

$$\begin{aligned} S^{xx}(\mathbf{Q}_{2D}, \omega) &= A_1(\mathbf{Q}_{2D})\delta(\omega - \omega_{\boldsymbol{q}}) + A_2(\mathbf{Q}_{2D}) f_x(\mathbf{Q}_{2D}, \omega) \\ S^{zz}(\mathbf{Q}_{2D}, \omega) &= B(\mathbf{Q}_{2D}) f_z(\mathbf{Q}_{2D}, \omega) \end{aligned} \tag{65}$$

Here $f_x(\mathbf{Q}_{2D}, \omega)$ and $f_z(\mathbf{Q}_{2D}, \omega)$ are simple functions describing the two continua. They are both normalized functions of frequency which are zero for $\omega < \omega_{\boldsymbol{q}}$ but − in contrast with the two-magnon continuum in linear spin wave theory − have no restriction placed on their upper energy limit. The QMC calculations yield the one-magnon energies $\omega_{\boldsymbol{q}}$, the relative spectral weights of the one-magnon and multimagnon components of the total $S(\mathbf{Q}_{2D}, \omega)$ as well as the parameters determining f_x and f_z.

In order to simulate the effect of the instrumental energy resolution, the numerical spectra for $(\pi/2, \pi/2)$ and $(\pi, 0)$ from [37] (Kindly provided by A. W. Sandvik) were smoothed by convolution with a Gaussian of the same width as the peaked part of the transverse experimental spectrum

at $(\pi/2, \pi/2)$. The smoothed spectra were then scaled to obtain the best possible agreement with the total (one-magnon plus multimagnon) transverse data at $(\pi/2, \pi/2)$ and $(\pi, 0)$ simultaneously. The $\mathbf{Q}_{2D}$-resolution could not be incorporated since Sandvik and Singh did not study the detailed dependence of their numerical spectra for T and L on $\mathbf{Q}_{2D}$.

With these approximations, we obtain excellent agreement between the QMC spectra and the experimental data for both transverse and longitudinally polarized spin excitations at both wavevectors investigated. In particular, the QMC data captures the zone boundary dispersion and the one-magnon intensity mismatch between the two wavevectors. Further, but less convincingly − the experimental errorbars having the magnitudes they do − the intensity above the transverse one-magnon peak at $(\pi, 0)$ is perfectly accounted for while the transverse two-magnon spectrum at $(\pi/2, \pi/2)$ is predicted to be closer to zero (The corresponding dashed lines are barely above background level in Fig. 31(a)). The agreement between the experimental data and the QMC spectra for $L(\mathbf{Q}_{2D}, \omega)$ is also very good at both wavevectors. To be quantitative, we have evaluated $\chi^2_{\rm red}$ for all for experimental spectra and find 1.48, 1.00, 1.01 and 0.68 for Fig 31 (a)-(d) in that order.

We must now address the central question of mutual consistency between the intensity ratios for zone boundary magnon seen in the time-of-flight and triple-axis experiments. In the former, we found a single-magnon spectral weight ratio of $I(\pi, 0)/I(\pi/2, \pi/2) = 0.46 \pm 0.12$ with the intensities $I(\mathbf{Q}_{2D}) = I_{\boldsymbol{q}}$ defined by Eq. (46). On the other hand, the triple axis results of Fig 31 gave two numbers: 0.67 ± 0.13 for the peak-intensity ratio (corresponding to $I^{\rm peak}(\pi/2, \pi/2)/I^{\rm peak}(\pi, 0) = 1.5 \pm 0.3$) and 0.92 ± 0.09 for the ratio of energy-integrated intensities (corresponding to $I^{\rm int}(\pi/2, \pi/2)/I^{\rm int}(\pi, 0) = 1.09 \pm 0.11$). Within the combined errorbars, the peak-intensity ratio is already consistent with the spectral weight ratio from the MAPS experiment. However, it is plagued by a large statistical error because it is based on just two measurements made at the peak positions. It is therefore prudent to investigate the issue of consistency more carefully.

First, let us consider the effect of resolution in the triple axis experiment. Our model calculation of the convolution of the one-magnon cross-section (63) − which predicts equal intensities at the two points considered and neglects the zone boundary dispersion − with the resolution function calculated on the basis of the Cooper Nathans prescription [7] provided essentially identical lineshapes in terms of energy-width and peak-intensities at the two wavevectors $(\pi, 0)$ and $(\pi/2, \pi/2)$ (red lines in Fig. 31). Thus, to within the accuracy of our determination of the resolution function and assuming that the ~ 1 meV dip in the single-magnon dispersion does not appreciably alter the resolution conditions, neither the observed difference in peak-intensities nor the difference energy-integrated intensities between the two points studied in the triple axis experiment is due to differences in resolution conditions. This observation eases comparison with the intensities seen in the time-of-flight experiment. Consider now, that the $\mathbf{Q}_{2D}$-resolution of the MAPS spectrometer is better than that of the triple-axis spectrometer due to the small isotropic pixel elements. This implies that the $\mathbf{Q}_{2D}$-projection of the resolution ellipsoid integrates over a larger portion of $\mathbf{Q}_{2D}$-space in the triple-axis experiment. Next, we note that the observed single-magnon intensity variation with $\mathbf{Q}_{2D}$, shown in Fig. 19, is apparently flatter near $(\pi/2, \pi/2)$ than near $(\pi, 0)$ where we have the large intensity dip. In this situation, the larger resolution ellipsoid volume of a triple-axis spectrometer will tend to increase the peak-intensity at $(\pi, 0)$ relative to that seen in the time-of-flight experiment by collecting contributions from the higher-intensity regions close to $(\pi, 0)$. If anything, the opposite will occur at $(\pi/2, \pi/2)$, i.e. the larger resolution ellisoid can cause a decrease in the peak-intensity in the triple-axis experiment relative to the time-of-flight experiment. The net effect of these considerations is that one can expect a smaller peak intensity ratio between $(\pi, 0)$ and $(\pi/2, \pi/2)$ in the time-of-flight experiment than in the triple-axis experiment in agreement with our observations.

Further, we should recall that in the time-of-flight experiment there was a source of error of magnitude $5 - 10\%$ on the observed intensities, caused by our inability to distinguish the expected variation of the polarization factor in the neutron scattering cross-section. Adding this factor on top of the resolution argument given above, it is fair to say that there is consistency between the spectral weight ratio 0.46 ± 0.12 found at MAPS and the peak-intensity ratio 0.67 ± 0.13 found at IN22, and that most likely both are consistent with the QMC prediction 0.705 indicted in Fig. 19(b).

How about the ratio of integrated intensities in the triple axis experiment? Whereas the peak-intensity in a scan through a dispersion surface depends strongly on the orientation of the resolution

ellipsoid, the integrated intensity in such a scan should be a more robust measure of the intensity. The prototypical manifestation of this can be seen in some of the constant-$\hbar\omega$ scans presented in this chapter, e.g. in Fig. 29(a) and (c), where one of the two counterpropagating single-magnon peaks is sharp and intense, whereas the other in broader and weaker. We have noted that in Fig. 31(a)-(b) an apparent $\sim 30\%$ lineshape increase at $(\pi, 0)$ compensates for the decrease in peak-intensity discussed above, yielding the quoted 0.92 ± 0.09 ratio between the energy-integrated intensities. On the other hand, we have also seen that our calculated resolution function predicts equal energy widths at the two wavevectors. Thus it is natural to speculate, as we did on page 69 that the broadening at $(\pi, 0)$ has an intrinsic component. Recapitulating the arguments put forward there, the effect of the zone boundary dispersion, which will be picked up by the $\mathbf{Q}_{2D}$-resolution is one candidate contributor. Another is finite transverse continuum scattering just above the single magnon peak at $(\pi, 0)$. In connection with the latter possibility it is particularly interesting to note that both series expansions [34], QMC [37] and the π-flux phase theory [86] predict the existence of a stronger multimagnon continuum at $(\pi, 0)$ than at $(\pi/2, \pi/2)$, and that further the latter two approaches tell us that the spectral weight of the transverse continuum at $(\pi, 0)$ is concentrated closer to the single-magnon peak than is the case at $(\pi/2, \pi/2)$, thereby giving rise to a lineshape broadening. The conjecture that there is a finite transverse multimagnon component at $(\pi, 0)$ is supported by the excellent agreement between the data in Fig. 31(b) and the combined QMC single-magnon plus multimagnon prediction. Further, such a contribution would act to decrease the single-magnon contribution to the energy-integrated intensity at $(\pi, 0)$, and by doing so improve the agreement with the time-of-flight ratio, the ratio of peak-intensities and with the single-magnon ratio 0.705 given by QMC. The MAPS data at $(\pi, 0)$ displayed in Fig. 15(f) is well acounted for by a fit based on the cross-section (45), and does not appear to exhibit any clear broadening towards high energies. This is however not a cause for serious concern since the expected effect − if at all present − is small even in the polarized triple axis experiment, and would be substantially more difficult to identify in a time-of-flight experiment where the effects of nuclear scatter must also be taken into consideration.

In conclusion to the above lines of thought, we have seen that the intensity ratios for single-magnon scattering at $(\pi, 0)$ and $(\pi/2, \pi/2)$ are most likely consistent with each other. There is some circumstantial evidence that transverse multimagnon continuum scattering makes a contribution to the integrated intensity and width of the single-magnon peak seen at $(\pi, 0)$ in the triple-axis experiment, but − truth be told − we cannot be sure without further experiments and theoretical guidance.

Continuing our investigation of the numerical work in [37], we note that QMC goes beyond spin wave theory in the sense that magnon-magnon interactions are taken into account to all orders of the $1/S$-expansion of the latter approach. The source of error in QMC lies not in approximations, but in computation time which in turn translates into lattice size. The authors of [37] study lattice sizes up to 32×32 sites at a low temperature $k_B T = J/32$ (With $J = 6.18$ meV for CFTD, this corresponds to $T = 2.2$ K and is just above the sample temperature in our experiments). They claim to have then reached a point where further lattice size increase will not change the results appreciably. If this is so and the numerical errors are small, the QMC data can be regarded as essentially exact representations of the excitation spectra of a 2DQHAFSL with magnon-magnon interactions fully accounted for. Taken to order $1/S^2$, spin wave theory yields $Z_c \simeq 1.18$ and a single-magnon energy which on the zone boundary $H + K = \pi$ is either constant [26] or varies by a small amount [28]. Given these contradictory results and since we have seen that QMC and experiment agree very well in CFTD, it is relevant to take a close look at what predictions are made by QMC [37, 84].

The magnon-magnon interactions have their most dramatic effect at $(\pi, 0)$ where they reduce the single-magnon energy to $\omega_{\boldsymbol{Q}} \simeq 2.16J$ (compared to $\omega_{\boldsymbol{Q}} = 2Z_c J = 2.36J$) and $\simeq 40\%$ of the total transverse spectral weight is transferred to the transverse continuum. By comparison, the continuum exhausts only $\simeq 13\%$ of the total transverse spectral weight at $(\pi/2, \pi/2)$ and the single-magnon energy $\omega_{\boldsymbol{Q}} \simeq 2.40J$ is changed much less. The momentum variation of $\hbar\omega_{\boldsymbol{q}}$ was included in both Fig. 16 and Fig. 31 and corresponds to a zone boundary dispersion of 10%.

Let us denote the energy-integral of the one-magnon contribution to $S^{xx}(\mathbf{Q}_{2D}, \omega)$ in Eq. (65) by $A_1(\mathbf{Q}_{2D})$, and the energy-integrated transverse and longitudinal continuum spectral weights by $A_2(\mathbf{Q}_{2D})$ and $B(\mathbf{Q}_{2D})$ respectively. Then we have $S^{xx}(\mathbf{Q}_{2D}) = A_1(\mathbf{Q}_{2D}) + A_2(\mathbf{Q}_{2D})$ and $S^{zz}(\mathbf{Q}_{2D}) = B(\mathbf{Q}_{2D})$. Using the numerical data [84] we can then work out the relative energy-integrated spectral weights of single-magnon and multimagnon excitations for $\mathbf{Q}_{2D} = (\pi/2, \pi/2)$

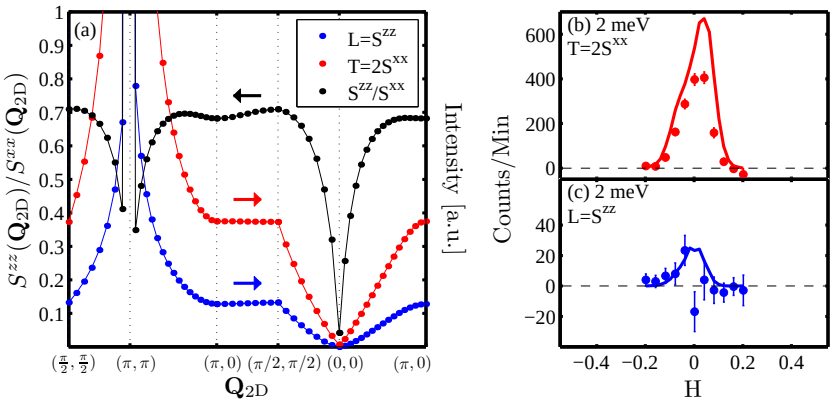

Figure 32: (a) Extended version of Figure 1 in [37], based on numerical data supplied by Sandvik [84]. In addition to the ratio $S^{zz}(\mathbf{Q}_{2D})/S^{xx}(\mathbf{Q}_{2D})$, we have also plotted the total energy-integrated transverse and longitudinal spectral weights (in arbitrary units), along a triangular path in reciprocal space. (b) and (c) show $T(\mathbf{Q}_{2D},\omega)$ and $L(\mathbf{Q}_{2D},\omega)$ at $\hbar\omega = 2$ meV for a constant-energy scan through (010). Counting times were ~ 3 minutes per point per polarization channel.

and $\mathbf{Q}_{2D} = (\pi, 0)$. At $(\pi/2, \pi/2)$ we find $A_1 = 0.6389$, $A_2 = 0.0993$, $B = 0.2618$ whereas the numbers for $(\pi, 0)$ are $A_1 = 0.4504$, $A_2 = 0.2953$, $B = 0.2542$. These integrals were used in fixing the relative (integrated) intensities of the QMC lines in Fig. 31 and − as we have seen − are in excellent agreement with the experimental data. In particular they lead to an intensity ratio of $0.4504/0.6389 = 0.705$ between magnons at $(\pi, 0)$ and $(\pi/2, \pi/2)$, and this ratio was included in Fig. 19.

Let us finally follow [37] and look at the $\mathbf{Q}_{2D}$-dependence of $2L/T = S^{zz}(\mathbf{Q}_{2D})/S^{xx}(\mathbf{Q}_{2D})$. Figure 32(a) reproduces and extends figure 1 of that paper and shows that longitudinally polarized spin excitations account for $30-35\%$ of the total spectral weight over the part of the full Brillouin zone where the single magnon energy is large. On approaching (π, π) both L and T grow rapidly, and would become divergent exactly at (π, π). These divergences are easily rationalized: That of L is related to the long-range magnetic order which would occur in an infinite lattice, whereas that of T takes place even in spin wave theory, where the weight of the single-magnon excitations near the zone center tends to infinity as $1/Q_{2D}$. The ratio $2L/T$ is divergent at (π, π), but is finite for small values of $[\mathbf{Q}_{2D} - (\pi, \pi)]$. Upon approaching (π, π), it further exhibits a drop from the values taken for wavevector transfers near the zone boundary. Thus, the single-magnon excitation exhaust the total spectral weight near the zone center.

Since Fig. 32(a) deals with energy integrated quantities, we cannot immediately relate its predictions to our experimental results for low energies, but note that unless significant additional longitudinal spectral weight is present at energies outside our experimental window of 9 meV near the zone center, a rapidly increasing L in the limit $\mathbf{Q}_{2D} \to (\pi, \pi)$ would seen to contrast sharply with Fig. 21 which shows an apparant absence of longitudinal scattering at the lowest energy $\hbar\omega = 2$ meV for wavevectors in the vicinity of (010). The data on which this is based are shown in Fig. 32(b)-(c). It is clear that the model calculation (with $\Delta S^z = 0.2$) overestimates the experimental response by a large amount in the case of $T(\mathbf{Q}_{2D},\omega)$. For $L(\mathbf{Q}_{2D},\omega)$, the experimental errorbars do not allow a distinction between the model calculation and a flat line at zero counts per minute. By contrast, the experimental data for $\hbar\omega = 3$ meV around (010) included in Fig. 30 are rather well described by the model for both channels, and L is clearly non-zero. The absence of longitudinal excitations at 2 meV and their reappearance at 3 meV is not simply a result of counting statistics as we counted for a longer time at 2 meV. There are also discrepancies between model and experiment at low energies for wavevector near (030), but since our data quality is best for wavevectors near (010) we focus our attention at the 2 meV data in Fig. 32(b) and (c) and outline two possible explanations for the apparent absence of longitudinal spin fluctuations at the lowest energies probed.

First, we should remember that the spin fluctuation spectrum of CFTD has a low energy gap of $\Delta = 0.38$ meV in the single-magnon excitations caused most likely by a Dzyaloshinsky-Moriya antisymmetric exchange interaction. In a simple picure, we would expect a gap in the two-magnon spectrum of $2\Delta = 0.76$ meV, but this does not explain the absence of longitudinally polarized

scattering at $\hbar\omega = 2$ meV. More generally, we are unaware of an argument to exclude that a Dzyaloshinsky-Moriya interaction or another subdominant term in the Hamiltonian may cause the longitudinal spin fluctuations to dwindle away at an energy scale beyond 2Δ. The suggestion that such terms might be responsible for the observed gap is however subject to restrictions. For example, Fig. 70(b) shows that next-nearest neighbor interaction affect the single-magnon intensities at low energy transfers. Similarly we must expect couplings beyond nearest neighbors to influence the two-magnon response, but being continuously connected to the $J' = 0$ limit by Eqs. (133)-(136), they cannot cause the observed low-energy gap in $L(\mathbf{Q}_{2D}, \omega)$.

As stated previously, the QMC results are in essence exact baring numerical error, but shed little light on the microscopic nature of the ground state. A second, perhaps rather speculative, possibility why we see $L \simeq 0$ at the lowest energy transfers is that the ground state of the 2DQHAFSL has qualitatively similarities with the π-flux phase state which we encountered in our analysis of time-of-flight data in chapter 4. Here we saw that its predictions for the dispersion [85] and amplitude [83] of the spin wave excitations have characteristics resembling those of the experimental data, i.e. a zone boundary dispersion (Fig. 16) and a large reduction in the spectral weight of the sharp single-magnon excitation at $(\pi, 0)$ relative to $(\pi/2, \pi/2)$ (Fig. 19).

Using the random phase approaximation, Ho and coworkers [86] calculated the full spectrum of transversely polarized excitations in the π-flux phase state at $T = 0$ K. It has two components: The first is a sharp, gapless, spin wave dispersion surface formed by bound states of particles and holes in the underlying bands of chargeless lattice fermions (loosely termed spinons) obtained by diagonalizing an effective Hamiltonian which combines the π-flux phase with a spin density wave. Ho *et al.* refer to these excitations as RVB-excitons, thereby hinting at a link between the π-flux phase description of the Heisenberg model and the resonating valence band state suggested by Anderson as a new type of insulator [15] and later as a suitable platform from which to understand the high-temperature superconductors [16]. The connection is more clearly presented in [88]. It is the dispersion and amplitude of these excitations which we discussed in chapter 4. Second, at energies above the spin wave dispersion there is a broad continuum formed by (non-bound) spinon pair excitations. Between the two components of the transversely polarized spin excitations there is a momentum-dependent gap. This gap vanishes at (π, π) implying the absence of a transverse continuum scattering at the lowest energies. What we observe in Fig. 32(c) is the absence of longitudinally polarised low-energy excitations. Unfortunately, Ho *et al.* do not calculate $S^{zz}(\mathbf{Q}_{2D}, \omega)$, but one might consider that it could have gap similar to that in $S^{+-}(\mathbf{Q}_{2D}, \omega)$. However, we should not overdo comparisons with the π-flux phase approach to the 2DQHAFSL since it − although it does have qualitative similarities to the data presented in this and the previous chapters − appears to have trouble predicting the quantitative details. Further developments of the theory are thus desirable. In particular, detailed calculations of $S^{zz}(\mathbf{Q}_{2D}, \omega)$ would be useful in clarifying to what extent the π-flux phase model agrees with our experimental data over the full range of energies investigated. Ho and coworkers also do not give the relative weights of the spin wave and continuous parts of the transverse excitation spectrum, which would have allowed a direct comparison with QMC and with our data. Still, the qualitative similarities to the experimental single-magnon spectrum of CFTD make the π-flux phase description of the Heisenberg Hamiltonian an interesting alternative to the more traditional approaches.

5.4 Conclusion

In this and the previous two chapters we have made an effort to study and understand the spin excitation spectrum of $Cu(DCOO)_2{\cdot}4D_2O$. In chapter 3 we showed that CFTD is a good manifestation of the two-dimensional quantum ($S = 1/2$) Heisenberg antiferromagnet on a square lattice. This realization allows us to interpret the results of our neutron scattering studies of CFTD in terms of theories designed to shed light of this important problem in theoretical physics. Chapter 3 further described experiments in which the spin excitation spectrum was studied in three materials thought to be good realizations of the 2DQHAFSL. In two of these, CFTD and $Sr_2Cu_3O_4Cl_2$ it was discovered that in sharp contrast with the predictions of linear spin wave theory − arguably the simplest theoretical model with which we can attempt to fit the experimental data − for the nearest neighbor Heisenberg model, the single-magnon energies along the magnetic zone boundary were not all identical. Rather, the single-magnon energy goes through a minimum at $(\pi, 0)$ and reaches a maximum at $(\pi/2, \pi/2)$, thus giving rise to a zone boundary dispersion. Not so in La_2CuO_4 − the third system discussed and the prototypical high-T_c parent compound. Although

this material also displays a zone boundary dispersion, in this case the sign is different: The spin wave energy in La_2CuO_4 is higher at $(\pi, 0)$ than at $(\pi/2, \pi/2)$. This behaviour can be understood by conceding that in addition to the main nearest neighbor interaction there is an important additional term in the spin Hamiltonian of La_2CuO_4. By constrast, the observations in CFTD and $Sr_2Cu_3O_4Cl_2$ are in excellent agreement with sophisticated theories and numerical techniques for the pure Heisenberg model. Thus, there is no need to include additional couplings amongst the spins in CFTD or $Sr_2Cu_3O_4Cl_2$. Since these two materials are understood to be ideal physical realizations of the 2DQHAFSL, it was concluded that the zone boundary dispersion they display is an integral property of the $S = 1/2$, square lattice Heisenberg model. Yet, in CFTD, the existing data on the spin excitation spectra left something to be desired. The purpose of the experiments reported in chapters 4 and 5 was to extend the borders of our knowledge about the spin fluctuations in CFTD, and by doing so breaking new ground in the ongoing research on the 2DQHAFSL.

The central results of the time-of-flight experiment which is the subject of chapter 4 are summarized in figures 16 and 19 and substantially extend our knowledge about the 2DQHAFSL. They do so by plotting not only the dispersion of the lowest energy spin excitations, but also the associated spectral weights versus $\mathbf{Q}_{2D}$. Moreover, the experimental conditions allowed these properties to be probed along the zone boundary, something which had not been done in previous experiments on CFTD. Figure 16 confirms the the existence of a zone boundary dispersion of magnitude $7 \pm 1\%$ along the zone boundary. The high energy part of the observed single-magnon dispersion, including the zone boundary, is in excellent accord with the dispersion derived from a series expansion approach to the Heisenberg model. Assuming the value $Z_c = 1.18$, we found $J = 6.16$ meV for the nearest neighbor exchange integral. Along the [11] direction of reciprocal space exclusively, we could fit the data using the dispersion relation derived from linear spin wave theory with only nearest neighbor interactions included. Again assuming $Z_c = 1.18$, this fit lead to $J = 6.18 \pm 0.02$ meV, a value slightly smaller than has previously been reported. The main discovery of chapter 4 is contained in Fig. 19 which shows the spectral weights of the spin fluctuations. Here it is seen, that the zone boundary dispersion between $(\pi/2, \pi/2)$ and $(\pi, 0)$ is accompanied by a large reduction in the spectral weight of the magnons propagating with wavevector $(\pi, 0)$. Quantitatively, we found a spectral weight ratio of 0.46 ± 0.12 between magnons at $(\pi, 0)$ and $(\pi/2, \pi/2)$, but this results does not include a 5-10% error in our intensity analysis.

Linear spin wave theory cannot account for both the zone boundary dispersion and the intensity drop at $(\pi, 0)$ even when next nearest neighbor interaction terms are added to the spin Hamiltonian. However, series expansion techniques, Quantum Monte Carlo and an approach known as the π-flux phase ansatz do have features resembling the observations. Based solely on the result of chapter 4 none of the above appear capable of explaining all the results in quantitative detail. Having established the existence of anomalies − relative to linear spin wave theory − in both the dispersion and spectral weight of single-magnon excitations at $(\pi, 0)$, a natural question was whether higher-energy multimagnon excitations could be identified, and if so, whether they would also display anomalous behaviour.

To study such excitations most efficiently, we employed polarized neutron scattering to separate the transversely and longitudinally polarized magnetic excitations from each other and from scattering of nuclear origin. These experiments are the subject of chapter 5 and the main results are reported in figure 13 and 31. The former deals with properties of the transverse and longitudinal excitation spectra at energies extending to $\hbar\omega \sim J$. Figure 13 shows for the first time that the 2DQHAFSL displays a well-defined and intense spectrum of longitudinally polarized spin excitations at energies above the main single-magnon branch. To model the experimental transverse and longitudinal excitation spectra we used linear spin wave theory within which they hold information about one-magnon and two-magnon processes respectively. Convoluting the linear spin wave theory cross-section with the experimental resolution fuction we found that for energies $\hbar\omega \sim J$ both transverse and longitudinal excitation spectra are excellently accounted for with only a single scale factor for the intensities. Only at the lowest energies probed did the linear spin wave model fail, since here we observed an apparent gap in the longitudinal excitations near (π, π). We speculated that this could be a telltale sign of deviations of the ground state of the 2DQHAFSL away from the Néel state, but less dramatic explantions should clearly also be considered.

The excitation spectra at zone boundary energies and above were studied at the two high-symmetry position $(\pi, 0)$ and $(\pi/2, \pi/2)$ on the magnetic zone boundary. The results are presented in Fig. 31. They are reasonably well accounted for by linear spin wave theory except for the anomalies in single-magnon energies and spectral weight at $(\pi, 0)$. Even better agreement is

obtained by comparing with the transverse and longitudinal excitation spectra of the 2DQHAFSL calculated using Quantum Monte Carlo algorithms. These numerical results appear to capture the high-energy excitation spectrum essentially perfectly, including the anomalies seen at $(\pi, 0)$. Importantly, we argued that the intensity ratios between zone boundary single-magnon excitations seen in the time-of-flight and polarized triple axis experiments were mutually consistent with each other and with QMC.

The impressive agreement between our observations and QMC prompted us to make the bold suggestion that a lineshape broadening observed at $(\pi, 0)$ in two separate polarized experiments could plausibly be caused − at least in part − by finite transverse continuum scattering. There are several independent supporting pieces of theoretical evidence suggesting that magnon-magnon interactions have their most dramatic effect at $(\pi, 0)$, but other factors could well contribute to the broadening at $(\pi, 0)$. It should also be mentioned, that in addition to the lineshape broadening, we have observed that the transverse response at energies beyond 16 meV is above zero at both $(\pi, 0)$ and (π, π). This surplus intensity could also be taken as evidence for the presence of a transverse continuum, but in itself is insufficient for firm conclusions to be drawn. Summing up, the identification of a continuum of transversely polarized spin excitations is much less certain than that of the continuum of longitudinally polarized excitions which seem unambiguous at all energies above $J/2 \simeq 3$ meV. Since transverse continuum scattering cannot be separated from one-magnon scattering using polarization analysis, progress in attempts to identify it must be based on identifying its detailed structure as a function of $\mathbf{Q}_{2\mathrm{D}}$ and $\hbar\omega$. For this, we need high-precision QMC computations at more wavevectors than are currently available.

An important immediate consequence of our identification of a strong longitudinally polarized multimagnon spectrum in the 2DQHAFSL is that it should be included explicitly in attempts to understand the anomalous Raman scattering and optical absorption lineshapes which were discussed in chapter 3. Broadly speaking, the main themes in the attempts to understand these experiments are multimagnon excitations and cyclic-exchange interactions on the square plaquettes, whereas linear spin wave theory always failed to provide the broad lineshapes observed. These were experiments performed on high-T_c parent compounds, in one of which it has been learned through neutron scattering that ring-exchange couplings are indeed present, but for which excitation continua have yet to be confirmed. Despite the possibility that additional exchange couplings are present in all cuprates and that therefore they cannot − as has traditionally been the case − be viewed as bona fide examples of the 2DQHAFSL, it appears plausible, by continuity, that the longitudinally polarized excitations we have identified in CFTD, where no cyclic exchange is present, should also be present, in some form, in these materials. If this conjecture is accepted, it becomes obvious that Raman scattering and optical absorption experiments on CFTD would be an important intermediate step in clarifying the effects of multimagnons and zone boundary anomalies on optical spectroscopy in the high-T_c materials. In linear spin wave theory, there is a singularity in the one-magnon density of states at the zone boundary and this dominates the two-magnon Raman spectrum. It is reasonable to assume that when the density of states does not have a singularity at the zone boundary energy, or when the singularity is rounded, as would be the case in CFTD, LSCO and $Sr_2Cu_3O_4Cl_2$ on account of the zone boundary dispersions, the Raman spectrum will look broader. In addition to this effect, higher-energy excitation continua would act to further broaden the optical spectra. The neutron scattering results for CFTD presented in the preceding chapters could be used at input in detailed theoretical calculations of the expected lineshapes in optical spectroscopies.

Summing up, we have learned that linear spin wave theory provides accurate predictions of the low-energy transverse and longitudinal spin excitations. However, it fails at higher energies where we see a zone boundary dispersion and a dramatic reduction in the single-magnon spectral weight at $(\pi, 0)$. Quantum Monte Carlo is in impressive agreement with the observed high-energy longitudinal and transverse response, but does not provide direct insight on the nature of the ground state. To shed some light on the latter, we have taken note of qualitative similarities between our data and the predictions of the π-flux phase description of the Heisenberg model. Here, the magnons of linear spin wave theory are viewed as bound $s = 1/2$ spinon pairs while the transverse continuum − if it were to be unambiguously detected − would correspond to unbound spinon pairs. This would be a highly interesting anology with one-dimensional antiferromagnets in which spinons are well established [89], and could even have potential implication for the high-T_c superconductors for which spinons have been conjectured to play a role [16, 90]. A second hint on the nature of the ground state correlations is provided by the twin figures 7 and 10 which are

however meant as little more than cartoon images of how to think of the origin of zone boundary dispersions in the infinite-U and finite U limits of the Hubbard model Eq. (42) respectively. They are based on the simple idea that although the Néel state is not the quantum mechanical ground state of the 2DQAHFSL, it cannot be a bad starting point for the variational calculus indicated (by mixing other states with the Néel state) since linear spin wave theory − which explicitly assumes the Néel state as the ground state − has been quite succesful in predicting the physical properties of real materials thought to be described by the 2DQHAFSL model. The dispersion and spectral weight computed using series expansion techniques [34] also have qualitative and − in the case of the dispersion − quantitative similarities with our experimental results. Figure 7 can be seen as an illustration of the microscopic physics underlying these series expansions [35]. If we now recall that both QMC and exact diagonalization studies of the Heisenberg model needed finite lattice sizes to produce a zone boundary dispersion [56], perhaps it is fair to speculate that local pictures such as Figs. 7 and 10 can provide some qualitative insight into the nature of the respective ground states.

6 High-T_c superconductivity

The subject of high-temperature superconductivity was born in 1986 when Bednorz and Müller discovered superconductivity below a critical temperature T_c of about 30 K in the compound $La_{2-x}Ba_xCuO_4$ [91]. At that time, the highest known transition temperature superconductor was Nb_3Ge with $T_c = 23.2$ K, and the accepted BCS theory of superconductivity predicted that transition temperatures above roughly 30 K were impossible, so the discovery of a 30 K superconductor came as a surprise.

In quick succession following the initial report by Bednorz and Müller, a number of groups reported superconductivity at higher and higher temperatures in a number of materials, all of which shared the common structural characteristic of having two-dimensional CuO_2-planes as basic building blocks. In 1987, the technologically important liquid nitrogen barrier at 77 K was broken with the discovery of the $YBa_2Cu_3O_{6+y}$ (YBCO) family of superconductors, some of which had critical temperatures around 90 K. Today, the list of these so-called high-T_c cuprate superconductors is extremely long, but the steep increase in the maximum T_c has come to a dead halt: The highest critical temperature at ambient pressure is 138 K and was observed in 1995 in $Hg_{0.8}Tl_{0.2}Ba_2Ca_2Cu_3O_{8.33}$. The compound $HgBa_2Ca_2Cu_3O_8$, discovered in 1993, has $T_c = 134$ K at ambient pressure. A year later it was reported to hold a record T_c of 164 K under 30 GPa applied pressure. While the original reports of a 30 K superconductor were marginally within the reach of BCS theory, transitions temperatures elevated to the level of 100 K are most certainly not.

In parallel with the dedicated materials efforts leading to the discoveries of these materials, a large number of experimental and theoretical physicists around the world have studied the physical properties of the high-temperature superconductors intensely in order to address the key question: Which physical processes cause superconductivity to develop in the high-temperature superconductors? This problem is still unsolved. When or if it is solved, the individuals laying the foundation for the solution will certainly be honored with the Nobel prize in physics as did Bednorz and Müller in 1987. Almost 20 years following the discovery of high-temperature superconductivity, the field is still a very active area of research, with a great many people producing and attempting to bring together the pieces of the jigsaw puzzle. The number of pieces is enormous and still growing, making it difficult − at best − to give a fair account of what progress has been made.

In chapter 7, we shall describe neutron scattering experiments performed to study the spin excitation spectrum of two members of the $La_{2-x}Sr_xCuO_4$ family of superconductors. In order to better understand the significance of the findings of these experiments, this introductory chapter is designed to give a reasonably short, coherent presentation of what seems at the time of writing to be some of the main pieces in the puzzle. For completeness and in order to facilitate an understanding of how high-T_c superconductors are different from the BCS superconductivity observed in the elements, it is natural to start by a brief review of the history and major breakthroughs in superconductivity as the subject was understood prior to 1986. This is done in section 6.1.

Having discussed the basic phenomenology of the superconducting state, section 6.2 is dedicated to a description of the physics observed in the high-T_c superconductors. Particular emphasis will be put on discussing how the latter are different from conventional BCS superconductors. This will naturally bring to the forefront a part of the common phase diagram of these materials commonly referred to as the pseudogap phase. Another theme in section 6.2 is the existence of magnetically ordered phases in the cuprate phase diagram. Given that neutron scattering − through Fouriers theorem − can be employed to study both the temporal and spatial dependences of magnetism, it is only natural that neutron scattering has emerged as one of the most influential experimental techniques used in the study of the cuprates.

Section 6.3 is devoted to a presentation of what is already known about the spin fluctuation spectra of high-temperature superconductors. While this is still an extensive body of work, it is limited in volume by the fact that detailed spectroscopic information requires large single crystalline samples. Unfortunately, nature has been cruel enough only to allow the growth of suitably sized samples of a few superconducting cuprate families, notably $La_{2-x}Sr_xCuO_4$ (LSCO) and $YBa_2Cu_3O_{6+y}$. Observations of spin fluctuations in other cuprates are rather more scarce, but they do exist. The main point in section 6.3 is that in recent years, evidence has appeared which points to important similarities between the excitation spectra in LSCO, YBCO and other materials. To interpret these similaries, we must discuss the theoretical models that have been developed to calculate the excitation spectra of high-temperature superconductors. For presentational pur-

poses, this is done partly in section 6.3 and partly in section 6.4. The latter section shows how theoretical attempts to model the observed spin fluctuation spectra in the cuprates can be broadly divided into two classes. One class of models believe in the reality of a real-space texturing of the charge carriers in the CuO_2 planes into patterns known as stripes, ladders, checkerboards etc. The second class is more conventional and is based on evaluating the susceptibility of Fermi liquids with well defined quasiparticles. Finally, section 6.5 concludes the chapter with a summary and an outline of the most important questions to be investigated in chapter 7.

6.1 Superconductivity

In this section, we describe some of the key characteristics of the superconductivity seen in the elements and more generally in the vast majortity of superconductors known prior to 1986. We also outline the underlying theoretical framework which succesfully describes these materials. Our exposition is based on reference [92].

Superconductivity was discovered in 1911 by Kamerlingh-Onnes in a study of the electrical resistance of mercury. It is a state characterized by zero electrical resistivity for sufficiently small dc currents below a transition temperature T_c. A second defining property of superconductors is their ability to completely expel magnetic flux from their bulk in sufficiently small external magnetic fields (the Meissner or Meissner-Ochsenfeld effect). Only metallic elements become superconducting at low temperatures, but materials that are good metals at room temperature typically have a low T_c if indeed they become superconducting at all. Magnetic metals do not become superconducting.

Following early and rather successful phenomenological theories, a vital clue to understanding the microscopic origin of superconductivity in the elements came with the discovery of the isotope effect, which shows that T_c in a given element depends on the weight of the nucleus. This meant that lattice degrees of freedom must play an essential role in establishing superconductivity. Following this, Bardeen, Cooper and Schrieffer managed to develop the microscopic theory which now bears their names (the BCS theory of superconductivity). In essence this theory says, that the metallic state has an instability towards superconductivity if some physical process gives rise to an attractive interaction between electrons. If such an attractive interaction exists, it is possible for a pair of electrons to overcome their mutual Coulomb repulsion and instead become attractively coupled. The attractive interaction leads to the formation of an entity known as a Cooper pair, which is a boson with charge $-2e$ and mass $2m_e$. The center of mass momentum of a Cooper pair is zero, i.e. the crystal momenta of the constituent electrons are the opposites $\hbar\mathbf{k}$ and $-\hbar\mathbf{k}$. The spatial wavefunction has s-wave symmetry and the spin part of the wavefunction is a singlet $(|\uparrow\downarrow\rangle - |\downarrow\uparrow\rangle)/\sqrt{2}$.

In the elements, the mechanism behind the establishment of an overall attractive electron-electron interaction is the virtual exchange of phonons, i.e. lattice vibrations (This is why good conductors typically do not become superconducting at low temperatures: The electron-phonon coupling parameter g in such systems is too small for the phonon-mediated attractive electron-electron interactions to outcomptete the repulsive Coulomb interaction. Yet, it is also the smallness of g that allow them to be good conductors, because electrons are then scattered weakly be lattice vibrations). Only electrons with energies in a narrow band surrounding the Fermi energy ϵ_F partake in the formation of Cooper pairs. The energy width of this band is set by the Debye frequency $\hbar\omega_D \ll \epsilon_F$. A simple variational calculation, in which electrons with opposite crystal momenta and spins and with energies within $\hbar\omega$ of the Fermi energy are coupled by an attractive interaction V, shows that Cooper pairing leads to a lowering of the total energy from that of the metallic ground state. It does so by smearing the Fermi-surface in the following sense: Let $v_{\mathbf{k}}$ be the (variational) amplitude for the two-electron state in which both $(\mathbf{k},\uparrow)$ and $(-\mathbf{k},\downarrow)$ are occupied and let $u_{\mathbf{k}}$ be the amplitude for the state in which none of these one-electron states are occupied. The metallic ground state is the defined by $v_{\mathbf{k}} = 1$ and $u_{\mathbf{k}} = 0$ for $|\mathbf{k}| \leq k_F$ and $v_{\mathbf{k}} = 0$ and $u_{\mathbf{k}} = 1$ for $|\mathbf{k}| \geq k_F$. In the variational ground state for superconductivity, $u_{\mathbf{k}}$ and $v_{\mathbf{k}}$ are continuous functions of $|\mathbf{k}|$ around k_F and so in particular $v_{\mathbf{k}}$ has non-zero values for $|\mathbf{k}| \geq k_F$. and $u_{\mathbf{k}}$ has non-zero values for $|\mathbf{k}| \leq k_F$. The extra kinetic energy of this configuration compared to the metallic Fermi liquid ground state is compensated by the gain in potential energy arising from phonon exchange. BCS-superconductivity can therefore be said to be potential energy driven.

The elementary excitations from the BCS ground state are fermions. In the parlor of the metallic state out of which superconductivity develops, an excitation of momentum $\mathbf{k}$ is like a normal state particle if $|\mathbf{k}| \gg k_F$ and like a hole if $|\mathbf{k}| \ll k_F$. For $|\mathbf{k}| \simeq k_F$ however, an excitation

is part hole, part particle because of the smearing of the amplitudes $u_{\mathbf{k}}$ and $v_{\mathbf{k}}$. The excitation spectrum is given by

$$E_{\mathbf{k}} = \sqrt{\epsilon_{\mathbf{k}}^2 + \Delta_{\mathbf{k}}^2} \tag{66}$$

where $\epsilon_{\mathbf{k}}$ is the normal state electronic dispersion, and the quantity $\Delta_{\mathbf{k}}$ is the so-called superconducting energy gap which is zero in the normal state and rises continuously with decreasing temperature below T_c to a maximum value $\Delta = 1.76\, k_B T_c$ at $T = 0$ K. $\Delta_{\mathbf{k}}$ has the significance of being the energy required to split up a Cooper pair with momentum $\hbar\mathbf{k}$. As such it is a measure of the stability of the superconducting ground state. The opening of a gap on the Fermi surface protects the symmetry-broken superconducting state. For s-wave superconductors, $\Delta_{\mathbf{k}}$ is independent of $\mathbf{k}$, but this is not a necessary condition in the theoretical BCS framework. It is also not a necessary condition that the attractive part of the electron-electron interaction is mediated by phonon-exchange. In particular, other bosons, e.g. magnons, could in principle do just as well. Experimentally, an elegant way to determine Δ is by quasiparticle tunneling experiments.

The behavior of superconductors in external fields lead to an important distinction between so-called type I and type II superconductors. The experimental characteristics of these two types of superconductors are as follows: For both types, below a lower critical field H_{c1} the field $\mathbf{B}$ in the bulk of the superconductor is identically zero. In other words, the external field $\mathbf{H}$ is completely compensated by a magnetization $\mathbf{M}$ in the opposite direction. This is the Meissner effect. For type I materials, H_{c1} also marks the field at which superconductivity ceases to exist. By contrast, superconductivity continues to exist in type II materials up to an upper critical field H_{c2} (which can be much larger than H_{c1}) at which it finally breaks down. In the range $H_{c1} \leq H \leq H_{c2}$, magnetic flux penetrates the sample in the form of vortices, each of which carry a quantum Φ_0 of flux (see Eq. (70) below). As H increases, the vortex density grows and superconductivity becomes unfavored at H_{c2} when the spatial extent of the vortices overlap significantly. To appreciate the origin of this phenomenology, we need to take a brief look at the London theory of superconductivity.

London made the bold step of proposing the existence of a macroscopic wavefunction $\psi(\mathbf{r}, t) = \psi_0(\mathbf{r}, t) \exp(iS(\mathbf{r}, t))$ describing the Cooper pairs in the superconducting state. Based on a Schrödinger equation fulfilled by ψ, one can derive an expression for the electric supercurrent density, i.e. the current density of Cooper pairs

$$\mathbf{J}_e = \frac{e\hbar}{m_e} \mid\psi\mid^2 \nabla S - \frac{2e^2}{m_e} \mid\psi\mid^2 \mathbf{A} \tag{67}$$

in terms of the gradient of the phase function $S(\mathbf{r}, t)$ and the vector potential $\mathbf{A}$ in terms of which the magnetic field is $\mathbf{B} = \nabla \times \mathbf{A}$. The quantity $\mid\psi\mid^2 = n_C$ is the density of Cooper pairs, which in turn is half of n_s, the density of superconducting electrons.

There is a fundamental issue to consider in connection with the London equation (67). It has to do with the requirement that $S(\mathbf{r}, t)$ should always be single valued in a simply connected specimen, i.e. in a sample which does not have holes (e.g. a vortex or a physical hole) in it. For multiply connected geometries on the other hand, S need not be single valued, and may change by any multiple of 2π around a contour encircling a hole. Focusing on a simply connected specimen, the terms containing ∇S in Eq. (67) can be eliminated by a gauge transformation which leaves observables such as $\mathbf{B}$ and $\mathbf{J}_e$ unaltered. The transformation introduces a new gauge transformed vector potential $\mathbf{A}_1$ and a new phase function S_1 through $\mathbf{A} = \mathbf{A}_1 + \nabla\chi$ and $S = S_1 + 2e\chi/\hbar$. Here χ is a scalar function which can be chosen at will since it does not affect $\mathbf{B}$ and $\mathbf{J}_e$. In particular, if we choose $\chi = \hbar S/2e$, Eq. (67) can be reduced to $\mathbf{J}_e = -(2e^2/m_e) \mid\psi\mid^2 \mathbf{A}_1$. The Meissner effect now drops out of the algebra as follows: First, we take the curl of the transformed London equation. This gives $\mathbf{B} + m_e/(2e^2 n_C) \nabla \times \mathbf{J}_e$. Eliminating $\mathbf{J}_e$ using the Maxwell equation $\nabla \times \mathbf{B} = \mu_0 \mathbf{J}_e$ and the mathematical identity $\nabla \times \nabla \times = -\nabla^2$ we finally get a differential equation for the variation of $\mathbf{B}$ inside our simply connected superconductor

$$\nabla^2 \mathbf{B} = \frac{\mathbf{B}}{\lambda_L^2} \tag{68}$$

$$\lambda_L = \sqrt{\frac{m_e}{2\mu_0 n_s e^2}} \tag{69}$$

A simple calculational example brings out the significance of the length scale λ_L that emerged from these manipulations. For a plane surface immersed in a parallel external field, the solution

to Eq. (68) is $\mathbf{B}(x) = \mathbf{B}_0 \exp(-x/\lambda_L)$, where $\mathbf{B}_0$ is the value of the field at the surface $x = 0$ of the superconductor and x is the distance from the surface. The solution shows that inside the superconductor, the field drops of exponentially with distance from the surface over the characteristic length scale λ_L, known therefore as the London penetration depth. Experimentally, λ_L is of order 100 Å, so for bulk samples magnetic flux is completely expelled below H_{c1} except for a small surface layer. In less mathematical terms, flux expulsion occurs because the superconductor responds to the external field by setting up a screening supercurrent $\mathbf{J}_e$ within λ_L of the surface. The field generated by these currents completely compensates the external field everywhere inside, except near the surface. In other words, the superconductor displays perfect diamagnetism. The penetration depth λ_L can be measured by e.g. small-angle neutron scattering or muon spin relaxation in the intermediate field regime $H_{c1} < H < H_{c2}$.

In the interest of completeness, it is timely at this point to admit that the London equation (67) relating the current density $\mathbf{J}_e$ to $\mathbf{A}$ evaluated at the same point $\mathbf{r}$ is only valid for sufficiently impure alloys. As suggested by Pippard, for cleaner materials on should employ a non-local relationship in which $\mathbf{J}_e$ is related to the values of $\mathbf{A}$ inside a region of extent ξ_P. The range ξ_P is then related to the mean free path l and a material dependent constant ξ_0 by $\xi_P^{-1} = \xi_0^{-1} + l^{-1}$, so that for a dirty material $\xi_P = l$ and the general non-local relation between $\mathbf{J}_e$ and $\mathbf{A}$ reduces to the London equation.

Let us now consider multiple-connected superconductors, and in particular the behavior around a vortex. It is easily shown that in order for $\psi(\mathbf{r}, t)$ to be single-valued, the circulation $\oint \mathbf{v}_s dl$ of the supercurrent velocity $\mathbf{v}_s = \mathbf{J}_e/(2e^2 \mid \psi \mid^2)$ around a closed contour encircling the vortex is equal to nh with h Planck's constant and n an integer. The value of n does not depend on the particular path around the vortex. Using the London equation one can then derive the magnetic flux Φ through the vortex:

$$\Phi = n\Phi_0 \qquad \text{with} \qquad \Phi_0 = \frac{h}{2e} \tag{70}$$

$\Phi_0 = 2.07 \times 10^{-15}$ V s is known as the flux quantum. Equation (70) shows that the flux through a single vortex is quantized. In fact, evaluating the energy associated with the superflow and field patterns around the vortex leads to the conclusion that for a given external field $\mathbf{H}$, $n = 1$ is thermodynamically favored over higher values of n and therefore $\Phi = \Phi_0$. Thus, the energy is always minimized by a distribution of vortices, each carrying a single flux quantum. Φ_0 can be determined experimentally by SQUID magnetometry. This fixes the charge − appearing in the denominator of Eq. (70) − of the objects from which the superconducting state is built, i.e. it proves the existence of charge $2e$ Cooper pairs. In deriving the superflow around the vortex one finds that it diverges on approaching the vortex center. Clearly this does not make sense. In reality, there is a core radius $\xi(T)$ − known as the coherence length − which cuts off the flow velocity at a critical value v_c at the distance $\xi(T)$ from the center. The value of v_c then depends only on $|\psi|^2$ and on the so-called Ginzburg-Landau parameter

$$\kappa = \frac{\lambda_L}{\xi} \tag{71}$$

i.e. on the ratio of the London penetration depth $\lambda_L(T)$ to the core radius $\xi(T)$. In the Ginzburg-Landau theory $\xi(T)$ is the characteristic length scale for changes in the density of Cooper pairs $|\psi|$ and has the same temperature dependence as the London penetration depth: Both diverge as T_c is approached from below, leaving κ as a material-dependent constant.

The theoretical framework predicts that $\mathbf{B}$ drops off continuously from a constant value at the vortex center to zero over a distance of λ_L, as before. The Cooper pair density $\mid \psi \mid$ rises continuously from zero at the vortex center to a constant value outside a core region of size $\sim \xi$, so that superconductivity is essentially suppressed within the core. Since the suppression occurs on account of the screening supercurrents, a natural, necessary condition for the existence of vortices would be $\lambda_L > \xi$. A full calculation of the surface energy of an interface between normal and superconducting regions leads to the exact criterion $\kappa > 1/\sqrt{2}$ for vortices to develop. Type II superconductors are therefore superconductors with $\kappa > 1/\sqrt{2}$ whereas Type I superconductors have $\kappa < 1/\sqrt{2}$. The physical interpretation of the type II phenomenology is then the following: For external fields $0 \leq H \leq H_{c1}$, we are in the Meissner state of complete flux expulsion. For fields above H_{c1}, flux penetrates in vortices, each of which carry precisely one flux quantum Φ_0. The number of vortices is then proportional to H. At H_{c1} a finite density of flux lines appears

and gives rise to a large reduction in the magnetization of the sample. On further increasing H and thereby the vortex density, vortex-vortex interactions become appreciable and cause the formation of ordered flux line lattices. The latter can be detected directly by small-angle neutron scattering. At H_{c2} superconductivity finally breaks down as the vortex cores begin to overlap. This argument shows that $\xi(T)$ must be intimately connected to H_{c2}. The relevant equation is $\mu_0 H_{c2} = \Phi_0/(2\pi\xi(T)^2)$. In the elements, ξ is typically larger than λ_L, although of the same order of magnitude. Thus, almost all superconducting elements belong to the type I class, niobium and vanadium being exceptions to the rule.

6.2 High T_c superconductors – an introduction

Having discussed the superconductivity in what we shall refer to as "conventional" superconductors, we move on to discuss the properties of the high-T_c superconductors. This is a major undertaking, but we shall attempt to keep the presentation short, while taking care not to oversimplify it to the point of where the enormous range of unusual phenomena these materials display is lost from sight. In writing this part of this chapter, we are relying mostly on a number of review articles [42, 65, 93, 94, 95, 96] – and references therein.

The natural place to start our discussion of high-T_c cuprates is to consider their crystal structures. The common structural elements in these materials are square (or approximately square) lattice CuO_2 layers. Different cuprates contain different numbers of adjacent CuO_2 layers, leading to a classification into single-layer, bilayer, trilayer (and so on) superconductors. The CuO_2 layers are separated from each other by layers of other material, which act as charge reservoirs when the systems are chemically doped. To exemplify, Fig. 33 displays the crystal structures of single-layer $La_{2-x}Sr_xCuO_4$ and bilayer $YBa_2Cu_3O_{6+y}$ – the latter in two variants differing in their oxygen content. In LSCO, the coordination of each Cu ion is completed by two apical oxygens residing inside the charge reservoirs. In YBCO on the other hand, each Cu ion residing inside a bilayer (i.e. the CuO_2 layers above and below the central Y atom) is coordinated to just one apical oxygen in addition to the four in-plane oxygen neighbors. In still other cuprates there are no out-of-plane oxygen nearest-neighbors at all [65]. The simple implication is that the essential electronic units of interest are the 2D CuO_2 planes. There is a general trend that T_c increases as one moves from single-layer materials to bilayer materials to trilayer materials etc., but since single-layer superconducting cuprates with very high values of T_c do exist in nature, the key ingredients in the mechanism for high-temperature superconductivity should be sought in the single-layer physics, with the charge reservoir chemistry acting as a tuning factor on properties such as the optimum T_c within a given cuprate family.

Both LSCO and YBCO have tetragonal as well as orthorhombic phases. At low doping levels LSCO has a high-temperature tetragonal phase (HTT. Space group I4/mmm) and a structural phase transition to a low temperature orthorhombic phase (LTO. Space group Cmca) at a temperature which decreases with increasing x from 530 K at $x = 0$ [97] to 0 K near $x = 0.21$ [98]. The structural transition is caused by tilting of the CuO_6 octahedron in the center of the tetragonal unit cell shown in Fig. 33(a) around one of the two tetragonal [110] axes. YBCO with $y = 0$ is tetragonal but upon oxygenation becomes orthorhombic as the distribution of the excess oxygens starts to form Cu-O chains running along **b**. It is however only the CuO_2 layers which are interesting from the viewpoint of superconductivity, since chain layers are not present in all superconducting cuprates.

Moving from structural to electronic properties, it probably not an exaggeration to say that since they were discovered, the cuprate superconductors have been studied using all spectroscopic tools known to modern solid state physics, and that each of these techniques have yielded results which are at odds with what one observes in materials described successfully by BCS theory. This does not mean that the superconductivity observed in the cuprates is completely different from the superconductivity of a well-behaved BCS superconductor. In fact, the phenomenology of the superconducting states have many similarities, the most important of course being the sharing of the two defining characteristics of superconductivity – zero resistance and the Meissner effect. The perfect diamagnetism revealed by the Meissner effect is present only at the lowest external fields. For higher fields, superconductivity does not break down, i.e. type II behavior is found. In fact, the Ginzburg-Landau parameter $\kappa \gg 1/\sqrt{2}$, because the superconducting coherence length ξ is very small, of order 10 Å, in these materials. With London penetration depths of order $100 - 1000$ Å we find $\kappa \sim 10 - 100$. Because ξ is so small, huge critical fields H_{c2} are required to achieve

the overlapping vortex cores needed to finally destroy superconductivity. As a function of doping, the maximum H_{c2}-values for LSCO and YBCO are $H_{c2} \simeq 62$ T and $H_{c2} \simeq 110$ T respectively for magnetic fields applied perpendicular to the CuO_2 planes.

Turning to microscopics, Bitter decoration studies of YBCO have revealed a flux lattice of hexagonal symmetry at low fields and, more importantly, that each vortex carries a single unit of the flux quantum $\Phi_0 = h/2e$, rather than e.g. $\Phi_0/2$ [100]. Thus, the fundamental particles responsible for the vortex formation have a charge consistent with Cooper pairs of electrons or holes as in conventional superconductors. More precise determinations of the quanta of flux in these materials come from SQUID measurements and give the same answer. The temperature dependence of the Knight shift below T_c revealed that the spin part of the Cooper pair wave function is a singlet [101] – once again conventional behavior. The remaining question relates to the symmetry of the orbital part of the wavefunction, and here something different happens: The spatial wavefunction has $l = 2$, i.e. it has d-wave symmetry rather than the conventional s-wave symmetry. More precisely, evidence for a $d_{x^2-y^2}$ pairing state comes from various phase sensitive measurements, and from direct determination of the $\mathbf{k}$ dependence of the superconducting gap function $\Delta_{\mathbf{k}}$ by angle resolved photoemission spectroscopy (ARPES). Details on the orbital symmetry can be found in e.g. [65, 102, 103, 104]. Although d-wave pairing is unusual, it is not at odds with anything in the BCS theory, and in particular is not evidence against a phononic pairing mechanism. Figure 34 schematically shows the Fermi surface (blue lines) and $d_{x^2-y^2}$ gap (red lines) of the superconducting cuprates as determined by ARPES. Because the filled states with $\epsilon_{\mathbf{k}} < 0$ in Eq. (66) are located in the regions surrounding the four (π, π) points, there exist states (nodal quasiparticles) along the [11] and $[1\overline{1}]$ directions which have $E_{\mathbf{k}} = 0$ even deep inside the superconducting state where the gap $\Delta_{\mathbf{k}} = \Delta_0(\cos \mathbf{k}_x - \cos \mathbf{k}_y)/2$ is fully developed (As will be mentioned below, the gap does not always have this exact mathematical form, but always changes sign on the line $\mathbf{k}_x = \mathbf{k}_y$).

We have now seen that apart from the d-wave symmetry of the spatial part of the superconducting wavefunction, there is little qualitative difference between the superconducting states of the high-T_c cuprates and conventional superconductors. There are however dramatic differences between the normal states from which superconductivity develop, and differences in the response to impurities. In BCS superconductors, even a small concentration of magnetic impurities cause superconductivity to vanish. The effect of nonmagnetic impurities is much less severe. By contrast, in the cuprates magnetic impurities have little effect on superconductivity, whereas tiny amounts of nonmagnetic impurities such as zinc cause T_c to drop to zero. This appears to be a telltale

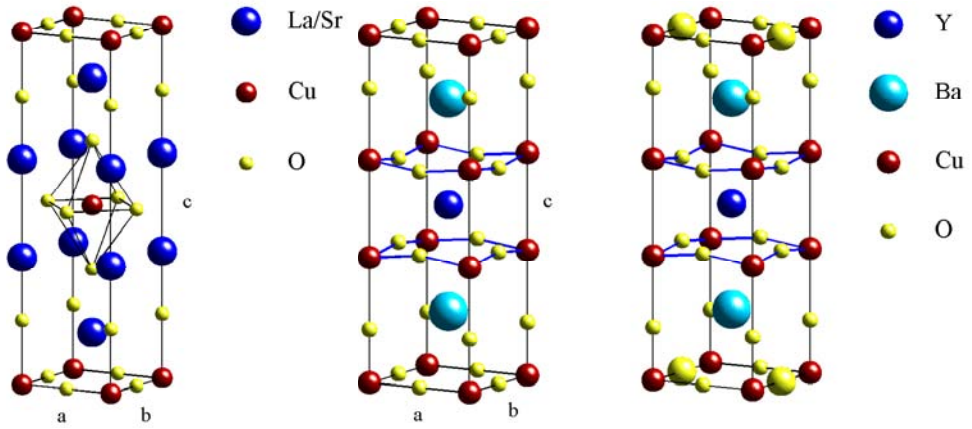

Figure 33: Unit cells of $La_{2-x}Sr_xCuO_4$ (left) and $YBa_2Cu_3O_{6+y}$ (center and right). LSCO: The CuO_6 octahedron involved in the tetragonal to orthorhombic structural phase transition is at the center of the cell. In the transition to the orthorhombic phase, these octahedra rotate around a tetragonal [110] direction, see e.g. [97]. There are two formula units and two CuO_2 layers per unit cell, and therefore one CuO_2 layer per formula unit. YBCO: The centermost structure is the tetragonal phase of YBCO seen for low oxygen contents. Upon oxygenation there is a transition to an orthorhombic phase (right). In the latter phase, Cu-O chain structures develop along the crystallographic $\mathbf{b}$ direction as indicated by the larger sized oxygen atoms. At full oxygenation $y = 1$, the Cu-O chains are filled and disorder stemming from finite chain segments is suppressed [99]. The buckled Cu_2O_4 bilayer is indicated by thick blue lines. There is one formula unit per unit cell, and each cell contains one bilayer unit and one chain-layer unit. The chain layers are irrelevant to the development of high-temperature superconductivity. Thus, for comparisons with other cuprates, YBCO contains two CuO_2 layers per formula unit and per unit cell.

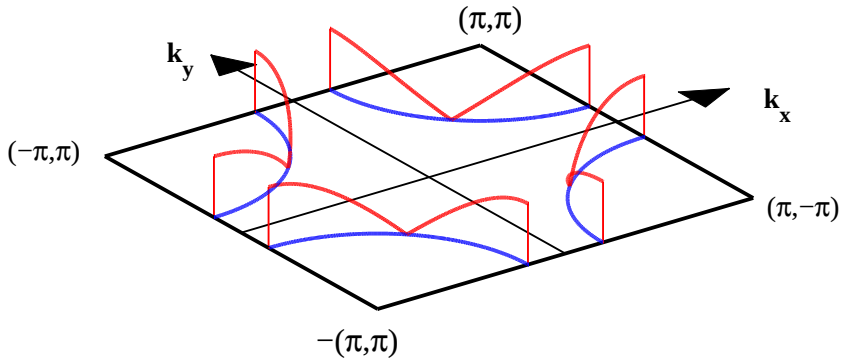

Figure 34: Generic Fermi surface and superconducting gap for superconducting cuprates. The blue lines indicate the Fermi surface measured in the normal state. The $d_{x^2-y^2}$ symmetry of the gap function $\Delta_{\mathbf{k}} = \Delta_0(\cos \mathbf{k}_x - \cos \mathbf{k}_y)/2$ implies that with hole pockets centered on the four (π, π) points, there are gap nodes along the [11] and $[1\overline{1}]$ directions. Red lines show the absolute values $|\Delta_{\mathbf{k}}|$ of the superconducting gap, which is at a maximum near the antinodal $(\pi, 0)$ points.

sign that something very different is going on in the cuprates, and suggests that magnetism may play a role for superconductivity. In order to discuss the peculiar normal state properties of the high-T_c superconductors it is useful first to present what is called the generic phase diagram [105] of these materials. This is shown in Fig. 35. The quantity p on the horizontal axis is the concentration of doped carriers per Cu in the CuO_2 planes. What is thought to be "generic" about the phase diagram is really just the four phases (or regions) it contains: An antiferromagnetic phase (AF), a superconducting phase (SC), a Fermi liquid phase and a pseudogap phase. Genericness is also expected for the characteristic scales on the doping axis, but only for so-called hole-doped cuprates, which are the ones we will be considering. For electron-doped cuprates, the antiferromagnetic phase appears to be more robust and extends to higher values of p. There is little or no genericness about the temperature scale. The particular scales shown are the ones relevant for LSCO where the doping level p equals the strontium doping level x, as we shall discuss below.

Let us consider the electronic structure of La_2CuO_4. Free Cu has the electronic configuration $[Ar]3d^{10}4s^1$. Since La always donates three electrons, and oxygen requires two, it is necessary for each Cu atom to donate an additional two electrons in order to maintain overall charge neutrality. The configuration of the resulting Cu^{2+} ions in La_2CuO_4 must therefore be $3d^9$, and application of Hunds rules lead to $L = 2$, $S = 1/2$. Let us now consider doping La_2CuO_4 with strontium, leading to compounds with the chemical formula $La_{2-x}Sr_xCuO_4$. When a La^{3+} ion is replaced by a Sr^{2+} ion, the Cu ions in the CuO_2 plane must donate an additional electron to the insulating spacer layer. Because our focus is on the physics of the CuO_2 layers, it is most natural to view the Sr doping process as one of hole-doping the CuO_2 planes. What is important for our purposes is that per Sr replacing a La, one hole is added per copper, i.e. $p = x$. In other cuprates, such as YBCO, the relationship between the hole (or electron) doping level p and the concentration of chemically substituted elements or oxygenation level can be more complex.

Let us now return to the phase diagram in Fig. 35 for a quick overview. First, it contains an antiferromagnetic phase with commensurate magnetic Bragg reflections at $\mathbf{Q}_{2D} = (\pi, \pi)$. For hole-doped cuprates such as LSCO and YBCO this phase occupies only a tiny sliver of the phase diagram extending to $p \simeq 0.02$. Upon introducing more holes into the CuO_2 planes, superconductivity sets in at $p \simeq 0.055$. The superconducting transition temperature then rises with increasing p, reaches a maximum at $p_{\text{optimal}} \simeq 0.16$ and gradually drops to zero near $p \simeq 0.29$. It is common practice to refer to samples with hole-doping levels $p \simeq p_{\text{optimal}}$ as optimally doped, and to samples with $p < p_{\text{optimal}}$ and $p > p_{\text{optimal}}$ as underdoped and overdoped respectively. The remaining regions of the phase diagram are a Fermi liquid phase on the overdoped side and a pseudogap phase on the underdoped side below a temperature scale T^*. The generic phase diagram exists in many guises. For example, one sometimes encounters the name "strange metal" for the state at temperatures above the T^*-line in the underdoped and optimally doped regions. For some cuprate families there are additional features not present in our version of the phase diagram. Particularities of the LSCO family of superconductors will be mentioned in section 6.3.

In chapter 3 we mentioned that the parent compound La_2CuO_4 is an antiferromagnet. The

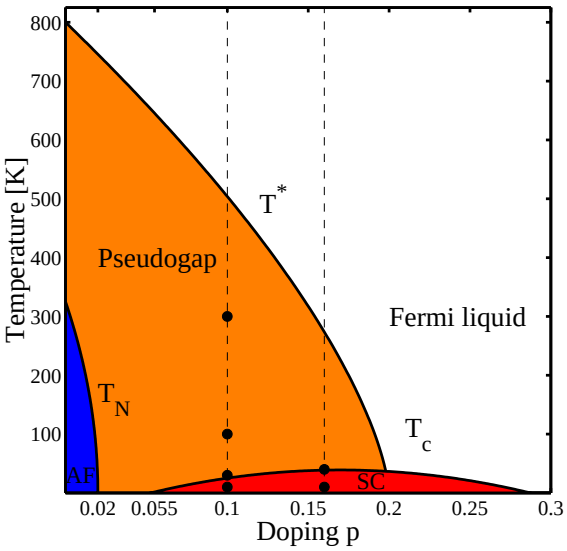

Figure 35: Generic cuprate phase diagram, here exemplified by $La_{2-x}Sr_xCuO_4$ in which the hole doping level p equals x. AF denotes the antiferromagnetic Mott-Hubbard phase and SC denotes the superconducting state. Not shown in this schematic phase diagram is a depression of T_c in the vicinity of $x = 1/8$ and the so-called spin glass region at low temperatures between the antiferromagnetic and superconducting phases. Both these features are seen experimentally in Sr and Ba-doped La_2CuO_4. The black dots mark the positions in the phase diagram at which we study the spin excitation spectrum $\chi''(\mathbf{Q}, \omega)$ in chapter 7.

same goes for the parent compounds of other cuprate families. The antiferromagnetic order doubles the unit cell and yields Bragg peaks at $\mathbf{Q}_{2D} = (\pi, \pi)$. Even though $T_N(x = 0) = 325 \pm 5$ K for La_2CuO_4 [44], the transition temperature drops very rapidly with hole-doping and commensurate antiferromagnetism has vanished already at $p \simeq 0.02$. This immediately sends a loud message that the mere existence of antiferromagnetism at the lowest doping levels owes itself to very special conditions, namely the physics of the Mott-Hubbard insulator. To appreciate this, we must take a brief look at the electronic energy level diagram [93]. We noted above, that the electronic configuration for Cu^{2+} is $3d^9$. Crystal field effects imply that in the solid, the five d-orbitals of copper are non-degenerate with the $3d_{x^2-y^2}$ orbital having the highest energy. Thus, the nine 3d electrons fill each of the $3d_{xz}$, $3d_{yz}$, $3d_{xy}$ and $3d_{z^2}$ orbitals with 2 electrons (one with spin "up" and one with spin "down"), leaving one electron for the $3d_{x^2-y^2}$ orbital, which is therefore half-filled. So far we have neglected interactions between different orbitals which lead to the formation of energy bands rather than discrete energy levels. In the cuprate superconductors, the energy of the oxygen 2p orbitals is nearly the same as that of the copper 3d orbitals. In this case, when bands are formed and electrons accommodated into them, one would expect a situation where the O 2p-derived band extends to an energy almost equal to that of the highest-energy occupied states in the Cu $3d_{x^2-y^2}$-derived band. However, even this expectation fails because it neglects interactions between electrons, something which one cannot do in these materials. Thus, the conventional wisdom encoded in band-theory would predict the cuprate parents to be metallic since the $3d_{x^2-y^2}$-band is half-filled. However, experimentally one finds them to be insulators. A natural platform from which to understand the insulating behavior is the one-band Hubbard model discussed already in chapter 3. For easy reference we shall write it down again

$$H_{\text{Hubbard}} = -t \sum_{\langle i,j \rangle, \sigma} (c^\dagger_{i\sigma} c_{j\sigma} + \text{H.c.}) + U \sum_i n_{i\uparrow} n_{i\downarrow} \tag{72}$$

The operators $c^\dagger_{i\sigma}$ and $c_{i\sigma}$ create and annihilate electrons with spin $\sigma \in \{\uparrow, \downarrow\}$ at site number i. The summation in the first term is over nearest neighbor sites of the square lattice. The operator $n_{i\sigma} = c^\dagger_{i\sigma} c_{i\sigma}$ counts the number of electrons in the spin state σ at site i. The first term in (72) describes the kinetic energy associated with process in which electrons jump between nearest neighbor sites while keeping their spin state. What causes the cuprate parent compounds to be electrically insulating is the prominence of the second term, which represents a large Coulomb energy penalty for two electrons with opposite spins occupying the same site. In the cuprate parents, the number of holes in the $3d_{x^2-y^2}$ band precisely equals the number of sites. When

U is large it is then clear that energy minimization is achieved by never allowing two electrons onto the same site. On the other hand, the spin degrees of freedom of the electrons are not restricted in the same manner. In particular virtual hopping between nearest neighbor sites is allowed by the Pauli principle when the electrons involved have antiparallel spins. As discussed in chapter 3, a second order perturbation expansion of Eq. (72) in the large-U and half-filling limits leads to antiferromagnetic Heisenberg interactions with an effective nearest neighbor interaction $J = 4t^2/U > 0$ between the $S = 1/2$ spins of the localized 3d electrons. This explains why the cuprate parent compounds are antiferromagnets. The insulating behavior is clearly related to the large on-site Coulomb repulsion which prevents two electrons from occupying the same site. In terms of the energy level diagram, U causes the half-filled $3d_{x^2-y^2}$ band to split into two bands (lower and upper Hubbard bands) located on either side of the chemical potential. With no unfilled states available immediately above the chemical potential, the undoped cuprate parents become (charge-transfer) insulators. The insulating gap is of order $U \simeq 2$ eV.

The above arguments hint that upon hole doping the insulating behavior will quickly give way to metallic conduction as it becomes possible for the electrons to jump to adjacent empty sites. In the process, the conditions required for antiferromagnetism will also be degraded. This argument is believed to explain why insulating behavior and commensurate antiferromagnetism vanish quickly with p in the hole-doped cuprates. Antiferromagnetism appears more robust in electron-doped cuprates, and this example suggests that the simple arguments presented above for Eq. (72) do not exhaust the range of physical behaviors the Hamiltonian (72) can induce. Indeed, one very influential approach to high-T_c superconductivity views the problem as intimately connected to the quantum phase transitions between a whole range of possible ordered phases in doped two-dimensional Mott-insulators [96]. One of these orders – the so-called stripe phase – will be discussed further in section 6.3.4.

The superconducting phase, as mentioned already, is essentially conventional except for the extreme scales of T_c, H_{c2} and ξ. The carriers of supercurrent are charge $2e$ Cooper pairs, the wavefunctions of which are singlets with respect to the spin, and have a spatial $d_{x^2-y^2}$ symmetry. The latter reflects itself in the superconducting gap function $\Delta_{\mathbf{k}}$ which can be measured with ARPES and is of the form $\Delta_{\mathbf{k}} = \Delta_0(\cos \mathbf{k}_x - \cos \mathbf{k}_y)/2$ (More precisely, this is only strictly true in overdoped and optimally doped cuprates. A component proportional to $(\cos 2\mathbf{k}_x - \cos 2\mathbf{k}_y)$ develops in the underdoped regime and coexists with the dominant $(\cos \mathbf{k}_x - \cos \mathbf{k}_y)$ term. The relative importance of this subdominant term increases with underdoping, leading to a decrease in the slope – along the Fermi surface – of the gap function $\Delta_{\mathbf{k}}$ at the nodal point in the electronic spectrum [65]). However, the doping dependence of the maximum gap Δ_0 is unusual. In BCS theory, the s-wave superconducting gap scales with T_c according to $\Delta = 1.76\, k_B T_c$ at $T = 0$ K. In the cuprates, Δ_0 decreases monotonically with increasing doping even in the underdoped regime where T_c is an increasing function of p. This is but one of many peculiar experimental observations in the abnormal normal state in the pseudogap region of the phase diagram, to which we now turn. It is a commonly held view that the key to understanding high-temperature superconductivity lies in sorting out what goes on in the pseudogap phase [65]. We start by mentioning what is probably the most celebrated of the unconventional properties of the cuprates: At optimal doping, the electronic part of the in-plane dc-resistivity ρ_{ab} is linear in T over several decades in temperature, see e.g. [106], and extrapolates to zero resistance at $T = 0$ K. This is in sharp contrast with the low-temperature behavior $\rho = \rho_0 + aT^2$ expected in Landau Fermi liquid theory. Recent detailed thermodynamic and transport measurements on heavily overdoped ($x = 0.3$), nonsuperconducting LSCO reveal that beyond the superconducting dome the ground state is indeed a Fermi liquid, although a highly correlated one [107]. In particular, the low-temperature resistivities ρ_{ab} and ρ_c are both proportional to T^2. By contrast, in the underdoped regime, deviations away from $\rho_{ab} \propto T$ occur: Upon reducing the hole-doping level p from optimal doping towards the underdoped side of the phase diagram, downward deviations from the linear-T high-temperature behavior sets in at a temperature T^* which increases with decreasing p [108], reaching temperatures near 700 K in the severely underdoped limit of LSCO, as indicated in Fig. 35. It is as if electron-electron scattering mechanisms become less effective in degrading electrical currents below T^*. A natural explanation for this is that a gap (decreasing with increasing doping) is developing in the electronic spectrum outside the superconducting phase.

What is the pseudogap? The name refers to a whole range of crossover phenomena seen in a number of experimental techniques probing the electronic spin or charge spectra [42]. These phenomena have in common that they point towards the gradual opening of gaps in the relevant

spectra at a temperature T^* which is higher than T_c and grows upon underdoping. To make matters more complex, there is evidence for an even higher crossover temperature scale T^0 and thereby for the existence of more than one type of pseudogap [42]. Usually, "pseudogap" is taken to refer to the lowest temperature phenomenon associated with T^*. For completeness, it should also be mentioned, that even when focusing solely on these phenomena, different techniques generally do not lead to the same values for the characteristic crossover temperature T^*. In addition to the transport studies briefly mentioned above, experimental techniques giving evidence for one or more pseudogaps include

- ARPES, which is sensitive to the density of filled single-electron states as a function of energy and momentum.
- Tunneling spectroscopy, which is sensitive to the density of both filled and unfilled single-electron states as a function of energy. Momentum space information can be obtained by Fourier transformation of STM signals acquired over a sufficiently large surface area.
- Specific heat, which is sensitive to the linear specific heat coefficient γ which in turn depends on the density of electronic states at the Fermi level.
- Nuclear magnetic resonance (NMR), which is sensitive to various momentum space averages of the low energy magnetic susceptibility $\chi(\mathbf{Q}, \omega \simeq 0)$.
- Neutron scattering, which is sensitive to the momentum and energy dependence of the imaginary part $\chi''(\mathbf{Q}, \omega)$ of the susceptibility.

We shall not enter into a discussion of the manners in which each of the techniques listed above probe the spin or charge pseudogaps. The reader is referred to [42] for an extensive review. Instead, we shall briefly talk about ARPES, which in a sense can be viewed as an electronic analogue of neutron scattering (Results from neutron scattering are discussed in section 6.3) since these techniques have both momentum and energy sensitivity.

ARPES measures the single-particle spectral function $A(\mathbf{k}, \omega)$ which in turn is related to the imaginary part of electron Greens function. The latter can often be calculated theoretically allowing direct comparisons with experiment to be made. ARPES can be used to measure the momentum dependence of the normal state Fermi surface as well as any gap opening on the Fermi surface. Thus, as mentioned above, ARPES has confirmed the $\mathrm{d}_{x^2-y^2}$-symmetry of the superconducting gap $\Delta_{\mathbf{k}}$, with the maximum gap Δ_0 not scaling with T_c and gap nodes along the $\langle 11 \rangle$ directions as seen in Fig. 34 [65].

In the normal state, the pseudogap is revealed both along the nodal [11] and along the antinodal [10] directions of the Brillouin zone, although in different ways. A typical ARPES spectrum as a function of $\hbar\omega$ at $(\pi, 0)$ for an underdoped cuprate in the superconducting phase consist of a gap near the Fermi level, a sharp coherence peak, then a small energy-interval where the photocurrent is depressed and finally a broader low-intensity peak followed by a high-energy incoherent part. This structure is referred to as a "peak-dip-hump" structure. Upon heating above T_c, the peak-dip-hump structure disappears, but the gap remains even in the normal state up to a temperature T^*. Hence, it is a pseudogap. Perhaps even more surprising, this gap has been found to have the same $\mathrm{d}_{x^2-y^2}$ symmetry in momentum space as the superconducting gap, and the minimum gap locus coincides with the normal state Fermi surface. Thus, the superconducting gap appears to develop smoothly from the pseudogap. However, it does not do so in a simple manner. Rather than the energy scale of the pseudogap simply increasing with decreasing temperature, the nodal and antinodal directions develop very differently: The pseudogap "closes" with increasing temperature in the regions near the nodal direction, but "fills in" near the antinodal direction, leaving the pseudogap energy scale independent of temperature at $(\pi, 0)$ [65]. The net effect is that as the temperature is increased above T_c, the nodal points of the superconductor develop into so-called "Fermi arcs". Only as T^* is reached do these arcs recover the full Fermi surface [109].

How could the pseudogap be understood? Broadly speaking, there are two kinds of theories. They are schematically presented and contrasted in Fig. 36.

The first class of theories regards the pseudogap temperature T^* as a temperature where electrons form Cooper pairs. In BCS theory, pairing is a necessary but not a sufficient condition for superconductivity to arise. In addition to pairing, phase coherence between the Cooper pairs is required. In conventional superconductors, the associated energy scales are identical, but this

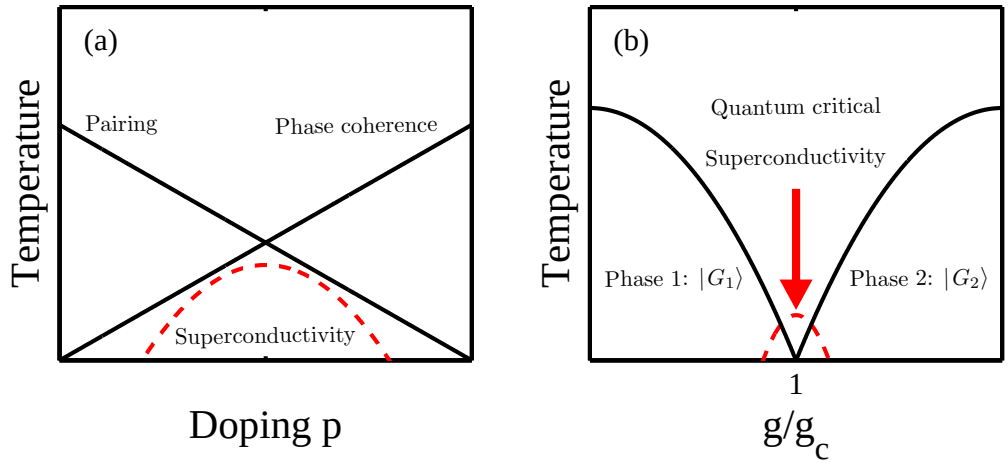

Figure 36: Two views of the high-T_c phase diagram. (a) Precursor pairing scenario. In BCS theory superconductivity requires pairing correlations to produce Cooper pairs and phase coherence between these pairs. In conventional superconductors, this would happen at the same temperature, but in cuprates the situation could be different. The measured pairing scale $\Delta_0 \propto T^*$ decreases with increased doping, but the low carrier density for a doped Mott insulator is expected to cause fluctuations in the superconducting phase through $N\phi \geq \hbar$. This would hinder superconductivity above a phase coherence line which increases monotonically with doping. (b) Generic quantum critical phase diagram [110]. The tuning parameter g can be thought of as e.g. applied field, pressure or chemical doping. For $g/g_c < 1$, the ground state is $|G_1\rangle$ and for $g/g_c > 1$ it is $|G_2\rangle$. The two phases are separated by a quantum critical point at $g = g_c$. For all temperatures above the two phase boundaries, the physical observables are strongly influenced by the quantum fluctuations caused by the quantum critical point at g_c. In the case of the cuprate high temperature superconductors, one might want to modify this phase diagram slightly by replacing the phase line delimiting the $|G_2\rangle$-phase by a crossover line delimiting a region with Landau Fermi-liquid properties.

is not necessarily so in the cuprates. There is a simple argument why superconducting phase fluctuations, preventing superconductivity at the pairing temperature scale T^* (which scales with the maximum superconducting gap Δ_0) should be important in the underdoped regime: If the cuprates are considered as doped Mott insulators, the number of carriers is small at low doping levels. Since the number operator is the conjugate to the phase operator, a low carrier density translates directly into large phase fluctuations. Since the pairing scale T^* decreases approximately linearly with doping, and the phase coherence line, according to the above argument, rises linearly from $p = 0, T = 0$ K, it is easy to imagine a situation where the two lines cross at optimal doping and divide the phase diagram into four separate quadrants, with the superconducting phase – a compromise between the pairing and phase coherence scales – occupying the lowest quadrant, as illustrated in Fig. 36(a) [94, 65].

An interpretation of the pseudogap regime as one with preformed pairs naturally explains why the pseudogap has the same symmetry as the superconducting gap. It also explains why the NMR Knight shift, which is sensitive to singlet formation, starts to decrease at T^* rather than at T_c as it does in conventional superconductors. In this picture, the pseudogap energy (seen in ARPES and tunneling) is simply the energy needed to dissociate one of the preformed Cooper pairs. On the other hand, it is more problematic for the precursor pairing scenario to explain the presence of Fermi arcs in the pseudogap region, although progress along this line has been made. A concrete example of a phase diagram resembling Fig. 36(a) has been proposed within the RVB model [16], where T^* is interpreted as the scale at which spins pair into singlet valence bonds, thus producing a gap in the spin excitation spectrum. From the point of view of constructing a superconducting state, the elegance of RVB ideas lie in the fact that the singlet bonds can be regarded as real-space Cooper pairs. Figure 37 shows a RVB picture with short range valence bonds only.

In terms of independent experimental evidence for a low carrier density in the underdoped regime, muon spin relaxation studies of relaxation rate $\sigma \propto \lambda_L^{-2} \propto n_s/m^*$ (We have replaced the real electron mass m_e in Eq. (69) by an effective mass m^* which in cuprates is found to be just a few times m_e) in several cuprate families shows a linear relation between T_c and n_s/m^* in the underdoped regime where there is also an approximate linear relation between T_c and p. The end result is an essentially linear relation between the density of superconducting electrons and the concentration of doped holes. This is not a self-evident result since there are not x but $1+x$ holes per copper site. For a recent perspective on these μSR studies and their broader relevance, see

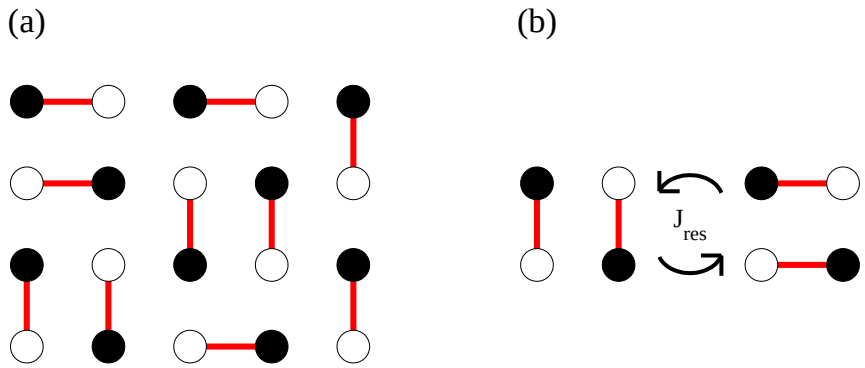

Figure 37: Schematic resonating valence bond (RVB) picture relevant to the insulating cuprate parent compounds. (a): A short-range resonating valence bond state consists of coherent superpositions of configurations of the type shown. Each red line represents a spin singlet formed by electrons on nearest neighbor sites of the bipartite square lattice. Each site is bonded to precisely one nearest neighbor. (b): By resonating between the two singlet configurations shown, a pair of valence bonds can lower their energy by an amount $J_{\rm res}$, related to the matrix elements connecting different configurations, see e.g. [15, 90].

[111].

In the second class of models, the pseudogap phenomenon is attributed to the presence of electronic phases other than superconductivity. In general, such phases may or may not be in direct competition with superconductivity. They need not even be long-range ordered: The fluctuations associated with the proximity of a second ordered phase are sufficient to produce observable effects. One way to think about such an ordered phase is in terms of quantum criticality. Figure 36(b) shows the generic phase diagram for a quantum critical point. The parameter g can be thought of as e.g. applied field, pressure or chemical doping. Tuning g causes a quantum phase transition between different ground states. For $g/g_c < 1$, the ground state is $|G_1\rangle$ and for $g/g_c > 1$ it is $|G_2\rangle$. The two ordered phases (bounded by solid black lines) are separated by a quantum critical point at $g = g_c$. In each phase, the excitations contain information on the nature of the underlying ground state. For temperatures above the two phase boundaries, the physical observables are severely influenced, even at elevated temperatures, by quantum fluctuations associated with the existence of the quantum critical point at $T = 0$ K and $g = g_c$. It is thought that superconductivity may sometimes arise in the region surrounding the quantum critical point (dashed red line), see e.g. [112], but emergent superconductivity is not in itself implied by quantum criticality.

In the context of high-temperature superconductivity, if quantum criticality ultimately lies at the heart of the subject, phenomena such as the linear T-resistivity can plausibly be explained by the a strong coupling of the electronic degrees of freedom to the quantum fluctuations associated with a quantum critical point hidden somewhere underneath the superconducting dome. In favor of interpreting the pseudogap physics as a signature of incipient order and quantum criticality, it has been reported that upon suppressing superconductivity through chemical doping, the superconducting dome collapses around the T^*-line which appears to go to zero at $p \simeq 0.19$ [113]. Within such a picture, it is possible to reconcile the Fermi arc phenomenology with specific heat data and the drop of T_c in the underdoped regime: The specific heat is sensitive to the density of states at the Fermi level. If some sort of electronic order removes the states available for pairing as p is reduced below the critical hole-concentration (thus leading to the Fermi arcs), the number of states available for superconducting pairing will decrease upon underdoping, thus causing T_c to drop. There is even a concrete example of quantum critical scaling behavior in the dynamic susceptibility $\chi''(\mathbf{Q}, \omega)$ of LSCO [114], but in this case the alleged critical point may not be the same as the one discussed above.

What could be the competing order? The main candidate discussed in the literature is the so-called stripe phase. We shall treat this phase further below in the context of the two competing models for explaining the excitation spectra in the high-temperature superconductors. For now, suffice it to say, that in the stripe model and related models, the holes doped into the CuO_2 planes have a tendency to distribute themselves in spatially inhomogeneous patterns. In the stripe scenario, the doped holes arrange themselves into one-dimensional rivers of charge, thus leaving behind regions with the same local structure as the Mott insulator at $p = 0$. In the simplest view, these areas should then be two-dimensional insulating antiferromagnets. A related idea is that the

doped holes form a two-dimensional checkerboard pattern. There is experimental support for both the stripe and checkerboard phases, primarily from neutron scattering [115, 116] and scanning tunneling microscopy [117, 118] studies, but controversies surround the interpretation of the data, so many important issues (Do stripe or checkerboard states exist in all cuprates? Are they relevant to the broader issues of high-T_c superconductivity? If this is the case: How are they relevant?) remain unsettled. At the very least, scanning tunneling microscopy on clean $Bi_2Sr_2CaCu_2O_{8+x}$ (Bi2212) surfaces provides strong evidence for significant electronic disorder on the nanoscale, an observation suggestive of competing electronic orders [119, 120].

The central question to be addressed is this: If the pseudogap signifies the existence of another electronic phase, why has it not been possible to unambiguously identity it over extended portions of the phase diagram? A plausible answer is that the electronic order in question is not long-range ordered, but is present only in fluctuating form. In this case, one should ask whether it is possible to force it to become static in order to characterize it. More generally put [95]: How can one detect fluctuating order in the high-T_c superconductors? If the incipient order is considered to compete with superconductivity, then it stands to reason that if superconductivity is suppressed or destroyed, the signatures of the second phase should become stronger. Of particular interest in this respect are Zn-substitution studies and magnetic field studies of the vortex phase [121, 122, 123, 117]. Heating above T_c of course also destroys superconductivity, but in terms of identifying phases, the $T = 0$ K response should yield less ambiguous results.

To conclude this section we point out, that from the fact that BCS theory does not seem to apply to the high-temperature superconductors [94], and since their superconductivity arises through the doping of a Mott insulator, it is quite reasonable to assume that strong electron-electron interactions must play an essential part in any theory of the pseudogap phenomenon and high-temperature superconductivity. However, the presence of strong interactions not only leads to the Mott insulator and, upon doping, to strong phase fluctuations, it also has a strong tendency towards the formation of competing orders [94]. Thus, the two views on the pseudogap phenomena sketched above are generally not mutually exclusive. On the other hand, far into the overdoped regime, the transport properties appear to be accounted for within the Fermi liquid description, which has been eminently successful in describing conventional metals and underpins BCS theory. From this point of view, it would also seem reasonable for a theory to start from a Fermi liquid description of the overdoped regime, and subsequently incorporating strong interactions using suitable approximation schemes. The two approaches to formulating theories for cuprate high-temperature superconductivity outlined above differ very much in their points of departure. The first is a strong-coupling approach, in which the main thing is the various real-space ordered phases which can develop from the Hubbard model (72) or related models. The second is a weak-coupling approach in which one attempts to understand the physics of the cuprates starting from well-defined quasiparticles in the overdoped regime, i.e. from ordered structures in reciprocal space.

6.3 Neutron scattering from high-T_c superconductors

This section is intended to give an overview of the neutron scattering studies that have been performed on cuprates, but in order not to present experimental data without any basis in theory, we shall also, here and in section 6.4, discuss the theories that have been developed in attempts to model the neutron scattering data. In the previous section we mentioned how attempts at understanding theoretically what high-T_c superconductivity is about at the most fundamental level, can be divided into two classes: A strong coupling approach, starting from the $p = 0$ limit of the phase diagram in Fig. 35, and a weak-coupling approach starting from the overdoped regime where it is believed that the ground state is a Fermi liquid. These two approaches are reflected in two basic classes of models aimed at the more narrow problem of explaining the neutron scattering data. The strong-coupling theories focus on well-defined structures in real-space, whereas the weak-coupling theories focus on well-defined structures in reciprocal space. In both cases, the object to be calculated is the imaginary part $\chi''(\mathbf{Q}, \omega)$ of the generalized susceptibility, or alternatively the scattering function $S(\mathbf{Q}, \omega)$ to which it is related through the fluctuation-dissipation theorem Eq. (17). Chapter 2 showed that when corrections are made for the effects of the finite instrumental resolution, $S(\mathbf{Q}, \omega)$ is precisely what is being measured in a neutron scattering experiment.

6.3.1 Crystal structures and issues of notation

Before starting our discussion of neutron scattering data, it is useful to make a few remarks regarding notation. As discussed in [98], according to standard conventions the space groups of the high-temperature tetragonal (HTT) and low-temperature orthorhombic phase (LTO) of LSCO are I4/mmm and Cmca respectively. In these space groups, the axis perpendicular to the CuO_2 planes are **c** and **b** respectively. In order to avoid confusion, we shall use a fixed notation, in which the CuO_2 planes are always perpendicular to **c**. For the orthorhombic phase this is achieved by using the nonstandard space group Bmab rather than Cmca. In the tetragonal to orthorhombic phase transition, the CuO_6 octahedra rotate around a tetragonal [110] axis, to form a staggered rotation pattern, in which the rotation is uniform within a given orthorhombic **bc**-plane [97]. In the process, the lengths of the two in-plane diagonals in Fig. 33(a) become unequal and these are the orthorhombic lattice vectors **a** and **b** in the LTO phase. For the particular doping levels $x = 0.10$ and $x = 0.16$ studied in the next chapter, the orthorhombic (Bmab) lattice constants are approximately $a = 5.3241(1)$ Å, $b = 5.3706(1)$ Å and $c = 13.1700(1)$ Å for $x = 0.1000$ and $a = 5.3247$ Å, $b = 5.3437(1)$ Å and $c = 13.2057(1)$ Å for $x = 0.1625$ [98]. Since there are two equivalent tilt directions within each tetragonal CuO_2 layer, twinning occurs unless special care is taken to avoid it [97].

A second note on notation has to do with how to identify points and distances in reciprocal space. In reading through the literature on high-temperature superconductors, several notations are encountered. In particular, different authors refer to the location of antiferromagnetic Bragg peaks in different manners. The picture gets more blurry still when incommensurate peaks are discussed. To keep the notation consistent with chapters 3-5, we have chosen whenever the **c**-axis component of the total neutron momentum transfer **Q** is irrelevant to use the same notation as in those chapters. This means, that antiferromagnetic Bragg peaks are denoted (π, π) and that the [10] directions are along the nearest neighbor Cu-Cu bonds, i.e. parallel to the tetragonal lattice vectors **a** and **b** in Fig. 33, or along the diagonals of the orthorhombic unit cell indicated by solid black lines in Fig. 38.

6.3.2 Antiferromagnetic order and spin waves in La_2CuO_4 and $YBa_2Cu_3O_{6+y}$

The subfield of neutron scattering from cuprates was started by the work of Vaknin and coworkers on the magnetic structure of the cuprate parent compound La_2CuO_4 (although with slightly reduced oxygen content) [124]. Acting on magnetic susceptibility anomalies pointing to possible antiferromagnetic order at low temperatures, Vaknin *et al.* used powder neutron diffraction to directly confirm this suspicion. The lowest-$|\mathbf{Q}|$ magnetic peak occurred at the orthorhombic (100) position. There was no peak at the (010) position. Neither (100) nor (010) are allowed structural Bragg reflections. The low-temperature magnetic structure was determined by analyzing the peak intensities of the antiferromagnetic Bragg peaks within a model, where the magnetic moments are assumed to reside on Cu^{2+} sites only. It was concluded that the Cu^{2+} spin directions are along the orthorhombic [010] axis (in which case the (010) reflection becomes unobservable as a consequence of the polarization factor in the neutron scattering cross-section) with the antiferromagnetic modulation direction being [100]. The magnetic structure is shown in figure 38. With a sensible assumption for the form factor $F(\mathbf{Q})$, Vaknin *et al.* also determined the low-temperature magnitude of the ordered sublattice moment to be $0.48 \pm 0.15 \mu_B$, approximately half the classically expected value. Using polarized neutron scattering, Mitsuda *et al.* unambiguously showed that the powder peaks analyzed by Vaknin and coworkers were magnetic in origin, and confirmed the large reduction in the ordered moment [125]. The discovery of conventional antiferromagnetic order in La_2CuO_4 put to rest a very early suggestion that the ground state in this material could be the resonating valence band state [16] since this does not break spin rotational symmetry.

Shortly after the work of Vaknin, Shirane and coworkers studied the spin fluctuations in undoped and oxygen-stoichiometric La_2CuO_4 single crystals. They used both two-axis and triple axis neutron scattering to infer that the dynamic fluctuations in this systems are highly two-dimensional [126], with rods of magnetic intensity extending along the $\mathbf{c}^*$ axis, away from the 3D magnetic Bragg peaks at (100). With the discovery of two dimensionality of cuprate magnetism, the reduction in the sublattice moment [124, 125] is most readily rationalized in terms of quantum fluctuations in a square lattice of Heisenberg coupled $S = 1/2$ spins − as discussed at length in chapter 3. Using polarized neutron scattering, Endoh *et al.* [127] subsequently proved the magnetic origin of the 2D scattering rods for temperatures above the Néel temperature T_N. Shirane

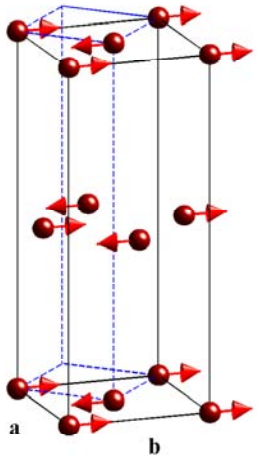

Figure 38: Magnetic structure of La_2CuO_4 as determined from powder neutron scattering by Vaknin and coworkers [124]. In the antiferromagnetic phase, the Cu^{2+} moments orient themselves along the orthorhombic **b** axis, and form ferromagnetic sheets which alternate along the orthorhombic **a** axis. The dashed blue lines indicate the size and orientation of the tetragonal unit cell seen in Fig. 33

et al. also attempted to observe counterpropagating antiferromagnetic spin waves in La_2CuO_4 but were unable to resolve them at 20 meV. This implied a lower limit on the spin wave velocity c_s (see section 3.1.1) of 0.4 eV Å. Subsequent low-energy inelastic triple axis measurements by Birgeneau *et al.* [128], lead to the conclusion $c_s \geq 0.6$ eV Å.

After these preliminary studies, a set of experiments by Aeppli, Hayden and coworkers combined triple axis [54, 62] and time-of-flight [63] neutron scattering techniques to study the spin waves in La_2CuO_4 for energies extending all the way to the zone boundary. In particular, they were able to resolve counterpropagating spin wave modes, and through their separation at low energy transfers obtain $c_s = 0.85 \pm 0.03$ eV Å. The spin waves were found to be well-defined all the way to the zone boundary and their dispersion was in excellent agreement with the theoretical prediction Eq. (37) for the square lattice, $S = 1/2$ Heisenberg model. A comparison of Eq. (37) with the experimental data lead to an effective nearest-neighbor exchange constant $J_{\rm eff} = 153 \pm 4$ meV. However, this neglects the quantum correction factor Z_c of the spin wave energy scale within linear spin wave theory. Assuming $Z_c = 1.18$, the zone boundary spin wave energy $\hbar\omega_{\rm ZB} = 2Z_cJ$ lead to $J = 132 \pm 4$ meV as the best estimate of the real nearest-neighbor exchange interaction. The next study of the spin wave spectrum of La_2CuO_4 was by Coldea and coworkers [44] who – as discussed at length in chapter 3 – identified a large ring-exchange term in the Hamiltonian of La_2CuO_4. The experimental and theoretical spin-off of relevance to high-temperature superconductivity following from this discovery has been ideas that there could be real staggered electronic current patterns flowing around the elementary plaquettes of the superconductors obtained from doping the insulating parent compounds. At the present stage there is however only little evidence for these "d-density wave" scenarios.

We turn now to the YBCO-family of superconductors. YBCO, shown in Fig. 33(b)-(c) is structurally and chemically more complex owing to the presence of both bilayers and chain layers. Although the chain layers may have a one-dimensional magnetic response of their own [129], the magnetism relevant for comparisons with LSCO and other cuprate families is that of the bilayers. The bilayer structure of YBCO and other cuprates implies the existence of two scattering channels depending on the symmetry of the spin fluctuations under reflection in the mirror plane between the two layers, see e.g. [130, 131]: The "acoustic" channel contains information about spin fluctuations which are odd under reflection in the mirror plane, corresponding to antiferromagnetic correlations between the bilayer planes. The "optic" channel contains information about spin fluctuations which are even under reflection in the mirror plane, and correspond to ferromagnetic correlations between the bilayer planes. Denoting the distance between the planes of the bilayers by d, the different symmetries of fluctuations in the acoustic and odd channels lead to the appearance of bilayer structure factors $\sin^2(Q_c\,d/2)$ and $\cos^2(Q_c\,d/2)$ which modify the intensities of acoustic and optical excitations respectively as a function of the component Q_c of $\mathbf{Q}$ along the **c**-axis. The

imaginary part of the generalized susceptibility can then be written

$$\chi''(\mathbf{Q},\omega) = \chi''_{\rm ac}(\mathbf{Q}_{\rm 2D},\omega)\sin^2(Q_c\,d/2) + \chi''_{\rm op}(\mathbf{Q}_{\rm 2D},\omega)\cos^2(Q_c\,d/2) \tag{73}$$

where we note the decoupling of Q_c from the in-plane momentum transfer $\mathbf{Q}_{\rm 2D}$. This equation shows, that one can study $\chi''_{\rm ac}(\mathbf{Q}_{\rm 2D},\omega)$ and $\chi''_{\rm op}(\mathbf{Q}_{\rm 2D},\omega)$ individually by orienting the sample in a manner permitting scans to be made in which Q_c equals odd or even multiples of π/d respectively.

The above comments regarding bilayer structure factors apply to all bilayer cuprates. Now, we restrict our attention to YBCO and to studies of spin waves in the antiferromagnetic parent compounds. Low energy studies of $YBa_2Cu_3O_{6.3}$ ($T_N = 260 \pm 5$ K) by Tranquada and coworkers revealed the existence of spin waves in the acoustic channel, from which rough estimates of three important exchange constants were derived. The in-plane nearest neighbor exchange constant was estimated to be $J = 80^{+60}_{-30}$ meV, with the large errors resulting from inability to separate counter-propagating spin waves. For the coupling $J_{\perp,1}$ between the two layers forming a bilayer, a lower limit of 2 meV was deduced from the absence of optical excitations at the highest energy investigated. Finally, the coupling $J_{\perp,2}$ between next-nearest neighbor layers, i.e. between layers in neighboring bilayer was found to be four orders of magnitude smaller than the dominant exchange interaction J [132]. A subsequent experiment by Shamoto *et al.* on $YBa_2Cu_3O_{6.15}$ ($T_N = 410 \pm 3$ K) extending to higher energies, but still seeing only acoustic fluctuations, improved upon these estimates. They found $J = 120 \pm 20$ meV, $J_{\perp,1} \geq 8$ meV and $J_{\perp,2} = 0.04 \pm 0.02$ meV [133]. To understand why the values of J, $J_{\perp,1}$ and $J_{\perp,2}$ can be compared between $YBa_2Cu_3O_{6.15}$ and $YBa_2Cu_3O_{6.3}$ it is necessary to be aware, that the phase diagram of $YBa_2Cu_3O_{6+y}$ as a function of $y \neq p$ can roughly be divided into three regimes, see e.g. [132]: At low y, there is an antiferromagnetic phase extending to $y \simeq 0.40$ after which superconductivity sets in. Inside the antiferromagnetic phase, T_N varies relatively slowly with y, suggesting that $y = 0.15$ samples are not substantially different from $y = 0.30$ samples. The phase boundary of the superconducting phase above $y \simeq 0.4$ has two broad plateaus. At intermediate y we find superconductors with transition temperatures around 60 K whereas for y-values approaching 1, we find superconductors with $T_c \simeq 90$ K. The optimal T_c corresponds to $y = 0.93$. Underdoped samples are samples with $y < 0.93$ whereas overdoped samples have $y > 0.93$. Finally, Hayden and coworkers [134] used time-of-flight neutron scattering to study the high-frequency spin wave response of $YBa_2Cu_3O_{6.15}$ ($T_N \simeq 400$ K). For the first time, an optical spin wave response was seen at energies above 74 ± 5 meV. Analyzing the data within linear spin wave theory they obtained $J = 125 \pm 5$ meV and from the expected optical zone center excitation gap $\hbar\omega_g = 2(JJ_{\perp,1})^{1/2}$ derived $J_{\perp,1} = 11 \pm 2$ meV. It should noted, that the value $J = 125 \pm 5$ meV does not include quantum corrections as did the value $J = 132 \pm 4$ meV found for LSCO [63]. Therefore it is more relevant to compare it to the unrenormalized value $J_{\rm eff} = 153 \pm 4$ meV. As noted in section 3.3.4, the presence of exchange interactions coupling spins beyond their nearest neighbors complicates the deduction of the raw exchange parameters since one should in principle include one quantum renormalization factor per exchange interaction, the values of which should be determined self-consistently [70].

The main message here is that the nearest neighbor effective exchange constants of antiferromagnetic samples of LSCO and YBCO, although not identical, are of the same order of magnitude. In YBCO, there is a significant interplane interaction inside a given bilayer, but the bilayers themselves are only very weakly coupled, as are the single CuO_2 layers in LSCO. Both in LSCO and in YBCO, three-dimensional antiferromagnetic order is achieved by a "pancake" process: Once the correlated area of the antiferromagnetic order within a given plane exceeds a certain limit, the smallness of the interlayer (or interbilayer) coupling is overcome and three-dimensional long-range order develops. Upon doping the antiferromagnets to form metallic superconductors, there is a dramatic decrease of the in-plane spin-spin correlation length and therefore, in the superconductors, the layers or bilayers are magnetically decoupled and the neutron scattering signals are essentially incoherent superpositions of one-layer or one-bilayer signals [130]. We note in passing, that the mathematics of [134] shows that in the absence of interplane interactions within a bilayer, one would have $\chi''_{\rm ac}(\mathbf{Q}_{\rm 2D},\omega) = \chi''_{\rm op}(\mathbf{Q}_{\rm 2D},\omega)$ in the notation of Eq. (73), in which case the bilayer structure factors disappear as expected for isolated layers.

6.3.3 Incommensurate spin fluctuations and spin gap in LSCO

Having discussed the antiferromagnetic parent compounds and neutron scattering of them at length, it is time we return to the superconducting cuprates. The next issue we want to dis-

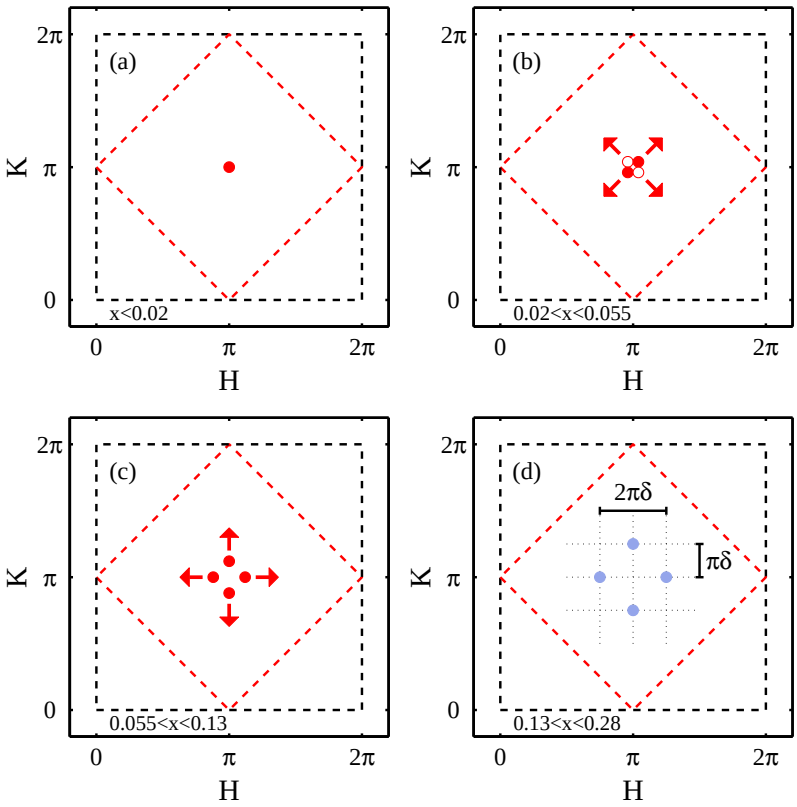

Figure 39: Evolution of the symmetry patterns of magnetic Bragg scattering (red circles) and low-energy fluctuations (blue circles) across the phase diagram of $La_{2-x}Sr_xCuO_4$. As in Fig. 6, the black and red dashed lines delimit the nuclear and magnetic zones. (a) The antiferromagnetic order observed for doping levels $0 < x < 0.02$ gives rise to a single Bragg reflection at (π, π). The low-energy excitations are conventional spin waves. (b) In the non-superconducting regime between $x \simeq 0.02$ and $x \simeq 0.055$, neutron scattering reveals four Bragg spots displaced symmetrically away from (π, π) along the [11] directions, i.e. along the diagonals of the elementary plaquettes. Open and filled symbols are used to emphasize that in this doping range and with this peak displacement direction it has been experimentally proven that each orthorhombic twin domain contributes one set of incommensurate peaks [138]. As x increases, these peaks move away from (π, π) as indicated by the red arrows. (c) In the superconducting regime for doping levels $0.055 < x \leq 0.13$, four diffraction peaks are seen displaced away from (π, π) along the [10] directions, i.e. along the nearest neighbor Cu-Cu directions. As x is increased, the peaks move away from (π, π) as indicated by the red arrows. (d) In the superconducting phase for $0.13 < x < 0.28$, there is no longer magnetic order, but low-energy fluctuations with the same symmetry as in (c) persist. The $\mathbf{Q}_{2D}$-space loci of these incommensurate fluctuations no longer vary with x, but remain at $(\pi(1 \pm \delta), \pi)$ and $(\pi, \pi(1 \pm \delta))$ with a fixed $\delta \sim 0.24$.

cuss is the reciprocal space symmetry of the low-energy magnetic scattering in LSCO, and how the intensity of these fluctuations is affected by superconductivity.

As have been repeatedly stated above, the commensurate antiferromagnetism of the Mott insulator is fragile, and vanishes quickly upon hole doping. Using elastic, quasielastic and inelastic neutron scattering Birgeneau *et al.* were able to show that even though 3D magnetic order vanishes quickly, strong antiferromagnetic correlations persist well into the superconducting phase in the form of rods of inelastic scattering along the normal to the CuO_2 planes. In the process, they reported indications, admittedly at the very limit of the statistical quality of the data, that the magnetic response in the superconducting phase was no longer commensurate as in La_2CuO_4, but incommensurate [128]. This initial (possible) observation was quickly confirmed by Yoshizawa *et al.* [135] and Thurston *et al.* [136]. In the latter paper, the incommensurate structure was found to be independent of the out-of-plane component of $\mathbf{Q}$ and to vary with $|\mathbf{Q}|$ in a manner consistent with the Cu^{2+} form factor variation. These facts are strongly suggestive of a magnetic origin, and are very difficult to reconcile with scattering from phonons. The full symmetry pattern of the incommensurate scattering was reported a few years later by Cheong and coworkers [137]: Using inelastic neutron scattering it was found, that there are four incommensurate peaks surrounding (π, π), symmetrically displaced along the [10] and [01] directions of the square lattice reciprocal space, i.e. along the directions defined by the Cu-O-Cu bonds, see Fig. 39(d).

Following early observations of gap-like behavior of the incommensurate magnetic peaks in LSCO [136, 139], later experiments directly correlated the opening of this "spin gap" Δ_s with the onset of superconductivity at T_c in near-optimally doped samples [140]. In other words, the spin gap opens at T_c. Following this discovery, a discussion developed on the question of whether or not the spin-gap was clean, in the sense of there being no magnetic scattering at energies below Δ_s [141, 142, 143, 144]. To properly address this question, one should consider both extrinsic and intrinsic causes for scattering below Δ_s. As sample quality improved, the first issue seems to have been resolved in favor of a clean gap [142, 143, 144]. The second issue, regarding the intrinsic signal is more complex, and is connected to the question of the origin of the incommensurate peaks. If $\chi''(\mathbf{Q}_{2D}, \omega)$ is interpreted as originating in particle-hole excitations, the incommensurate peaks arise as a consequence of dynamic nesting of parallel parts of the Fermi surface. In such a picture, the simplest expectation would be that the spin-gap is $\mathbf{Q}_{2D}$-dependent in a manner which reflects the $d_{x^2-y^2}$ symmetry of the superconducting gap function $\Delta_{\mathbf{k}}$. Thus, the spin-gap should in general be dispersive, and in particular, it should have nodes at the wavevectors connecting the nodes of $\Delta_{\mathbf{k}}$, see e.g. [145, 146]. However, studies of Δ_s in optimally doped LSCO by Lake and coworkers showed that there is little or no dispersion in the spin-gap, which therefore appears to have s-wave symmetry [144]. In particular, the spin gap at the location of the incommensurate peaks was clean and had a magnitude $\Delta_s = 6.7$ meV, the precise numerical value being dependent on how Δ_s is defined [144]. A clean gap has also been seen in slightly overdoped LSCO, but there does not appear to be any evidence for the existence of a spin gap in underdoped LSCO, see [147].

The opening of the spin gap at T_c is accompanied by increased scattering at energies above Δ_s. This was shown clearly in $La_{1.86}Sr_{0.14}CuO_4$ by Mason *et al.* [148], who also reported a clear $\mathbf{Q}_{2D}$-space sharpening of the incommensurate peak signal immediately above the spin gap Δ_s. The latter behavior, dubbed the "coherence effect", was explained by phase space arguments in a Fermi liquid nesting picture. These results were later verified in $La_{1.84}Sr_{0.16}CuO_4$ by Lake *et al.* [144]. More generally, the fact that spectral weight suppression below Δ_s is correlated with spectral weight increases above Δ_s suggest that the spin gap signifies a spectral weight transfer from low energies to high energies along the incommensurate peaks. Since $S(\mathbf{Q}, \omega) = (n(\omega) + 1)\chi''(\mathbf{Q}, \omega)$ must satisfy the sum rule

$$\frac{\int d\mathbf{Q}\, d(\hbar\omega)\, \mathrm{Tr}(S^{\alpha\beta}(\mathbf{Q}, \omega))}{\int d\mathbf{Q}} = S(S+1) \qquad \text{per copper atom} \tag{74}$$

it is clear that the spectral weight lost below the spin gap, must go somewhere. Intuitively, it is most natural that it should go where the susceptibility is large in the first place, i.e. along the incommensurate peaks. Although there are quite a few studies of the spin gap in LSCO, there has not been a study to demonstrate the full extent of the spectral weight transfer, in the sense of verifying Eq. (74). One of the main results obtained from the experiments reported in chapter 7 and published in [149] is precisely such a verification. Another central theme in chapter 7 is whether or not the incommensurate peaks have a dispersion. Until very recently, it has generally been accepted that they did not (see e.g. [114, 116]), although one study by Petit *et al.* [150] exists, in which the authors report a sharp incommensurate to commensurate crossover at $\hbar\omega \simeq 25 - 30$ meV in optimally doped $La_{2-x}Sr_xCuO_4$. The results reported in the next chapter together with a study of the excitation spectrum of $La_{1.875}Ba_{0.125}CuO_4$ ($T_c = 3 - 6$ K) [151] in its normal state, disprove the reigning view that the incommensurate modes have no dispersion.

Following Lake *et al.* , a possible explanation for the spin gap lies in singlet formation. According to this point of view, the low-energy degrees of freedom above T_c are depleted by Cooper pair formation. Transforming a singlet into a triplet is a $\Delta S = 1$ process and is associated with a finite energy cost. According to Lake *et al.* , this energy is the spin gap energy, and its independence of $\mathbf{Q}_{2D}$, contrasting the $d_{x^2-y^2}$ symmetry of the charge excitations probed by ARPES, can be seen as a sign that the two types of excitations are independent in the cuprates. Such exotic spin-charge separated states are known to exist in one-dimensional electron systems, e.g. Luther-Emery liquids [144], and have also been postulated for the cuprates.

6.3.4 Stripes

In 1995 Tranquada and coworkers, in a diffraction study of $La_{1.48}Nd_{0.4}Sr_{0.12}CuO_4$ (LNSCO), presented the first evidence for an interpretation of the incommensurate fluctuation patterns in LSCO in terms of a real space picture of spatially segregated spins and charges, dubbed "stripes",

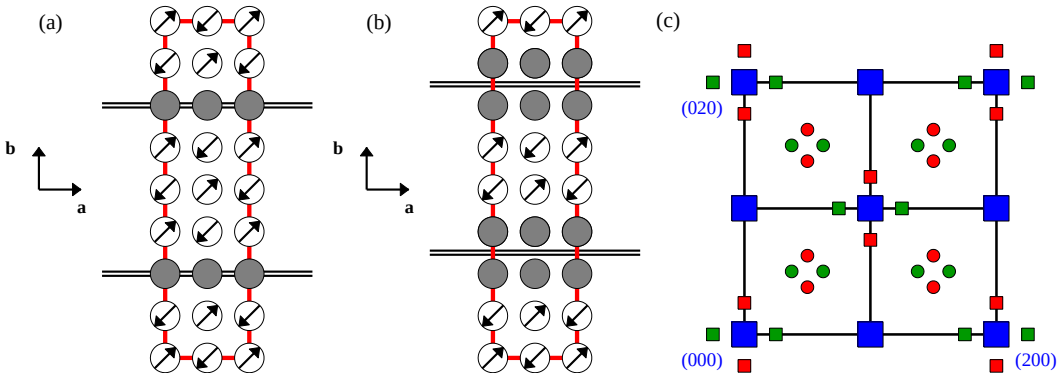

Figure 40: (a)-(b): Schematic illustration of a stripe phase in LSCO adapted from [115]. The Cu-O bond directions **a** and **b** are horizontal and vertical. The stripe unit cell for a doping level of x=1/8 is indicated by the solid red lines. In a stripe picture, the doped holes congregate onto rivers of charge running along the Cu-O bonds in $La_{2-x}Sr_xCuO_4$ (Indicated by double solid black lines) and along the diagonal of the elementary NiO_4 plaquettes in the $La_{2-x}Sr_xNiO_4$ family. In between the charge stripes there is local antiferromagnetic order, with the charge stripes being antiphase domain walls for the magnetic order. This implies that the charge unit cell is half the size of the spin unit cell. In (a) the stripes are site-centered, whereas in (b) they are bond-centered. In both (a) and (b), we have suggested that the spin direction in the hole-poor regions is identical to that of La_2CuO_2 shown in Fig. 38. This is consistent with the observed spin structure in (spin) stripeordered La_2CuO_{4+y} [155]. (c): The expected diffraction pattern (in the tetragonal notation relevant to $La_{2-x-y}Nd_ySr_xCuO_4$) for a crystal in which stripes along **a** and **b** exist in equal proportion. The solid blue square are allowed and forbidden nuclear Bragg reflections. The remaining red and green symbols correspond to two separate stripe directions. The circles are magnetic Bragg peaks caused by spin stripe order and displaced from $(1/2, 1/2, 0)$ by $\delta_s = 1/8$ along the [100] and [010] directions. The squares are structural Bragg peaks due to charge stripe order. In neutron scattering, the latter peaks originate from the nuclear charge displacements induced by the electronic inhomogeneity of the stripe ordering. By contrast, X-rays are directly sensitive to the periodicity of the distortion in the electron charge distribution. In both cases, as a direct consequence of the magnetic unit cell having twice the extent of the charge unit cell, the charge order Bragg satellites are displaced from the allowed nuclear Bragg reflections by $2\delta_s$ perpendicular to the respective stripe directions.

instead of a dynamic nesting scenario [115]. This has been an extremely influential idea (to the point that one may speak of a new subfield, coined "stripology"), so we shall spend some time presenting the model in its details.

Figure 40 illustrates the stripe model for a doping level $x = 1/8$ of LSCO. The basic idea is that upon doping the Mott-insulator at $x = 1/8$, the doped holes have a tendency to form ordered patterns of the type shown. The earliest theoretical illustrations of this tendency were due to Zaanen and Gunnarsson [152], Schulz [153] and Poilblanc and Rice [154], all of whom used the Hartree-Fock approximation to study Hubbard models in various guises. At $x = 1/8$, the picture is this: Instead of delocalizing over the CuO_2-planes, the doped holes form rivers of charge (charge stripes) running along the Cu-O-Cu direction. The charge stripes may be either centered on Cu sites (site-centered stripes) as shown in Fig. 40(a) or centered on the Cu-O-Cu bonds (bond-centered stripes) as shown in Fig. 40(b). In both cases, the regions between the charged stripes have the same local structure as the undoped Mott-insulator. This gives two possibilities: Either the charge stripes are domain walls for the antiferromagnetic order or they are not. Put differently: Either the spin unit cells are twice the size of the charge unit cells, or they have the same size. These two cases are illustrated for the case of site-centered stripes in Fig. 41(a) and (b) respectively. Theoretically, Zaanen and Gunnarson found that the lowest energy is achieved by having a spin unit cell twice as large as the charge unit cell. A simplistic and commonly used argument for the preference of case (a) over case (b) concerns the energy cost of sideways, meandering motion of a charge stripe. Figure 41(c) and (d) shows the effect of such transverse stripe motion (reflecting the dislike of the doped holes of being localized) away from the configurations shown in (a) and (b) respectively. Whereas there is an energy cost associated with the meandering motion in both cases because antiferromagnetic bonds are broken, the cost is greatest in case (d) where a ferromagnetic bond (encircles in solid blue lines) is formed. Taking the preference for antiphase domain walls for granted, the repeat distance at $x = 1/8$ along the line transverse to the stripe direction is precisely eight lattice constants, whereas the charge repeat distance is four lattice constants.

Diffraction from stripes In a neutron diffraction experiment, an ordered structure such as this would give rise to two sets of Bragg peaks: Magnetic Bragg peaks displaced away from (π, π) along

the direction perpendicular to the stripe direction and structural Bragg peaks displaced away from the nuclear Bragg reflections $(2\pi, 0)$ along the same direction. This is illustrated in Fig. 40(c) where we are using a tetragonal notation to index the various types of reflections because this brings the connection between the displacement vectors and real-space stripe repeat distances out most clearly. In this notation (π, π) and $(2\pi, 0)$ correspond to $(1/2, 1/2, 0)$ and $(1, 0, 0)$ respectively, but since the latter is not an allowed Bragg reflection in $La_{2-x}Sr_xCuO_4$, the satellite peaks corresponding to charge order are expected around $(2, 0, 0)$ and other allowed nuclear reflections instead. In fact, by contrast with X-rays, neutrons are not directly sensitive to the charge order. However, charge ordered states such as those indicated in Fig. 40 are expected to induce nuclear displacement patterns with the same real-space periodicity as that of the charge stripes, and these can be detected by neutron scattering. If the real-space charge stripe distance is N_c lattice constants along **b**, as in Fig. 40(a), then the nuclear satellite peaks due to charge stripes are expected to be displaced away from allowed Bragg reflections by $\Delta\mathbf{Q}_c = \pm(1/N_c)(0, 1, 0) = \pm\delta_c(0, 1, 0)$. Since the charge stripes are domain walls for the spin order, the magnetic repeat distance perpendicular to the stripe direction is always twice the charge repeat distance, i.e. $N_s = 2N_c$. Consequently, satellite peaks giving evidence of spin stripe order will be displaced by $\Delta\mathbf{Q}_s = \Delta Q_s/2 = \pm 1/2(1/N_c)(0, 1, 0) = \pm\delta_s(0, 1, 0)$ away from the commensurate antiferromagnetic point $(1/2, 1/2, 0)$. For LSCO with $x = 1/8$ there is one doped hole per eight Cu sites. Thus, in the arrangement of Fig. 40(a), there is one doped hole for every two sites along the stripes. Since each Cu site can accommodate two holes and one hole is already present as in La_2CuO_4, the presence of one additional hole per two Cu sites on the stripe makes it "quarter-filled" in terms of electrons. In this particular case $N_c = 4$ and $N_s = 8$, so according to the above argument, we expect charge and spin displacement vectors equal to $\Delta\mathbf{Q}_c = \pm(1/4)(0, 1, 0)$ and $\Delta\mathbf{Q}_s = \pm(1/8)(0, 1, 0)$ respectively, in the case where the stripes run along **a**. We note in particular that for LSCO indexed in the tetragonal notation, $\delta_s = x = p$. If for one reason or the other stripes running along **a** and **b** are present in equal proportion, then the total expected diffraction diagram Fig. 40(c) contains equal intensity charge and spin satellite peaks displaced along [100] and [010] resulting from stripes along **b** and **a** respectively.

In going from the tetragonal notation to our favored square lattice reciprocal space notation of Fig. 39, we must multiply all reciprocal space lengths by 2π. This gives rise to a factor of two difference between the numerical values of the magnitudes of the displacement vectors in the two notations since the peak displacement parameter δ in square lattice reciprocal space is defined as shown in Fig. 39(d), i.e. the magnetic satellite peaks are located at $(\pi(1 \pm \delta), \pi)$ and $(\pi(1 \pm \delta), \pi)$ (We have dropped the subscript on δ in order to keep a notation which does not explicitly suggest a stripe interpretation). To give a concrete example, the quarter-filled stripes discussed above correspond to $\delta_s = 1/8$ in tetragonal notation, but to $\delta = 1/4$ in square lattice notation. In other words, interpreting incommensurate magnetic peaks in neutron scattering data in terms of a stripe picture while using the notation defined in Fig. 39(d), the real-space charge stripe distance is $1/\delta$ in units of the lattice constant.

Stripes in $La_{2-x-y}Nd_ySr_xCuO_4$ Having set the stage, let us return to a description of the work of Tranquada *et al.* [115]. Their basic idea was this: Maybe the correct way to interpret the inelastic incommensurate quartet of magnetic excitations observed in $La_{2-x}Sr_xCuO_4$ was not in terms of particle-hole excitations across a nested Fermi surface, but in terms of spin fluctuations in stripe environments such as those shown in Figs. 40(a) and (b). An independent motivation for this idea came from the so-called "1/8 conundrum". This refers to the observation, that in $La_{2-x}Ba_xCuO_4$, there is a suppression of T_c to zero in the immediate neighborhood of $x = p = 1/8$. In $La_{2-x}Sr_xCuO_4$, T_c is also suppressed near $x = p = 1/8$, but not all the way to $T = 0$ K. If the doped holes self-organize into stripe patterns, it is natural to speculate that 1/8-conundrum originates in the fact that precisely at this doping level, the stripes would be commensurate with the lattice with a charge stripe repeat distance of four lattice constants, which could in turn mean that charge stripes enjoy a particular stability. Implicit in this picture is the idea that static charge stripes compete with superconductivity.

By the magic of chemistry, in $La_{2-x-y}Nd_ySr_xCuO_4$, co-doping with neodymium on the La sites has several effects (In the original stripe picture, these effects are seen as interconnected) which should lead to increased stripe stability. Most importantly, Nd-doping causes a second low-temperature structural transition (on cooling) from the LTO structure of $La_{2-x}Sr_xCuO_4$ to a low-temperature tetragonal (LTT) structure, which appears to be essential for a well-developed $p = 1/8$-suppression of T_c (LBCO also has the LTT structure). In addition to the structural transition, co-

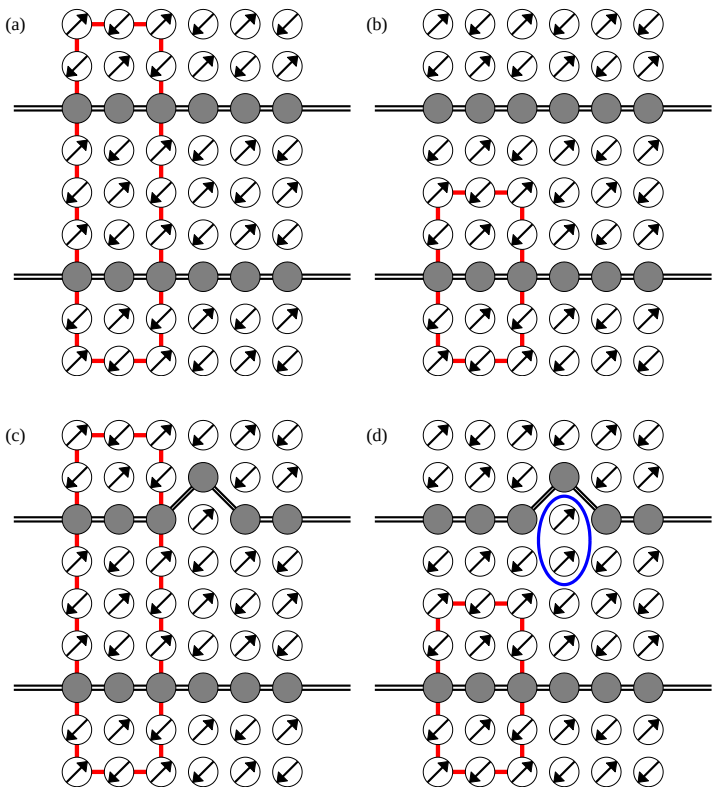

Figure 41: Meandering stripes. Panel (a) reproduces Fig. 40(a), i.e. it shows the ordered configuration for antiphase stripes, where the spin direction flips across the charge stripe, making the magnetic unit cell (red lines) twice the size of the charge unit cell. Panel (b) shows an ordered configuration in which the spin configuration on sites next to the stripe along the perpendicular in-plane direction is the same. In this case, the magnetic unit cell has the same size as the charge unit cell, which in turn is half the size of the magnetic unit cell in panel (a). In panels (c) and (d), we allow for transverse movement of the doped holes, which in the ordered phases (a) and (b) reside strictly on straight lines. For the antiphase stripe case in panel (c), there is an energy cost associated with the breaking of antiferromagnetic bonds $J\mathbf{S}_i \cdot \mathbf{S}_j$ with $J > 0$. For the in-phase stripe case in panel (d), there is still an energy cost associated with broken antiferromagnetic bonds, but also an extra cost caused by the formation of an unfavorable configuration with parallel nearest neighbor spins. As a result, transverse motion is energetically less costly for antiphase stripes, and this lowers the energy of configuration (a) relative to configuration (b).

doping $La_{2-x}Sr_xCuO_4$ with Nd causes an increased width in x of the T_c anomaly observed in LSCO, as well as an overall decrease of T_c. Thus, in the particular compound $La_{1.48}Nd_{0.4}Sr_{0.12}CuO_4$ investigated by Tranquada and coworkers, the LTO-LTT first-order transition occurs at 70 K and $T_c = 3 - 4$ K [156]. Using neutron diffraction, they observed both static spin order and static charge order as reflected by a Bragg peak pattern such as that shown in Fig. 40(c). Static incommensurate magnetic order had never been observed in any member of the LSCO family prior to this experiment, but the real key discovery was charge order, reflected in incommensurate Bragg satellites displaced from the nuclear peaks by precisely twice the distance of the incommensurate magnetic satellites from the antiferromagnetic point. These charge peaks were subsequently also observed in hard X-ray diffraction studies of LNSCO by von Zimmermann *et al.* [157].

The experimental evidence outlined above is highly suggestive of the soundness of an interpretation of the inelastic incommensurate magnetic peaks observed in superconducting LSCO as resulting from spin fluctuations in a real-space stripe picture, where the charge stripes are antiphase domain walls for the antiferromagnetic order. Further support for this idea comes from the order of the observed transitions in LNSCO. Upon cooling the sample in the LTO phase, the LTO-LTT first order transition occurs at 70 K. In the interpretation of Tranquada *et al.* , this provides a lattice pinning potential for the charge stripes which indeed become observable only at a lower temperature $\sim$ 60 K. At this temperature, there are no magnetic satellite peaks. Upon further cooling to $\sim$ 50 K, the magnetic satellite peaks become observable long before the final low-temperature superconducting transition. Since charge order precedes spin order, the stripes are said to be "charge-driven" [115, 158]. This is a very important constraint since one can argue theoretically using Landau theory [159, 94], that if the spins order first, i.e. if the transition is

"spin-driven", then charge order has to set in at the same temperature, as occurs in the spin-density wave (SDW) transition in chromium. By contrast, if the charges order first, then the spins need not order at the same temperature. Thus, the charge-driven ordering of spins and charges in LNSCO is qualitatively different from a SDW transition, which would be the weak-coupling equivalent of stripes. Moreover, the argument shows that if spin stripes exist, then charge stripes must necessarily also exist, whereas the opposite is not the case. It has been argued that if incommensurate inelastic magnetic peaks are associated with fluctuating spin stripes, then a study of their properties indirectly yields information about fluctuating charge stripes [95].

To finish our treatment of [115, 158], it should be mentioned that the magnetic order observed at low-temperatures has a correlation length of ~ 170 Å and a low-temperature ordered moment of $0.10 \pm 0.03\mu_B$, which is a significant fraction of the ordered moment $0.48 \pm 0.15\mu_B$ observed by Vaknin *et al.* in the commensurate antiferromagnet La_2CuO_{4-y}. A later comparative study of three crystals of $La_{1.6-x}Nd_{0.4}Sr_xCuO_4$ with varying Sr content x showed a clear anticorrelation between T_c and the low-temperature ordered moment in the stripe phase, i.e. clearly suggesting a competition between static charge stripes and superconductivity [156]. Further, we emphasize that in the interpretation of Tranquada and collaborators, the orthogonal set of (corresponding) incommensurate magnetic and structural peaks indicated by red and green circles in Fig. 40(c) are due to orthogonal stripes in adjacent CuO_2 planes, made favorable by the specific pattern of rotations of the CuO_6 octahedra in the LTT phase.

Stripes in nickelates The original experiment on stripe phases of LNSCO crystals had a prehistory. Before stripes were seen in cuprates, the same signatures had already been detected in the isostructural nickelates $La_2NiO_{4.125}$ and $La_{1.8}Sr_{0.2}NiO_4$. There are however important differences between the LSCO and LSNO families. First and foremost, nickelates do not become superconductors upon hole-doping their Mott-insulating antiferromagnetic parent La_2NiO_4. Second, the Ni^{2+} ions in La_2NiO_4 carry spin $S = 1$ which should suppress quantum effects relative to the $S = 1/2$ Cu^{2+} counterparts in LSCO. Third, the nickelate stripes run along $\mathbf{a} + \mathbf{b}$, i.e. along the diagonals of the NiO_2 plaquettes, an arrangement referred to as "diagonal stripes", whereas the stripe structures shown in Fig. 40 are called "vertical" stripes. Fourth, nickelate stripes are more well-defined in the sense that the low-temperature ordered moment is closer to that of the parent compound La_2NiO_4 than is the case even for LNSCO, which is the best cuprate stripe system. On the one hand, this makes it easier to probe the stripe order, but on the other hand, it probably removes the nickelates further from the limit in which the cuprates belong. Despite the differences, the structural similarity between LSCO and LSNO families, and the existence of stripe order in both is a good reason to suspect that the nickelate stripology is potentially relevant to the cuprate superconductors as well. Most relevant to our experiments in LSCO reported in the following chapter are measurements by Bourges *et al.* [160] and by Boothroyd *et al.* [161] of the high-energy spin dynamics in nickelates with well-developed stripe order. Both experiments revealed that the high-energy excitations are in fact well described by linear spin wave theory. In particular, counterpropagating spin wave branches were observed. In chapter 7 we shall see that the spin excitation spectra of underdoped and optimally doped LSCO cannot be explained by such simple theories, since we do not see any evidence of counterpropagating spin wave branches.

Mechanism for stripe formation What is the mechanism behind stripe formation? At present, stripe phases are believed to arise roughly as follows: Consider a single hole in an antiferromagnetic background. Its motion will be restricted because this would leave behind a trail of broken antiferromagnetic bonds. In the case of a finite hole density, global phase separation would solve this problem: Not only would the energy cost of broken bonds be reduced as much as possible, the holes would also gain kinetic energy by being able to move freely. However, there would be a very large Coulomb energy cost associated with such a configuration, so the system must find a compromise. It is intuitively clear that this must lead to a new length-scale, such as the interstripe spacing. Stripes are not the only possible result of this compromise (Checkerboard states would be another), but they are very common outcomes of numerical and theoretical studies, see e.g. [94].

Static incommensurate order in LSCO So far, we have discussed the evidence for stripes in what appears to be a remote, almost non-superconducting corner of the phase diagram of LNSCO systems. Following the discovery of static stripes in $La_{1.6-x}Nd_{0.4}Sr_xCuO_4$, a number of neutron

scattering experiments on $La_{2-x}Sr_xCuO_4$, starting with [162] for $x = 0.12$ have provided evidence that static spin stripe order is present in underdoped LSCO, at all doping levels between $x = 0.02$ and $x = 0.13$. However, in none of these experiments has it been possible to also detect the charge order peaks seen by Tranquada in LNSCO, or by Fujita and coworkers in systems of the chemical formula $La_{2-x-y}Ba_ySr_xCuO_4$ system [163]. Since LSCO has the LTO structure at low temperatures, the demonstrations of static spin order simultaneously disproved the conjecture of Tranquada and coworkers [115] that the LTT structure is a necessary precondition for stripe order.

Concerning the static spin stripe order and low-energy spin fluctuations in LSCO, there are two important points to make. The first concerns the evolution of the symmetry of the observed static or dynamic incommensurate signals across the phase diagram. We illustrate this in Fig. 39. As we have already mentioned, for doping levels up to $x \simeq 0.02$, LSCO is a commensurate antiferromagnet characterized by a unit cell doubling reflected in magnetic Bragg peaks at (π, π)-positions, as indicated in Fig. 39(a). For hole-dopings levels in the insulating, spin-glass regime $0.02 < x < 0.055$ there are incommensurate magnetic Bragg peaks around (π, π), but they are rotated by 45 degrees (as first reported by Wakimoto *et al.* for $x = 0.05$ [164]) relative to the stripes shown in Fig. 40 [138]. In other words, they are diagonal stripes, similar to those observed in nickelates. In Fig. 39(b) we illustrate that there are four peaks around each (π, π) position, but this is an oversimplification. In fact, Matsuda *et al.* [138] very carefully demonstrated that different low-temperature orthorhombic domains of their twinned LSCO samples each give one set of incommensurate peaks. In other words, the intrinsic signal in non-superconducting underdoped LSCO is one-dimensional. This one-dimensional signal appears to be universally found in the insulating spin-glass regime [138, 165, 166]. In the superconducting state, but very close to the phase transition to superconducting order at $x \simeq 0.055$, Fujita *et al.* [166] report a coexistence of the one-dimensional diagonal stripe order discussed above, with a quartet of "vertical stripes" of the type studied by Tranquada *et al.* in LNSCO. For higher doping levels, the signal from diagonal stripes disappears, and one is left with quartets of incommensurate peaks of the vertical type [162, 167, 168, 169], as shown in Fig. 39(c). The static incommensurate order persist all the way to $x = 0.13$. No report of static order at higher doping levels have surfaced. Instead, there are inelastic incommensurate magnetic peaks with the parallel stripe symmetry, as indicated by the change of coloration between Figs. 39(c) and (d). These fluctuations develop a spin gap when the sample becomes superconducting. It appears, that just as there are no reports of static magnetic order above $x = 0.13$, there are also no reports of spin gap behavior below $x = 0.14$.

The second point we want to make regarding the nature of the static magnetic order and low-energy fluctuations in LSCO concerns the doping evolution of the peak splitting. In a detailed study of the low-energy excitations in superconducting samples of LSCO, Yamada and coworkers showed that the incommensurability δ indexed in tetragonal notation is related to the doping level x by the relationship $\delta \simeq x$ for $0.06 \leq x \leq 0.12$ and then saturates at $\delta \simeq 0.12$ for higher doping levels. Since T_c also increases with doping in the underdoped regime, Yamada *et al.* found $\delta \propto T_c$ [116], thus showing a direct correlation between two observable properties of superconducting LSCO, and by doing so, suggesting an intimate connection between magnetism and superconductivity. However, when evaluating the importance of this observed correlation, it should be mentioned that in the overdoped regime, $\delta \sim 0.12$ even though T_c tends zero [116]. In connection with the linear relationship $\delta \propto x$ for $x \leq 0.12$, we should recall that in our discussion of the ideal case $x = 1/8$ in Fig. 40 we found the identity $\delta = x$ (In a real crystal, the intrinsic δ may become blurred by disorder in the stripe spacings). Thus, in a stripe picture, $\delta \simeq x$ means that upon hole-doping, the stripes move closer together, and nothing else happens. The saturation $\delta \sim 0.12$ seen for higher doping levels would then imply that once the charge-stripe distance has reached $1/(2\delta) \sim 4$ lattice constants − as in Figs. 40(a) and (b) − the stripes do not move closer to each other anymore. What happens to the excess doped holes is an open question. Perhaps a transition takes place between the configurations shown in Figs. 40(a) and (b). Another possibility is that the excess holes simply start filling the remaining available sites on the charge stripe. On the overdoped side of the phase diagram, recent experiments by Wakimoto *et al.* suggest that the low-energy incommensurate spin fluctuations disappear at the same doping level as superconductivity [170].

The observation of a linear relation between δ and x in underdoped superconductors is very interesting, and finds a natural explanation in the stripe picture, as we have just seen. In fact, a very similar phenomenon is found in the spin-glass regime. Because the incommensurate peak positions in this regime are rotated by 45 degrees relative to the pattern seen in the supercon-

ducting phase, we must use a different notation to describe them: The incommensurate peaks indicated by filled and open red squares in Fig. 39(b) occur at two separate corresponding sets of positions $\mathbf{Q}_{\mathrm{A}} = \pm\left(\pi(1+\epsilon/\sqrt{2}), \pi(1+\epsilon/\sqrt{2})\right)$ and $\mathbf{Q}_{\mathrm{B}} = \pm\left(\pi(1+\epsilon/\sqrt{2}), \pi(1-\epsilon/\sqrt{2})\right)$. With this convention, ϵ is defined in the same manner as δ in the sense that both equal the distance from (π, π) measured in units of π. It turns out that the incommensurabilities ϵ of the one-dimensional modulations observed in the spin-glass regime follow exactly the same law $\epsilon \propto x$ [138, 166] as reported by Yamada *et al.* [116] for the superconducting phase. Further, the incommensurabilities in the spin-glass and superconducting states are smoothly connected ($\epsilon \simeq \delta$) precisely at the phase boundary between the insulating spin glass and superconducting phases [166]. Consequently, a plot of peak-separation from (π, π) versus x is linear all the way from $x \sim 0.02$ to $x \sim 0.12$ after which it saturates. This monotonic doping dependence is suggested by red arrows in Fig. 39(b) and (c). A study of the doping dependence of the ordered magnetic moment over the same range, reveals that the moment decreases monotonically and without anomalies across the insulator-superconductor transition at $x \sim 0.055$. At $x \simeq 0.12$, the moment is enhanced and the incommensurate peaks are resolution limited in momentum space [168], indicating a special stability of the static incommensurate magnetism around this particular doping [171]. It is interesting to note, that lower energy probes such as μSR, NMR and NQR provide evidence for exactly the same trends [172], with the important quantitative difference that these techniques often lead to lower values of the magnetic ordering temperatures. This discrepancy is commonly taken to be a direct consequence of the lower frequencies probed. In fact, from this low-energy point of view, what we have called "static spin stripes" are more often viewed as glassy and disordered states, with the possible exception of the particularly stable magnetism near $x = 0.12$ [172].

Summing up, the observed linearity between the inverse period of incommensurate spin fluctuations and the hole doping x is consistent with a stripe scenario in which diagonal stripes and vertical stripes are preferred in the insulating spin glass and superconducting regimes respectively. If we assume that stripes are the cause of both static and inelastic incommensurate magnetic peaks, we can say the following: The stripes are static below $x \simeq 0.13$. Above this doping, they are replaced by stripe fluctuations with the same momentum space symmetry. These fluctuating stripe signatures disappear together with superconductivity on the overdoped side of the phase diagram near $x \simeq 0.29$. From these facts, it would appear that parallel stripes are intimately connected to superconductivity. However, it is unclear whether they are also the cause of superconductivity. On the one hand, the general anticorrelation between T_c and the ordered moment [156, 171] favors a competitive relationship, but since optimal doping occurs in the regime with no static order, one could also argue that stripes in their fluctuating form may not compete with superconductivity, and could possibly be an ingredient in the mechanism for high-temperature superconductivity.

Finally, it should be emphasized, that although we have mostly discussed stripes from the viewpoint of neutron diffraction and spectroscopy, the notion that stripes exist and are an integral part of cuprate physics in general, is supported by a wealth of other techniques. For a review, see [95]. We should also stress, that if stripes really exist, they could plausibly be held responsible for the $\mathbf{Q}_{2\mathrm{D}}$-independence of the spin gap [144], which alongside the $d_{x^2-y^2}$ symmetry of the orbital wavefunction of Cooper pairs led Lake *et al.* to speculate that spins and charges could be decoupled in the cuprates: Since stripes are one-dimensional objects, certain aspects of the physics of 1D electron gases, such as spin-charge separation could plausibly occur when 1D objects are embedded in the two-dimensional CuO_2 planes of the cuprates.

6.3.5 Probing the interplay between superconductivity and stripes

In section 6.2 we mentioned how one view of the peculiar physics observed in the pseudogap region of the phase diagram hold that these effects are caused by a competition between superconductivity and one or more additional electronic orders. The stripe states discussed above are the most obvious candidates for a competing order. Indeed we have already mentioned how T_c and the ordered moment in the stripe phase are anticorrelated: When spin stripes are well-defined, superconductivity becomes weak. Since spin stripe order requires charge stripe order by Landau theory, we can imagine that the electrons are torn between a tendency to create Cooper pairs and superconductivity and a tendency towards creating electronic nanoscale inhomogeneity in the form of charge stripes. In this section, we discuss the results of experiments designed to probe this competition. They do so by studying the effect of intense external magnetic fields on the static and dynamic incommensurate spin response. The idea underlying these experiments is that in strongly

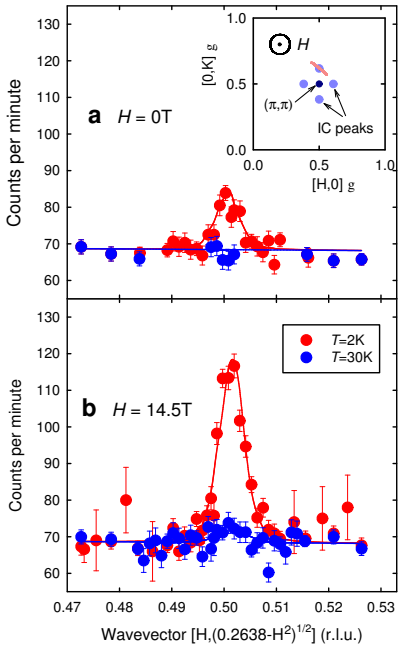

Figure 42: Diffraction signal in $La_{1.90}Sr_{0.10}CuO_4$ ($T_c = 29K$) from [122]. The scan direction is shown in the inset. (a) In zero external field, $H = 0$ T, there is a small elastic incommensurate signal at $T = 2$ K (red symbols), which vanishes upon heating to $T = 30$ K $> T_c$ (blue symbols). (b) A $H = 14.5$ T magnetic field perpendicular to the CuO_2 planes causes a large increase in the magnetic signal at $T = 2$ K, but does not induce static order above the zero-field T_c. Both the zero-field and the field-induced signals are resolution limited, implying an in-plane correlation length in excess of 400 Å.

correlated systems such as these, one may imagine that antiferromagnetic [173] or perhaps stripe fluctuations are generated when superconductivity is destroyed.

First, we describe inelastic scattering experiments. Lake *et al.* [121] studied optimally doped $La_{1.84}Sr_{0.16}CuO_4$ (In fact, the same crystals we have used for some of the time-of-flight experiments reported in the next chapter) in magnetic fields up to $H = 7.5$ T ($H_{c2} \simeq 62$ T), applied perpendicular to the CuO_2 planes. First, it was found that a 7.5 T field causes the superconducting spin gap $\Delta_s = 6.7$ meV to close. Subtracting the zero-field signal for $T \ll T_c$ from the in-field signal at the same temperature reveals that the field-induced signal is centered on an energy lower than Δ_s and confined to energies below Δ_s. In other word, the field induces fluctuations that are slower, and in fact also longer ranged in real-space, than the fluctuations seen in the normal state without a field. This behavior is consistent with a greater tendency towards stripe order. Second, the temperature dependence of the incommensurate signal at a given $\hbar\omega < \Delta$ in 7.5 T field tracks the temperature dependence of the irreversibility line in the same field. The irreversibility line is the temperature-field phase boundary separating a high-temperature superconducting region with mobile vortices and a low-temperature region in which a static vortex lattice is formed. Macroscopic superconducting phase coherence and perfect conductivity is only established below the irreversibility line. The identical temperature dependences of the in-field, subgap magnetic signal and the irreversibility line was interpreted as direct evidence for freezing of the spins residing inside the cores of vortices with radius $\xi \sim 20$ Å [121]. Subsequent experiments by other groups on slightly overdoped LSCO with $x = 0.17$ [174] and $x = 0.18$ [175], going to $H = 5$ T and $H = 10$ T respectively, confirm the results that the spin gap filling tracks the irreversibility temperature rather than T_{c2}. However, in neither study was the field induced signal confined to within the spin gap. Instead, the spectral weight redistribution is centered on the spin gap energy Δ_s [174] itself, and takes place over a significantly larger range of $\hbar\omega$ than reported in [144].

Next, we turn to diffraction studies of the effect of a magnetic field. The first report of a magnetic field effect on the elastic signal was by Katano *et al.* who saw a $\sim 50\%$ increase of the incommensurate peak in a field of 10 T in a $La_{1.90}Sr_{0.10}CuO_4$ sample which even in zero field had an anomalously suppressed $T_c = 12$ K. They did not study the field dependence of the enhancement of the signal, but the intensity enhancement suggests a competitive relation between superconductivity and the cause − stripes or Fermi surface nesting − of the incommensurate peaks in LSCO. The

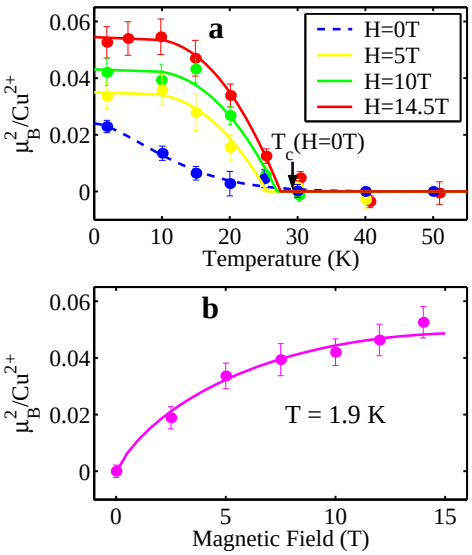

Figure 43: Temperature and field dependence of the induced magnetic moment in $La_{1.90}Sr_{0.10}CuO_4$ ($T_c = 29$ K) from [122]. (a) Temperature dependence of the squared magnetic moment associated with the measured intensities of the incommensurate profiles in Fig. 42. (a) The blue symbols represent measured zero-field intensities. The dashed blue line is a guide to the eye. The remaining symbols represent the field-induced intensities (defined as the in-field signal minus the zero-field signal) in an external field applied perpendicular to the CuO_2 planes. The solid lines through the these data are fits to mean-field theory. By normalizing to the scattering from a transverse acoustic phonon, the intensities have been converted to the corresponding ordered magnetic moment squared per Cu^{2+} ion. Within the experimental accuracy, the incommensurate peak signal drops to background level around $T_c(H = 0\text{T})$. for all values of the field. (b) Field dependence at $T = 1.9$ K of the field-induced incommensurate signal. The solid line is a fit to a theoretical expression derived by Demler, Sachdev and Zhang in a model based on competing orders [177], as described in the text.

field dependence of the signal enhancement, crucial in comparing experiment to various theories, was determined by Lake and coworkers [122] (which includes the present author. See also [176]) at a temperature of 2 K and magnetic fields as high as 14.5 T in underdoped $La_{1.90}Sr_{0.10}CuO_4$. Figure 42 displays the results of constant-$2\theta_S$ scans through a single incommensurate peak above and below T_c in zero field (panel (a)) and with $H = 14.5$ T (panel (b)). Subtracting the zero-field static signal from the in-field signal reveals the field-induced signal. The field dependence of the induced signal is proportional to $m^2\,(H/H_{c2})\ln(H_{c2}/H)$ with $m^2 = 0.12\mu_B^2$ per Cu^{2+}, and $H_{c2} = 45$ T. This form was suggested by Demler, Sachdev and Zhang in a model based on competing superconducting and stripe/spin density wave orders [177]. The temperature and field-dependences of the field-induced signal are displayed in Figs. 43(a) and (b). The data suggest, that the normal state which would have occurred in the absence of superconductivity is not a normal metal with a Fermi surface, but an insulating stripe phase. This interpretation of the data is supported by high-field resistivity measurements by Bobinger *et al.* showing an insulator-to-metal transition in the field-induced normal states around optimal doping [178]. In the underdoped regime, the resistivity shows an insulating upturn at low temperatures, consistent with charge localization. More generally, the data from [122] support a view of the underdoped cuprates as dominated by competing electronic (stripe and superconducting) orders. Another very interesting observation brought to light by [122] is that the field induced signal has exactly the same $\mathbf{Q}_{2D}$-space symmetry as the zero-field signal, but has a peak width so narrow in $\mathbf{Q}_{2D}$ that the correlated regions of what in the most likely interpretation is stripe order, must be greater than 400 Å . This correlation length is in turn significantly greater than the vortex cores size $\xi \sim 20$ Å and also greater than the ~ 130 Å distance between the vortices at 14.5 T. Thus, the data suggest that the incommensurate field-induced signal is not, as was suggested in the earliest SO(5) models [173], confined to the vortex cores, but most likely precipitates the order in a much larger regions centered on the vortices.

The idea that stripe order is created around the vortices received direct support from STM measurements by Hoffman *et al.* , who found modulations in the local density of electronic states in extended halos around the vortices. The modulation period was close to four lattice constants, as would be expected if the field-induced signal was due to stripes with a magnetic repeat distance

of eight lattice constants. To bring forth these structures, Hoffman and coworkers subtracted the signal from a large zero-magnetic-field field-of-view from the in-field image of the same region [117]. Although suggestive, interpreting the STM results in terms of stripes is not wholly unproblematic: Since STM is sensitive only to the charges in the topmost CuO_2 layers (typically of $Bi_2Sr_2CaCu_2O_{8+x}$), stripe order in this single layer should break the symmetry of rotations by $\pi/2$. Yet, to the best of our knowledge such broken symmetries have not been seen either in a field or without a field. In fact, recent STM data give direct evidence of checkerboard order in lightly hole-doped $Ca_{2-x}Na_xCuO_2Cl_2$.

Following the experiments of Lake *et al.* , Khaykovich and coworkers studied the interplay of superconductivity and stripe order in excess oxygen doped La_2CuO_{4+y} [123, 179] by applying intense magnetic fields perpendicular to the CuO_2 planes. Their results are very similar to those reported in [122], and support the same conclusion, namely a repulsive coupling between stripe/SDW order and superconducting order on the level of Ginzburg-Landau theory. Several other neutron scattering studies of the effect of a magnetic field on static magnetic order in cuprates have been performed, but here we want to mention another type of experiment. Excess oxygen doped La_2CuO_{4+y} has the highest T_c (42 K) in the LSCO family. This is thought to be related to the staging behavior [180] these compounds exhibit as a function of y: The excess oxygens form an ordered lattice in the interstitial regions of the crystal. The degree of quenched dopant-disorder in this lattice is believed to lead to variations in T_c. By controlling the cooling rate from high-temperatures, the level of interstitial oxygen disorder can be controlled. Lee *et al.* used this to their advantage by comparing the values of T_c as well as the SDW/stripe intensities in the same sample prepared with varying oxygen disorder [181]. First, the sample was slowly cooled to obtain a low-disorder, high-T_c sample, and the incommensurate intensities were recorded. Then, the sample was heated to room temperature, before being quench-cooled to low temperatures again. This gives a sample with a high degree of disorder, and a lower (by ~ 5 K) superconducting transition temperature. Remarkably, the incommensurate intensities then increase by an amount comparable to the effect of a 7.5 T field seen by Khaykovich *et al.* [123].

Having presented evidence that stripes are realities in the $La_{2-x}Sr_xCuO_4$ family, and having mentioned that superconductivity can sometimes develop around a quantum critical point [112], we should not neglect to mention a polarized an unpolarized neutron scattering experiment by Aeppli *et al.* , which demonstrated E/T-scaling of the normal-state, low-energy incommensurate fluctuations in near optimally doped $La_{1.86}Sr_{0.14}CuO_4$ [114]. E/T-scaling being a generally expected property near quantum critical points, in effect these data are indirect evidence that a quantum critical point connected to stripe order is lurking somewhere in a generalized phase diagram of LSCO, incorporating co-doping axes, a magnetic field axis etc. Thus, the alleged critical point may very well not be easily accessible, but according to the general theory of quantum critical points, its sphere of influence can be very large anyway, and is a plausible cause for the many anomalous properties of the cuprates.

In this subsection we have provided arguments in favor of models in which stripe- or spin-density-wave order compete with superconductivity. To our knowledge, models in which the incommensurate magnetic peaks seen by neutron scattering in LSCO are derived from dynamic nesting have yet to come up with plausible explanations for the observations discussed above. To sum up, the general picture seems to be that when the stripe order is strong, the superconducting order is correspondingly weak.

6.3.6 The excitation spectrum of $YBa_2Cu_3O_{6+y}$

Having spent a lot of space on the order and excitations in the $La_{2-x}Sr_xCuO_4$ family of high-temperature superconductors, we shall now move on to describe what has been observed in superconductors belonging to the $YBa_2Cu_3O_{6+y}$ family. We want to do this because in chapter 7 we shall present data in support of the notion that the spin excitation spectra in LSCO and YBCO are in fact quite similar. Given that both systems are built from square CuO_2 planes and derive from insulating antiferromagnets with nearest-neighbor exchange constants J of the same order of magnitude, this is exactly what one would naively expect, but in fact, the similarities in the excitation spectra of the two systems have only recently begun to emerge. Of course, this does not invalidate the research done prior to the discovery of these similarities, and indeed, if the excitation spectrum of YBCO bears qualitative resemblance to that of LSCO, any feature in the YBCO spectrum is potentially relevant to LSCO as well. Therefore, a description of the excitation

spectrum of YBCO can serve as a guideline when interpreting LSCO data, and as such warrants exposition. One the other hand, it is the properties of LSCO that are of greatest interest to us, so our discussion of YBCO will be shorter than that of LSCO.

While incommensurate spin fluctuations are the most widely studied features in LSCO, the focus of interest in YBCO has for many years been the so-called "resonance mode" or simply "resonance". The resonance was discovered in 1991 by Rossat-Mignod and collaborators in optimally doped $YBa_2Cu_3O_{6.92}$ [182]. In the interest of a coherent presentation, let us anneal away some of the discrepancies between early experiments and present a popular contemporary view (based on [183]) of the peak identified in [182], before stepping back to discuss a small number of key experiments: At optimal doping, the resonance feature is centered on $E_{\rm res} = 41$ meV and on the commensurate wavevector $\mathbf{Q}_{\rm 2D} = (\pi, \pi)$ where it becomes visible when the sample is cooled below T_c. It occurs in the acoustic channel of Eq. (73) only, and is sharp in $\hbar\omega$ but broad in $\mathbf{Q}_{\rm 2D}$ with a corresponding in-plane correlation length of ~ 15 Å [183].

The magnetic origin of the resonance below T_c was proven by Mook *et al.* [184], although the conclusions drawn were later refined by Fong *et al.* [185]. Mook and coworkers used polarized neutron scattering to distinguish the pristine signatures of the magnetic spectrum in general and those of the resonance in particular from coherent and incoherent inelastic scattering processes involving nuclei. They found a sharp and intense resonance below T_c preceded for $T > T_c$ by a broader and less intense peak-like feature. Fong and collaborators took advantage of the differing dependences on the modulus of $\mathbf{Q}$ of the magnetic and nuclear scattering cross-sections to verify the magnetic origin of the signal below T_c and to argue that the precursor peak above T_c reported by Mook *et al.* was in fact a phonon.

Subsequent experiments by Dai *et al.* [186], Fong *et al.* [187] and Bourges *et al.* [188] reported resonance modes seen in crystals with varying degrees of underdoping. In the underdoped regime, $E_{\rm res}$ appears to be proportional to T_c, but on approaching optimal doping, the linearity breaks down and $E_{\rm res}$ becomes insensitive to changes in T_c [183]. In the linear regime, Bourges *et al.* reported a constant ratio $E_{\rm res}/k_BT_c = 4.9 \pm 0.2$.

Even more interestingly, in underdoped YBCO, the doping dependence of the resonance onset temperature appears to track the doping dependence of the pseudogap temperature T^* determined by transport and NMR measurements [189, 183]: As a function of decreasing hole content, the temperature dependence of the spectral weight at (π, π) and $E_{\rm res}$ shows a larger and larger pre-transitional regime below T^*, before (for all doping levels) giving way to a more rapid intensity increase on cooling below T_c. At optimal doping, Dai *et al.* find $T^* = T_c$ [189] and the resonance only occurs below T_c as originally reported by Rossat-Mignod and collaborators. By evaluating the mean-squared fluctuating moment $\langle m^2_{\rm res}\rangle = (3/(2\pi)) \int d(\hbar\omega)\, \chi''_{\rm res}(\omega)\, (n(\omega)+1)$ associated with the resonance at all temperatures, Dai *et al.* demonstrated a direct correlation between the electronic contribution $C_{\rm el}(T)$ to the specific heat and the derivative $d\langle m^2_{\rm res}\rangle/dT$. In other words, the more gradual entropy release in the underdoped regime, compared to optimal doping, is reflected in the more gradual intensity change of the resonance. This shows that the exchange energy of the resonance is approximately sufficient to account for the pseudogap anomalies in the electronic specific heat across the phase diagram of YBCO [189] and may account for the condensation energy E_C (given by the difference $(F_{\rm n} - F_{\rm sc})_{T=0}$ between the extrapolated $T = 0$ K Helmholtz free energy of the normal state and the free energy of the superconducting state) gained by the system when it goes superconducting [190]. In an experiment following the same line of thought, Dai *et al.* subsequently showed that a 6.8 T magnetic field applied along the crystallographic **c**-axis of an underdoped $YBa_2Cu_3O_{6.6}$ crystal (with a corresponding effective hole-doping $p \simeq 0.1$), causes the resonance to loose intensity. The in-field temperature dependence of the resonance intensity tracks that of the in-field electronic specific heat [191].

In the underdoped regime, the intensities of the scattering at energies immediately above and below the resonance decrease upon entering the superconducting state [186, 187], reflecting a narrowing in energy of the resonance below T_c [189], but also the opening of a spin gap Δ_s on cooling [183]. Dai *et al.* reported the relation $\Delta_s/k_BT_c \simeq 3.8$, valid for all but the lowest doping levels. For comparison, $\Delta_s/k_BT_c \simeq 2$ for the optimally doped LSCO samples investigated in [144]. Recently, a very thorough study of underdoped $YBa_2Cu_3O_{6.5}$, specially treated to achieve minimal structural disorder from the oxygenation of the Cu-O chain layers, showed that the opening of the spin gap coincides with the superconducting transition temperature T_c [99]. The spin gap in this so-called ortho-II YBCO manifests itself as a suppression but not an elimination of the spectral weight below an energy Δ_s. Most importantly, the spectral weight which is suppressed at low energies

upon entering the superconducting state is within errors identical to the net weight gained by the resonant mode in the same temperature interval. In other words, the origin of the resonance, according to Stock *et al.* , is simply the transfer of spectral weight from energies below the spin gap to energies above the spin gap [99].

Since the onset temperature of the resonance appears to be the pseudogap temperature T^* [189] and since its position scales with T_c, it is clear that its very existence is intimately tied in with superconductivity, Cooper pair creation, and the pseudogap [189, 191]. However, it is very unclear exactly how. In the SO(5) theory of superconductivity [192], the increase of antiferromagnetic correlations reflected by the resonance is viewed as the mechanism by which high-T_c superconductors find a way to lower their energy relative to the normal state [193]. As discussed above, this idea finds support in the work of Dai *et al.* [189]. Whether this particular theory is right or not, it is natural that significant effort has gone into searches for resonant modes in cuprate families other than YBCO, for if a resonance is not present in all cuprate high-T_c materials, it can have nothing to do with the elusive mechanism lying at the root of the problem. Such searches were rewarded in 1999 when Fong and coworkers found a resonant mode in the bilayer superconductor $Bi_2Sr_2CaCu_2O_{8+x}$ [194] − a favorite of surface sensitive techniques such as ARPES and STM because it cleaves easily and gives clean surfaces (However, because it cleaves so easily it is also difficult to grow the large single-crystals necessary for inelastic neutron scattering). The resonance found in Bi2212 (T_c = 91 K for the near optimally doped sample studied) has very similar characteristic to the YBCO resonance at similar hole-doping p: It occurs at $\mathbf{Q}_{2D} = (\pi, \pi)$ and only in the acoustic scattering channel. It is centered on $E_{res} = 43$ meV but is much broader in both energy and in-plane momentum than the resonance in optimally doped YBCO. Thus, the total integrated resonance intensity is also much larger in Bi2212 than in YBCO. Further, the appearance of the resonance coincides with T_c to within errors, and examination of its intensity at symmetry equivalent points in reciprocal space is consistent with the copper form factor variation, thus supporting a magnetic origin [194]. Following the discovery of a Bi2212 resonance, it has also been seen in overdoped Bi2212 by He and coworkers who report that E_{res} in Bi2212 scales with T_c ($E_{res}/k_BT_c \simeq 5.4$) rather than with p [195]. It has also been found in strongly underdoped Bi2212 by Mesot *et al.* [196] who find that the neutron resonance energy compares favorably with ARPES experiments in which the difference between the "peak" energy and the "hump" energy in the peak-dip-hump structures found for wavevectors near $(\pi, 0)$, is interpreted as an independent measure of the energy of a collective mode with wavevector (π, π) which interacts with the electrons.

While the discovery of a resonant mode in Bi2212 proved unambiguously that the resonance is not just a peculiarity relevant only to YBCO, the possibility still existed that it was caused by the bilayer structure shared by $Bi_2Sr_2CaCu_2O_{8+x}$ and $YBa_2Cu_3O_{6+y}$. In particular, no commensurate resonance has ever been reported in $La_{2-x}Sr_xCuO_4$, the only other cuprate which has been studied as hard as YBCO. Fong *et al.* speculated, that this is due to a higher degree of structural disorder in LSCO. The logical possibility that the resonance is confined to bilayer cuprates was thrown aside following the discovery (through truly heroic efforts in the alignment phase of the experiment) by He *et al.* of a resonance in the single layer cuprate $Tl_2Ba_2CuO_{6+\delta}$ which has a transition temperature of $\sim 92.5 \pm 2$ K [197]. The signatures of the $Tl_2Ba_2CuO_{6+\delta}$ resonance follow the now familiar pattern: It is centered on $\mathbf{Q}_{2D} = (\pi, \pi)$ and comes into existence at T_c to within the experimental precision. The mode energy is $E_{res} \simeq 47$ meV, slightly higher than in YBCO and Bi2212.

So far we have discussed the resonance and its characteristic as if it were the only feature in the cuprate excitation spectrum. In fact, the weight of the resonance in $YBa_2Cu_3O_{6.6}$ accounts only $\sim 1\%$ of the total moment squared $S(S+1)$ per Cu residing in a CuO_2 layer [131] when both acoustic and optic excitations are taken into account. In $YBa_2Cu_3O_{6.5}$, the latter retain a gap of $\Delta_{op} \sim 53$ meV at low temperatures [188], similar in magnitude to the optic gap 74 ± 5 meV observed by Hayden *et al.* in antiferromagnetic $YBa_2Cu_3O_{6.15}$ [134]. Until recently, the optic and acoustic spectra were thought to consist predominantly of continuum contributions [198], on top of which the acoustic resonance is added. However, in recent years it has become clear, that these continua have their own internal structure. For example, it now appears that in addition to the acoustic resonance, there is also a resonance in the optical channel [199], but the most surprising new insights have been gained in the acoustic channel as we shall see.

This new development begun with the discovery by Dai *et al.* [200] and Mook *et al.* [201] in $YBa_2Cu_3O_{6.6}$ of an incommensurate quartet of peaks with the same $\mathbf{Q}_{2D}$-symmetry as those

seen in LSCO [201]. These incommensurate peaks were found in $\chi''(\mathbf{Q}_{2D},\omega)$ at energies above the spin gap Δ_s, but below the resonance energy. Not only do these incommensurate peaks lie at $(\pi(1\pm\delta),\pi)$ and $(\pi,\pi(1\pm\delta))$, the value of the incommensurability parameter $\delta = 0.21\pm0.02$ is also identical to δ characterizing the low-energy incommensurate spin fluctuations in $La_{2-x}Sr_xCuO_4$ at a comparable level of hole doping, $x = p = 0.10$ [201]. Even the incommensurate peak widths and $\mathbf{Q}_{2D}$ integrated intensities are similar in magnitude. The significance of these observations is obvious. They point to a larger degree of universality between the spin fluctuations of the LSCO and YBCO families than had previously been believed to exist, thereby strengthening the case for a magnetic mediated pairing common to all cuprate families. It also begs the question whether stripes exist in YBCO, and if so, what their relation to the resonance mode is. Alternatively, if stripes do not exist, how are the incommensurate peaks produced?

Subsequently the incommensurate structure below the resonance has been confirmed in several YBCO samples across the phase diagram [202, 203, 204, 183, 99]. In all of these studies, the symmetry of the subresonance incommensurate pattern is the same as reported by Mook an coworkers [201]. However, there are obviously more twists to the story. First of all, plotting the incommensurability parameter δ versus hole doping p as did Yamada for the low-energy incommensurate peaks in LSCO [116], Dai *et al.* found a linear relationship $\delta \propto p$ for underdoped samples, whereas δ saturates at approximately 0.2 for $p \geq 0.10$ [183], corresponding − in a stripe picture − to a real-space charge stripe distance of $1/\delta = 5$ lattice constants. Thus, although there are clear qualitatively similarities to the case of LSCO, there is a small quantitative difference in the saturation value of δ which in LSCO is closer to 0.25 corresponding to a charge stripe distance of four lattice constants.

The second point to be made regarding the subresonance incommensurate peaks in YBCO superconductors is that they have been demonstrated by Bourges and coworkers to evolve continuously as a function of $\mathbf{Q}_{2D}$ and $\hbar\omega$ into the resonance at higher energies [203]. Therefore, the incommensurate peaks and the resonance are one and the same. In the original publication, Bourges *et al.* claimed that the incommensurate peaks in their near-optimally doped $YBa_2Cu_3O_{6.85}$ sample vanish above T_c giving way to a response function $\chi''_{ac}(\mathbf{Q}_{2D},\omega)$ peaked at (π,π) at all energy transfers between 25 and 50 meV ($E_{res} = 41$ meV). Subsequent experiments on the same sample by Bourges, Rønnow and coworkers found that the incommensurate peaks persist to temperatures above T_c [56], whereas Dai *et al.* are of the opinion that the intensities of the incommensurate peaks track the temperature dependence of the resonance as a function of doping, i.e. existing above T_c in underdoped samples in a pretransitional regime which shrinks to zero as optimal doping is approached [183].

Finally, a third point is the momentum dependence of $\chi''_{ac}(\mathbf{Q}_{2D},\omega)$ above the resonance. Arai and coworkers presented evidence that the response at energies above the commensurate resonance in underdoped $YBa_2Cu_3O_{6.7}$ becomes incommensurate again, with the same symmetry as the incommensurate peaks observed for $\hbar\omega < E_{res}$ [202]. The incommensurability δ above the resonance was found to be an increasing function of $\hbar\omega$, but the peaks are simultaneously becoming broader and are much less intense than those below E_{res}. For completeness, it should also be mentioned that Arai *et al.* claimed that at the resonance energy, the single peak observed could also consist of two separate peaks, overlapping only due to finite energy resolution. In other words, this would imply that there is no resonance, but only incommensurate peaks.

How should these observations be understood? In terms of fluctuating stripes or perhaps in terms of dynamic nesting? Independent evidence for the former comes from neutron scattering measurements by Mook, Dai and Doğan of static charge order in highly underdoped $YBa_2Cu_3O_{6.35}$ [205]. The charge order peaks they observed have a modulation vector δ_c which within errors is identical to $2\delta_s$ for the incommensurate inelastic magnetic peaks observed in the same compound, as expected in a stripe picture. Further, the charge stripe order persists to room temperature [205]. A second piece of evidence favoring stripes comes from direct observations of one-dimensionality of the magnetic peaks: Using a detwinned sample of underdoped, orthorhombic $YBa_2Cu_3O_{6.6}$ in which the domain size ratios are known, Mook *et al.* were able to establish that the quartet of incommensurate peaks belong to separate twin domains [206]. The fluctuation spectrum of each twin domain contains only two incommensurate peaks.

We have here given a lengthy, but not exhaustive review of the fluctuation spectra of cuprate superconductors. In general, issues concerning the full spectrum of spin fluctuations $\chi''(\mathbf{Q}_{2D},\omega)$ have been postponed. In particular, this includes a number of very recent studies [207, 151, 208, 209] probing the spin excitation spectra over a large range of energy transfers using time-of-flight

spectrometers, but also older some older work [210, 150]. These studies can be directly compared to our experimental results, and fit better in chapter 7, although some will be mentioned briefly in the next section.

6.4 Theories for the spin fluctuation spectra of cuprate superconductors

In this section, we shall discuss the basics of two classes of models designed to explain the spin fluctuation spectra of the cuprates. The division into two "classes" of models is certainly an oversimplification, but is relevant in the sense that there is certainly a distinctive difference in the foundation from which they start. One class, which we could term "stripe models" assume the existence of ordered real-space structures such as stripes, whereas in the second class, which we term "dynamic nesting" models, the ordered structure exists in momentum space, in the form of well-defined Fermi-surfaces, gap-functions etc. We will begin by describing the dynamic nesting models.

6.4.1 Dynamic nesting models

A quantitative treatment of neutron scattering from the viewpoint of Fermi surface based models starts from an electronic dispersion $\epsilon_{\mathbf{k}}$, measured from the Fermi level, and a superconducting gap function $\Delta_{\mathbf{k}}$. These two quantities combine in the quasiparticle energy $E_{\mathbf{k}}$ given by $E_{\mathbf{k}} = (\epsilon_{\mathbf{k}}^2 + \Delta_{\mathbf{k}}^2)^{1/2}$. Knowing these quantities, it is possible to perform a direct computation of the noninteracting susceptibility $\chi_0(\mathbf{q},\omega)$ using an expression from BCS theory, see e.g. [211, 212]

$$\chi_0(\mathbf{q},\omega) = \chi_0^{(\mathrm{hh})}(\mathbf{q},\omega) + \chi_0^{(\mathrm{pp})}(\mathbf{q},\omega) + \chi_0^{(\mathrm{ph})}(\mathbf{q},\omega) \tag{75}$$

$$\chi_0^{(\mathrm{hh})}(\mathbf{q},\omega) = \sum_{\mathbf{k}} \frac{1}{4}\Big(1 - \frac{\epsilon_{\mathbf{k}}\epsilon_{\mathbf{k+q}} + \Delta_{\mathbf{k}}\Delta_{\mathbf{k+q}}}{E_{\mathbf{k}}E_{\mathbf{k+q}}}\Big)\frac{1 - f(E_{\mathbf{k+q}}) - f(E_{\mathbf{k}})}{\omega + (E_{\mathbf{k+q}} + E_{\mathbf{k}}) + i\delta} \tag{76}$$

$$\chi_0^{(\mathrm{pp})}(\mathbf{q},\omega) = \sum_{\mathbf{k}} \frac{1}{4}\Big(1 - \frac{\epsilon_{\mathbf{k}}\epsilon_{\mathbf{k+q}} + \Delta_{\mathbf{k}}\Delta_{\mathbf{k+q}}}{E_{\mathbf{k}}E_{\mathbf{k+q}}}\Big)\frac{f(E_{\mathbf{k+q}}) + f(E_{\mathbf{k}}) - 1}{\omega - (E_{\mathbf{k+q}} + E_{\mathbf{k}}) + i\delta}. \tag{77}$$

$$\chi_0^{(\mathrm{ph})}(\mathbf{q},\omega) = \sum_{\mathbf{k}} \frac{1}{2}\Big(1 + \frac{\epsilon_{\mathbf{k}}\epsilon_{\mathbf{k+q}} + \Delta_{\mathbf{k}}\Delta_{\mathbf{k+q}}}{E_{\mathbf{k}}E_{\mathbf{k+q}}}\Big)\frac{f(E_{\mathbf{k+q}}) - f(E_{\mathbf{k}})}{\omega - (E_{\mathbf{k+q}} - E_{\mathbf{k}}) + i\delta} \tag{78}$$

The function f is the distribution function for fermions $f(E) = 1/(\exp(E/k_BT) + 1)$, and the infinitesimal complex quantity $i\delta$ ensures the convergence of the summations. The three terms (76)-(78) correspond to quasiparticle pair annihilation, quasiparticle pair creation and quasiparticle scattering respectively. Other colloquial names for the three susceptibility components $\chi_0^{(\mathrm{hh})}(\mathbf{q},\omega)$, $\chi_0^{(\mathrm{pp})}(\mathbf{q},\omega)$ and $\chi_0^{(\mathrm{ph})}(\mathbf{q},\omega)$ are the (quasi)hole-hole, particle-particle and particle-hole channels, hence the superscripts. The factors appearing inside parenthesis are so-called coherence factors, which reflect the mixing in BCS theory of normal state particles and holes. Note in passing the structural similarity of Eqs. (75)-(78) to Eqs. (133)-(136) for the inelastic part of the longitudinal scattering cross-section calculated in the linear spin wave approximation. The similarity immediately suggests that $\chi_0(\mathbf{q},\omega)$ will contain continuum contributions.

In the absence of a gap, $\Delta_{\mathbf{k}} = 0$, Eq. (75) reduces to the ordinary Lindhard function

$$\chi_0(\mathbf{q},\omega) = \sum_{\mathbf{k}} \frac{f(\epsilon_{\mathbf{k+q}}) - f(\epsilon_{\mathbf{k}})}{\omega - (\epsilon_{\mathbf{k+q}} - \epsilon_{\mathbf{k}}) + i\delta} \tag{79}$$

from which the coherence factors have vanished since there is no longer particle-hole mixing. In particular, neutrons are insensitive to particle-particle and hole-hole processes above T_c

The superconducting and normal state susceptibilities $\chi_0(\mathbf{q},\omega)$ in Eqs. (75) and (79) are non-interacting susceptibilities. To obtain the susceptibilities with which to compare neutron scattering data, it may be necessary to use approximations such as the random phase approximation (RPA)

$$\chi(\mathbf{q},\omega) = \frac{\chi_0(\mathbf{q},\omega)}{1 - U(\mathbf{q})\chi_0(\mathbf{q},\omega)} \tag{80}$$

where $U(\mathbf{q})$ describes residual interactions between the quasiparticles. In the case we are interested in, $U(\mathbf{q})$ would typically be of magnetic origin. Finally, with or without residual interactions, neutron scattering is directly sensitive only to the imaginary component of the susceptibility (80),

through the fluctuation-dissipation theorem Eq. (17). We can clearly see that in models of this type, the details of the neutron scattering cross section arise as a consequence of the combined influences of the specific shape of the Fermi surface and the symmetry of the gap (through the non-interacting susceptibility χ_0) and residual interactions, typically the strong Cu-Cu exchange interactions (through $U(\mathbf{q})$).

The assumptions underlying the above equations is of course, that well-defined quasiparticles exist. Angle resolved photoemission spectroscopy tells us that this is always the case below T_c where the single-particle spectral function $A(\mathbf{k},\omega)$, to which ARPES is sensitive, displays a peak close to the Fermi surface. In the overdoped regime, good quasiparticles also appear to exist in the normal state, but for underdoped and optimally doped cuprates this is not so. At the very least, there are increasing conceptual problems in applying Eq. (79) as the doping level is reduced from the overdoped side of the phase diagram.

Models such as the above have been successful, at least qualitatively, in reproducing the YBCO resonance [213] and low-energy incommensurate spin fluctuations in LSCO [211] separately, but following the discovery of incommensurate fluctuations in YBCO below the resonance, the experimental constraints on any such model have become more severe, because the resonance and incommensurate peaks must be continuously connected. Moreover, it should be possible to compare model calculations with neutron scattering data in absolute units once $\chi''(\mathbf{q},\omega)$ has been computed. Finally, previous practice has shown that in order to obtain agreement with experiment, the effects of instrumental resolution may have to be included explicitly [211].

As a specific example of the BCS-RPA approach applied to YBCO, we shall discuss the work of Norman [212, 214], who rather than taking the dispersion $\epsilon_{\mathbf{k}}$ from some microscopic calculation, fits real ARPES data to a tight-binding dispersion. Using $\epsilon_{\mathbf{k}}$ derived in this manner as well as an experimentally determined gap function $\Delta_{\mathbf{k}}$ of $\mathrm{d}_{x^2-y^2}$ symmetry, $\chi_0(\mathbf{q},\omega)$ is computed from Eq. (78). This noninteracting susceptibility is however found to be numerically too small to explain the experimental observations in YBCO. Thus, the RPA is used to obtain the interacting susceptibility. Two functional forms are tried out: A "Hubbard-like" approximation $U(\mathbf{q}) = J$ and a "tJ-like" approximation $U(\mathbf{q}) = -1/2J(\cos(q_x a)+\cos(q_y a))$ equal to $J(\mathbf{q})$, the Fourier transform of the nearest neighbor magnetic interaction strengths. The game then is to see which $U(\mathbf{q})$ yields agreement with the incommensurate and commensurate structures seen in YBCO near (π,π). To obtain realistic descriptions of the data, J appearing in both models for $U(\mathbf{q})$ is adjusted to force the denominator of (80) to be close to zero at (π,π). Moreover, the parameters of the tight-binding dispersion were adjusted slightly to give Fermi surfaces with varying degrees of flatness in the nodal [11] direction. Norman finds that indeed it is possible to obtain a $\chi''(\mathbf{q},\omega)$ which agrees with the experimental observations [202], i.e. incommensurate responses above and below the resonance energy E_{res} with $\delta(\hbar\omega > E_{\mathrm{res}}) > \delta(\hbar\omega < E_{\mathrm{res}})$.

While the results found by Norman seem to describe the experimental observations in YBCO rather well we note that they are highly dependent on the exact Fermi surface shape. Moreover, the effects of all interactions are effectively accounted for already in the tight binding fits to experimental ARPES data, which probe natures own diagonalization of the true microscopic Hamiltonian − whatever it might be. Viewed in this way, the use of the RPA appears unjustified. However, a more fair attitude to [212, 214], is to regard the results as proofs of principle that to explain the experimental observations it is not strictly necessary to invoke collective magnetic excitations such as spin-waves stemming from the commensurate antiferromagnetic regions between charge stripes.

Other theoreticians have used ideas similar to the above to compute the susceptibility, i.e. first computing χ_0 under various assumptions (a d-wave superconducting gap function being a common assumption), and subsequently incorporating strong antiferromagnetic correlations through Eq. (80), or analogous expressions [215, 216, 217] to obtain an interacting susceptibility χ, the imaginary part of which contains low-energy incommensurate peaks connected continuously to a commensurate resonance. Typically, the resonance is interpreted as a collective $S = 1$ mode, consisting of a particle-hole pair, bound together by an attractive exchange interaction. This bound state exists only at energies below the lower energy limit of a continuum of unbound particle-hole excitations (The lower limit of the continuum is $\mathbf{Q}_{2\mathrm{D}}$-dependent in a manner reflecting the $\mathrm{d}_{x^2-y^2}$ symmetry of the superconducting gap). This is the case in [216] where the lowest energy incommensurate peaks are of particle-hole nature, but change their character with increasing energy as they merge with the resonance, as sketched in Fig. 44(a).

The theories discussed above all employ the RPA. For completeness it should be mentioned that Abrikosov has argued [218] that the use of the RPA is unjustified and that the resonance

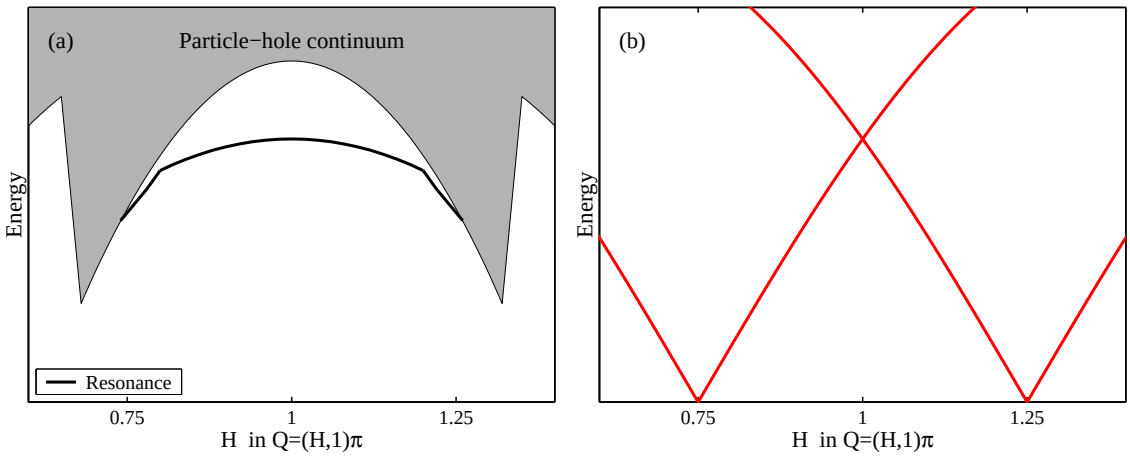

Figure 44: Schematic views on incommensurate and commensurate spin responses. (a) Itinerant model. Both incommensurate and commensurate peaks are seen as parts of the same collective $S = 1$ mode, pulled below a continuum of particle-hole excitations by an attractive interaction, see e.g. [216]. (b) Localized model. Conventional spin wave excitations emerging from incommensurate positions $(\pi(1\pm\delta), \pi)$ and $(\pi, \pi(1\pm\delta))$ (only the former two are seen for momenta $(H, 1)\pi$) cross at (π, π) thereby yielding an intensity increase at this isolated point, see e.g. [219]. In stripe-based models, the 1D nature of the problem implies, that there are two rather than four incommensurate peaks to be accounted for.

and off-resonance incommensurability can be explained solely from a realistic parameterization of the bandstructure near $(\pi, 0)$ where ARPES has reported the existence of a flat band (extended saddle point). In this approach, the resonance at (π, π) simply reflects electronic transitions from a saddle point near $(\pi, 0)$ to another saddle point near e.g. $(0, -\pi)$.

6.4.2 Stripe models

We turn now to a description of spin-based models, starting with a simplistic account of how one can get a commensurate resonance. This can happen simply by having spin wave branches (possibly gapped) emerge from the incommensurate positions $(\pi(1 \pm \delta), \pi)$ and $(\pi, \pi(1 \pm \delta))$. At the high-symmetry point (π, π), there will be an intensity increase due to the crossing of the branches [219], see Fig. 44(b). According to such a picture, it should be possible at the lowest energies to observe spin excitations dispersing in the direction away from (π, π). Batista, Ortiz and Balatsky consider various concrete models in which the spin state is incommensurate (in the sense that the lowest energy spin excitations occur at incommensurate wavevectors) to predict general consequences of such a state. For example, if δ_0 denotes the incommensurability at the lowest energies, then one should find $E_{\rm res} \propto \delta_0$ for small δ_0. For $La_{1.90}Sr_{0.10}CuO_4$ a commensurate resonance is predicted at $14 - 16$ meV, but it is suggested that disorder may wash it out [219]. It should be noted that in none of the concrete incommensurate models treated in [219] do charges or superconductivity play any significant role.

Next, we should discuss models [220, 221] in which the spin wave excitations from ordered stripe phases of the type discussed in section 6.3.4 are investigated. These models are very interesting since in the nickelates, which are the best characterized systems known to display static spin stripe order, the high-energy spin excitations appear to be well-described by spin wave theory [160, 161]. In particular, spin waves propagating both towards (π, π) and away from (π, π) are seen. These observations contrast sharply with those of LSCO, where stripe order is presumably less stable and where spin excitations dispersing away from (π, π) are not seen (see [151] and the results presented in the next chapter). Both stripe-model calculations [220, 221] consider vertical as well as diagonal stripes. Carlson, Yao and Campbell [221] calculate the spin wave spectra for both site-centered and bond-centered stripes whereas Krüger and Scheidl [220] consider only site-centered stripes. In both cases, the idea is simply to compute the full (linear) spin wave spectrum for different stripe unit cells and inter- and intra stripe couplings.

Both papers find that they can obtain a commensurate resonance in the manner sketched in Fig. 44(b), but Carlson and coworkers discuss that the level crossing is more likely to occur in the case of diagonal stripes (as observed in nickelates and in the insulating spin-glass phase of LSCO) than

for vertical stripes (as observed in superconducting cuprates). This difference is caused by a greater tendency for level repulsion in the latter case. Both papers also find that the intensities associated with magnons dispersing towards the left and towards the right in Fig. 44(b) are identical for all cases of orientation, center-position and stripe periodicity (the models are restricted to stripes-distances measured in integer lattice constants). In addition to counterpropagating acoustic spin waves at low energies near each of the four incommensurate peaks, there are generally optical spin waves at higher energies. Krüger and Scheidl find that the resonance energy $E_{\rm res}$ depends not only on the stripe periodicity as in [219], but also on the interstripe exchange interaction. For LSCO, they predict a resonance energy in the range $40 - 52$ meV [220].

The stripe calculations discussed above contain several predictions relevant to experiments in the cuprates. If the stripe picture is right, it should be possible to observe both counterpropagating spin waves at low energies and a commensurate resonance mode. However, if they are not seen, it may not imply the complete failure of these models since they completely neglect any coupling the spin degrees of freedom might have to the charge degrees of freedom. In particular, superconducting order is neglected. Moreover, as these are one-dimensional approaches they do not directly give rise to the four isolated incommensurate peaks seen in experiments on superconducting cuprates.

Still more focused models of stripes have been developed by Uhrig, Schmidt and Grüninger [222, 223] and by Vojta and Ulbricht [224]. Both models work explicitly with bond-centered charge stripes separated by two-leg spin-ladders, i.e. with states similar to that shown in Fig. 40(b). In models of isolated two-leg ladders, the natural excitations would be "triplons". These are linear combinations of states in which one energy-minimizing singlet, formed along a rung of the ladder, is excited into one of the three triplets states. Triplons therefore come in three flavors. Since each singlet-triplet transition is associated with a finite energy cost, the triplon spectrum is gapped. Introducing a weak ferromagnetic inter-ladder coupling constant J' on top of the single-ladder Hamiltonian (consisting − in the case of [222, 223] − of conventional separate Heisenberg couplings along the legs and rungs of the ladder, and augmented by a ring-exchange term similar to Eq. (43)) can give rise to overall magnetic order if it is sufficiently large. In terms of the excitation spectrum in a system with ladders along both perpendicular Cu-Cu directions, the gapped 1D triplon spectrum softens around the experimentally observed incommensurate peak positions as the inter-ladder coupling increases. Uhrig, Schmidt and Grüninger tune the coupling precisely to the critical point where the excitation energy at these points reaches zero (corresponding to a transition from a paramagnetic to a magnetically ordered state), and then compute the full excitation spectrum. They find, that at low energies the excitations are magnons which disperse away from incommensurate peak positions. The inter-ladder coupling J' introduces a weak dispersion transverse to the ladder direction and thereby gives rise to a saddle point at $\mathbf{Q}_{\rm 2D} = (\pi, \pi)$, which corresponds to the resonance. At higher energies, there is little effect of the inter-ladder coupling and the excitation spectrum resembles that of a single isolated ladder. In other words, the response at high energy is triplon-like, revealing the one-dimensional nature of the underlying electronic stripe structure [222, 223]. Coupling to charges is generally expected to be relevant, but Uhrig and coworkers discuss that when static charge order is present or when the resonance lies below the particle-hole continuum, the damping due to charges can be substantially reduced. It is speculated that the resonance mode of LSCO lies within the continuum where it becomes overdamped and plausibly non-observable in a neutron scattering experiment [222]. Vojta and Ulbricht obtain very similar conclusions in their model, although they focus on the concept of bond-order inside the the hole-poor, spin-rich ladders [224], a very fashionable theme in theories of doped Mott insulators [96]. An important result of this theory is that matrix element effects cause the low-energy magnons propagating in the direction away from (π, π) to loose their intensity much more rapidly that the magnons propagating towards (π, π). It is interesting that this can happen even without considering the damping effect of spin-charge coupling which is thrown away from the outset in the spin-only theories [220, 221, 222, 223, 224]. Spin-charge coupling was considered by Seibold and Lorenzana [225] who used the Hubbard model to study the spin excitation spectrum when static bond-centered vertical stripes are enforced, i.e. in a picture intermediate between the localized (spin-only) and itinerant (dynamic nesting) limits that have been discussed above. Most interestingly from an experimental viewpoint, they too find an excitation spectrum which at low energies looks like magnons but with the important difference compared to [220, 221] that the branches dispersing away from (π, π) loose their intensity very quickly because of the coupling to charge degrees of freedom. By contrast, the branches dispersing towards (π, π) remain intense and merge to form a commensurate resonance as in [219, 220, 221, 222, 223, 224]. The effect of

d-wave superconductivity on the damping of spin excitations derived from lattice electrons in a spin- and charge-striped environment was studied by Andersen and Hedegård [226]. In their model, the spatially heterogeneous stripe structure is obtained as the mean-field solution of an extended Hubbard model in which a tendency towards superconductivity is induced by an attractive nearest neighbor coupling between electrons of opposite spin. In this model, when stripes coexist with d-wave pairing the spin-wave branches dispersing away from (π, π) fall inside the d-wave particle-hole continuum, causing them to become strongly damped. On the other hand, in the absence of d-wave pairing, both the excitations dispersing away from (π, π) and those dispersing towards (π, π) should be observable. The damping effect of the particle-hole continuum is expected to play a role not only in the superconducting phase, but also in the pseudogap phase in underdoped cuprates. An attractive feature of the model calculations of [226] is that they are able to reproduce experimentally observed features in techniques as distinct as STM, ARPES and neutron scattering.

Treating the coupled spin and charge degrees of freedom in a Landau theory, Vojta and Sachdev have shown [227] that states with charge ordering wavevectors $(\pi/2, 0)$ and $(0, \pi/2)$ (as observed in LNSCO [115]) yield essentially the same spin excitation spectrum (similar to that obtained in [224] and [222, 223]) whether the charges are centered on copper sites as in Fig. 40(a) or on oxygen sites as in Fig. 40(b). By contrast, a 4×4 checkerboard ordered state (with the same charge ordering wavevectors) yields a completely different spin excitation spectrum in which the low-energy incommensurate peaks are rotated 45 degrees away from the positions at which they are observed experimentally in superconducting cuprates. Vojta and Sachdev expect their theory to remain valid when the ordering wave vectors differ from $(\pi/2, 0)$ and $(0, \pi/2)$, as well as when the charge order is fluctuating rather than static [227]. This is important because it implies that the results should be valid even for $La_{2-x}Sr_xCuO_4$ with $x > 0.13$ where no static spin order is observed.

Perhaps the most intriguing experimentally verifiable prediction made by the ladder models [222, 223, 224] is that above the resonance, the spin response rotates by 45 degrees relative to the response below the resonance. In other words, while the peaks in the subresonance response are displaced from (π, π) along the [10] directions, the response above $E_{\rm res}$ is displaced along [11]. Although we have postponed a discussion of the most recent experiments on the full excitation spectrum of the cuprates, it would be unfair to hide that precisely this behavior, a 45 degree rotation of the high-energy spin response, has been seen in stripe-order $La_{1.875}Ba_{0.125}CuO_4$ by Tranquada *et al.* [151] and in underdoped $YBa_2Cu_3O_{6.6}$ ($p \simeq 0.1$) by Hayden *et al.* [207]. Continuing in the spirit of sweeping as little as possible under the rug, we should also state that these experiments and the spin-ladder theories, which model the results rather well, do not stand unchallenged: Experiments on oxygen ordered $YBa_2Cu_3O_{6.5}$ by Stock *et al.* [208] find that the magnetic response above the resonance energy looks very much like isotropic spin waves dispersing away from (π, π), i.e. a two-dimensional response rather than a one-dimensional triplon spectrum. Further, in near-optimally doped $YBa_2Cu_3O_{6.85}$, Hinkov and coworkers find a high-energy spectrum with the same two-dimensional symmetry as reported in [208], but with one-dimensional modulations in the intensities [209]. Thus, from the experimental standpoint, the issues are far from settled.

6.5 Summary and outline of important issues

In this long chapter, we have tried to get around the high-T_c problem in general, but have focused mainly on the state of our knowledge of the two-dimensional spin fluctuation spectra, described by $\chi''(\mathbf{Q}_{\rm 2D}, \omega)$. The main message which should be brought along to the next chapter is this: The excitation spectra of the cuprate families $La_{2-x}Sr_xCuO_4$ and $YBa_2Cu_3O_{6+y}$, which are by far the most widely studied systems, were for a long time considered to be qualitatively different, and were consequently thought to be governed by different physical phenomena, but it now appears that there is a larger degree of universality between the systems, pointing to the existence of a single common cause of the different aspects of the cuprate excitation spectra. We have discussed candidate theories with which these spectra should be compared, and have seen that they can be broadly divided into two classes. In the first, the incommensurate peaks and the resonance are believed to arise from dynamic nesting processes involving particles and holes. In the second, the key players are spins residing in hole-poor regions separated by hole-rich stripes.

Let us briefly summarize the experimental situation: Previously, the spectrum of $La_{2-x}Sr_xCuO_4$ was considered to consist of a quartet of non-dispersive [114, 116] incommensurate peaks at $(\pi(1 \pm \delta), \pi)$ and $(\pi, \pi(1 \pm \delta))$ [137]. Figure 45(a) shows this situation schematically in the sense

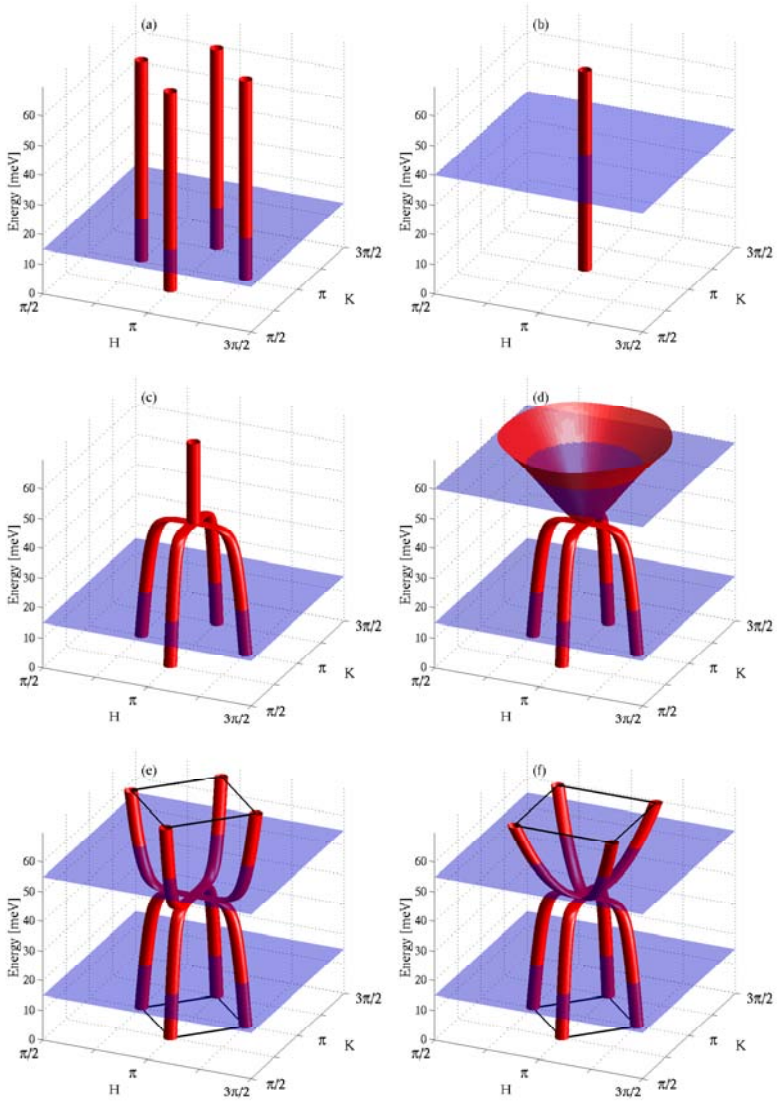

Figure 45: Schematic illustration of various possible symmetries of the spin excitation spectra $\chi''(\mathbf{Q}_{2D},\omega)$ as described in the text. All issues concerning the energy- and temperature dependences of the intensities and $\mathbf{Q}_{2D}$-space widths of the peaks have been neglected. Further, for YBCO we are only showing the acoustic response $\chi''_{ac}(\mathbf{Q}_{2D},\omega)$. The blue planes intersecting the dispersions in (a)-(f) are constant energy slices. By analyzing the characteristic symmetries of the $\mathbf{Q}_{2D}$-space distributions of intensity in a sequence of such slices, it is in principle possible to single out the correct model. (a)-(b) The excitation spectra of $La_{2-x}Sr_xCuO_4$ and $YBa_2Cu_3O_{6+y}$ respectively, as they were viewed prior to the discovery of incommensurate peaks in the acoustic response of YBCO. (c) YBCO with incommensurate peaks of the same symmetry as in (a) below E_{res}, smoothly connected to the commensurate resonance, and remaining commensurate above E_{res}. (d) YBCO with incommensurate peaks below E_{res} and isotropic spin waves above. (e) YBCO with incommensurate peaks of the same symmetry as in (a) both above and below E_{res}. (f) YBCO with incommensurate peaks above E_{res} which are rotated by 45 degrees relative to the incommensurate response below E_{res}.

that low-energy spin gaps [141, 142, 143, 144] and peak broadening with increasing energy [114] the have been neglected. The incommensurability parameter δ describing the low-energy response was found to scale with T_c in the underdoped regime [116]. Similarly, prior to the discovery [200, 201] of incommensurate peaks in YBCO it was believed that the acoustic response $\chi''_{\rm ac}(\mathbf{Q}_{\rm 2D},\omega)$ consisted solely of antiferromagnetic fluctuations around the commensurate (π,π) position, as shown schematically in Fig. 45(b), which neglects spin gaps, broadening as well as the energy dependence of the commensurate intensity. The latter contains a low-temperature peak − the resonance − at an energy $E_{\rm res}$ which scales with T_c in the underdoped regime [188, 183]. In recent years, it has been discovered that not only do incommensurate peaks exist below the resonance energy in YBCO superconductors with the same orientation as those seen in LSCO [200, 201, 183, 99], they also disperse with increasing energy and connect smoothly to the resonance mode [203]. With these informations in hand, one would expect the symmetry of the excitation spectrum to be as shown in Fig. 45(c). However, even this appears to be an oversimplification since there exist reports that the response for $\hbar\omega > E_{\rm res}$ becomes incommensurate again, either with the same symmetry as below $E_{\rm res}$ [202] or rotated by 45 degrees [207]. These viewed are illustrated in Figs. 45(d) and (e) respectively. Finally, there are also reports that the response above $E_{\rm res}$ in YBCO resemble isotropically dispersing spin wave, as shown in Fig. 45(f) with either isotropic [208] or anisotropic [209] intensity distributions. A recent experiment on $La_{1.875}Ba_{0.125}CuO_4$ suggests that the high-energy excitations in this system resembles Fig. 45(d) in the normal state.

Thus far, the experimental situation suggests that perhaps the cuprates have a common excitation spectrum. However, to truly put this conclusion on a firm basis, it is necessary to find a dispersion in the positions of the incommensurate peaks of LSCO as well as identifying the LSCO equivalent of the resonance modes that have been identified in YBCO as well as in $Bi_2Sr_2CaCu_2O_{8+x}$ and $Tl_2Ba_2CuO_{6+\delta}$. In the next chapter, we study the spin excitations of optimally doped $La_{1.84}Sr_{0.16}CuO_4$ and underdoped $La_{1.90}Sr_{0.10}CuO_4$ in order to try to do precisely this. We will try to extract as much information about $\chi''(\mathbf{Q}_{\rm 2D},\omega)$ as possible, but the focus will be the following list of key questions:

- Incommensurate peaks: Do the incommensurate peaks in LSCO systems disperse as a function of $\hbar\omega$? If so, is the dispersion $\delta(\omega)$ different from or similar to the various dispersions that have been reported in YBCO and LBCO?
- Resonance mode: Does LSCO have a commensurate resonance, carrying substantial spectral weight in the superconducting state?
- Temperature dependence: How does the excitation spectrum evolve with temperature? In particular, how does the onset of superconductivity affect $\chi''(\mathbf{Q}_{\rm 2D},\omega)$?
- Doping dependence: Do the answers to the above questions vary with hole-doping concentration?

Having addressed the issues listed, we must consider which class of theory describes the experimental observations better: Real-space stripe or ladder theories or perhaps a dynamic nesting picture? Finally, we should consider the implications − if any − of our data on broader issues such as the nature of the pseudogap phase, and the origin of superconductivity itself. With these comments, we close the chapter.

7 The spin excitation spectrum of $La_{2-x}Sr_xCuO_4$

In this chapter we present the results of two time-of-flight experiments aimed at studying the evolution with energy transfer and temperature of the spin excitation spectra of underdoped and optimally doped $La_{2-x}Sr_xCuO_4$. The quantity we are interested in is the imaginary part $\chi''(\mathbf{Q}_{2D},\omega)$ of the generalized magnetic susceptibility. Through the fluctuation-dissipation theorem Eq. (17), $\chi''(\mathbf{Q}_{2D},\omega)$ is related to the scattering function $S(\mathbf{Q}_{2D},\omega)$, which apart from resolution considerations and the factors in Eq. (15) is what is measured in a neutron scattering experiment. As for the studies of CFTD reported in chapter 4, we used the MAPS spectrometer shown in Fig. 3 for these experiments. The two-dimensionality of the magnetic correlations in LSCO along with the large reciprocal space coverage made possible by the 16 m^2 MAPS detector banks allows us to map out $\chi''(\mathbf{Q}_{2D},\omega)$ to a very high degree of precision within the experimental window chosen. We focus predominantly on clarifying the evolution of the excitations below $\hbar\omega = 40$ meV, but for underdoped LSCO we present data extending to 80 meV. In particular, we wish to address the questions raised in section 6.5 of the previous chapter.

The main issue on the table is the evolution with $\hbar\omega$ of the $\mathbf{Q}_{2D}$-space symmetry of the excitations. Figure 45 shows schematically how it is possible to distinguish between a number of different possible symmetries by analyzing the data in the form of constant energy slices. Figure 46 displays eight examples of such constant energy slices from experiments on both $La_{1.90}Sr_{0.10}CuO_4$ (panels (a)-(d)) and $La_{1.84}Sr_{0.16}CuO_4$ (panels (e)-(h)). Inspection of such images can immediately give qualitatively correct answers to some of the key questions. Without going into details at this stage, it is clear that the overall structure of $\chi''(\mathbf{Q}_{2D},\omega)$ is similar for the two compositions, and that intensity changes resulting from the onset of superconductivity are only detectable at the lowest energies shown.

The rest of the chapter is organized as follows: Section 7.1 contains experimental details of relevance for the understanding of the experiments. In section 7.2, we introduce our notation and define a few useful quantities. Next, in section 7.3 we attempt to obtain a preliminary overview of the data before moving on, in section 7.4, to a description of the model we have used in the analysis proper and of the methods employed in extracting the physical quantities of interest from the experimental data. Having obtained a basic appreciation of the contents of the data set, we present our experimental results in section 7.5. In section 7.6 we discuss the significance of the experimental findings before drawing final conclusions in section 7.7.

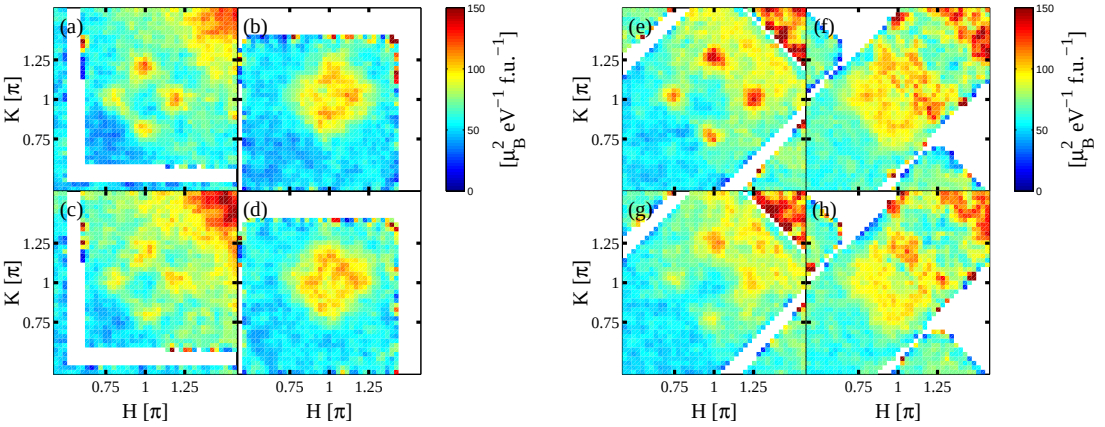

Figure 46: Color maps from experiments on $La_{1.90}Sr_{0.10}CuO_4$ ($T_c = 29$ K. Panels (a)-(d)) and $La_{1.84}Sr_{0.16}CuO_4$ ($T_c = 38.5$ K. Panels (e)-(h)) of the central parts of the 2D Brillouin zone displayed in Fig. 39. For both compositions the raw intensities were averaged over four Brillouin zones and in 4 meV energy windows centered on (a) $\hbar\omega = 10$ meV for $T = 10$ K; (b) $\hbar\omega = 30$ meV for $T = 10$ K; (c) $\hbar\omega = 10$ meV for $T = 30$ K; (d) $\hbar\omega = 30$ meV for $T = 30$ K; (e) $\hbar\omega = 10$ meV for $T = 10$ K; (f) $\hbar\omega = 30$ meV for $T = 10$ K; (g) $\hbar\omega = 10$ meV for $T = 40$ K; (h) $\hbar\omega = 30$ meV for $T = 40$ K. The factors appearing in Eq. (82) were divided out in order to present the data in the form of $\chi''(\mathbf{Q}_{2D},\omega)$ in units $\mu_B^2\,\mathrm{eV}^{-1}\mathrm{f.u.}^{-1}$.

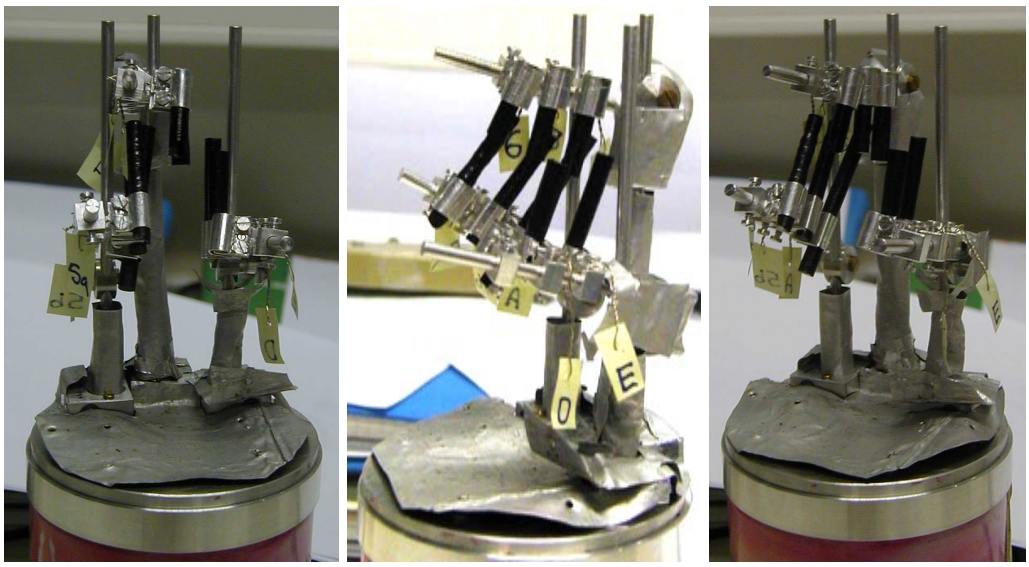

Figure 47: Pictures showing the composite mount used for the MAPS experiment on optimally doped LSCO. The nine single crystals have a total mass of 18.7 grams and were comounted using high-energy X-rays. In the leftmost picture, the crystallographic $\mathbf{c}^*$ axis, normal to the CuO_2 planes, is approximately in the left-right direction. In the experiment, the mount was oriented with $\mathbf{c}^*$ parallel to $\mathbf{k}_i$.

7.1 Experimental details

All samples used were grown in optical image furnaces in the laboratories of H. Takagi at the University of Tokyo. Under these growth conditions, they form black cylindrical rods as seen in Fig. 47. Visually inspecting and comparing the most recently grown (underdoped, $p = x = 0.10$) to the oldest (optimally doped, $x = 0.16$) crystals, it is immediately evident that the surface roughness is much higher in the older samples. It may be that this reflects a higher degree of inhomogeneity in the oldest samples, but if so, the inhomogeneity must be of a character which has little or no effect on bulk properties quantities such as T_c, since the reported values are consistent with the best published values for the two concentrations $p = x$ of doped holes per copper site ($T_c = 29$ K for $La_{1.90}Sr_{0.10}CuO_4$ and $T_c = 38.5$ for $La_{1.84}Sr_{0.16}CuO_4$).

The composite mounts used for the MAPS experiments were aligned at room temperature by the use of a high energy X-ray source at ILL, Grenoble. The total mosaic spread of each mount was ~ 1.5 degrees. In Fig. 47 we show pictures of the $La_{1.84}Sr_{0.16}CuO_4$ mount which comprised nine single crystals with a total mass of 18.7 grams. These crystals had previously been used by Lake and coworkers to investigate the spin gap Δ_s and to study how $\chi''(\mathbf{Q}_{2D}, \omega)$ at energies around Δ_s is affected by the application of a strong magnetic field applied perpendicular to the CuO_2 planes [144, 121]. The $x = 0.10$ mount was more compact, consisting of four crystals with a total mass of 19.76 grams arranged side by side on a single aluminium plate. All four crystals came from a new batch, and had never been studied by neutron scattering before. Subsequent experiments have found them to exhibit static magnetic order, as is common in underdoped LSCO [228].

At MAPS the samples were mounted on the cold finger of a continuous cycle refrigerator and lowered into the sample chamber with the CuO_2 planes perpendicular to $\mathbf{k}_i$. As discussed in section 2.3, this orientation is very efficient for studying two-dimensional magnetic correlations. The $x = 0.16$ samples were oriented with their orthorhombic [100] and [010] axes along the horizontal and vertical directions perpendicular to $\mathbf{k}_i$, whereas for $x = 0.10$ the orthorhombic [110] and $[\bar{1}10]$ were along the vertical and horizontal. Although $La_{2-x}Sr_xCuO_4$ is orthorhombic at low temperature we make no distinctions between the orthorhombic $\mathbf{a}^*$ and $\mathbf{b}^*$ axes in the experiments reported here since the samples studied are generally found to be twinned. With the incident energy $E_i = 55$ meV chosen for $x = 0.16$ and used also for the main part of the $x = 0.10$ experiment, the respective sample orientations imply that five and four magnetic zone centers $\mathbf{Q}_{2D} = (\pi, \pi)$ are projected onto the MAPS detector banks. These correspond to orthorhombic wavevectors $(\pm 10L)$ and $(0 \pm 1L)$ and (for $x = 0.16$) $(30L)$.

For optimally doped LSCO, two runs were made with $E_i = 55$ meV and a Fermi chopper frequency of 250 Hz. At $T = 10$ and 40 K respectively, we counted for 62 and 64 hours. In the

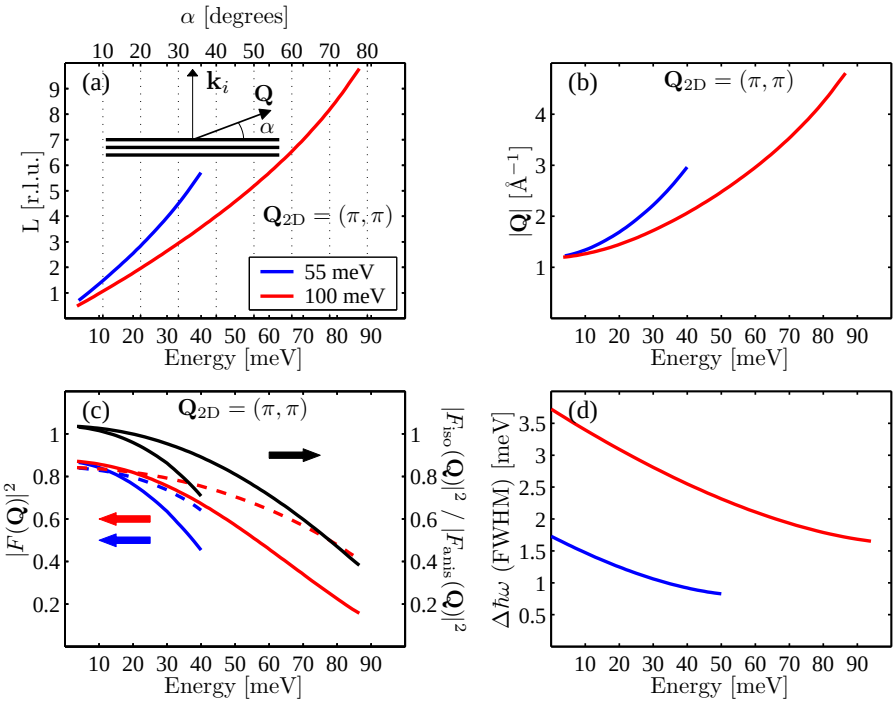

Figure 48: (a) The energy dependence of L versus neutron energy transfer at $\mathbf{Q}_{2D} = (\pi, \pi)$ for $E_i = 55$ meV (blue lines) and $E_i = 100$ meV (red lines). The top axis displays the corresponding angle α between the neutron momentum transfer $\mathbf{Q}$ and the CuO_2 planes. (b) Energy dependence of the length of $\mathbf{Q}$ when $\mathbf{Q}_{2D} = (\pi, \pi)$. (c) Energy dependences of the isotropic and anisotropic [133, 229] squared Cu^{2+} form factors at $\mathbf{Q}_{2D} = (\pi, \pi)$ (full and dashed lines respectively). The full black lines represent the ratios of the squared isotropic form factors to the squared anisotropic form factors for the two incident energies used. (d) Energy dependence of the energy resolution (FWHM) as a function of neutron energy transfer. The red and blue lines in (b)-(d) refer to the incident energy E_i as in (a).

experiment on underdoped LSCO, four runs at $T = 10$, 30, 100 and 300 K were made under the same experimental conditions as used in the experiment on optimally doped LSCO. The counting times were 18, 44, 39 and 21 hours respectively. Finally, a single 22 hour run at $T = 10$ K was made on underdoped LSCO with $E_i = 100$ meV and a Fermi chopper frequency of 350 Hz. The energy resolutions of the two instrument configurations used are displayed in Figure 48(d).

As described in section 4.1, at the end of a time-of-flight experiment a number of manipulations are carried out to remove bad detectors, correct for variations in the detector efficiencies and to place the observed intensities on an absolute scale. After these corrections, the data are output as $(k_i/k_f)\left(d^2\sigma/(d\Omega\ dE_f)\right)_{\rm tot}$ in units of mbarn sr^{-1} meV^{-1} f.u.$^{-1}$.

For the experiments reported in this chapter, the 147456 available pixels were binned together in groups of four, so that after the removal of bad detectors, the resulting data files contained 32922 (32871) individually addressable pixels for $x = 0.16$ ($x = 0.10$). For the runs with $E_i = 55$ meV, the number of energy bins per pixel element was 110 (120) for $x = 0.16$ ($x = 0.10$), spanning energy transfers $\hbar\omega$ from -4.75 to 49.75 meV (-9.75 to 49.75 meV) in steps of 0.5 meV. The $E_i = 55$ meV data sets obtained from these runs thus contained a total of 3621420 (3944520) closely spaced points on the time-of-flight parabola. For the single data set obtained with $E_i = 100$ meV in the experiment on underdoped LSCO, there were 32871 pixel elements, each probing the response in 105 energy bins between -9.5 and 94.5 meV. This run therefore probed 3451455 points on the time-of-flight parabola.

7.2 Definitions and notation

For the purposes of our analysis, we write the total cross-section $\left(d^2\sigma/(d\Omega\ dE_f)\right)_{\rm tot}$ as a sum of two terms

$$\left(\frac{d^2\sigma}{d\Omega\ dE_f}\right)_{\rm tot} = \left(\frac{d^2\sigma}{d\Omega\ dE_f}\right)_{\rm mag} + \left(\frac{d^2\sigma}{d\Omega\ dE_f}\right)_{\rm bg} \tag{81}$$

with the understanding that $\left(d^2\sigma/(d\Omega\ dE_f)\right)_{\rm mag}$ is the cross-section for the peaked part of the magnetic spectrum which our analysis yields information about. Magnetic scattering without any clear $\mathbf{Q}_{\rm 2D}$-dependence over the range of momenta we are investigating will not be captured by the analysis and effectively forms part of a background cross-section $\left(d^2\sigma/(d\Omega\ dE_f)\right)_{\rm bg}$, which is otherwise dominated by phonon scattering.

To analyze the magnetic scattering in quantitative detail, we employ the standard notation for absolute unit measurements in cuprate high-temperature superconductors [188, 198, 130]

$$\frac{k_i}{k_f}\left(\frac{d^2\sigma}{d\Omega\ dE_f}\right)_{\rm mag} = (\gamma r_0)^2\ |F(\mathbf{Q})|^2\ \left(\frac{2}{\pi g^2\mu_B^2}\right)[n(\omega)+1]\,\chi''_{\rm iso}(\mathbf{Q},\omega) \tag{82}$$

It should be emphasized that Eq. (82) is only strictly valid for magnetically disordered systems where the identity $\sum_{\alpha\beta}(\delta_{\alpha\beta} - \hat{\mathbf{Q}}_\alpha\hat{\mathbf{Q}}_\beta)\chi''_{\alpha\beta}(\mathbf{Q},\omega) = (2/3){\rm Tr}\left(\chi''_{\alpha\beta}(\mathbf{Q},\omega)\right)$ holds. The quantity $\chi''_{\rm iso}(\mathbf{Q},\omega)$ in Eq. (82) is the isotropic susceptibility [188, 130] defined as one-third of the trace of the tensorial susceptibility $\chi''_{\alpha\beta}(\mathbf{Q},\omega)$:

$$\chi''_{\rm iso}(\mathbf{Q},\omega) = \frac{1}{3}{\rm Tr}\left(\chi''_{\alpha\beta}(\mathbf{Q},\omega)\right) \tag{83}$$

With these definitions, the fluctuation-dissipation theorem Eq. (17) takes the modified form

$$S^{\alpha\beta}(\mathbf{Q},\omega) = \frac{n(\omega)+1}{\pi(g\mu_B)^2}\,\chi''_{\alpha\beta}(\mathbf{Q},\omega) \tag{84}$$

and the total moment sum rule Eq. (74) becomes

$$\begin{aligned} S(S+1) &= \frac{\int d\mathbf{Q}\,d(\hbar\omega)\,{\rm Tr}\left(S^{\alpha\beta}(\mathbf{Q},\omega)\right)}{\int d\mathbf{Q}} \\ &= \frac{3\hbar}{\pi(g\mu_B)^2}\frac{\int d\mathbf{Q}\,d\omega\ [n(\omega)+1]\,\chi''_{\rm iso}(\mathbf{Q},\omega)}{\int d\mathbf{Q}} \end{aligned} \tag{85}$$

per copper ion [130]. Introducing the local (isotropic) susceptibility $\chi''_{\rm iso}(\omega)$ defined by

$$\chi''_{\rm iso}(\omega) = \frac{\int d\mathbf{Q}\,\chi''_{\rm iso}(\mathbf{Q},\omega)}{\int d\mathbf{Q}} \tag{86}$$

we can rephrase Eq. (85) in terms of the mean-squared fluctuating moment per copper site $\langle m^2\rangle = (g\mu_B)^2 S(S+1)$

$$\langle m^2\rangle = \frac{3\hbar}{\pi}\int\frac{d\omega\,\chi''_{\rm iso}(\omega)}{1-\exp(-\hbar\omega/k_BT)} \tag{87}$$

For systems in which the magnetic correlations are two-dimensional, $\chi''_{\rm iso}(\mathbf{Q},\omega)$ is independent of the component of $\mathbf{Q}$ normal to the 2D plane, and the local susceptibility (86) can be equated with the Brillouin zone averaged susceptibility

$$\chi''_{\rm iso}(\omega) = \chi''_{\rm iso,2D}(\omega) = \frac{\int d\mathbf{Q}_{\rm 2D}\,\chi''_{\rm iso}(\mathbf{Q},\omega)}{\int d\mathbf{Q}_{\rm 2D}} \tag{88}$$

In the notation of Eq. (82), $(\gamma r_0)^2 = 0.2905$ is assigned the unit barn sr^{-1} [230]. Since $(k_i/k_f)\left(d^2\sigma/(d\Omega\ dE_f)\right)_{\rm mag}$ has the units mbarn sr^{-1} meV^{-1} per formula unit, the units of $\chi''_{\rm iso}(\mathbf{Q},\omega)$ become μ_B^2 eV^{-1} f.u.$^{-1}$. Henceforth, we shall drop the subscript "iso" on the susceptibilities.

When reducing the data from $(k_i/k_f)\left(d^2\sigma/(d\Omega\ dE_f)\right)_{\rm mag}$ to $\chi''(\mathbf{Q},\omega)$ we assume $g = 2$ and use the isotropic form factor for free Cu^{2+} ions. We make this choice despite evidence [133, 229] suggesting that the correct form of $|F(\mathbf{Q})|^2$ in cuprate high-T_c superconductors is not that of free Cu^{2+} ions, but rather an anisotropic form, reflecting the planar nature of highest-energy occupied orbitals responsible for magnetic scattering. Figure 48(c) displays both the isotropic and anisotropic form factors for neutron wavevector transfers $\mathbf{Q}$ such that the in-plane component $\mathbf{Q}_{\rm 2D}$ is fixed at (π,π) around which the magnetic scattering is strongest. It is evident that for

high energy transfers a significant difference develops between the two squared form factors, with $|F_{\rm iso}(\mathbf{Q})|^2$ dropping more rapidly with increasing $\hbar\omega$ than the anisotropic squared form factor $|F_{\rm anis}(\mathbf{Q})|^2$. By contrast, at the lowest energies $|F_{\rm iso}(\mathbf{Q})|^2 \leq |F_{\rm anis}(\mathbf{Q})|^2$. These difference are easily explained: Figures 48(a) shows that for fixed $\mathbf{Q}_{\rm 2D} = (\pi, \pi)$ the out-of-plane component of $\mathbf{Q}$ grows rapidly with increasing $\hbar\omega$. Therefore, when $\hbar\omega$ approaches E_i the angle α, defined in Fig. 48(a), between $\mathbf{Q}$ and the CuO_2 planes becomes very large. In this situation, effects of the planar nature of the orbitals responsible for the magnetic scattering should become observable through $|F(\mathbf{Q})|^2$. If these orbitals are less extended along the out-of-plane direction than along the in-plane directions, then the squared form factor, being defined in Eq. (14) as the Fourier transform of the normalized density of unpaired electrons, should drop less rapidly along $\mathbf{Q}_z$ than along any in-plane direction. We have chosen to work with the isotropic formfactor throughout for reasons of computational simplicity (The program used for carrying out resolution corrected least-squares fits of our data only includes the isotropic form factor as a standard option for computing intensities). Having completed the analysis, we can then return to comment on what influence the anisotropic form factor would have had. It is clear that any conclusions drawn concerning intensity differences (at the same value of $\hbar\omega$) between data obtained under the same experimental conditions, but at different temperatures, are not affected qualitatively by the choice of formfactor. Quantitatively, we generally do expect differences, but these can be estimated from the black curves in Fig. 48(c) since the magnetic scattering remain concentrated around $\mathbf{Q}_{\rm 2D} = (\pi, \pi)$ at all energies investigated.

7.3 Broad-brush overview of the data

Before turning to a full analysis of the data, it is useful to take advantage of the wide coverage of $(\mathbf{Q}, \omega)$ space to obtain an overview of the data set. This is the aim of the present section, where the data are presented in various averaged formats chosen to emphasize different aspects of the the problems involved in extracting information about the magnetic fluctuation spectra.

7.3.1 Phonons

The overall goal of the experiment is to study the imaginary part $\chi''(\mathbf{Q}_{\rm 2D}, \omega)$ of the generalized magnetic susceptibility, but it is of great importance for us to have an idea about the importance of coherent phonon scattering in the MAPS data set, and in particular to be aware of the energies at which the time-of-flight parabola intersects intense phonon branches. This is so because phonon scattering can potentially be mistaken for magnetic scattering in situations where it is not possible to unambiguously identify the former via its temperature dependence or via its $\mathbf{Q}$ dependence.

While the $\mathbf{Q}$-space coverage of MAPS is large, we cannot in a single setting of the instrument measure the entire phonon density of states. Yet, as we shall now see, by indiscriminately averaging the total scattering $(k_i/k_f)\left(d^2\sigma/(d\Omega\, dE_f)\right)_{\rm tot}$ (Coherent and incoherent. Magnetic and nuclear) over $\mathbf{Q}_{\rm 2D}$ in the four Brillouin zones closest to the origin, we find surprisingly good qualitative agreement, in terms of the positions of the main phonon branches, between our data and a model calculation of the phonon density of states in undoped La_2CuO_4, which in turn compares fairly well with experimental measurements of the same quantity [231].

Figure 49 displays data from the $La_{1.90}Sr_{0.10}CuO_4$ experiment, obtained with different incident energies and at different temperatures. Panel (a) shows data collected at $T = 10$, 30, 100 and 300 K with $E_i = 55$ meV, whereas panel (b) shows data collected with $E_i = 100$ meV at $T = 10$ K. These plots are constructed by using the Matlab package Mslice (see section 4.2) to average the intensities over the available parts of the four Brillouin zones closest to the origin. It should be noted, that when $\hbar\omega$ increases, the $\mathbf{Q}$ space coverage of MAPS is gradually reduced, as can be seen from Fig. 4. This implies, that the $\mathbf{Q}_{\rm 2D}$-space averages shown in Fig. 49 are averages over a fraction of these four zones which decreases with increasing $\hbar\omega$ for a given E_i. Therefore, we cannot expect a favorable quantitative comparison with the theoretically or experimentally determined phonon density of states. This failure is only aggravated by the fact that the time-of-flight parabola will generally not intersect all of the $3N$ three-dimensional phonon dispersion branches expected for a unit cell containing N atoms.

However, even with these severe restrictions, Fig. 49 shows that the peak positions in our experimental data agree reasonably well with the calculated and measured peak positions in the phonon density of states, reported in [231] for La_2CuO_4 (which in turn has a slightly different phonon spectrum than $La_{1.90}Sr_{0.10}CuO_4$ [231]). For the reasons outlined above, it is not surprising

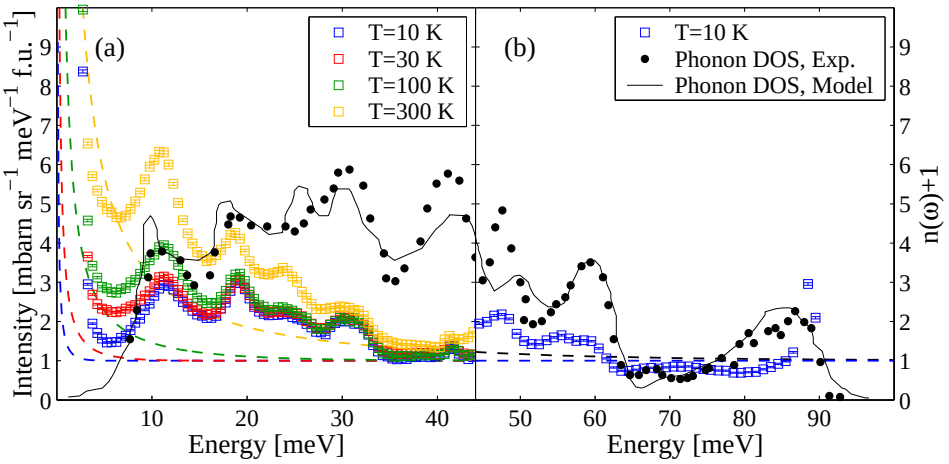

Figure 49: Comparison of time-of-flight data from $La_{1.90}Sr_{0.10}CuO_4$ with the phonon density of states of undoped La_2CuO_4 below a cut-off energy of $\sim$ 90 meV. The squares are experimental data obtained by averaging $(k_i/k_f)\left(d^2\sigma/(d\Omega\ dE_f)\right)_{\rm tot}$ over the parts of the four Brillouin zones closest to the origin which are projected onto the MAPS detector banks at a given $\hbar\omega$. (a) $E_i = 55$ meV. Blue squares: $T = 10$ K. Red squares: $T = 30$ K. Green squares: $T = 100$ K. Yellow squares: $T = 300$ K. (b) $E_i = 100$ meV. Blue squares $T = 10$ K. Blue, red, green and yellow dashed lines in (a) and (b) represent the Bose occupation factors $[n(\omega) + 1]$ for $T = 10$, 30, 100 and 300 K respectively. The black lines and circles are from [231] and represent a model calculation of the phonon density of states and experimental data of the same quantity.

that our measured peak intensities do not agree with the calculated and measured phonon density of states. Nor is it surprising that the 10 K data in (a) and (b) do not match at 44 meV since the difference in incident energies E_i implies that the time-of-flight parabola intersects different part of the phonon spectrum. Having said this, the temperature dependence of the spectra displayed in panel (a) clearly demonstrates that there is substantial scattering from phonons even at the lowest temperatures.

The main message of Fig. 49 is that when analyzing our data in order to extract information about $\chi''(\mathbf{Q}_{\rm 2D}, \omega)$, we must carefully consider the possibility of phonon contributions at the energies where the averages displayed in Fig. 49 show peaks. The large Bose occupation factors for the lowest energy phonons at high temperatures means that they can make it impossible to discern magnetic scattering even if it is present. On the other hand, such phonons are easily identifiable via their temperature dependence.

7.3.2 Energy averaged magnetic scattering

Next, we shall investigate the $\mathbf{Q}_{\rm 2D}$-dependence of the scattering near the magnetic zone center (π, π). Figure 50 displays averages over large energy intervals of the total observed scattering $(k_i/k_f)\left(d^2\sigma/(d\Omega\ dE_f)\right)_{\rm tot}$ inside the section of the square lattice reciprocal space shown in grey in the inset. The intensity at a given point is an average over both energy and over momentum transfer components perpendicular to the cut direction, as indicated by the solid black lines inside the grey area in the inset (See also Fig. 55). The energy intervals used in the averaging process are chosen to be as large as possible for a given E_i while avoiding the possible contaminating influence of the incoherent scattering centered on $\hbar\omega = 0$. By averaging $(k_i/k_f)\left(d^2\sigma/(d\Omega\ dE_f)\right)_{\rm tot}$ over large ranges of energy transfer $\hbar\omega$, any details such as a dispersion in the incommensurate peak positions are likely to be washed out. Despite this problem, the plots allow us to glean useful information about the nature of the magnetic fluctuations at different time-scales and their evolution with temperature.

To analyze the data, we have fitted the profiles in Fig. 50 with a sum of two symmetric Gaussians displaced from (π, π) and superimposed on a background, which for simplicity is assumed to be quadratic in the distance from (π, π) along $[1\overline{1}]$. In presenting the data in Fig. 50, the level of the flat part of the fitted background is indicated by solid colored lines on the left-hand axes. Furthermore, the data have been offset vertically for a clearer presentation. At this stage, we are not taking resolution corrections into consideration. Moreover, we assume that $\chi''(\mathbf{Q}_{\rm 2D}, \omega)$ has the fourfold symmetry shown in Fig. 39(d). With the cuts running along the $[1\overline{1}]$ direction of the square lattice reciprocal space, the energy-averaged peak displacement parameter $\langle\delta\rangle$ defined as

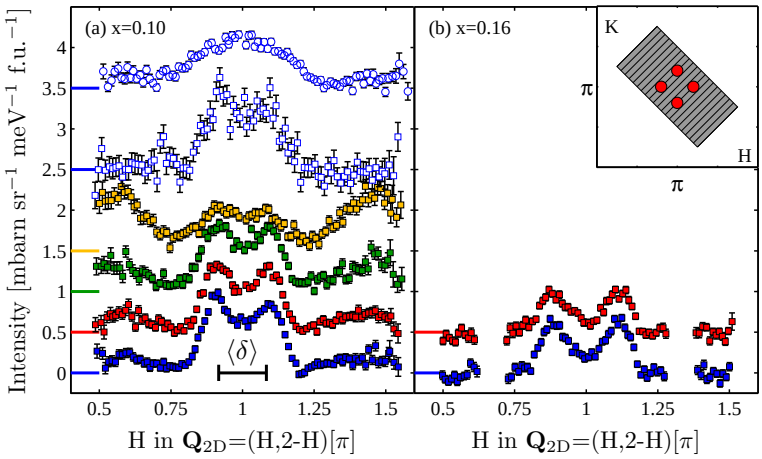

Figure 50: Averages of the intensities $(k_i/k_f)\left((d^2\sigma/(d\Omega\ dE_f))\right)_{\rm tot}$ seen in underdoped and optimally doped LSCO at different temperatures. To obtain these plots, $(k_i/k_f)\left((d^2\sigma/(d\Omega\ dE_f))\right)_{\rm tot}$ was averaged over large energy ranges $E_1 \leq \hbar\omega \leq E_2$ and over the components of the 2D wavevector transfer $\mathbf{Q}_{\rm 2D}$ perpendicular to the cut-direction. (a) $La_{1.90}Sr_{0.10}CuO_4$. Filled blue, red, green and yellow squares were obtained with an incident energy $E_i = 55$ meV at $T = 10$, 30, 100 and 300 K respectively. $(k_i/k_f)\left(d^2\sigma/(d\Omega\ dE_f)\right)_{\rm tot}$ was averaged between $E_1 = 4$ meV and $E_2 = 40$ meV. The open blue squares and circles were obtained at $T = 10$ K with $E_i = 100$ meV and with $(k_i/k_f)\left(d^2\sigma/(d\Omega\ dE_f)\right)_{\rm tot}$ averaged over the ranges 6-40 meV and 40-85 meV respectively. (b) $La_{1.84}Sr_{0.16}CuO_4$. Blue and red squares were obtained at $T = 10$ and 40 K respectively with an incident energy $E_i = 55$ meV and for energy transfers between 4 and 40 meV. For clarity, the data have been offset from the solid blue, red, green and yellow lines which represent the flat parts of a quadratic model for the backgrounds, as explained in the text. The inset shows the region of the Brillouin zone probed. The intensity of each point in (a) and (b) represents an average over energy and over all momenta inside one of the rectangular grey boxes oriented with their long axis parallel to [11].

in Fig. 39(d) is equal to the distance between two peaks when projected onto a nearest neighbor Cu-Cu direction.

First, let us compare the low-$\hbar\omega$ averages indicated by squares in Figure 50(a). It is clear that at all temperatures from $T = 10$ K to $T = 300$ K, the energy-averaged response is incommensurate. The $T = 10$ K spectra obtained with $E_i = 55$ meV and $E_i = 100$ meV are consistent except for the values of $\langle\delta\rangle$ which are $\langle\delta\rangle = 0.167 \pm 0.002$ for $E_i = 55$ meV and $\langle\delta\rangle = 0.154 \pm 0.006$ for $E_i = 100$ meV. The discrepancy is most likely caused by the (π, π) regions crossing the gaps between the MAPS detector banks for low energy transfers in the case $E_i = 100$ meV. For the data taken with $E_i = 55$ meV, the peak positions show no change from $T = 10$ K to 100 K. Within the errors of the fit, they are consistent with $\langle\delta\rangle = 0.166 \pm 0.001$. At $T = 300$ K, the peaks have moved slightly closer to (π, π) and $\langle\delta\rangle = 0.152 \pm 0.006$. Concomitantly with this decrease in $\langle\delta\rangle$ with increasing temperature, there is a marked decrease in the fitted peak amplitudes, whereas the widths are temperature-independent. It should be pointed out that because of uncertainties in the background determination (In particular, our crude assumption of a quadratic background does not capture what appears to be coherent phonon scattering near $H = 0.6$ and $H = 1.4$), we cannot have much faith in the absolute values of the fitted peak intensities, but we note that since the Bose occupation factors have not been divided out in Fig. 50(a)-(b) there may well be a substantial intensity decrease with increasing temperature.

The above observations concerning the energy-averaged low-energy response in underdoped LSCO can be directly transferred to the data on the optimally doped composition shown in Fig. 50(b). There is a slight intensity reduction with increasing temperature, but the peak widths and peak separations are temperature independent. For the latter we find $\langle\delta\rangle = 0.215 \pm 0.003$.

Finally, we note that the high-energy response indicated by open blue circles in Fig. 50(a) appears qualitatively different from the incommensurate low-energy response (open and filled blue squares) at the same temperature, $T = 10$ K. It appears to the eye that the response is commensurate, but in fact the cut-profile is fit equally well with a single, broad commensurate peak at (π, π) and by two overlapping incommensurate peaks separated by $\langle\delta\rangle = 0.178 \pm 0.008$ (as witnessed by the values $\chi^2_{\rm red} = 1.48$ and 1.34 respectively of the reduced chi-squared goodness-of-fit measure). This result is a first sign of the difficulties inherent in identifying the nature of the high-energy response: A crossover from incommensurate to commensurate scattering with increasing $\hbar\omega$ may

well be misinterpreted as simply an effect of broadening, and vice versa. The data presented in Fig. 50 are clearly insufficient to unambiguously identify the symmetry of $\chi''(\mathbf{Q}_{2D}, \omega)$ at high energies. To proceed further along these lines, it is necessary to model the response function $\chi''(\mathbf{Q}_{2D}, \omega)$ in a more sophisticated manner than in the simple one-dimensional analysis above and to make allowance for the effects of finite instrumental resolution.

7.3.3 Color images of $\chi''(\mathbf{Q}_{2D}, \omega)$

Having looked at the spin fluctuations averaged over large energy ranges, let us return to Fig. 46 in order to study what happens in the much narrower ranges $8 - 12$ and $28 - 32$ meV. To obtain these images, the intensities $(k_i/k_f)\left(d^2\sigma/(d\Omega\ dE_f)\right)_{\rm tot}$ in the four Brillouin zones closest to the origin of reciprocal space were averaged and corrections (of both magnetic and background contributions to $\left(d^2\sigma/(d\Omega\ dE_f)\right)_{\rm tot}$) were made for various factors − including the Bose occupation factor $(n(\omega) + 1)$ − in the cross-section Eq. (82). Having converted the data in this manner, they are presented as $\chi''(\mathbf{Q}_{2D}, \omega)$ in units of μ_B^2 eV^{-1} per formula unit, with the understanding that there is also a non-magnetic background contribution present. Panels 46(a)-(d) display data from the experiment on underdoped LSCO while panels (e)-(h) display data from the experiment on optimally doped LSCO. As stated in the introduction, inspection of such images can immediately give a rough idea about the structure of $\chi''(\mathbf{Q}_{2D}, \omega)$ and about the changes caused by the onset of superconductivity below T_c.

Several things should be noted about the data presented in Fig. 46. First, we note that the absolute unit values of $\chi''(\mathbf{Q}_{2D}, \omega)$ are of the same order of magnitude at both energy transfers investigated and are also comparable between $x = 0.10$ and $x = 0.16$. Second, superimposed on a background that generally increases with $|\,\mathbf{Q}\,|$ (i.e. from lower left corners to the upper right corners), we observe that in both underdoped and optimally doped LSCO the response at $\hbar\omega = 10$ meV is incommensurate with well-defined and roughly isotropic (i.e. circular) peaks with the symmetry of Fig. 39(d), and with essentially no scattering above the background level at the commensurate (π, π) position. This is the case for temperatures both below and just above the superconducting transition temperatures T_c as can be seen by comparing panels (a) and (c) (for $x = 0.10$) and (e) and (g) (for $x = 0.16$). The incommensurability parameter δ defined in Fig. 39(d) is clearly smaller for the underdoped $La_{1.90}Sr_{0.10}CuO_4$ sample than for the optimally doped $La_{1.84}Sr_{0.16}CuO_4$ sample. This observation is in broad agreement with the notion that δ increases with the hole-doping concentration $p = x$ in underdoped samples and then saturates at a value close to 0.24 (in square lattice notation). We note in passing that this behavior was originally reported to hold for $\hbar\omega \leq 3.5$ meV and was expected − based on the assumption of zero dispersion in the incommensurate peak pattern with $\hbar\omega$ (see Fig. 45(a)) − to remain valid for energies above this range [116]. The data presented in Fig. 46 are consistent with this notion as are the low-temperature energy-averaged incommensurability parameters $\langle\delta\rangle = 0.166 \pm 0.001$ (for $x = 0.10$) and $\langle\delta\rangle = 0.215 \pm 0.003$ (for $x = 0.16$) derived from our simplistic analysis of the data in Fig. 50.

Third, going from $\hbar\omega = 10$ meV to 30 meV, panels (b), (d), (f) and (h) show that the response function $\chi''(\mathbf{Q}_{2D}, \omega)$ broadens significantly into a squarish pattern and appears to move closer to the zone center. This observation is consistent with the fact that the values of $\langle\delta\rangle$ quoted in the previous paragraph fall short of the values reported by Yamada *et al.* [116] ($\delta \sim 0.20$ and $\delta \sim 0.25$ for $x = 0.10$ and $x = 0.16$ respectively) for low energy transfers. By contrast with the situation for $\hbar\omega = 10$ meV, there is clearly finite spectral weight above the background level at (π, π). However, a careful inspection shows that $\chi''(\mathbf{Q}_{2D}, \omega)$ is slightly depressed at (π, π) compared with the surrounding regions (This is more evident for $x = 0.16$ than for $x = 0.10$), showing that in fact the response remains incommensurate at $\hbar\omega = 30$ meV in both underdoped and optimally doped LSCO for both $T = 10$ K and immediately above T_c.

Fourth, as we observed for $\hbar\omega = 10$ meV, the response at 30 meV for $x = 0.10$ is concentrated in a smaller portion of $\mathbf{Q}_{2D}$-space than is the case for the optimally doped sample, suggesting that a simple scaling of the $x = 0.16$ color maps by the ratios of the measured parameters δ at e.g. $\hbar\omega = 10$ meV would roughly reproduce the $x = 0.10$ color maps. This experimental observation agrees well with the theoretical expectations in spin-based models of the cuprate excitation spectra, see e.g. [219], and with recent calculations of the spin excitations characterizing lattice electrons residing in a spin- and charge-striped environment [226]. In both cases, the upshot is that the real-space distance between the stripes is the key quantity determining the characteristic energy-scales of the excitations.

Fifth, the intensity changes induced by cooling from immediately above T_c to our base temperature 10 K can be studied by comparing the color maps of $\chi''(\mathbf{Q}_{2D}, \omega)$ for a given doping level and energy transfer at the two temperatures, i.e. by comparing panels (a) and (c), (b) and (d), (e) and (g), (f) and (i). At $\hbar\omega = 10$ meV, spectral weight changes are clearly visible for $x = 0.16$ and also, but to a lesser extent, for the underdoped sample. In both cases, the locus of the intensity increase appears to coincide with the normal state incommensurate peak positions. By contrast, little or no intensity change takes place at $\hbar\omega = 30$ meV for either hole concentration.

In considering how to interpret this information, it is important to realize that for the energies and temperatures investigated in Fig. 46, all intensity changes must have their origin elsewhere than in the Bose occupation factor $(n(\omega) + 1)$, since the latter hardly changes between 10 K and $T \simeq T_c$ for the two compositions, and moreover has already been divided out in Fig. 46. Because we have not studied the detailed temperature dependence of $\chi''(\mathbf{Q}_{2D}, \omega)$, when interpreting the data we have to somehow address the question of whether intensity changes detected on cooling from T_c to base temperature simply represent a monotonic continuation of intensity changes taking place already in the normal state for $T \geq T_c$, or whether they set in abruptly at T_c and are consequently direct reflections of the strong electron-electron correlations implied by superconductivity. Finally, there is the third logical possibility, suggested by the high-T_c phase diagram and the temperature dependence of the YBCO resonance mode [189], that the intensity changes set in at the pseudogap temperature $T^* \geq T_c$. For optimally doped LSCO, we can let ourselves be guided by existing literature which concludes that the opening of a spin gap at T_c is accompanied by spectral weight shifting to energies above the spin gap. This picture has been verified for both $La_{1.86}Sr_{0.14}CuO_4$ [142, 148] and $La_{1.84}Sr_{0.16}CuO_4$ [144, 121], and tells us that at least at optimal doping, the intensity shifts up to $\hbar\omega \sim 15$ meV are not simply a monotonic continuation of the temperature-dependence in the normal state, but arise directly as a consequence of superconductivity. By continuation, it stands to reason that any intensity shifts we may find at energies above and beyond $\hbar\omega \simeq 15$ meV in optimally doped LSCO are also a result of superconductivity. For underdoped LSCO, we may expect the situation to be less clear-cut since there appears to be no low-temperature spin gap [147].

7.3.4 Color images of $(k_i/k_f)(d^2\sigma/(d\Omega\ dE_f))_{\rm tot}$

We end this section by presenting a series of color images of $(k_i/k_f)(d^2\sigma/(d\Omega\ dE_f))_{\rm tot}$ spanning the full range of temperatures and energies investigated in the two experiments. Figures 51, 52 and 53 all display data obtained with an incident energy $E_i = 55$ meV. With this incident energy, we focus on the response below $\hbar\omega \sim 40$ meV. For optimally doped LSCO, Fig. 51 shows the measured intensities at $T = 10$ and 40 K for five different energy transfers. For the underdoped composition, Figs. 52 and 53 shows the intensities measured at the same five values of $\hbar\omega$ for $T = 10$, 30, 100 and 300 K. Finally, Fig. 54 displays data from underdoped LSCO obtained at $T = 10$ K with a higher incident energy $E_i = 100$ meV, which allows us to study the spin excitations for energies as high as ~ 80 meV. Just as the data presented in Fig. 46, these images were obtained by averaging the intensities in the four Brillouin zone of the square lattice closest to the origin.

Absolute unit comparisons with $La_{1.875}Ba_{0.125}CuO_4$ and $YBa_2Cu_3O_{6.6}$ Clearly, the data in Figs. 51-54 allow a variety of comparisons to be made, but before turning to these we wish to emphasize that they can also be compared to color images contained in two recent high-profile publications dealing with the (predominantly high-energy) spin responses of stripe-ordered $La_{1.875}Ba_{0.125}CuO_4$ [151] and underdoped YBCO [207]. When comparing with these papers it is important to note that the quantities being presented are not identical: Whereas Tranquada and coworkers present color images of $(k_i/k_f)(d^2\sigma/(d\Omega\ dE_f))_{\rm tot}$ of LBCO in (absolute) units of mbarn sr^{-1} meV^{-1} f.u.$^{-1}$ [151], Hayden *et al.* plot color images of $\chi''(\mathbf{Q}_{2D}, \omega)$ of YBCO in units of μ_B^2 eV^{-1} f.u.$^{-1}$ and present fits of $(k_i/k_f)(d^2\sigma/(d\Omega\ dE_f))_{\rm tot}$ in units of mbarn sr^{-1} meV^{-1} f.u.$^{-1}$ [207]. Because the formula unit of YBCO contains two Cu ions residing in CuO_2 planes whereas the formula units of LSCO and LBCO contains just one copper atom, YBCO intensities and susceptibilities quoted per formula unit must always be divided by two before being compared to similar quantities reported for LSCO and LBCO. The bilayer structure of YBCO leads to an additional complicating factor: For YBCO, the total moment sum rule involves the sum of the acoustic and optical contributions to Eq. (73). If there were no optical excitations, $\chi''_{\rm op}(\mathbf{Q}_{2D}, \omega) = 0$, the acoustic spectral weight would need to be divided by an additional factor of two before comparisons

with single-layer cuprates can be made. This follows because the modulation factor $\sin^2(Q_c\, d/2)$ in Eq. (73) averages to 1/2 over the out-of-plane direction. When finite optical spectral weight is present, comparisons become more tricky.

Since underdoped LSCO is presumably more similar to LBCO than to YBCO, we have elected to present our color plots in terms of $(k_i/k_f)(d^2\sigma/(d\Omega\ dE_f))_{\rm tot}$ rather than in terms of $\chi''(\mathbf{Q}_{\rm 2D},\omega)$. With this choice, the absolute unit intensities in the color images Figs. 52 and 54 should be quantitatively comparable to those of the color images in [151]. For the reasons mentioned above, intensity comparisons between Figs. 51 and 54 and the constant-$\hbar\omega$ cuts presented in Fig. 2 (g)-(l) of [207] for YBCO are only semi-quantitative. The same applies to comparisons between the susceptibility data of our Fig. 46 and Fig. 2 (a)-(f) of [207].

With these comments in mind, the (absolute unit) intensity comparisons reveal that the overall intensity scales of our two experiments and those reported in [151, 207] are all consistent. However, we note that at the lowest energies probed by Tranquada *et al.* ($\hbar\omega = 6\pm2$, Fig. 2(a) in [151]), there is slightly less peak-over-background intensity than in our Fig. 52(f). This minor discrepancy may reflect that the static magnetic order is stronger in LBCO than in our underdoped LSCO sample, and that therefore some of the low-energy weight observed in LSCO has shifted to $\hbar\omega = 0$ meV in LBCO. For higher energy transfers, the intensities in Fig 2 of [151] appear quantitatively consistent with our data on underdoped LSCO at similar energies.

Choosing the color scale Since it appears to have become standard practice [151, 201, 207, 208] to present results of (time-of-flight) studies of the spin fluctuations in cuprates superconductors in terms of such color images, we wish to emphasize the simple but important point that changes in the color scale cause different aspects of the data to come into prominence. This means that − at the very least − great care must be taken not to over-interpret such images, and that a presentation of raw images must always be backed up by concrete analysis.

The color images we present in Figs. 51-54 differ from the color images published by Hayden *et al.* [207] not only in the units used, but also in the treatment of phonon scattering. Hayden and coworkers make an effort to remove the phonon contamination prior to plotting the color maps. By contrast, in our color images the phonon scattering is still present and is clearly visible for some energies and temperatures.

A second, related comment regards the color scales used in Figs. 51-54 versus those used in [207] and [151]: Since the phonon contribution to the total observed scattering has been removed in the images in [207], they are presented using a color scale including negative as well as positive intensities. With this color scale, the remnant magnetic contributions ideally exist on top of a flat background at zero intensity units. By contrast, Tranquada and coworkers do not remove the phonon scattering, and present their images using a color scale chosen (for each $\hbar\omega$) to emphasize changes in the symmetry of the intensity distribution with increasing $\hbar\omega$ [151]. The resulting color plots are suggestive of a 45 degree rotation of the magnetic response at high-energy transfers (See Fig. 45(f)) relative to the incommensurate low energy response. However, we argue that the changes with $\hbar\omega$ of the color scale employed in [151] along with the restricted field of view used, means that this conclusion − and the spin-ladder theories that have followed from it − is more robust for underdoped YBCO [207] than in LBCO where the spin and charge stripe order is presumably static [163].

We present our color images using a color scale which always extends from zero mbarn $\rm sr^{-1}$ $\rm meV^{-1}$ $\rm f.u.^{-1}$. The maximum of the color scale is in each case chosen as a compromise between the desire to facilitate comparisons between different energies, dopings and temperatures (In other words: Changing the color scale as rarely as possible) and the necessity of sometimes changing the scale to keep track with the evolution of the intensity distribution as a function of $\hbar\omega$ and temperature. This choice of color scale makes it important always to keep in mind that underneath the magnetic features, there is a phonon-related background, the intensity of which follows the Bose occupation factor $n(\omega)+1$, as illustrated by Fig. 49.

Let us now turn to a description of the evolution with energy, temperature and doping of the data in Figs. 51-54. We start by looking at the energy dependence of the observed low-temperature intensity distributions in $La_{1.90}Sr_{0.10}CuO_4$ and $La_{1.84}Sr_{0.16}CuO_4$ and at the changes caused by the onset of superconductivity. Next, we focus solely on underdoped LSCO and investigate the development of the intensity distribution as a function of temperature from $T = 10$ K through $T = 30$ and 100 K to room temperature, $T = 300$ K. Finally, we describe the spin dynamics at energies above $\hbar\omega \sim 35$ meV.

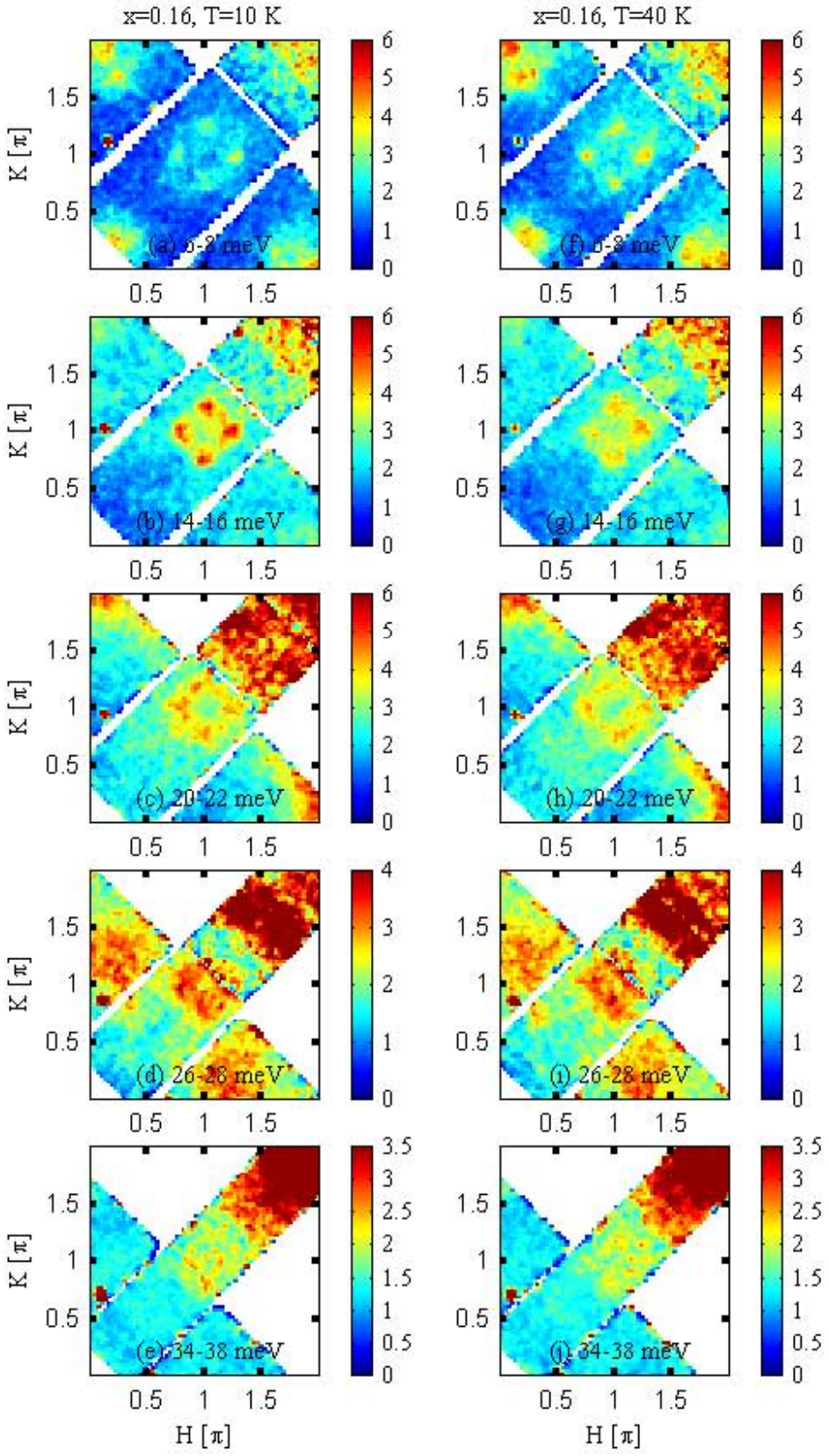

Figure 51: Color images of the intensities $(k_i/k_f)(d^2\sigma/(d\Omega\ dE_f))_{\rm tot}$ in mbarn sr^{-1} meV^{-1} f.u.$^{-1}$ in optimally doped LSCO (T_c = 38.5 K), measured with E_i = 55 meV at T = 10 K (panels (a)-(e)) and T = 40 K (panels (f)-(j)). Note the variation of the color scale.

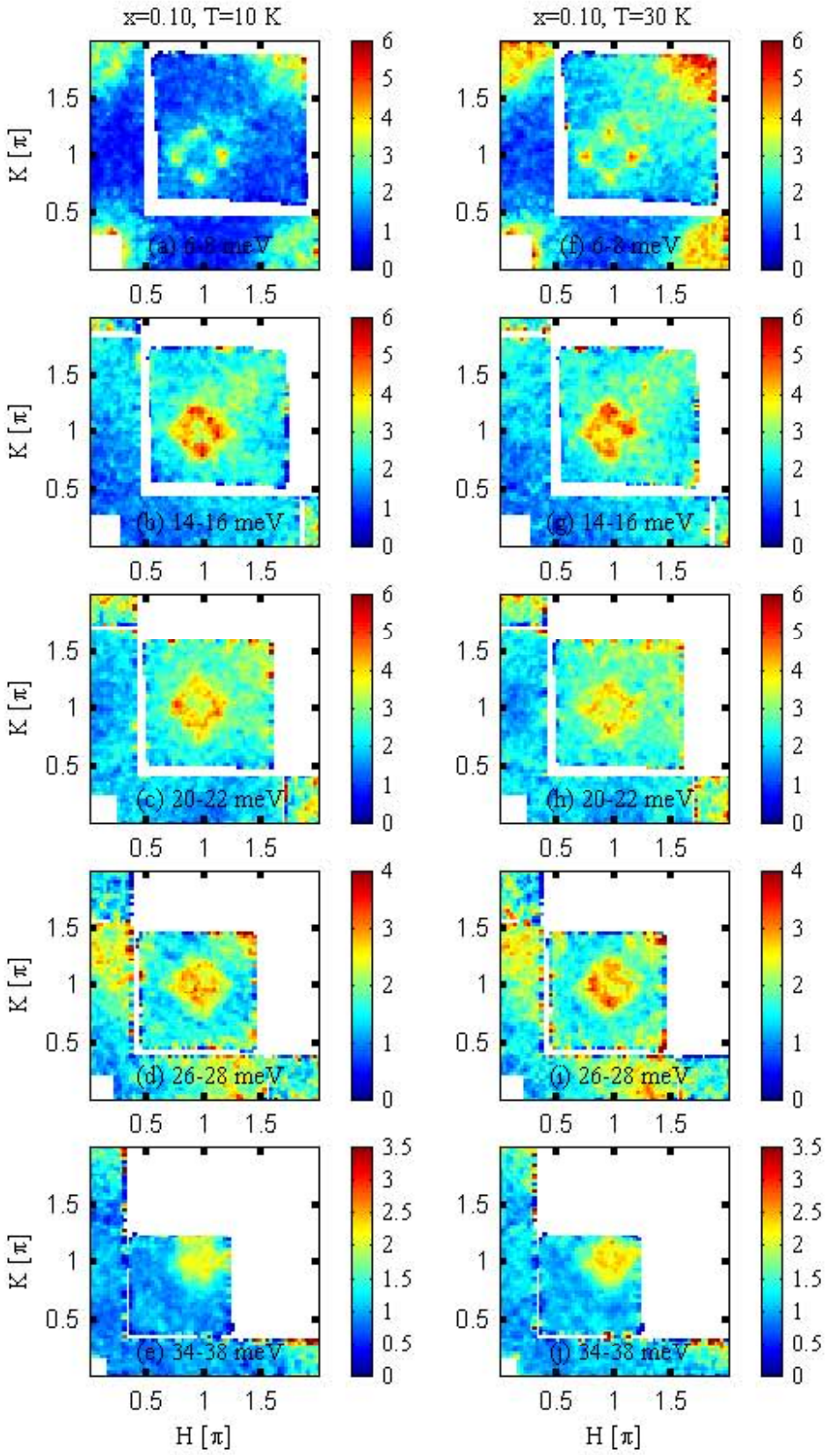

Figure 52: Color images of the intensities $(k_i/k_f)(d^2\sigma/(d\Omega\ dE_f))_{\rm tot}$ in mbarn sr^{-1} meV^{-1} f.u.$^{-1}$ in underdoped LSCO ($T_c = 29$ K), measured with $E_i = 55$ meV at $T = 10$ K (panels (a)-(e)) and $T = 30$ K (panels (f)-(j)). Note the variation of the color scale.

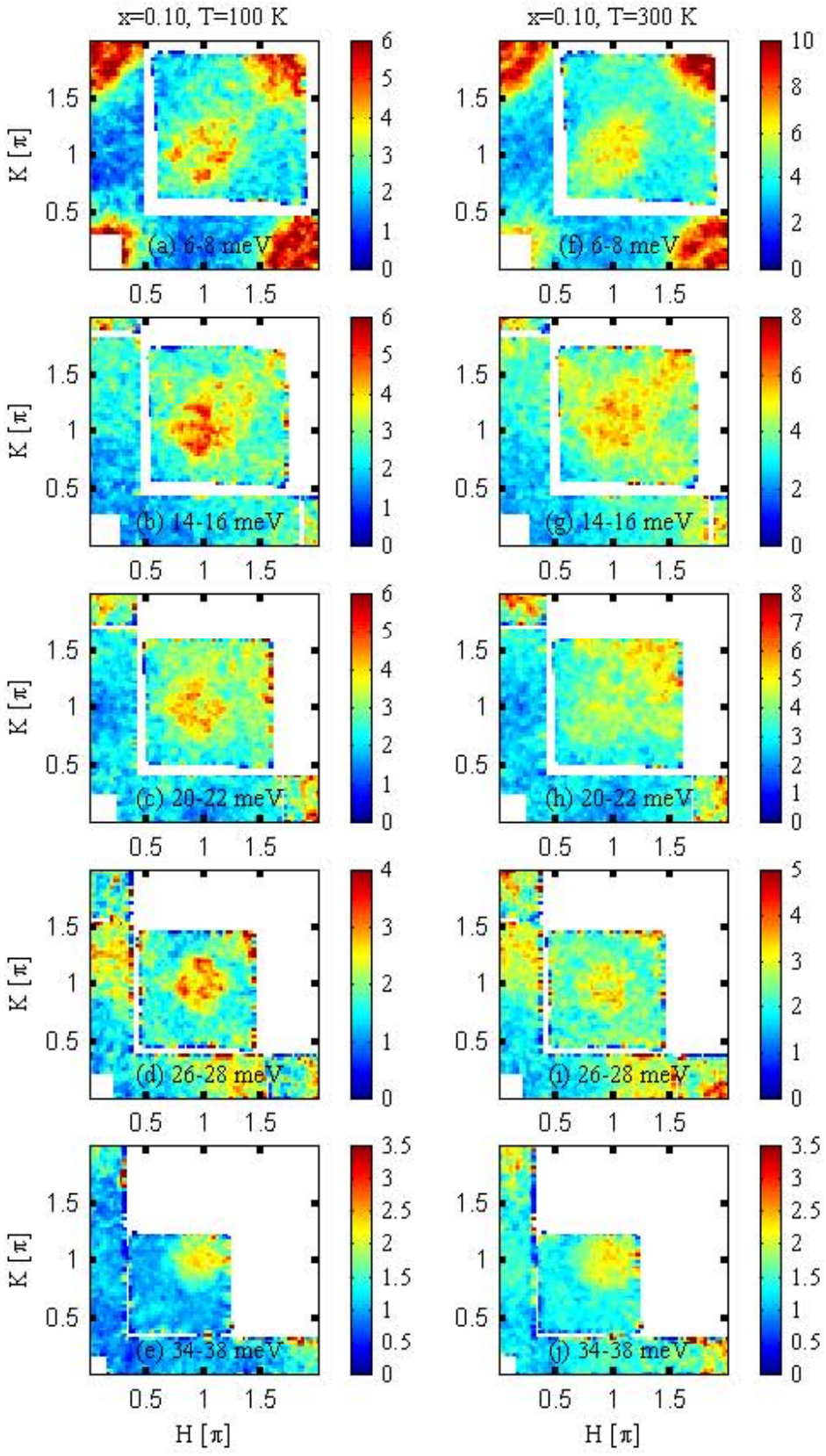

Figure 53: Color images of the intensities $(k_i/k_f)(d^2\sigma/(d\Omega\ dE_f))_{\rm tot}$ in mbarn sr^{-1} meV^{-1} f.u.$^{-1}$ in underdoped LSCO (T_c = 29 K), measured with E_i = 55 meV at T = 100 K (panels (a)-(e)) and T = 300 K (panels (f)-(j)). Note the variation of the color scale.

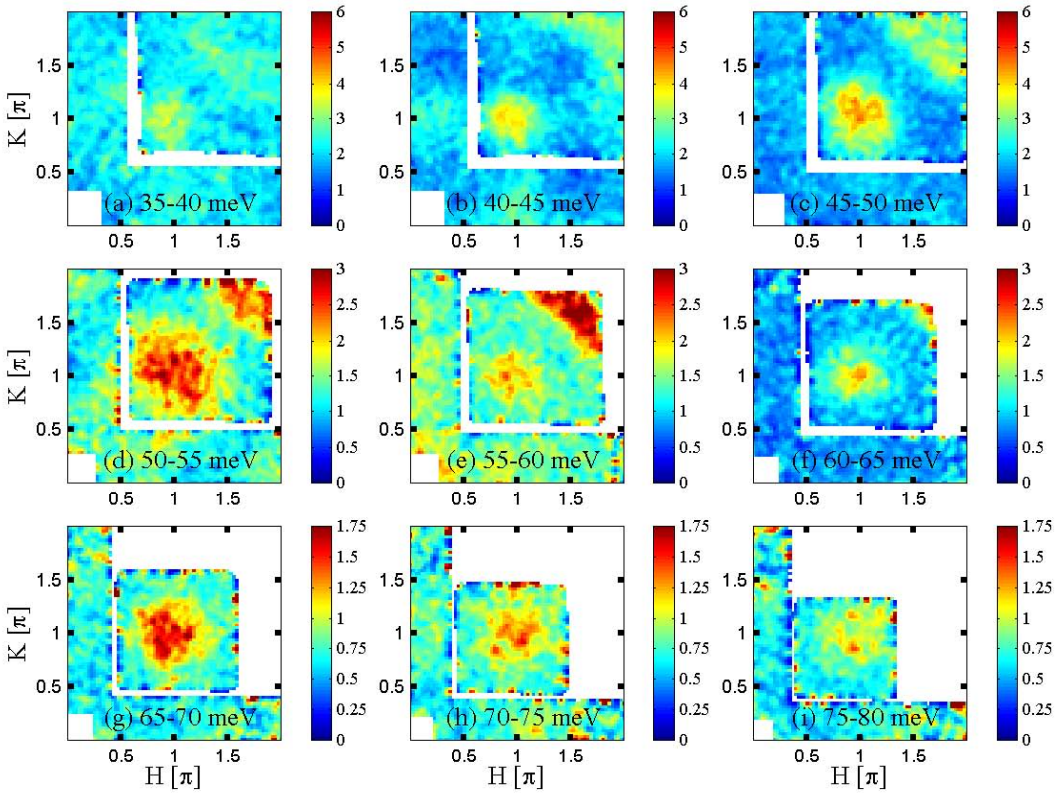

Figure 54: Color images of the intensities $(k_i/k_f)(d^2\sigma/(d\Omega\ dE_f))_{\rm tot}$ in mbarn sr^{-1} meV^{-1} f.u.$^{-1}$ in underdoped LSCO ($T_c = 29$ K), measured with $E_i = 100$ meV at $T = 10$ K. Note the variation of the color scale.

Low-temperature response in $La_{1.90}Sr_{0.10}CuO_4$ and $La_{1.84}Sr_{0.16}CuO_4$ For energies below $\hbar\omega \sim 38$ meV, the spin excitation spectra of optimally doped LSCO in the superconducting and normal states can be visualized with the aid of Fig. 51.

In the energy-range $6-8$ meV shown in Fig. 51(a) we see weak but clear signs of a quartet of incommensurate peaks. The symmetry of the intensity distribution in $\mathbf{Q}_{2D}$-space is that of Fig. 39(d). In particular, there is not much intensity present at $\mathbf{Q}_{2D} = (\pi, \pi)$. Upon going to $\hbar\omega = 14-16$ meV (panel (b) of Fig. 51), we observe that the quartet of incommensurate peaks has gained intensity. At $\hbar\omega = 20-22$ meV, (panel (c)), the quartet has become broader, but the intensity maxima are still displaced from (π, π) along $\langle 10\rangle$ directions. Consequently, there is a local minimum in the magnetic response at (π, π). Also visible in this energy range is an intense phonon background in the high-angle detector bank seen in the upper right corner. At $\hbar\omega = 26-28$ meV (panel (d)), the response has broadened further and now appears to have the symmetry of a square surrounding (π, π). There are still hints of a weak intensity depression at (π, π). Note that in going from panel (c) to panel (d) in Fig. 51 the color scale was changed. Yet another color scale change takes place upon going to panel (e) which shows the intensity distribution at $\hbar\omega = 34-38$ meV where there are only weak signatures of scattering in the region around (π, π).

In the normal state at $T = 40$ K, i.e. immediately above T_c, we observe that the response in the range $6-8$ meV (Fig. 51(f)) is incommensurate just as it is in the superconducting state at the same energies (Fig. 51(a)). However, the intensities of the four peaks are clearly larger in the normal state at $T = 40$ K than in the superconducting state at $T = 10$ K. By contrast, when we compare the superconducting and normal state responses at $\hbar\omega = 14-16$ meV (panels (b) and (g)) the picture has turned around: There is now more scattering below than above T_c. These are the well-known signatures of the opening of a spin gap below T_c. Intensity is removed below the spin gap Δ_s and shifted to energies above the gap [144, 148]. In the very same optimally doped LSCO crystals used for our experiment, Lake *et al.* have determined the low-temperature value $\Delta_s = 6.7$ meV [144], which falls inside the intensity range averaged over in Fig. 51(a) and (f). Our data allow us to track the intensity redistribution associated with superconductivity and the spin gap to higher energies than has previously been possible. In the range $\hbar\omega = 20-22$ meV,

we can see by comparing panels (c) and (h) in Fig. 51 that there is still slightly more intensity in the superconducting state than in the normal state. On the other hand, at $26-28$ meV, there appears to be little or no difference − in terms of intensity and $\mathbf{Q}_{2D}$-space symmetry − in the response around (π,π) between the superconducting and normal states (Fig. 51(d) and (i)). The same comment applies to the weak intensities seen in panels (e) and (j).

Let us now turn to the data for underdoped LSCO at $T = 10$ and 30 K shown in Fig. 52. By contrast with the optimally doped case shown in Fig. 51, any signature of a spin gap in the underdoped sample is much less evident at $\hbar\omega = 6-8$ meV in Fig. 52(a) and (f), although there does appear to be a slight intensity increase of the normal state response at $T_c+1 = 30$ K over the superconducting response at 10 K. At $14-16$ meV (panels (b) and (g)), there are no clear intensity differences between the incommensurate features. Between 20 and 22 meV, there appears to be slightly more intensity in the superconducting state than in the normal state and the intensity profiles resemble a square surrounding (π,π). At $\hbar\omega = 26-28$ meV and $34-38$ meV, the profiles become progressively less intense. They also seem to develop intricate internal structures, but with the color scales chosen it is likely that these structures are simply reflections of statistical fluctuations in the neutron count rates. It will be noted that the intensities in the range $34-38$ meV are larger for underdoped than for optimally doped LSCO and appear to be concentrated in a smaller portion of $\mathbf{Q}_{2D}$-space.

A common characteristic of the spin fluctuation spectra of underdoped and optimally doped LSCO present at all energies and temperatures in Figs. 51 and 52 is the overall symmetry and development of the intensity pattern: With increasing $\hbar\omega$, incommensurate peak profiles with the symmetry of Fig. 39(d) develop into diffuse square-like shapes surrounding (π,π). The edges of these squares run along $\langle 11\rangle$ directions, i.e. along the directions joining nearest neighbor (in $\mathbf{Q}_{2D}$-space) neighbor incommensurate low-energy peaks. It is also evident that we are not observing an isotropic broadening of the low-energy incommensurate peaks with increasing $\hbar\omega$. Instead, the "center of gravity" of the intensity profiles moves inwards, i.e. towards $\mathbf{Q}_{2D} = (\pi,\pi)$, where the response increases as a function of increasing $\hbar\omega$. By contrast, there are no obvious intense components of the spin fluctuation spectra dispersing in the directions away from (π,π) relative to the low-energy peak positions as one would have expected if the spin excitations were related in a simple manner to conventional, isotropic antiferromagnetic spin waves. Thus, the color images allow us to infer that the dominant spin excitations are dispersive and move towards (π,π) with increasing $\hbar\omega$.

Temperature evolution of the response in $La_{1.90}Sr_{0.10}CuO_4$ Having described the magnetic response of underdoped LSCO below ~ 38 meV in the superconducting state and immediately above T_c, we turn to an investigation of Fig. 53 which illustrates the intensity distributions in $La_{1.90}Sr_{0.10}CuO_4$ at $T = 100$ and 300 K respectively at the same energy transfers as in Figs. 51 and 52. When inspecting these images, it should be noted that it has been necessary to change the color scales used for the $T = 300$ K data in Figs 53(f)-(j) in order to prevent the magnetic signal around (π,π) from being overwhelmed by background scattering from lattice degrees of freedom.

At $T = 100$ K, Fig. 53(a) shows that the response is incommensurate at $6-8$ meV. The peak widths appear broadened relative to the $T = 10$ and 30 K cases displayed in Fig. 52(a) and (f). Increasing the temperature to 300 K (Fig. 53(f)) causes a dramatic change: The incommensurate structure is now no longer evident and the symmetry of the intensity distribution is more similar to that observed for $\hbar\omega \sim 30$ meV at $T = 10$ and 30 K. Comparing Fig. 52(a) and (f) to Fig. 53(a) and (f) it is also evident that the scattering near $(2\pi,0)$ and equivalent positions is related to phonons since its intensity grows with increasing temperature. Moving to $14-16$ meV (panels (b) and (g) of Fig. 53), the intensity distributions again appear to broaden and gradually loose definition relative to the low-temperature data at the same energies, displayed in panels (b) and (g) of Fig. 52. However, the effect is less dramatic in the range $14-16$ meV than at $6-8$ meV. Thus, the influence of increasing temperature on the low-energy incommensurate profiles are strongest at low energy transfers and gradually become less prominent with increasing $\hbar\omega$. As a rough rule-of-thumb, the symmetry in $\mathbf{Q}_{2D}$-space of the excitations at an energy $\hbar\omega$ and for the temperatures $T = 30$, 100 and 300 K appears to be equivalent to the symmetry observed at $T = 10$ K at an energy transfer $\sim \sqrt{\hbar\omega^2 + (k_BT)^2}$. Such E/T-scaling behavior has previously been reported by Aeppli and coworkers for the widths of the low-energy, normal-state spin fluctuations in near-optimally doped $La_{1.86}Cu_{0.14}CuO_4$ where it was interpreted as a signature of a nearby quantum critical point [114].

In comparing the $14-16$ meV data presented in Fig. 53(b) to the data displayed in Fig. 52(b) and (g), it appears that there is more intensity at $T = 100$ K than at lower temperatures. However, this is most likely explained by the existence of a non-zero phonon background below the magnetic features. This conclusion is supported by the 300 K data in Fig. 53(g), which shows clear signs of phonon scattering in the form of broad lines of scattering extending from (π, π) along the $\langle 11 \rangle$ directions. Moreover, for $\hbar\omega \sim 15$ meV, Fig. 49 shows that a larger phonon background at $T = 100$ K than at lower temperatures is consistent with the influence of the Bose occupation factor in the cross-section for phonon scattering.

At energies above 20 meV (panels (c)-(e) and (h)-(j) of Fig. 53) the symmetries of the intensity distributions in $\mathbf{Q}_{2D}$-space appear to be the same at $T = 100$ and 300 K. They are consistent with the squarish patterns seen at high-energies in Fig. 52, although the differences in the color scales make it hard to draw firm conclusions. For $\hbar\omega = 20-22$ meV, the intensities appear to be larger at 100 K than at 300 K (panels (c) and (h)), but at higher energies even this difference tends to vanish. Thus, the spectra obtained in the range $\hbar\omega = 34-38$ are equivalent in terms of both their $\mathbf{Q}_{2D}$-space symmetries and (approximately) in terms of their intensities at all temperatures from $T = 10$ to 300 K.

Generally, a comparison of the $T = 300$ K data shown in Fig. 53(f)-(j) with the data obtained at the same energy transfers but at lower temperatures (Fig. 52 and Fig. 53(a)-(e)), reveals that phonon scattering is a great cause for concern at high temperatures. In fact, for many values of $\hbar\omega$, a quantitative analysis of the magnetic contribution to the total observed scattering at 300 K was found to be impossible. At such energies, we are left with the important but limited information that can be extracted by inspection of the color images in Fig. 53(f)-(j).

High-energy response in $\mathbf{La_{1.90}Sr_{0.10}CuO_4}$ Finally, we turn to figure 54 for an investigation of the low-temperature response of underdoped LSCO above $\hbar\omega \sim 35$ meV. The nine panels in this figure show the evolution with energy in steps of 5 meV from $\hbar\omega = 37.5$ meV to 77.5 meV.

The most prominent feature in these data is a sharp peak in the intensity around $\mathbf{Q}_{2D} = (\pi, \pi)$ in the range $\hbar\omega = 45-50$ meV (Fig. 54(c)). At first sight, one might be tempted to think that this feature could be the long sought after commensurate resonance mode of LSCO. However, we believe (but cannot definitively prove) that the effect arises as a consequence of an intense phonon branch being intersected by the time-of-flight parabola in this energy range. In support of this interpretation, we note that in the $40-45$ meV color map shown in Fig. 54(b) there are hints of broad lines of scattering extending from (π, π) along $\langle 10 \rangle$ directions. By analogy with panel (g) of Fig. 53 where we noted similar broad lines along the $\langle 11 \rangle$ directions (which could be unambiguously identified as phonons due to their temperature evolution), we expect the lines in Fig. 54(b) to be phonon related as well, and to be connected to the intense feature at (π, π) for $\hbar\omega = 45-50$ meV. We also emphasize, that in panel (d) of Fig. 54 which shows the response at energies immediately above the $45-50$ meV feature, the intensity distribution is broader in $\mathbf{Q}_{2D}$-space than at any other energy investigated. This observation is not consistent with any known phenomenology of the resonance modes in $YBa_2Cu_3O_{6+y}$, $Bi_2Sr_2CaCu_2O_{8+x}$ and $Tl_2Ba_2CuO_{6+\delta}$. Furthermore, the experimental phonon density of states data [231] contained in Fig. 49 indicates a sharp peak around $\hbar\omega = 47$ meV. This peak position is in excellent agreement with our $\mathbf{Q}_{2D}$-space averaged data in the same figure. Finally, we note that Tranquada *et al.* [151] mention potential problems with phonon scattering around 47 meV. For these reasons, we consider phonon scattering to seriously jeopardize quantitative analysis of our data between 40 and 55 meV. Therefore, we focus our attention only on the data contained in panels (a) and (e)-(i) of Fig. 54.

Recently, the nature of the high-energy response has become a subject of much debate [151, 207, 208, 209]. The studies of $La_{1.875}Ba_{0.125}CuO_4$ by Tranquada *et al.* [151] and of $YBa_2Cu_3O_{6.6}$ by Hayden *et al.* [207] reported that the symmetry of the high-energy response rotates 45 degrees with respect to that of the low-energy response. At low energy transfers these authors see well-defined incommensurate peaks with the symmetry of Fig. 39(d), whereas at high energies they observe much broader, square patterns surrounding (π, π) with more or less well-defined peaked incommensurate features inside the squares. The squares and peaks are rotated by 45 degrees (see Fig. 45(f) for a schematic illustration), so that the edges of the square run along $\langle 10 \rangle$ directions rather than along $\langle 11 \rangle$ directions. On the other hand, studies of oxygen-ordered $YBa_2Cu_3O_{6.5}$ by Stock *et al.* [208] and of near-optimally doped $YBa_2Cu_3O_{6.85}$ by Hinkov *et al.* [209] have concluded that the excitations at energies above the YBCO resonance mode are more closely similar to isotropically dispersing spin wave excitations. In the former case, the intensity distribution of

these spin waves was reported to be isotropic around (π,π) [208], whereas in the latter case [209], a one-dimensional anisotropy of the spin-wave intensities was found.

From the data presented in Fig. 54, it is very hard to say anything conclusive about the $\mathbf{Q}_{2D}$-space symmetry of the high-energy magnetic scattering in underdoped LSCO. The data displayed in Fig. 52(a)-(e) indicate that the signatures of well-defined incommensurate peaks disappear at lower energy transfers and become replaced by intensity patterns resembling squares. These squares are centered on (π,π) and their edges are parallel to $\langle 11\rangle$. The magnetic signal observed above ~ 35 meV in panels (a) and (e)-(i) of Fig. 54 is a broad feature centered around (π,π). Assigning a definite $\mathbf{Q}_{2D}$-space symmetry to the intensity distributions at the energies of these images is nearly impossible, but a tentative conclusion would be that the rotated square symmetry of [151, 207] is less likely than both isotropic spin waves [208] and a continuation to higher $\hbar\omega$ of the squares with edges along $\langle 11\rangle$, which are observed below ~ 35 meV.

7.4 Data analysis

To model the data presented in the previous section we have chosen the phenomenological lineshape

$$\chi''(\mathbf{Q},\omega)=\chi''(\mathbf{Q}_{2D},\omega)=\chi''_{\delta}(\omega)\sum_{\delta}\frac{\kappa^4(\omega)}{\left(\kappa^2(\omega)+\left[\mathbf{Q}_{2D}-\mathbf{Q}_{\delta}(\omega)\right]^2\right)^2} \tag{89}$$

The sum runs over four incommensurate reciprocal lattice positions $\mathbf{Q}_{\delta}(\omega)$ with the symmetry shown in Fig. 39(d), i.e. $\mathbf{Q}_{\delta}(\omega)\in\{(\pi\,(1\pm\delta(\omega))\,,\pi)\,,(\pi,\pi\,(1\pm\delta(\omega)))\}$. Allowance is made for broadening and dispersion, reflected in $\hbar\omega$-dependent width and incommensurability parameters $\kappa(\omega)$ and $\delta(\omega)$. At each energy transfer we assume that the four incommensurate peaks have equal intensity. Thus, only one peak intensity parameter $\chi''_{\delta}(\omega)$ enters Eq. (89). Note that the out-of-plane component of $\mathbf{Q}$ is absent on the right-hand side of Eq. (89). Thus, the spin fluctuation spectrum is assumed to be two-dimensional, and we have consequently written $\chi''(\mathbf{Q},\omega)=\chi''(\mathbf{Q}_{2D},\omega)$.

It is important to stress that we do not claim that the spin fluctuation spectrum of LSCO can be adequately modeled by Eq. (89) over the extended energy intervals investigated in this chapter. The spirit of the analysis which we have carried out is merely to choose a lineshape suitable for a rough description of the crossover from sharp incommensurate peaks at low energy to the significantly broader scattering profiles seen at higher energies.

Specifically, the use of Eq. (89) prevents us from addressing issues such as whether there exists systematic intensity differences between the four incommensurate peaks surrounding a given zone center wavevector $\mathbf{Q}_{2D}$, as expected in a stripe scenario (See Fig. 40). Because each LSCO crystal is typically found to be twinned and since we may easily have mixed up orthorhombic **a** and **b** axes in the alignment of the 4 and 9 crystals used for the experiments, the restriction of having only one amplitude parameter is a minor one.

The actual data fitted to the model (82) were in the form of constant energy cuts and were created using Mslice. The majority of our fits were performed using transverse cuts. By "transverse" we mean cuts in $\mathbf{Q}_{2D}$-space along $[1\overline{1}]$ directions, as illustrated in Fig. 55(a). To check the consistency of the results obtained by analyzing transverse cuts, we have also analyzed the data by using longitudinal cuts, i.e. cuts along the [11] direction as shown in Fig. 55(b).

The reason for working primarily with transverse cuts lies in considerations of the origin of the background scattering lying underneath the magnetic features which we attempt to model using Eq. (89): We expect the background cross-section $\left(d^2\sigma/(d\Omega\;dE_f)\right)_{\rm bg}$ to consist predominantly of contributions from processes in which a neutron creates (for $\hbar\omega>0$ meV) coherent and incoherent one-phonon or multi-phonon excitations. Being a displacement mode, one-phonon scattering grows as $|\,\mathbf{Q}\,|^2$ [1]. If the dispersion of a particular phonon branch is not to shallow, it can be expected to give rise to peaks in constant-$\hbar\omega$ cuts. By contrast, in coherent multiphonon processes the crystal momentum and energy transferred by the neutron to the sample is shared by two or more phonons, leading to multiphonon cross-sections which are featureless as a function of $\hbar\omega$ and simply add to the overall background level in a given constant-$\hbar\omega$ cut. The dependence of the $N_{\rm ph}$-phonon intensity on $|\,\mathbf{Q}\,|$ is generally expected to become more rapid, e.g. $I_{N_{\rm ph}}\propto|\,\mathbf{Q}\,|^{2N_{\rm ph}}$, as the number of phonons $N_{\rm ph}$ involved grows [1]. In terms of extracting the parameters characterizing magnetic scattering, the advantage of transverse over longitudinal constant-$\hbar\omega$ cuts lies in the fact that for the former, all points are at approximately the same $|\,\mathbf{Q}\,|$. Consequently, multiphonon scattering

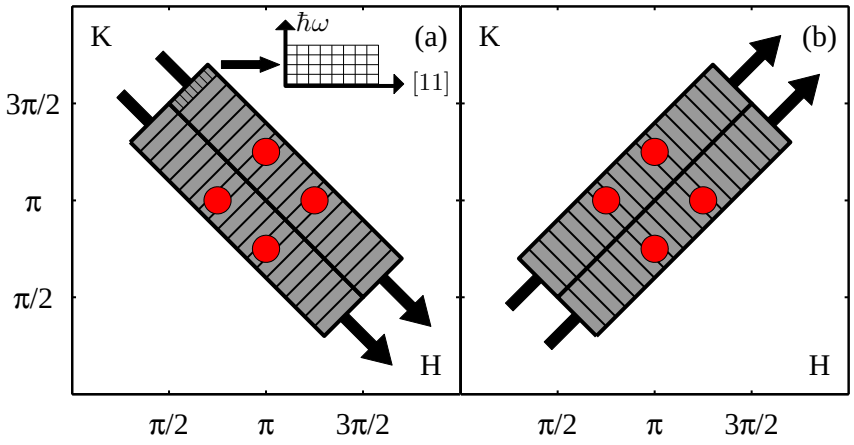

Figure 55: Geometry in $\mathbf{Q}_{2D}$-space of (a) constant-$\hbar\omega$ transverse cut-files (b) constant-$\hbar\omega$ longitudinal cut-files. The grey area represents the total region of $\mathbf{Q}_{2D}$-space probed. In most cases, we have chosen to subdivide this area into two cut-files, as indicated by the arrows. To ensure that all magnetic intensity is included in the analysis, the cut-files are arranged back-to-back and their widths in $\mathbf{Q}_{2D}$-space transverse to the direction of the arrows are chosen to be large enough for the grey area to enclose the majority of the peak-over-background intensity visible in color maps such as those shown in Fig. 46. Each cut-file contains a user-defined number of points along the cut-direction. In the cases shown, there are 20 points in each cut. For each of these points, the intensity is computed by averaging the intensities of all detectors inside the area of (for the case of transverse cuts) $([11], \hbar\omega)$-space defined by the user when choosing the energy window and transverse $\mathbf{Q}_{2D}$-space width of the cut. In the case shown schematically in (a), each point in a cut corresponds to an average over 8 pixels, each of which probes three different energy-transfer intervals.

should vary little across such a cut and the background is expected to be flat unless the time-of-flight parabola happens to intersect a one-phonon branch in the same interval of energy-transfers. For longitudinal cuts on the other hand, the background should increase with $|\mathbf{Q}|$. It is because flat backgrounds are preferable for obtaining good, stable fits, that we have mostly used transverse cuts in our analysis.

Although transverse cuts are generally easier to fit, there are good reasons to analyze longitudinal cuts as well. For the experiment on optimally doped LSCO, one advantage of longitudinal cuts over transverse becomes evident at high energy transfers: Upon going to higher values of $\hbar\omega$, the location on the MAPS detector banks of the interesting region around $\mathbf{Q}_{2D} = (\pi, \pi)$ containing magnetic intensity moves to higher scattering angles $2\theta_S$. With the sample orientation chosen for the $x = 0.16$ experiment, it happens that when $\hbar\omega$ approaches 30 meV, one of the four equivalent (π, π) regions ($\mathbf{Q} = (\pm 10L)$ and $\mathbf{Q} = (0 \pm 1L)$) starts to move into the high-angle bank of the spectrometer (as can be seen in e.g. Fig. 46(f) and (h)) whereas the three others begin to leave the low-angle detector banks altogether. For magnetic scattering taking place in the high-angle detector banks, transverse cuts become quite difficult to analyze because the number of pixels containing scattering at the background level is reduced. It is even possible − because the magnetic signal broadens with $\hbar\omega$ − that there are no pixels available to define the background with reasonable accuracy. In this situation, it is critical to be able to analyze longitudinal cuts as a double-check on the analysis of transverse cuts. In the $x = 0.10$ experiment, similar problems with the background determination come into prominence at high energy transfers when the four (π, π) regions approach the corners of the MAPS detector banks. In this case also, it is important to analyze longitudinal cuts as a cross-check.

For both doping levels, the main problem in analyzing longitudinal cuts is the increase in background scattering from phonons as a function of $|\mathbf{Q}|$. When the magnetic response is weak, broad and superimposed on a background with a strong curvature, sensible fits can be hard to achieve. With the sample orientation used in the $x = 0.16$ experiment, wavevectors around $\mathbf{Q} = (30L)$ ($\mathbf{Q}_{2D} = (\pi, \pi)$) fall onto the high-angle detector bank, and could in principle be analyzed by using longitudinal cuts. However, the drop in the Cu^{2+} form factor with $|\mathbf{Q}|$ combined with strongly increasing background scattering as a function of $|\mathbf{Q}|$ make it very difficult to extract sensible information from such fits. For this reason, we have only analyzed magnetic scattering occurring around the four lowest-$|\mathbf{Q}|$ zone centers $\mathbf{Q} = (\pm 10L)$ and $\mathbf{Q} = (0 \pm 1L)$.

To extract reliable information about $\chi''(\mathbf{Q}_{2D}, \omega)$ from analysis of cut-files it is critical to take

resolution effects explicitly into account. These corrections are affected by the Tobyfit least-squares fitting program [82] described in section 4.2.2. The program convolves a user-defined model cross-section with the instrumental resolution function calculated on the basis of the fixed instrument lengths and moderator characteristics along with the chosen chopper frequency and incident energy E_i. The resulting calculated cross-section is subsequently fitted to the experimental data using the least-squares method [232].

For our model cross-section, we use Eq. (89) multiplied by the Bose occupation factor $[n(\omega)+1]$ and by the isotropic Cu^{2+} form factor. Equation (82) shows that apart from numerical factors this cross-section equals the magnetic contribution $(k_i/k_f)(d^2\sigma/d\omega\ dE_f)_{\mathrm{mag}}$ to the total observed intensity $(k_i/k_f)(d^2\sigma/d\omega\ dE_f)_{\mathrm{tot}}$.

As explained in section 4.2.2 and illustrated in Fig. 55(a), the cut-files used as input to Tobyfit retain full information about the values of $\mathbf{Q}$ and $\hbar\omega$ of all detectors contributing to any given point in a cut-file. When fitting, the program uses all these numbers and not just the nominal energy and the single $\mathbf{Q}_{\mathrm{2D}}$-values projected onto the axis defining the direction of the cut. This means, that effectively we are performing fits on a finite surface element in a four-dimensional space spanned by $\hbar\omega$ and the three Cartesian components of $\mathbf{Q}$, constrained by the equation for the time-of-flight parabola Eq. (23). With our working assumption that $\chi''(\mathbf{Q},\omega)$ is independent of the component of $\mathbf{Q}$ perpendicular to the CuO_2 planes, we can use this to our advantage by creating cuts in the side-by-side fashion shown in Fig. 55 and fitting them simultaneously. In this case, we are effectively − in a single Tobyfit session − fitting $\chi''(\mathbf{Q},\omega) = \chi''(\mathbf{Q}_{\mathrm{2D}},\omega)$ over the entire grey area in Fig. 55 and over an energy window of our choice.

From each Tobyfit session − involving the fitting of a single cut-file or two or more simultaneously fitted cut-files − we extract

- A peak displacement parameter $\delta(\omega)$
- A width parameter $\kappa(\omega)$
- A peak intensity parameter $\chi''_\delta(\omega)$
- Parameters describing the background variation
- A goodness of fit measure χ^2_{red}

The peak displacement parameter $\delta(\omega)$ quantifies the separation of the dominant spin excitations from $\mathbf{Q}_{\mathrm{2D}} = (\pi,\pi)$ at each $\hbar\omega$. The peak width parameter $\kappa(\omega)$ is related to the correlation length $\xi(\omega)$ − equal to the inverse half-width at half maximum (HWHM) of the peak profile − for spin excitations at the particular energy transfer $\hbar\omega$ by

$$\xi(\omega) = \frac{1}{\left(\sqrt{2}-1\right)^{1/2}\kappa(\omega)} \tag{90}$$

This energy dependent correlation length should not be confused with the thermodynamic correlation length $\xi(T)$ measured in two-axis experiments, where one integrates over all energy transfers modulo energy cutoffs determined by E_i and the magnetic form factor. Instead, $\xi(\omega)$ is the correlation length for spin fluctuations on the time scale $2\pi/\omega$. Correcting for the constant factors in Eq. (82) (with $\mu_B = 1$) the peak intensity parameter $\chi''_\delta(\omega)$ in Eq. (89) can be expressed in absolute units μ_B^2 eV^{-1} $\mathrm{f.u.}^{-1}$. At each energy transfer, the fitted values of $\chi''_\delta(\omega)$, and $\kappa(\omega)$ allow us to derive the local susceptibility $\chi''(\omega)$ in Eq. (86) in absolute units μ_B^2 eV^{-1} $\mathrm{f.u.}^{-1}$. As was noted in section 7.2, the local susceptibility of a system with purely two-dimensional correlations is identical to the Brillouin zone averaged susceptibility $\chi''_{\mathrm{2D}}(\omega)$ defined by Eq. (88).

Once the local or Brillouin zone averaged susceptibilities have been determined at all energies investigated, we can integrate over $\hbar\omega$ according to Eq. (87) in order to evaluate the fraction of the mean-squared fluctuating moment $\langle m^2\rangle$ per copper site responsible for the fluctuations observed the energy window investigated. Moreover, since $\chi''(\omega)$ can be evaluated at all temperatures and for both compositions studied, we can investigate the evolution of $\langle m^2\rangle$ with hole-doping and temperature in absolute units.

7.4.1 Different modes of analysis

There are several manners in which to approach the analysis. For example, it has already been mentioned that one can use both longitudinal and transverse cuts to analyze the same data, and that doing so is important for cross-checking the results obtained using either method. More generally, the way the background scattering is treated leads to a distinction between different modes of analysis. Furthermore, since the magnetic part of the total observed spectrum broadens and weakens with increasing $\hbar\omega$, it can be useful to symmetrize the data around $\mathbf{k}_i$ to obtain better counting statistics.

In analyzing the data from each of the two experiments, we have attempted many different plans of attack, combining the ideas listed above. Generally speaking, all modes of analysis were found to lead to consistent results in terms of the parameters appearing in Eq. (89) and derived quantities such as the local susceptibility $\chi''(\omega)$.

We emphasize, that this consistency between the methods should not be mistaken for equivalence. Either method has its shortcomings and may fail in some energy-transfer intervals because of the interference of strong phonon-scattering. However, the overall trends with $\hbar\omega$ of the quantities derived from the analysis were found to be robust. Using several different method to analyze the same data is in effect an attempt to circumnavigate the problems caused by the inability of our phenomenological model Eq. (89) to account for all features of the observed intensity distribution. Background problems related to phonons manifest themselves in slightly erratic variations with $\hbar\omega$ in the parameters derived from fits of the data. What is important is that since we cannot expect to provide a mathematically accurate description of all magnetic and non-magnetic contributions to the observed intensity distribution, we must accept a certain degree of numerical scatter in our results. Analyzing the data using a variety of strategies allows a consistent "average" mental picture to be obtained, which can act to guide further analysis.

Background models The simplest method of analysis is to treat the background scattering as local to each cut, and include it in the fitting procedure. The background is then allowed to vary along the cut-direction, but not along perpendicular $\mathbf{Q}_{2\mathrm{D}}$-directions. Thus, when fitting transverse cuts the variation of the background along the longitudinal direction is ignored, and vice versa. Because the background generally varies most rapidly along the longitudinal $\mathbf{Q}$ direction, one may argue that since we have mostly analyzed transverse cuts, this simple method is systematically wrong. On the other hand, the width of the transverse scans along the longitudinal direction is relatively small, see Fig. 55, and therefore the background should in most cases not vary too dramatically along this direction. Furthermore, by choosing to fit two transverse cuts at each energy transfer $\hbar\omega$, each of which is allowed to have its own local background level, the variation along $|\mathbf{Q}|$ is at least partially accounted for. Finally, in the interest of keeping the number of parameters to be fitted at a minimum, we have considered it an unnecessary complication to treat the background as varying along two $\mathbf{Q}_{2\mathrm{D}}$-space directions and along $\hbar\omega$. In practice, depending on circumstances (which are judged by inspection of the cuts at each energy), the local background model is chosen to be flat, sloping or even quadratic in the $\mathbf{Q}_{2\mathrm{D}}$-component along the cut-direction.

An alternative method consists in attempting to use the large $\mathbf{Q}$ coverage of MAPS to model the background in order to subtract this contribution from the data before fitting. One then hopes to get a background level of zero at all energies, thereby reducing the number of parameters to be fitted. In practice we have carried out this program as follows: For each energy interval to be fitted, we selected the regions of $\mathbf{Q}$-space for which the MAPS detectors have $|\mathbf{Q}|$-values between limits set by the lowest and highest $|\mathbf{Q}|$ in the two transverse cuts at that energy. Next, we exclude from this $\mathbf{Q}$-space region all detectors used for the transverse cuts themselves, and remove by hand any signal in the remaining region that is clearly spurious or likely to be due to coherent phonon scattering. Then, we plot the intensities of the remaining detectors as a function of their respective $|\mathbf{Q}|$-values and fit these data to a quadratic lineshape $a(\omega) + b(\omega)\,|\mathbf{Q}| + c(\omega)\,|\mathbf{Q}|^2$ (Using a different combination of terms does not alter the final results of the analysis). Keeping the fitted coefficients $a(\omega)$, $b(\omega)$ and $c(\omega)$, we then revert to the original data file, subtract the appropriate global background function $\sum_\omega \left(a(\omega) + b(\omega)\,|\mathbf{Q}| + c(\omega)\,|\mathbf{Q}|^2\right)$ and only then create the cut-files to be fitted.

There are several problems with this method. First, it implicitly assumes that the background has no structure along the transverse $\mathbf{Q}$-direction. This is not always the case. The method fails to give a background level of zero when the background curves or slopes along the cut-direction.

Therefore, even for the background corrected data, it is still necessary to allow for background variations along the transverse direction, treating the background as local to each cut. By doing so, the background is effectively allowed to vary along two perpendicular directions: The variation perpendicular to the cut-direction is treated prior to creating the cut-files, whereas the variation along the cut-direction is treated by Tobyfit. In principle this makes the background subtraction approach preferable to the method involving no background subtraction. However, the regions of **Q**-space employed to fix the variation of the background along the longitudinal direction, even though they have the same $|\,\mathbf{Q}\,|$ as the transverse cuts, are quite far away in reciprocal space, and in practice sometimes contain significantly less or more scattering than the background in the cut-regions, which in turn leads to under- or over-subtraction. In this case one may doubt whether the background subtraction procedure is more reliable than the approach of simply having one local background model per cut. Another difficulty with the background subtraction is that it does not take care of the continuity of the background in any give detector as a function of $\hbar\omega$, as by construction the background is evaluated only once for each value of $|\mathbf{Q}|$. We have found that choosing a small energy bin size for the background evaluation reduces but does not eliminate this particular problem.

We estimate that when phonon scattering is relatively weak, i.e. at low temperatures, the background subtraction procedure discussed above is slightly preferable to analyzing the raw data without background corrections.

Symmetrization Because the four $\mathbf{Q}_{2\mathrm{D}} = (\pi, \pi)$-regions we are fitting are equivalent, one can symmetrize them to improve statistics. More precisely, this is done by rotating equivalent zones around $\mathbf{k}_i$, into one and the same zone. There is a small systematic error involved in doing so when the sample is not perfectly aligned. Upon symmetrization, misalignments get mixed in with the peak width and position. Whether or not this is acceptable depends on the magnitude of the misalignment, but also on its type. For example, misalignment in the degree of freedom corresponding to rotation around $\mathbf{k}_i$ does not matter, but rotation around the vertical axis and around the horizontal axis perpendicular to $\mathbf{k}_i$ do. By comparing fits of low energy data (obtained with and without symmetrization) where sharp incommensurate peaks dominate the spectrum, we have found that misalignments of the type mentioned above cannot be very large. Thus, although the values of the peak width and incommensurability obtained from analysis of symmetrized data can in principle have contributions from misalignment, the comparisons mentioned above and the general consistency found between various fitting-strategies tell us that this is not a serious problem. Importantly, it does not influence the results for the parameters in Eq. (89).

The chosen methods Most of our analysis was carried out with two (primarily transverse) cut-files per nominal energy transfer $\hbar\omega$, which were simultaneously fitted in Tobyfit. The width of the area in $\mathbf{Q}_{2\mathrm{D}}$-space averaged over for each point in a single cut file was generally chosen to be $(\sqrt{2}/5)\pi$, one fifth of the distance from $(0, 0)$ to (π, π). Figure 55 shows that with two such cuts arranged back-to-back, the interesting region around (π, π) is quite well covered. However, because the intensity distribution broadens with increasing $\hbar\omega$ it is relevant to ask if working with a fixed cut-width allows us to average over all the magnetic intensity of interest. We have checked this by choosing a value of the momentum component over which we are averaging to be larger than the standard value $(\sqrt{2}/5)\pi$ (per cut). The relevant fits are then repeated with the new $\mathbf{Q}_{2\mathrm{D}}$-space width. If the parameters derived from the fits do not change appreciably, we are well justified in believing that the original fits with a $\mathbf{Q}_{2\mathrm{D}}$-space width equal to $(\sqrt{2}/5)\pi$ are sufficiently broad to yield accurate results. In all cases investigated, we found no significant changes when using a larger $\mathbf{Q}_{2\mathrm{D}}$-space width.

In the initial stages of the data analysis, we used 2 meV energy bins for each cut-file, but later we switched to 4 meV bins in order to reduce the numerical scatter in the results. We found that this could be done without loss of generality in the sense that the results obtained at a given $\hbar\omega$ using with a bin-size of 4 meV are consistent with the averages of the results at the two neighboring $\hbar\omega$-points taken from analysis using a bin-size of 2 meV.

Having made remarks about background corrections, symmetrization, $\mathbf{Q}_{2D}$-space averaging as well as the choice of energy bin-size, let us list the particular methods used to obtain the data presented in section 7.5:

- Data for underdoped and optimally doped LSCO taken with $E_i = 55$ meV at $T = 10$, 30 and 40 K were analyzed using a method involving the combination of symmetrization and background subtraction. The energy bin-size was 4 meV and two back-to-back transverse cuts of width $(\sqrt{2}/5)\pi$ were fitted simultaneously for each $\hbar\omega$ below $\hbar\omega = 30$ meV. For energies in the range $30 - 40$ meV only the transverse cut at low-$|\mathbf{Q}_{2D}|$ could be fitted because the number of background points was insufficient for the high-$|\mathbf{Q}_{2D}|$ cut.
- Data taken with $E_i = 100$ meV at $T = 10$ K and data taken with $E_i = 55$ meV at $T = 100$ and 300 K were analyzed using symmetrization, but with no background subtraction attempted. In these cases as well, two 4 meV bin-size, transverse cuts of width $(\sqrt{2}/5)\pi$ were used at all energies.

7.5 Results

We have now presented all the essential informations required for a proper understanding of the data analysis and it is time to describe our results. We do so in a number of subsections, each of which deals with a specific problem concerning the evolution of the spin excitation spectra of underdoped and optimally doped LSCO. A more in-depth discussion of the significance of the experimental findings is contained in section 7.6.

In section 7.5.1 we focus on identifying the behavior of $\chi''(\mathbf{Q}_{2D}, \omega)$ in underdoped and optimally doped LSCO at low temperatures and at energies below ~ 40 meV. We also study the changes in $\chi''(\mathbf{Q}_{2D}, \omega)$ in this energy range caused by heating the samples to immediately above their superconducting transitions temperatures. Because we have only obtained data at two temperatures ($T = 10$ and 40 K) for optimally doped LSCO, section 7.5.1 contains all our results for the hole-doping concentration $p = x = 0.16$. For underdoped LSCO, we have obtained data at four temperatures and this allows us to investigate more closely the evolution of $\chi''(\mathbf{Q}_{2D}, \omega)$ with temperature. Section 7.5.2 contains a description of the results of this part of our work. Next, section 7.5.3 contains a brief presentation of the scarce information that have been obtained for the low-temperature behavior of $\chi''(\mathbf{Q}_{2D}, \omega)$ at energies above 35 meV. Finally, section 7.5.4 summarizes all our results for the hole-doping level $p = x = 0.10$.

7.5.1 Low-temperature response in $La_{1.90}Sr_{0.10}CuO_4$ and $La_{1.84}Sr_{0.16}CuO_4$

We start by presenting a series of examples of resolution corrected fits of data from optimally doped and underdoped LSCO. The intensities are given in terms of $(k_i/k_f)\left(d^2\sigma/(d\Omega\, dE_f)\right)\Big)_{\text{mag}}$ in absolute units, mbarn sr^{-1} meV^{-1} f.u.$^{-1}$. Each panel in figure 56 contains two transverse cuts: One taken at base temperature $T = 10$ K (blue symbols) and one taken immediately above T_c (red symbols). They were produced by correcting the raw data for an estimate of the background intensity and subsequently symmetrizing the corrected data around $\mathbf{k}_i$. The least-squares fitting program Tobyfit was used to carry out resolution corrected fits using our model cross-section Eq. (82) with $\chi''_{\text{iso}}(\mathbf{Q}, \omega)$ given by Eq. (89). At all values of the energy transfer $\hbar\omega$ below 30 meV, we fitted the two transverse cuts indicated in Fig. 55(a) simultaneously. At higher values of the energy transfer, only the cut with the lowest value of $|\mathbf{Q}_{2D}|$ in Fig. 55(a) was fitted. All data shown in Fig. 56 correspond to this lowest-$|\mathbf{Q}_{2D}|$ cut. The line defining the average trajectory in $\mathbf{Q}_{2D}$-space of these cuts is centered on the point $\mathbf{Q}_{2D} = 0.9(\pi, \pi)$. The twin cut which is simultaneously fitted in Tobyfit is centered on $\mathbf{Q}_{2D} = 1.1(\pi, \pi)$. In Fig. 56, we have chosen the labels on the horizontal axes to correspond to this center-line, defining the average wavevector for each point in a given cut.

The blue and red lines in the Fig. 56 are examples of resolution corrected fits of the superconducting and normal state data respectively. The background correction procedure does not work perfectly and the flat parts of the fitted remnant backgrounds have been subtracted from the data to ease comparisons. The quality of the fits are excellent at all energy transfers as witnessed by values of the goodness-of-fit parameter χ^2_{red} which lie between 0.90 and 2.26 for the fits involved in producing the lines in Fig. 56, and are typically found to be around 1.50. We emphasize, that these values of χ^2_{red} correspond (at low energies) to the simultaneous fit of two transverse cut-files

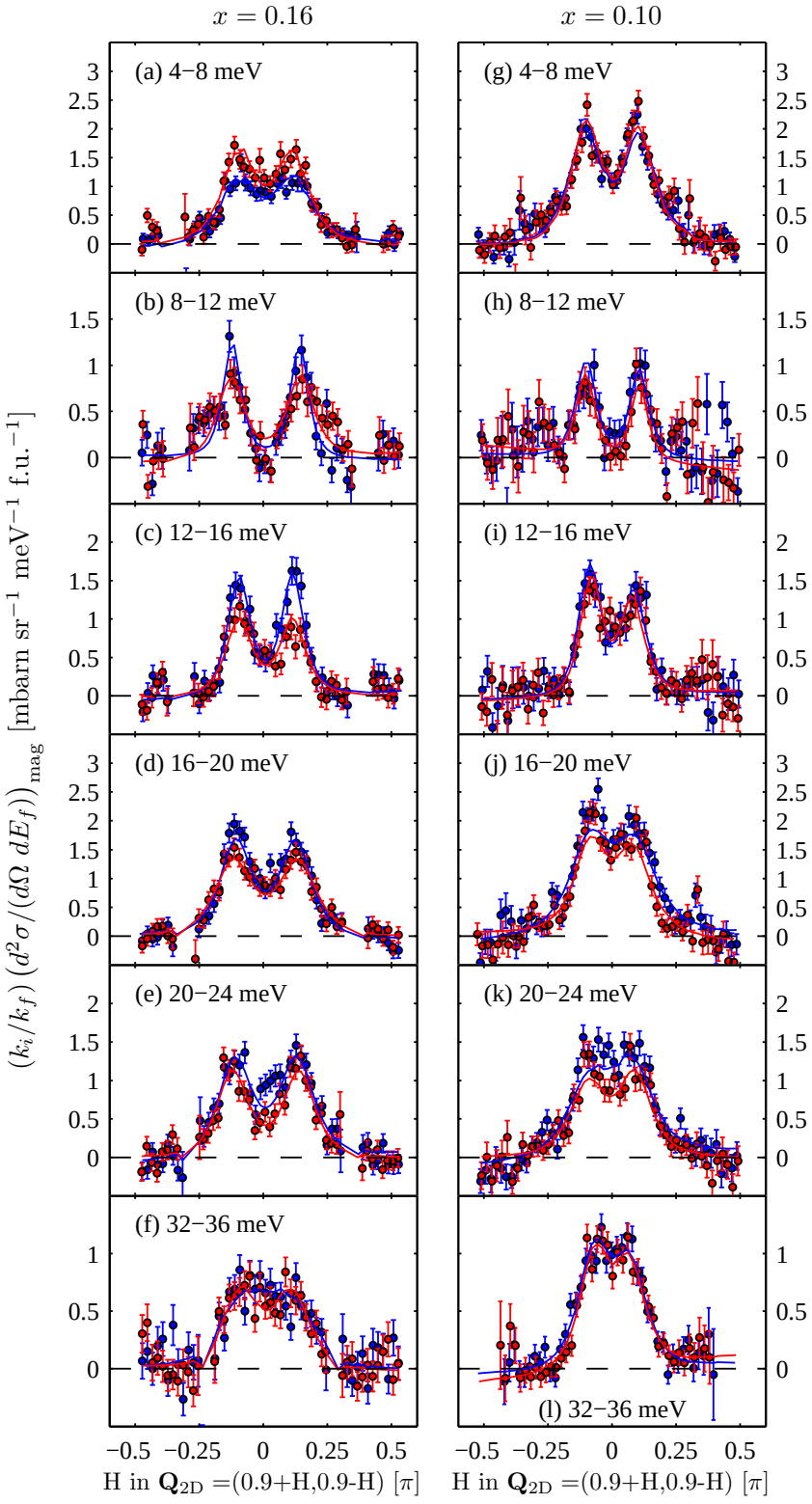

Figure 56: Examples of fits of $(k_i/k_f)\left(d^2\sigma/(d\Omega\ dE_f)\right)_{\rm mag}$ for $x = 0.16$ and $x = 0.10$ using the model defined by Eqs. (82) and (89). Panels (a)-(f) show fits for $T = 10$ K (blue circles and lines) and $T = 40$ K (red circles and lines) at different energy transfers for optimally doped LSCO ($T_c = 38.5$ K). Panels (g)-(l) show fits at $T = 10$ K (blue circles and lines) and $T = 30$ K (red circles and lines) at the same energy transfers for underdoped LSCO ($T_c = 29$ K). All cuts are transverse with a width of $(\sqrt{2}/5)\pi$ perpendicular to the cut-direction (corresponding to Fig. 55(a)) and were produced after subtracting an estimate of the phonon background at each energy. As described in section 7.4.1, this phonon subtraction procedure is not perfect and leaves a small remnant background. In order to ease comparisons between the $x = 0.10$ and $x = 0.16$ data, the fitted values of the flat part of this remaining background has been subtracted from the data shown.

spanning a substantial portion of $\mathbf{Q}_{2D}$-space around (π, π). When inspecting any single cut it should always be kept clearly in mind that because of this parallel fitting procedure (which is sensitive to details in $\chi''(\mathbf{Q}_{2D}, \omega)$ along all directions of the square lattice reciprocal space) there can be small apparent discrepancies between the data and the fitted lines, as well as between the data and the numerical values of fitted parameters such as the incommensurability $\delta(\omega)$. Such deviations are simply reflections of the fact that two cuts were fitted simultaneously and that the data points in the twin cut are also affecting the fit.

There is an important technical point to note in connection with the use of Eq. (82). By contrast with optimally doped LSCO, underdoped LSCO displays weak static order with ordered sublattice moments below $0.1\mu_B$ per copper [171]. In principle, this means that we cannot employ Eq. (82) which is only strictly valid for magnetically disordered systems. However, there are several arguments in favor of using Eq. (82) anyway: First and foremost, it is convenient to use the same formulae for the analysis of underdoped and optimally doped LSCO at all temperatures in order to facilitate comparisons. Second, although there is evidence for magnetic order in underdoped LSCO, the value of the ordered moment is very small, implying that these systems are quite close to the disordered limit where Eq. (82) is valid. Third, as mentioned in chapter 6, experiments using lower energy probes such μSR, NMR and NQR generally do not agree with the conclusions inferred from neutron scattering experiments that there is true long-range magnetic order. Instead, such studies view the "static" magnetism seen by neutron diffraction as a disordered, slowly fluctuating spin-glass phase of matter. Fourth, even if there is long-range magnetic order in underdoped LSCO, the moment direction is not known. Thus, the use of a generalized version of Eq. (82), valid also for magnetically ordered systems, would require assumptions to be made about the direction of the moment. Fifth, even if the moment direction was known, the samples we are studying are generally twinned. A proper analysis would then also require quantitative corrections for the domain population fractions to be made. Sixth, experimentally we have not found any evidence for systematic differences between the incommensurate fluctuations along perpendicular directions in reciprocal space as one would have expected for a statically ordered magnetic systems. Finally, any effect of a finite ordered moment would not influence inferences drawn about the $\mathbf{Q}_{2D}$-space symmetry of the spin fluctuations which is the property we are primarily interested in. Furthermore, any influence on the intensity information is likely to reveal itself in the results of analysis performed using Eq. (82). Summing up, we believe that although we could in principle be making a systematic error when using Eq. (82) for underdoped LSCO, there are empirical reasons to expect that the error is small, but would not go unnoticed if present.

Energy dependence and spin gap Let us now turn to describe the cuts in Fig. 56. The data for optimally doped $La_{1.84}Sr_{0.16}CuO_4$ collected in panels (a)-(f) clearly display the characteristic signatures of the opening of a spin gap Δ_s in the superconducting state, as could also be inferred from the color images in Fig. 51: In the lowest energy interval shown ($4 - 8$ meV, panel (a)) the intensities in the superconducting state at $T = 10$ K are clearly smaller than in the normal state at $T = 40$ K. The intensity differences are largest at the positions of the incommensurate magnetic peaks. At the center of the cut, i.e. at $\mathbf{Q}_{2D} = 0.9(\pi, \pi)$, there is also a small intensity difference. Judging from the fits, this difference is perfectly accounted for by the finite width of the incommensurate peaks. At higher energy transfers ($8-12$, $12-16$ and $16-20$ meV in panels (b)-(d) of Fig. 56), the signal in the superconducting state is clearly larger than the normal state signal. At energy transfers $\hbar\omega = 20 - 24$ meV, panel (e) shows that the intensities at the incommensurate peak positions are close to being identical, but there is slightly more scattering between the peaks in the superconducting state. Thus, we can infer that the spectral weight redistribution caused by the opening of the spin gap affects $\chi''(\mathbf{Q}_{2D}, \omega)$ for energies up to $\sim 20 - 25$ meV. At the highest energy transfer shown, ($\hbar\omega = 32 - 36$ meV, panel (f)) the data in the superconducting and normal states are indistinguishable to the eye. This behavior was also clear from Fig. 51(e). We note that while visually there is no difference between the data at $\hbar\omega = 32 - 36$ meV, Tobyfit detects a slightly smaller incommensurability in the superconducting state, and therefore the fits at $T = 10$ and 40 K are not identical.

Having described the spin gap behavior of optimally doped LSCO, we can compare with the data for underdoped $La_{1.90}Sr_{0.10}CuO_4$ at $T = 10$ and 30 K in panels (g)-(l). For this hole-doping level, previous experiments have found no evidence of a spin gap at low energies, see e.g. [147], and indeed our time-of-flight data indicate very few differences between the response in the superconducting state and at a temperature immediately above T_c. For $\hbar\omega = 20 - 24$ meV (panel

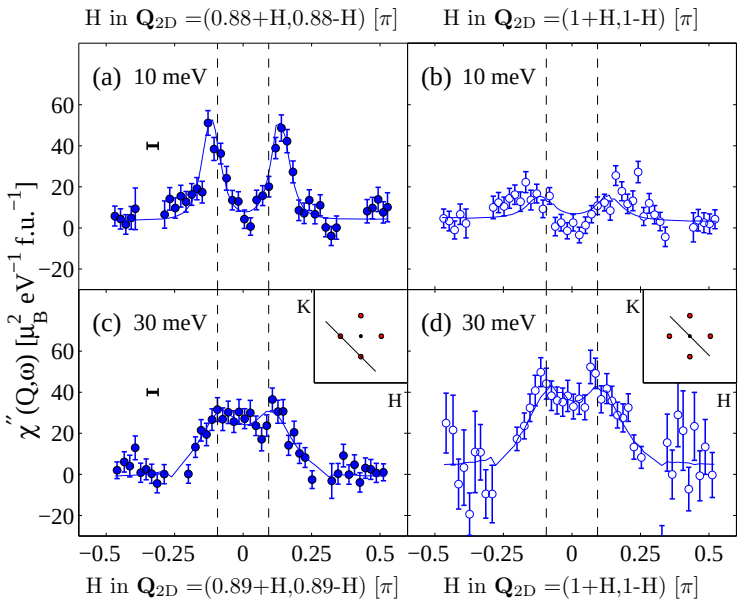

Figure 57: Constant-$\hbar\omega$ cuts through the susceptibility data presented in Fig. 46(e) and (f). The centers of the $\mathbf{Q}_{2D}$-space trajectories of the cuts are shown in the two insets. Note that the scan centers in (a) and (b) are slightly displaced from each other. Solid lines are fits of our model Eq. (89). The vertical dashed lines are the fitted peak positions at $\hbar\omega = 30 \pm 2$ meV. The horizontal bars in (a) and (c) represent the instrumental momentum resolution (FWHM).

(k)) there does appear to be slightly more intensity at $T = 10$ K than at $T = 30$ K, but as we shall learn below, there is no difference between the response at the two temperatures (outside the errorbars) to within the accuracy with which the phenomenological lineshape (89) is capable of describing it.

Comparing the spin fluctuation spectra between underdoped and optimally doped LSCO, the overall impression from Fig. 56 is that there is slightly more intensity for $x = 0.10$ than for $x = 0.16$. This observation agrees well with the energy integrated spectra shown in Fig. 50. For the response at energies above 30 meV it is also in accord with a comparison of the $34-38$ meV images shown in panels (e) and (j) of Figs. 51 and 52. A peculiarity displayed by the $\hbar\omega = 8-12$ meV data in Fig. 56(b) and (h) in both normal and superconducting states is the presence of very sharp peak profiles which cause the response between the two peaks to drop almost to background level. Later in the chapter we shall argue that at this energy transfer there are problems with background scattering from phonons (See Fig. 49) and that this is the cause of the sharpness of the peaks. At low temperatures, the problems are not severe and do not prevent information from being obtained. However, care must be taken when interpreting data obtained at temperatures high enough for the Bose occupation factor $n(\omega) + 1$ to differ significantly from unity, as is the case for $T = 100$ and 300 K.

Dispersion Next, we turn to a central result of this chapter: The development with $\hbar\omega$ of the positions of the loci of maximum intensity in constant energy slices such as those shown in Figs. 51 and 52. When inspecting these color images we argued in favor of the existence of a dispersion of the dominant spin fluctuations in the direction towards (π, π). We will now present evidence for the existence of such a dispersion. In Fig. 57 we show four examples of transverse, constant-$\hbar\omega$ cuts through the $T = 10$ K susceptibility data which were displayed in the form of color images in Fig. 46(e) and (f). In the same manner as the plots shown in Fig. 56, the data in Fig. 57 have been background corrected and symmetrized before cuts were produced and fitted. The average trajectories of the cuts in $\mathbf{Q}_{2D}$-space are indicated schematically in the insets of Fig. 57. The data in panels (a) and (b) are cuts taken at $\hbar\omega = 10 \pm 2$ meV and run through the sharp incommensurate peaks seen in Fig. 46(e) and through the center of the zone at $\mathbf{Q}_{2D} = (\pi, \pi)$ respectively. The data in panels (c) and (d) correspond to $\hbar\omega = 30 \pm 2$ meV and follow almost identical paths in reciprocal space. For this plot, we have deviated from our standard practice of using two transverse cuts with an width $(2/\sqrt{5})\pi$ transverse to the cut direction. This has been done in order to directly

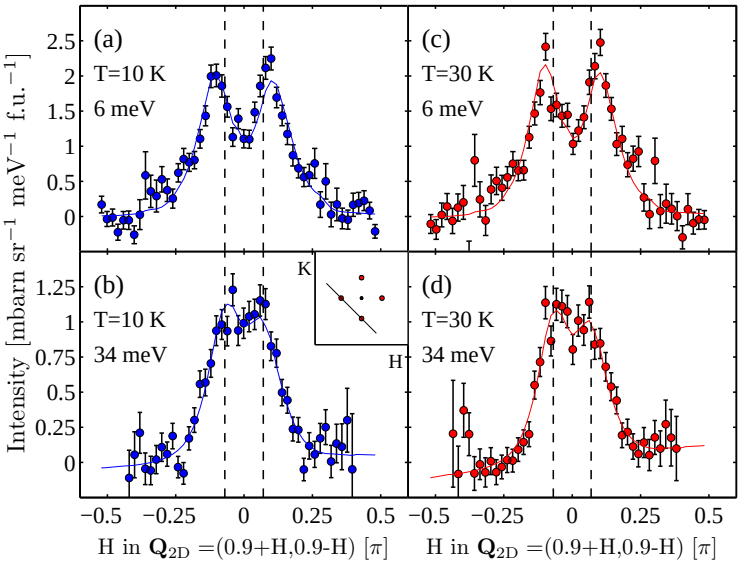

Figure 58: Magnetic contributions $(k_i/k_f)\left(d^2\sigma/(d\Omega\, dE_f)\right)_{\rm mag}$ to the total observed intensity $(k_i/k_f)\left(d^2\sigma/(d\Omega\, dE_f)\right)_{\rm tot}$ at $T = 10$ and 30 K for underdoped LSCO ($T_c = 29$ K). As in Figs. 56 and 57, the flat parts of the fitted backgrounds have been subtracted. (a) $T = 10$ K, $\hbar\omega = 6 \pm 2$ meV. (b) $T = 10$ K, $\hbar\omega = 34 \pm 2$ meV. (c) $T = 30$ K, $\hbar\omega = 6 \pm 2$ meV. (d) $T = 30$ K, $\hbar\omega = 34 \pm 2$ meV. The solid lines through the data represent fits of the model cross-section defined by Eqs. (82) and (89). The vertical dashed lines represent the fitted peak positions at $\hbar\omega = 34 \pm 2$ for each temperature separately. The centers of the $\mathbf{Q}_{2D}$-space trajectories of the cuts are shown in the inset.

investigate the response at (π, π) and at the points midway between the incommensurate peaks.

The solid blue lines are fits of the susceptibility data to Eq. (89). The dashed vertical lines indicate the fitted peak positions of the dominant spin excitations at $\hbar\omega = 30$ meV. It is clear that the locations of these lines are inconsistent with the positions of the well-defined low-energy incommensurate peaks in panel (a), even when the instrumental $\mathbf{Q}_{2D}$-resolution (horizontal bars in panels (a) and (c)) is taken into account. Thus, our model tells us that between $\hbar\omega = 10$ and 30 meV, the dominant spin fluctuations have moved slightly closer to (π, π). There are no indications of magnetic features dispersing in the direction away from (π, π) relative to the low-energy incommensurate peak positions.

A comparison between panels (b) and (d) gives more detailed information about the nature of the evolution of $\chi''(\mathbf{Q}_{2D}, \omega)$ with energy. At 10 meV (panel (b)) there is only very little intensity between the incommensurate peaks and almost none at (π, π), but at 30 meV (panel (d)) the "edges" of the square-like structure in Fig. 46(f) are no sharper than the "corners" of the square (panel (c)). In fact, because the cut through $\mathbf{Q}_{2D} = (\pi, \pi)$ in panel (d) picks up the tails of all four broadened features surrounding (π, π) it becomes more intense than the cut along the edge of the square shown in panel (c).

Figure 58 shows examples of constant energy cuts at $\hbar\omega = 6 \pm 2$ and 34 ± 2 meV at $T = 10$ K (panels (a) and (b)) and $T = 30$ K (panels (c) and (d)). These cuts are presented in terms of intensities $(k_i/k_f)\left(d^2\sigma/(d\Omega\, dE_f)\right)_{\rm mag}$ and were obtained after background corrections and symmetrization. At both temperatures, the low-energy data consist of two incommensurate peaks whereas the high-energy response is a "flat-topped". As in Fig. 57, the dashed lines indicate the values obtained from Tobyfit of the peak positions within the model Eq. (89). Once again, it is clear that these high-energy loci of magnetic scattering are different from the positions of the sharp incommensurate peaks seen at lower energies. Thus, the spin fluctuations in underdoped LSCO also display a slight dispersion towards (π, π) with increasing energy. Figure 58 shows that this dispersive behavior is present both in the superconducting state at $T = 10$ K and in the normal state at $T = 30$ K. Since the $\mathbf{Q}_{2D}$-resolution varies slowly with $\hbar\omega$ (as shown by the horizontal bars in panels (a) and (c) of Fig. 57), the fact that the resolution corrected fits in Fig. 58 account very well for the increased intensity between the peaks at $\hbar\omega = 34$ meV implies that this effect is caused by the combination of dispersion and intrinsic broadening of the incommensurate modes.

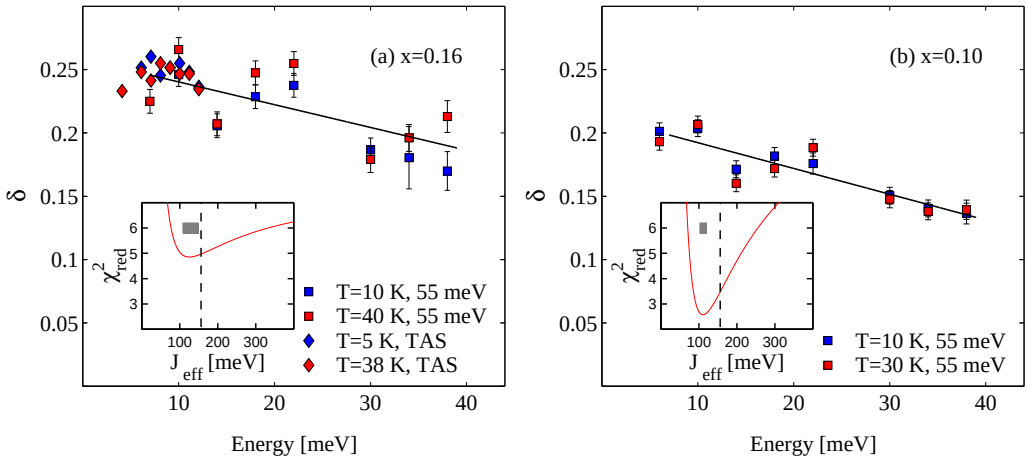

Figure 59: Incommensurability parameter $\delta(\omega)$ defined as in Fig. 39(d). (a) Optimally doped LSCO ($T_c = 38.5$ K). Blue and red squares represent our time-of-flight data at $T = 10$ and 40 K respectively. Blue and red diamonds represent triple axis measurements on the same crystals by Lake *et al.* [234] at $T = 5$ and 38 K respectively. Because of the appearance of a low energy spin gap $\Delta_s = 6.7$ meV in these crystals [144], it is not possible to define δ for energies $\hbar\omega$ below $\sim \Delta_s$ in the superconducting state. (b) Underdoped LSCO ($T_c = 29$ K). Blue and red squares represent our time-of-flight experiments at $T = 10$ and 30 K respectively. The solid lines in (a) and (b) are two-parameter fits of all time-of-flight data points (both normal and superconducting state data) to a straight line. As explained in the text, the slope of this line can be converted to an effective exchange constant $J_{\rm eff}$ for the low energy incommensurate peaks. The best fits are obtained with $J_{\rm eff} = 125^{+23}_{-17}$ meV and $J_{\rm eff} = 111^{+9}_{-8}$ meV for $x = 0.16$ and $x = 0.10$ respectively. These confidence intervals are indicated by grey boxes in the insets which show goodness-of-fit values $\chi^2_{\rm red}$ (red lines) for one-parameter fits to a straight line, in which $J_{\rm eff}$ is held fixed. As discussed in the text, the vertical dashed lines at $J = 156$ meV correspond to the quantum renormalized nearest neighbor exchange integral in the parent antiferromagnet La_2CuO_4 [63].

Model parameters extracted from the analysis The dispersions suggested by the data in Figs. 57 and 58 are clearly subtle effects. We have chosen to analyze these data based on the phenomenological model Eq. (89) although it may well be argued that this model is not the most natural choice for a description of the broadened square-like structures observed at high energies. The basic problem for all potential models is how to distinguish between the observed dramatic broadening with $\hbar\omega$ and the combination of such a broadening and a small peak shift towards (π, π). In addition, any remnant effects of phonon scattering can act to obscure the results of the data analysis based on Eq. (89), but again: Any other model would suffer from similar difficulties.

The use of Eq. (89) is motivated by the seemingly continuous evolution with $\hbar\omega$ of the symmetry of the intensity distributions from incommensurate peaks at low energies to broader features at high-energies. This evolution can be seen in color images such as those in Figs. 51 and 52 and is a robust property of the spin excitation spectra of both underdoped and optimally doped LSCO. Having chosen the particular lineshape (89) to model this crossover with $\hbar\omega$, the parameters extracted from fits to experimental data will now be presented without further consideration of whether or not a better model could be designed. We start by presenting result for the parameter $\delta(\omega)$ (See Fig. 39(d)) quantifying the $\mathbf{Q}_{\rm 2D}$-space separation of the dominant spin excitation from $\mathbf{Q}_{\rm 2D} = (\pi, \pi)$ in units of π. We then present the values of the half-width at half maximum of the peak profiles and of its inverse, the inelastic correlation length $\xi(\omega)$ defined in Eq. (90). Next, we describe the energy dependence of the fitted peak-amplitude parameter $\chi''_\delta(\omega)$ before focusing our attention on the local susceptibility $\chi''(\omega)$. The errorbars on the fitted parameters $\delta(\omega)$, $\kappa(\omega)$ and $\chi''_\delta(\omega)$ are the ones extracted from the resolution corrected least-squares fits of (89). Errorbars on derived quantities such as the local susceptibility were calculated from these statistical errors using standard methods for propagation of errors [233].

Figure 59 summarizes our results for the energy dependence of δ in optimally doped LSCO at $T = 10$ and 40 K and for underdoped LSCO at $T = 10$ and 30 K. We have not analyzed data in the energy range $\hbar\omega = 26 \pm 2$ meV on account of a strongly sloping phonon background in transverse cuts (visible as increased intensities near $\mathbf{Q}_{\rm 2D} \simeq (5/4, 1/4)\pi$ in panels (d) and (j) of Figs. 51-53) which the background subtraction procedure, being designed to account only for background variations along the longitudinal direction in $\mathbf{Q}_{\rm 2D}$-space, does not remove. We point out that inspection of the transverse cuts in this energy range reveals signatures of incommensurate spin

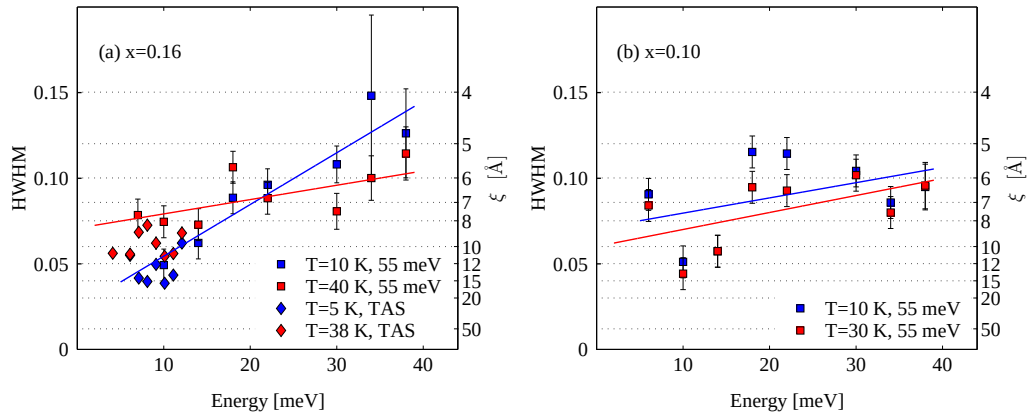

Figure 60: Half-width at half maximum (HWHM. Without units) of the fitted incommensurate peak profiles in 2D reciprocal space and the corresponding inelastic correlation lengths $\xi(\omega) = a/(2\pi)$ HWHM$(\omega)^{-1}$. (a) Optimally doped LSCO ($T_c = 38.5$ K). Blue and red squares represent our time-of-flight data at $T = 10$ and 40 K respectively. Blue and red diamonds represent triple axis measurements on the same crystals by Lake *et al.* [234] at $T = 5$ and 38 K. Because of the appearance of a low energy spin gap $\Delta_s = 6.7$ meV in these crystals [144], it is not possible to define the correlation length for energies $\hbar\omega$ below $\sim \Delta_s$ in the superconducting state. (b) Underdoped LSCO ($T_c = 29$ K). Blue and red squares represent our time-of-flight experiments at $T = 10$ and 30 K respectively. The solid blue and red lines in (a) and (b) are fits to a straight line for the correlation length data at each temperature separately.

fluctuations, but nevertheless we have chosen not to include these data in our analysis because information about widths and intensities would be strongly influenced by uncertainties in the background determination.

In panel (a) of Fig. 59, we are able to supplement our time-of-flight data on optimally doped LSCO by data from triple axis experiments performed and analyzed by B. Lake *et al.* [234] using the same model lineshape Eq. (89). These experiments were performed on the same nine crystals used in our experiment and should therefore be directly comparable. Although there is some numerical scatter in the (two) time-of-flight values of δ in the energy region where the data sets overlap, the time-of-flight and triple axis values of δ are not inconsistent. It can also be seen that the energy-by-energy variation of the time-of-flight values of δ at the two doping levels and for both temperatures plotted in Fig. 59 track each other. While this behavior could be intrinsic to the magnetic response, it is more likely to be a reflection of common underlying phonon-related scattering processes which are not adequately accounted for by the model we use to fit the background remaining after the (non-perfect) background subtraction procedure. Regardless of these variations, the fitted values of δ certainly display an overall decreasing trend with increasing $\hbar\omega$ which is outside the statistical errorbars. Thus, the energy dependence of the fitted values of δ support the conclusion inferred from the color maps in Fig. 51 and from the transverse cuts displayed in Fig. 57, namely the existence of a dispersion in the incommensurate peak positions.

For both underdoped and optimally doped LSCO, we have fitted the combined $T = 10$ K and $T \simeq T_c$ data to a straight line. The resulting curves are shown as solid black lines in Fig. 59. By analogy with the spin wave velocity $c_s = \sqrt{2}J$ of a classical square lattice antiferromagnet (see section 3.1.1), we can convert the slope of the fitted line to an effective velocity $c_{\rm eff}$ and thereby to an effective exchange interaction $J_{\rm eff}$ characterizing the inwards dispersion of the incommensurate spin excitations of LSCO. For the optimally doped composition, the energy variation of δ is best fit with an effective exchange $J_{\rm eff} = 125^{+23}_{-17}$ meV. The errorbars on this estimate were obtained by fixing $J_{\rm eff}$ and fitting only the offset $\delta(\hbar\omega = 0)$. Having done this for a large range of values of $J_{\rm eff}$ we find the errorbars from the condition $\delta\chi^2_{\rm red}\ (N_p - N_{\rm par}) = 1$ [232] where N_p is the number of points to be fitted and $N_{\rm par} = 1$ is the number of parameters fitted. The inset in Fig. 59 shows the reduced goodness-of-fit parameter $\chi^2_{\rm red}$ versus $J_{\rm eff}$. For underdoped LSCO (panel (b) of Fig. 59) a similar procedure leads to an effective exchange $J_{\rm eff} = 111^{+9}_{-8}$ meV, which is consistent with the value derived for the optimally doped composition. The confidence intervals on the determinations of $J_{\rm eff}$ are shown by grey boxes in the insets and can be compared with the value $J = 156 \pm 5$ meV characterizing the spin waves in the undoped parent insulator La_2CuO_4 [63]. This exchange constant J is quantum renormalized in the sense discussed in chapter 3, i.e. it is the product of a bare exchange interaction $J_{\rm bare}$ and a quantum renormalization factor $Z_c = 1.18$

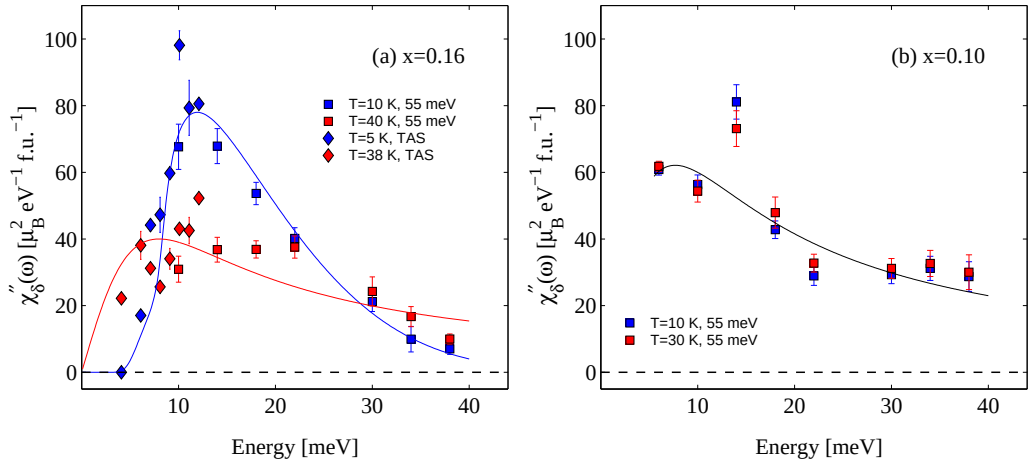

Figure 61: Peak amplitude $\chi''_\delta(\omega)$ in absolute units μ_B^2 eV^{-1} f.u.$^{-1}$. (a) Optimally doped LSCO ($T_c = 38.5$ K). Blue and red squares represent our time-of-flight data at $T = 10$ and 40 K respectively. Blue and red diamonds represent triple axis measurements on the same crystals by Lake *et al.* [234] at $T = 5$ and 38 K. The blue and red solid lines are guides to the eye for the superconducting and normals states respectively. (b) Underdoped LSCO ($T_c = 29$ K). Blue and red squares represent our time-of-flight experiments at $T = 10$ and 30 K respectively. The solid black line is a guide to the eye for both temperatures.

for the spin wave velocity. It is the renomalized exchange constant J which − when inserted in the dispersion relation derived from linear spin wave theory − yields the correct spin wave energies. The values $J_{\rm eff}$ quoted for the incommensurate spin fluctuations in LSCO do not include any attempt to correct for multiplicative quantum renormalization factors since no existing theory predicts the relevant renormalization factor $Z_{\rm inc}$. For comparisons with La_2CuO_4 it is therefore best to quote the effective values $J_{\rm eff}$ which yield the correct dispersions of the the incommensurate modes.

Figure 60 displays the fitted values of the half-width at half maximum of the peak profiles in $\mathbf{Q}_{\rm 2D}$-space, expressed in the same unitless format as δ. To obtain the inelastic correlation length $\xi(\omega)$ in units of Å we must take the inverse of the HWHM and multiply by $a/(2\pi)$ where $a \simeq 3.77$ Å is the nearest neighbor Cu-Cu separation. The resulting numbers for the correlation length are shown on the right-hand axes. As in Fig. 59, panel (a) contains both our time-of-flight neutron scattering data for optimally doped LSCO and results for the HWHM derived by Lake *et al.* from triple axis neutron scattering data [234]. Panel (b) contains our results for underdoped LSCO.

Just as we saw for the incommensurability parameter $\delta(\omega)$, the time-of-flight data points are scattered by a greater amount than seems consistent with the statistical errorbars obtained from Tobyfit. On the other hand, Fig. 60(a) shows that the low-energy values of the HWHM are reasonably consistent with the triple axis data. Fitting straight lines through the combined time-of-flight and triple axis data for the superconducting and normal states (we assume that the small differences between the normal and superconducting state temperatures in the two experiments do not matter for the physical properties of interest) results in the solid blue and red lines in Fig 60. According to the triple axis data, the spin excitations in the superconducting state for energies immediately above $\Delta = 6.7$ meV become more coherent, i.e. longer-ranged, in real space. This so-called "coherence effect" was noted by Mason *et al.* in near-optimally doped LSCO [148]. The time-of-flight data for both optimally doped and underdoped LSCO also appear to suggest a decreased peak width around 10 meV (See Fig. 56), but as stated earlier there are reasons to believe that in this case phonon scattering is involved in producing the effect. For geometrical reasons, our time-of-flight experiments do not probe the same three-dimensional wavevector transfer $\mathbf{Q}$ as the experiment of Mason and coworkers and therefore there is not necessarily an inconsistency. We will return to the issue of phonon scattering at $\hbar\omega = 10$ meV in section 7.5.4. The fits of the correlation length data to solid lines indicates that the high-energy value of ξ does not depend sensitively on temperature or doping and has a numerical value in the range $5 - 6$ Å .

Next, we turn to investigate the energy dependence of the amplitude parameter $\chi''_\delta(\omega)$ in absolute units, μ_B^2 eV^{-1} f.u.$^{-1}$. Figures 61(a) and (b) display the parameters extracted from the least-squares fitting routine. Panel (a) also contains the triple axis data described in connection

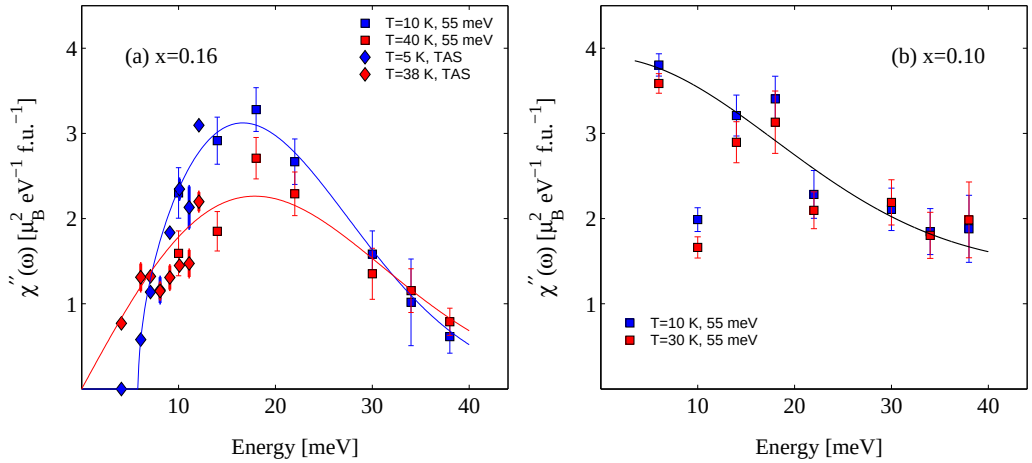

Figure 62: Local susceptibility $\chi''(\omega)$ in absolute units μ_B^2 eV^{-1} f.u.$^{-1}$. (a) Optimally doped LSCO ($T_c = 38.5$ K). Blue and red squares represent our time-of-flight data at $T = 10$ and 40 K respectively. Blue and red diamonds represent triple axis measurements on the same crystals by Lake *et al.* [234] at $T = 5$ and 38 K. The blue and red solid lines are guides to the eye for the superconducting and normals states respectively. (b) Underdoped LSCO ($T_c = 29$ K). Blue and red squares represent our time-of-flight experiments at $T = 10$ and 30 K respectively. The solid black line is a guide to the eye for both temperatures.

with Figs. 59 and 60. Using a single, temperature independent parameter, these data were scaled to match the time-of-flight data in the region of overlap. This is necessary because the triple axis data are not in absolute units.

We have previously noted that the energy dependences of δ in underdoped and optimally doped LSCO are qualitatively very similar and are quantitatively accounted for by spin wave velocities of the same order of magnitude. We have also seen that (apart from the coherence effect seen clearly in the triple axis data only) the correlation lengths $\xi(\omega)$ of the spin excitations in both the superconducting and normal states have similar energy dependences in underdoped and optimally doped LSCO. By contrast, the temperature dependences of the peak amplitudes $\chi''_\delta(\omega)$ are qualitatively different at the two hole-doping levels. For optimally doped LSCO, the data in Fig. 61(a) show that the opening of a spin gap Δ_s at T_c (indicated by the triple axis data and by the drop to zero of the solid blue guide to the eye for the superconducting state amplitude) is accompanied by the formation of a peak at $\hbar\omega = 12 \pm 2$ meV in the amplitude parameter $\chi''_\delta(\omega)$. This peak formation can also be seen clearly in Fig. 51(b) as well as in the cuts shown in Fig. 56(b) and (c). On the other hand, the normal state amplitudes in optimally doped LSCO varies much less rapidly as a function of energy. Its energy-dependence is qualitatively similar to that of the normal and superconducting state amplitudes in underdoped LSCO displayed in Fig. 61(b). Within the experimental errorbars, the onset of superconductivity has no influence at all on the peak amplitude in the underdoped samples. This behavior was anticipated from the color maps in Fig. 52 and from the transverse cuts in Fig. 56(g)-(l) and stands in sharp contrast to the spin gap behavior seen in Fig. 61(a).

We have now described the energy dependence of the parameters derived directly from the Tobyfit sessions. Using these parameters it is now straightforward to derive the values of the local susceptibility $\chi''(\omega)$ defined by Eq. (86). Since the amplitude parameter $\chi''_\delta(\omega)$ was expressed in absolute units (μ_B^2 eV^{-1} f.u.$^{-1}$) so are the resulting local susceptibility plots shown in Fig. 62.

Given the strong similarity between the correlation length data in the superconducting and normal state of underdoped LSCO it is no surprise that the energy dependence of the local susceptibility in $La_{1.90}Sr_{0.10}CuO_4$, shown in Fig. 62(b) tracks that of the amplitude $\chi''_\delta(\omega)$ shown in Fig. 61(b). Within the errorbars there is no difference between the superconducting and normal state response at any energy. Averaged over the range below ~ 30 meV there does appear to be slightly more intensity in the superconducting than in the normal state. By contrast, the local susceptibility of optimally doped LSCO in the superconducting state displays a peak around $\hbar\omega = 18 \pm 2$ meV with a half-width at half maximum of 12 ± 2 meV. Thus, the spectral weight redistribution caused by the opening of the spin gap affects the response at energies as high as ~ 30 meV.

Having determined $\chi''(\omega)$ in absolute units, it is interesting to inquire whether or not there

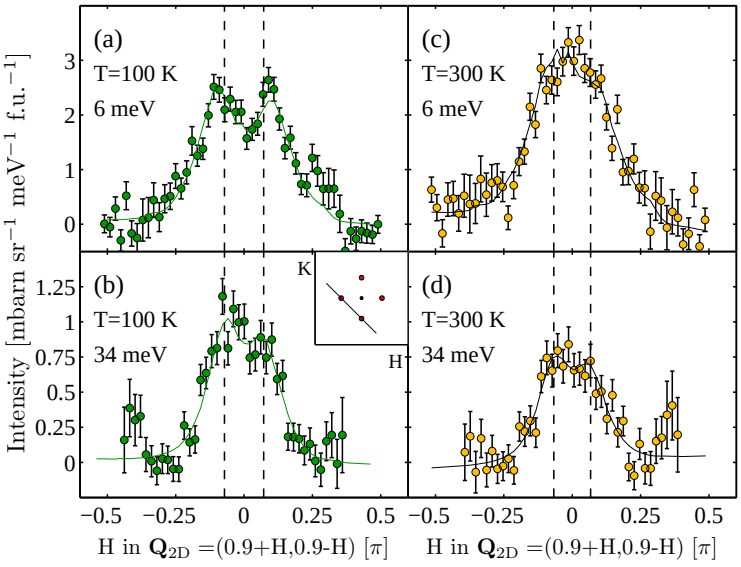

Figure 63: Magnetic contributions $(k_i/k_f)\left(d^2\sigma/(d\Omega\, dE_f)\right)_{\rm mag}$ to the total observed intensity $(k_i/k_f)\left(d^2\sigma/(d\Omega\, dE_f)\right)_{\rm tot}$ at $T = 100$ and 300 K for underdoped LSCO ($T_c = 29$ K). The flat parts of the fitted backgrounds have been subtracted. (a) $T = 100$ K, $\hbar\omega = 6 \pm 2$ meV. (b) $T = 100$ K, $\hbar\omega = 34 \pm 2$ meV. (c) $T = 300$ K, $\hbar\omega = 6 \pm 2$ meV. (d) $T = 300$ K, $\hbar\omega = 34 \pm 2$ meV. The solid lines through the data represent fits of the model cross-section defined by Eqs. (82) and (89). The vertical dashed lines represent the fitted peak positions at $\hbar\omega = 34 \pm 2$ for each temperature separately. The centers of the $\mathbf{Q}_{2D}$-space trajectories of the cuts are shown in the inset.

is spectral weight conservation in optimally doped LSCO upon going from the normal state at $T = 40$ K into the superconducting state at $T = 10$ K. We can investigate this issue by employing Eq. (87) to evaluate the mean-squared fluctuating moment responsible for the fluctuations in our experimental window below 40 meV. Combining our time-of-flight data with the triple axis data provided by Lake *et al.* [234] we find $\langle m^2 \rangle = 0.053 \pm 0.005 \mu_B^2$ per formula unit in the normal state and $\langle m^2 \rangle = 0.061 \pm 0.005 \mu_B^2$ per formula unit in the superconducting state (In computing these integrals we have corrected for the use (in Tobyfit) of the isotropic Cu^{2+} form factor instead of the more correct anisotropic form factor. This is done my multiplying the local susceptibilities $\chi''(\omega)$ in Fig. 62(a) by the black curve terminating at $\hbar\omega = 40$ meV in panel (c) of Fig. 48. This is justified since the magnetic response is concentrated around $\mathbf{Q}_{2D} = (\pi, \pi)$ at all energies). Thus, we have found that upon entering the superconducting state, there is no change within the errors of the mean-squared-fluctuating moment of optimally doped LSCO. The spectral weight lost below the spin gap is simply shifted to higher energies. In section 7.5.4, we investigate the mean-squared-fluctuating moment of underdoped LSCO.

7.5.2 Temperature evolution of the response in $La_{1.90}Sr_{0.10}CuO_4$

In the previous section we provided a detailed description of the energy dependence of the imaginary part $\chi''(\mathbf{Q}_{2D}, \omega)$ of the generalized susceptibility, analyzed using the phenomenological model Eq. (89). There were two primary results: First, we identified a dispersion in the incommensurate magnetic peak positions: With increasing $\hbar\omega$, the peaks broaden and move towards $\mathbf{Q}_{2D} = (\pi, \pi)$ with a characteristic velocity $\sqrt{2} J_{\rm eff}$ where $J_{\rm eff} \simeq 110 - 125$ meV for both compositions. Based on the fitted values of δ displayed in Fig. 59, the dispersions in the incommensurate peak positions seem to be identical in the superconducting and normal states of both underdoped and optimally doped LSCO. The second central finding of section 7.5.1 was the observation that the intensity redistribution caused by the opening of a spin gap below T_c in optimally doped LSCO is spectral weight conserving. By contrast, we saw that in underdoped LSCO the onset of superconductivity below $T_c = 29$ K has no observable effects on the local susceptibility. In this and the following two sections we present the remainder of our results for $\chi''(\mathbf{Q}_{2D}, \omega)$ in underdoped LSCO. We start by demonstrating that the dispersive incommensurate peaks exist even at $T = 100$ K in underdoped LSCO.

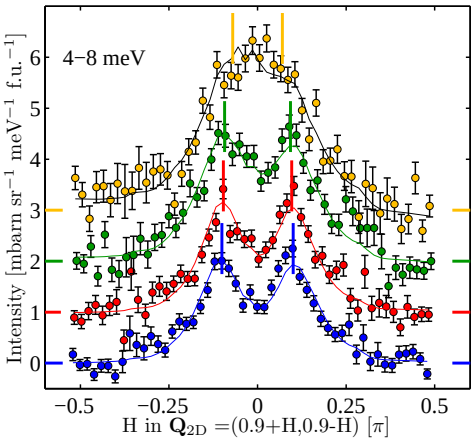

Figure 64: Low-energy magnetic intensity $(k_i/k_f)\left(d^2\sigma/(d\Omega\ dE_f)\right)_{\rm mag}$ in underdoped LSCO (T_c = 29 K) at the four temperatures investigated. The blue, red, green and yellow symbols are transverse cuts taken at $\hbar\omega = 6 \pm 2$ meV for T = 10, 30, 100 and 300 K respectively. The trajectories of the cuts are identical and were defined in Figs. 58 and 63. The fitted flat background levels have been subtracted and the resulting curves have been offset vertically as indicated by the colored lines on the axes. The solid lines through the data are fits to our model cross-section defined by Eqs. (82) and (89). The fitted peak positions are indicated by the solid vertical line-segments which are colored according to the data they describe.

Figure 63 displays transverse cuts obtained at T = 100 and 300 K in the energy intervals 6 ± 2 and 34 ± 2 meV. At these elevated temperatures we did not use the background correction procedure, but still symmetrized the data around $\mathbf{k}_i$. The values of the goodness-of-fit measure $\chi^2_{\rm red}$ for the four fits (1.27, 1.34, 1.45 and 0.97 for panels (a)-(d) respectively) testify to the excellent quality of the fits. Precisely as in Figs. 57 and 58, the dashed vertical lines indicate the fitted peak position for the data obtained at high energy transfer, $\hbar\omega = 34 \pm 2$ meV. At T = 100 K, it appears that the lines do not match the peak positions at $\hbar\omega = 6 \pm 2$ meV in panel (a). By analogy with Fig. 58 this observation suggest that the dispersive incommensurate modes survive to this temperature. On the other hand, the data presented in panels (c) and (d) appear to indicate that the dispersion has vanished at room temperature.

Next, we focus on the temperature dependence of the response in the lowest energy-range we have studied. Figure 64 displays equivalent transverse constant-energy cuts at 6 ± 2 meV for the four temperatures investigated. These four cuts have all been presented before in Figs. 58 and 63. By plotting them together, we can bring forward a dramatic effect of temperature on the lowest energy fluctuations. At T = 10, 30 and 100 K the response is clearly incommensurate. By contrast, at T = 300 K there are no longer clear-cut signatures of incommensurate peaks. Instead, it now appears that the peak in the response occurs midway between the positions at which the incommensurate peaks occur at lower temperatures, but the peak profile in Fig. 63(c) retains the flat-topped character of two broad overlapping peaks. Analyzing the data in terms of Eq. (89), we find that the temperature dependence of the peak positions is very slow between T = 10 and T = 100 K. The fitted peak positions appear to shift slightly towards (π, π) as indicated by the colored solid line segments in Fig. 64, but in fact they remain equivalent within the errorbars. The peak widths derived from the fits are also identical within the errors between T = 10 and 100 K, but at 300 K it is substantially larger than at lower temperatures. Finally, the peak amplitude parameter $\chi''_\delta(\omega)$ drops rapidly as a function of temperature, but is compensated by the increase in the Bose occupation factor. This compensation is the reason why the intensities $(k_i/k_f)\left(d^2\sigma/(d\Omega\ dE_f)\right)_{\rm mag}$ in Fig. 64 are largest at the highest temperature.

The temperature dependence of the response of underdoped LSCO at $\hbar\omega = 6 \pm 2$ meV shown in Fig. 64 is remarkably similar to data from a triple axis experiment by Fujita *et al.* [163] on $La_{1.875}Ba_{0.125}CuO_4$ − a system which displays charge stripe order at low temperature and for which Tranquada *et al.* reported a rotation by 45 degrees of the high energy response [151]. At the same energy transfer investigated by us in Fig. 64, Fujita *et al.* found that the incommensurate peaks move closer together with increasing temperature. At T = 200 K there are still signatures of incommensurate peaks in LBCO, but the response is much broader than at low temperatures. For our purposes it is interesting to note that these results were interpreted as implying the existence

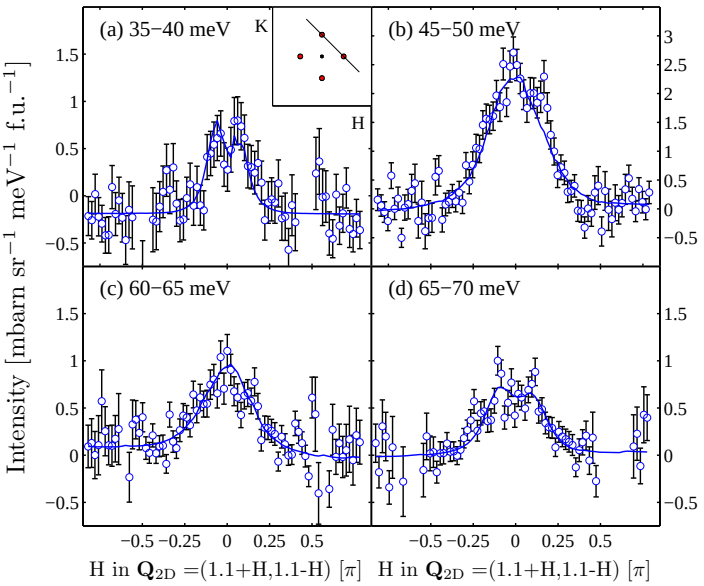

Figure 65: High-energy magnetic intensity $(k_i/k_f)\left(d^2\sigma/(d\Omega\, dE_f)\right)_{\rm mag}$ in underdoped LSCO ($T_c = 29$ K). The data were obtained at $T = 10$ K with an incident energy $E_i = 100$ meV. The cuts are transverse and their centers run along the trajectory shown in the inset. Panels (a)-(d) display the response at $\hbar\omega = 37.5 \pm 2.5$ meV, $\hbar\omega = 47.5 \pm 2.5$ meV, $\hbar\omega = 57.5 \pm 2.5$ meV and $\hbar\omega = 67.5 \pm 2.5$ meV respectively. The solid blue lines are fits to the model cross-section defined by Eqs. (82) and (89). Note that the intensity scale is different in panel (b) than in panels (a) and (c)-(d), and that the horizontal scale in all panels differs from that used for $E_i = 55$ meV data in previous figures.

of dynamic charge stripes above the charge ordering temperature in LBCO [163].

7.5.3 High-energy response in $La_{1.90}Sr_{0.10}CuO_4$

In this section, we present a few examples of transverse cuts obtained with an incident neutron energy $E_i = 100$ meV for energy transfers greater than 35 meV. The corresponding color images were presented in Fig. 54. Figure 65 shows four constant energy transverse cuts at $35 - 40$ meV, $45 - 50$ meV, $60 - 65$ meV and $65 - 70$ meV. The most remarkable feature in these cuts is the fact that the response at $45 - 50$ meV, shown in Fig. 65(b) is substantially more intense than in the three other energy ranges. In section 7.3.4 we discussed that the origin of this intense peak is most likely to be found in phonon scattering. We shall not repeat the arguments presented earlier in favor of this interpretation. Because of the intense, most likely phonon related scattering in this energy interval the data in the energy range $40 - 55$ meV cannot be trusted and has not been analyzed further.

The data shown in Fig. 65(a), (c) and (d) reveal little about the nature of the high-energy response in LSCO. The solid lines represent fits using our model lineshape Eq. (89). As can be seen, we obtain quite good fits of the data, but this proves little since any broad feature would fit the same data well. We have tried to fit the high-energy data set using both a model consisting of a single commensurate peak at (π, π) and using a model consisting of a quartet of 45 degree rotated incommensurate peaks as reported in [151, 207], but neither gives a better description of the data than Eq. (89). Based on inspection of the data in Fig. 65(a), (c) and (d) and on the color images in Fig. 54 our best guess would be that the response at energies above ~ 35 meV is either commensurate or retains the unrotated square symmetry characteristic of the lower energy fluctuations. However, based on resolution corrected fits, we cannot tell which model is more appropriate.

7.5.4 Summary for $La_{1.90}Sr_{0.10}CuO_4$

Having discussed all our data for underdoped LSCO, we can now assemble the pieces in the form of summary plots for the peak separation, width and amplitude as well as for the local susceptibility.

Figure 66(a) contains all our results for the energy dependence of the peak separation parameter δ. The data for $T = 10$ and 30 K were already presented in Fig. 59, and we have discussed

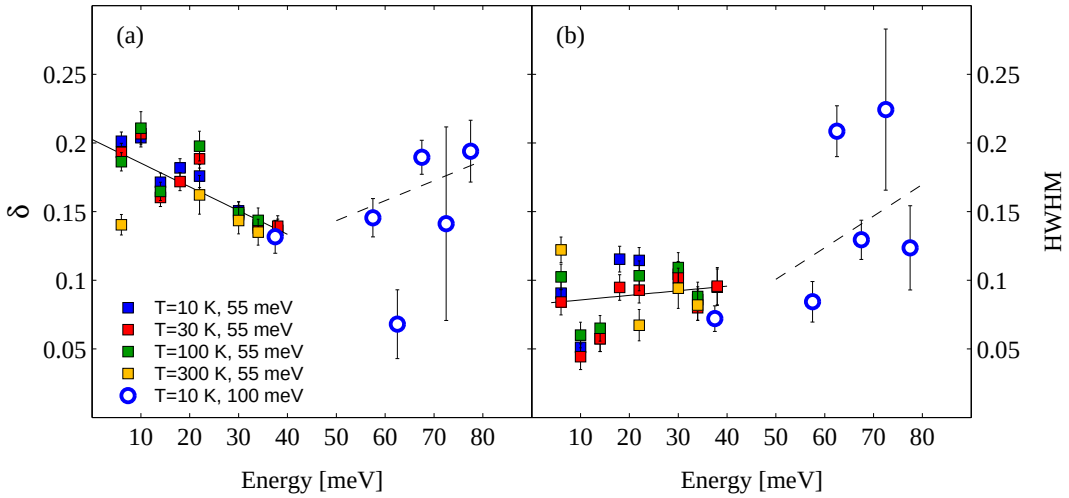

Figure 66: Summary plot for the dispersion and peak width in $La_{1.90}Sr_{0.10}CuO_4$. Filled blue, red, green and yellow squares correspond to $T = 10$, 30, 100 and 300 K respectively, and were obtained with $E_i = 55$ meV. The open blue circles represent results obtained at $T = 10$ K with $E_i = 100$ meV. (a) Incommensurability parameter $\delta(\omega)$. (b) Half-width at half maximum (HWHM) of the fitted peak profiles. The solid and dashed lines are guides to the eye. In the energy range around $30 - 40$ meV, the high temperature data points fall on top of the low temperature points.

how they provide strong evidence for an inwards dispersion in the incommensurate peak positions. In Fig. 66(a) we have added the results obtained at $T = 100$ and 300 K with an incident energy $E_i = 55$ meV as well as $T = 10$ K results obtained with $E_i = 100$ meV.

Figure 63 shows that the fitted peak positions at $\hbar\omega = 34 \pm 2$ meV at $T = 100$ K appear to be inconsistent with the peak separation at $\hbar\omega = 6 \pm 2$ meV. This suggests that the dispersion we have identified at $T = 10$ and 30 K persists to even higher temperatures. Figure 66(a) supports this: Although the numerical scatter in the fitted values of δ derived from the least-squares fits is larger for $T = 100$ K than at lower temperatures, they follow the same overall decreasing trend with increasing $\hbar\omega$. In particular, at energies above 30 meV the values of δ are indistinguishable from the values obtained at $T = 10$ and 30 K. For the data obtained at $T = 300$ K, quantitative analysis becomes much more troublesome on account of strongly increased background scattering. Thus, at this temperature we could only obtain reasonable fits at four energy transfers. For the energy range $\hbar\omega = 6 \pm 2$ meV, Fig. 64 demonstrated a dramatic temperature evolution of the spin excitations. The cuts obtained at $T = 300$ K at this energy are qualitatively different from those obtained at lower temperature. The 300 K spectrum appears flat-topped instead of having clear signatures of well-separated incommensurate peaks as do the lower temperature spectra. Thus, comparing the room temperature spectra for $\hbar\omega = 6 \pm 2$ and 34 ± 2 meV in Fig. 63(c) and (d), there are no longer any visible signs of a dispersion in the spin excitations. These observations are reflected in the four $T = 300$ K data points in Fig. 66(a). The low-energy value of δ falls much below that of the $T = 10$, 30 and 100 K data at the same energy transfer. By contrast, the $T = 300$ K values of δ at $\hbar\omega = 22 \pm 2$, 30 ± 2 and 34 ± 2 meV are generally consistent with the values obtained at these energies for lower temperatures. Finally, using Eq. (89) to fit the high-energy data set obtained with $E_i = 100$ meV away from the phonon contaminated region $40 - 55$ meV, we find that the values of δ appear to follow a generally increasing trend with increasing temperature, as indicated by the dashed guide to the eye. As noted in section 7.5.3, the response at these energies can also be fitted with a single commensurate peak, but we point out, that the use of Eq. (89) finds empirical support in the fact that we obtain an overall consistent description of the response around $35 - 40$ meV measured with both $E_i = 55$ meV and $E_i = 100$ meV.

Panel (b) of Fig. 66 contains all our data for the peak width. As was the case for the peak separation parameter δ, the energy dependences of the width at $T = 100$ and 300 K are reasonably consistent with our findings for $T = 10$ and 30 K, the most prominent exception to this rule being the room temperature response at $\hbar\omega = 6 \pm 2$ meV where the peak width is larger than at lower temperatures. For the high-energy response at $T = 10$ K, we find that the peak width increases with increasing $\hbar\omega$ (as indicated by a dashed guide to the eye), but is consistent with the $E_i = 55$ meV data at $35 - 40$ meV.

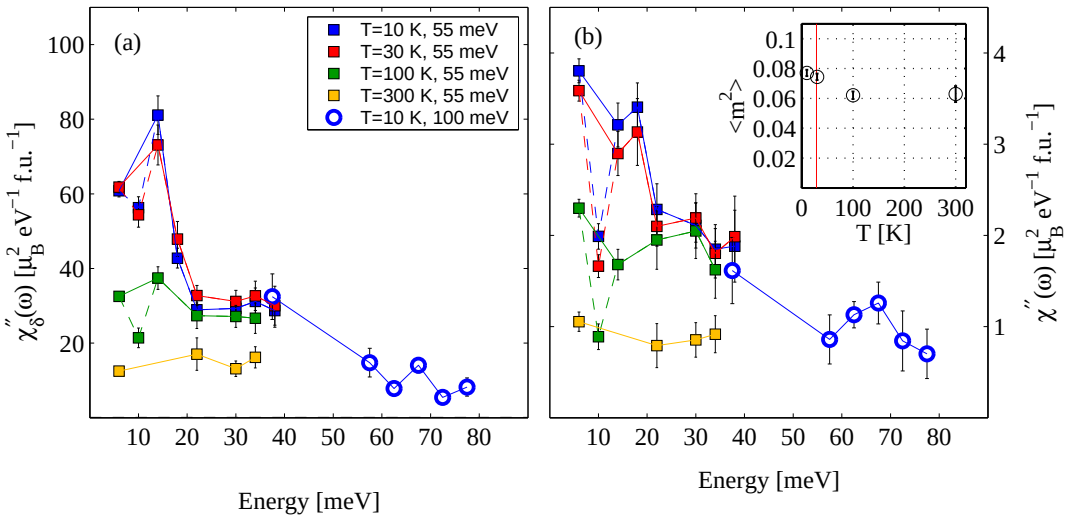

Figure 67: Summary plot for the energy dependence of the the peak amplitude and local susceptibility in $La_{1.90}Sr_{0.10}CuO_4$. Filled blue, red, green and yellow squares correspond to $T = 10$, 30, 100 and 300 K respectively, and were obtained with $E_i = 55$ meV. The open blue circles represent results obtained at $T = 10$ K with $E_i = 100$ meV. (a) Peak intensity parameter $\chi''_\delta(\omega)$ in absolute units. (b) Local susceptibility $\chi''(\omega)$ in absolute units. The data points in (a) and (b) are joined by solid colored lines except for the points at $\hbar\omega = 10$ meV which are believed to be strongly affected by phonon scattering and are connected to the neighboring points by dashed lines. The inset shows the temperature dependence of the fluctuating moment $\langle m^2 \rangle$ (in units of μ_B^2 f.u.$^{-1}$) responsible for the spin fluctuations in the energy range $6 - 34$ meV. The vertical red line in the inset indicates the superconducting transition temperature $T_c = 29$ K.

Combining panels (a) and (b) of Fig. 66 which together describe the $\mathbf{Q}_{2D}$-space structure of the excitations, we find confirmation of the point made in connection with the color images in Figs. 51-53 that the symmetry of the excitation spectrum above $\sim$ 30 meV is independent of temperature.

Figure 67(a) and (b) summarizes our result for the peak amplitude $\chi''_\delta(\omega)$ and for the local susceptibility $\chi''(\omega)$ respectively. Whereas the values of the peak separation and peak width shown in Fig. 66 are identical within the errorbars at most values of $\hbar\omega$, the amplitude of the magnetic signal decreases substantially as the samples are heated from T_c to room temperature. Fig. 67(a) shows that the values of the peak amplitude for $T = 100$ K deviate from the $T = 10$ and 30 K curves for energies below $\hbar\omega \sim 20$ meV. By contrast, at all energies where sensible fits could be obtained, the $T = 300$ K amplitudes are substantially lower than for $T = 10$, 30 and 100 K. For the high-energy data obtained at $T = 10$ K with $E_i = 100$ meV, we once again find good agreement in the range $\hbar\omega = 37.5 \pm 2.5$ meV with the $T = 10$ K data obtained with $E_i = 55$ meV.

Figure 67(b) shows the local susceptibility $\chi''(\omega)$ for all temperatures and energies investigated. The results generally track the energy dependence of the amplitude parameter displayed in Fig. 67(a), but are also affected by the energy dependence of the peak width in Fig. 66(b). As a result, the local susceptibility at both $T = 10$, 30 and 100 K go through a pronounced minimum at $\hbar\omega = 10$ meV. In all cases, this minimum interrupts an otherwise reasonably monotonic energy dependence of $\chi''(\omega)$. We believe that this effect is caused by the influence of phonon scattering, and that therefore it is fair to neglect the data points at $\hbar\omega = 10$ meV in further considerations of the data. In favor of such an interpretation, we note that when attempting to analyze data at $T = 300$ K and $\hbar\omega = 10$ meV, it was found that background scattering completely overwhelms any magnetic signal. Similar but less severe problems were experienced in the analysis of the $T = 100$ K data at the same energy. Furthermore, inspection of Fig. 49 shows that both the experimental phonon density of states data and the model calculation of the same quantity [231] indicate that the lowest-energy peak in the phonon spectrum occurs at $\hbar\omega \simeq 10$ meV. Moreover, in the $\mathbf{Q}_{2D}$-integrated intensities obtained from the MAPS data and shown in the same figure, the first peak also occurs around 10 meV. Finally, if Mslice is used to plot the MAPS data as a function of momentum and energy, an approximately non-dispersive band is clearly seen to pass through (π, π) around 10 meV. The intensity of this band increases with increasing temperature and is therefore almost certainly phonon related. For the reasons outlined above, we are well justified in

neglecting all data points obtained at 10 meV, and shall do so in the remainder of this chapter.

Returning to Fig. 66, we emphasize that although the $\hbar\omega = 10$ meV data point has the highest values of δ, its neglect does not remove the decreasing trend of δ with increasing $\hbar\omega$. Thus, the solid lines through the low energy data in Fig. 66(a) and (b) represent fits to a straight line for all data points obtained with $E_i = 55$ meV, except for the $\hbar\omega = 10$ meV data and the $\hbar\omega = 6$ meV data for $T = 300$ K and is clearly decreasing with increasing $\hbar\omega$.

Let us now refocus on Fig. 67(b). From the values of the local susceptibility obtained with $E_i = 55$ meV, we can numerically evaluate Eq. (87) between $\hbar\omega = 6$ and 34 meV (neglecting the phonon-infected $\hbar\omega = 10$ meV point) to derive the value of mean-squared-fluctuating moment $\langle m^2 \rangle$ responsible for the spin fluctuations observed in this range. For $T = 10$, 30, 100 and 300 K respectively we find $\langle m^2 \rangle = 0.077 \pm 0.002\, \mu_B^2$ f.u.$^{-1}$, $0.074 \pm 0.002\, \mu_B^2$ f.u.$^{-1}$, $0.062 \pm 0.003\, \mu_B^2$ f.u.$^{-1}$, and $0.063 \pm 0.005\, \mu_B^2$ f.u.$^{-1}$, These values are plotted versus temperature in the inset of Fig. 67(b). It is clear that a significant reduction in $\langle m^2 \rangle$ occurs between T_c and 100 K. An evaluation of Eq. (87) for the high energy data between 37.5 and 77.5 meV yields $\langle m^2 \rangle = 0.032 \pm 0.004\, \mu_B^2$ f.u.$^{-1}$. Finally, the total $T = 10$ K mean-squared fluctuating moment between $\hbar\omega = 6$ and 77.5 meV is $\langle m^2 \rangle = 0.108 \pm 0.004\, \mu_B^2$ f.u.$^{-1}$. The quoted values of $\langle m^2 \rangle$ were obtained after correcting the local susceptibility data in Fig. 67(b) for the use (in Tobyfit) of the isotropic Cu^{2+} form factor instead of the anisotropic form factor, i.e. by multiplying with the appropriate black curves in Fig. 48(c).

7.6 Discussion

In the previous section we presented our experimental results. In this section, the aim is to present an interpretation of these results and to put them in context by discussing their relation to other neutron scattering experiments and, more broadly, to the field of high-temperature superconductivity. It is logical to subdivide our discussion into issues relating to the $\mathbf{Q}_{2D}$-space symmetry of the spin excitations and issues relating to their intensities.

7.6.1 Dispersion

We start with the $\mathbf{Q}_{2D}$-space symmetry of the excitations. To aid the discussion, Fig. 68 summarizes our results for the dispersion of the incommensurate modes below 40 meV in the superconducting states of underdoped and optimally doped LSCO. In panel (a) our data for $La_{1.84}Sr_{0.16}CuO_4$, supplemented by the triple axis data of B. Lake *et al.* [234] are plotted together with data from experiments on near-optimally doped $YBa_2Cu_3O_{6.85}$ [204]. By comparing the dispersions observed in LSCO and YBCO we bring forth the key conclusion of this chapter, namely that the dispersion we have identified in optimally doped LSCO is remarkably similar to that which characterizes the excitations below the resonance mode in YBCO at a comparable hole-doping level (At different doping levels, similar subresonance incommensurate excitations are observed in YBCO [183, 201, 202, 203]). In both systems, the excitations disperse inwards, and do so with similar effective velocities. In panel (c), we plot our results for the dispersion in $La_{1.90}Sr_{0.10}CuO_4$ together with the low-energy part of of the excitation spectrum of $La_{1.875}Ba_{0.125}CuO_4$ reported by Tranquada *et al.* [151]. The errorbars on the LBCO data do not represent the error in the determination of the peak position but the widths (HWHM) of Gaussians peaks fitted to the data. It is clear that the dispersions of the excitations in the two materials are consistent in this case also. Finally, in panels (b) and (d) we replot the dispersions of the incommensurate peaks in LSCO below T_c on top of shaded regions representing the fitted peak widths (FWHM). Also shown in these plots are dispersion cones for antiferromagnetic spin waves (projected onto the axis of the plot and displaced to originate from $\mathbf{Q}_{2D} = (\pi, \pi(1 \pm 1/4))$ and $\mathbf{Q}_{2D} = (\pi, \pi(1 \pm 1/5))$ in panels (b) and (d) respectively) with the quantum renormalized exchange constant $J = 156$ meV characterizing undoped La_2CuO_4 [63]. Two important conclusions may be drawn from a comparison with the spin wave dispersion curves. First, it is clear that for both underdoped and optimally doped LSCO, the shift towards $\mathbf{Q}_{2D} = (\pi, \pi)$ with increasing $\hbar\omega$ of the loci of magnetic scattering is of the same order of magnitude as that observed for antiferromagnetic spin waves in La_2CuO_4 dispersing along $\langle 10 \rangle$ directions. Second, the low-energy excitation spectrum of LSCO is clearly unlike antiferromagnetic spin waves in the sense that there is no evidence of modes dispersing in the direction away from (π, π), i.e. tracking the outermost part of the (displaced) spin wave dispersion curve of La_2CuO_4.

Combining the low-energy data presented for LSCO, YBCO and LBCO in Fig. 68(a) and (c) with the striking similarity between the 45 degree rotated high-energy spin fluctuations of

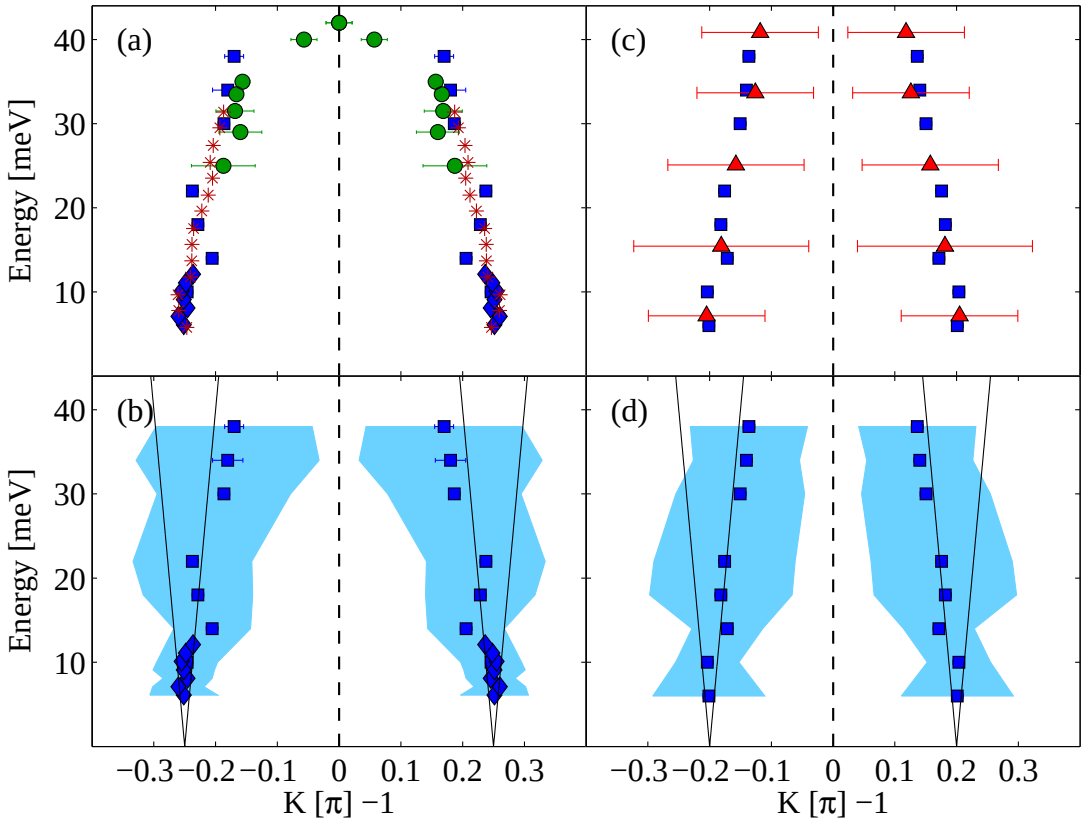

Figure 68: Summary plot for the dispersions observed in $La_{1.84}Sr_{0.16}CuO_4$ and $La_{1.90}Sr_{0.10}CuO_4$ below $\hbar\omega = 40$ meV at $T = 10$ K. (a) Optimally doped LSCO. The blue squares are our time-of-flight results. At the lowest energies, they are supplemented by triple axis data from experiments on the same crystals by Lake *et al.* [234] (blue diamonds). The green circles are from experiments on near-optimally doped YBCO [204]. The stars represent half the wavevector of the most prominent features observed along the [10] direction in low-temperature STM experiments on $Bi_2Sr_2CaCu_2O_{8+\delta}$ [235]. (b) Optimally doped LSCO. The blue squares are our time-of-flight results. The shaded blue regions represent the fitted FWHM at each energy. The solid lines indicate antiferromagnetic spin waves dispersing symmetrically away from $\mathbf{Q}_{2D} = (\pi, (1 \pm 1/4)\pi)$ with a spin wave velocity corresponding to the (quantum renormalized) exchange constant $J = 156$ meV observed in La_2CuO_4 [63]. (c) Underdoped LSCO. The blue squares are the results of our time-of-flight experiments. The red triangles represent the low-energy dispersion observed by Tranquada *et al.* [151] in spin and charge-stripe ordered $La_{1.875}Ba_{0.125}CuO_4$. The errorbars on the latter data represent the HWHM of Gaussian fits, i.e. they correspond to the shaded blue regions in panels (b) and (d). (d) Underdoped LSCO. The blue squares and the shaded regions have the same meaning as in (b). The solid lines represent antiferromagnetic spin waves with $J = 156$ meV dispersing away from $\mathbf{Q}_{2D} = (\pi, (1 \pm 1/5)\pi)$.

stripe-ordered $La_{1.875}Ba_{0.125}CuO_4$ [151] and underdoped $YBa_2Cu_3O_{6.6}$ [207], it is natural to conclude that the cuprate superconductors have a common spin fluctuation spectrum. This supposed universal spin fluctuation spectrum consists of low-energy incommensurate modes which disperse towards $\mathbf{Q}_{2D} = (\pi, \pi)$ where they intersect (yielding a region in $(\mathbf{Q}_{2D}, \omega)$-space with a high density of states where − in our interpretation − the commensurate resonance modes in $YBa_2Cu_3O_{6+y}$ [182], $Bi_2Sr_2CaCu_2O_{8+x}$ [194] and $Tl_2Ba_2CuO_{6+\delta}$ [197] form, see below), whereupon the high-energy spectrum has a 45 degree rotated structure [151, 207]. As we have mentioned previously, the $\mathbf{Q}_{2D}$-space symmetry of the high-energy fluctuation spectrum is still a controversial issue, with some studies of YBCO claiming that excitations above the resonance energy resemble spin waves in terms of their dispersion [208, 209]. Our data for energies $\hbar\omega \geq 40$ meV do not shed much light on this topic, but are also not statistically inconsistent with a 45 degree rotation of the high-energy spin fluctuation spectrum. Thus, although the nature of the high-energy spectrum remains unsettled, in the following we assume the existence of a universal spin fluctuation spectrum with the characteristics described above, and ask what type of theory predicts such a spectrum. Having done so, we discuss what constraints our experimental results place on such theories.

In section 6.4 we encountered some of the theories which are on the market. Various approaches start from a dynamic nesting picture of particle-hole excitations across a Fermi surface with a superconducting energy gap $\Delta_{\mathbf{k}}$ with d-wave symmetry [212, 214, 215, 216, 217, 218], whereas others

treat the problem as one of localized spins in a stripe [220, 221] or ladder [222, 223, 224, 227] environment. Given the combined experimental evidence obtained from neutron scattering, ARPES, STM and other experiments for both stripes and quasiparticles in cuprate superconductors (See e.g. [65, 95]), it appears most appropriate to start from a model of electrons forming inhomogeneous spatial patterns, and such ideas have also found theoretical expression [225, 226].

To our knowledge, while dynamic nesting theories have predicted an inwards dispersion below the resonance energy $E_{\rm res}$ in YBCO as well as an outwards dispersion above $E_{\rm res}$, none have predicted the 45 degree rotation of the high-energy spectrum observed in [151, 207]. Because several models involving stripes or ladders are able to explain such a rotation of the high-energy spectrum [222, 223, 224, 225, 227], the $\mathbf{Q}_{\rm 2D}$-space symmetry of the excitations observed by Tranquada *et al.* [151] and Hayden *et al.* [207] point towards a crucial role for charge-ordered states such as those assumed in these models. Furthermore, since charge-stripe ordered states have been observed directly using neutron and X-ray diffraction in both $La_{1.48}Nd_{0.4}Sr_{0.12}CuO_4$ [115, 157], $La_{1.875}Ba_{0.125}CuO_4$ [163] and in $YBa_2Cu_3O_{6.35}$ [205] and also find support from other sources (as discussed in chapter 6 and in [95]) this is not a surprising conclusion. The real issue is whether nanoscale (spin or charge) texturing of the CuO_2-planes plays a fundamental role for superconductivity in the cuprates to arise. Such grand issues cannot be settled from our data alone. A more modest question which we must pose ourselves is what constraints our experimental results put on further theoretical developments.

First, we point to the strong similarity between the measured temperature dependence of the low-energy response in underdoped LSCO displayed in Fig. 64 and similar measurements in $La_{1.875}Ba_{0.125}CuO_4$ by Fujita and coworkers [163]. Because LBCO is known to display charge stripe order at low temperature, whereas − to our knowledge − charge order Bragg peaks have never been reported in systems with the chemical formula $La_{2-x}Sr_xCuO_4$, this observation provides circumstantial evidence for charge stripe correlations in LSCO. More precisely, Fujita *et al.* argue that the continuous loss of incommensurate magnetic signatures in LBCO caused by warming to high temperatures from the low-temperature charge-stripe ordered state (through a charge-ordering transition which is believed to be induced by a structural orthorhombic-to-tetragonal phase transition) reflects the presence of a temperature-dependent mixture of charge-stripe spacings [163]. If these arguments and the supporting model calculations [163] are accepted, then it stands to reason that disordered change stripes exist in LSCO at all temperatures, and most likely remain dynamic because there is no structural distortion to pin them. On the other hand, it is known that magnetic fields applied perpendicular to the CuO_2 planes strongly enhance the associated spin stripe order parameter in underdoped LSCO [122, 123, 179] and also induces periodic modulations in the density of states of charged quasiparticles [117].

Disorder in the charge stripe distance has recently been discussed [226] as an explanation of the existence of features in the nodal [11] direction in ARPES experiments on stripe ordered $La_{2-x-y}Nd_ySr_xCuO_4$ [236], where one would naively expect none. This is important because the same model [226] captures prominent aspects of our experimental data on LSCO for energies below 40 meV, namely the existence of a dispersion towards (π,π) and the absence of an excitation branch dispersing in the direction away from (π,π). In improving the empirical basis for such theories, unambiguously establishing the existence of charge stripe correlations in LSCO is of crucial importance. Perhaps our low-energy observations is a step in this direction.

Next, we turn to the temperature dependence of the dispersion of the incommensurate modes. In both optimally doped and underdoped LSCO our data show that the existence of a dispersion does not depend on the simultaneous existence of superconductivity. In underdoped LSCO, the dispersion survives to $T = 100$ K, far above $T_c = 29$ K. Although we have insufficient low-energy data at $T = 300$ K to prove this, the difference in the fitted values of δ between $\hbar\omega = 22$ meV and higher energies seen in Fig. 66(a) suggest that a dispersion may even exist at room temperature above a threshold energy below which thermal stripe disordering − in the sense discussed above − significantly affects the fluctuations.

Previous experiments on YBCO have reported the existence of incommensurate scattering below the resonance energy in the normal state in both underdoped [99, 183] and near-optimally doped [204] samples. Our experiments show analogous behavior in underdoped and optimally doped LSCO, and indicate that the effective exchange constant $J_{\rm eff}$ quantifying the velocity of the dispersion towards $\mathbf{Q}_{\rm 2D} = (\pi,\pi)$ is remarkably insensitive to temperature changes at both doping levels. This robustness of the dispersion suggests that the energy scale responsible for the incommensurate modes in LSCO (and because of the universality of the low-energy spectrum, also

in other cuprates) is much higher than $k_B T_c$. Moreover, the proximity of the effective exchange constants $J_{\text{eff}} = 125^{+23}_{-17}$ meV ($x = 0.16$) and $J_{\text{eff}} = 111^{+9}_{-8}$ meV ($x = 0.10$) to $J = 156 \pm 5$ meV obtained by Hayden *et al.* for undoped La_2CuO_4 [63] can be taken as evidence that the spin physics of the superconductors is closely akin to that of the insulating parent compounds. On a general level, this observation favors theories of cuprate high-temperature superconductivity which take their origin in the physics of the Mott insulator at $x = 0$ over theories which start from the opposite regime of a conventional Fermi liquid description (Transport measurements indicate that the latter type of theory is more suitable in the strongly overdoped regime [107]). In particular, it suggests that models involving stripes or ladders are more likely to provide an accurate description of the spin excitations in cuprate superconductors than are models based on dynamic nesting.

A second important point concerning the temperature evolution of the spin excitations is that we do not at any temperature or doping level observe spin excitation branches dispersing in the direction away from (π, π). Instead, the response for $\hbar\omega \leq 40$ meV appears to consist of modes which broaden in $\mathbf{Q}_{2\text{D}}$ while dispersing towards (π, π) as indicated in panels (b) and (d) of Fig. 68 for $T \ll T_c$ in optimally doped and underdoped LSCO respectively. As we have stated previously, this proves that the low-energy excitations in LSCO are unlike conventional spin waves from antiferromagnetically correlated spins residing in charge-striped geometries [220, 221]. On the other hand, spin wave theory accurately describes the high-energy excitations in isostructural and non-superconducting $S = 1$ nickelates [160, 161] which are known to host well-developed stripe order. In particular, both counterpropagating modes are observed in these systems. In section 6.4.2 we discussed how different models based on stripes and ladders have attempted to account for the absence of the mode dispersing away from (π, π) in the cuprates. In the work of Andersen and Hedegård [226], the origin of this effect is believed to lie in the damping influence of a d-wave particle-hole continuum. The problem with such an interpretation is how to explain the absence of counterpropagating modes above T_c, but this difficulty may be healed by the existence of the pseudogap phase at the temperatures and doping levels we have investigated. In a one-band Hubbard model description developed by Seibold and Lorenzana, the effect is caused by spin-charge coupling emerging naturally from the computations after all parameters are fixed [225]. By contrast, in a spin-only model put forward by Vojta and Ulbricht [224] the effect is caused by an enhancement (through matrix element effects) of the response around (π, π), rather than a decrease of the response away from (π, π). Whatever the correct explanation may be, our results make clear that phase coherent superconductivity is not involved. This is not necessarily an argument in favor of spin-only approaches such as [224] since any theory must eventually account for the influence of charges.

Let us now turn to the doping dependence of the dispersion. As is made clear by Fig. 68 there is negligible change in the slope of the dispersion between underdoped, (weakly) magnetically ordered $La_{1.90}Sr_{0.10}CuO_4$ and optimally doped, magnetically disordered $La_{1.84}Sr_{0.16}CuO_4$. A semiquantitative analysis yielded the values $J_{\text{eff}} = 111^{+9}_{-8}$ meV ($x = 0.10$) and $J_{\text{eff}} = 125^{+23}_{-17}$ meV ($x = 0.16$) for the effective exchange constants determining the excitation velocities. These numbers are identical within errors, and are not far from the value $J = 130 \pm 5$ meV found by Hayden *et al.* for $La_{1.86}Sr_{0.14}CuO_4$ by fitting the highest-energy, shortest-wavelength excitations to a linear spin wave model [210, 198]. On the other hand, the values derived for the three superconducting specimens are slightly reduced relative to the value $J = 156 \pm 5$ meV found for the antiferromagnetic spin waves in La_2CuO_4 [63]. A modest reduction is natural since the hole-doping process − whether it occurs in a homogeneous or in an inhomogeneous manner − destroys the completely localized nature of the $S = 1/2$ spins in the Mott insulator, effectively weakening nearest neighbor spin correlations. In any case, the qualitative and quantitative similarity between the dispersions of underdoped and optimally doped LSCO (in addition to the similarities with the low-energy spectra of magnetically disordered, near-optimally doped YBCO [203] and charge-stripe ordered LBCO [151]) immediately proves that static spin order is irrelevant for the existence of a dispersion. In the light of the preceding discussion we would infer that fluctuating stripe or ladder order is present at both doping levels studied.

Theoretically, the excitation spectra computed by Seibold and Lorenzana [225] depend little on the periodicity and phase (bond-centering or site-centering) of the stripes, but static magnetic order is a precondition in their model. Therefore, it cannot explain why we observe the same dispersion in optimally doped LSCO as in underdoped LSCO. In other models [222, 223], a number of coupling parameters are fine-tuned to force the system to a quantum critical point separating the magnetically ordered two-leg ladder state from a paramagnetic state. Only then is the excitation

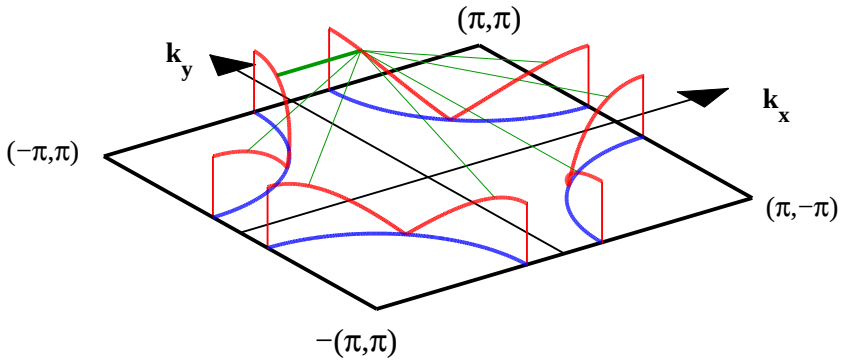

Figure 69: Generic Fermi surface and superconducting gap function $\Delta_{\mathbf{k}}$ for superconducting cuprates. As in Fig. 34 the blue lines indicate the Fermi surface measured in the normal state whereas the red lines show the absolute values of the $d_{x^2-y^2}$ superconducting gap $\Delta_{\mathbf{k}}$. Hole pockets are centered on the four (π, π) points. The solid green lines represent the STM wavevectors discussed in the text. The thick green line parallel to [10] is the particular wavevector corresponding to the stars in panel (a) of Fig. 68.

spectrum calculated. Such theories can in principle only describe one particular doping level. For more realistic comparisons with our data, they should be extended into both the disordered and ordered regimes.

To round off our discussion of $\mathbf{Q}_{2D}$-space symmetry of the inelastic magnetic scattering in LSCO, we point to a possible correlation between the dispersion we have observed and dispersions observed in STM experiments [235, 237, 238] probing the quasiparticle density of states on clean surfaces of (typically) $Bi_2Sr_2CaCu_2O_{8+\delta}$ (Bi2212).

Figure 69 reproduces Fig. 34 of chapter 6 but also contains seven wavevectors connecting points on the quasiparticle dispersion surface Eq. (66) with $\epsilon_{\mathbf{k}} = 0$ for wavevectors on the Fermi surface. Scattering from random defects leads to quantum interference between quasiparticle states with the same energy $E_{\mathbf{k}}$, i.e. connected by the green lines in Fig. 69. The interference patterns become visible in large spatial field-of-view maps of the conductance when charges are made to tunnel between the topmost CuO_2 layer of Bi2212 and the STM tip with the bias voltage set to fulfill the condition $eV = E_{\mathbf{k}}$. By Fourier transforming such images the group of J. C. Davis have succeeded in identifying all seven wavevectors in Fig. 69 [237]. By tracking the dispersions of the wavevectors with bias voltage, they could subsequently invert the whole picture to obtain the Fermi surface and superconducting gap. In doing so they found excellent agreement with the Fermi surface and gap measured by ARPES [237]. In panel (a) of Fig. 68 we have plotted the dispersion (measured with positive bias voltage, i.e. by pulling electrons out of filled states, in experiments on optimally doped "as-grown" Bi2212 [235]) of the wavevector indicated by a thick green line along [10] in Fig. 69. The only difference is that we have divided the wavevector scale by a factor of two. After this division, the STM dispersion falls on top of the dispersion of the incommensurate modes of optimally doped LSCO, displaced from (π, π) along the same $\langle 10 \rangle$ direction.

There is no real justification for dividing the STM wavevector by two, although such a factor is known from diffraction experiments on charge-stripe ordered cuprates [115, 163, 205], see Fig. 40(c). The almost identical dispersions obtained after dividing by two are most likely coincidental. For example, in underdoped Bi2212 the hole pockets around the (π, π) points would shrink relative to the optimally doped case since there are fewer holes. This would in turn cause the (thick green) wavevector along [10] to increases its length whereas the parallel neutron scattering wavevector $\delta\pi\,(1, 0)$ becomes shorter. Thus, in this case, the STM and neutron dispersions would not fall on top of each other after division of the former by two.

One could also argue that we observe a dispersion which does not change with temperature, whereas the STM dispersions discussed above should become invisible when the superconducting gap vanishes. However, this runs into the counterargument that STM shows cuprate (Bi2212) surfaces to be intrinsically disordered on the nanoscale [119, 120]. The nature of this inhomogeneity is such that for a given nominal doping, various nanoscale regions display conductance spectra characteristic of a range of doping levels (as reflected by the superconducting energy gaps) around the average, nominal level. Because of this spread of effective doping levels, it is slightly unclear what should be understood by "the vanishing of the superconducting gap".

The reason for not immediately writing off the correlation between STM and neutron dis-

persions shown in Fig. 68(a) is that in nanoscale regions with the lowest effective doping, STM reveals the harmonious coexistence (in the same nanoscale regions) of quasiparticle interference patterns of the type discussed above with non-dispersive quasiparticle density of states modulations which are more likely to be associated with an electronic ordering phenomenon correlating with the enigmatic pseudogap phase [238]. The energy-independent wavevectors of these modulations in strongly underdoped nano-regions in Bi2212 are parallel to $\langle 10 \rangle$ and their magnitudes reveal that the characteristic length scale for the electronic order in question is in the range $4-5$ lattice constants [238]. Electronic ordering phenomena with the same characteristic length scale and orientation have been observed above T_c [239] and around vortex cores [117] where superconductivity is destroyed locally by the application of a magnetic field. Thus, the picture emerging from STM experiments is that there exists an electronic phase with a length scale of $4-5$ lattice constants and a characteristic orientation parallel to the nearest neighbor Cu-Cu direction. This electronic order competes with superconductivity and comes into prominence as soon as the latter is suppressed via underdoping, heating or application of a magnetic field. Given the typical length scale of the phenomenon, the competing electronic order could quite possibly be the stripe or ladder order which − as discussed above − is also a likely candidate for the origin of the dispersing incommensurate modes observed by neutron scattering. This conjecture is strongly supported by the field-induced static antiferromagnetic order in underdoped LSCO [122, 123, 179], but from the STM standpoint "checkerboard" ordered states are also much en vogue [118, 238].

7.6.2 Intensities

Having discussed the dispersion of the incommensurate peaks, we now turn our attention to the observed intensities. It should be pointed out from the outset that in all calculations we have neglected variations in the Debye-Waller factor $\exp(-2W)$ in Eq. (15). This is justified by the small magnitudes and slow temperature dependence of the isotropic Debye-Waller temperature factors [98].

For optimally doped LSCO we have investigated the spectral weight changes which occur when the samples enter their superconducting state and a spin gap Δ_s opens in the imaginary part $\chi''(\mathbf{Q}_{2D},\omega)$ of the generalized susceptibility. These issues have been investigated before [144, 148]. The new information brought to light by our experiments is that the spectral weight changes caused by the onset of superconductivity affect $\chi''(\mathbf{Q}_{2D},\omega)$ for energies as high as ~ 30 meV. Furthermore, we have discovered that the intensity redistribution conserves spectral weight. Thus, the mean-squared fluctuating moment $\langle m^2 \rangle$ evaluated using Eq. (87) for energies below 40 meV is identical within errors in the superconducting state at $T = 10$ K and in the normal state at $T = 40$ K. The spectral weight lost below the spin gap Δ_s for $T \ll T_c$ is merely shifted to higher energy transfers, forming a broad peak in the local susceptibility $\chi''(\omega)$ centered at $\hbar\omega = 18 \pm 2$ meV and with a width of 12 ± 2 meV (HWHM), see Fig. 62(a). For $La_{1.86}Sr_{0.14}CuO_4$, Hayden *et al.* have previously reported a peak in $\chi''(\omega)$ centered at $\hbar\omega = 22 \pm 5$ meV, but in that study the temperature dependence of the local susceptibility was not investigated [210]. Our observation of spectral weight conservation through the superconducting transition in optimally doped LSCO parallels a recent study of oxygen-ordered, underdoped ortho-II $YBa_2Cu_3O_{6.5}$ where similar spectral weight conservation was found to apply to the formation of the resonance mode [99]. In other words, the resonance in YBCO is most likely formed when spectral weight is pushed to higher energies by the gradual formation of a spin gap [99].

Turning this argument around, it is interesting to ask whether the peak we have observed at 18 ± 2 meV in optimally doped LSCO is the long-sought LSCO resonance mode. To answer this, we should recall the experimental characteristics, presented in section 6.3.6, of the resonance mode in YBCO. Besides being magnetic in origin, the YBCO resonance occurs in the acoustic response function $\chi''_{ac}(\mathbf{Q}_{2D},\omega)$ and is centered on $\mathbf{Q}_{2D} = (\pi,\pi)$. The resonance intensity always increases with decreasing temperature, but the detailed temperature dependence varies with hole-doping concentration. At optimal doping the resonance first appears below T_c, but a progressively wider pretransitional regime with finite resonance intensity in the normal state develops in underdoped samples.

Let us now compare with the situation in optimally doped LSCO. First of all, it is well-known and easily established by polarization analysis that the incommensurate inelastic peaks in LSCO are magnetic. Second, the YBCO resonance is commensurate whereas the peak in the local susceptibility of LSCO derives from four incommensurate wavevectors. Third, while we have not

measured the detailed temperature dependence of the spectral weight at $\hbar\omega = 18 \pm 2$ meV, the temperature dependence of the incommensurate peak intensity has previously been measured in magnetically disordered LSCO samples with slightly lower hole-concentration and agrees with the temperature dependence of the YBCO resonance at optimal doping. Thus, for $La_{1.86}Sr_{0.14}CuO_4$ Mason and coworkers have demonstrated that the spectral weight increase at $\hbar\omega = 15$ meV sets in at T_c, i.e. at the same temperature where the spin gap starts to open [148]. Finally, since LSCO is a single-layer compound, comparisons of absolute unit intensities between LSCO and YBCO are complicated by the presence of finite optical spectral weight in YBCO, a detailed knowledge of which is necessary for completely accurate comparisons. In all cases, YBCO intensities quoted per formula unit must be divided by two to account for the fact that YBCO has two coppers in CuO_2 planes per formula unit whereas LSCO has one, see Fig. 33.

Using Eq. (87), we can can evaluate the absolute value $\delta\langle m^2\rangle$ of the spectral weight shifted into the peak centered at $\hbar\omega = 18 \pm 2$ meV in the superconducting transition. Including corrections for the use of the isotropic form factor, we find $\delta\langle m^2\rangle = 0.010 \pm 0.005\, \mu_B^2\ (CuO_2)^{-1}$. This value is of the same order of magnitude as $\delta\langle m^2\rangle = 0.03 \pm 0.02\ (CuO_2)^{-1}$ quoted by Dai *et al.* for both underdoped $YBa_2Cu_3O_{6.6}$ and optimally doped $YBa_2Cu_3O_{6.93}$ [189] as well as $\delta\langle m^2\rangle = 0.03\ (CuO_2)^{-1}$ given by Stock *et al.* for oxygen-ordered $YBa_2Cu_3O_{6.5}$ [99]. The close similarity between these values lends support to an interpretation of the peak in the local susceptibility in Fig. 62(a) as an incommensurate resonance mode in optimally doped LSCO. Furthermore, it is striking that the peak energy $\hbar\omega = 18 \pm 2$ meV is identical within errors to the resonance energy $E_{\rm res} = 41$ meV [189] of optimally doped YBCO scaled by the ratio (38.5K/92.5K) of the superconducting transition temperatures. Finally, in underdoped YBCO it has been shown that modest magnetic fields $H \ll H_{c2}$ applied perpendicular to the CuO_2 planes significantly suppress the resonance intensity [191]. In a similar manner, a number of magnetic field studies of LSCO samples near optimal doping [121, 174, 175] have established that modest fields cause the spin gap to close. In an experiment by Tranquada *et al.* [175] on a slightly overdoped $La_{1.82}Sr_{0.18}CuO_4$ sample, the zero-field signal in the superconducting state was peaked at incommensurate wavevectors at an energy $\hbar\omega \simeq 9$ meV. The application of a magnetic field caused the incommensurate signal at this energy to decrease in amplitude and broaden in $\mathbf{Q}_{\rm 2D}$. The combination of these two effects and the observation by Mason *et al.* [148] that the opening of the spin gap Δ_s below T_c (in zero field) is accompanied by a sharpening (the "coherence effect") of the incommensurate response in $La_{1.86}Sr_{0.14}CuO_4$ immediately above Δ_s led Tranquada and coworkers to suggest an incommensurate resonance at $\hbar\omega = 9$ meV in $La_{1.82}Sr_{0.18}CuO_4$ [175]. Clearly, this suggestion is in line with our data, but we have added further credence to the concept of incommensurate resonance modes in $La_{2-x}Sr_xCuO_4$ by studying the spectral weight redistribution over a large range of energy transfers and by computing the absolute value of the spectral weight associated with such a resonance mode in optimally doped LSCO, showing that it is similar to the spectral weights of resonance modes in YBCO at various hole-doping levels.

A resonance mode at $\hbar\omega = 15$ meV has been predicted by Kao, Si and Levin in an RPA calculation of the neutron scattering cross-section [217], but the resonance is commensurate rather than incommensurate. Similarly, spin-based models discussed by Batista, Ortiz and Balatsky [219] predict commensurate resonance modes in this energy range. More to the point, Morr and Pines have used a spin-fermion model to predict an incommensurate resonance-like feature in the range $8-18$ meV for LSCO [145]. In this model, antiferromagnetically coupled spins interact with charge carriers via an RPA-like coupling term [145, 146]. This causes incommensurate spin excitations to become damped in a manner which differs between the superconducting and normal states. Although this model is interesting and its prediction for the incommensurate peak amplitude bears a striking resemblance to our results in Fig. 61(a), it suffers from several drawbacks. For example, the incommensurate wavevector (at which the resonance-like peak occurs) is not independently predicted but is chosen to match experiment. Moreover, the spin gap Δ_s is predicted to have nodes at the wavevectors connecting the nodes of the d-wave superconducting gap $\Delta_{\mathbf{k}}$, whereas experimentally a $\mathbf{Q}_{\rm 2D}$-independent spin gap is observed [144].

Summing up, the picture we envisage is that the cuprates have a common, universal spin fluctuation spectrum (at least for energies below ~ 40 meV), but with spin gaps of unequal magnitude. In YBCO, spin gap formation pushes low-energy spectral weight into an energy-range where overlapping dispersive modes (incommensurate at lower energies) lead to a high density of states. Therefore, the YBCO resonance (and the commensurate resonance modes in Bi2212 and $Tl_2Ba_2CuO_{6+\delta}$) appears very intense. On the other hand, because the spin gap Δ_s of LSCO is

smaller than that of YBCO, the spectral weight lost below the gap, although comparable in its magnitude $\delta\langle m^2\rangle$ to that of YBCO, is transferred to a quartet of incommensurate wavevectors at lower energy transfers than the YBCO resonance energy. Because each of these wavevectors is responsible for only a fourth of the total resonance weight $\delta\langle m^2\rangle$, an incommensurate resonance will appear to be substantially less bright in constant-$\hbar\omega$ scans or cuts than one which is commensurate.

If the peak in $\chi''(\omega)$ at $\hbar\omega = 18 \pm 2$ meV is an incommensurate equivalent of the higher-energy commensurate resonance modes in YBCO, Bi2212 and $Tl_2Ba_2CuO_{6+\delta}$, then one controversy [190, 240] in the high-T_c conundrum could be on its way to being resolved. It has been claimed by Kee, Kivelson and Aeppli [190] that the apparent non-existence of a resonance mode in LSCO is inconsistent with the fact that the putative signatures of scattering off a resonance mode in e.g. ARPES (where the resonance energy is believed to be related to the "peak-dip-hump" structure discussed in section 6.3.6) are observed in LSCO as well. Therefore, it was suggested, the resonance mode does not reveal itself in ARPES or other spectroscopies, the underlying reason being that its spectral weight $\delta\langle m^2\rangle_{\rm res}$ constitutes at most a few percent of the total available spectral weight obtained by integrating Eq. (87) over all frequencies [190]. In answer to this claim, Abanov and coworkers argued that despite the small spectral weight of the resonance, the fermionic self-energy due to scattering off such a mode can well be large and is unrelated to its spectral weight [240]. This would imply that ARPES and other spectroscopies should be able to observe the signatures of resonance modes. Consequently, if the peak at $\hbar\omega = 18 \pm 2$ meV which we have observed in optimally doped LSCO is a resonance mode, then it should be observable in ARPES experiments. It is then interesting to inquire whether there are observable consequences caused by the appearance of this resonance at incommensurate rather than commensurate wavevectors. More generally, everything which is known about the resonance modes of YBCO, Bi2212 and $Tl_2Ba_2CuO_{6+\delta}$ ought to be checked for LSCO with particular emphasis on understanding whether the incommensurate nature of the LSCO resonance is correlated with the fact that T_c is lower in LSCO than in YBCO, Bi2212 and $Tl_2Ba_2CuO_{6+\delta}$.

The picture outlined above is appealing, but does not treat the case of underdoped LSCO where no spin gap is seen below $x = 0.13$. In the following we discuss this case, based on the data for $La_{1.90}Sr_{0.10}CuO_4$ shown in Fig. 67. First we note that in accordance with our expectations, the absence of a spin gap implies that no peak develops in $\chi''(\omega)$ below T_c. Thus, for $T = 10$ and 30 K we have derived the values $\langle m^2\rangle = 0.077 \pm 0.002\ \mu_B^2\ (CuO_2)^{-1}$ and $\langle m^2\rangle = 0.074 \pm 0.002\ \mu_B^2\ (CuO_2)^{-1}$ respectively for the mean-squared fluctuating moment evaluated in the range $6-34$ meV. On the other hand, a spectral weight reduction does occurs upon heating to $T = 100$ and 300 K. At these two temperatures we find $\langle m^2\rangle = 0.062 \pm 0.003\ \mu_B^2\ (CuO_2)^{-1}$ and $\langle m^2\rangle = 0.063 \pm 0.005\ \mu_B^2\ (CuO_2)^{-1}$ respectively. These numbers show that from T_c to 100 K a non-zero amount $\delta\langle m^2\rangle = 0.012 \pm 0.004\ \mu_B^2\ (CuO_2)^{-1}$ of spectral weight is lost. The range of energies and temperatures probed in our experiment do not allow us to tell what has happened to this spectral weight. There are two possibilities. First: If our model − defined by Eqs. (82) and (89) − is valid in underdoped LSCO, then the excess spectral weight found at low energies for $T = 10$ and 30 K must have been transferred from energies above 40 meV or from other wavevectors. The second possibility is that our model does not work at $T = 10$ and 30 K and that this is the cause of the change in the values of the mean-squared fluctuating moment.

It is noteworthy that the absolute value of $\delta\langle m^2\rangle$ is comparable to the value $\delta\langle m^2\rangle = 0.010 \pm 0.005\ \mu_B^2\ (CuO_2)^{-1}$ associated with the incommensurate magnetic resonance in optimally doped LSCO. Given that the resonance mode in underdoped YBCO becomes observable at a temperature corresponding to the pseudogap temperature T^* rather than at T_c [189], one might speculate whether the difference signal (10 K−100 K) in Fig. 67(b) is also a resonance, setting in above T_c. If so, then such a resonance is not related to spin gap formation, and requires another physical mechanism.

Since underdoped LSCO is known to be weakly magnetically ordered at low temperatures, a more plausible explanation for the spectral weight loss between $T = 30$ and 100 K involves a tendency towards antiferromagnetic order which suppresses the spin gap completely. In this scenario, the apparent loss of spectral weight reflects a change of the polarization factor in the neutron scattering cross-section below an ordering temperature T_N at which the magnetic moments select a preferred direction. Although this direction is not known from experiment, the concomitant change in the polarization factor (which is not embodied by Eq. (82)) can well be imagined to cause an increase in the total spectral weight detected below T_N. In particular, a moment direction parallel to the orthorhombic [010] direction − as in La_2CuO_4 [124] − is qualitatively consistent

with our observations in the sense that the increase in spectral weight happens at low energy transfers where Fig. 48(a) shows $\mathbf{Q}$ to be nearly parallel to the CuO_2-planes and to $\mathbf{Q}_{2D} = (\pi, \pi)$ which in turn corresponds to $\mathbf{Q} = (0 \pm 1L)$ and $\mathbf{Q} = (\pm 10L)$ (both wavevectors being relevant to our argument because LSCO crystals are typically twinned). In underdoped LSCO, T_N is typically found (by neutron diffraction) to be comparable to T_c, see e.g. [122, 155], so the fact that $\langle m^2 \rangle$ changes between T_c and 100 K (but is unchanged between $T = 10$ and 30 K as well as between $T = 100$ and 300 K) is in accord with the idea that the spectral weight loss is caused by magnetic ordering between these two temperatures.

In a variation of the latter idea, one could find inspiration in the STM evidence for nanoscale phase separation and suggest that no spin gap is observed in nominally underdoped LSCO because the nano-regions displaying "underdoped" conductance spectra are dominated by the competing electronic order (i.e. static stripe order) and outweigh the response from the nano-regions displaying "optimally doped" conductance spectra and no competing order. By contrast, in nominally optimally doped LSCO, the response of underdoped nano-regions could be outweighed by the response of electronically distinct nano-regions displaying optimally doped and overdoped behavior. Given the short coherence lengths of the incommensurate spin fluctuations, displayed in Fig. 60 and 66(b) this is not an altogether unnatural suggestion, and is further supported by the fact that low-frequency probes (e.g. μSR, NMR and NQR) typically reveal a slow, glassy spin dynamics in underdoped LSCO rather than static long-range order [172].

Irrespective of the origin of the spectral weight loss in underdoped LSCO, it is clear that from the point of view of intensity considerations the excitation spectra of underdoped and optimally doped LSCO are completely different. This is so in spite of the fact that the excitation spectra appear equivalent from the point of view of their $\mathbf{Q}_{2D}$-space symmetry, with the effective velocity of the dispersions in the incommensurate modes below 40 meV being surprisingly insensitive to temperature and doping. A successful theory for the cuprate spin fluctuation spectra should be capable of accounting for both this robustness of the dispersion and the differences in the temperature dependences of the intensity distributions. To carry out this program, the coupling between spins and electrons must be explicitly considered. Therefore, even though spin-only theories [222, 223, 224] yield excellent agreement with the observed dispersions in LBCO [151], $YBa_2Cu_3O_{6.6}$ [207] and – for low energies – our LSCO data, by construction they cannot account for the spectral weight shift we observe in optimally doped LSCO. In this respect, models involving electrons in striped geometries [225, 226, 227] are more favorable.

Because it assumes static stripe order, the model developed by Andersen and Hedegård [226] is in principle incapable of accurately accounting for the situation in optimally doped LSCO where there is no static magnetic order. For underdoped LSCO where static order does exist, it is predicted that the presence of the pseudogap phase causes the normal state response function $\chi''(\mathbf{Q}_{2D}, \omega)$ to be a broadened version of the superconducting state response [226]. This comes close to the essentially identical excitation spectra we observe for $T = 10$ and 30 K, but for temperatures above the pseudogap temperature T^*, the model predicts that it should become possible to observe excitation branches dispersing in the direction away from (π, π). Thus, if $T = 100$ or 300 K are above T^*, we should have found traces of such modes. Since we have not, it would seem that either $T^* \geq 300$ K or something is missing from the model. A second prediction made by [226] is that in the superconducting state the intensity of the excitation branches in $\chi''(\mathbf{Q}_{2D}, \omega)$ display a prominent peak $\mathbf{Q}_{2D} = (\pi, \pi)$. This is inconsistent with our results, but it is possible that the experimental window $\hbar\omega \leq 40$ meV in which we have obtained data at several temperatures is too narrow to observe the predicted maximum. In the model developed by Seibold and Lorenzana [225], the effect of superconductivity on the intensities of the excitations is not considered explicitly. Their computed excitation spectra for $p = 1/8$ contains multiple peaks in $S(\omega)$ (equal to $\chi''(\omega)$ at $T = 0$ K), and overall appears different from our experimental data for underdoped LSCO at $T = 10$ K (with $E_i = 55$ meV and $E_i = 100$ meV). Vojta and Sachdev [227] discuss the spin excitation spectra in the presence of both static and fluctuating charge (bond) order. In their model, superconductivity is expected to give rise to a spin gap in the spectrum of magnetic excitations – inconsistent with the experimental evidence for underdoped LSCO – but detailed calculations are lacking.

A general idea for how to account for the qualitative difference in the temperature dependences of the intensities in underdoped and optimally doped $La_{2-x}Sr_xCuO_4$ is to ascribe it to the existence of a quantum critical point slightly above $x = 0.13$, separating a magnetically ordered and superconducting from a magnetically disordered and superconducting phase [177]. This notion is

supported both by inelastic neutron scattering experiments by Aeppli and coworkers [114] revealing E/T-scaling in $La_{1.86}Sr_{0.14}CuO_4$, and by very recent high-field neutron diffraction experiments by Khaykovich and coworkers in which static antiferromagnetism was induced by a magnetic field in $La_{1.856}Sr_{0.144}CuO_4$ – a system which is magnetically disordered in zero-field [241]. In such a scenario, the spin gap in optimally doped LSCO is caused by critical slowing down of quantum spin fluctuations on approaching the critical point [241]. Our data are clearly consistent with (but do not prove) the existence of a quantum critical point between $x = 0.10$ and $x = 0.16$ in the phase diagram of $La_{2-x}Sr_xCuO_4$.

7.7 Conclusion and outlook

We have performed time-of-flight neutron scattering experiments on underdoped and optimally doped high-temperature superconductors $La_{2-x}Sr_xCuO_4$ with $x = 0.10$ ($T_c = 29$ K) and $x = 0.16$ ($T_c = 38.5$ K) respectively. The goal of the experiments was to obtain detailed information about the imaginary part $\chi''(\mathbf{Q}_{2D}, \omega)$ of the generalized magnetic susceptibility, which from previous experiments was known to be dominated by a quartet of incommensurate peaks surrounding the antiferromagnetic zone center $\mathbf{Q}_{2D} = (\pi, \pi)$. We focused on the energy range $\hbar\omega \leq 40$ meV and have found a number of interesting results.

First of all, the incommensurate peaks in both magnetically ordered, underdoped LSCO and in magnetically disordered, optimally doped LSCO are dispersive. As $\hbar\omega$ increases, the loci of magnetic scattering move closer to $\mathbf{Q}_{2D} = (\pi, \pi)$. By contrast with the expectations for antiferromagnetic spin waves, we observe no signs of magnetic scattering dispersing in the direction away from (π, π). The characteristic velocities of the dispersions towards (π, π) are identical within errors in underdoped and optimally doped LSCO. The numerical values of the effective exchange constants J_{eff} quantifying the velocity of the dispersions are only slightly reduced relative to the quantum renormalized exchange constant $J = 156 \pm 5$ meV describing the spin wave excitations of the antiferromagnetic parent compound La_2CuO_4. For underdoped and optimally doped LSCO we find $J_{\text{eff}} = 111^{+9}_{-8}$ meV and $J_{\text{eff}} = 125^{+23}_{-17}$ meV respectively. The existence and velocity of the dispersion does not depend on the simultaneous existence of phase coherent superconductivity. In underdoped LSCO, a dispersion is present even at $T = 100$ K.

The proper context of our results for the dispersing incommensurate modes is revealed by comparisons with neutron scattering experiments on other cuprate high-temperature superconductors with and without magnetic order. In the experimental window $\hbar\omega \leq 40$ meV, the dispersion we have found in optimally doped LSCO is qualitatively and quantitatively similar to the dispersion of the incommensurate peaks below the resonance mode in magnetically disordered, near-optimally doped $YBa_2Cu_3O_{6.85}$. The dispersion below 40 meV in underdoped LSCO is nearly identical to the dispersion in the same energy-range in the charge-stripe ordered cuprate $La_{1.875}Ba_{0.125}CuO_4$. Thus, for energies below 40 meV our results point to the existence of a universal spin excitation spectrum in all high-temperature superconductors. Based solely on experiments probing higher energy transfers, the existence or non-existence of a universal magnetic excitation spectrum is still under debate. We have obtained some data for underdoped LSCO in the superconducting state and for energies above 40 meV, but they do not contribute to resolving the controversy surrounding the high-energy spectrum.

The intensities of the dispersing incommensurate modes have been investigated in absolute units at selected temperatures in both underdoped and optimally doped LSCO. It was known from previous experiments that at optimal doping, a spin gap opens in the superconducting state and is accompanied by increased intensities at energies above the spin gap. We have found that the spectral weight lost below the spin gap is transferred to energies above the spin gap. Thus, spectral weight is conserved on cooling through the superconducting transition. The spectral weight transferred from below to above the spin gap energy is concentrated in a broad peak around $\hbar\omega = 18 \pm 2$ meV in the local susceptibility $\chi''(\omega)$. Its magnitude in absolute units is $\delta\langle m^2\rangle = 0.010 \pm 0.005\ \mu_B^2\ (CuO_2)^{-1}$. Given that similar spectral weight conservation has been demonstrated to apply to the resonance mode in $YBa_2Cu_3O_{6.5}$ which has a spectral weight $\langle m^2\rangle$ of the same order of magnitude, we suggest that a plausible interpretation of the peak in the local susceptibility in the superconducting state of optimally doped LSCO, is that it represents the long sought resonance mode in LSCO. In such a scenario, the only difference between LSCO, YBCO and other cuprate families concerns the energy scale, the $\mathbf{Q}_{2D}$-space symmetry of the excitation spectrum being universal. The resonance is formed when spectral weight is pushed to

higher energies by the formation of a spin gap. The smaller spin gap in LSCO relative to YBCO means that the resonance becomes incommensurate rather than commensurate. In support of this picture, our experiments on underdoped LSCO, for which previous experiments have failed to detect a spin gap, revealed no difference between the local susceptibilities at $T = 10$ K and at T_c. On heating $La_{1.90}Sr_{0.10}CuO_4$ from T_c to $T = 100$ K, low-energy spectral weight of magnitude $\delta\langle m^2\rangle = 0.012 \pm 0.004\ \mu_B^2\ (CuO_2)^{-1}$ is lost without a detectable compensating gain at the energies and wavevectors investigated. We suggest that this effect is most likely caused by a breakdown of our model when $La_{1.90}Sr_{0.10}CuO_4$ develops magnetic order at low temperatures.

In their totality, our experimental results provide strong constraints on theories for the spin excitation spectra of high-temperature superconductors. At present no existing theory is capable of explaining both the robustness of the dispersion in the incommensurate magnetic excitations to changes in temperature and doping, and the qualitative differences in the temperature dependence of the corresponding intensities. The most promising theories are based on nanoscale texturing of the CuO_2 planes into stripe or ladder structures of spins and electrons.

In the future, the key issue to be investigated experimentally is whether or not the cuprate high-temperature superconductors have a universal spin excitation spectrum over a larger range of energy transfers than have been probed in this chapter. In particular, it should be clarified whether the high-energy excitation spectrum of $La_{2-x}Sr_xCuO_4$ is rotated by 45 degrees as reported for $La_{1.875}Ba_{0.125}CuO_4$ and $YBa_2Cu_3O_{6.6}$ or whether it resembles spin waves as reported for oxygen-ordered $YBa_2Cu_3O_{6.5}$ and for near-optimally doped $YBa_2Cu_3O_{6.85}$. In the light of the plausible existence of a quantum critical point in the phase diagram of $La_{2-x}Sr_xCuO_4$, the doping dependence of the high-energy spectrum is also of great interest.

Yet another central issue relating to the $\mathbf{Q}_{2D}$-space symmetry of the magnetic excitation spectra of cuprate high-temperature superconductors has to do with the experimental absence of low-energy magnetic scattering dispersing in the direction away from $\mathbf{Q}_{2D} = (\pi, \pi)$. Since such modes have been observed in stripe-ordered but non-superconducting $S = 1$ nickelates, a proper understanding of the reasons for their absence in cuprates could lead to important steps ahead in comprehending the interplay between stripe order and superconductivity, which is potentially at the root of the high-T_c conundrum. To this end, studies of the spin excitation spectrum of $La_{2-x}Sr_xCuO_4$ in the overdoped regime, far from the pseudogap phase, would be very interesting.

More generally, understanding the intricate relationships between the dispersive magnetic excitations probed by neutron scattering, the quasiparticle dispersions measured by ARPES and the dispersive and non-dispersive quasiparticle density of states modulations observed in STM experiments should be a matter of high priority in the theoretical community.

Finally, concerning our interpretation of the peak in the local susceptibility of optimally doped LSCO as a reflection of an incommensurate resonance mode, further experiments (using both neutron scattering and other probes) are necessary to map out the doping and temperature dependence of the effect. This should allow quantitative comparisons to be drawn with the well-characterized resonance modes of YBCO and Bi2212 as well as with theory, and is important for unveiling the underlying reason for the absence of a spin gap in underdoped, magnetically ordered LSCO.

A Derivation of the neutron scattering cross-section in linear spin wave theory

In this appendix, we derive the cross-section for one- and two-magnon scattering in an antiferromagnet. The mathematics is pretty elemental, but provides the natural starting point for our investigations of the spin excitation spectrum in $Cu(DCOO)_2{\cdot}4D_2O$ and as such warrants a reasonably detailed exposition. Before presenting the derivations in sections A.2 and A.3 we briefly outline some of the main developments of spin wave theory.

A.1 Spin wave theory

The object of spin wave theory is to find the elementary excitations of spin Hamiltonians. For antiferromagnets on simple lattices it rests on two central assumptions

- The ground state has a finite sublattice moment.
- The magnitude of quantum fluctuations about the classical Néel state is small.

Thus the theory start from a particular assumed ground state − the Néel state − with long-range spin order. This state is the natural ansatz when we consider antiferromagnets on bipartite lattices. In this case all spins on sublattice A (B) are along the positive (negative) z-direction and the nearest neighbours of all A (B) sites are B (A) sites. It is chosen despite the fact that whenever $\mathbf{S}_i^+\mathbf{S}_j^- + \mathbf{S}_i^-\mathbf{S}_j^+$ terms are present in the spin Hamiltonian the Néel state cannot be the true quantum mechanical ground state because such terms give rise to non-diagonal matrix elements. The second assumption listed above is tantamount to the assumption that there there is nevertheless a substantial overlap between the Néel state and the true ground state. These issues were discussed at greater length in section 3.1. Here, we will continue by indicating some of the more important developments of spin wave theory for the antiferromagnetic Heisenberg model. Because the Mermin Wagner theorem tells us that no long-range order can exist at finite temperatures in a system with continuous degrees of freedom such as the Heisenberg model, the discussion that follows applies strictly to $T = 0$ K.

It should be noted that because different papers employ slightly different notations, We have made appropriate corrections to the expressions in this appendix in order to simplify the presentation.

Following earlier work for ferromagnets, a 1952 paper by Anderson provided a semiclassical treatment of antiferromagnetic spin waves (single-magnons), improving on older treatments of the same problem by taking into account zero-point fluctuations [21]. Both 1D, 2D and 3D cases were treated and it was shown that the ground state energies obtained with corrections for the zero-point energies of the quantized oscillators, lay between the rigorous limits Eq. (32). For the simple lattices (linear chain, square lattice and simple cubic) considered in [21], $z = 2D$, and the ground state energy is

$$E_g^{\mathrm{A}} = -\frac{N}{2} z J S^2 \left(1 + \frac{c}{S}\right) \tag{91}$$

The factor c is given by an average over $N/2$ wavevectors $\boldsymbol{q}$ in the first Brillouin zone and represents the effect of the zero-point fluctuations

$$c \;=\; \frac{2}{N}\sum_{\boldsymbol{q}} \left(1 - (1-\gamma_{\boldsymbol{q}}^2)^{1/2}\right) \tag{92}$$

with $\gamma_{\boldsymbol{q}} = (1/z)\sum_{\boldsymbol{\delta}} e^{i\boldsymbol{q}\cdot\boldsymbol{\delta}}$ − a sum of exponential factors involving the z nearest neighbour vectors $\boldsymbol{\delta}$. The ground state ($T = 0$ K) sublattice magnetization M was found to be reduced from the classical ($S \to \infty$) saturation value $(N/2)g\mu_B S$. For the square and simple cubic lattices Anderson found

$$M^{\mathrm{A}} = \frac{N}{2} g\mu_B \left(S - \frac{c'}{2}\right) = \frac{N}{2} g\mu_B S \left(1 - \frac{c'}{2S}\right) \tag{93}$$

The magnitude of the reduction is determined by a factor c', which is also an average over $N/2$ wavevectors in the first Brillouin zone

$$c' = \frac{2}{N}\sum_{\boldsymbol{q}} \left(\frac{1}{(1-\gamma_{\boldsymbol{q}}^2)^{1/2}} - 1\right) \tag{94}$$

In chapter 3 we set $g\mu_B$ to unity and employ the notation $m = (2/N)M$ for the sublattice moment per spin.

It is noteworthy that the reduction factors c and c' depend only on the lattice symmetry and not on the spin quantum number S. Equations (91) and (93) show that the effects of the latter vanish as the classical limit $S \to \infty$ is approached. Here, the classical results $E_g = -\frac{N}{2}zJS^2$ and $M = (N/2)g\mu_B S$ become exact as one would expect. Numerical evaluation yields $c = 0.1579$ and $c' = 0.3932$ for the square lattice [21, 26]. The latter result implies that even disregarding spin wave interactions, quantum zero-point fluctuations reduce the sublattice magnetization by $\sim 40\%$ relative to $S = 1/2$. More dramatically, c' diverges for the linear chain, signifying the breakdown of the fundamental assumption of spin wave theory that the sublattice moment is finite. It is very surprising that in spite of this gross failure, the ground state energy calculated from spin wave theory (with $c = 0.363$ for the 1D case) is very close to the exact result of Bethe and Hulthén (see e.g. [22]). Taken at face value this would appear to suggests that spin wave theory performs well at low temperatures even in extreme cases in terms of spin quantum number and dimensionality. While this conclusion is somewhat oversimplified, it does have a certaim amount of truth to it.

In terms of z and $\gamma_{\boldsymbol{q}}$, the single-magnon dispersion relation in linear spin wave theory is [21]

$$\hbar\omega_{\boldsymbol{q}}^{\mathrm{A}} = zJS\left(1-\gamma_{\boldsymbol{q}}^2\right)^{1/2} \tag{95}$$

This result will be derived in section A.2 of this appendix. Here we just note that while (95) is gapless for all S, one of the more prominent failures of spin wave theory occurs in the $S = 1$ linear chain where the excitation spectrum in fact has a (Haldane) gap.

Shortly after the work of Anderson, Kubo [23] used the Holstein Primakoff transformation [24] (see section A.2) to calculate thermodynamic properties (such as the sublattice moment and the magnetic susceptibilities in fields along and perpendicular to the axis of the ordered moment) of Heisenberg antiferromagnets at finite temperatures. In the process, he demonstrated the equivalence of Andersons semiclassical approach to that of Holstein and Primakoff, when spin wave interactions are neglected. Further, he computed the first correction term to the ground state energy − arising because of spin wave interactions − by including the order $1/(2S)$ term in the Holstein Primakoff expansion (see Eq. (105)). The result

$$E_g^{\mathrm{K}} = -\frac{N}{2}zJS^2\left(1+\frac{c}{S}+\frac{c^2}{4S^2}\right) \tag{96}$$

shows that the first order correction is negligible compared to the zeroth order correction even for $S = 1/2$.

These treatments of the antiferromagnetic Heisenberg model were later refined by Oguchi [25], who calculated the quantum renormalizations of the ground state energy, sublattice magnetization and spin wave dispersion in the presence of spin wave interactions up to order $1/(2S)$ in the Holstein Primakoff expansion. The results involve the quantum renormalization factors (92) and (94)

$$E_g^{\mathrm{O}} = E_g^{\mathrm{K}} \tag{97}$$

$$M^{\mathrm{O}} = M^{\mathrm{A}} \tag{98}$$

$$\omega_{\boldsymbol{q}}^{\mathrm{O}} = \omega_{\boldsymbol{q}}^{\mathrm{A}}\left(1+\frac{c}{2S}\right) \tag{99}$$

Since Oguchi used the same method as Kubo, the ground state energy should be the same and indeed this is borne out by (97). More surprisingly, Eq. (98) shows that to first order in $1/(2S)$, the sublattice magnetization is unaffected by interactions and remains at the value derived by Anderson. Finally, Eq. (99) shows that in the extreme quantum limit $S = 1/2$ interactions give rise to a **q**-independent renormalization of the energy scale for single-magnon excitations. Its numerical value for a square lattice of $S = 1/2$ spins is $Z^{\mathrm{O}} = (1 + c) = 1.1579$. Comparing with (95) we can then define an effective exchange coupling J_{eff}

$$J_{\mathrm{eff}} = Z^{\mathrm{O}}J \tag{100}$$

The quantum renormalization factor for the spin wave velocity c_s − not to be mistaken for the number c in Eq. (92) − is commonly referred to as Z_c. First order corrections for spin wave interactions yielding a **q**-independent energy renormalization, we can write $Z_c = Z^{\mathrm{O}}$.

Following the discovery of high-T_c materials and the initial realization that La_2CuO_4 is rather well represented by the two-dimensional quantum $S = 1/2$ Heisenberg antiferromagnet on a square lattice (2DQHAFSL) [124, 127], Igarashi [26] went one order further in the Holstein Primakoff expansion for the $S = 1/2$ square lattice, i.e. to order $(1/2S)^2$, correcting earlier work [242] in which Umklapp processes were treated incorrectly. By numerically evaluating the resulting expressions computed to this order, he managed to obtain the quantum renormalisation factor for (amongst other properties) the spin wave velocity c_s, and to compute the sublattice magnetization

$$Z_c^{\mathrm{I}} = Z^{\mathrm{O}} + \frac{0.0215 \pm 0.0002}{(2S)^2} = 1.1794 \pm 0.0002 \tag{101}$$

$$M^{\mathrm{I}} = \frac{N}{2} g\mu_B \left(S - \frac{c'}{2} + \frac{0.0035}{(2S)^2} \right) = 0.3069 \tag{102}$$

As shown in [26], these results compare very favorably with those of other theoretical approaches to the Heisenberg model. One may note, that the second order corrections are significantly smaller than the first order corrections. It is possible, although it does not represent a mathematical proof, that this fact implies the rapid convergence of the Holstein Primakoff series for the physical quantities of interest. If so, the truncation of these series after e.g. the $1/(2S)^2$ term would be validated.

A.2 Linear spin wave theory: Dispersion

In this section we use linear spin wave theory to derive the dispersion relation for single-magnon excitations of the square lattice Heisenberg antiferromagnet. Our starting point is a spin Hamiltonian with nearest neighbour in-plane exchange J, next-nearest neighbour in-plane exchange J' and interlayer coupling J_c

$$\begin{aligned} H &= H^{\mathrm{NN}} + H^{\mathrm{NNN}} + H^{\mathrm{c}} \\ &= J \sum_{\mathrm{nn}} \mathbf{S}_{\boldsymbol{i}} \cdot \mathbf{S}_{\boldsymbol{j}} + J' \sum_{\mathrm{nnn}} \mathbf{S}_{\boldsymbol{i}} \cdot \mathbf{S}_{\boldsymbol{j}} + J_c \sum_{\mathrm{c}} \mathbf{S}_{\boldsymbol{i}} \cdot \mathbf{S}_{\boldsymbol{j}} \end{aligned} \tag{103}$$

Introducing raising and lowering operators $\mathbf{S}_{\boldsymbol{j}}^{\pm} = \mathbf{S}_{\boldsymbol{j}}^{x} \pm (-1)^{1/2} \mathbf{S}_{\boldsymbol{j}}^{y}$, we can rewrite each interaction $\mathbf{S}_{\boldsymbol{i}} \cdot \mathbf{S}_{\boldsymbol{j}} = \mathbf{S}_{\boldsymbol{i}}^{z} \mathbf{S}_{\boldsymbol{j}}^{z} + (\mathbf{S}_{\boldsymbol{i}}^{+} \mathbf{S}_{\boldsymbol{j}}^{-} + \mathbf{S}_{\boldsymbol{i}}^{-} \mathbf{S}_{\boldsymbol{j}}^{+})/2$. The effect of the operators $\mathbf{S}_{\boldsymbol{j}}^{\pm}$ is to increase or decrease the z-component of the spin angular momentum: If $|m\rangle$ is an eigenstate of $\mathbf{S}_{\boldsymbol{i}}^{z}$ and $\mathbf{S}_{\boldsymbol{i}}^{2}$ with eigenvalues m and $S(S+1)$ respectively, then $\mathbf{S}_{\boldsymbol{i}}^{\pm} |m\rangle = \sqrt{(S \mp m)(S \pm m + 1)}\, |m \pm 1\rangle$.

To obtain the elementary excitations of the Hamiltonian (103), we assume that its many-body quantum ground state is the Néel state and refer to the sublattice on which all spins are along the positive (negative) z-direction as sublattice A (B). The next step is to implement the Holstein Primakoff transformation (see e.g. [22] or the original paper [24]) in which the spin operators $\mathbf{S}_{\boldsymbol{i}}$ and $\mathbf{S}_{\boldsymbol{j}}$ ($\boldsymbol{i} \in$A and $\boldsymbol{j} \in$B) are rewritten in powers of bosonic creation and annihilation operators $\mathbf{a}_{\boldsymbol{i}}^{\dagger}$, $\mathbf{b}_{\boldsymbol{j}}^{\dagger}$, $\mathbf{a}_{\boldsymbol{i}}$ and $\mathbf{b}_{\boldsymbol{j}}$

$$\begin{aligned} \mathbf{S}_{\boldsymbol{i}}^{+} &= \sqrt{2S \left(1 - \frac{\mathbf{a}_{\boldsymbol{i}}^{\dagger} \mathbf{a}_{\boldsymbol{i}}}{2S} \right)}\, \mathbf{a}_{\boldsymbol{i}} & \mathbf{S}_{\boldsymbol{j}}^{+} &= \mathbf{b}_{\boldsymbol{j}}^{\dagger} \sqrt{2S \left(1 - \frac{\mathbf{b}_{\boldsymbol{j}}^{\dagger} \mathbf{b}_{\boldsymbol{j}}}{2S} \right)} \\ \mathbf{S}_{\boldsymbol{i}}^{-} &= \mathbf{a}_{\boldsymbol{i}}^{\dagger} \sqrt{2S \left(1 - \frac{\mathbf{a}_{\boldsymbol{i}}^{\dagger} \mathbf{a}_{\boldsymbol{i}}}{2S} \right)} & \mathbf{S}_{\boldsymbol{j}}^{-} &= \sqrt{2S \left(1 - \frac{\mathbf{b}_{\boldsymbol{j}}^{\dagger} \mathbf{b}_{\boldsymbol{j}}}{2S} \right)}\, \mathbf{b}_{\boldsymbol{j}} \\ \mathbf{S}_{\boldsymbol{i}}^{z} &= S - \mathbf{a}_{\boldsymbol{i}}^{\dagger} \mathbf{a}_{\boldsymbol{i}} & \mathbf{S}_{\boldsymbol{j}}^{z} &= -S + \mathbf{b}_{\boldsymbol{j}}^{\dagger} \mathbf{b}_{\boldsymbol{j}} \end{aligned} \tag{104}$$

The Holstein Primakoff approximation consists in formally expanding the square roots in powers of $(\mathbf{a}_{\boldsymbol{i}}^{\dagger} \mathbf{a}_{\boldsymbol{i}}/2S)$ and $(\mathbf{b}_{\boldsymbol{j}}^{\dagger} \mathbf{b}_{\boldsymbol{j}}/2S)$

$$\left(2S \left(1 - \frac{\mathbf{a}_{\boldsymbol{i}}^{\dagger} \mathbf{a}_{\boldsymbol{i}}}{2S} \right) \right)^{1/2} = \overbrace{(2S)^{1/2}}^{\text{Anderson 1952}} \left(\underbrace{\overbrace{1}^{\text{Oguchi 1960}} - \frac{1}{2} \left(\frac{\mathbf{a}_{\boldsymbol{i}}^{\dagger} \mathbf{a}_{\boldsymbol{i}}}{2S} \right) - \frac{1}{8} \left(\frac{\mathbf{a}_{\boldsymbol{i}}^{\dagger} \mathbf{a}_{\boldsymbol{i}}}{2S} \right)^2}_{\text{Igarashi 1992}} + \ldots \right) \tag{105}$$

Expanding to zeroth order, i.e. simply replacing the summation on the right hand side of Eq. (105) by unity results in linear spin wave theory [21, 23, 243]. Expanding to higher order amounts to taking interactions between spin waves into account and was done by Oguchi to order $1/(2S)$ [25] and by Igarashi to order $1/(2S)^2$ [26] as discussed in section A.1. It seems natural to assume that successive terms become smaller and smaller, but there is no general theorem to this effect.

When truncating the series after any finite number of terms, well-known problems arise (see e.g. [14]). They have to do with the separability of the physical subspace consisting of $2S+1$ eigenstates of $\mathbf{S}_{\boldsymbol{i}}^z$ from unphysical states generated by the bosonic ladder operators $\mathbf{a}_{\boldsymbol{i}}^\dagger$, $\mathbf{a}_{\boldsymbol{i}}$, $\mathbf{b}_{\boldsymbol{i}}^\dagger$ and $\mathbf{b}_{\boldsymbol{i}}$ which act on a Hilbert space spanned by the infinitely many eigenstates of the spin-deviation operators $\mathbf{n}_{\boldsymbol{i}} = \mathbf{a}_{\boldsymbol{i}}^\dagger \mathbf{a}_{\boldsymbol{i}}$ (for sites on sublattice A) and $\mathbf{n}_{\boldsymbol{i}} = \mathbf{b}_{\boldsymbol{i}}^\dagger \mathbf{b}_{\boldsymbol{i}}$ (for sites on sublattice B). This separability is built into (104) (For example: Take a spin on sublattice A and assume it has had $2S$ spin deviations excited, i.e. $\mathbf{a}_{\boldsymbol{i}}^\dagger \mathbf{a}_{\boldsymbol{i}}$ has the eigenvalue $2S$ corresponding to $\mathbf{S}^z$ having the eigenvalue $-S$. Further reductions in the eigenvalue of $\mathbf{S}^z$ would be unphysical and indeed (104) shows that $\mathbf{S}^- \,|n_{\boldsymbol{i}} = 2S\rangle = 0$) but is lost as soon as the series is truncated. However, looking at Eq. (105) we see that if the ground state expectation values of the operators $\mathbf{n}_{\boldsymbol{i}} = \mathbf{a}_{\boldsymbol{i}}^\dagger \mathbf{a}_{\boldsymbol{i}}$ are small compared to $2S$ ($= 1$ for $S = 1/2$), the unphysical states generated by $\mathbf{S}_{\boldsymbol{i}}^+$ and $\mathbf{S}_{\boldsymbol{i}}^-$ are likely to have a negligible effect on the results. The validity of the Holstein Primakoff transformation of the problem rests on this condition.

Continuing in the spirit of linear spin wave theory we approximate

$$\begin{aligned} \mathbf{S}_{\boldsymbol{i}}^+ &\simeq \sqrt{2S}\,\mathbf{a}_{\boldsymbol{i}} & \mathbf{S}_{\boldsymbol{j}}^+ &\simeq \sqrt{2S}\,\mathbf{b}_{\boldsymbol{j}}^\dagger \\ \mathbf{S}_{\boldsymbol{i}}^- &\simeq \sqrt{2S}\,\mathbf{a}_{\boldsymbol{i}}^\dagger & \mathbf{S}_{\boldsymbol{j}}^- &\simeq \sqrt{2S}\,\mathbf{b}_{\boldsymbol{j}} \\ \mathbf{S}_{\boldsymbol{i}}^z &= S - \mathbf{a}_{\boldsymbol{i}}^\dagger \mathbf{a}_{\boldsymbol{i}} & \mathbf{S}_{\boldsymbol{j}}^z &= -S + \mathbf{b}_{\boldsymbol{j}}^\dagger \mathbf{b}_{\boldsymbol{j}} \end{aligned} \tag{106}$$

Inserting in (103) and keeping only terms to second order in the creation and annihilation operators we obtain for the nearest neighbour, in-plane interaction

$$\begin{aligned} H^{\mathrm{NN}} = \; & E_0^{\mathrm{NN}} + \sum_{(l,m,n)\in A} JS[(4\mathbf{a}_{lmn}^\dagger \mathbf{a}_{lmn} + \mathbf{b}_{l+1mn}^\dagger \mathbf{b}_{l+1mn} + \mathbf{b}_{l-1mn}^\dagger \mathbf{b}_{l-1mn} \\ & + \mathbf{b}_{lm+1n}^\dagger \mathbf{b}_{lm+1n} + \mathbf{b}_{lm-1n}^\dagger \mathbf{b}_{lm-1n}) \\ & + (\mathbf{a}_{lmn}\mathbf{b}_{l+1mn} + \mathbf{a}_{lmn}^\dagger \mathbf{b}_{l+1mn}^\dagger + \mathbf{a}_{lmn}\mathbf{b}_{l-1mn} + \mathbf{a}_{lmn}^\dagger \mathbf{b}_{l-1mn}^\dagger \\ & + \mathbf{a}_{lmn}\mathbf{b}_{lm+1n} + \mathbf{a}_{lmn}^\dagger \mathbf{b}_{lm+1n}^\dagger + \mathbf{a}_{lmn}\mathbf{b}_{lm-1n} + \mathbf{a}_{lmn}^\dagger \mathbf{b}_{lm-1n}^\dagger)] \end{aligned} \tag{107}$$

where $E_0^{\mathrm{NN}} = -2NJS^2$ is the classical ($S \to \infty$) ground state energy of the nearest neighbour Heisenberg model. The summation over all lattice sites (labelled by their Cartesian coordinates $\mathbf{r} = (l, m, n)$) on sublattice A takes care of all nearest neighbour interactions without double counting problems. Expressions similar to (107) may be derived for H^{NNN} and H^{c}. For the former the summation is over all spins and double counting is corrected for by division by two. The classical ground state energy for the total Hamiltonian H is $E_0 = E_0^{\mathrm{NN}} + E_0^{\mathrm{NNN}} + E_0^{\mathrm{c}} = -2NJS^2 + 2NJ'S^2 - NJ_cS^2$. The sign change in the contribution from H^{NNN} is due to the fact that this interaction couples spins on the same sublattice. If we consider the physical situation of interest where nearest neighbour interactions are dominant, antiferromagnetic and orders of magnitude larger than J_c, the expression for the classical ground state energy reflects the fact that antiferromagnetic next-nearest neigbour interactions $J' > 0$ cannot be satisfied in the Néel state and consequently tend to destablize it. Such frustrated interactions lead to increased quantum fluctuations. By contrast, ferromagnetic next-nearest neighbour interactions stabilize the Néel state.

To proceed from (107), it is convenient to enter reciprocal space by introducing Fourier transformed operators $\mathbf{a}_{\boldsymbol{q}}^\dagger$, $\mathbf{a}_{\boldsymbol{q}}$, $\mathbf{b}_{\boldsymbol{q}}^\dagger$ and $\mathbf{b}_{\boldsymbol{q}}$

$$\begin{aligned} \mathbf{a}_q^\dagger &= \left(\frac{2}{N}\right)^{1/2} \sum_{\boldsymbol{r}\in A} e^{i\boldsymbol{q}\cdot\boldsymbol{r}} \mathbf{a}_{\boldsymbol{r}}^\dagger & \mathbf{b}_q^\dagger &= \left(\frac{2}{N}\right)^{1/2} \sum_{\boldsymbol{r}\in B} e^{-i\boldsymbol{q}\cdot\boldsymbol{r}} \mathbf{b}_{\boldsymbol{r}}^\dagger \\ \mathbf{a}_q &= \left(\frac{2}{N}\right)^{1/2} \sum_{\boldsymbol{r}\in A} e^{-i\boldsymbol{q}\cdot\boldsymbol{r}} \mathbf{a}_{\boldsymbol{r}} & \mathbf{b}_q &= \left(\frac{2}{N}\right)^{1/2} \sum_{\boldsymbol{r}\in B} e^{i\boldsymbol{q}\cdot\boldsymbol{r}} \mathbf{b}_{\boldsymbol{r}} \end{aligned} \tag{108}$$

The inverse transforms read

$$\begin{aligned} \mathbf{a}_r^\dagger &= \left(\frac{2}{N}\right)^{1/2} \sum_{\boldsymbol{q}} e^{-i\boldsymbol{q}\cdot\boldsymbol{r}} \mathbf{a}_{\boldsymbol{q}}^\dagger & \mathbf{b}_r^\dagger &= \left(\frac{2}{N}\right)^{1/2} \sum_{\boldsymbol{q}} e^{i\boldsymbol{q}\cdot\boldsymbol{r}} \mathbf{b}_{\boldsymbol{q}}^\dagger \\ \mathbf{a}_r &= \left(\frac{2}{N}\right)^{1/2} \sum_{\boldsymbol{q}} e^{i\boldsymbol{q}\cdot\boldsymbol{r}} \mathbf{a}_{\boldsymbol{q}} & \mathbf{b}_r &= \left(\frac{2}{N}\right)^{1/2} \sum_{\boldsymbol{q}} e^{-i\boldsymbol{q}\cdot\boldsymbol{r}} \mathbf{b}_{\boldsymbol{q}} \end{aligned} \tag{109}$$

The summations over $\boldsymbol{q}$ extend over $N/2$ wavevectors in the first Brillouin zone. Inserting in (107) we find

$$\begin{aligned} H^{\mathrm{NN}} &= E_0^{\mathrm{NN}} + 4JS \sum_{\boldsymbol{q}} (\mathbf{a}_{\boldsymbol{q}}^\dagger \mathbf{a}_{\boldsymbol{q}} + \mathbf{b}_{\boldsymbol{q}}^\dagger \mathbf{b}_{\boldsymbol{q}}) \\ &\quad + 2JS \sum_{\boldsymbol{q}} (\cos(\boldsymbol{q}\cdot\boldsymbol{a}) + \cos(\boldsymbol{q}\cdot\boldsymbol{b})) (\mathbf{a}_{\boldsymbol{q}} \mathbf{b}_{\boldsymbol{q}} + \mathbf{a}_{\boldsymbol{q}}^\dagger \mathbf{b}_{\boldsymbol{q}}^\dagger) \end{aligned} \tag{110}$$

where $\boldsymbol{a}$ and $\boldsymbol{b}$ are the basis vectors of the square lattice under consideration. Expressions similar to (110) can be derived for H^{NNN} and H^{c}. They all take the same form, consisting of a term proportional to the sum of number operators for the $\mathbf{a_q}$ and $\mathbf{b_q}$ bosons, i.e. $(\mathbf{a_q^\dagger a_q} + \mathbf{b_q^\dagger b_q})$ and another term proportional to the combination $(\mathbf{a_q b_q} + \mathbf{a_q^\dagger b_q^\dagger})$. Collecting terms and omitting the classical ground state energy E_0, the Hamiltonian (103) can be expressed as a sum of $N/2$ independent Hamiltonians $H_{\boldsymbol{q}}$

$$H = \sum_{\boldsymbol{q}} H_{\boldsymbol{q}} \tag{111}$$

with $H_{\boldsymbol{q}} = A_{\boldsymbol{q}}(\mathbf{a}_{\boldsymbol{q}}^\dagger \mathbf{a}_{\boldsymbol{q}} + \mathbf{b}_{\boldsymbol{q}}^\dagger \mathbf{b}_{\boldsymbol{q}}) + B_{\boldsymbol{q}}(\mathbf{a}_{\boldsymbol{q}} \mathbf{b}_{\boldsymbol{q}} + \mathbf{a}_{\boldsymbol{q}}^\dagger \mathbf{b}_{\boldsymbol{q}}^\dagger)$. For the particular Hamiltonian (103), $A_{\boldsymbol{q}}$ and $B_{\boldsymbol{q}}$ are given in terms of the interaction strengths J, J' and J_c by

$$\begin{aligned} A_{\boldsymbol{q}} &= 2S(2J - 2J' + J_c) + 4J'S \cos(\boldsymbol{q}\cdot\boldsymbol{a}) \cos(\boldsymbol{q}\cdot\boldsymbol{b}) \\ B_{\boldsymbol{q}} &= 2S[J(\cos(\boldsymbol{q}\cdot\boldsymbol{a}) + \cos(\boldsymbol{q}\cdot\boldsymbol{b})) + J_c \cos(\boldsymbol{q}\cdot\boldsymbol{c})] \end{aligned} \tag{112}$$

Having reduced the problem of finding the excitated states of H to that of finding those of a set of $N/2$ Hamiltonians $H_{\boldsymbol{q}}$, the final step consists of tranforming from the non-diagonal bosonic operators $\mathbf{a}_{\boldsymbol{q}}$ and $\mathbf{b}_{\boldsymbol{q}}$ to operators $\boldsymbol{\alpha}_{\boldsymbol{q}}$ and $\boldsymbol{\beta}_{\boldsymbol{q}}$ in terms of which the Hamiltonians $H_{\boldsymbol{q}}$ are readily diagonalised. This step is known as a Bogoliubov transformation (see e.g. [22]). The operators $\boldsymbol{\alpha}_{\boldsymbol{q}}$ and $\boldsymbol{\beta}_{\boldsymbol{q}}$ are introduced by writing

$$\begin{aligned} \mathbf{a}_{\boldsymbol{q}}^\dagger &= -u_{\boldsymbol{q}} \boldsymbol{\alpha}_{\boldsymbol{q}}^\dagger + v_{\boldsymbol{q}} \boldsymbol{\beta}_{\boldsymbol{q}} \\ \mathbf{a}_{\boldsymbol{q}} &= -u_{\boldsymbol{q}} \boldsymbol{\alpha}_{\boldsymbol{q}} + v_{\boldsymbol{q}} \boldsymbol{\beta}_{\boldsymbol{q}}^\dagger \\ \mathbf{b}_{\boldsymbol{q}}^\dagger &= v_{\boldsymbol{q}} \boldsymbol{\alpha}_{\boldsymbol{q}} - u_{\boldsymbol{q}} \boldsymbol{\beta}_{\boldsymbol{q}}^\dagger \\ \mathbf{b}_{\boldsymbol{q}} &= v_{\boldsymbol{q}} \boldsymbol{\alpha}_{\boldsymbol{q}}^\dagger - u_{\boldsymbol{q}} \boldsymbol{\beta}_{\boldsymbol{q}} \end{aligned} \tag{113}$$

The coefficients $u_{\boldsymbol{q}}$ and $v_{\boldsymbol{q}}$ are real numbers. Along with the transformation (114), we demand that the new operators also describe bosonic modes, i.e. they must satisfy the Boson commutation relations $[\boldsymbol{\alpha}_{\boldsymbol{q}}, \boldsymbol{\alpha}_{\boldsymbol{q}}^\dagger] = 1$ and $[\boldsymbol{\beta}_{\boldsymbol{q}}, \boldsymbol{\beta}_{\boldsymbol{q}}^\dagger] = 1$. This implies $[\mathbf{a}_{\boldsymbol{q}}, \mathbf{a}_{\boldsymbol{q}}^\dagger] = u_{\boldsymbol{q}}^2 - v_{\boldsymbol{q}}^2 = 1$ which is trivially satisfied with the parameterization $u_{\boldsymbol{q}} = \cosh\theta_{\boldsymbol{q}}$ and $v_{\boldsymbol{q}} = \sinh\theta_{\boldsymbol{q}}$. Inserting the expressions (114) in the Hamiltonians $H_{\boldsymbol{q}}$ we arrive at

$$\begin{aligned} H_{\boldsymbol{q}} &= 2A_{\boldsymbol{q}} v_{\boldsymbol{q}}^2 + 2B_{\boldsymbol{q}} u_{\boldsymbol{q}} v_{\boldsymbol{q}} \\ &\quad + [A_{\boldsymbol{q}}(u_{\boldsymbol{q}}^2 + v_{\boldsymbol{q}}^2) - 2B_{\boldsymbol{q}} u_{\boldsymbol{q}} v_{\boldsymbol{q}}](\boldsymbol{\alpha}_{\boldsymbol{q}}^\dagger \boldsymbol{\alpha}_{\boldsymbol{q}} + \boldsymbol{\beta}_{\boldsymbol{q}}^\dagger \boldsymbol{\beta}_{\boldsymbol{q}}) \\ &\quad + [B_{\boldsymbol{q}}(u_{\boldsymbol{q}}^2 + v_{\boldsymbol{q}}^2) - 2A_{\boldsymbol{q}} u_{\boldsymbol{q}} v_{\boldsymbol{q}}](\boldsymbol{\alpha}_{\boldsymbol{q}} \boldsymbol{\beta}_{\boldsymbol{q}} + \boldsymbol{\alpha}_{\boldsymbol{q}}^\dagger \boldsymbol{\beta}_{\boldsymbol{q}}^\dagger) \end{aligned} \tag{114}$$

The first two terms are corrections to the classical ground state energy. The diagonalization condition $B_{\boldsymbol{q}}(u_{\boldsymbol{q}}^2 + v_{\boldsymbol{q}}^2) - 2A_{\boldsymbol{q}} u_{\boldsymbol{q}} v_{\boldsymbol{q}} = 0$ amounts to the demand $\tanh 2\theta_{\boldsymbol{q}} = B_{\boldsymbol{q}}/A_{\boldsymbol{q}}$. By rewriting $A_{\boldsymbol{q}} = C_{\boldsymbol{q}} \cosh 2\theta_{\boldsymbol{q}}$ and $B_{\boldsymbol{q}} = C_{\boldsymbol{q}} \sinh 2\theta_{\boldsymbol{q}}$ the coefficient $[A_{\boldsymbol{q}}(u_{\boldsymbol{q}}^2 + v_{\boldsymbol{q}}^2) - 2B_{\boldsymbol{q}} u_{\boldsymbol{q}} v_{\boldsymbol{q}}]$ equals $C_{\boldsymbol{q}} = ((A_{\boldsymbol{q}} + B_{\boldsymbol{q}})(A_{\boldsymbol{q}} - B_{\boldsymbol{q}}))^{1/2}$. This concludes the diagonalisation as we now have

$$H_{\boldsymbol{q}} = 2A_{\boldsymbol{q}} v_{\boldsymbol{q}}^2 + 2B_{\boldsymbol{q}} u_{\boldsymbol{q}} v_{\boldsymbol{q}} + \hbar\omega_{\boldsymbol{q}}(\boldsymbol{\alpha}_{\boldsymbol{q}}^\dagger \boldsymbol{\alpha}_{\boldsymbol{q}} + \boldsymbol{\beta}_{\boldsymbol{q}}^\dagger \boldsymbol{\beta}_{\boldsymbol{q}}) \tag{115}$$

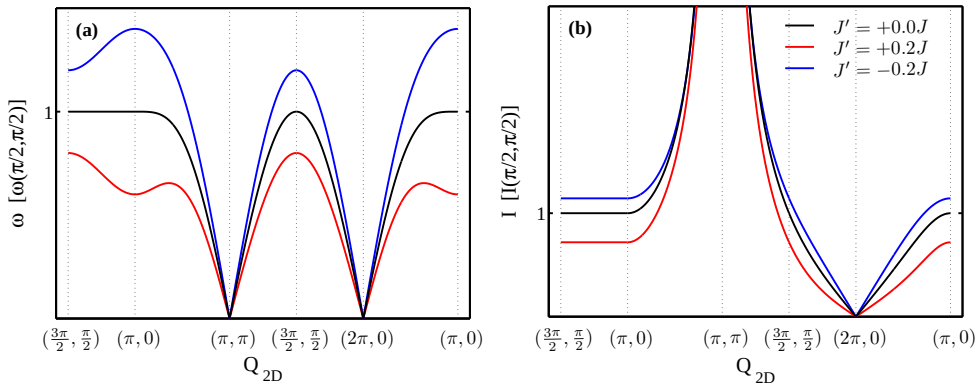

Figure 70: Linear spin wave theory dispersion and intensities calculated from the formulae (116) and (128). We use $J_c = 0$ throughout and plot the results for $J' = 0$ (solid black lines), $J' = +0.2J$ (solid red lines) and $J' = -0.2J$ (solid blue lines). The single-magnon dispersion and its intensity shown in panels (a) and (b) respectively are normalized by their values at $\mathbf{Q}_{2D} = (\pi/2, \pi/2)$ (or equivalently $\mathbf{Q}_{2D} = (3\pi/2, \pi/2)$) for the pure nearest neighbor Heisenberg model $J' = J_c = 0$. Note that an antiferromagnetic next-nearest-neighbor interaction J' leads to a local minimum in the spin wave dispersion at $\mathbf{Q}_{2D} = (\pi, 0)$. By contrast, with a ferromagnetic J' the dispersion has a local minimum at $\mathbf{Q}_{2D} = (\pi/2, \pi/2)$. In both these cases there is a dispersion along the magnetic zone boundary but in the former $\omega(\mathbf{Q}_{2D})$ goes through a local maximum along the path $(\pi, \pi) \rightarrow^{1} (\pi, 0)$. Turning to the intensities in panel (b), one first notes that antiferromagnetic next-nearest-neighbor interactions $J' > 0$ lead to a lowering of the single-magnon intensities at all wavevectors compared to the pure nearest-neighbor case $J' = 0$, whereas $J' < 0$ gives increased intensities. In neither of the cases $J' > 0$ or $J' < 0$ are the magnetic zone boundary dispersions seen in panel (a) accompanied by anomalies in the spin wave intensities between $(\pi/2, \pi/2)$ and $(\pi, 0)$. A non-zero out-of-plane coupling J_c leads to modulations of the spin wave energies and intensities along the $\mathbf{c}^*$-direction.

with the energy $\hbar\omega_{\boldsymbol{q}}$ given by

$$\hbar\omega_{\boldsymbol{q}} = \sqrt{(A_{\boldsymbol{q}} + B_{\boldsymbol{q}})(A_{\boldsymbol{q}} - B_{\boldsymbol{q}})} \tag{116}$$

This result agrees with an RPA treatment of the Hubbard model [244] apart from a factor 2 difference between the definitions of J_c. The latter can however be explained by the fact that what is considered in [244] is the double-layer cuprate $YBa_2Cu_3O_{6+y}$ where a given spin interacts only with one out-of-plane neighbour. Agreement is obtained if we divide our J_c by two. Further, (116) gives the correct dispersion for the Heisenberg model on a cubic lattice if $J_c = J$ and $J' = 0$.

The coefficients $u_{\boldsymbol{q}}$ and $v_{\boldsymbol{q}}$ can be conveniently expressed in terms of $A_{\boldsymbol{q}}$ and $\omega_{\boldsymbol{q}}$

$$u_{\boldsymbol{q}} = \sqrt{\frac{1}{2}\left(\frac{A_{\boldsymbol{q}}}{\hbar\omega_{\boldsymbol{q}}} + 1\right)} \qquad v_{\boldsymbol{q}} = \pm\sqrt{\frac{1}{2}\left(\frac{A_{\boldsymbol{q}}}{\hbar\omega_{\boldsymbol{q}}} - 1\right)} \tag{117}$$

The minus sign is chosen when $B_{\boldsymbol{q}}$ is negative. If $J' = 0$ and $J_c = 0$, Eq. (116) reduces to (95).

Let us examine the dispersion relation (116). Figure 70(a) displays $\hbar\omega_{\boldsymbol{q}}$ along the high symmetry directions of the first Brillouin zone in 2D, which was shown in Fig. 6). Energies are given in units of the spin wave energy at $(\pi/2, \pi/2)$ (or equivalently $(3\pi/2, \pi/2)$) for the pure Heisenberg model $J' = J_c = 0$ for which the equal energy contour for the highest single-magnon energy $E_{\max} = 4SJ = 2J$ follows the boundary of the magnetic Brillouin zone surrounding the antiferromagnetic wavevector $\mathbf{Q}_{2D} = (\pi, \pi)$ (dashed red line in Fig. 6). In particular, the energies at the high symmetry points $(\pi, 0)$ and $(\pi/2, \pi/2)$ are equal. This ceases to be the case when next-nearest neighbour interactions J' are included. If J' is antiferromagnetic, we saw previously that the classical ground state energy is increased, reflecting increased frustration and decreased stability of the Néel state. Correspondingly, the spin wave energies at $(\pi, 0)$ and $(\pi/2, \pi/2)$ are both decreased, but by unequal amounts, $\hbar\omega(\pi, 0) < \hbar\omega(\pi/2, \pi/2)$, i.e. a dispersion develops along the magnetic zone boundary. On the other hand, ferromagnetic exchange interactions J' lead to an increase in the spin wave energies at both points in reciprocal space, but with $\hbar\omega(\pi, 0) > \hbar\omega(\pi/2, \pi/2)$. An important qualitative differerence between the two cases is that for J' antiferromagnetic, $\hbar\omega_{\boldsymbol{q}}$ goes through a local maximum between (π, π) and $(\pi, 0)$. Stated differently, there is a local depression in the single-magnon dispersion surface at $(\pi, 0)$. According to (113), a non-zero J_c leads to a dispersion in the spin wave energies along the $\mathbf{c}^*$-direction. Owing to the smallness of this coupling in CFTD we shall not consider it any further.

A.3 Linear spin wave theory: Intensities

To calculate the spin wave intensities we recall from chapter 2 that neutron scattering intensities are proportional to the Fourier transform in time and space of two-point spin correlation functions

$$\left(\frac{d^2\sigma}{d\Omega\, dE'}\right)^{(\alpha\beta)} \propto \frac{1}{2\pi\hbar}\sum_{\boldsymbol{r}} e^{i\mathbf{Q}\cdot\boldsymbol{r}}\int dt\, e^{-i\omega t}\frac{1}{Z}\sum_n e^{-E_n/k_BT}\langle n\,|\,\mathbf{S}^\alpha_{\mathbf{0}}(0)\mathbf{S}^\beta_{\boldsymbol{r}}(t)\,|\,n\rangle \tag{118}$$

In our case, there are only three combinations (α,β) to be computed: $(\alpha,\beta)=(+,-)$, $(-,+)$ and (z,z). This follows because the z-component of the total spin operator $\mathbf{S}^z_{\rm tot}=\sum_{\boldsymbol{i}}\mathbf{S}^z_{\boldsymbol{i}}$ commutes with the Hamiltonian H. Therefore, eigenstates of H are also eigenstates of $\mathbf{S}^z_{\rm tot}$. Since the remaining combinations $(\alpha,\beta)=(+,+)$, $(+,z)$, $(z,+)$, $(-,-)$, $(-,z)$ and $(z,-)$ have in common that the combination of spin operators $\mathbf{S}^\alpha_{\mathbf{0}}(0)\mathbf{S}^\beta_{\boldsymbol{r}}(t)$ appearing on the right hand side of (118) change the eigenvalue of $\mathbf{S}^z_{\rm tot}$ the corresponding matrix elements must vanish identically.

Having already diagonalised H in terms of independent bosonic modes, the calculations involved in finding out the intensities are straightforward. The $(+,-)$ and $(-,+)$ components yield the single-magnon intensities. The (z,z) component gives the intensity of the magnetic Bragg reflection associated with the time-independent, ordered part of $\mathbf{S}^z$ as well as the intensity of scattering from three different types of two-magnon processes: Two-magnon creation, two-magnon annihilation and mixed magnon creation annihilation processes. At the lowest temperatures, Bose occupation factors show that we need only consider the contribution from two-magnon creation [245].

We now proceed to give the calculation of $\langle n\,|\,\mathbf{S}^+_{\mathbf{0}}(0)\mathbf{S}^-_{\boldsymbol{r}}(t)\,|\,n\rangle$. We take the site $\boldsymbol{r}=\mathbf{0}$ to reside on sublattice A. For sites $\boldsymbol{r}$ that are also on sublattice A, we use Eqs. (106), (109) and (114) to successively rewrite $\langle n\,|\,\mathbf{S}^+_{\mathbf{0}}(0)\mathbf{S}^-_{\boldsymbol{r}}(t)\,|\,n\rangle$

$$\begin{aligned}
\langle n\,|\,\mathbf{S}^+_{\mathbf{0}}(0)\mathbf{S}^-_{\boldsymbol{r}}(t)\,|\,n\rangle_{\boldsymbol{r}\in\mathrm{A}} &= 2S\,\langle n\,|\,\mathbf{a}_{\mathbf{0}}(0)\mathbf{a}^\dagger_{\boldsymbol{r}}(t)\,|\,n\rangle \\
&= \frac{4S}{N}\sum_{\boldsymbol{q}\boldsymbol{q}'} e^{-i\boldsymbol{q}'\cdot\boldsymbol{r}}\langle n\,|\,\mathbf{a}_{\boldsymbol{q}}e^{iHt/\hbar}\mathbf{a}^\dagger_{\boldsymbol{q}'}e^{-iHt/\hbar}\,|\,n\rangle \\
&= \frac{4S}{N}\sum_{\boldsymbol{q}\boldsymbol{q}'} e^{-i\boldsymbol{q}'\cdot\boldsymbol{r}} \\
&\quad\times\langle n\,|\,(-u_{\boldsymbol{q}}\boldsymbol{\alpha}_{\boldsymbol{q}}+v_{\boldsymbol{q}}\boldsymbol{\beta}^\dagger_{\boldsymbol{q}})e^{iHt/\hbar}(-u_{\boldsymbol{q}'}\boldsymbol{\alpha}^\dagger_{\boldsymbol{q}'}+v_{\boldsymbol{q}'}\boldsymbol{\beta}_{\boldsymbol{q}'})e^{-iHt/\hbar}\,|\,n\rangle \\
&= \frac{4S}{N}\sum_{\boldsymbol{q}\boldsymbol{q}'} e^{-i\boldsymbol{q}'\cdot\boldsymbol{r}}\Big[\langle n\,|\,u_{\boldsymbol{q}}u_{\boldsymbol{q}'}\boldsymbol{\alpha}_{\boldsymbol{q}}e^{iHt/\hbar}\boldsymbol{\alpha}^\dagger_{\boldsymbol{q}'}e^{-iHt/\hbar}\,|\,n\rangle \\
&\quad+\langle n\,|\,v_{\boldsymbol{q}}v_{\boldsymbol{q}'}\boldsymbol{\beta}^\dagger_{\boldsymbol{q}}e^{iHt/\hbar}\boldsymbol{\beta}_{\boldsymbol{q}'}e^{-iHt/\hbar}\,|\,n\rangle\Big]
\end{aligned} \tag{119}$$

The eigenstates $|\,n\rangle$ are defined by the set of $2\times N/2$ expectation values $n^\alpha_{\boldsymbol{q}_n}$ and $n^\beta_{\boldsymbol{q}_m}$ for the number operators $\hat{n}^\alpha_{\boldsymbol{q}_n}=\alpha^\dagger_{\boldsymbol{q}_n}\alpha_{\boldsymbol{q}_n}$ and $\hat{n}^\beta_{\boldsymbol{q}_m}=\beta^\dagger_{\boldsymbol{q}_m}\beta_{\boldsymbol{q}_m}$, i.e. $|n\rangle = |n^\alpha_{\boldsymbol{q}_1}n^\alpha_{\boldsymbol{q}_2}\ldots n^\alpha_{\boldsymbol{q}_{N/2}}n^\beta_{\boldsymbol{q}_1}n^\beta_{\boldsymbol{q}_2}\ldots n^\beta_{\boldsymbol{q}_{N/2}}\rangle$. Making use of the well known properties of ladder operators

$$\begin{aligned}
\boldsymbol{\alpha}_{\boldsymbol{q}_n}\,|\ldots n^\alpha_{\boldsymbol{q}_{n-1}}n^\alpha_{\boldsymbol{q}_n}n^\alpha_{\boldsymbol{q}_{n+1}}\ldots\rangle &= \sqrt{n^\alpha_{\boldsymbol{q}_n}}\,|\ldots n^\alpha_{\boldsymbol{q}_{n-1}}n^\alpha_{\boldsymbol{q}_n}-1\;n^\alpha_{\boldsymbol{q}_{n+1}}\ldots\rangle \\
\boldsymbol{\alpha}^\dagger_{\boldsymbol{q}_n}\,|\ldots n^\alpha_{\boldsymbol{q}_{n-1}}n^\alpha_{\boldsymbol{q}_n}n^\alpha_{\boldsymbol{q}_{n+1}}\ldots\rangle &= \sqrt{n^\alpha_{\boldsymbol{q}_n}+1}\,|\ldots n^\alpha_{\boldsymbol{q}_{n-1}}n^\alpha_{\boldsymbol{q}_n}+1\;n^\alpha_{\boldsymbol{q}_{n+1}}\ldots\rangle
\end{aligned} \tag{120}$$

we obtain

$$\langle n\,|\,\mathbf{S}^+_{\mathbf{0}}(0)\mathbf{S}^-_{\boldsymbol{r}}(t)\,|\,n\rangle_{\boldsymbol{r}\in\mathrm{A}} = \frac{4S}{N}\sum_{\boldsymbol{q}} e^{-i\boldsymbol{q}\cdot\boldsymbol{r}}\left[u^2_{\boldsymbol{q}}(n^\alpha_{\boldsymbol{q}}+1)e^{i\omega_{\boldsymbol{q}}t}+v^2_{\boldsymbol{q}}n^\beta_{\boldsymbol{q}}e^{-i\omega_{\boldsymbol{q}}t}\right] \tag{121}$$

For a site $\boldsymbol{r}$ on the B sublattice a similar calculation yields

$$\langle n\,|\,\mathbf{S}^+_{\mathbf{0}}(0)\mathbf{S}^-_{\boldsymbol{r}}(t)\,|\,n\rangle_{\boldsymbol{r}\in\mathrm{B}} = -\frac{4S}{N}\sum_{\boldsymbol{q}} e^{-i\boldsymbol{q}\cdot\boldsymbol{r}}u_{\boldsymbol{q}}v_{\boldsymbol{q}}\left[(n^\alpha_{\boldsymbol{q}}+1)e^{i\omega_{\boldsymbol{q}}t}+n^\beta_{\boldsymbol{q}}e^{-i\omega_{\boldsymbol{q}}t}\right] \tag{122}$$

For the $(-+)$ component the equivalent results are

$$\langle n\,|\,\mathbf{S}^-_{\mathbf{0}}(0)\mathbf{S}^+_{\boldsymbol{r}}(t)\,|\,n\rangle_{\boldsymbol{r}\in\mathrm{A}} = \frac{4S}{N}\sum_{\boldsymbol{q}} e^{i\boldsymbol{q}\cdot\boldsymbol{r}}\left[u^2_{\boldsymbol{q}}n^\alpha_{\boldsymbol{q}}e^{-i\omega_{\boldsymbol{q}}t}+v^2_{\boldsymbol{q}}(n^\beta_{\boldsymbol{q}}+1)e^{i\omega_{\boldsymbol{q}}t}\right] \tag{123}$$

$$\langle n\,|\,\mathbf{S}^-_{\mathbf{0}}(0)\mathbf{S}^+_{\boldsymbol{r}}(t)\,|\,n\rangle_{\boldsymbol{r}\in\mathrm{B}} = -\frac{4S}{N}\sum_{\boldsymbol{q}} e^{i\boldsymbol{q}\cdot\boldsymbol{r}}u_{\boldsymbol{q}}v_{\boldsymbol{q}}\left[n^\alpha_{\boldsymbol{q}}e^{-i\omega_{\boldsymbol{q}}t}+(n^\beta_{\boldsymbol{q}}+1)e^{i\omega_{\boldsymbol{q}}t}\right] \tag{124}$$

The next step is to insert these four expressions in Eq. (118). The sums and integrals are elementary. Thermal averages of the occupation numbers $n^{\alpha}_{\boldsymbol{q}}$ and $n^{\alpha}_{\boldsymbol{q}}$ lead to Bose occupation factors $n^{\alpha/\beta}(\omega_{\boldsymbol{q}}) = (e^{\hbar\omega^{\alpha/\beta}_{\boldsymbol{q}}/k_BT} - 1)^{-1}$. In what is hopefully obvious notation these manipulations lead us to

$$\left(\frac{d^2\sigma}{d\Omega\, dE'}\right)^{(+-)} \propto 2S\Big[(u^2_{\mathbf{Q}} - u_{\mathbf{Q}}v_{\mathbf{Q}})(n^{\alpha}(\omega_{\mathbf{Q}}) + 1)\delta(\hbar\omega - \hbar\omega_{\mathbf{Q}}) + (v^2_{\mathbf{Q}} - u_{\mathbf{Q}}v_{\mathbf{Q}})n^{\beta}(\omega_{\mathbf{Q}})\delta(\hbar\omega + \hbar\omega_{\mathbf{Q}})\Big] \tag{125}$$

$$\left(\frac{d^2\sigma}{d\Omega\, dE'}\right)^{(-+)} \propto 2S\Big[(u^2_{-\mathbf{Q}} - u_{-\mathbf{Q}}v_{-\mathbf{Q}})n^{\alpha}(\omega_{-\mathbf{Q}})\delta(\hbar\omega + \hbar\omega_{-\mathbf{Q}}) + (v^2_{-\mathbf{Q}} - u_{-\mathbf{Q}}v_{-\mathbf{Q}})(n^{\beta}(\omega_{-\mathbf{Q}}) + 1)\delta(\hbar\omega - \hbar\omega_{-\mathbf{Q}})\Big] \tag{126}$$

where the neutron wavevector transfer $\mathbf{Q}$ has been reintroduced. Finally, taking into account the symmetries in the problem $\omega_{\mathbf{Q}} = \omega_{-\mathbf{Q}}$, $u_{\mathbf{Q}} = u_{-\mathbf{Q}}$, $v_{\mathbf{Q}} = v_{-\mathbf{Q}}$ and writing $n(\omega_{\mathbf{Q}}) = n^{\alpha}(\omega_{\mathbf{Q}}) = n^{\beta}(\omega_{\mathbf{Q}})$ we are able to calculate the $(\alpha, \beta) = (x, x)$ and (y, y) components of the cross-section. The identity $(d^2\sigma/d\Omega\, dE')^{(xx)} + (d^2\sigma/d\Omega\, dE')^{(yy)} = 1/2[(d^2\sigma/d\Omega\, dE')^{(+-)} + (d^2\sigma/d\Omega\, dE')^{(-+)}]$ is easily verified. Using that $(d^2\sigma/d\Omega\, dE')^{(xx)} = (d^2\sigma/d\Omega\, dE')^{(yy)}$ by symmetry, the end result becomes

$$\left(\frac{d^2\sigma}{d\Omega\, dE'}\right)^{(xx)} \propto \frac{S}{2}\,(u_{\mathbf{Q}} - v_{\mathbf{Q}})^2\Big[(n(\omega_{\mathbf{Q}}) + 1)\delta(\hbar\omega - \hbar\omega_{\mathbf{Q}}) + n(\omega_{\mathbf{Q}})\delta(\hbar\omega + \hbar\omega_{\mathbf{Q}})\Big] \tag{127}$$

It is an evaluation of this expression which leads to the sign convention for $v_{\boldsymbol{q}}$ in Eq. (117). The occupation factor $n(\omega_{\mathbf{Q}})$ is zero at $T = 0$ K showing that only the one-magnon creation term proportional to $(n(\omega_{\mathbf{Q}}) + 1)\delta(\hbar\omega - \hbar\omega_{\mathbf{Q}})$ matters at the lowest temperatures.

One would expect the total $\mathbf{Q}$ and $\hbar\omega$-integrated single-magnon spectral weight to be proportional to the expectation value $\langle \mathbf{S}^{x\,2}_{\boldsymbol{i}} + \mathbf{S}^{y\,2}_{\boldsymbol{i}}\rangle$ [246]. This quantity can be readily computed, and the $T = 0$ K result $S(1 + 2\Delta S^z)$ is seen to contain one term of order ΔS^z. It turns out that if one were to include the first order correction term in the Holstein Primakoff expansion (105) one would find (in addition to the energy scale renormalization by the numerical factor $Z^{\mathrm{O}} = (1 + c) = 1.1579$ which was discussed in section A.1) that the prefactor $S/2$ in (127) is replaced by $(S - \Delta S^z)/2$ [247]. To obtain this result all terms quartic in the bosonic ladder operators are decoupled in an RPA fashion, e.g. $\mathbf{a}^{\dagger}_{\boldsymbol{q}}\mathbf{a}_{\boldsymbol{q}'}\mathbf{b}^{\dagger}_{\boldsymbol{p}}\mathbf{b}_{\boldsymbol{p}'} = \langle \mathbf{a}^{\dagger}_{\boldsymbol{q}}\mathbf{a}_{\boldsymbol{q}'}\rangle\mathbf{b}^{\dagger}_{\boldsymbol{p}}\mathbf{b}_{\boldsymbol{p}'} + \langle \mathbf{a}^{\dagger}_{\boldsymbol{q}}\mathbf{b}^{\dagger}_{\boldsymbol{p}}\rangle\mathbf{a}_{\boldsymbol{q}'}\mathbf{b}_{\boldsymbol{p}'} + \langle \mathbf{a}^{\dagger}_{\boldsymbol{q}}\mathbf{b}_{\boldsymbol{p}'}\rangle\mathbf{b}^{\dagger}_{\boldsymbol{p}}\mathbf{a}_{\boldsymbol{q}'} + \mathbf{a}^{\dagger}_{\boldsymbol{q}}\mathbf{a}_{\boldsymbol{q}'}\langle \mathbf{b}^{\dagger}_{\boldsymbol{p}}\mathbf{b}_{\boldsymbol{p}'}\rangle + \ldots$ As a direct consequence of the replacement of $S/2$ by $(S - \Delta S^z)/2$ the value of $\langle \mathbf{S}^{x\,2}_{\boldsymbol{i}} + \mathbf{S}^{y\,2}_{\boldsymbol{i}}\rangle$ is changed to $(S - \Delta S^z)(1 + 2\Delta S^z)$. Because this expression contains an additional term of order ΔS^z, what is here revealed is that in order to obtain a theory which is consistent to order ΔS^z we are in fact forced to keep the first order terms in the Holstein Primakoff expansion when computing the transverse spectral weight. Thus, to order ΔS^z the correct result for the intensities of single-magnon excitations is

$$\left(\frac{d^2\sigma}{d\Omega\, dE'}\right)^{(xx)} \propto \frac{S - \Delta S^z}{2}\,(u_{\mathbf{Q}} - v_{\mathbf{Q}})^2\Big[(n(\omega_{\mathbf{Q}}) + 1)\delta(\hbar\omega - \hbar\omega_{\mathbf{Q}}) + n(\omega_{\mathbf{Q}})\delta(\hbar\omega + \hbar\omega_{\mathbf{Q}})\Big] \tag{128}$$

For the pure nearest neighbor Heisenberg model $J' = J_c = 0$, Eq. (128) reduces to

$$\left(\frac{d^2\sigma}{d\Omega\, dE'}\right)^{(xx)} \propto \frac{S - \Delta S^z}{2}\sqrt{\frac{1 - \gamma_{\mathbf{Q}}}{1 + \gamma_{\mathbf{Q}}}}\,\Big[(n(\omega_{\mathbf{Q}}) + 1)\delta(\hbar\omega - \hbar\omega_{\mathbf{Q}}) + n(\omega_{\mathbf{Q}})\delta(\hbar\omega + \hbar\omega_{\mathbf{Q}})\Big] \tag{129}$$

This is a well-known result of linear spin wave theory according to which the single-magnon intensity diverges as the inverse $\mathbf{Q}_{\mathrm{2D}}$-space distance from (π, π) positions and goes to zero linearly as a function of the $\mathbf{Q}_{\mathrm{2D}}$-space distance from $(2\pi, 2\pi)$ positions.

In Fig. 70(b) we use solid lines to plot the single-magnon intensities in the three cases $J' = 0$, $J' = +0.2J$ and $J' = -0.2J$ for $T = 0$ K. The interplane coupling J_c has been set to zero and the intensities are normalized to their value at $\mathbf{Q}_{\mathrm{2D}} = (\pi/2, \pi/2)$ for the nearest neighbor model (129). The most important finding is that finite next-nearest neighbour interactions do not lead to variations in the single-magnon intensities along the magnetic zone boundary. Since equations (113) imply that $\hbar\omega_{\boldsymbol{q}} = A_{\boldsymbol{q}}$ along this path, this result follows directly from (117) and

(128). On the other hand we do find that finite next-nearest neighbor interactions are accompanied by changes in the numerical values of the intensities at all wavevectors, relative to the nearest-neighbor case $J' = 0$. If they are antiferromagnetic, $J' > 0$, the single-magnon intensities are decreased over the whole Brillouin zone while ferromagnetic interactions $J' < 0$ lead to increased intensities. Had we not included the first order term in the Holstein Primakoff expansion in our derivation of $(d^2\sigma/d\Omega\, dE')^{(xx)}$ we would have found − using Eq. (127) rather than (128) − no difference between the numerical values of the intensities of zone boundary magnons between the three cases. Further, (127) predicts single-magnon intensities which inside the magnetic Brillouin zone surrounding (π, π) are greater (smaller) for $J' > 0$ ($J' < 0$) than for $J' = 0$ in constrast with the prediction of the correct expression (128). Since the total integrated single-magnon intensity is dominated by the divergence at (π, π) we would therefore be led to the false conclusion that antiferromagnetic (ferromagnetic) next-nearest-neighbor interactions increase (decrease) the total single-magnon scattering relative to the case $J' = 0$. What saves us is of course the fact that ΔS^z is larger (smaller) for $J' > 0$ ($J' < 0$) than for $J' = 0$ and therefore the decrease (increase) in the prefactor $S - \Delta S^z$ outweighs the increase (decrease) in the integral of the $\mathbf{Q}$-dependent factor $(u_{\mathbf{Q}} - v_{\mathbf{Q}})^2$. A final comment relating to Eq. (128) is that the inclusion of a finite out-of-plane interaction J_c gives rise to modulations in the intensities along the $\mathbf{c}^*$ direction only.

Having computed the single-magnon intensities, we move on to the longitudinal component $(d^2\sigma/d\Omega\, dE')^{(zz)}$. For $\boldsymbol{r} \in$ A and $\boldsymbol{r} \in$ B respectively we find

$$\begin{aligned}
\langle n|\mathbf{S}^z_{\mathbf{0}}(0)\mathbf{S}^z_{\boldsymbol{r}}(t)|n\rangle_{\boldsymbol{r}\in\mathrm{A}} &= \langle n|(S-\mathbf{a}^\dagger_{\mathbf{0}}\mathbf{a}_{\mathbf{0}})(S-e^{iHt/\hbar}\mathbf{a}^\dagger_{\boldsymbol{r}}\,\mathbf{a}_{\boldsymbol{r}}\,e^{-iHt/\hbar})|n\rangle \qquad (130)\\
&= S^2 - S\langle n|e^{iHt/\hbar}\,\mathbf{a}^\dagger_{\boldsymbol{r}}\mathbf{a}_{\boldsymbol{r}}\,e^{-iHt/\hbar}|n\rangle - S\langle n|\mathbf{a}^\dagger_{\mathbf{0}}\mathbf{a}_{\mathbf{0}}|n\rangle\\
&\quad +\langle n|\mathbf{a}^\dagger_{\mathbf{0}}\mathbf{a}_{\mathbf{0}}\,e^{iHt/\hbar}\,\mathbf{a}^\dagger_{\boldsymbol{r}}\mathbf{a}_{\boldsymbol{r}}\,e^{-iHt/\hbar}|n\rangle\\
\langle n|\mathbf{S}^z_{\mathbf{0}}(0)\mathbf{S}^z_{\boldsymbol{r}}(t)|n\rangle_{\boldsymbol{r}\in\mathrm{B}} &= \langle n|(S-\mathbf{a}^\dagger_{\mathbf{0}}\mathbf{a}_{\mathbf{0}})(-S+e^{iHt/\hbar}\mathbf{b}^\dagger_{\boldsymbol{r}}\,\mathbf{b}_{\boldsymbol{r}}\,e^{-iHt/\hbar})|n\rangle \qquad (131)\\
&= -S^2 + S\langle n|e^{iHt/\hbar}\,\mathbf{b}^\dagger_{\boldsymbol{r}}\mathbf{b}_{\boldsymbol{r}}\,e^{-iHt/\hbar}|n\rangle + S\langle n|\mathbf{a}^\dagger_{\mathbf{0}}\mathbf{a}_{\mathbf{0}}|n\rangle\\
&\quad -\langle n|\mathbf{a}^\dagger_{\mathbf{0}}\mathbf{a}_{\mathbf{0}}\,e^{iHt/\hbar}\,\mathbf{b}^\dagger_{\boldsymbol{r}}\mathbf{b}_{\boldsymbol{r}}\,e^{-iHt/\hbar}|n\rangle
\end{aligned}$$

The first three terms in each of the above expressions leads to elastic scattering. The last terms contain both elastic and inelastic contributions. Collecting all elastic contributions we find

$$\begin{aligned}
\left(\frac{d^2\sigma}{d\Omega\, dE'}\right)^{(zz)}_{\hbar\omega=0} \propto\ & \delta(\hbar\omega)\frac{(2\pi)^3}{v_m}\sum_{\boldsymbol{\tau}}\delta(\mathbf{Q}-(\boldsymbol{\tau}-\boldsymbol{\tau}_{\mathrm{AFM}})) \qquad (132)\\
&\times\Big[S^2 - 2S\frac{2}{N}\sum_{\boldsymbol{q}}\left(u^2_{\boldsymbol{q}}n(\omega_{\boldsymbol{q}}) + v^2_{\boldsymbol{q}}\left(n(\omega_{\boldsymbol{q}})+1\right)\right)\\
&+\Big(\frac{2}{N}\sum_{\boldsymbol{q}}\left(u^2_{\boldsymbol{q}}n(\omega_{\boldsymbol{q}}) + v^2_{\boldsymbol{q}}\left(n(\omega_{\boldsymbol{q}})+1\right)\right)\Big)^2\Big]
\end{aligned}$$

where v_m is the volume of the magnetic unit cell, equal to twice the volume v_0 of the structural unit cell. The sum over $\boldsymbol{\tau}$ extends over all structural Bragg reflections and $\boldsymbol{\tau}_{\mathrm{AFM}}$ is the wavevector of any magnetic Bragg reflection. Note that the quantity in the square bracket should equal $(S - \Delta S^z)^2 = S^2 - 2S\Delta S^z + \Delta S^{z\,2}$, so that the reduction in the ordered moment is given by $\Delta S^z = (2/N)\sum_{\boldsymbol{q}}\left(u^2_{\boldsymbol{q}}n(\omega_{\boldsymbol{q}}) + v^2_{\boldsymbol{q}}\left(n(\omega_{\boldsymbol{q}})+1\right)\right)$. The latter result can be confirmed by straightforward evaluation of any of the expectation values $\langle\mathbf{a}^\dagger_{\boldsymbol{r}}\mathbf{a}_{\boldsymbol{r}}\rangle$ or $\langle\mathbf{b}^\dagger_{\boldsymbol{r}}\mathbf{b}_{\boldsymbol{r}}\rangle$. For $T = 0$ K and in the limit $J' = J_c = 0$ it reduces to $\Delta S^z = c'/2$ with c' given by (94). Comparing with Eq. (93) we see that this is indeed the expected result. Upon increasing ΔS^z, the sublattice moment drops and reaches zero near $J'/J = 0.38$. Going to second order in the Holstein Primakoff expansion, Igarashi has shown that the Néel state is actually more stable against the quantum fluctuations caused by frustrating antiferromagnetic next-nearest neighbor interactions than suggested by linear spin wave theory [248].

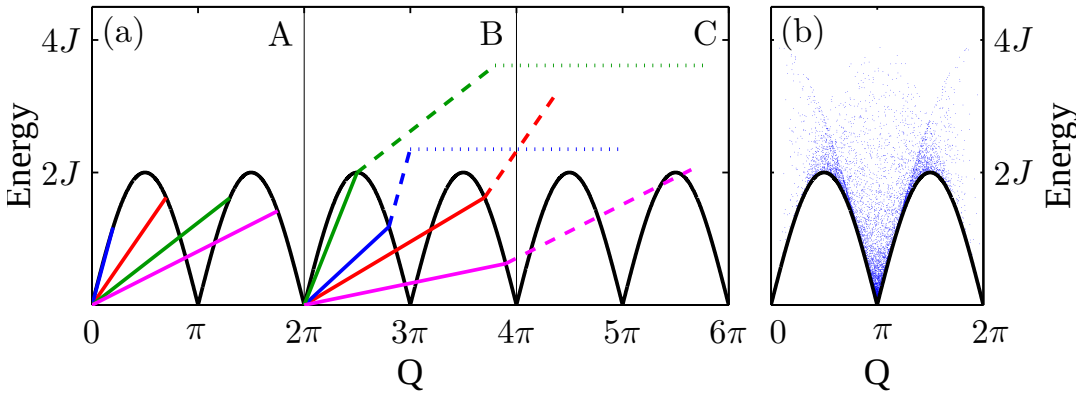

Figure 71: (a) Schematic illustration of how to calculate the two-magnon spectrum for processes where two magnons are created using the Monte Carlo routine described in the text. For simplicity, we consider the dispersion relation $\hbar\omega_{\boldsymbol{q}} = 2J\sqrt{1-\cos(Q)^2}$ of the 1D Heisenberg chain [21]. This dispersion is plotted as solid black lines in three Brillouin zones which we denote A, B and C. These are Brillouin zones of a three-dimensional crystal but we plot only the projection of the three-dimensional wavevectors along the chain axis. To generate two-magnon events we start by choosing two wavevectors $\mathbf{Q}_1$ and $\mathbf{Q}_2$ (one in zone A, one in zone B) at random and calculate the theoretical weight of the corresponding two-magnon process by using Eq. (135). The solid colored (red,blue,green and magenta) lines in zones A and B represent pairs of random (projected) $\mathbf{Q}$-vectors. With lattice constants set to unity, all three components of the sum $\mathbf{Q}_{\rm tot} = \mathbf{Q}_1 + \mathbf{Q}_2$ of the wavevectors of each pair $(\mathbf{Q}_1, \mathbf{Q}_2)$ can range anywhere between 0 to 4π, whereas the sum $\hbar\omega_1 + \hbar\omega_2$ of energies prescribed by the δ-function in (135) lies between 0 and $4J$ − twice the single-magnon energy at the magnetic zone boundary (which in 1D consists of the two points $Q = \pi/2$ and $Q = 3\pi/2$). The high-energy end-points of the colored dashed lines represent these sums. Having calculated $\mathbf{Q}_{\rm tot}$ and $\hbar\omega_{\rm tot} = \hbar\omega_1 + \hbar\omega_2$, the wavevector transfer is projected onto the Brillouin zone C when neccesary (blue and green dotted lines). The Monte Carlo procedure described in the text generates two-magnon events with a probability distribution corresponding to the theoretical expectation Eq. (135). (b) 10600 two-magnon events generated as described above. The two-magnon continuum resides above the single-magnon branch and extends to $4J$ as expected.

Collecting all inelastic contributions to the (zz) component of the cross section gives

$$\left(\frac{d^2\sigma}{d\Omega\, dE'}\right)^{(zz)}_{\hbar\omega\neq 0} = \left(\frac{d^2\sigma}{d\Omega\, dE'}\right)^{(zz)}_{\rm (aa)} + \left(\frac{d^2\sigma}{d\Omega\, dE'}\right)^{(zz)}_{\rm (cc)} + \left(\frac{d^2\sigma}{d\Omega\, dE'}\right)^{(zz)}_{\rm (ca)} \tag{133}$$

$$\left(\frac{d^2\sigma}{d\Omega\, dE'}\right)^{(zz)}_{\rm (aa)} \propto \frac{2}{N}\sum_{\boldsymbol{q}} \frac{1}{2}(u_{\boldsymbol{q}} v_{\boldsymbol{q}+\mathbf{Q}} - u_{\boldsymbol{q}+\mathbf{Q}} v_{\boldsymbol{q}})^2 \times n(\omega_{\boldsymbol{q}}) n(\omega_{\boldsymbol{q}+\mathbf{Q}})\, \delta(\hbar\omega + \hbar\omega_{\boldsymbol{q}} + \hbar\omega_{\boldsymbol{q}+\mathbf{Q}}) \tag{134}$$

$$\left(\frac{d^2\sigma}{d\Omega\, dE'}\right)^{(zz)}_{\rm (cc)} \propto \frac{2}{N}\sum_{\boldsymbol{q}} \frac{1}{2}(u_{\boldsymbol{q}} v_{\boldsymbol{q}+\mathbf{Q}} - u_{\boldsymbol{q}+\mathbf{Q}} v_{\boldsymbol{q}})^2 \times \left(n(\omega_{\boldsymbol{q}}) + 1\right)\left(n(\omega_{\boldsymbol{q}+\mathbf{Q}}) + 1\right)\, \delta(\hbar\omega - \hbar\omega_{\boldsymbol{q}} - \hbar\omega_{\boldsymbol{q}+\mathbf{Q}}) \tag{135}$$

$$\left(\frac{d^2\sigma}{d\Omega\, dE'}\right)^{(zz)}_{\rm (ca)} \propto \frac{2}{N}\sum_{\boldsymbol{q}} (u_{\boldsymbol{q}} u_{\boldsymbol{q}+\mathbf{Q}} - v_{\boldsymbol{q}} v_{\boldsymbol{q}+\mathbf{Q}})^2 \times n(\omega_{\boldsymbol{q}})\left(n(\omega_{\boldsymbol{q}+\mathbf{Q}}) + 1\right)\, \delta(\hbar\omega + \hbar\omega_{\boldsymbol{q}} - \hbar\omega_{\boldsymbol{q}+\mathbf{Q}}) \tag{136}$$

The first two terms, Eq. (134) and (135) are due to scattering processes in which two magnons are annihilated and created respectively, whereas Eq. (136) describes processes in which one magnon is created and another annihilated. Because these three types of processes involve two magnons their mathematical expressions contain two occupation factors. At low temperatures the only significant contribution comes from double-creation processes Eq. (135). The fact that a summation over $\mathbf{q}$ is involved for every neutron wavevector transfer $\mathbf{Q}$, tells us that Eqs. (134)-(136) describe continuum scattering, i.e. scattering that is spread out over $\mathbf{q}$ and $\hbar\omega$ rather than concentrated along a well defined dispersion as in the case of the one-magnon contribution. The expression obtained for the double-creation term agrees with that given by Tennant *et al.* [245] except for a trivial factor of two explained by the number of terms included in the summations over $\boldsymbol{q}$.

We shall now explain how one can use a simple Monte Carlo routine to compute the one- and two-magnon cross-sections for the pure 1D Heisenberg model with dispersion $\hbar\omega = 2J(1-\cos Q)^{1/2}$.

For simple demonstrational purposes we ignore that spin wave theory is known to fail in one dimension [21], and that the actual spin excitation spectrum is quantitatively different, see [249]. Following Tennant *et al.* [245] the two-magnon continuum is calculated in the following manner:

- Choose two random $\mathbf{Q}$ vectors $\mathbf{Q}_1$ and $\mathbf{Q}_2$ in the three dimensional Brillouin zone. For the problem at hand it is only the component of $\mathbf{Q}$ along the chain that is relevant. However, since spin chains exist within three-dimensional crystals it is advisable to use three-dimensional vectors.

- Calculate the weight of the process $(\mathbf{Q}_1, \mathbf{Q}_2)$ in question by using Eq. (133). Since at low temperatures, we need only take double-creation processes (135) into consideration, it suffices to evaluate $W^{\mathrm{cc}}_{\mathbf{Q}_1\mathbf{Q}_2} = (1/2)(u_{\mathbf{Q}_1}v_{\mathbf{Q}_2} - u_{\mathbf{Q}_2}v_{\mathbf{Q}_1})^2\,(n(\omega_{\mathbf{Q}_1})+1)\,(n(\omega_{\mathbf{Q}_2})+1)$.

- Compute the ratio $w^{\mathrm{cc}}_{\mathbf{Q}_1\mathbf{Q}_2}$ of $W^{\mathrm{cc}}_{\mathbf{Q}_1\mathbf{Q}_2}$ to the weight $W^{\mathrm{cc}}_{\mathrm{max}}$ of the most likely event, i.e. that which maximizes the weight function $W^{\mathrm{cc}}_{\mathbf{Q}_1\mathbf{Q}_2}$.

- Generate a random number r between 0 and 1, and compare it to $w^{\mathrm{cc}}_{\mathbf{Q}_1\mathbf{Q}_2}$. If $r < w^{\mathrm{cc}}_{\mathbf{Q}_1\mathbf{Q}_2}$, the the event $(\mathbf{Q}_1, \mathbf{Q}_2)$ is accepted. Otherwise it is discarded.

- For an accepted event $(\mathbf{Q}_1, \mathbf{Q}_2)$, calculate the total energy $\hbar\omega_{\mathrm{tot}} = \hbar\omega_{\mathbf{Q}_1} + \hbar\omega_{\mathbf{Q}_2}$ and wavevector $\mathbf{Q}_{\mathrm{tot}} = \mathbf{Q}_1 + \mathbf{Q}_2$. Inspection of Eq. (135) reveals that the energy limits of the longitudinal continuum are zero and twice the zone boundary energy, giving a total energy bandwidth of $4J$. Each component of the total wavevector lies between 0 and 4π (lattice constants are set to unity) and we must fold it back into the first Brillouin zone by subtraction of a reciprocal lattice wavevector $\mathbf{G}$ whenever necessary.

- Repeat this sequence until a large number of two-magnon events have been accepted.

A schematic illustration of this Monte Carlo routine is provided in Fig. 71. It is clear that for each Q, two-magnon states exist only at energies higher than the single-magnon dispersion relation $\hbar\omega = 2J(1-\cos Q)^{1/2}$. Moreover, we note that the two-magnon spectral weight is not uniformly distributed but has internal structure with local maxima slightly above the single-magnon energies, larger two-magnon cross-section near $Q = \pi$ than near $Q = 0$ and $Q = 2\pi$ as well as substantial spectral weight at the magnetic zone boundary points $Q = \pi/2$ and $Q = 3\pi/2$.

The one-magnon cross-section may be calculated in the same manner: First, a random wavevector $\mathbf{Q}$ is generated and its weight calculated using Eq. (128). This weight is then divided by that of the most likely one-magnon event, the resulting ratio $w^{\mathrm{c}}_{\mathbf{Q}}$ compared to a random number r and so on. Extending the procedure outlined above to two spatial dimensions is straightforward and this approach was used to calculate both the transverse and longitudinal cross-sections for use in fitting the polarized CFTD data presented in chapter 5. Figure 26 in that chapter is the analogue of Fig. 71(b) for the 2D case and is qualitatively similar.

An important technical comment regards the handling of divergencies in the weights of the most likely one- or two-magnon events. For the expressions (128) and (135) respectively and in two dimensions these occur when $\mathbf{Q}_{\mathrm{2D}} = (\pi, \pi)$ and e.g. when $(\mathbf{Q}_{\mathrm{2D},1}, \mathbf{Q}_{\mathrm{2D},2}) = ((0,0),(\pi,\pi))$ If $w^{\mathrm{c}}_{\mathrm{max}}$ or $w^{\mathrm{cc}}_{\mathrm{max}}$ were allowed to be infinite, no events would ever be accepted. To handle this difficulty, it is necessary to introduce artificial cutoffs to make the maximum weights finite. There is a certain freedom of choice involved in how to implement this constraint, but of course any method chosen should not be allowed to introduce grossly unphysical features in the Monte Carlo clouds. In the end, what is important from the point of view of data analysis is that the cutoff must not be allowed to give results which are qualitatively or − to any significant degree − qualitatively different at the energies and wavevectors of interest from those one could have obtained from analytic treatments of (128) and (135). For the neutron clouds used in analyzing the data presented in chapter 5 the cutoffs were implemented simply by multiplying $A_{\boldsymbol{q}} = 4JS$ by a number less than one part in a thousand larger than unity. This trick makes the maximum weights finite but also yields a small gap at (π, π) in the single-magnon spectrum and a related small small energy gap at all wavevectors between the single-magnon dispersion branch and the onset of two-magnon scattering (see Fig. 26). Otherwise everything is left unchanged and the fits performed using these Monte Carlo event clouds do not suffer.

The calculations in this appendix have illustated by way of example that in the linear spin wave approximation, processes involving an even number of magnons contribute to $S^{zz}(\mathbf{Q},\omega)$ whereas

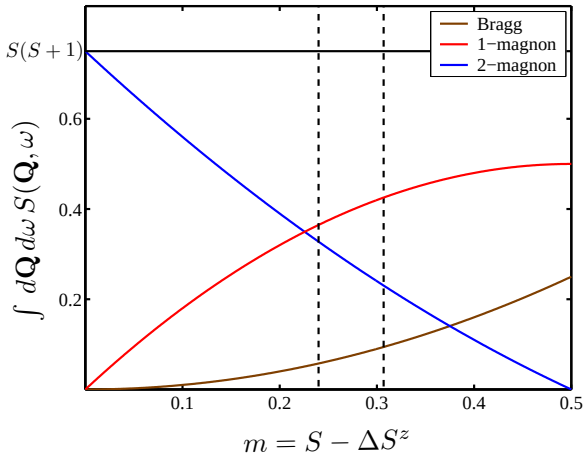

Figure 72: Integrated intensities in linear spin wave theory for the pure Heisenberg model as a function of the magnitude of the ordered moment m. The Bragg contribution is localized in both $\mathbf{Q}$ and ω and integrates to $(S-\Delta S^z)^2$. The single-magnon contribution is spread out on the dispersion surface Eq. (116) and integrates to $(S-\Delta S^z)(2\Delta S^z+1)$. The two-magnon contribution is spread out over a continuous range in both momentum and energy and integrates to $\Delta S^z(\Delta S^z+1)$ [245]. The sum of the three contributions always equals $S(S+1) = 3/4$. As discussed in the text, the validity of these results must break down in the limit $m \to 0$. The two dashed vertical lines indicate respectively the theoretical prediction $m = 0.3069$ for a 2DQHAFSL [26] and the experimental value $m = 0.24 \pm 0.01$ (assuming $g = 2$) reported for CFTD [80].

processes involving an odd number of magnons are involved in $S^{+-}(\mathbf{Q},\omega)$ and $S^{-+}(\mathbf{Q},\omega)$. Tennant *et al.* [245] note that multimagnon processes involving three or more magnons redistribute some of the transverse intensity into further continua at energies higher than twice the zone boundary energy. For the nearest-neighbour Heisenberg model, they give the $\mathbf{Q}$ and $\hbar\omega$-integrals of $S^{\alpha\beta}(\mathbf{Q},\omega)$ for zero-magnon (Bragg) scattering, one-magnon scattering and two-magnon scattering at $T = 0$ K, all in terms of the the reduction ΔS from $S = 1/2$

$$\begin{aligned} I_0 &= (S-\Delta S)^2 \\ I_1 &= (S-\Delta S)(2\Delta S+1) \\ I_2 &= \Delta S(\Delta S+1) \end{aligned} \tag{137}$$

Note that the sum total of these contributions equals $S(S+1)$ as it should. We have already derived the result for I_1 as the $T = 0$ K expectation value of $\langle \mathbf{S}_i^{x\,2} + \mathbf{S}_i^{y\,2}\rangle$. Analogous calculations of the expectation values of $\langle \mathbf{S}_i^z\rangle^2$ and $\langle \mathbf{S}_i^{z\,2}\rangle$ lead to the simple results $\langle \mathbf{S}_i^z\rangle^2 = (S-\Delta S^z)^2$ and $\langle \mathbf{S}_i^{z\,2}\rangle = (S-\Delta S^z)^2 + \Delta S^z(1+\Delta S^z)$ which in turn implies $\langle \mathbf{S}_i^{z\,2}\rangle - \langle \mathbf{S}_i^z\rangle^2 = \Delta S^z(1+\Delta S^z)$. Thus we see that the integrated Bragg, one-magnon and two-magnon intensities I_0, I_1 and I_2 are given by the expectation values of $\langle \mathbf{S}_i^z\rangle^2$, $\langle \mathbf{S}_i^{x\,2} + \mathbf{S}_i^{y\,2}\rangle$ and $\langle \mathbf{S}_i^{z\,2}\rangle - \langle \mathbf{S}_i^z\rangle^2$ respectively. This serves to emphasize yet again the necessity of including the first-order term in the Holstein Primakoff expansion (105) when computing the single-magnon intensities. Without this term we would have found $I_1 = S(2\Delta S+1)$ and $\langle \mathbf{S}_i^{x\,2} + \mathbf{S}_i^{y\,2} + \mathbf{S}_i^{z\,2}\rangle = I_0 + I_1 + I_2 = S(S+1) + \Delta S^z(2\Delta S^z+1)$, which would have revealed an inconsistency in the approach. The correction to I_1 introduced by the first order term in (105) is exactly large enough to ensure that we get the correct result for the sublattice moment length $\langle \mathbf{S}_i^{x\,2} + \mathbf{S}_i^{y\,2} + \mathbf{S}_i^{z\,2}\rangle = S(S+1)$.

In Fig. 72 we plot the three expressions (138) as a function of the reduction ΔS in the ordered sublattice moment in the ground state. If there were no quantum fluctuations the sublattice moment per spin would be at the saturation value $m = 1/2$. In this case the total spectral weight is divided between Bragg scattering and single-magnon scattering in the proportion $S^2 : S$ and there is no two-magnon scattering. In other words, the existence of two-magnon scattering is intimately tied to a finite quantum reduction of the sublattice moment. As m is reduced from saturation, more and more spectral weight is shifted from the Bragg peak and single-magnon dispersion branch into the two-magnon continuum until at $m = 0$, the spectral weight of two-magnon excitations exhaust the total available $S(S+1)$. In this limit there is no long-range magnetic order and so the theory breaks down. Presumably the breakdown occurs already at finite values of m when the condition $\Delta S^z = \langle \mathbf{a}_i^\dagger \mathbf{a}_i\rangle \ll 2S = 1$ for the validity of the Holstein Primakoff expansion Eq. (105) becomes questionable.

B Flipping ratio R and effective polarization $P_{\rm eff}$ in polarized neutron scattering

In this appendix, we introduce and demonstrate in a simple way some of the concepts necessary for interpreting results from polarized triple axis experiments. After finishing this appendix, we have been made aware of a more general calculation [250] which contains the results reported here as a subset.

Imagine that there are $N_u(\mathbf{r})$ neutrons with $s^z = +1/2$ and $N_d(\mathbf{r})$ neutrons with $s^z = -1/2$ inside a small volume element around a particular spatial coordinate $\mathbf{r}$ on the idealized beam path from neutron source to detector. We can then define a spatially varying polarization vector $\mathbf{P}(\mathbf{r})$ of magnitude

$$P(\mathbf{r}) = \frac{N_u(\mathbf{r}) - N_d(\mathbf{r})}{N_u(\mathbf{r}) + N_d(\mathbf{r})} \tag{138}$$

and oriented along the z-direction. We can further represent the spin state of the beam at $\mathbf{r}$ by a vector

$$s_b(\mathbf{r}) = \begin{bmatrix} n_u(\mathbf{r}) \\ n_d(\mathbf{r}) \end{bmatrix} \tag{139}$$

where $n_u = N_u/(N_u + N_d)$ and $n_d = N_d/(N_u + N_d)$ are the fractional numbers of $s^z = +1/2$ and $s^z = -1/2$ neutrons. Clearly we have $n_u + n_d = 1$ and the polarization of the beam is $P = n_u - n_d$.

Let us think of some source of depolarization, i.e. some mechanism by which spin $s^z = +1/2$ neutrons are transformed to $s^z = -1/2$ neutrons and vice versa. Our goal is to find a matrix equation to represent the depolarization process. To do this we imagine that at point $\mathbf{r}_1$ the polarization state is $s_b(\mathbf{r}_1)$. At point $\mathbf{r}_2$ further downstream the beam path the polarization state has changed to $s_b(\mathbf{r}_2)$ as a result of all depolarization processes occuring between $\mathbf{r}_1$ and $\mathbf{r}_2$. The combined influence of the latter are represented by a 2-by-2 matrix $\Pi_{\mathbf{r}_1 \to \mathbf{r}_2}$. The elements of $\Pi_{\mathbf{r}_1 \to \mathbf{r}_2}$ must depend on some measure p for the degree of depolarization taking place between $\mathbf{r}_1$ and $\mathbf{r}_2$. We take $p = 1$ and $p = 0$ to correspond to no and full depolarization respectively. For symmetry reasons the diagonal elements of $\Pi_{\mathbf{r}_1 \to \mathbf{r}_2}$ must be identical and the same applies to the two off-diagonal elements. The further requirement that we have $n_u + n_d = 1$ at both $\mathbf{r}_1$ and $\mathbf{r}_2$ reduces the number of independent entries to one. Denoting this quantity $\pi(p)$ we have the matrix equation

$$s_b(\mathbf{r}_2) = \Pi_{\mathbf{r}_1 \to \mathbf{r}_2}(p) s_b(\mathbf{r}_1) \tag{140}$$

$$\begin{bmatrix} n_u(\mathbf{r}_2) \\ n_d(\mathbf{r}_2) \end{bmatrix} = \begin{bmatrix} \pi(p) & 1-\pi(p) \\ 1-\pi(p) & \pi(p) \end{bmatrix} \begin{bmatrix} n_u(\mathbf{r}_1) \\ n_d(\mathbf{r}_1) \end{bmatrix} \tag{141}$$

Next, we make the assumption that π depends linearly on p, i.e. $\pi(p) = \pi_1 + \pi_2 p$. We then imagine that it is possible to prepare a fully polarized initial beam e.g. $s_b(\mathbf{r}_1) = \begin{bmatrix} 1 \\ 0 \end{bmatrix}$ and deduce the numerical values of π_1 and π_2 by equating the left and right-hand sides in the extreme cases $p = 1$ (which must lead to $s_b(\mathbf{r}_2) = \begin{bmatrix} 1 \\ 0 \end{bmatrix}$) and $p = 0$ (which must lead to $s_b(\mathbf{r}_2) = \begin{bmatrix} 1/2 \\ 1/2 \end{bmatrix}$). We arrive at

$$\Pi_{\mathbf{r}_1 \to \mathbf{r}_2} = \frac{1}{2} \begin{bmatrix} (1+p) & (1-p) \\ (1-p) & (1+p) \end{bmatrix} \tag{142}$$

which is the desired result. Importantly, the product of two matrices of form (142) with $p = p_1$ and $p = p_2$ respectively, remains on the same form, but with $p = p_1 p_2$.

In terms of depolarization of the beam we can decompose a triple axis experiment into three steps

1. Depolarization of an initially perfectly polarized beam along its path to the sample position. We represent this by a number p_i and matrix Π_i.

2. Depolarization by the sample itself, represented by a depolarization factor $(1 - d)$ and a matrix $(1 - \Delta)$. $d = 0$ corresponds to no depolarization and $d = 1$ to full depolarization.

3. Depolarization of the beam leaving the sample along its path to the detector. We represent this by a number p_f and a matrix Π_f.

All three matrices are of the general form (142) with diagonal entries $(1+p_i)/2$, $(1+(1-d))/2$ and $(1+p_f)/2$ respectively.

The sample may of course also scatter neutrons. Such processes are represented by a matrix Σ for which spin-flip (SF) and non-spin-flip (NSF) processes give rise to finite off-diagonal and diagonal matrix elements $\sigma_{\rm SF}$ and $\sigma_{\rm NSF}$ respectively (For simplicity, we allow only two independent entries in Σ. The extension to the general case is trivial). If the off-diagonal elements of Σ are non-zero, the polarization state of the beam is transformed by the scattering process, otherwise it is unchanged. To exemplify, coherent nuclear scattering is non-spin-flip scattering and so per definition does not change the spin state of the neutron. It is represented by a matrix with off-diagonal elements equal to zero. By contrast, nuclear spin incoherent scattering is two-thirds spin-flip and one-third non-spin-flip. Modulo an overall multiplicative factor, the corresponding matrix has 1/3 in the diagonal and 2/3 in the off-diagonal elements. A perfectly spin-up-polarized ($n_u = 1$) incident beam will be transformed to a beam with $n_u = 1/3$ and $n_d = 2/3$, thus leading to $P = -1/3$. In the general case electronic magnetic scattering has both spin-flip and non-spin flip components but with the guide field at the sample position oriented along the scattering vector $\mathbf{Q}$ all magnetic scattering occurs in the spin-flip channel. In this special case the diagonal elements of the matrix describing electronic magnetic scattering from the sample would be zero.

In situations where either the diagonal or off-diagonal matrix elements are zero, we can measure the combination $p_i(1-d)p_f$ directly and show that it has the significance of an effective polarization of the given spectrometer setup. The polarization vector of the exit beam will generally be

$$s_b^{\rm final} = \mathcal{N}\left(\Pi_f\,(1-\Delta)\,\Sigma\,\Pi_i\,s_b^{\rm incident}\right) \tag{143}$$

The symbol $\mathcal{N}(\cdots)$ means that the vector argument must be normalized according to $n_u + n_d = 1$. This explicit normalization is necessary because unlike Eq. (142), the matrix Σ does not conserve the length of the beam polarization vector. Let us now assume $\sigma_{\rm SF} = 0$ and $\sigma_{\rm NSF} = 1$ and $s_b^{\rm incident} = \begin{bmatrix}1\\0\end{bmatrix}$. The normalization in Eq. (143) ensures that our result for the beam polarization does not depend on the chosen numerical value of $\sigma_{\rm NSF}$. To compute $s_b^{\rm final}$ we must evaluate the product $\Pi_f\,(1-\Delta)\,\Sigma\,\Pi_i\,s_b^{\rm incident}$. Since Σ is the unit matrix, this is simply a product of three matrices of the form (142) times $s_b^{\rm incident}$. Using the property of products of such matrices mentioned above one finds

$$\begin{aligned} s_b^{\rm final} &= \frac{1}{2}\mathcal{N}\left(\begin{bmatrix}(1+p_i(1-d)p_f)\\(1-p_i(1-d)p_f)\end{bmatrix}\right)\\ &= \frac{1}{2}\begin{bmatrix}(1+p_i(1-d)p_f)\\(1-p_i(1-d)p_f)\end{bmatrix} \end{aligned} \tag{144}$$

and a final polarization $P = p_i(1-d)p_f$. In the case of pure SF scattering ($\sigma_{\rm SF} = 1$ and $\sigma_{\rm NSF} = 0$) an analogous calculation gives a final polarization $P = -p_i(1-d)p_f$.

Experimentally, one requires a measure for the effective degree of polarization $P_{\rm eff}$ of a given spectrometer configuration. This is obtained by preparing an incident beam with $s_b^{\rm incident} = \begin{bmatrix}1\\0\end{bmatrix}$ and then taking the ratio of the NSF to SF count rates for scans across a region of $(\mathbf{Q},\omega)$-space where $\sigma_{\rm NSF} \neq 0$ and $\sigma_{\rm SF} = 0$. Since the SF count rate would be zero were it not for beam depolarization, this ratio is a natural measure and is known as the flipping ratio R. Its significance as a measure of $P_{\rm eff}$ and the explicit calculations above show that $P_{\rm eff} = p_i(1-d)p_f$, i.e.

$$R = \frac{n_u^{\rm final}}{n_d^{\rm final}} = \frac{(1+P_{\rm eff})}{(1-P_{\rm eff})} = \frac{1+p_i(1-d)p_f}{1-p_i(1-d)p_f} \tag{145}$$

In practice, a typical procedure for measuring R using non-spin-flip scattering processes would be to scan the wavevector transfer $\mathbf{Q}$ or the energy transfer $\hbar\omega$ across a coherent phonon dispersion branch with the guide field at the sample position along $\mathbf{Q}$. An alternative procedure would be to scan $\mathbf{Q}$ or $\hbar\omega$ across a region with finite spin-flip scattering and no non-spin-flip scattering, still with the guide field along $\mathbf{Q}$. In this case R would be defined as the ratio of spin-flip scattering to non-spin flip scattering and one would get the same result

$$R = \frac{n_d^{\rm final}}{n_u^{\rm final}} = \frac{(1-P_{\rm eff})}{(1+P_{\rm eff})} = \frac{1+p_i(1-d)p_f}{1-p_i(1-d)p_f} \tag{146}$$

It would also be possible to deduce $P_{\rm eff}$ from nuclear spin incoherent scattering (from e.g. vanadium) for which the expected final polarization would be $-p_i(1-d)p_f/3 = -P_{\rm eff}/3$.

References

[1] G. L. Squires, *Introduction to the theory of thermal neutron scattering* (Dover Publications, Inc., 1996).

[2] G. Shirane, S. M. Shapiro, and J. M. Tranquada, *Neutron scattering with a triple-axis spectrometer* (Cambridge University Press, 2002).

[3] L. V. Hove, *Correlations in space and time and Born approximation scattering in systems of interacting particles*, Phys. Rev. **95**, 249 (1954).

[4] L. V. Hove, *Time-dependent correlations between spins and neutron scattering in ferromagnetic crystals*, Phys. Rev. **95**, 1374 (1954).

[5] R. M. Moon, T. Riste, and W. C. Koehler, *Polarization analysis of thermal neutron scattering*, Phys. Rev. **181**, 920 (1969).

[6] P. M. Chaikin and T. C. Lubensky, *Principles of condensed matter physics* (Cambridge University Press, 1995).

[7] M. J. Cooper and R. Nathans, *The resolution function in neutron diffractometry I. The resolution function of a neutron diffractometer and its application to phonon measurements*, Acta Cryst. **23**, 357 (1967).

[8] N. J. Chesser and J. D. Axe, *Derivation and experimental verification of the normalized resolution function for inelastic neutron scattering*, Acta Cryst. A **29**, 160 (1973).

[9] M. Popovici, *On the resolution of slow-neutron spectrometers. IV: The triple-axis spectrometer resolution function, spatial effects included*, Acta Cryst. A **31**, 507 (1975).

[10] C. G. Windsor, *Pulsed neutron scattering* (Taylor & Francis Ltd., 1981).

[11] R. S. Eccleston, in *Neutron data booklet*, edited by A.-J. Dianoux and G. Lander (Institut Laue-Langevin, 2002), Chap. Time-of-flight inelastic neutron scattering.

[12] E. Merzbacher, *Quantum mechanics* (John Wiley & sons, 1970).

[13] P. W. Anderson, *Limits on the energy of the antiferromagnetic ground state*, Phys. Rev. **83**, 1260 (1951).

[14] E. Manousakis, *The spin-1/2 Heisenberg antiferromagnet on a square lattice and its application to the cuprous oxides*, Rev. Mod. Phys. **63**, 1 (1991).

[15] P. W. Anderson, *Resonating valence bonds: A new kind of insulator?*, Mat. Res. Bull. **8**, 153 (1973).

[16] P. W. Anderson, *The resonating valence bond state in La_2CuO_4 and superconductivity*, Science **235**, 1196 (1987).

[17] R. Coldea, D. A. Tennant, K. Habicht, P. Smeibidl, C. Wolters, and Z. Tylczynski, *Direct measurement of the spin Hamiltonian and observation of condensation of magnons in the 2D frustrated quantum magnet Cs_2CuCl_4*, Phys. Rev. Lett. **88**, 137203 (2002).

[18] S. Stringari, *Spin excitations and sum rules in the Heisenberg antiferromagnet*, Phys. Rev. B **49**, 6710 (1994).

[19] R. R. P. Singh and D. A. Huse, *Microscopic calculation of the spin-stiffness constant for the spin-1/2 square-lattice Heisenberg antiferromagnet*, Phys. Rev. B **40**, 7247 (1989).

[20] C. M. Canali and M. Wallin, *Spin-spin correlation functions for the square-lattice Heisenberg antiferromagnet at zero temperature*, Phys. Rev. B **48**, 3264 (1993).

[21] P. W. Anderson, *An approximate quantum theory of the antiferromagnetic ground state*, Phys. Rev. **86**, 694 (1952).

[22] K. Yosida, *Theory of magnetism* (Springer-Verlag Berlin Heidelberg, 1996).

[23] R. Kubo, *The spin-wave theory of antiferromagnetics*, Phys. Rev. **87**, 568 (1952).

[24] T. Holstein and H. Primakoff, *Field dependence of the intrinsic domain magnetization of a ferromagnet*, Phys. Rev. **58**, 1098 (1940).

[25] T. Oguchi, *Theory of spin-wave interactions in ferro- and antiferromagnetism*, Phys. Rev. **117**, 117 (1960).

[26] J. i. Igarashi, $1/S$ *expansion for the thermodynamic quantities in a two-dimensional Heisenberg antiferromagnet at zero temperature*, Phys. Rev. B **46**, 10763 (1992).

[27] C. M. Canali and S. M. Girvin, *Theory of Raman scattering in layered cuprate materials*, Phys. Rev. B **45**, 7127 (1992).

[28] C. M. Canali, S. M. Girvin, and M. Wallin, *Spin-wave velocity renormalization in the two-dimensional Heisenberg antiferromagnet at zero temperature*, Phys. Rev. B **45**, 10131 (1992).

[29] H. M. Rønnow, Ph.D. thesis, Risø National Laboratory, 2000.

[30] R. R. P. Singh, *Thermodynamic parameters of the T=0, spin-*$1/2$ *square-lattice Heisenberg antiferromagnet*, Phys. Rev. B **39**, 9760 (1989).

[31] J. D. Reger and A. P. Young, *Monte Carlo simulations of the spin-*$1/2$ *Heisenberg antiferromagnet on a square lattice*, Phys. Rev. B **37**, 5978 (1988).

[32] J. i. Igarashi, $1/S$ *expansion for dynamic structure factors in a two-dimensional Heisenberg antiferromagnet at zero temperature*, J. Phys.: Condens. Matter **4**, 10265 (1992).

[33] R. R. P. Singh, *Transverse-spin correlations and single-mode approximation for the square-lattice* $S = 1/2$ *Heisenberg model*, Phys. Rev. B **47**, 12337 (1993).

[34] R. R. P. Singh and M. P. Gelfand, *Spin-wave excitation spectra and spectral weights in square lattice antiferromagnets*, Phys. Rev. B **52**, 15695 (1995).

[35] C. Broholm and G. Aeppli, *Dynamic correlations in quantum magnets*, Preprint (2004).

[36] O. F. Syljuåsen and H. M. Rønnow, *Quantum renormalization of high-energy excitations in the 2D Heisenberg model*, J. Phys. Condens. Matter **12**, 405 (2000).

[37] A. W. Sandvik and R. R. P. Singh, *High-energy magnon dispersion and multimagnon continuum in the two-dimensional Heisenberg antiferromagnet*, Phys. Rev. Lett. **86**, 528 (2001).

[38] K. B. Lyons, P. E. Sulewski, P. A. Fleury, H. L. Carter, A. S. Cooper, G. P. Espinosa, Z. Fisk, and S.-W. Cheong, *High-energy spin and charge excitations in* La_2CuO_4, Phys. Rev. B **39**, 9693 (1989).

[39] S. Sugai, M. Sato, T. Kobayashi, J. Akimitsu, T. Ito, H. Takagi, S. Uchida, S. Hosoya, T. Kajitani, and T. Fukuda, *High-energy spin excitations in the insulating phases of high-*T_c *superconducting cuprates and* La_2NiO_4, Phys. Rev. B **42**, 1045 (1990).

[40] J. D. Perkins, J. M. Graybeal, M. A. Kastner, R. J. Birgeneau, J. P. Falck, and M. Greven, *Mid-infrared optical absorption in undoped lamellar copper oxides*, Phys. Rev. Lett. **71**, 1621 (1993).

[41] B. H. Bransden and J. C. Joachain, *Physics of atoms and molecules* (Longman Scientific & Technical, 1994).

[42] T. Timusk and B. Statt, *The pseudogap in high-temperature superconductors*, Rep. Prog. Phys **62**, 61 (1999).

[43] K. B. Lyons, P. A. Fleury, J. P. Remeika, A. S. Cooper, and T. J. Negran, *Dynamics of spin fluctuations in lanthanum cuprate*, Phys. Rev. B **37**, 2353 (1988).

[44] R. Coldea, S. M. Hayden, G. Aeppli, T. G. Perring, C. D. Frost, T. E. Mason, S.-W. Cheong, and Z. Fisk, *Spin waves and electronic interactions in* La_2CuO_4, Phys. Rev. Lett. **86**, 5377 (2001).

[45] M. Roger and J. M. Delrieu, *Cyclic four-spin exchange on a two-dimensional square lattice: Possible applications in high-T_c superconductors*, Phys. Rev. B **39**, 2299 (1989).

[46] J. Lorenzana and G. A. Sawatzky, *Phonon assisted multimagnon optical absorption and long lived two-magnon states in undoped lamellar copper oxides*, Phys. Rev. Lett. **74**, 1867 (1995).

[47] S. Chakravarty, B. I. Halperin, and D. R. Nelson, *Low-temperature behavior of two-dimensional quantum antiferromagnets*, Phys. Rev. Lett. **60**, 1057 (1988).

[48] S. Chakravarty, B. I. Halperin, and D. R. Nelson, *Two-dimensional quantum Heisenberg antiferromagnet at low temperatures*, Phys. Rev. B **39**, 2344 (1989).

[49] M. Greven, R. J. Birgeneau, Y. Endoh, M. A. Kastner, M. Matsuda, and G. Shirane, *Neutron scattering study of the two-dimensional spin $S = 1/2$ square-lattice Heisenberg antiferromagnet $Sr_2CuO_2Cl_2$*, Z. Phys. B **96**, 465 (1995).

[50] M. Greven, R. J. Birgeneau, Y. Endoh, M. A. Kastner, B. Keimer, M. Matsuda, G. Shirane, and T. R. Thurston, *Spin correlations in the 2D Heisenberg antiferromagnet $Sr_2CuO_2Cl_2$: Neutron scattering, Monte Carlo simulations and theory*, Phys. Rev. Lett. **72**, 1096 (1994).

[51] B. Keimer, N. Belk, R. J. Birgeneau, A. Cassanho, C. Y. Chen, M. Greven, M. A. Kastner, A. Aharony, Y. Endoh, R. W. Erwin, and G. Shirane, *Magnetic excitations in pure, lightly doped, and weakly metallic La_2CuO_4*, Phys. Rev. B **46**, 14034 (1992).

[52] R. J. Birgeneau, M. Greven, M. A. Kastner, Y. S. Lee, B. O. Wells, Y. Endoh, K. Yamada, and G. Shirane, *Instantaneous spin correlations in La_2CuO_4*, Phys. Rev. B **59**, 13788 (1999).

[53] H. M. Rønnow, D. F. McMorrow, and A. Harrison, *High-temperature magnetic correlations in the 2D S=1/2 antiferromagnet copper formate tetradeuterate*, Phys. Rev. Lett. **82**, 3152 (1999).

[54] G. Aeppli, S. M. Hayden, H. A. Mook, Z. Fisk, S.-W. Cheong, D. Rytz, J. P. Remeika, G. P. Espinosa, and A. S. Cooper, *Magnetic dynamics of La_2CuO_4 and $La_{2-x}Ba_xCuO_4$*, Phys. Rev. Lett. **62**, 2052 (1989).

[55] Y. J. Kim, A. Aharony, R. J. Birgeneau, F. C. Chou, O. Entin-Wohlman, R. W. Erwin, M. Greven, A. B. Harris, M. A. Kastner, I. Y. Korenblit, Y. S. Lee, and G. Shirane, *Ordering due to quantum fluctuations in $Sr_2Cu_3O_4Cl_2$*, Phys. Rev. Lett. **83**, 852 (1999).

[56] H. M. Rønnow, D. F. McMorrow, R. Coldea, A. Harrison, I. D. Youngson, T. G. Perring, G. Aeppli, O. F. Syljuåsen, K. Lefmann, and C. Rischel, *Spin dynamics of the 2D spin 1/2 quantum antiferromagnet copper deuteroformate tetradeuterate (CFTD)*, Phys. Rev. Lett. **87**, 037202 (2001).

[57] E. F. Shender, *Antiferromagnetic garnets with fluctuationally interacting sublattices*, Sov. Phys. JETP **56**, 178 (1982).

[58] J. Villain, *Order as an effect of disorder*, J. Phys. (Paris) **41**, 1263 (1980).

[59] S. J. Clarke, A. Harrison, T. E. Mason, and D. Visser, *Characterisation of spin-waves in copper(II) deuteroformate tetradeuterate: a square lattice $S = 1/2$ Heisenberg antiferromagnet*, Solid State Commun. **112**, 561 (1999).

[60] M. S. Seehra, *Two dimensional magnetic behavior of Copper Formate Tetrahydrate*, Physics Lett. A **28**, 754 (1969).

[61] R. B. Flippen and S. A. Friedberg, *Low-temperature magnetic susceptibility of some hydrated formates of Cu^{++} and Mn^{++}*, J. Chem. Phys. **38**, 2652 (1963).

[62] S. M. Hayden, G. Aeppli, H. A. Mook, S.-W. Cheong, and Z. Fisk, *Spin dynamics in the two-dimensional antiferromagnet La_2CuO_4*, Phys. Rev. B **42**, 10220 (1990).

[63] S. M. Hayden, G. Aeppli, R. Osborn, A. D. Taylor, T. G. Perring, S.-W. Cheong, and Z. Fisk, *High-energy spin waves in La_2CuO_4*, Phys. Rev. Lett. **67**, 3622 (1991).

[64] J. P. Goff, A. M. Toader, M. Roger, N. Shannon, S. M. Hayden, and J. R. Stewart, *Ring-exchange in high-temperature superconductors*, ILL annual report p. 22 (2003).

[65] M. R. Norman and C. Pépin, *The electronic nature of high temperature cuprate superconductors*, Rep. Prog. Phys **66**, 1547 (2003).

[66] M. S. Hybertsen, E. B. Strechel, M. Schluter, and D. R. Jennison, *Renormalization from density-functional theory to strong-coupling models for electronic states in Cu-O materials*, Phys. Rev. B **41**, 11068 (1990).

[67] A. Singh and P. Goswami, *Spin-wave spectrum in La_2CuO_4: Double occupancy and competing interaction effects*, Phys. Rev. B **66**, 092402 (2002).

[68] N. M. R. Peres and M. A. N. Araújo, *Spin-wave dispersion in La_2CuO_4*, Phys. Rev. B **65**, 132404 (2002).

[69] P. Sengupta, R. T. Scalettar, and R. R. P. Singh, *High-energy magnon dispersion in the half-filled Hubbard model: A comparison with La_2CuO_4*, Phys. Rev. B **66**, 144420 (2002).

[70] A. A. Katanin and A. P. Kampf, *Spin excitations in La_2CuO_4: Consistent description by inclusion of ring exchange*, Phys. Rev. B **66**, 100403 (2002).

[71] A. A. Katanin and A. P. Kampf, *Theoretical analysis of magnetic Raman scattering in La_2CuO_4: Two magnon intensity with the inclusion of ring exchange*, Phys. Rev. B **67**, 100404 (2002).

[72] R. Kiriyama, H. Ibamoto, and K. Matsuo, *The crystal structure of cupric formate tetrahydrate $Cu(HCO_2)_2\cdot 4H_2O$*, Acta Crystallogr. **7**, 482 (1954).

[73] K. Okada, M. I. Kay, D. T. Cromer, and I. Almodovar, *Crystal structure by neutron diffraction and the antiferroelectric phase transition in Copper Formate Tetrahydrate*, J. Chem. Phys. **44**, 1648 (1966).

[74] R. L. Martin and H. Waterman, *Magnetic properties of copper(II) salts. Part IV. Remarkable magnetic behaviour of copper(II) formate and its hydrates*, J. Chem Soc. 1359 (1959).

[75] H. Kobayashi and T. Haseda, *The magnetic properties of cupric formate tetrahydrate at low temperatures*, J. Phys. Soc. Jpn. **18**, 541 (1963).

[76] K. Yamagata and T. Sakai, *Magnetization process of nearly 2-dimensional $Cu(HCOO)_2\cdot 4H_2O$ and $Cu(HCOO)_2\cdot 2(NH_2)_2CO\cdot 2H_2O$. I Mechanism of field-induced transition*, J. Phys. Soc. Jpn. **49**, 2165 (1980).

[77] P. van der Leeden, P. A. van Dalen, and W. J. M. de Jonge, *Investigation of the magnetic state of $Cu(COOH)_2\cdot 4D_2O$ at* 4.2° *K by a proton resonance study*, Physica **33**, 202 (1967).

[78] M. S. Seehra, *New method for measuring the static magnetic susceptibility by paramagnetic resonance*, Rev. Sci. Instrum. **39**, 1044 (1968).

[79] K. Yamagata, Y. Kozuka, and T. Morita, *Magnetization process of nearly 2-dimensional $Cu(HCOO)_2\cdot 4H_2O$ and $Cu(HCOO)_2\cdot 2(NH_2)_2CO\cdot 2H_2O$. II Estimation of magnetic parameters*, J. Phys. Soc. Jpn. **50**, 421 (1981).

[80] N. Burger, H. Fuess, and P. Burlet, *Neutron diffraction study of the antiferromagnetic phase of Copper Formate Tetradeuterate*, Solid State Commun. **34**, 883 (1980).

[81] A. Dupas and J.-P. Renard, *Zero-point spin deviation and spontaneous sublattice magnetization in the two-dimensional antiferromagnet $Cu(HCOO)_2\cdot 4D_2O$*, Phys. Lett. A **33**, 470 (1970).

[82] T. G. Perring, *Tobyfit version 2.0. Least squares fitting to single crystal data at HET, MARI and MAPS* (Manual, 2000).

[83] O. F. Syljuåsen and P. A. Lee, *Anomalous spin excitation spectrum of the Heisenberg model in a magnetic field*, Phys. Rev. Lett. **88**, 207207 (2002).

[84] A. W. Sandvik, Personal communications (2003-2004).

[85] T. C. Hsu, *Spin waves in the flux-phase description of the $S = 1/2$ Heisenberg antiferromagnet*, Phys. Rev. B **41**, 11379 (1990).

[86] C.-M. Ho, V. N. Muthukumar, M. Ogata, and P. W. Anderson, *Nature of spin excitations in two-dimensional Mott insulators: Undoped cuptrates and Other Materials*, Phys. Rev. Lett. **86**, 1626 (2001).

[87] H. M. Rønnow, Personal communications (2003).

[88] I. Affleck and J. B. Marston, *Large-n limit of the Heisenberg-Hubbard model: Implications for high-T_c superconductors*, Phys. Rev. B **37**, 3774 (1988).

[89] D. A. Tennant, T. G. Perring, R. A. Cowley, and S. E. Nagler, *Unbound spinons in the $S = 1/2$ antiferromagnetic chain $KCuF_3$*, Phys. Rev. Lett. **70**, 4003 (1993).

[90] D. S. Rokhsar and S. A. Kivelson, *Superconductivity and the quantum hard-core dimer gas*, Phys. Rev. Lett. **61**, 2376 (1988).

[91] J. G. Bednorz and K. A. Müller, *Possible high T_c superconductivity in the Ba-La-Cu-O system*, Z. Phys. B **64**, 189 (1986).

[92] D. R. Squires and J. Tilley, *Superfluidity and superconductivity* (Institute of physics publishing, 1990).

[93] R. J. Cava, *Oxide superconductors*, J. Am. Ceram. Soc **83**, 5 (2000).

[94] E. W. Carlson, V. J. Emery, S. A. Kivelson, and D. Orgad, *Concepts in high temperature superconductivity*, cond-mat/0311058; Review chapter in 'The Physics of Superconductors. Vol II: Superconductivity in Nanostructures, High-T_c and Novel Superconductors, Organic Superconductors' edited by K. H. Bennemann and J. B. Ketterson (Springer-Verlag, 2004) .

[95] S. A. Kivelson, I. P. Bindloss, E. Fradkin, V. Oganesyan, J. M. Tranquada, A. Kapitulnik, and C. Howald, *How to detect fluctuating stripes in the high-temperature superconductors*, Rev. Mod. Phys. **75**, 1201 (2003).

[96] S. Sachdev, *Order and quantum phase transitions in the cuprate superconductors*, Rev. Mod. Phys **75**, 913 (2003).

[97] M. A. Kastner, R. J. Birgeneau, G. Shirane, and Y. Endoh, *Magnetic, transport, and optical properties of monolayer copper oxides*, Rev. Mod. Phys. **70**, 897 (1998).

[98] P. G. Radaelli, D. G. Hinks, A. W. Mitchell, B. A. Hunter, J. L. Wagner, B. Dabrowski, K. G. Vandervoort, H. K. Viswanathan, and J. D. Jorgensen, *Structural and superconducting properties of $La_{2-x}Sr_xCuO_4$ as a function of Sr content*, Phys. Rev. B **49**, 4163 (1994).

[99] C. Stock, W. J. L. Buyers, R. Liang, D. Peets, Z. Tun, D. Bonn, W. N. Hardy, and R. J. Birgeneau, *Dynamic stripes and resonance in the superconducting and normal phases of $YBa_2Cu_3O_{6.5}$ ortho-II superconductor*, Phys. Rev. B **69**, 014502 (2004).

[100] P. L. Gammel, D. J. Bishop, G. J. Dolan, J. R. Kwo, C. A. Murray, L. F. Schneemeyer, and J. V. Waszczak, *Observation of hexagonally correlated flux quanta in $YBa_2Cu_3O_7$*, Phys. Rev. Lett. **59**, 2592 (1987).

[101] S. E. Barrett, D. J. Durand, C. H. Pennington, C. P. Slichter, T. A. Friedmann, J. P. Rice, and D. M. Ginsberg, *^{63}Cu Knight shifts in the superconducting state of $YBa_2Cu_3O_{7-\delta}$ ($T_c = 90\,K$)*, Phys. Rev. B **41**, 6283 (1991).

[102] D. J. v. Harlingen, *Phase-sensitive tests of the symmetry of the pairing state in the high-temperature superconductors - Evidence for $d_{x^2-y^2}$ symmetry*, Rev. Mod. Phys. **67**, 515 (1995).

[103] D. J. Scalapino, *The case for $d_{x^2-y^2}$ pairing in the cuprate superconductors*, Physics Reports **250**, 329 (1995).

[104] A. Damascelli, Z. Hussain, and Z.-X. Shen, *Angle-resolved photoemission studies of the cuprate superconductors*, Rev. Mod. Phys. **473**, 2003 (75).

[105] J. L. Tallon, C. Bernhard, H. Shaked, R. L. Hitterman, and J. D. Jorgensen, *Generic superconducting phase behaviour in high-T_c cuprates: T_c variation with hole concentration in $YBa_2Cu_3O_{7-\delta}$*, Phys. Rev. B **51**, 12911 (1995).

[106] S. Martin, A. T. Fiory, R. M. Fleming, L. F. Schneemeyer, and J. V. Waszczak, *Normal-state transport properties of $Bi_{2+x}Sr_{2-y}CuO_{6\pm\delta}$ crystals*, Phys. Rev. B **41**, 846 (1990).

[107] S. Nakamae, K. Behnia, N. Mangkorntong, M. Nohara, H. Takagi, S. J. C. Yates, and N. E. Hussey, *Electronic ground state of heavily overdoped nonsuperconducting $La_{2-x}Sr_xCuO_4$*, Phys. Rev. B **68**, 100502 (2003).

[108] T. Ito, K. Takenaka, and S. Uchida, *Systematic deviation from T-linear behaviour in the in-plane resistivity of $YBa_2Cu_3O_{7-y}$: Evidence for dominant spin scattering*, Phys. Rev. Lett. **70**, 3995 (1993).

[109] M. R. Norman, H. Ding, M. Randeria, J. C. Campuzano, T. Yokoya, T. Takeuchi, T. Takahashi, T. Mochiku, K. Kadowaki, P. Guptasarma, and D. G. Hinks, *Destruction of the Fermi surface in underdoped high-T_c superconductors*, Nature **392**, 157 (1998).

[110] S. Sachdev, *Quantum phase transitions* (Cambridge University Press, 1999).

[111] Y. J. Uemura, *Condensation, excitation, pairing, and superfluid density in high-T_c superconductors: Magnetic resonance mode as a roton analogue and a possible spin-mediated pairing*, cond-mat/0406301 .

[112] N. D. Mathur, F. M. Grosche, S. R. Julian, I. R. Walker, D. M. Freye, R. K. W. Haselwimmer, and G. G. Lonzarich, *Magnetically mediated superconductivity in heavy fermion compounds*, Nature **394**, 39 (1998).

[113] J. L. Tallon, J. W. Loram, G. V. M. Williams, J. R. Cooper, I. R. Fisher, J. D. Johnson, M. P. Staines, and C. Bernhard, *Critical doping in overdoped High-T_c superconductors: a quantum critical point?*, Phys. Status Solidi B **215**, 531 (1999).

[114] G. Aeppli, T. E. Mason, S. M. Hayden, H. A. Mook, and J. Kulda, *Nearly singular magnetic fluctuations in the normal state of a high-T_c cuprate superconductor*, Science **278**, 1432 (1997).

[115] J. M. Tranquada, B. J. Sternlieb, J. D. Axe, Y. Nakamura, and S. Uchida, *Evidence for stripe correlations of spins and holes in copper oxide superconductors*, Nature **375**, 561 (1995).

[116] K. Yamada, C. H. Lee, K. Kurahashi, J. Wada, S. Wakimoto, S. Ueki, H. Kimura, Y. Endoh, S. Hosoya, G. Shirane, R. J. Birgeneau, M. Greven, M. A. Kastner, and Y. J. Kim, *Doping dependence of the spatially modulated dynamical spin correlations and the superconducting transition temperature in $La_{2-x}Sr_xCuO_4$*, Phys. Rev. B **57**, 6165 (1998).

[117] J. E. Hoffman, E. W. Hudson, K. M. Lang, V. Madhavan, H. Eisaki, S. Uchida, and J. C. Davis, *A four unit cell periodic pattern of quasiparticle states surrounding vortex cores in $Bi_2Sr_2CaCu_2O_{8+\delta}$*, Science **295**, 466 (2002).

[118] T. Hanaguri, C. Lupien, Y. Kohsaka, D.-H. Lee, M. Azuma, M. Takano, H. Takagi, and J. C. Davis, *A "checkerboard" electronic crystal state in lightly hole-doped $Ca_{2-x}Na_xCuO_2Cl_2$*, Nature **430**, 1001 (2004).

[119] S. H. Pan, J. P. O'Neal, R. L. Badzey, C. Chamon, H. Ding, J. R. Engelbrecht, Z. Wang, H. Eisaki, S. Uchida, A. K. Gupta, K.-W. Ng, E. W. Hudson, K. M. Lang, and J. C. Davis, *Microscopic electronic inhomogeneity in the high-T_c superconductor $Bi_2Sr_2CaCu_2O_{8+x}$*, Nature **413**, 282 (2001).

[120] K. M. Lang, V. Madhavan, J. E. Hoffman, E. W. Hudson, H. Eisaki, S. Uchida, and J. C. Davis, *Imaging the granular structure of high-T_c superconductivity in underdoped $Bi_2Sr_2CaCu_2O_{8+x}$*, Nature **414**, 412 (2002).

[121] B. Lake, G. Aeppli, K. N. Clausen, D. F. McMorrow, K. Lefmann, N. E. Hussey, N. Mangkorntong, M. Nohara, H. Takagi, T. E. Mason, and A. Schröder, *Spins in the vortices of a high-temperature superconductor*, Science **291**, 1759 (2001).

[122] B. Lake, H. M. Rønnow, N. B. Christensen, G. Aeppli, K. Lefmann, D. F. McMorrow, P. Vorderwisch, P. Smeibidl, N. Mangkorntong, T. Sasagawa, M. Nohara, H. Takagi, and T. E. Mason, *Antiferromagnetic order induced by an applied magnetic field in a high-temperature superconductor*, Nature **415**, 299 (2002).

[123] B. Khaykovich, Y. S. Lee, R. W. Erwin, S.-H. Lee, S. Wakimoto, K. J. Thomas, M. A. Kastner, and R. J. Birgeneau, *Enhancement of long-range magnetic order by magnetic field in in superconducting* $La_{2-x}Sr_xCuO_{4+y}$, Phys. Rev. B **66**, 014528 (2002).

[124] D. Vaknin, S. K. Sinha, D. E. Moncton, D. C. Johnston, J. M. Newsam, C. R. Safinya, and J. H. E. King, *Antiferromagnetism in* La_2CuO_{4-y}, Phys. Rev. Lett. **58**, 2802 (1987).

[125] S. Mitsuda, G. Shirane, S. K. Sinha, D. C. Johnston, M. S. Alvarez, D. Vaknin, and D. E. Moncton, *Confirmation of antiferromagnetism in* La_2CuO_{4-y} *with polarised neutrons*, Phys. Rev. B **36**, 822 (1987).

[126] G. Shirane, Y. Endoh, R. J. Birgeneau, M. A. Kastner, Y. Hidaka, M.Oda, M. Suzuki, and T. Murakami, *Two-dimensional antiferromagnetic quantum spin-fluid state in* La_2CuO_4, Phys. Rev. Lett. **59**, 1613 (1987).

[127] Y. Endoh, K. Yamada, R. J. Birgeneau, D. R. Gabbe, H. P. Jenssen, M. A. Kastner, C. J. Peters, P. J. Picone, T. R. Thurston, J. M. Tranquada, G. Shirane, Y. Hidaka, M. Oda, Y. Enomoto, M. Suzuki, and T. Murakami, *Static and dynamic spin correlations in pure and doped* La_2CuO_4, Phys. Rev. B **37**, 7443 (1988).

[128] R. J. Birgeneau, D. R. Gabbe, H. P. Jenssen, M. A. Kastner, P. J. Picone, T. R. Thurston, G. Shirane, Y. Endoh, M. Sato, K. Yamada, Y. Hidaka, M. Oda, Y. Enemoto, M. Suzuki, and T. Murakami, *Antiferromagnetic spin correlations in insulating, metallic and superconducting* $La_{2-x}Sr_xCuO_4$, Phys. Rev. B **38**, 6614 (1988).

[129] H. A. Mook, P. Dai, K. Salama, D. Lee, F. Doğan, G. Aeppli, A. T. Boothroyd, and M. E. Mostolloer, *Incommensurate one-dimensional fluctuations in* $YBa_2Cu_3O_{6.93}$, Phys. Rev. Lett. **77**, 370 (1996).

[130] H. F. Fong, P. Bourges, Y. Sidis, L. P. Regnault, J. Bossy, A. Ivanov, D. L. Milius, I. A. Aksay, and B. Keimer, *Spin susceptibility in underdoped* $YBa_2Cu_3O_{6+x}$, Phys. Rev. B **61**, 14773 (2000).

[131] G. Aeppli, S. M. Hayden, P. Dai, H. A. Mook, R. D. Hunt, T. G. Perring, and F. Doğan, *The weight of various features in the magnetic spectra of cuprates*, Phys. Status Solidi **215**, 519 (1999).

[132] J. M. Tranquada, G. Shirane, B. Keimer, S. Shamoto, and M. Sato, *Neutron scattering study of magnetic excitations in* YBa_2CuO_{6+x}, Phys. Rev. B **40**, 4503 (1989).

[133] S. Shamoto, M. Sato, J. M. Tranquada, B. J. Sternlieb, and G. Shirane, *Neutron-scattering study of antiferromagnetism in* $YBa_2Cu_3O_{6.15}$, Phys. Rev. B **48**, 13817 (1993).

[134] S. M. Hayden, G. Aeppli, T. G. Perring, H. A. Mook, and F. Doğan, *High-frequency spin waves in* $YBa_2Cu_3O_{6.15}$, Phys. Rev. B **54**, 6905 (1996).

[135] H. Yoshizawa, S. Mitsuda, H. Kitazawa, and K. Katsumata, *An incommensurate magnetic diffuse scattering in superconducting* $La_{1.92}Sr_{0.08}CuO_{4-\delta}$, J. Phys. Soc. Jpn. **57**, 3686 (1988).

[136] T. R. Thurston, R. J. Birgeneau, M. A. Kastner, N. W. Preyer, G. Shirane, Y. Fujii, K. Yamada, Y. Endoh, K. Kakurai, M. Matsuda, Y. Hidaka, and T. Murakami, *Neutron scattering study of the magnetic excitations in metallic and superconducting* $La_{2-x}Sr_xCuO_{4-y}$, Phys. Rev. B **40**, 4585 (1989).

[137] S.-W. Cheong, G. Aeppli, T. E. Mason, H. Mook, S. M. Hayden, P. C. Canfield, Z. Fisk, K. N. Klausen, and J. L. Martinez, *Incommensurate magnetic fluctuations in* $La_{2-x}Sr_xCuO_4$, Phys. Rev. Lett. **67**, 1791 (1991).

[138] M. Matsuda, M. Fujita, K. Yamada, R. J. Birgeneau, M. A. Kastner, H. Hiraka, Y. Endoh, S. Wakimoto, and G. Shirane, *Static and dynamic spin correlations in the spin-glass phase of slightly doped* $La_{2-x}Sr_xCuO_4$, Phys. Rev. B **62**, 9148 (2000).

[139] G. Shirane, R. J. Birgeneau, Y. Endoh, P. Gehring, M. A. Kastner, K. Kitazawa, H. Kojima, I. Tanaka, R. R. Thurston, and K. Yamada, *Temperature dependence of the magnetic excitations in* $La_{1.85}Sr_{0.15}CuO_4$ *(*$T_c = 33$ *K)*, Phys. Rev. Lett. **63**, 330 (1989).

[140] T. E. Mason, G. Aeppli, and H. A. Mook, *Magnetic dynamics of superconducting* $La_{1.86}Sr_{0.14}CuO_4$, Phys. Rev. Lett. **68**, 1414 (1992).

[141] T. R. Thurston, P. M. Gehring, G. Shirane, R. J. Birgeneau, M. A. Kastner, Y. Endoh, M. Matsuda, K. Yamada, H. Kojima, and I. Tanaka, *Low-energy incommensurate spin excitations in superconducting* $La_{1.85}Sr_{0.15}CuO_{4-y}$, Phys. Rev. B **46**, 9128 (1992).

[142] T. E. Mason, G. Aeppli, S. M. Hayden, A. P. Ramirez, and H. A. Mook, *Low energy excitations in superconducting* $La_{2-x}Sr_xCuO_4$, Phys. Rev. Lett. **71**, 919 (1993).

[143] K. Yamada, S. Wakimoto, G. Shirane, C. H. Lee, M. A. Kastner, S. Hosoya, M. Greven, Y. Endoh, and R. J. Birgeneau, *Direct observation of a magnetic gap in superconducting* $La_{1.85}Sr_{0.15}CuO_4$ *(*T_c*=37.3 K)*, Phys. Rev. Lett. **75**, 1626 (1995).

[144] B. Lake, G. Aeppli, T. E. Mason, A. Schröder, D. F. McMorrow, K. Lefmann, M. Isshiki, M. Nohara, H. Takagi, and S. M. Hayden, *Spin gap and magnetic coherence in a clean high-temperature superconductor*, Nature **400**, 43 (1999).

[145] D. Morr and D. Pines, *Magnetic coherence in cuprate superconductors*, Phys. Rev. B **61**, R6483 (2000).

[146] D. Morr and D. Pines, *Magnetic coherence as a universal feature of cuprate superconductors*, Phys. Rev. B **62**, 15177 (2000).

[147] R. Gilardi, S. Streule, A. Hiess, H. M. Rønnow, M. Oda, N. Momono, M. Ido, and J. Mesot, *Spin dynamics in the mixed phase of* $La_{2-x}Sr_xCuO_4$ *(*$x = 0.10$*,* $x = 0.17$*)*, Physica B **350**, 72 (2004).

[148] T. E. Mason, A. Schröder, G. Aeppli, H. A. Mook, and S. M. Hayden, *New magnetic coherence effect in superconducting* $La_{2-x}Sr_xCuO_4$, Phys. Rev. Lett. **77**, 1604 (1996).

[149] N. B. Christensen, D. F. McMorrow, H. M. Rønnow, B. Lake, S. M. Hayden, G. Aeppli, T. G. Perring, M. Mangkorntong, M. Nohara, and H. Takagi, *Dispersive excitations in the high-temperature superconductor* $La_{2-x}Sr_xCuO_4$, Phys. Rev. Lett. **93**, 147002 (2004).

[150] S. Petit, A. H. Moudden, B. Hennion, A. Vietkin, and A. Revcolevschi, *Spin dynamics study of* $La_{2-x}Sr_xCuO_4$ *by inelastic neutron scattering*, Physica B **234**, 800 (1997).

[151] J. M. Tranquada, H. Woo, T. G. Perring, H. Goka, G. D. Gu, G. Wu, M. Fujita, and K. Yamada, *Quantum magnetic excitations from stripes in copper oxide superconductors*, Nature **429**, 534 (2004).

[152] J. Zaanen and O. Gunnarsson, *Charged magnetic domain lines and the magnetism of high-*T_c *oxides*, Phys. Rev. B **40**, 7391 (1989).

[153] H. J. Schulz, *Incommensurate antiferromagnetism in the two-dimensional Hubbard model*, Phys. Rev. Lett. **64**, 1445 (1989).

[154] D. Poilblanc and T. M. Rice, *Charged solitons in the Hartree-Fock approximation to the large-U Hubbard model*, Phys. Rev. B **39**, 9749 (1989).

[155] Y. S. Lee, R. J. Birgeneau, M. A. Kastner, Y. Endoh, S. Wakimoto, K. Yamada, R. W. Erwin, S.-H. Lee, and G. Shirane, *Neutron-scattering study of spin-density wave order in the superconducting state of excess-oxygen doped* La_2CuO_{4+y}, Phys. Rev. B **60**, 3643 (1999).

[156] J. M. Tranquada, J. D. Axe, N. Ichikawa, A. R. Moodenbaugh, Y. Nakamura, and S. Uchida, *Coexistence of, and competition between, superconductivity and charge-stripe order in* $La_{1.6-x}Nd_{0.4}Sr_xCuO_4$, Phys. Rev. Lett. **78**, 338 (1997).

[157] M. v. Zimmermann, A. Vigliante, T. Niemöller, N. Ichikawa, T. Frello, J. Madsen, P. Wochner, S.Uchida, N. H. Andersen, J. M. Tranquada, D. Gibbs, and J. R. Schneider, *Hard X-ray diffraction study of charge stripe order in* $La_{1.48}Nd_{0.4}Sr_{0.12}CuO_4$, Europhysics Letters **41**, 629 (1998).

[158] J. M. Tranquada, J. D. Axe, N. Ichikawa, Y. Nakamura, S. Uchida, and B. Nachumi, *Neutron-scattering study of stripe-phase order of holes and spins in* $La_{1.48}Nd_{0.4}Sr_{0.12}CuO_4$, Phys. Rev. B **54**, 7489 (1996).

[159] O. Zachar, S. A. Kivelson, and V. J. Emery, *Landau theory of stripe phases in cuprates and nickelates*, Phys. Rev. B **57**, 1422 (1998).

[160] P. Bourges, Y. Sidis, M. Braden, K. Nakajima, and J. M. Tranquada, *High-energy spin dynamics in* $La_{1.69}Sr_{0.31}NiO_4$, Phys. Rev. Lett. **90**, 147202 (2003).

[161] A. T. Boothroyd, D. Prabhakaran, P. G. Freeman, S. J. S. Lister, M. Enderle, A. Heiss, and J. Kulda, *Spin dynamics in stripe-ordered* $La_{5/3}Sr_{1/3}NiO_4$, Phys. Rev. B **67**, 100407 (2003).

[162] T. Suzuki, T. Goto, K. Chiba, T. Shinoda, T. Fukase, H. Kimura, K. Yamada, M. Ohashi, and Y. Yamaguchi, *Observation of modulated magnetic long-range order in* $La_{1.88}Sr_{0.12}CuO_4$, Phys. Rev. B **57**, 3229 (1998).

[163] M. Fujita, H. Goka, K. Yamada, J. M. Tranquada, and L. P. Regnault, *Stripe order, depinning and fluctuations in* $La_{1.875}Ba_{0.125}CuO_4$ *and* $La_{1.875}Ba_{0.075}Sr_{0.05}CuO_4$, Phys. Rev. B **70**, 104517 (2004).

[164] S. Wakimoto, G. Shirane, Y. Endoh, K. Hirota, S. Ueki, K. Yamada, R. J. Birgeneau, M. A. Kastner, Y. S. Lee, P. M. Gehring, and S.-H. Lee, *Observation of incommensurate magnetic correlations at the lower critical concentration for superconductivity in* $La_{2-x}Sr_xCuO_4$ *(x=0.05)*, Phys. Rev. B **60**, 769 (1999).

[165] S. Wakimoto, R. J. Birgeneau, M. A. Kastner, Y. S. Lee, R. Erwin, P. M. Gehring, S. H. Lee, M. Fujita, K. Yamada, Y. Endoh, K. Hirota, and G. Shirane, *Direct observation of a one-dimensional static spin modulation in insulating* $La_{1.95}Sr_{0.05}CuO_4$, Phys. Rev. B **61**, 3699 (2000).

[166] M. Fujita, K. Yamada, H. Hiraka, P. M. Gehring, S.-H. Lee, S. Wakimoto, and G. Shirane, *Static magnetic correlations near the insulating-superconducting phase boundary in* $La_{2-x}Sr_xCuO_4$, Phys. Rev. B **65**, 064505 (2002).

[167] H. Matsushita, H. Kimura, M. Fujita, K. Yamada, K. Hirota, and Y. Endoh, *Sr concentration dependence of incommensurate elastic magnetic peaks in* $La_{2-x}Sr_xCuO_4$, J. Phys. Chem. Solids **60**, 1071 (1999).

[168] H. Kimura, K. Hirota, H. Matsushita, K. Yamada, Y. Endoh, S.-H. Lee, C. F. Majkrzak, R. Erwin, G. Shirane, M. Greven, Y. S. Lee, M. A. Kastner, and R. J. Birgeneau, *Neutron-scattering study of static antiferromagnetic correlations in* $La_{2-x}Sr_xCu_{1-y}Zn_yO_4$, Phys. Rev. B **59**, 6517 (1999).

[169] H. Kimura, H. Matsushita, K. Hirota, Y. Endoh, K. Yamada, G. Shirane, Y. S. Lee, M. A. Kastner, and R. J. Birgeneau, *Neutron scattering study of incommensurate elastic magnetic peaks in* $La_{1.88}Sr_{0.12}CuO_4$, J. Phys. Chem. Solids **60**, 1067 (1999).

[170] S. Wakimoto, H. Zhang, K. Yamada, I. Swainson, H. Kim, and R. J. Birgeneau, *Direct relation between the low-energy spin excitations and superconductivity of overdoped high-*T_c *superconductors*, Phys. Rev. Lett. **92**, 217004 (2004).

[171] S. Wakimoto, R. J. Birgeneau, Y. S. Lee, and G. Shirane, *Hole concentration dependence of the magnetic moment in superconducting and insulating* $La_{2-x}Sr_xCuO_4$, Phys. Rev. B **63**, 172501 (2001).

[172] M.-H. Julien, *Magnetic order and superconductivity in* $La_{2-x}Sr_xCuO_4$*: a review*, Physica B **329-333**, 693 (2003).

[173] D. P. Arovas, A. J. Berlinsky, C. Kallin, and S.-C. Zhang, *Superconducting vortex with antiferromagnetic core*, Phys. Rev. Lett. **79**, 2871 (1997).

[174] R. Gilardi, A. Hiess, N. Momono, M. Oda, M. Ido, and J. Mesot, *Unusual interplay between copper-spins and vortex dynamics in slightly overdoped* $La_{1.83}Sr_{0.17}CuO_4$, Europhysics Letters **66**, 840 (2004).

[175] J. M. Tranquada, C. H. Lee, K. Yamada, Y. S. Lee, L. P. Regnault, and H. M. Rønnow, *Evidence for an incommensurate magnetic resonance in* $La_{2-x}Sr_xCuO_4$, Phys. Rev. B **69**, 174507 (2004).

[176] B. Lake, H. M. Rønnow, N. B. Christensen, G. Aeppli, K. Lefmann, D. F. McMorrow, P. Vorderwisch, P. Smeibidl, N. Mangkorntong, T. Sasagawa, M. Nohara, H. Takagi, and T. E. Mason, *Antiferromagnetic vortex state in a high-temperature superconductor*, cond-mat/0104026 .

[177] E. Demler, S. Sachdev, and Y. Zhang, *Spin ordering quantum transitions of superconductors in a magnetic field*, Phys. Rev. Lett. **87**, 067202 (2001).

[178] G. S. Bobinger, Y. Ando, A. Passner, T. Kimura, M. Okuya, J. Shimoyama, K. Kishio, K. Tamasaku, N. Ichikawa, and S. Uchida, *Insulator-to-metal crossover in the normal state of* $La_{2-x}Sr_xCuO_4$ *near optimal doping*, Phys. Rev. Lett. **77**, 5417 (1996).

[179] B. Khaykovich, R. J. Birgeneau, F. C. Chou, R. W. Erwin, M. A. Kastner, S.-H. Lee, Y. S. Lee, P. Smeibidl, P. Vorderwisch, and S. Wakimoto, *Effect of a magnetic field on long-range magnetic order in stage-4 and stage-6 superconducting* La_2CuO_{4+y}, Phys. Rev. B **67**, 054501 (2003).

[180] B. O. Wells, Y. S. Lee, M. A. Kastner, R. J. Christianson, R. J. Birgeneau, K. Yamada, Y. Endoh, and G. Shirane, *Incommensurate spin fluctuations in high-transition temperature superconductors*, Science **277**, 1067 (1997).

[181] Y. S. Lee, F. C. Chou, A. Tewary, M. A. Kastner, S. H. Lee, and R. J. Bigeneau, *Neutron scattering study of the effects of dopant disorder on the superconductivity and magnetic order in stage-4* La_2CuO_{4+y}, Phys. Rev. B **69**, 020502 (2004).

[182] J. Rossat-Mignod, L. P. Regnault, C. Vettier, P. Bourges, P. Burlet, J. Bossy, J. Y. Henry, and G. Lapertot, *Neutron-scattering study of the* $YBa_2Cu_3O_{6+x}$ *System*, Physica C **185**, 86 (1991).

[183] P. Dai, H. A. Mook, R. D. Hunt, and F. Doğan, *Evolution of the resonance and incommensurate spin fluctuations in superconducting* $YBa_2Cu_3O_{6+x}$, Phys. Rev. B **63**, 054525 (2001).

[184] H. A. Mook, M. Yethiraj, G. Aeppli, T. E. Mason, and T. Armstrong, *Polarized neutron determination of the magnetic excitations in* $YBa_2Cu_3O_7$, Phys. Rev. Lett. **70**, 3490 (1993).

[185] H. F. Fong, B. Keimer, P. W. Anderson, D. Reznik, F. Doğan, and I. A. Aksay, *Phonon and magnetic neutron scattering at 41 meV in* $YBa_2Cu_3O_7$, Phys. Rev. Lett. **75**, 316 (1995).

[186] P. Dai, M. Yethiraj, H. A. Mook, T. B. Lindemer, and F. Doğan, *Magnetic dynamics in underdoped* $YBa_2Cu_3O_{7-x}$*: Direct observation of a superconducting gap*, Phys. Rev. Lett. **77**, 5425 (1996).

[187] H. F. Fong, B. Keimer, D. L. Milius, and I. A. Aksay, *Superconductivity-induced anomalies in the spin excitation spectra of underdoped* $YBa_2Cu_3O_{6+x}$, Phys. Rev. Lett. **78**, 713 (1997).

[188] P. Bourges, Y. Sidis, H. F. Fong, L. P. Regnault, J. Bossy, A. Ivanov, and B. Keimer, *Shifting of the magnetic-resonance peak to low energy in the superconducting state of underdoped* $YBa_2Cu_3O_{6.8}$, Europhys. Lett. **38**, 313 (1997).

[189] P. Dai, H. A. Mook, S. M. Hayden, G. Aeppli, T. G. Perring, R. D. Hunt, and F. Doğan, *The magnetic excitation spectrum and thermodynamics of high-T_c superconductors*, Science **284**, 1344 (1999).

[190] H.-Y. Kee, S. A. Kivelson, and G. Aeppli, *Spin-1 neutron resonance peak cannot account for electronic anomalies in the cuprate superconductors*, Phys. Rev. Lett. **88**, 257002 (2002).

[191] P. Dai, H. A. Mook, S. M. Hayden, G. Aeppli, and F. Doğan, *Resonance as a measure of pairing correlations in the high-T_c superconductor* $YBa_2Cu_3O_{6.6}$, Nature **406**, 965 (2000).

[192] S.-C. Zhang, *A unified theory based on SO(5) symmetry of superconductivity and antiferromagnetism*, Science **275**, 1089 (1997).

[193] E. Demler and S.-C. Zhang, *Quantitative test of a microscopic mechanism of high-temperature superconductivity*, Nature **396**, 733 (1998).

[194] H. F. Fong, P. Bourges, Y. Sidis, L. P. Regnault, A. Ivanov, G. D. Gu, N. Koshizuka, and B. Keimer, *Neutron scattering from magnetic excitations in* $Bi_2Sr_2CaCu_2O_{8+\delta}$, Nature **398**, 588 (1999).

[195] H. He, Y. Sidis, P. Bourges, G. D. Gu, A. Ivanov, N. Koshizuka, B. Liang, C. T. Lin, L. P. Regnault, E. Schoenherr, and B. Keimer, *Resonant spin excitation in an overdoped high temperature superconductor*, Phys. Rev. Lett. **86**, 1610 (2001).

[196] J. Mesot, N. Metoki, M. Böhm, A. Hiess, and K. Kadowaki, *The magnetic resonance in underdoped Bi2212 and its relation to the electronic spectra: an inelastic neutron scattering study*, Physica C **341-348**, 2105 (2000).

[197] H. He, P. Bourges, Y. Sidis, C. Ulrich, L. P. Regnault, S. Pailhès, N. S. Berzigiarova, N. N. Kolesnikov, and B. Keimer, *Magnetic resonant mode in the single-layer high-temperature superconductor* $Tl_2Ba_2CuO_{6+\delta}$, Science **295**, 1045 (2002).

[198] S. M. Hayden, G. Aeppli, P. Dai, H. A. Mook, T. G. Perring, S.-W. Cheong, Z. Fisk, F. Doğan, and T. E. Mason, *Absolute measurement of high-frequency magnetic dynamics in high-T_c superconductors*, Physica B **241-243**, 765 (1998).

[199] S. Pailhès, Y. Sidis, P. Bourges, V. Hinkov, A. Ivanov, C. Ulrich, L. P. Regnault, and B. Keimer, *Resonant magnetic excitations at high-energy in superconducting* $YBa_2Cu_3O_{6.85}$, Phys. Rev. Lett. **93**, 167001 (2004).

[200] P. Dai, H. A. Mook, and F. Doğan, *Incommensurate magnetic fluctuations in* $YBa_2Cu_3O_{6.6}$, Phys. Rev. Lett. **80**, 1738 (1998).

[201] H. A. Mook, P. Dai, S. M. Hayden, G. Aeppli, T. G. Perring, and F. Doğan, *Spin fluctuations in* $YBa_2Cu_3O_{6.6}$, Nature **395**, 580 (1998).

[202] M. Arai, T. Nishijima, Y. Endoh, T. Egami, S. Tajima, K. Tomimoto, Y. Shiohara, M. Takahashi, A. Garrett, and S. M. Bennington, *Incommensurate spin dynamics of underdoped superconductor* $YBa_2Cu_3O_{6.7}$, Phys. Rev. Lett. **83**, 608 (1999).

[203] P. Bourges, Y. Sidis, H. F. Fong, L. P. Regnault, J. Bossy, A. Ivanov, and B. Keimer, *The spin excitation spectrum in superconducting* $YBa_2Cu_3O_{6.85}$, Science **288**, 1234 (2000).

[204] H. M. Rønnow, L. P. Regnault, C. Ulrich, B. Keimer, M. Ohl, P. Bourges, and Y. Sidis, *Incommensurate antiferromagnetic fluctuations in superconducting* $YBa_2Cu_3O_{6.85}$, ILL annual report p. 18 (2000).

[205] H. A. Mook, P. Dai, and F. Doğan, *Charge and spin structure in* $YBa_2Cu_3O_{6.35}$, Phys. Rev. Lett. **88**, 097004 (2002).

[206] H. A. Mook, P. Dai, F. Doğan, and R. D. Hunt, *One-dimensional nature of the magnetic fluctuations in $YBa_2Cu_3O_{6.6}$*, Nature **404**, 729 (2000).

[207] S. M. Hayden, H. A. Mook, P. Dai, T. G. Perring, and F. Doğan, *The structure of the high-energy spin excitations in a high-transition-temperature superconductor*, Nature **429**, 531 (2004).

[208] C. Stock, W. J. L. Buyers, R. A. Cowley, P. S. Clegg, R. Coldea, C. D. Frost, R. Liang, D. Peets, D. Bonn, W. N. Hardy, and R. J. Birgeneau, *From dynamic stripes to spin-waves: The high-energy inelastic spectrum in superconducting $YBa_2Cu_3O_{6.5}$*, cond-mat/0408071 .

[209] V. Hinkov, S. Pailhès, P. Bourges, Y. Sidis, A. Ivanov, A. Kulakov, C. T. Lin, D. P. Chen, C. Bernhard, and B. Keimer, *Two-dimensional geometry of spin excitations in the high-transition-temperature superconductor $YBa_2Cu_3O_{6+x}$*, Nature **430**, 650 (2004).

[210] S. M. Hayden, G. Aeppli, H. A. Mook, T. G. Perring, T. E. Mason, S.-W. Cheong, and Z. Fisk, *Comparison of the high-frequency magnetic fluctuations in the insulating and superconducting $La_{2-x}Sr_xCuO_4$*, Phys. Rev. Lett. **76**, 1344 (1996).

[211] N. Bulut and D. J. Scalapino, *Weak-coupling analysis of the neutron-scattering spectral weight*, Phys. Rev. B **47**, 3419 (1993).

[212] M. R. Norman, *Relation of neutron incommensurability to electronic structure in high-temperature superconductors*, Phys. Rev. B **61**, 14751 (2000).

[213] D. Z. Liu, Y. Zha, and K. Levin, *Theory of neutron scattering in the normal and superconducting states of $YBa_2Cu_3O_{6+x}$*, Phys. Rev. Lett. **75**, 4130 (1995).

[214] M. R. Norman, *Magnetic collective mode dispersion in high-temperature superconductors*, Phys. Rev. B **63**, 092509 (2001).

[215] J. Brinckmann and P. A. Lee, *Slave boson approach to neutron scattering in $YBa_2Cu_3O_{6+y}$ superconductors*, Phys. Rev. Lett. **82**, 2915 (1999).

[216] F. Onufrieva and P. Pfeuty, *Spin dynamics of a two-dimensional metal in a superconducting state: Application to the high-T_c cuprates*, Phys. Rev. B **65**, 054515 (2002).

[217] Y.-J. Kao, Q. Si, and K. Levin, *Frequency evolution of neutron peaks below T_c: Commensurate and incommensurate structure in $La_{1.85}Sr_{0.15}CuO_4$ and $YBa_2Cu_3O_{6.6}$*, Phys. Rev. B **61**, 11898 (2000).

[218] A. A. Abrikosov, *Fine structure of the neutron maximum in high-temperature superconducting cuprates*, Phys. Rev. B **62**, 15156 (2000).

[219] C. D. Batista, G. Ortiz, and A. V. Balatsky, *Unified description of the resonance peak and incommensuration in high-T_c superconductors*, Phys. Rev. B **64**, 172508 (2001).

[220] F. Krüger and S. Scheidl, *Spin dynamics of stripes*, Phys. Rev. B **67**, 134512 (2003).

[221] E. W. Carlson, D. X. Yao, and D. K. Campbell, *Spin waves in striped phases*, Phys. Rev. B **70**, 064505 (2004).

[222] G. S. Uhrig, K. P. Schmidt, and M. Grüninger, *Unifying magnons and triplons in stripe-ordered cuprate superconductors*, cond-mat/0402659 .

[223] G. S. Uhrig, K. P. Schmidt, and M. Grüninger, *Magnetic excitations in the stripe phase of high-T_c superconductors*, cond-mat/0407648 .

[224] M. Vojta and T. Ulbricht, *Magnetic excitations in a bond-centered stripe phase: Spin waves far from the semiclassical limit*, Phys. Rev. Lett. **93**, 127002 (2004).

[225] G. Seibold and J. Lorenzana, *Magnetic fluctuations from stripes in cuprates*, cond-mat/0406589 .

[226] B. M. Andersen and P. Hedegård, *Spin dynamics in the stripe phase of the cuprates*, cond-mat/0411065 .

[227] M. Vojta and S. Sachdev, *Phenomenological lattice model for dynamic spin and charge fluctuations in the cuprates*, cond-mat/0408461 .

[228] B. Lake and coworkers, 2002-2003.

[229] T. Freltoft, G. Shirane, S. Mitsuda, J. P. Remeika, and A. S. Cooper, *Magnetic form factor of Cu in La_2CuO_4*, Phys. Rev. B **37**, 137 (1988).

[230] S. M. Hayden, R. Doubble, G. Aeppli, T. G. Perring, and E. Fawcett, *Strongly enhanced magnetic excitations near the quantum critical point of $Cr_{1-x}V_x$ and why strong exchange enhancement need not imply heavy fermion behaviour*, Phys. Rev. Lett. **84**, 999 (2000).

[231] S. L. Chaplot, W. Reichardt, L. Pintschovius, and N. Pyka, *Common interatomic potential model for the lattice dynamics of several cuprates*, Phys. Rev. B **52**, 7230 (1995).

[232] W. H. Press, S. A. Teukolsky, W. T. Vetterling, and B. P. Flannery, *Numerical recipes in Fortran 77, second edition* (Cambridge University Press, 1992).

[233] P. R. Bevington and K. R. Robinson, *Data reduction and error for the physical sciences, second edition* (McGraw-Hill Inc., 1992).

[234] B. Lake and coworkers, 1998-2000.

[235] J. E. Hoffman, K. McElroy, D.-H. Lee, K. M. Lang, H. Eisaki, S. Uchida, and J. C. Davis, *Imaging quasiparticle interference in $Bi_2Sr_2CaCu_2O_{8+\delta}$*, Science **297**, 1148 (2002).

[236] X. J. Zhou, T. Yoshida, S. A. Kellar, P. V. Bogdanov, E. D. Lu, A. Lanzara, M. Nakamura, T. Noda, T. Kakeshita, H. Eisaki, S. Uchida, A. Fujimori, Z. Hussain, and Z.-X. Shen, *Dual nature of the electronic structure of $(La_{2-x-y}Nd_ySr_x)CuO_4$ and $La_{1.85}Sr_{0.15}CuO_4$*, Phys. Rev. Lett. **86**, 5578 (2001).

[237] K. McElroy, R. W. Simmonds, J. E. Hoffman, D.-H. Lee, J. Orenstein, H. Eisaki, S. Uchida, and J. C. Davis, *Relating atomic-scale electronic phenomena to wave-like quasiparticle states in superconducting $Bi_2Sr_2CaCu_2O_{8+\delta}$*, Nature **422**, 592 (2003).

[238] K. McElroy, D.-H. Lee, J. E. Hoffman, K. M. Lang, E. W. Hudson, H. Eisaki, S. Uchida, J. Lee, and J. C. Davis, *Homogeneous nodal superconductivity coexisting with inhomogeneous charge order in strong underdoped $Bi_2Sr_2CaCu_2O_{8+\delta}$*, .

[239] M. Vershinin, S. Misra, S. Ono, Y. Abe, Y. Ando, and A. Yazdani, *Local ordering in the pseudogap state of the high-T_c superconductor $Bi_2Sr_2CaCu_2O_{8+\delta}$*, Science **303**, 1995 (2004).

[240] A. Abanov, A. V. Chubukov, M. Eschrig, M. R. Norman, and J. Schmalian, *Neutron Resonance in the Cuprates and its Effect on Fermionic Excitations*, Phys. Rev. Lett. **89**, 177002 (2002).

[241] B. Khaykovich, S. Wakimoto, R. J. Birgeneau, M. A. Kastner, Y. S. Lee, P. Smeibidl, P. Vorderwisch, and K. Yamada, *Field-induced transition between magnetically disordered and ordered phases of $La_{2-x}Sr_xCuO_4$*, cond-mat/0104026 .

[242] J. i. Igarashi and A. Watabe, *Dynamics of a two-dimensional Heisenberg antiferromagnet at zero temperature*, Phys. Rev. B **43**, 13456 (1991).

[243] J. v. Kranendonk and J. H. v. Vleck, *Spin waves*, Rev. Mod. Phys. **30**, 1 (1958).

[244] D. K. Morr, *Effect of next-nearest neighbor hopping on the spin dynamics in antiferromagnets*, Phys. Rev. B **58**, 587 (1998).

[245] D. A. Tennant, S. E. Nagler, D. Welz, G. Shirane, and K. Yamada, *Effects of coupling between chains on the magnetic excitation spectrum of $KCuF_3$*, Phys. Rev. B **52**, 13381 (1995).

[246] J. Jensen, Personal communications (2004).

[247] J. Jensen and A. R. Mackintosh, *Rare earth magnetism* (Oxford University Press, 1991).

[248] J. i. Igarashi, $1/S$ *expansion in a two-dimensional frustrated Heisenberg antiferromagnet*, J. Phys. Soc. Jpn. **62**, 4449 (1993).

[249] S. E. Nagler, D. A. Tennant, R. A. Cowley, T. G. Perring, and S. K. Satija, *Spin dynamics in the quantum antiferromagnetic chain compound* $KCuF_3$, Phys. Rev. B **44**, 12361 (1991).

[250] A. R. Wildes, *The polarizer-analyzer correction problem in neutron polarization analysis experiments*, Rev. Sci. Instrum. **70**, 4241 (1999).

List of papers

N. B. Christensen, H. M. Rønnow, D. F. McMorrow, A. Harrison, G. Aeppli, T. G. Perring, R. Coldea, L.P.Regnault, M. Enderle, *Quantum fluctuations in a simple two-dimensional antiferromagnet*, to be submitted to Physical Review Letters.

N. B. Christensen, D. F. McMorrow, H. M. Rønnow, B. Lake, S. M. Hayden, G. Aeppli, T. G. Perring, M. Mangkorntong, M. Nohara, H. Takagi, *Dispersive excitations in the high-temperature superconductor* $La_{2-x}Sr_xCuO_4$, Phys. Rev. Lett. **93**, 147002 (2004).

N. B. Christensen, D. F. McMorrow, H. M. Rønnow, A. Harrison, T. G. Perring, R. Coldea, *Deviations from linear spin wave theory in the 2D,* $S = 1/2$ *Heisenberg antiferromagnet CFTD*, J. Magn. Magn. Mater. **272-276**, 896 (2004).

K. Lefmann, B. Lake, G. Aeppli, S.-W. Cheong, N. B. Christensen, K. N. Klausen, S. Hayden, T. E. Mason, D. F. McMorrow, H. A. Mook, H. M. Rønnow, H. Takagi, *Static and dynamic spins in superconducting* $La_{2-x}Sr_xCuO_4$*: The Risø years*, J. Low Temp. Phys. **135**, 621 (2004).

B. Lake, G. Aeppli, N. B. Christensen, K. Lefmann, D. F. McMorrow, K. N. Clausen, H. M. Rønnow, P. Vorderwisch, P. Smeibidl, N. Mangkorntong, T. Sasagawa, M. Nohara, H. Takagi, N. E. Hussey *Effects of magnetic field on the cuprate high-*T_c *superconductor* $La_{2-x}Sr_xCuO_4$, Phys. Status. Solidi B **241** (6), 1223 (2004).

B. Lake, T. E. Mason, G. Aeppli, K. Lefmann, N. B. Christensen, D. F. McMorrow, K. N. Clausen, H. M. Rønnow, P. Vorderwisch, P. Smeibidl, N. Mangkorntong, N. E. Hussey, T. Sasagawa, M. Nohara, H. Takagi, A. Schrö der, *Vortex magnetism in the high-temperature superconductor* $La_{2-x}Sr_xCuO_4$, Int. J. Mod. Phys. B 16 **20-22**, 3155 (2002).

B. Lake, T. E. Mason, G. Aeppli, K. Lefmann, N. B. Christensen, D. F. McMorrow, K. N. Clausen, H. M. Rønnow, P. Vorderwisch, P. Smeibidl, N. Mangkorntong, N. E. Hussey, T. Sasagawa, M. Nohara, H. Takagi, A. Schrö der, *Field-induced antiferromagnetism in the high-temperature superconductor* $La_{2-x}Sr_xCuO_4$, Int. J. Mod. Phys. B 16 **20-22**, 3155 (2002).

B. Lake, H. M. Rønnow, N. B. Christensen, G. Aeppli, K. Lefmann, D. F. McMorrow, P. Vorderwisch, P. Smeibidl, N. Mangkorntong, T. Sasagawa, M. Nohara, H. Takagi, T. E. Mason, *Antiferromagnetic order induced by an applied magnetic field in a high-temperature superconductor*, Nature **415**, 299 (2002).

Bibliographic Data Sheet **Risø–PhD-7(EN)**

Title and author(s)

Neutron scattering studies of two-dimensional antiferromagnetic spin fluctuations in insulating and superconducting $S = 1/2$ systems

Niels Bech Christensen

ISBN

87–550–3407–1

ISSN

Dept. or group

Materials Research Department

Date

January 14, 2005

Groups own reg. number(s)

Project/contract No.

Sponsorship

Pages	Tables	Illustrations	References
191	1	72	250

Abstract (Max. 2000 char.)

Time-of-flight and polarized triple axis neutron scattering is used to probe the spin excitations of $Cu(DCOO)_2{\cdot}4D_2O$ and $La_{2-x}Sr_xCuO_4$.

The first part of the thesis contains an investigation of the excitation spectrum of the square lattice $S = 1/2$ Heisenberg antiferromagnet $Cu(DCOO)_2{\cdot}4D_2O$. Along the antiferromagnetic zone boundary a pronounced intensity variation is found for the dominant single-magnon excitations. This variation tracks an already known zone boundary dispersion. Using polarization analysis to separate the components of the excitation spectrum, a continuum of longitudinally polarized multimagnon excitations is discovered at energies above the single-magnon branch. At low energies, the findings are well described by linear spin wave theory. At high energies, linear spin wave theory fails and instead the data are very well accounted for by state-of-the-art Quantum Monte Carlo computations.

In the second part of the thesis, the spin excitation spectra of the high temperature superconductors $La_{1.90}Sr_{0.10}CuO_4$ and $La_{1.84}Sr_{0.16}CuO_4$ are characterized. The main discovery is that the excitations are dispersive at both doping levels. The dispersion strongly resembles that seen in other high-T_c superconductors. The presence of dispersive excitations does not require superconductivity to exist. For $La_{1.84}Sr_{0.16}CuO_4$, but not for $La_{1.90}Sr_{0.10}CuO_4$, the onset of superconductivity gives rise to a spectral weight shift which displays qualitative and quantitative similarities to the resonance mode observed in other high-T_c superconductors.

Descriptors

Neutron spectroscopy; Lanthanum compounds; Strontium compounds; Copper compounds; Antiferromagnetism; Superconductivity; Spin fluctuations; Quantum fluctuations; Low dimensionality

Available on request from:
Information Service Department, Risø National Laboratory
(Afdelingen for Informationsservice, Forskningscenter Risø)
P.O. Box 49, DK–4000 Roskilde, Denmark
Phone (+45) 46 77 46 77, ext. 4004/4005 · Fax (+45) 46 77 40 13
E-mail: risoe@risoe.dk

Mission

To promote an innovative and environmentally sustainable technological development within the areas of energy, industrial technology and bioproduction through research, innovation and advisory services.

Vision

Risø's research **shall extend the boundaries** for the understanding of nature's processes and interactions right down to the molecular nanoscale.

The results obtained shall **set new trends** for the development of sustainable technologies within the fields of energy, industrial technology and biotechnology.

The efforts made **shall benefit** Danish society and lead to the development of new multi-billion industries.